Transactions of the ASME®

Journal of Turbomachinery

Published Quarterly by The American Society of Mechanical Engineers

VOLUME 123 • NUMBER 1 • JANUARY 2001

TECHNICAL PAPERS

(Contents continued on inside back cover)

Editor, **T. H. OKIISHI (2003)**
Associate Editors
Gas Turbine (Review Chair)
R. NATOLE (2001)
Heat Transfer
R. BUNKER (2003)
Turbomachinery
R. ABHARI (2002)
R. DAVIS (2002)
C. KOCH (2002)
S. SJOLANDER (2002)

BOARD ON COMMUNICATIONS
Chairman and Vice-President
R. K. SHAH

OFFICERS OF THE ASME
President, **JOHN R. PARKER**

Executive Director, **D. L. BELDEN**

Treasurer, **J. A. MASON**

PUBLISHING STAFF
Managing Director, Engineering
CHARLES W. BEARDSLEY
Director, Technical Publishing
PHILIP DI VIETRO
Managing Editor, Technical Publishing
CYNTHIA B. CLARK
Managing Editor, Transactions
CORNELIA MONAHAN
Production Coordinator
VALERIE WINTERS
Production Assistant
MARISOL ANDINO

Transactions of the ASME, Journal of Turbomachinery (ISSN 0889-504X) is published quarterly (Jan., Apr., July, Oct.) by The American Society of Mechanical Engineers, Three Park Avenue, New York, NY 10016. Periodicals postage paid at New York, NY and additional mailing offices. POSTMASTER: Send address changes to Transactions of the ASME, Journal of Turbomachinery, c/o THE AMERICAN SOCIETY OF MECHANICAL ENGINEERS, 22 Law Drive, Box 2300, Fairfield, NJ 07007-2300.
CHANGES OF ADDRESS must be received at Society headquarters seven weeks before they are to be effective. Please send old label and new address.

STATEMENT from By-Laws. The Society shall not be responsible for statements or opinions advanced in papers or ... printed in its publications (B7.1, Par. 3).
COPYRIGHT © 2001 by the American Society of Mechanical Engineers. For authorization to photocopy material for internal or personal use under those circumstances not falling within the fair use provisions of the Copyright Act, contact the Copyright Clearance Center (CCC), 222 Rosewood Drive, Danvers, MA 01923, tel: 978-750-8400, www.copyright.com. Request for special permission or bulk copying should be addressed to Reprints/Permission Department.

INDEXED by Applied Mechanics Reviews and Engineering Information, Inc. Canadian Goods & Services Tax Registration #126148048

This journal is printed on acid-free paper, which exceeds the ANSI Z39.48-1992 specification for permanence of paper and library materials. ∞™
♲ 85% recycled content, including 10% post-consumer fibers.

Downloaded 01 Jun 2010 to 171.66.16.62. Redistribution subject to ASME license or copyright; see http://www.asme.org/terms/Terms_Use.cfm

(**Contents continued**)

Journal of Turbomachinery **Volume 123, Number 1** **JANUARY 2001**

ANNOUNCEMENT

The Influence of Transient Inlet Distortions on the Instability Inception of a Low-Pressure Compressor in a Turbofan Engine

Dirk C. Leinhos

Norbert R. Schmid

Leonhard Fottner

Institut für Strahlantriebe,
Universität der Bundeswehr München,
D-85577 Neubiberg, Germany

While studies on compressor flow instabilities under the presence of inlet distortions have been carried out with steady distortions in the past, the investigation presented here focuses on the influence of transient inlet distortions as generated by variable geometry engine intakes of super- and hypersonic aircraft on the characteristic and the nature of the instability inception of a LPC. The flow patterns (total pressure distortion with a superimposed co- or counterrotating swirl) of the distortions are adopted from a hypersonic concept aircraft. A LARZAC 04 twin-spool turbofan was operated with transient inlet distortions, generated by a moving delta wing, and steady total pressure distortions starting close to the LPC's stability limit until it stalled. High-frequency pressure signals are recorded at different engine power settings. Instabilities are investigated with regard to the inception process and the early detection of stall precursors for providing data for a future stability control device. It turned out that the transient distortion does not have an influence on the surge margin of the LPC compared to the steady distortion, but that it changes the nature of stall inception. The pressure traces are analyzed in the time and frequency domain and also with tools like Spatial FFT, Power Spectral Density, and Traveling Wave Energy. A Wavelet Transformation algorithm is applied as well. While in the case of clean inlet flow, the compressor exhibits different types of stall inception depending on the engine speed, stall is always initiated by spike-type disturbances under the presence of steady or transient distortions. Modal disturbances are present in the mid-speed range that do not grow into stall, but rather interact with the inlet flow and produce short length scale disturbances. The obtained early warning times prior to stall are adversely affected by transient distortions in some cases. The problem of appropriate thresholding becomes evident. The best warning times have been acquired using a statistical evaluation of the Wavelet coefficients, which might be promising to apply in a staged active control system. This system could include different phases of detection and actuation depending on the current precursor. [DOI: 10.1115/1.1330271]

Introduction

A reduction of the design surge margin of aeroengine compressors while maintaining sufficient engine dynamic and tolerance to inlet distortions is proposed to be one way of obtaining more efficient propulsion systems by either reducing the stage count or increasing the pressure ratio with the same number of stages. Since this requires a system that assures the aerodynamic stability of the compressor in all operating conditions, different schemes of active control systems have been proposed and tested for high-speed machines [1–4]. These systems rely on the early detection of incipient instabilities. Since engine accelerations and inlet distortions are the most important causes for a reduction of operating surge margin under real flight conditions, the influence of these effects on the instability inception has to be investigated. While recent studies on compressor instabilities during engine accelerations [5] and under the presence of inlet distortions [6–10] focused on steady distortions, the work presented in this paper was carried out using transient inlet distortions as generated by engine intakes of super- and hypersonic aircraft to evaluate their influence on the compressor characteristic and the stall inception process of the LPC of a twin-spool turbofan.

The flow patterns of the distortions exemplarily used in this study are adopted from the concept aircraft HTSM (Hypersonic Transport System Munich), which was designed in a German research program on hypersonic trans-atmospheric flight [11]. The HTSM was planned to be equipped with an air-breathing combined propulsion system for operation in turbo as well as in RAM mode. In the range from take-off to a flight Mach number of $M=2.8$ the transport system is powered by the turbo engines. Above this transition Mach number the RAM engines are active up to $M=6.8$. Turbo and RAM engines use the same intakes and nozzles, respectively. Figure 1 shows a cutaway of the proposed propulsion system with two Turbo-RAM combinations.

The extended flight envelope makes a variable intake geometry necessary in both the super- and subsonic sections. Inhomogeneous flow generated by the supersonic part of the intake may cause separation and thus the occurrence of additional secondary flow in the geometrically complex intake duct leading to nonsymmetric vortices and sectorial changes in total pressure and temperature. When adapting the intake to a different operating point, the moving ramp of the subsonic diffuser causes an unsteady secondary flow, resulting in a transient distortion mainly described by an increasing vortex that produces swirl at the LPC inlet. Also in the case of a malfunctioning ramp that moves into an extreme position one can think of similar consequences for the flow to the compressor.

Since the turbo engines of the HTSM have the same direction of rotation, but are installed off the centerline, the LPCs face the inlet conditions as mirror images, thus creating a corotating swirl

---

Contributed by the International Gas Turbine Institute and presented at the 45th International Gas Turbine and Aeroengine Congress and Exhibition, Munich, Germany, May 8–11, 2000. Manuscript received by the International Gas Turbine Institute February 2000. Paper No. 2000-GT-505. Review Chair: D. Ballal.

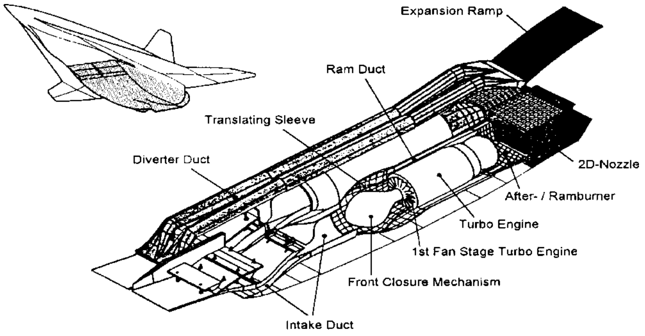

Fig. 1 Propulsion system of a hypersonic aircraft

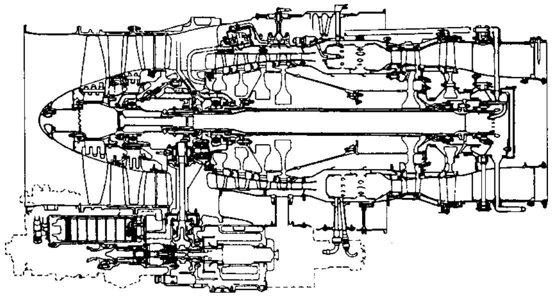

Fig. 3 LARZAC 04 C5 design point performance data

for those turbo engines installed on one side and counterrotating swirl for the others, respectively. In the following the corotating swirl will be referred to as CO case while the counterrotating swirl will be termed COUNTER case.

The test engine is subjected to transient inlet distortions generated by moving a nonsymmetric, half delta-wing with one edge parallel to the main flow and a huge winglet alongside the streamwise edge to prevent flow and a second vortex around this edge. It produces a single vortex through leading edge separation for AOA's above 6 deg. In order to generate additional sectorial total pressure deficits, two pieces of wire gauze are installed in the engine intake. The distortion generator is depicted in Fig. 2. Details of it and the influence of steady inlet distortions on the overall LPC and engine performance can be found in Schmid et al. [12].

Experimental Setup

Test Engine. The engine tests were carried out at the institute's ground test facility using the low-bypass twin-spool turbofan engine LARZAC 04 C5 (Fig. 3). It is designed with a two-stage, transonic LPC, a four-stage HPC, and single-stage HP and LP turbines. The core and bypass flow expand through separate nozzles, which allows an almost independent throttling of both compressors. In order to operate the LPC of the test engine away from its steady-state working line, it is throttled by continuously reducing the bypass nozzle area by radially moving in circle segments [13]. Important engine parameters are listed in Table 1.

Instrumentation and Data Acquisition. The test engine is equipped with two different types of instrumentation. A number of thermocouples as well as wall static pressure probes and total pressure probes, connected with standard pressure transducers, are installed throughout the engine. They represent the so-called low-frequency instrumentation. They enable calculating mass flows and a detailed gas path analysis for steady and transient operations. In addition, the spool speeds, the thrust, and the fuel flow are measured. An overview of the type and location of probes can be found in Schmid et al. [12] and Höss et al. [13]. The data correction and gas path analysis procedure for deriving compressor maps and running lines is described by Herpel and Fottner [14].

In addition to the conventional pressure probes, a number of high-frequency static wall and free-stream total pressure probes are installed at various positions throughout the LPC and the HPC (Fig. 4) in order to track pressure fluctuations during stall onset. Miniature piezo-resistive pressure transducers are incorporated into the front end of the probes, giving a minimum time lag and damping of the pressure signals when sampling. For the measurements presented in this paper five wall static pressure probes are installed 7 mm upstream of the first LPC rotor, equally spaced around the circumference at 332 deg (sensor 1), 44 deg (sensor 2), 116 deg (sensor 3), 188 deg (sensor 4), and 260 deg (sensor 5) (counting in the rotational direction of the rotor) for detecting spatial flow disturbances. The sensor positions relative to the flow pattern are presented in Fig. 5. With five sensors in one plane, spatial disturbances can be resolved up to the second harmonic. Other wall static pressure probes are located in the first LPC stator and one in front of the HPC (after the splitter casing) while a total pressure probe is situated at the LPC exit in front of the splitter casing. These probes allow conclusions about the axial extension of pressure fluctuations and the position at which they start. The axial positions of the sensors are shown in Fig. 4. Each of the eight signals from the pressure transducers is digitized with a sampling rate of 32.8 kHz and 13-bit resolution. Before being transferred to a storage device, it is filtered with a 12.8 kHz analog low pass filter. Details of the full high-frequency instrumentation are given in Höss et al. [13].

Table 1 LARZAC 04 C5 design point performance data

Thrust	13 kN
Turbine entry temperature	1403 K
Bypass ratio	1.13
Mass flow	27.64 kg/s
Π_{LPC} / Π_{HPC}	2.26 / 4.6
n_{LPC} / n_{HPC}	17500 RPM / 22561 RPM

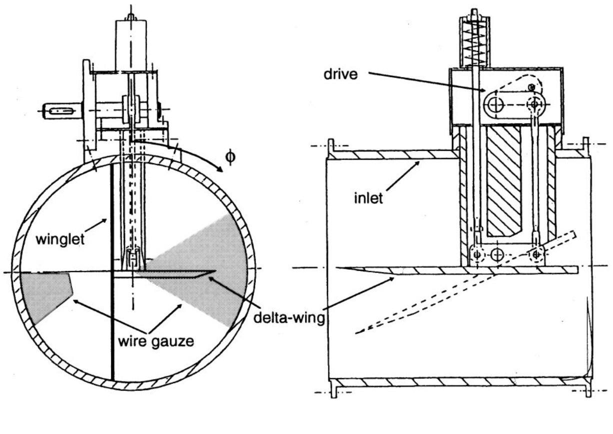

Fig. 2 Inlet distortion generator (CO configuration)

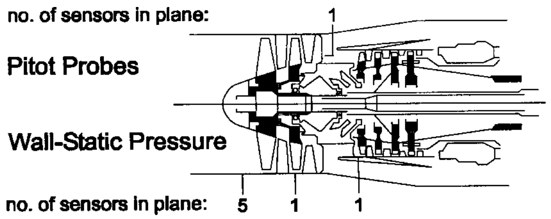

Fig. 4 Positions of miniature pressure probes

Table 2 Distortion parameters (delta-wing 20 deg AOA)

	CO distortion	COUNTER distortion
$DC(\varphi)_{max}$	0.50	0.50
$SC(\varphi)_{max}$	0.19	0.19

Inlet Distortions: Flow Pattern

The steady inlet distortion is generated by a nonsymmetric delta-wing under a high angle of attack and two pieces of wire gauze installed into the engine intake. The transient character of the distortion is achieved by changing the angle of attack of the delta-wing at a rate of roughly 1.5 deg/s, which is considered to be comparable to the pace at which real engine inlet geometries are adapted, thus increasing the single vortex. Two mirror image setups of the distortion generator were built to produce the CO and COUNTER flow patterns.

The maxima of the swirl ($SC\varphi$) and total pressure ($DC\varphi$) distortion coefficients, calculated within a sector of $\varphi_{\text{crit}} = 60$ deg in a plane one compressor radius upstream of the first stage using Eq. (1), for a fixed position of the delta-wing at 20 deg AOA are shown in Table 2.

$$DC(\varphi,x)|_{\varphi_{\text{crit}}} = \left| \frac{\overline{|p_t(x)-p_t(\varphi,x)|_{\max}}}{\overline{p_t(x)-p(x)}} \right|, \qquad SC(\varphi,x)|_{\varphi_{\text{crit}}} = \frac{\overline{|\nu_{\text{cross}}(\varphi,x)|_{\max}}}{\nu} \tag{1}$$

The flow patterns of the steady CO and COUNTER distortion relative to the sensor positions of the high-frequency instrumentation (viewed upstream) for $n_{\theta\,\text{LPC}}$=76 percent are shown in Fig. 5.

Relative cross-velocities (related to the axial velocity) indicating swirl are represented by vectors ($\nu_{\text{cross,rel}}$) while darker sectors show a higher total pressure deficit (local $pt(p_{t,\text{loc}})$ related to the momentum-averaged $p_t(p_{t,\text{mom}})$). Measurements were taken for steady and transient CO and COUNTER distortions at various engine speeds. While in the case of steady distortion the delta-wing was fixed at 20 deg AOA before the bypass throttle was closed continuously, the transient distortions were introduced to the LPC when it already operated stable close to its stability limit (because of previously closing the throttle) with the delta-wing starting at 0 deg AOA and then moving it until stall occurred (up to 22 deg AOA).

Analysis Methods

The signals from the high-frequency response sensors are subjected to different analyzing methods in order to give a full picture of the stall inception process. The data presented here are taken from the five wall static pressure probes at the LPC inlet only.

Temporal and Frequency Domain Techniques. The pressure signals are analyzed in the time domain using digital low- and bandpass FIR (Finite-Impulse-Response) filters. Single events like emerging spikes can be seen best in the time domain. They can also be tracked on their way around the annulus in order to identify sectors of damping or amplification. A Fast Fourier Transformation (FFT) is applied to each pressure trace while the set of five signals is subjected to a Spatial Fourier Transformation (SFT) as introduced by McDougall et al. [15] and Garnier et al. [16] for detecting dominant rotating spatial disturbances. The full spectrum of spatial disturbances is obtained by calculating the Power Spectral Density (PSD) of the spatial Fourier coefficients. Based on the PSD, Tryfonidis et al. [17] developed the concept of Traveling Wave Energy (TWE) as an indicator for the disturbance energy present in the flow. The PSD and TWE are also calculated for the recorded pressure signals.

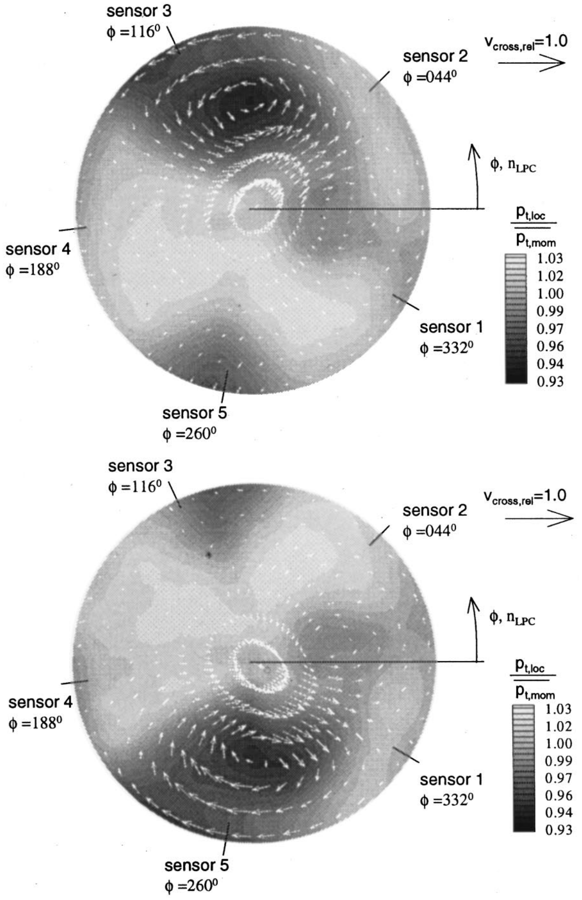

Fig. 5 Sensor position relative to the CO (top) and COUNTER (bottom) distortion (viewed upstream)

Wavelet Transformation. In addition to the Fourier-based analysis techniques, a Wavelet transformation (WT) is applied in order to improve the temporal resolution of single events. Because of its similarity to the footprint of a spike in the pressure signal of a wall static probe, the Daubechies wavelet as shown in Fig. 6

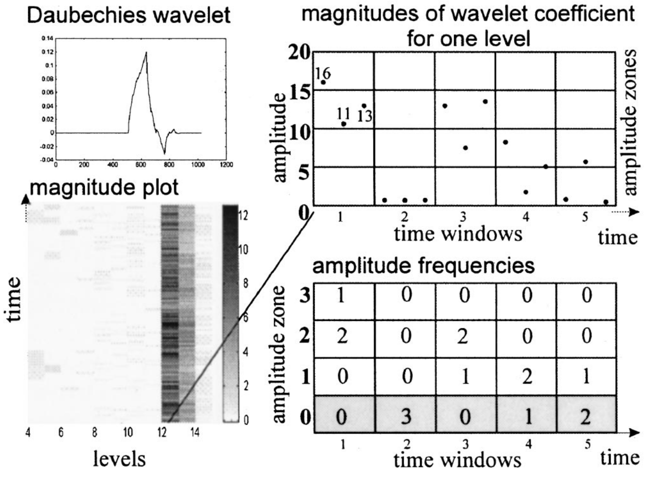

Fig. 6 Wavelet transformation and statistical evaluation

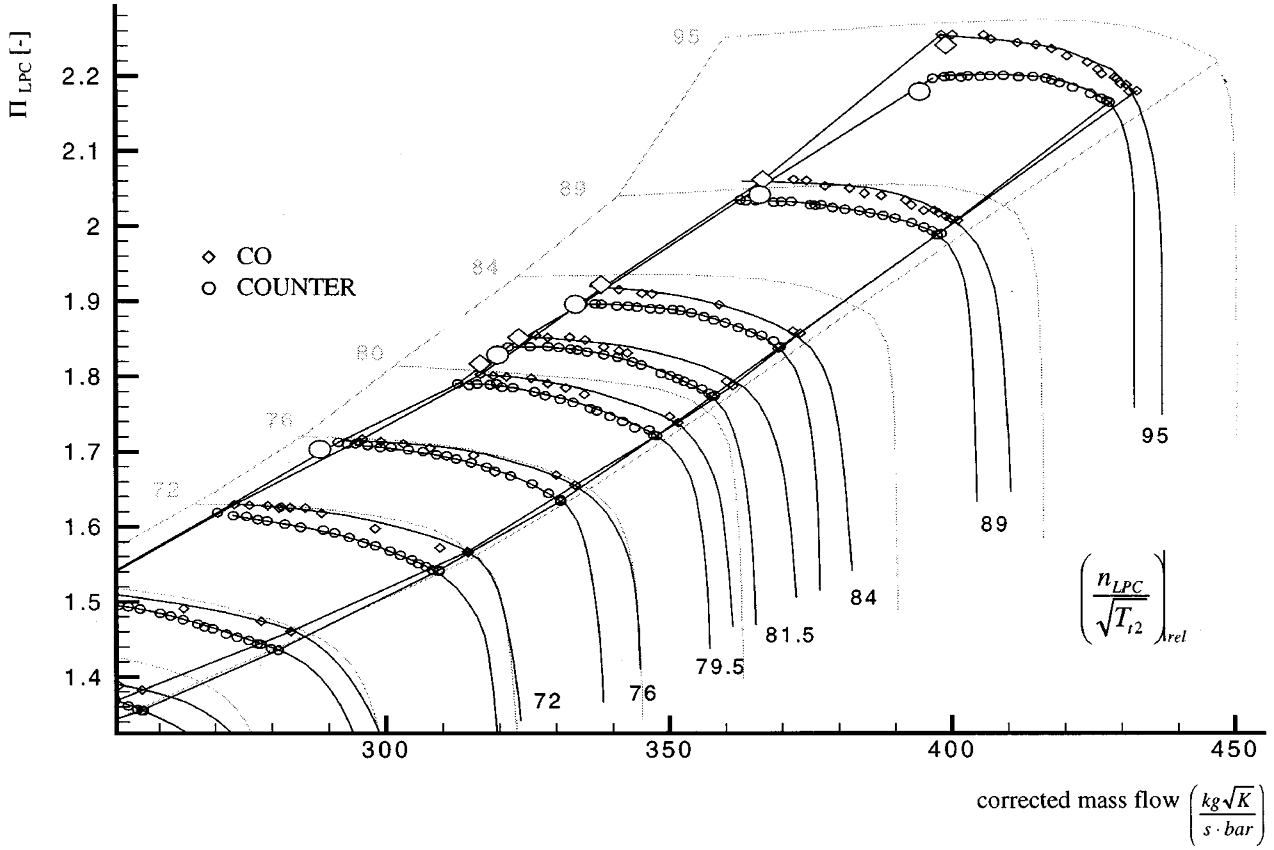

Fig. 7 Cutaway of the LPC compressor map

(upper left) is used. Details about the WT are given by Höss et al. [13]. Since a plot of the amplitudes of the wavelet coefficients (magnitude plot) as given in the lower left of Fig. 6 (e.g., levels 4 to 14 are shown in the lower left of Fig. 6; the darker the bars the higher the amplitude of the wavelet coefficient) alone does not allow an in-depth analysis of the stall inception process and does not improve the early warning time, Höss et al. [13] suggested a statistical evaluation of the magnitudes in order to obtain an integral indicator for compressor instability. The process for deriving this instability parameter for one level will be described in the following. For each level, which can be interpreted as a band of signal frequency, the amplitude range is divided into amplitude zones and the time range in time windows (upper right of Fig. 6). The wavelet coefficients whose amplitudes reside in each of the obtained boxes are counted, yielding the so-called amplitude frequency of occurrence. An amplitude frequency vector $\mathbf{f_a}$ is created by taking the values of all amplitude zones for a single time window. In order to reduce the influence of signal noise the frequency values for zone zero (gray shaded zone in the lower right of Fig. 6) are set to zero. In the example given in Fig. 6 this results in an amplitude frequency vector for the first time window of $\mathbf{f_{a1}} = [1\ 2\ 0\ 0]^t$ and for the second time window of $\mathbf{f_{a2}} = [0\ 0\ 0\ 0]^t$. The next step is to sum the components of the frequency vectors (e.g., $\mathbf{f_{a1}} = 3$). This value is then multiplied with the sum a_a of the amplitudes within one time window (e.g., $a_{a1} = 40$) yielding a frequency weighted value of the amplitudes of the wavelet coefficients wc_a (e.g., $wc_{a1} = 120$) for one level. This value is determined for every time window (a window length of 0.1s is used for the presented data) and plotted against time (see for instance Fig. 10). The result is similar as if summing all amplitudes within a time window but the presented method is less susceptible to single events. Subsequently the process is repeated for the other levels.

Since the levels of the WT are connected to signal frequencies by the equation $f = 2^{\text{Level}}$, levels 7 to 9 represent the LPC rotor frequency (depending on the spool speed) and levels 7 to 8 modal activities while spikes are best resolved by levels 11 to 13 (at the order of the blade frequency of the first rotor), which is identified as the relevant length scale for the creation of spikes. Höss et al. [13] showed that in the case of a clean inlet flow, the values for some levels started to rise for 0.5–1.5 s prior to stall, depending on the rotational speed, indicating the begin of the instability inception process regardless of the type of stall inception. In the case of steadily distorted flow, even longer early warning times were obtained [9]. In principle the WT can be used for online monitoring of compressor stability.

Experimental Results

LPC Measurements. The LPC map is presented in Fig. 7. The characteristics for clean inlet flow are shown in light gray, while the black map, numbers, and symbols represent the distorted inlet flow. The diamond symbols indicate the points of CO data, the circle symbols represent the COUNTER data. The lines of constant relative aerodynamic speeds are measured for stabilized condition from the nominal steady-state working line up to stall by closing the bypass throttle. Since it is not possible to de-throttle the compressor below the nominal working line, the speedlines have to be extrapolated in a reasonable way using energetic and efficiency considerations. The detailed description of the deterioration of the compressor map with steady distortions is given in Schmid et al. [12]. The larger, white-filled symbols near the surge lines represent the measured points of stall with transient inlet distortions. Since in the lower speed range the beginning of stall cannot be clearly identified while the engine is running, it

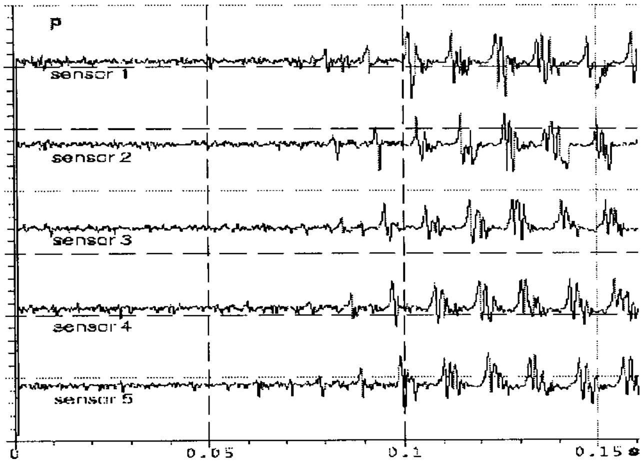

Fig. 8 Time series of static pressure, $n_{\theta \mathrm{LPC}}$=53 percent, CO, steady

was not possible to throttle the LPC to a stable point very close to the surge line and then initiate the instability by moving the delta-wing. Therefore, transient data are only available for speeds above $n_{\theta \mathrm{LPC}}=79.5$ percent in the CO and above $n_{\theta \mathrm{LPC}}=76$ percent in the COUNTER case. Some of these ''transient'' points do not coincide with the given speed lines because of slightly varying LPC speeds when the delta-wing is moving. With an increasing angle of attack, the delta-wing blocks the inlet, which decreases the mass flow through the LPC and the HPC, thus reducing the performance of the compressors which leads to lower pressure ratios. One can see that the ''transient'' points are located on the measured surge lines for steady distortions, CO, and COUNTER, respectively. Thus the surge margin decreases in the same way both for steady and transient distortions. Since the speed of the transient delta-wing is small compared to the rotor speed, the transient distortion seems to have steady character for the LPC and no significant difference compared to steady distortions occurs.

High Frequency-Measurements. As reported by Höss et al. [13], the type of stall inception in the LPC of the LARZAC 04 depends on the spool speed in the case of clean inlet flow. While in the low-speed range spikes triggered the instability and in the mid-speed range stall cells grew via modal waves, a disturbance rotating at rotor frequency initiated stall in the high-speed range. This disturbance is thought to be either a compressible mode of a modal wave or might come from rotor unbalancing. Under the presence of inlet distortions the behavior seems to be somewhat different. In the following the results of the transient inlet distortions will be discussed after addressing the stall inception with steady distortions generated with the same delta-wing (at 20 deg AOA) for each case.

CO (Steady). The pressure data from the five wall static pressure probes were intensely analyzed throughout the complete speed range. It then became clear that the stall inception behavior differs depending on the spool speed with respect to the geometric origin of the instability and the types of stall precursors present in the flow. The low-, mid-, and high-speed ranges revealed some differences. Representative speedlines for those were identified to be $n_{\theta \mathrm{LPC}}=53$, 79.5, and 95 percent. In the case of $n_{\theta \mathrm{LPC}}=53$ percent all analysis methods clearly showed a spike-type stall inception. Figure 8 depicts the time series of the wall static pressure sensor.

The critical spike is first detected at sensor 4, which is just outside the strong total pressure and swirl distortion as shown at the top of Fig. 5. There are also some spikes produced in the smaller pressure deficit with a small radial flow component close to sensor 5. Similar behavior has been observed in past studies [8,10] where it was concluded that short length scale disturbances are diminished when entering a distorted zone and grow again when leaving it. No continuously growing phase is found in either the FFT and SFT or in the PSD. The TWE yields an early warning time of 0.3s (45 rotor revolutions (revs)) and the instability parameter of the WT wc_a of 0.4 s for sensor 4 in level 11. Since sensor 4 is the most active location of spike production, this demonstrates the ability of the WT to resolve short length scale disturbances.

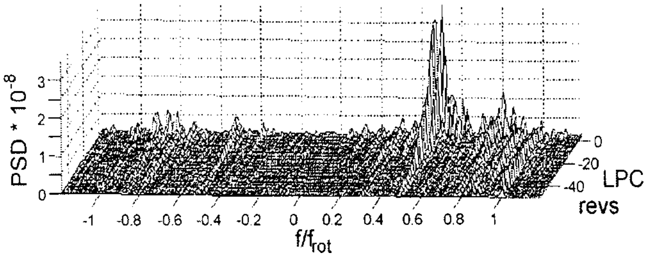

Fig. 9 PSD of SFT's second harmonic, $n_{\theta \mathrm{LPC}}$=79.5 percent, CO, steady

A different observation was made for $n_{\theta \mathrm{LPC}}=79.5$ percent where a rotating disturbance is present in the PSD of the second harmonic of the SFT (Fig. 9) at 50 percent f_{rot}. It grows for about 50 revs (0.22 s) prior to stall, whereas the TWE rises for 0.45 s. But in the time series and bandpass filtered signal no modal activity is visible. Rather, a spike emerges at sensor 1, which is located behind the smaller sector of total pressure deficit and where the cross-velocity component indicates a counterflow (Fig. 5). Also the second harmonic of the SFT does not grow smoothly into stall, although for some revolutions a constant phase speed of approximately 50 percent of f_{rot} can be detected. The statistical evaluation of the WT reveal levels 8, 9, and 11 rising at sensor 3. This might also indicate that there is long as well as short length scale disturbance activity. It gives a warning time of 0.5 s. One can therefore conclude that a modal wave is present but cannot claim for sure that it leads directly to the instability. It is more likely that the modal disturbance interacts with the distortion and produces spikes that finally trigger the stall. A similar observation is reported by Day et al. [6].

In the high-speed case ($n_{\theta \mathrm{LPC}}=95$ percent) again a typical spike-type stall inception was identified starting between sensors 3 and 4. Sensor 4 shows a great spike activity in the time series and the FFT, while no useful information can be obtained from the SFT and PSD, which shows just a noisy spectrum. But still the TWE of the first harmonic gives a warning time of 0.19 s (50 revs). The wc_a shows a significant increase for about 1 s (267 revs) at level 13 of sensors 2, 3, and 4, verifying the stalling via spikes. In Fig. 10 the wc_a (in arbitrary units) of level 13 at sensor 4 is plotted against time. The beginning of the instability is depicted at 2.66 s.

COUNTER (Steady). For the COUNTER case observations similar to the previous are made for the three speed ranges. However, it has to be pointed out that for $n_{\theta \mathrm{LPC}}=53$ percent, the warn-

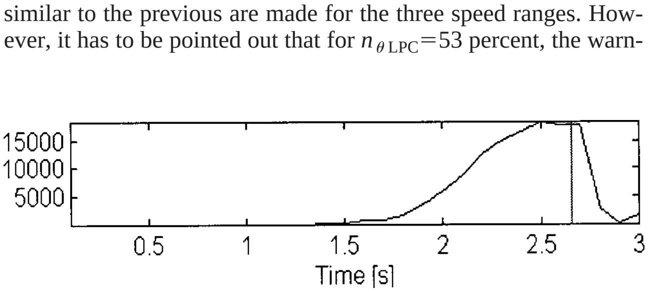

Fig. 10 The wc_a of level 13 at sensor 13 against time, $n_{\theta \mathrm{LPC}}$=95 percent, CO, steady

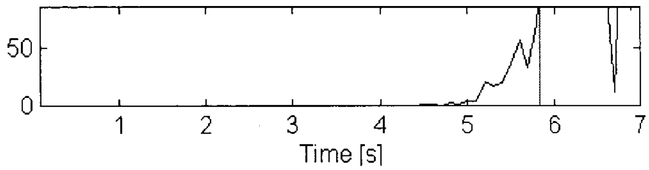

Fig. 11 The wc_a of level 11 at sensor 1 against time, $n_{\theta \mathrm{LPC}}$ =53 percent, COUNTER, steady

ing times obtained by the TWE decreased to 10 revs, whereas the wc_a of level 11 of sensor 1 indicates the increase of disturbances 0.75 s (115 revs) prior to stall as shown in Fig. 11. Looking at the flow pattern of the COUNTER distortion at the bottom of Fig. 5, one can see that sensor 1 is located at the exit of the sector of total pressure distortion with a rather large counterflow, which increases the relative flow angle onto the tip region of the blades, thus favoring the production of spikes.

For the mid-speed range ($n_{\theta \mathrm{LPC}}$=76 percent), some modal disturbances are found again in the PSD of the first harmonic rotating at 42 percent rotor speed. Since the stall cell runs around the annulus with f/f_{rot}=55 percent and level 11 rises for all sensors, it is likely that the modal disturbance does not grow smoothly into stall but rather promotes the development of spikes. The first harmonic of the SFT is shown in Fig. 12. There are sections of constant phase speed (between 40 and 50 percent of rotor speed) visible some revolutions before stall. The TWE gives an early warning time of 90 revs (0.4 s) and the wc_a of levels 7, 8, and 9 of sensor 4 (relatively calm region) for 220 revs (1 s).

The stall inception in the high-speed case is clearly driven by spikes. Neither the SFT nor the PSD indicate the existence of modal disturbances. The spectrum of the first harmonic is clearly dominated by the rotor frequency. The FFT shows that the signals from sensors 1 and 2 have the noisiest spectrum, where the critical spike is also found in the time plot. The TWE yields a 0.15 s (40 revs) warning time. The stability parameter of the WT increases for levels 11 to 13 for a couple of seconds prior to stall. Since this rise is quite peaky, it is difficult to define an exact warning time, which might be overcome by finding an appropriate threshold based on a larger data base. As an example, the wc_a of levels 11 (top) and 12 (bottom) at sensor 3 are depicted in Fig. 13.

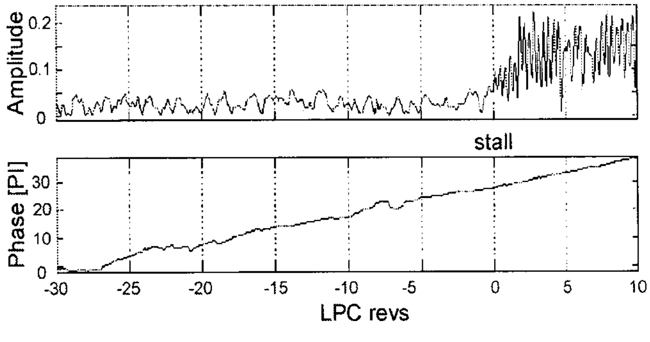

Fig. 12 SFT of first harmonic, $n_{\theta \mathrm{LPC}}$=76 percent, COUNTER, steady

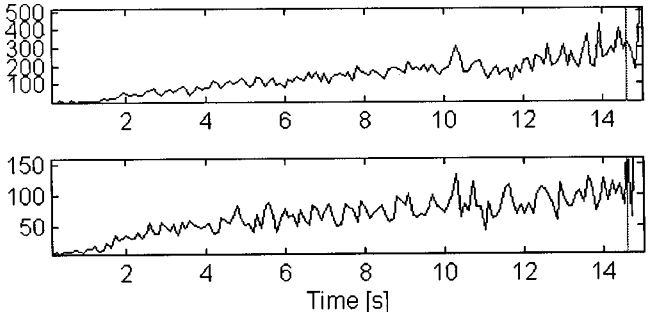

Fig. 13 The wc_a of level 11 (top) and 12 (bottom) at sensor 3 against time, $n_{\theta \mathrm{LPC}}$=95 percent, COUNTER, steady

CO (Transient). As mentioned above, data for transient inlet distortions could only be acquired in the mid and high-speed range. Therefore, the results will be reported for those two starting with the CO distortion. As in the steady case a disturbance rotating a f/f_{rot}=50 percent can be detected in the PSD of the second harmonic for almost the complete measuring time for $n_{\theta \mathrm{LPC}} = 80$ percent. Since the operating point when starting to move the delta-wing was already very close to the surge line, one can interpret this as a modal disturbance that is present because of the reduced damping of the system close to the stability limit. In Fig. 14 the differential PSD (DPSD), which is obtained by subtracting the negative part of the PSD-spectrum from the positive, shows the rise of this disturbance for as long as 1500 revs and also a strong increase just before stall. But one can also see that the rotating speed of the stall cell (at the back) is higher than $f/f_{\mathrm{rot}} = 50$ percent. This indicates that the instability does not grow smoothly out of the modal disturbance, which can be concluded as well from the time series and some activity in the upper level of the WT. It has also to be pointed out that it is somewhat peculiar that the speed of the mode is exactly 50 percent of the rotor speed in all the presented cases (though the spool speed is slightly varying), which is not true for clean inlet flow. Hence it might be suggested that the modal activity is amplified in interaction with the inlet distortion and thus an eigenfrequency of the compression system including the inlet flow condition. Since the TWE is already at rather high levels there is no real increase prior to stall leading to a mere 20 revs (0.09 s) warning time while the wc_a of level 7 at sensor 4 yields 90 revs (0.4 s).

The high-speed case is best represented by $n_{\theta \mathrm{LPC}}$=90 percent. Since the SFT reveals no constant phase speed and the PSD is very noisy, with only the rotor frequency being detectable in the first harmonic and levels 8-10 of the WT very active, it can be suggested that there is no modal disturbance and that stall is initiated by spikes. Similar to mid-speed the TWE wiggles around an almost constant level without any significant increase before stall, as shown in Fig. 15, where it is presented for the last 500 revs. The wc_a of levels 10 at sensor 4 exhibits a very noisy and un-

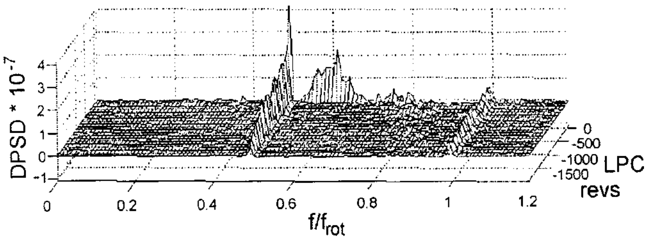

Fig. 14 DPSD of SFT's second harmonic, $n_{\theta \mathrm{LPC}}$=80 percent, CO, transient

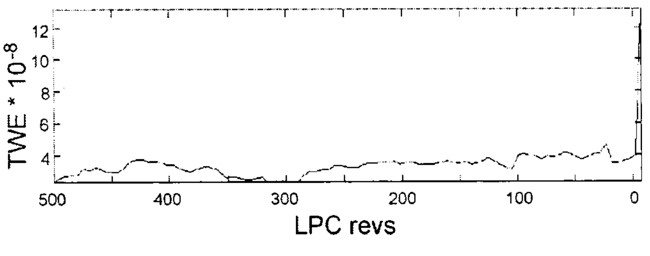

Fig. 15 TWE of SFT's first harmonic, $n_{\theta \mathrm{LPC}}$=95 percent, CO, transient

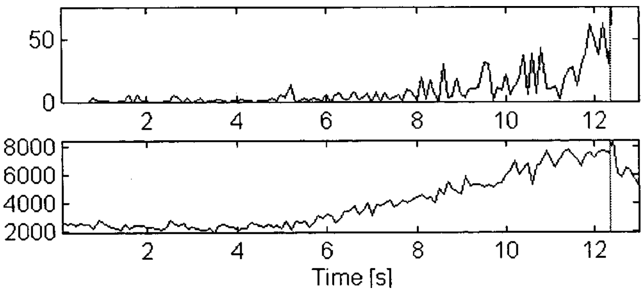

Fig. 16 The wc_a of level 9 (top) and 13 (bottom) at sensor 5 against time, $n_{\theta \mathrm{LPC}}$=80 percent, COUNTER, transient

steady rise (similar to steady CO) for some seconds, making it difficult to define a threshold. For a conservative thresholding (no decrease after that point in time) a warning time of around 0.15 s (40 revs) can be obtained.

COUNTER (Transient). Similar to the CO distortion, a second harmonic modal disturbance rotating at 50 percent of f_{rot} was found for $n_{\theta \mathrm{LPC}}$=76 percent in the COUNTER case. The same observations are made for the SFT and PSD, suggesting that the mode interacts with the inlet flow and produces spikes that eventually lead to the instability. As in the previous case, the TWE does not reveal any useful increase because it does not grow continuously but rather rises and falls over a longer period in time. The wc_a of levels 7 to 9 at sensor 1 and levels 7 to 13 at sensor 5 exhibit a noisy rise, which makes it hard to define a warning time. Assuming an appropriate thresholding, the wc_a of level 9 at sensor 5 (very active region) give 0.5 s (110 revs) as shown in Fig. 16 (top) while it increases for about 6 s at level 13. The sharp drop after the establishment of the stall cell indicates that the instabilities move to lower frequency bands.

Spikes in time series, the absence of a constant phase in the SFT, a very noisy PSD without any characteristic frequencies, and the high activity in the upper levels of the WT strongly suggest that spikes initiate stall in the high-speed case $n_{\theta \mathrm{LPC}}$=95 percent. In contrast with mid-speeds, the TWE gives, depending on the thresholding, a remarkable warning time of 50 revs (0.2 s) as shown in Fig. 17 where the TWE of the first harmonic is plotted for 2000 revs prior to stall. It is likely that the TWE can take advantage of a high number of spikes that emerge and survive for a short period. A peaky increase of the wc_a of levels 7 to 10 at sensor 2 and levels 9 to 10 at sensor 5 can be observed, suggesting that the size of the small length scale disturbances becomes bigger closer to stall and slowing them down. For a conservative thresholding the wc_a of level 8 at sensor 3 yields a warning time of 0.3 s (80 revs) while a strong increase in level 10 at sensor 2 can be detected 1 s (260 revs) prior to stall.

Summary and Conclusion

This study focuses on the problem of transient inlet distortion that might be encountered in actively controlled aeroengine compressors with reduced design surge margin. The stall inception process is analyzed and compared to the case of steady inlet distortions. The differences from previously obtained results for clean inlet flow are stated. While the operating range of the LPC, particularly the surge margin, is not adversely affected by the transient distortion, because of its relatively slow speed compared to the spool speeds, differences were found regarding the nature of stall precursor and hence the capability of methods for early detecting instabilities as they might be used in control devices. Methods based on the detection of spatial disturbances (PSD, TWE) did not give a useful warning time for CO and COUNTER transient distortions in the midspeed range (as opposed to the steady distortion) and only a short warning time (0.15 s) in the case of CO distortion in the high-speed range while a sufficient time (0.3 s) was obtained for the high-speed COUNTER distortion. Although the statistical evaluation of the WT gives longer warning times than the other methods in all cases, the problem of appropriate thresholding becomes evident. Nevertheless, employing a statistical wavelet analysis seems to be a promising approach for a future active stall control system, which could include different stages of detection and actuation depending on the current precursor.

While at low and high speeds spikes cause stall for steady and transient distortions (CO and COUNTER), it can be suggested by taking all analysis methods into account that modal disturbances are present in the midspeed range, but that they do not grow into rotating stall. Rather, they interact with the distortions favoring the development of spikes that eventually cause the instability.

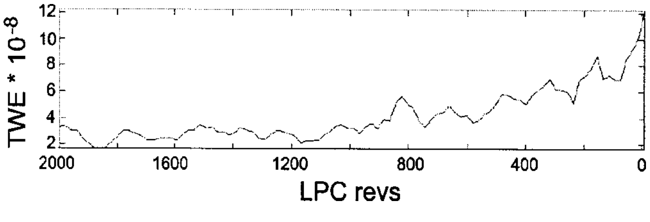

Fig. 17 TWE of SFT's first harmonic, $n_{\theta \mathrm{LPC}}$=95 percent, COUNTER, transient

Acknowledgments

This study was partly supported by the Deutsche Forschungs Gemeinschaft (DFG) as a project of the national research cooperation ''SFB 255'' of the TU München and the Universität der Bundeswehr München, which is gratefully acknowledged.

Nomenclature

T_t = total temperature, K
f = frequency, Hz
n = rotor speed
p, p_t = static pressure, total pressure, Pa
ν = free-stream velocity
Π = pressure ratio
$n_{\theta \mathrm{LPC}}$ = $(n_{\mathrm{LPC}}/\sqrt{T_{t\mathrm{LPC,inlet}}})_{\mathrm{relative}}$
wc_a = instability parameter of Wavelet transformation

Abbreviations

AOA = angle of attack
LPC = low-pressure compressor
HPC = high-pressure compressor
CO = corotating distortion
COUNTER = counterrotating distortion

References

[1] Freeman, C., Wilson, A., Day, I. J., and Swinbanks, M. A., 1998, ''Experiments in Active Control of Stall on an Aeroengine Gas Turbine,'' ASME J. Turbomach., **120**, pp. 637-647.
[2] Nelson, E. B., Paduano, J. D., and Epstein, A. H., 2000, ''Active Stabilization of Surge in an Axi-Centrifugal Turboshaft Engine,'' ASME J. Turbomach., **122**, pp. 485-493.
[3] Spakovszky, Z. S., Weigl, H. J., Paduano, J. D., van Schalkwyk, C. M., Suder, K. L., and Bright, M. M., 1999, ''Rotating Stall Control in a High-Speed Stage With Inlet Distortion: Part I – Radial Distortion,'' ASME J. Turbomach., **121**, pp. 510-516; ''Part II – Circumferential Distortion,'' ibid., pp. 517–524.
[4] Weigl, H. J., Paduano, J. D., Fréchette, A. G., Epstein, A. H., Greitzer, E. M., Bright, M. M., and Strazisar, A. J., 1998, ''Active Stabilization of Rotating Stall in a Transonic Single Stage Axial Compressor,'' ASME J. Turbomach., **120**, pp. 625-636.
[5] Höss, B., 1998, ''Zum Einfluß von Eintrittsstörungen auf das dynamische Leistungsverhalten von Turbostrahltriebwerken unter besonderer Berücksichtigung instabiler Verdichterstömungen,'' Dissertation, Universität der Bundeswehr München, Germany.
[6] Day, I. J., Breuer, T., Escuret, J., Cherrett, W., and Wilson, A., 1999, ''Stall Inception and the Prospects for Active Control in Four High Speed Compressors,'' ASME J. Turbomach., **121**, pp. 18-27.

[7] Hoying, D. A., 1993, ‘‘Stall Inception in a Multistage High Speed Axial Compressor,’’ Paper No. AIAA-93-2238.

[8] Jahnen, W., Peters, T., and Fottner, L., 1999, ‘‘Stall Inception in a 5-Stage HP-Compressor With Increased Load Due to Inlet Distortions,’’ ASME Paper No. 99-GT-440.

[9] Leinhos, D., Höss, B., and Fottner, L., 1998, ‘‘Rotating Stall Inception With Inlet Distortion in the Low Pressure Compressor of a Turbofan Engine,’’ *Proc. 19th AIMS Symposium*, Garmisch-Partenkirchen, Germany, May 4-7.

[10] Wilson, A. G., and Freeman, C., 1994, ‘‘Stall Inception and Development in an Axial Flow Aeroengine,’’ ASME J. Turbomach., **116**, pp. 217-225.

[11] Koelle, D. E., and Kuczera, H., 1990, ‘‘SÄNGER Space Transportation System–Progress Report 1990,’’ 41st IAF Congress, Dresden, Germany, Oct., IAF Paper No. 90-175.

[12] Schmid, N. R., Leinhos, D. C., and Fottner, L., 2000, ‘‘Steady Performance Measurements of a Turbofan Engine Under the Presence of Inlet Distortions With Co- and Counter-Rotating Swirl From the Intake Diffuser for Hypersonic Flight,’’ ASME Paper No. 2000-GT-11.

[13] Höss, B., Leinhos, D. C., and Fottner, L., 2000, ‘‘Stall Inception in the Compressor System of a Turbofan Engine,’’ ASME J. Turbomach., **122**, pp. 32-44.

[14] Herpel, Th., and Fottner, L., 1993, ‘‘A System for Monitoring, Measurement and Analysis of Transient Performance and Stall Phenomena of Gas Turbine Engines,’’ ICIASF ’93 Record, IEEE Publication 93CH3199-7.

[15] McDougall, N. M., Cumpsty, N. A., and Hynes, T. P., 1990, ‘‘Stall Inception in Axial Compressors,’’ ASME J. Turbomach., **112**, pp. 116-125.

[16] Garnier, V. H., Epstein, A. H., and Greitzer, E. M., 1991, ‘‘Rotating Waves as a Stall Inception Indication in Axial Compressors,’’ ASME J. Turbomach., **113**, pp. 290-302.

[17] Tryfonidis, M., Etchevers, O., Paduano, J. D., Epstein, A. H., and Hendricks, G. J., 1995, ‘‘Pre-Stall Behavior of Several High-Speed Compressors,’’ ASME J. Turbomach., **117**, No. 1, pp. 62-80.

Design and Test of a Semi-Passive Flow Control Device for Inlet Distortion Suppression

Link C. Jaw
Scientific Monitoring, Inc.,
Tempe, AZ 85259

William T. Cousins
Honeywell International,
Phoenix, AZ 85034

Dong N. Wu

David J. Bryg

Scientific Monitoring, Inc.,
Tempe, AZ 85259

Advanced turbine engines often operate with reduced stability margin to increase performance. Aircraft engine temperature and pressure inlet distortion have a major effect upon the stability of the compression system. Suppression of inlet distortion can provide a greater stability margin for the engine, thereby reducing operability restrictions on the engine by allowing closer operation to the stability limit. SMI has designed and tested a semi-passive distortion suppression system. The system uses flow injection to modify temperature and pressure inlet distortion. The prototype system was tested on a Honeywell T55 compressor rig. This paper presents both the design of the system and the test results. The test results show that this semi-passive distortion suppression system was able to reduce the surge margin degradation caused by the presence of pressure or temperature distortion. Special design considerations for this type of system are discussed, based upon the results of the prototype test. It is shown that distortion control can be a viable addition to the design of an aircraft engine. [DOI: 10.1115/1.1333091]

Introduction

Rotating stall and surge are two undesirable instabilities in gas turbine engines. Either instability can be initiated by poor inlet flow conditions in the engine. Nonuniform inlet conditions (known as distorted inlet conditions) can manifest themselves in either the temperature field, the pressure field, or both. Inlet distortion is caused by the design of the inlet itself, by the pitch and yaw angle of the aircraft, by the location of the engine inlets with respect to the airframe itself, or by the ingestion of wakes from other aircraft, or in the case of military aircraft, armaments.

Engines are designed to operate with a certain stability margin, that is, far enough from the stability limit of the compression system that surge or stall conditions will not be initiated. Quite often, advanced turbine engines operate with reduced stability margins to increase performance. However, there is a limit as to how much this stability margin can be reduced without jeopardizing the operability of the engine. Stability margin is reduced by many influences on the engine such as performing engine transients (thus raising the operating line), engine build tolerances, worn hardware, and inlet distortion. Generally, inlet distortion is a significant factor in the reduction of stability margin. Therefore, if the effect of inlet distortion on the engine can be reduced, the engine can operate closer to the stability limit, thus increasing performance without increasing the risk of compression system stability problems.

There are many ways that inlet distortion can be affected by external means. Since inlet distortion is either a maldistribution of flow (through a varying pressure field) or a maldistribution of temperature, affecting these by some external means is necessary to improve nonuniform inlet conditions. Suppression of inlet distortion can be considered either active or passive. Active suppression requires sensors, control computers, and actuators such as that presented by Jaw [1], and the systems of others [2,3]. Passive suppression, on the other hand, can be thought of as self-correcting flows due to the design of some sort of pressure equalizing system about the flowpath. Active suppression might be considered a more effective approach since it is a response to a measured nonuniformity in the flow, but it generally adds cost and weight to the engine. A compromise between active and passive suppressions is a passive, or hybrid, suppression system. A semi-passive system requires fewer actuators and sensors, because it provides most of the suppression effect through passive energy dissipation.

SMI has designed and tested a semi-passive distortion suppression system. The system, called the Distortion Suppression Plenum (DSP), is a plenum wrapped around the inlet duct of an engine. The DSP and the engine inlet duct are connected aerodynamically through a number of airflow passages. If the pressure inside the plenum is higher than the local static pressure of the air in the inlet duct, air will flow from the plenum to the inlet. On the other hand, if the local static pressure of the air in the inlet duct is higher than the plenum pressure, air will flow from the inlet to the plenum. This simple two-way flow exchange is the basic design parameter of the DSP. The pattern of the DSP flow passages can be varied to achieve the best result for a given operating condition.

If the pressure in the plenum is ‘‘controlled’’ to be slightly higher than the average pressure of the inlet duct, air will be forced into the flowpath, disrupting the distortion by adding momentum to the low-momentum air in the inlet. Increasing the momentum of inlet air in the low-momentum flowfield regions improves the nonuniformity of the inlet flow, thus reducing the degradation of stability margin by reducing the inlet distortion. Flow equalization between the plenum and the inlet can be expected to have a similar effect for temperature distortion, since the compression system stability (and the compressor map) is based upon corrected flow conditions.

The purpose of this paper is to report on both the design and on the test results of the Distortion Suppression Plenum designed by SMI.

Design of the DSP

The original idea for the DSP was to put flow injection holes on the plenum wall that separates the inlet duct and the external plenum. These holes are distributed equally about the circumfer-

---

Contributed by the International Gas Turbine Institute and presented at the 45th International Gas Turbine and Aeroengine Congress and Exhibition, Munich, Germany, May 8–11, 2000. Manuscript received by the International Gas Turbine Institute February 2000. Paper No. 2000-GT-45. Review Chair: D. Ballal.

ence of the duct. This circumferential pattern consists of 75 holes slanted 30 deg from the horizontal in the direction toward the engine face. Air injected through these holes imparts an axial momentum component to the inlet air based upon the difference in the static pressure field.

The tests with the DSP were conducted on a seven-stage Honeywell T55 compressor rig. To provide the greatest chance of success and to allow the easiest tracking of the inlet flow, the DSP was designed to affect the inlet flow with the T55 compression system running at 75 percent corrected speed. This was a speed of interest for several reasons. First, it is after the closure of the surge bleed in the engine cycle. Second, it is a speed at which engine surge behavior is still controlled by stalling of the front stages of the compression system, as discussed in the work by Cousins [4,5]. In addition, in the real engine environment, it is often at the lower speeds that many other destabilizing influences (such as the start of a rapid transient) combine with the effects of inlet distortion to provide a region of reduced stability margin. To assist in the determination of the proper hole size and flow injection angle, a computational fluid dynamic analysis was performed on the T55 compressor rig inlet duct. This analysis showed that by varying the amount of flow injected, the momentum increase achieved (and the effect of the injected jet) could reach all the way to the first-stage rotor or at lower flows, just affect the local flow in the inlet duct. This is an important consideration in the interpretation of the results that will be discussed later in this paper.

After further (CFD) simulations, interest developed in a second flow injection pattern. This was an axial hole pattern, consisting of longitudinally aligned holes slanted in the circumferential direction against the rotation of the compressor, providing a local counter-swirl component to the flow. The air injected through the axial-hole pattern forms a streamwise ''sheet'' of flow, intended to disrupt the distortion disturbance. These axial holes were also slanted 45 deg from the horizontal line. A total of five holes were drilled in the plenum wall in this pattern.

Figure 1 shows the DSP containing both the circumferential and the axial hole patterns. Figure 2 illustrates the flow directions of the injected air from the plenum to the inlet duct.

Fig. 1 The DSP showing the hole patterns

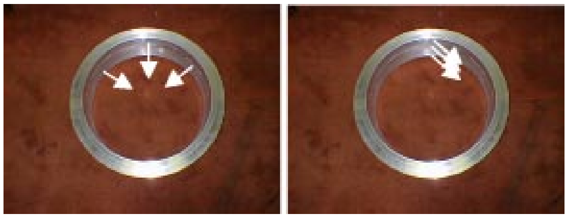

Fig. 2 Illustration of the designed flow patterns of the DSP

Test Setup and Results

Testing of the DSP was conducted on an Honeywell T55 compressor rig. The DSP formed a section of the inlet duct on the compressor rig. This section (with the DSP) was inserted in the inlet duct between two Marmon flanges as shown in Fig. 3. The DSP was also used as the base on which the SMI high-response air injection valve was mounted (Figs. 3 and 4). Three 0.625-in.-dia air supply lines were connected to the plenum to provide shop air to the part of the plenum encompassing the circumferential holes, as shown in Fig. 5. One additional line (of the same size) was connected to the part of the plenum encompassing the axial holes.

The compressor rig with the DSP installed is shown in Fig. 6. The airflow enters the rig from the left, through the annulus. A solid blockage plate is shown mounted on the distortion screen holder at the inlet during a calibration test.

The test plan was prepared to determine how much lost surge margin could be recovered using the DSP under both pressure and temperature distortion conditions at 75 percent compressor-corrected speed. Initially, pressure distortion was to be created by using a 90-deg extent distortion screen or the 90-deg blockage plate (shown installed in Fig. 6). A 90-deg temperature distortion was to be created by three specially designed upstream-facing flow-injection wands. These wands can be seen in Fig. 3 hanging into the flowpath directly behind the converging inlet and before the DSP. Using hot-air injection to form a temperature distortion pattern has been successful on other engine programs at Honeywell. In the case of the T55 compressor rig, a 90-deg distortion was chosen for several reasons. It was known from past tests that

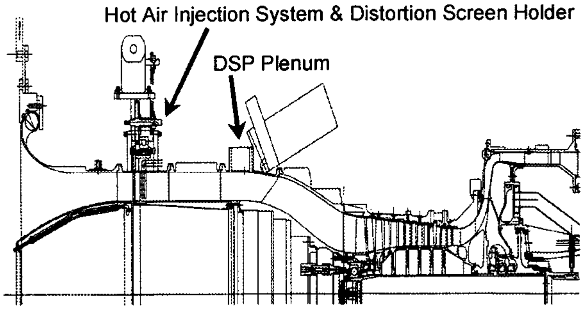

Fig. 3 T55 compressor rig layout

Fig. 4 Three-dimensional model of the DSP showing installation details

Fig. 5 Plenum airflow supply and distribution system

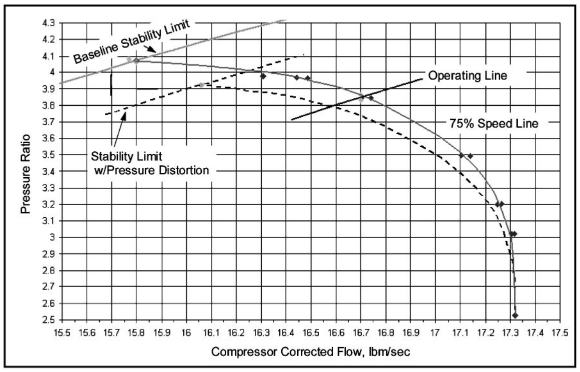

Fig. 7 Compressor map showing the baseline stability limit and the effect of pressure distortion

a 90-deg distortion pattern would produce an adequate change in the stability limit line of the compressor for this test series. In addition, since the T55 compressor rig contains four inlet struts, the 90-deg pattern was selected so the struts could be used to assist in the formation of the distortion profile. The struts produced a flow boundary that helped contain the injected air forming a cleaner pattern. Following flow-injection tests from the temperature distortion wands, it was found that the same level of pressure distortion could be produced by the injection of ambient air as that produced by the blockage plate. Producing pressure distortion in this manner reduced the test time and cost involved in changing out distortion screens and opening the rig inlet from the inlet suppression tank.

The test procedure involved three steps:

- identification of the compressor stability limit prior to any distortion application,
- identification of the stability limit after pressure and temperature distortion was introduced, and,
- identification of the new stability limit after the DSP started airflow injection into the inlet duct under both of the injection schemes (circumferential and axial).

First, the baseline stability limit (surge point) was determined at 75 percent compressor-corrected speed, as shown in Fig. 7. The slope of the limit line was drawn by obtaining the surge point at both 65 and 80 percent corrected compressor speed. The operating line used throughout the test series is also shown in the figure, and represents the engine operating line. This line is necessary to calculate constant speed surge margin. For a compressor rig test, the operating line can be set anywhere using the rig discharge plenum valve. Therefore, the results presented here for changes in the stability margin of the compressor are due only to the changes in the stability limit line, not changes that might occur to the operating line, since those cannot be determined by the rig test.

Also shown in Fig. 7 is the effect of the application of pressure distortion. For the distortion applied (which was approximately 5 percent circumferential distortion, $\Delta Pc/P$), the stability margin (or constant speed surge margin) was reduced 5.3 percent (from 11.7 percent to 6.4 percent).

The first set of tests investigated surge margin recovery by using the circumferential injection only. Three different injection flow rates were tested. The results showed that the circumferential hole pattern was able to affect the distorted inlet so that some of the stability margin was recovered; however, the amount of recovery was not linear with flow rate. The largest recovery (from 6.4 to 9.0 percent surge margin) was achieved using the DSP with the circumferential holes activated at a flow rate of 1.0 lbm/s, thereby gaining 2.6 percent surge margin. When the circumferential holes were activated at flow injection rates of both 1.6 lbm/s and 0.5 lbm/s, the recovered surge margin was not as great, as shown in Fig. 8.

The second set of tests investigated the effect of surge margin recovery by using axial injection. This series of tests used flow rates of 0.2 lbm/s, 0.3 lbm/s, and 0.4 lbm/s. Some stability margin was recovered in all cases as shown in Fig. 9, but the largest recovery resulted from the lowest flow rate. The surge margin

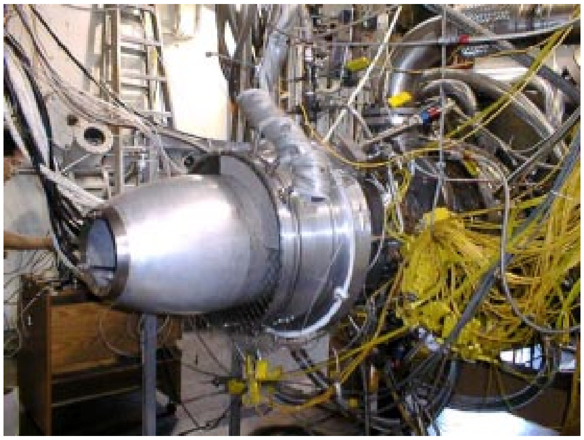

Fig. 6 Compressor rig showing the DSP installed

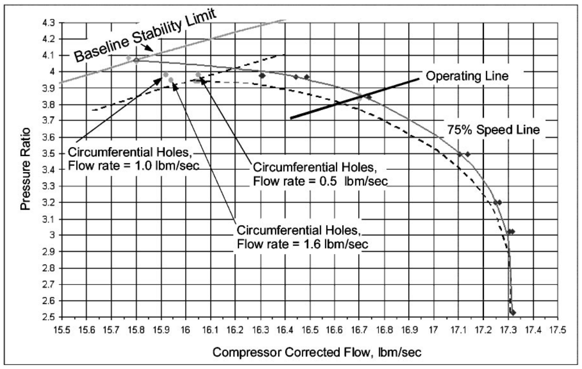

Fig. 8 Compressor map showing the surge margin recovery achieved using the circumferential holes in the DSP with pressure distortion

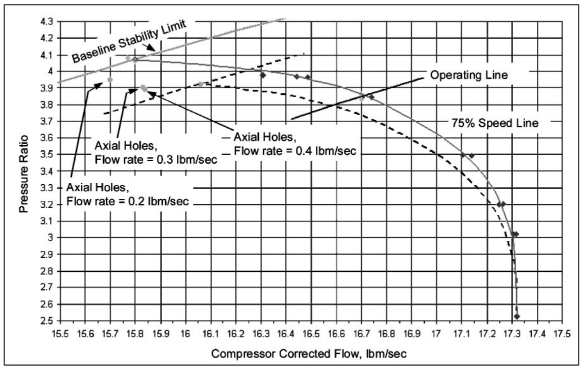

Fig. 9 Compressor map showing the surge margin recovery achieved using the axial holes in the DSP with pressure distortion

with the 0.2 lbm/s blowing was 9.7 percent, a 3.3 percent improvement in surge margin over the pressure distortion case without blowing.

Following the pressure distortion tests, examination of the effects of the DSP on temperature distortion proceeded. As mentioned previously, the generation of temperature distortion also generates pressure distortion due to the injection of air in the upstream direction from the hot air wands. Previous temperature distortion testing at Honeywell on other compression systems showed that the air must be injected in the upstream direction to achieve adequate mixing of the temperature distortion field. In some cases, the tests have been performed using screens in the undistorted temperature sector of the inlet to create the same pressure loss as the injected hot air, thus effectively eliminating the pressure distortion during the temperature distortion testing. Due to program timing and costs, this procedure was not used in this test series. Rather, determination of the effect of pressure distortion with ambient air at the same flow rate as used in the temperature distortion hot air injection was performed. Therefore, the goal for the DSP system was to get back to the stability limit line produced by pressure distortion alone. The baseline test with temperature distortion (approximately 4 percent circumferential distortion, $\Delta Tc/T$, which per the previous discussion, includes pressure distortion) produced a reduction in surge margin of 10.5 percent with 5.5 percent being due to the pressure distortion, as shown in Fig. 10.

Under both the temperature and the pressure distortion conditions, the circumferential injection recovered only a small amount of the lost surge margin. With 1.6 lbm/s flow rate through the circumferential holes, the surge margin recovered was only about 2 percent. Decreasing the flow rate caused this to get worse, as shown in Fig. 11.

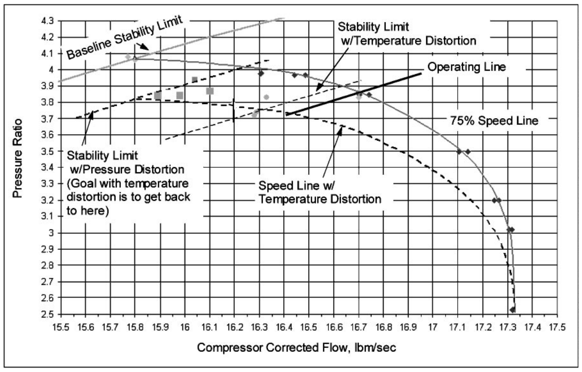

Fig. 10 Effect of temperature distortion generated by hot air injection on compression system stability

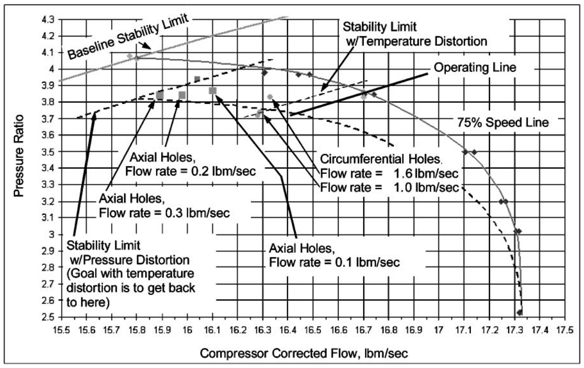

Fig. 11 Compressor map showing the surge margin recovery achieved using axial and circumferential holes in the DSP with temperature (and pressure) distortion

The most encouraging results for temperature and pressure distortion were achieved with the axial hole configuration. Flow rates of 0.1 lbm/s, 0.2 lbm/s, and 0.3 lbm/s were tested and the resultant surge margin recoveries were 3.3, 4.2, and 4.8 percent, respectively. For these flows, the actual surge margin values were 4.5, 5.4, and 5.7 percent, respectively. This recovery of the stability limit is shown in Fig. 11.

Discussion

Tests of the DSP indicated that blowing air in the axial and circumferential directions into the inlet of a compression system could have an effect on the stability margin of the compression system by improving the inlet distortion pattern.

Examination of the previously presented data shows that the axial flow injection was the most successful. Both the axial and the circumferential air injection affected the stability limit of the compressor in rather interesting ways.

The circumferential air injection showed the greatest recovery of stability margin at 1.0 lbm/s, while at both 1.6 lbm/s and at 0.5 lbm/s the recovery was less. One might be led to believe that there is a problem with the data, but careful examination of the physics associated with the flow injection and the impact of the injection on the first rotor of the compressor would indicate otherwise. The flow is injected into the flowpath at an angle of 30 deg from the axial direction. At the higher flow rates, the initial CFD work showed that the jet effect of the injected air could impact the tip of the first rotor. This being the case, it is expected that at the highest flow rate (1.6 lbm/s), the jet is causing a radial distortion at the first rotor which starts to cost stability margin.

In the case of the axial air injection, the air is injected toward the compressor face at an angle of 45 deg from a line tangent to the flow path wall. This imparts a flow vector that is opposite the direction of rotation of the rotor, therefore causing counterswirl to the first rotor. Counterswirl causes an increase in the incidence angle (and therefore loading) of the first stage of the compression system. Since the first stage is the stall trigger that initiates surge behavior at 75 percent corrected speed, it is not unexpected that there would be a loss in stability margin as the injected flow rate is increased, since it is imparting a greater and greater amount of counterswirl to the compression system. This is observed in the pressure distortion data where, as the injected air flow rate increased from 0.2 lbm/s to 0.4 lbm/s, the stability margin dropped.

There are some rather unique observations that can be made by examining the temperature (and by system design pressure) distortion data. This time, the circumferential air injection hardly had any effect at all. This is probably because the constant circumferential injection did not affect the maldistributed temperature profile since the injected air was all at a constant temperature. In the case of the axial air injection, however, the injected air is not uniform in the circumferential direction and therefore has a direct effect on the high-temperature region into which it is injecting a cooler flow. There is some question as to the exact flow physics occurring here. In the case of pressure distortion alone, raising the injected flow rate caused a decrease in the stability margin of the compressor. For the temperature and pressure combined distortion, the axial air injection brought the stability limit line almost all the way back to the stability limit line for the pressure-alone case.

A significant and major difference between the pressure-alone distortion case and the temperature distortion case with axial air injection is that the stability margin increased with increased injected flow rate under temperature distortion conditions, but decreased under pressure distortion conditions. One could question whether under the temperature distortion conditions (where there is also a pressure distortion due to the air injection), the increase in stability margin with increasing injected flow rate is due to affecting the pressure or the temperature distortion. It is the belief of the authors that since the temperature distortion (90-deg extent, high-temperature region) is convected with the flow and the axial air is being injected directly into this region, most of the benefit of the axial air injection under temperature distortion conditions comes from affecting the temperature distortion profile, not the pressure profile. This is further supported by the pressure distortion alone data where increasing flow rate decreased the stability margin.

Conclusions

A prototype of the Distortion Suppression Plenum (DSP) with two different hole patterns was designed and built. The prototype was then tested on a Honeywell T55 compressor rig, under both temperature and pressure distortion conditions.

Flow injection through circumferential holes was marginally effective for surge margin recovery under inlet distortion conditions. Proper tuning of the injection flow rate for a given operating condition may be needed to optimize the recovery of stability margin. Too much injection can lead to the formation of radial distortion, limiting the effectiveness of the DSP.

Flow injection through axial holes exhibited better capability in stability margin recovery, both for pressure and for temperature distortion. Under pressure distortion conditions, too much axial flow injection may cause counterswirl in the inlet, reducing the effectiveness of the DSP.

Axial flow injection into a temperature distortion field can reduce the circumferential temperature variation, thereby limiting the effect on the compression system.

A semi-passive distortion suppression with either an axial or circumferential hole pattern requires a flow control valve to deliver the flow being injected into the inlet duct. Since the pressure in the plenum must be higher than the pressure in the inlet duct, pressurized air is required to supply the DSP. This pressurized air has to come from either a compressor bleed port or some kind of external pump. In addition, this pressurized air may have to be cooled before it is injected at the inlet to reduce the possible degradation caused by the temperature distortion effects.

The compressor design parameters and the loading distribution of the compression system must be carefully considered in the design of a DSP, along with the compressor sensitivity to swirl and to radial distortion. CFD studies are critical for these considerations. In addition, the speed of the compressor will have an effect on how beneficial a DSP will be, since the stability limiting stage of the compression system is a function of the speed.

While these tests have shown that there is a potential to modify compressor inlet distortion through air injection, they have also shown that there are special concerns that must be addressed during the design of the injection system.

Acknowledgments

Scientific Monitoring, Inc., is grateful to the U.S. Army Aviation Applied Technology Directorate (AATD) for providing financial support and encouragement during the course of this project.

SMI would also like to thank Honeywell International for many valuable discussions and for its support of the T55 compressor rig testing. Particularly, we would like to acknowledge the support from Dr. Arun Sehra (now with NASA Glenn Research Center), Mr. John Dodge, Mr. Jim Sublett, Mr. Mike Holbrook, and Mr. John White.

Last, we thank Dr. Frank Q. Liu for his contributions in design, modeling, and test support.

References

[1] Jaw, L. C., et al., 1999, ‘‘A High-Response High-Gain Actuator for Active Flow Control,’’ Paper No. AIAA 99-2128.

[2] Epstein, A. H. et al., 1989, ‘‘Active Suppression of Aerodynamic Instabilities in Turbomachines,’’ AIAA J. Propulsion, **5**, No. 2, pp. 204–211.

[3] Day, I. J., 1993, ‘‘Active Suppression of Rotating Stall and Surge in Axial Compressors,’’ ASME J. Turbomach., **115**, pp. 40–47.

[4] Cousins, W. T., 1997, ‘‘The Dynamics of Stall and Surge Behavior in Axial-Centrifugal Compressors,’’ Ph.D. Dissertation, Virginia Polytechnic Institute and State University, Blacksburg, VA.

[5] Cousins, W. T., et al., 1995, ‘‘Surge and Stall Characteristics of AxialCentrifugal Compressors: The Enhancement to Engine Stability,’’ presented at the AGARD Symposium on Loss Mechanisms in Turbomachinery, Derby, UK.

Compressor Stability Enhancement Using Discrete Tip Injection

Kenneth L. Suder
NASA Glenn Research Center,
Cleveland, OH 44135

Michael D. Hathaway
US Army Vehicle Technology Directorate,
Cleveland, OH 44135

Scott A. Thorp

Anthony J. Strazisar

Michelle B. Bright

NASA Glenn Research Center,
Cleveland, OH 44135

Mass injection upstream of the tip of a high-speed axial compressor rotor is a stability enhancement approach known to be effective in suppressing stall in tip-critical rotors. This process is examined in a transonic axial compressor rotor through experiments and time-averaged Navier-Stokes CFD simulations. Measurements and simulations for discrete injection are presented for a range of injection rates and distributions of injectors around the annulus. The simulations indicate that tip injection increases stability by unloading the rotor tip and that increasing injection velocity improves the effectiveness of tip injection. For the tested rotor, experimental results demonstrate that at 70 percent speed the stalling flow coefficient can be reduced by 30 percent using an injected massflow equivalent to 1 percent of the annulus flow. At design speed, the stalling flow coefficient was reduced by 6 percent using an injected massflow equivalent to 2 percent of the annulus flow. The experiments show that stability enhancement is related to the mass-averaged axial velocity at the tip. For a given injected massflow, the mass-averaged axial velocity at the tip is increased by injecting flow over discrete portions of the circumference as opposed to full-annular injection. The implications of these results on the design of recirculating casing treatments and other methods to enhance stability will be discussed. [DOI: 10.1115/1.1330272]

Introduction

Aerodynamic stability is a fundamental limit in the compressor design process. Development of robust techniques for increasing stability has several benefits: enabling higher loading and fewer blades; increasing safety throughout a mission; increasing tolerance to stage mismatch during part-speed operation and speed transients; and opportunity to match stages at the compressor maximum efficiency point thus reducing fuel burn.

Many early approaches to increasing compressor stability consisted of some form of casing treatment [1–3] such as circumferential or axial skewed grooves. A number of recent investigations have focused on employing active control methodologies such as pitching inlet guide vanes [4,5], unsteady axisymmetric downstream bleed [6], unsteady upstream midspan injection [7], and unsteady upstream tip injection [8–11]. These methodologies are effective on compression systems in which stall is precipitated through modal pressure disturbances [12]. Actively controlling some aspect of the compressor flow field (e.g., flow angle, total pressure) to reduce or delay the growth rate of these disturbances has been demonstrated to be effective in extending the stable operating range of compressors.

Weigl and Spakovszky controlled stall in a single-stage transonic axial compressor through feedback control of the flow rate through 12 injectors uniformly spaced around the compressor annulus upstream of the rotor tip. Since the control valve for each injector was commanded to either open or close relative to a mean position, the injection consisted of a steady component with a superimposed unsteady component. Weigl's results are summarized in Fig. 1. The total massflow is the sum of the compressor annulus flow and the injected flow, P_S is the tip static pressure downstream of the rotor, and P_{tot} is the total pressure far upstream of the injectors. The data shown in Fig. 1 were acquired with a steady injection rate equal to 3.5 percent of the design speed choke flow. The results show that the total stability enhancement is due in large part to steady injection. Koch and Smith [13] and Lee and Greitzer [14] have also shown that steady injection in an appropriate location increases compressor stability. These previous investigations of steady injection form the motivation for the present work.

In the work of Weigl and in the present effort, the injected flow is supplied from an external source. In actual application, this flow would be bled from the rear of the compressor and recirculated to the rotor being controlled [11]. Since bleed extraction incurs a cycle penalty because work has been done on the bled air, there is a strong driver to minimize the amount of recirculation required for a given extension in stable operating range. The present investigation therefore addresses the following issues:

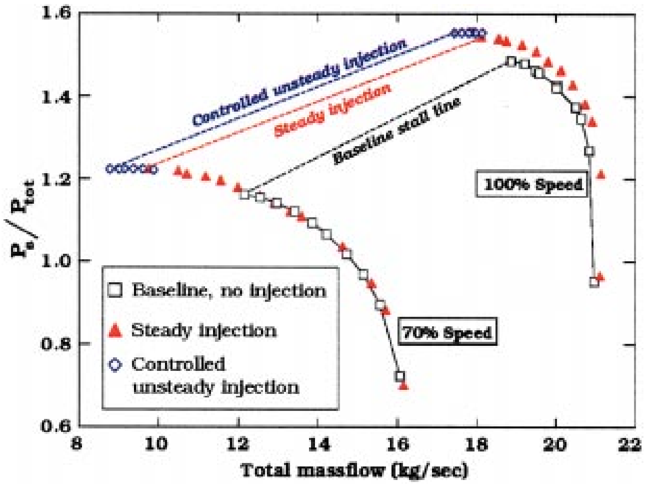

Fig. 1 Impact of steady and controlled unsteady tip injection on the stability limit of a transonic axial compressor stage as measured by [8]

Contributed by the International Gas Turbine Institute and presented at the 45th International Gas Turbine and Aeroengine Congress and Exhibition, Munich, Germany, May 8–11, 2000. Manuscript received by the International Gas Turbine Institute February 2000. Paper No. 2000-GT-650. Review Chair: D. Ballal.

- How does steady tip injection increase compressor stability?
- How does one maximize the stability increase for a given level of injected flow?

Time-average CFD simulations that employ a mass-injection model to simulate tip injectors were conducted to study the fluid mechanic processes through which tip injection increases stability. Using guidance from the CFD results, a parametric study of tip injection on a transonic axial compressor was then performed using the injection system previously used by Weigl and Spakovszky. Injection parameters that were varied include the number and distribution of injectors around the annulus, and the injected flow momentum and velocity.

Test Compressor and Measurements

Measurements were acquired in the NASA Glenn single-stage axial-flow compressor facility. The rotor tested, designated NASA Rotor 35, has 36 blades, an inlet tip radius of 25.4 cm, a hub–tip radius ratio of 0.70, an aspect ratio of 1.19, a tip solidity of 1.3, and an axial chord of 2.72 cm at the tip and 4.12 cm at the hub. The compressor was designed for axial inlet flow, and inlet relative Mach number is 1.48 at the tip at the design speed. The rotor tip clearance at design speed is 0.86 percent of tip chord. The compressor aerodynamic design and blade coordinates were reported by Reid and Moore [15].

Casing-mounted injectors, shown in Fig. 2, are located 55 mm (200 percent of rotor tip axial chord) upstream of the rotor. The injectors are designed to generate a jet along the casing upstream of the rotor [16]. Each injector penetrates 5.1 mm (6 percent span) from the casing into the flow field and is 57 mm wide (128 percent rotor pitch, 12.9 deg of arc along the casing). The injected flow is aligned with the inlet annulus flow in the downstream axial direction to minimize mixing between the annulus flow and the injected flow. The injectors are connected to a torus that is supplied with air at ambient temperature from an external source. During active stall control, the flow rate of each injector is controlled by an electromechanical valve. In the present work, the valve is set to 100 percent open and the injector flow rate is adjusted by changing the torus supply pressure. The injector exit velocity is calculated using a total and a static pressure measured at the exit of one injector at the injector centerline. A uniform velocity across the injector exit area (slug flow) is assumed. A survey of the injector exit flow distribution indicated that the exit flow fills only about 75 percent of the injector width and a comparison between the injector plenum flow rate measured with a venturi flow meter and the flowrate calculated with the slug flow velocity assumption confirmed this. Therefore, all of the experimental data analysis presented herein uses the slug flow velocity assumption with an effective injector width that is 75 percent of the geometric width.

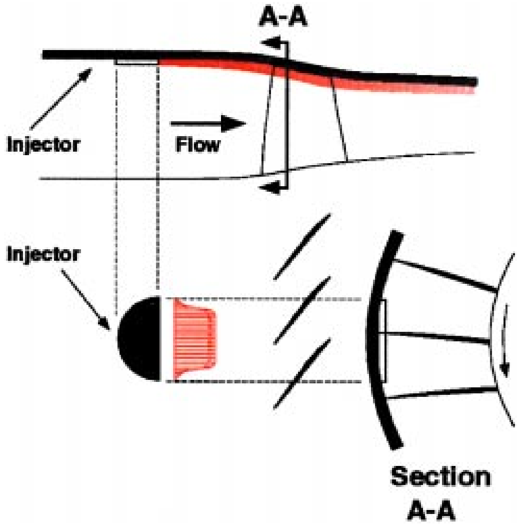

Fig. 2 Scale drawing of a discrete wall injector

Overall performance measurements are reported in terms of total-to-static pressure ratio based on casing static pressures measured at 12 points around the annulus at 125 percent of rotor chord. The injector exit static pressure closely matches the compressor casing static pressure upstream of the rotor as long as the injector exit flow is below its choking flow rate. All measurements reported herein are therefore obtained with the injectors operating below their choke point. Compressor massflow is measured with a calibrated orifice plate located far upstream of the compressor inlet plenum. Both the inlet massflow to the compressor and the injector massflow are corrected to standard day conditions. The sum of these corrected massflows is the total massflow rate through the rotor. Measurement uncertainties are: massflow 0.11 kg/s and pressure 0.10 N/cm^2.

Numerical Analysis

The Average Passage code (APNASA) developed by Adamczyk [17] is used for all CFD simulations. APNASA is a three-dimensional time-averaged Navier–Stokes code developed for multistage compressor analysis. The simulations are performed with two ''blade rows,'' wherein one blade row simulates the rotor flow field and the other blade row simulates the injectors. The body forces from one blade row are imposed on the other blade row and updated after every 100 iterations.

The mesh used is 147 axial×51 radial×41 tangential nodes with three cells in the rotor tip clearance gap. The rotor and injector meshes are identical axially and radially. The injector mesh has circumferentially uniform spacing with the spacing set to give 18 cells across the circumferential extent of the injector face. There are 14 cells across the radial extent of the injector face.

The version of APNASA used for this investigation includes provisions for source terms that are used to model the casing injectors, Turner and Saedi [18]. The source terms are set to provide the measured massflow from the injectors distributed uniformly over the cell centers covering the injector face (i.e., assuming slug flow). The upstream boundary condition for the flow field is obtained from surveys of the total pressure and total temperature distribution measured upstream of the rotor with zero injection. The downstream hub static pressure is adjusted in steps to develop a prediction of the rotor operating characteristics for various annulus massflow rates.

A Baldwin–Lomax turbulence model is used for all simulations. Convergence is achieved when the axisymmetric flow fields for both the rotor and injectors remain constant. Typically, 80 to 600 or more updates of the body force terms (increasing toward stall) are required for convergence. For operating points that are not close to stall, the convergence is well behaved. As stall is approached, the number of separated points in the flow field and other flow field parameters vary between updates. However, the simulation approaches a limit cycle in which the peak-to-peak amplitude of the flow field differences does not grow with increasing number of updates.

Numerical Results

The goal of the simulations is to provide insight into how tip injection increases the rotor stability in a time-average sense, rather than to provide a detailed analysis of the unsteady interaction between the injectors and the rotor. All simulations are performed for 100 percent of design speed with 12 injectors uniformly spaced around the circumference, directed in the downstream axial direction. Three configurations are analyzed:

Configuration	Injected Flow	Injector area
A (baseline)	0	-
B	5% rotor choke flow	full
C	5% rotor choke flow	half

Configuration *C* is analyzed to assess the impact of injected momentum on performance. In this configuration, the injector circumferential width is halved while holding the total injected massflow constant. This has the effect of doubling the injector exit velocity and momentum, since the momentum from a half-width injector in Configuration *C* is

$$\rho A_C(V_C)^2=\rho(A_B/2)(2V_B)^2=2\rho A_B(V_B)^2$$

The calculated operating characteristics are shown in Fig. 3, where the total mass flow is the sum of the inlet corrected massflow and the injector corrected massflow. APNASA results are consistent with the experimental trends observed by Weigl (shown in Fig. 1) in that the stalling massflow is reduced with steady injection. The simulation results for Configuration *C* indicate that the injector effectiveness is sensitive to the momentum and velocity of the flow leaving the injectors. Although the injector exit momentum doubles for this case, the circumferentially mass-averaged momentum increase at the rotor face over the radial extent of the injectors is only about 20 percent since the injectors occupy only a fraction of the circumference.

The circumferentially mass-averaged diffusion factor and incidence for Configurations *A* and *B* are compared in Fig. 4 over the outer portion of the span at the uninjected stall point. The operating conditions are points 1 and 2 in Fig. 3. The incidence and diffusion factors are determined along streamtubes based on circumferentially mass-averaged conditions evaluated approximately 2 percent chord upstream and downstream of the rotor leading and trailing edges. Diffusion factor is calculated as:

$$\mathrm{DF}=\left(1.0-\frac{\overline{W_{out}}}{\overline{W_{in}}}+\frac{\Delta\overline{W_\theta}}{2\sigma\overline{W_{in}}}\right)$$

where

$$\overline{W_{in}},\overline{W_{out}},\overline{W_\theta}$$

refer to mass-averaged rotor relative inlet, exit, and tangential velocity, respectively, and σ is rotor solidity. The diffusion factor and incidence are identical below 80 percent of span. In the outer 20 percent of span, tip injection reduces incidence and diffusion factor relative to the no-injection configuration and therefore allows the potential for stable operation at massflows below the baseline (no injection) stall point.

Spanwise distributions of rotor incidence and diffusion factor at the stall points for Configurations *A*, *B*, and *C* (see points 1, 3, and 4 in Fig. 3) are shown in Fig. 5. The configurations with injection are operating at substantially lower massflow rates than the baseline configuration, as is evident from the increased incidence and diffusion factors below 90 percent span. At the baseline stalling flow, the lower portion of the blade span is apparently not close to stall, since it is now able to operate at a lower massflow rate with the aid of rotor tip injection. Hathaway and Strazisar [19] evaluated the diffusion factor at the rotor tip as a function of the total rotor flow rate for Configurations *A*, *B*, and *C*. They found that the rotor tip controls stall for all three configurations and that stall occurs when the rotor tip diffusion factor reaches 0.75. For this rotor, tip injection reduces the diffusion factor at the tip for a given annulus massflow, therefore allowing further reductions in the overall massflow.

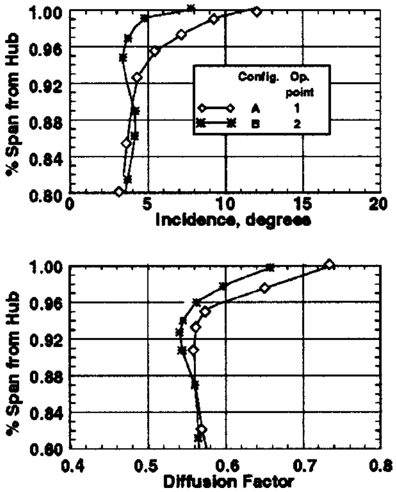

Fig. 4 Comparison of predicted incidence and diffusion factor near the blade tip at the baseline stalling massflow with and without tip injection

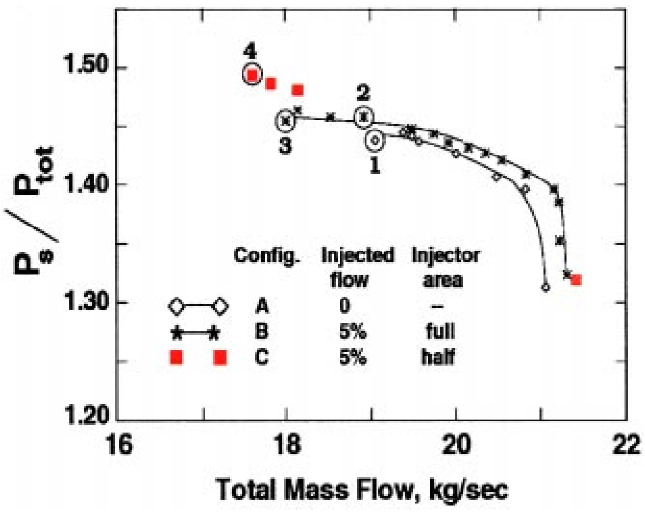

Fig. 3 Predicted design speed rotor performance with and without tip injection

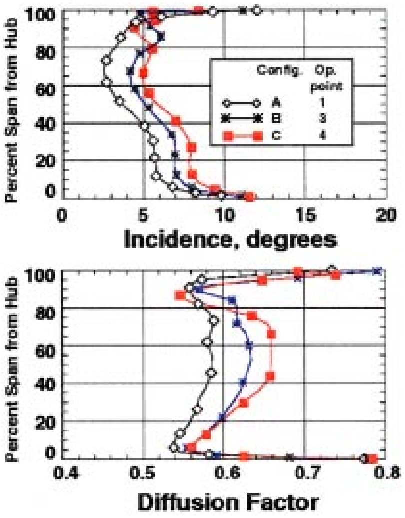

Fig. 5 Comparison of predicted incidence and diffusion factor across the blade span at the stalling massflows of Configurations *A*, *B*, and *C* (see Fig. 3)

In summary, the present simulations and those of Hathaway and Strazisar [19] indicate that:

- Tip injection lowers the incidence and blade loading at the tip.
- There is a critical tip diffusion factor at which the blade stalls with or without injection.
- For a given injected massflow, injector effectiveness increases when the injector exit velocity and momentum are increased by reducing injector area.

Experimental Results

The compressor casing was machined with penetrations for 12 injectors located every 30 deg around the annulus. In a previous investigation, we determined that 12 injectors are not needed for steady injection to be effective. Therefore in the present investigation we used various arrangements of 8, 6, 4, 3, and 2 injectors pointed in the downstream axial direction. For a given number of injectors, several arrangements around the annulus were tested. All injector arrangements are summarized in the appendix. When using fewer than eight injectors, the unused injectors are kept in the flow path. This practice keeps the total metal blockage of the injectors constant across the test matrix, so that changes in stalling flow between injector configurations are not due to varying metal blockage. The baseline (no injection) constant-speed operating characteristics are acquired with eight injectors in the flowpath.

Previous injection investigations also indicated that in a full-stage configuration, stall was triggered in some cases by the stator, probably due to excessive stator incidence angles at low massflows. To explore fully the ability of injection to reduce the stage stalling massflow would have required adjustment of the stator setting angle as the injection level was varied. Since the stator vanes in Stage 35 were not manufactured with vane actuation capability, we removed the stator for the present investigation, and acquired all measurements reported herein with the rotor operating in isolation.

The earlier work of Weigl et al. [8], Spakovszky et al. [9,10], and the simulations reported herein were performed with the original NASA Rotor 35 blading. However, all results presented below are for a modified version of Rotor 35 that was being used in a concurrent investigation of compressor blade refurbishment techniques. The leading edge of every other blade was cut back by 5 percent of chord and refinished with an elliptic leading edge. Comparison between limited stability enhancement data collected on Rotor 35 prior to its modification and the data reported herein indicates that the leading edge cutback does not affect the stability enhancement results.

Overall Performance Characteristics. The static-to-total pressure ratio characteristics for 70 and 100 percent speed are shown in Fig. 6 for several injector configurations. The total massflow is once again the sum of the annulus corrected massflow and the injector corrected massflow. In each case, the injectors are operating at their maximum (choking) flow rate. The performance characteristics for the various injector configurations lie on top of one another, which suggests that the stability enhancement can be quantified merely by the change in the stalling mass flow. We will concentrate our analysis on data acquired at 70 percent speed and then return to 100 percent speed to validate our understanding.

Radial Distribution of Blade Loading. The numerical simulations indicate that the stability enhancement results from an unloading of the rotor tip. To explore this behavior we grouped six injectors together so that one half of the circumference included injectors spaced 30 deg apart while the other half of the circumference had no injectors. We then acquired total pressure, total temperature, and flow angle surveys downstream of the rotor at two circumferential locations, one in the injected half of the circumference and one in the uninjected half. The surveys were acquired near the no-injection stall point with and without tip injection, and at a lower massflow achievable only with injection. These operating conditions are identified as points 1, 2, and 3 in Fig. 6. The flow through the injectors was maximized (choked injectors) for this exercise, resulting in an injected flow of approximately 2.8 percent of the annulus flow.

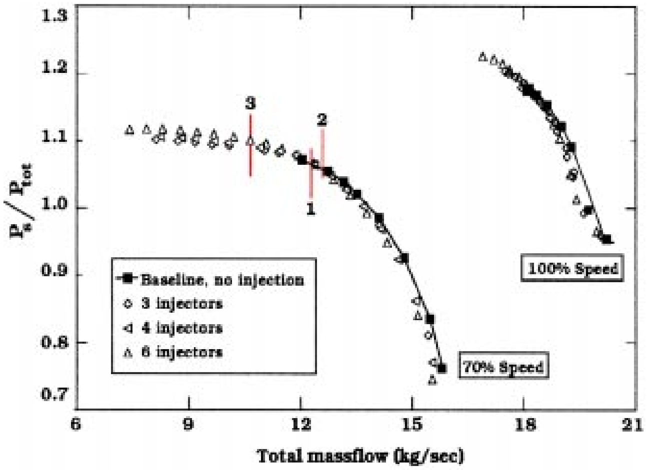

Fig. 6 **Measured rotor performance at 70 and 100 percent speed with and without tip injection**

The blade loading at operating conditions 1 and 2 is presented in Fig. 7(*a*) in terms of the diffusion factor. The swirl induced upstream of the rotor by the circumferentially nonuniform axial velocity created by the injectors is ignored in calculating the diffusion factor, since the CFD simulations indicate that the swirl angle is on the order of 2 deg. For the no-injection case, the diffusion factor reaches a maximum near 90 percent span, which implies the compressor is tip critical. The blade loading in the uninjected half of the annulus is nearly identical to the blade loading with no injection, where the slight difference in the tip is attributed to the inherent decrease in loading at the higher mass flow of operating condition 2. In the injected half of the annulus it is clear that injection reduces the blade loading at the tip.

A comparison of the blade loading at operating conditions 1 and 3 is presented in Fig. 7(*b*). As the annulus flow is reduced below the no-injection stalling flow, the blade loading in both the injected and uninjected regions increases across the span relative

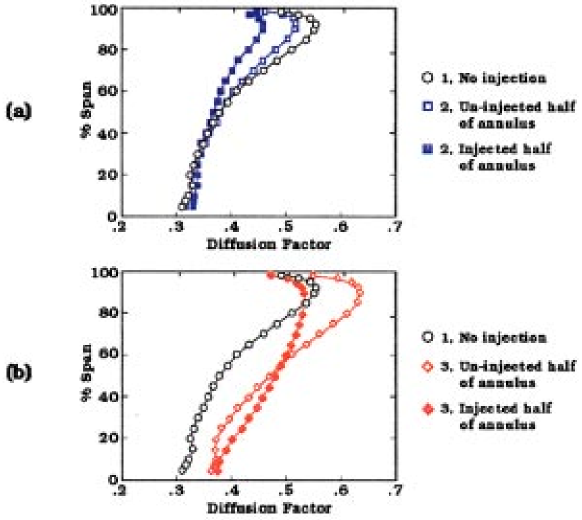

Fig. 7 **Comparison of diffusion factor measured in the injected and uninjected half of the annulus at 70 percent speed: (*a*) at operating points 1 and 2 depicted in Fig. 6, and (*b*) at operating points 1 and 3 depicted in Fig. 6**

to that at the no-injection stalling flow. The loading at the hub is identical in the injected and uninjected halves of the annulus. In the uninjected region, the blade loading at the tip significantly exceeds the critical tip diffusion factor exhibited at stall with no injection. However, the blade loading at the tip in the injected region approaches but does not exceed this critical diffusion factor. This result suggests that the compressor does not stall until the critical diffusion factor is exceeded in the injected half of the annulus.

In summary, tip injection effectively redistributes the blade loading by decreasing it at the tip and allowing it to increase over the remainder of the blade span, thereby extending the stable operating range for tip critical compressor rotors. These results are qualitatively consistent with those from the numerical simulations.

Operating Range Extension. Stall margin is used as a measure of the stable operating range for installed compressors, and is typically defined as either: (1) the change in massflow and pressure rise between the operating line and the stall line at a fixed rotational speed; or (2) the change in pressure rise between the operating line and the stall line at a fixed mass flow. However, an isolated rotor in a compressor rig test does not have an operating line. We therefore choose to quantify changes in stability as the normalized change in stalling flow coefficient,

$$\Delta\phi_{\text{stall}} = ((\phi_{\text{stall}})_b - (\phi_{\text{stall}}))/(\phi_{\text{stall}})_b\,,$$

where $(\phi_{\text{stall}})_b$ is the stalling flow coefficient for the baseline (no-injection) case. Note that this parameter is identical to the percentage change in the corrected stalling flow rate of the compressor since

$$\phi = V_x/U_t = m/(\rho A_a U_t)$$

where A_a is the annulus area, m is the sum of the annulus and injector massflow rates (corrected to standard-day conditions), ρ is the density at standard-day conditions, and U_t is the corrected tip speed.

Figure 8 summarizes the stable operating range extension measured at 70 percent speed as a function of injected massflow for varying injector numbers. The injected flow is normalized by the annulus flow at the baseline (no-injection) stall point. The results include data from all of the injector arrangements shown in the appendix. For the sake of clarity, we will not distinguish between the various injector arrangements for a given number of injectors at this time. For the 4, 6, and 8 injector configurations the mass flow was varied from no flow to the injector choking flow. For the 2 and 3 injector cases, the maximum range extension depicted in Fig. 8 corresponds to an injector exit Mach number of 0.8, because at an injector exit Mach number of 1 it was difficult to clearly identify stall. The maximum range extension is nearly identical for the 4, 6, and 8 injector cases. Maximum range extension is achieved with as few as four injectors using a total injected mass flow of less than 2 percent of the annulus flow. Adding more injectors merely increases the amount of injected air without significantly impacting the range extension.

Injection Parameters Controlling Range Extension. To explain the results shown in Fig. 8, it is useful to consider the impact of injector momentum, exit velocity, and spacing on range extension. One might suspect that the injected momentum is the controlling parameter affecting range extension in that a jet of high-momentum fluid will energize the low-momentum flow resulting from the endwall boundary layer and tip leakage vortex, thus reducing blockage. High endwall blockage has been attributed as a cause of stall by several investigators [20–24]. An equally valid argument could be made for the injection velocity being the controlling parameter, since the high-velocity jet from the injectors will reduce the blade incidence and therefore reduce the blade loading.

The arguments given above are based on steady-flow effects. Consideration of unsteady flow effects leads one to consider injector spacing as a potential parameter. Day [25] has shown that compressor stall is preceded by the growth of both long- and short-wavelength pressure perturbations. These disturbances grow in amplitude as they rotate around the annulus. Therefore, an alternative explanation for the stabilizing influence of the injectors is that they retard or disrupt the growth of these stall-precursive perturbations. These perturbations have more time to grow before they encounter another injector as the number of injectors is reduced. One would therefore expect that injector effectiveness would be reduced once the distance between injectors is increased beyond some critical value.

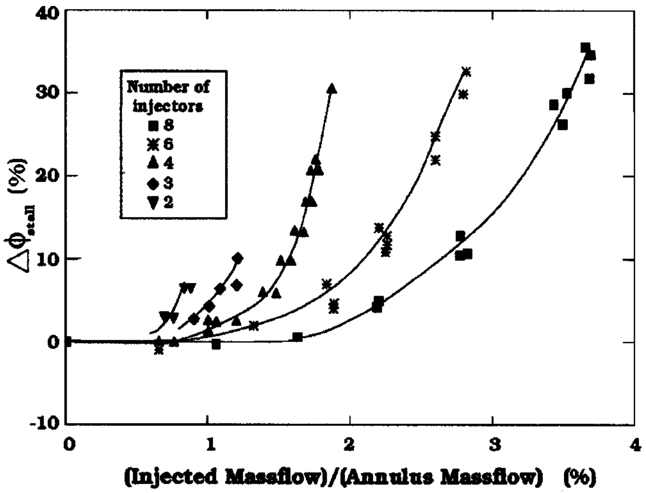

Fig. 8 Range extension measured at 70 percent speed as a function of injected massflow

Injector Spacing. Injector spacing effects were first explored by arranging a given number of injectors around the annulus in several different ways (see appendix). A typical result is shown in Fig. 9 for four arrangements of six injectors around the annulus. The injected flow is again normalized by the annulus flow at the baseline (no-injection) stall point. The solid-filled points indicate cases in which the stall point was difficult to determine. It is evident that for a given injector massflow, the range extension is independent of the injector arrangement. We found similar results for groups of 3, 4, and 8 injectors. Only in the case of two injectors does it seem to make a difference whether the injectors are located next to one another or separated by 180 deg. Graf et al. [26] and Cumpsty [27] have studied the effects of asymmetric

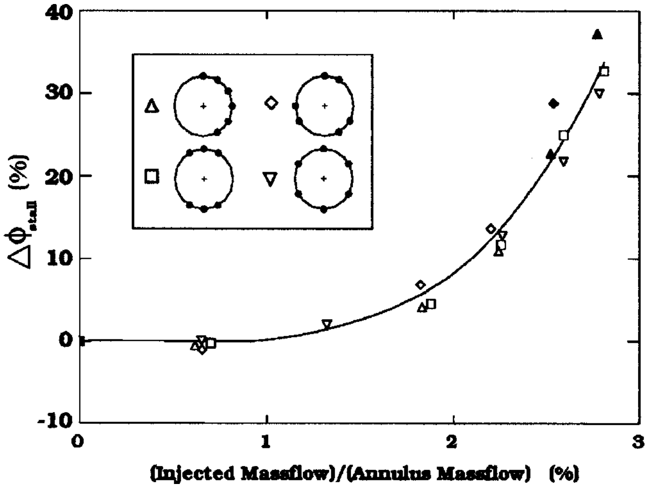

Fig. 9 Range extension measured at 70 percent speed as a function of injected massflow for various arrangements of six injectors around the annulus

inlet flows on compressor performance using nonuniform tip clearance and discrete casing treatment, respectively. In both cases, they found that the magnitude of changes in the compressor performance was related to the circumferential wavelength (i.e., the reduced frequency) of the asymmetry. The results shown here represent asymmetries with wavelengths ranging from one cycle per rev (six injectors grouped together) to six cycles per rev (six injectors evenly spaced), with no difference in compressor performance for a given injected massflow. We have no explanation for the discrepancy between our results and those of Graf and Cumpsty.

A second issue related to injector spacing is the observation from Fig. 8 that the maximum range extension achievable with choked injectors begins to roll off for the cases with fewer than four injectors. This may be an effect of the reduced circumferential coverage as the number of injectors is reduced or could be merely due to a decrease in total injected flow. We explored this issue by doubling the number of injectors while reducing the injector height by half so that the total injected massflow and injector exit velocity remained constant. For example, the total injected massflow and relative exit velocity of eight half-height injectors are the same as that of four full-height injectors. A comparison between half-height and full-height injectors is presented in Fig. 10, where the data points for the full-height and half-height cases are denoted by solid and open symbols, respectively. We see that eight half-height injectors provide the same maximum range extension as four full-height injectors. However, four and six half-height injectors provide a greater maximum range extension than two and three full-height injectors. These results suggest that the reduction in range extension with less than four full height injectors, as shown in Fig. 8, is not due to a decrease in total injected flow, but rather is linked to the circumferential coverage and spacing of the injectors.

Injector Mass, Momentum, and Velocity. To explore the role of mass, momentum, and exit velocity in extending stable operating range, we will consider the four injector configurations labeled *A*, *B*, *C*, and *D* in Fig. 10. The velocity, massflow, and momentum per injector are all coupled for the full-height injector cases *A*, *B*, and *C*: changing one of these parameters changes all three. Case *D*, which features eight half-height injectors, allows us to change the injector massflow and momentum while holding the injector exit velocity equal to that of Case *A*. Taking Case *A* as the ''baseline,'' we define the massflow and momentum per injector for Case *A* as

$$m=\rho A_A V_A \quad \text{and} \quad mv=\rho A_A (V_A)^2,$$

where A_A and V_A are the injector area and exit velocity, respectively. Using the velocity and area relationships defined below, we arrive at the results shown in Table 1.

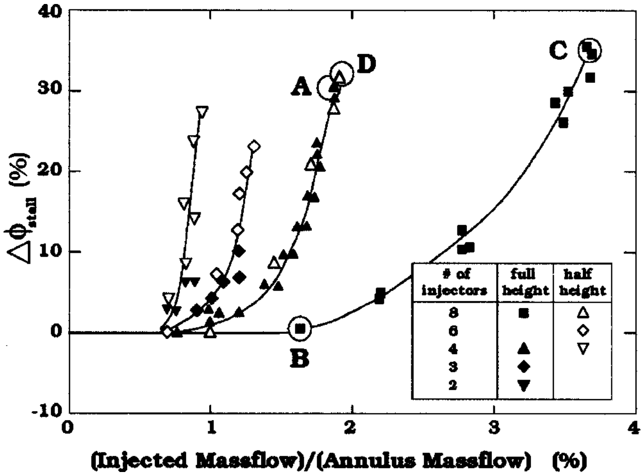

Fig. 10 Range extension measured at 70 percent speed for half-height and full-height injectors

Table 1 Summary of injection parameters

Parameter	Case A	Case B	Case C	Case D
No. of Injectors	4	8	8	8
Total Injected Massflow	4 m	4 m	8 m	4 m
Total Injected Momentum	4 mv	2 mv	8 mv	4 mv
Massflow per Injector	m	½ m	m	½ m
Momentum per Injector	mv	¼ mv	mv	½ mv
Injector Exit Velocity	V_A	½ V_A	V_A	V_A

$V_B=\frac{1}{2}V_A$	total injected massflow for *B* and *A* is the same, *B* has twice as many injectors as *A*
$V_C=V_A$	total injected massflow for *C* is twice that for *A*, *C* has twice as many injectors as *A*
$V_D=V_A$	total injected mass flow for *D* and *A* is the same, *D* has twice as many injectors as *A*, injector areas for *D* and *A* are related by $A_D=\frac{1}{2}A_A$

We will now examine each of the injection parameters in Table 1. Recall from Fig. 10 that cases *A*, *C*, and *D* have the same range extension while case *B* has substantially less range extension.

Total Injected Massflow:

- Compare cases *A*, *B*, *D*: same total flow with much reduced range extension for case *B*

$\therefore$ **Total injected massflow is not correlated to range extension**

Total Injected Momentum:

- Compare cases *A*, *C*: *C* has twice the momentum of *A* and the same range extension

$\therefore$ **Total momentum is not correlated to range extension**

Massflow per Injector:

- Compare Cases *B*, *D*: same massflow per injector with much reduced range extension for case *B*

$\therefore$ **Massflow per injector is not correlated to range extension**

Momentum per Injector:

- Compare cases *A*, *D*: *D* has half the momentum per injector of *A* and the same range extension

$\therefore$ **Momentum per injector is not correlated to range extension**

Injector Exit Velocity:

- Compare cases *A*, *C*, *D*: same injector exit velocity with the same range extension
- Compare cases *A*, *C*, *D* to *B*: *B* has lower injector exit velocity with less range extension

$\therefore$ **Injector exit velocity is possibly correlated to range extension**

To verify that the injector exit velocity is correlated to range extension, the data shown in Fig. 10 are analyzed in terms of the axial velocity mass-averaged over the outer 6 percent of the annulus height (i.e., the radial extent of the injectors). The mass-averaged axial velocity is defined as

$$\overline{V_z}=\frac{[\rho_i(N*W*V_i^2)+\rho_c(\pi D-N*W)*V_c^2]}{\rho_i(N*W*V_i)+\rho_c(\pi D-N*W)*V_c]}$$

where N is the number of injectors, W is the injector width, and D is the annulus diameter. V_i and ρ_i are the injected flow velocity and density, respectively, at the injector exit, and V_c and ρ_c are the annulus flow velocity and density at 97 percent span (the

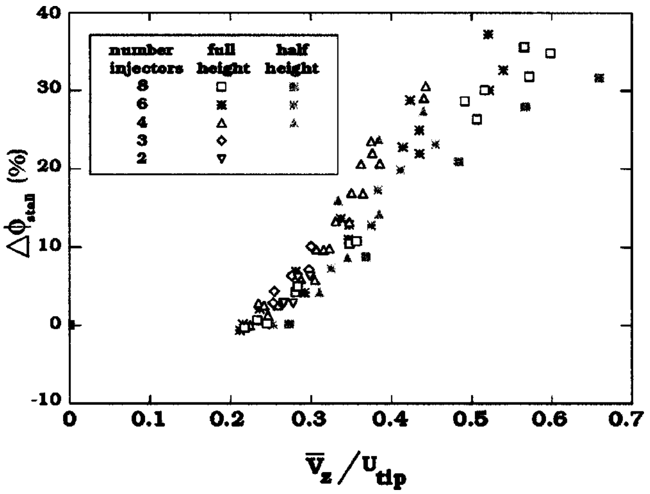

Fig. 11 Range extension measured at 70 percent speed as a function of mass-averaged axial velocity over the outer 6 percent span normalized by the tip speed

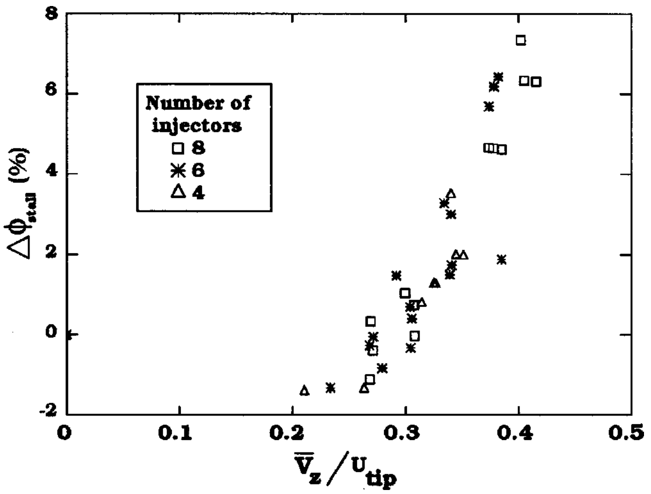

Fig. 12 Range extension measured at 100 percent speed as a function of mass-averaged axial velocity over the outer 6 percent span normalized by the tip speed

center of the injector height). While this analysis neglects mixing between the injected flow and the annulus flow, our aim here is to use the simplest analysis possible to assess the correlation between the axial velocity at the tip and the range extension. The mass averaging acknowledges the fact that as the number of injectors is decreased, the rotor spends less time in the high-velocity jet located downstream of an injector. Results for both full-height and half-height configurations, shown in Fig. 11, confirm that stability enhancement is directly related to the increase in the mass-averaged axial velocity at the rotor tip. The increased axial velocity reduces incidence, unloads the rotor tip, and acts to reduce the buildup of blockage at the rotor tip. Since this rotor is tip critical, all of these effects allow increased loading before the blade stalls, enabling a reduction in the stalling massflow.

Design Speed Results. Stability enhancement at 100 percent speed was investigated using 2, 3, 4, 6, and 8 injectors. The results are similar in character to those shown in Fig. 8 for 70 percent speed. However, no measurable range extension was achieved with fewer than four injectors. The range extension measured at design speed as a function of $\overline{V_z}$ is shown in Fig. 12. The results verify that range extension is correlated to the increase in mass-averaged axial velocity $\overline{V_z}$ near the blade tip at design speed as well as at 70 percent speed.

The maximum range extension obtained at design speed is significantly lower than that measured at 70 percent speed. With 4, 6, and 8 injectors, the maximum range extension, characterized by the change in stalling flow coefficient, at 100 percent speed is 3.5, 6.4, and 7.3 percent for injection massflows of 1.3, 1.9, and 2.5 percent of the annulus flow rate. The reduced injector effectiveness at design speed can be explained as follows. The choking velocity of the injector is fixed and independent of compressor speed. For a given number of choked injectors, $\overline{V_z}$ is reduced at increased compressor speeds due to the increased core velocity, V_c. Since the range extension is a function of the mass-averaged velocity $\overline{V_z}$, it follows that the range extension will be reduced as well. Since the injectors are choked at the point of maximum range extension, the only way to increase $\overline{V_z}$ is to add more injectors. In summary, the experimental results indicate that injector effectiveness is:

- Correlated with the increase in mass-averaged axial velocity at the tip, which is maximized when the injectors are choked.
- Independent of the injector arrangement around the annulus provided there are three or more injectors.

Applications

Steady tip injection has been demonstrated to be an effective means of extending the stable operating range of a tip critical compressor. The range extension reported herein is for a rotor operating in isolation. Tip injection redistributes the rotor loading across the span, which in turn impacts the loading distribution on the downstream stator. Therefore, it is conceivable that stall could initiate in the stator, and that without variable stator geometry, the maximum range extension in a stage would be reduced compared to that of a rotor in isolation. In a multistage configuration, range extension could also be reduced due to stage matching considerations.

In a multistage compressor, the injected air required to stabilize a given stage would be supplied by bleed from a downstream stage. In order to minimize the penalty in cycle efficiency incurred by extracting bleed air for injection, one could use a shut-off valve in the recirculation line, which would only enable injection ''on-demand'' during those times when increased stability is needed. We have shown that injector effectiveness is maximized when the injector is choked. Assuming no losses in the recirculation system, this choking condition requires that the bleed static pressure be roughly twice the static pressure at the injection location. The injected air will be heated when it is supplied by recirculation from a downstream stage. For a given corrected massflow of heated air, the increase in mass-averaged axial velocity (and therefore the range extension) obtained with choked injectors will be lower than that obtained in the present work with air injected at ambient temperature. This reduction in injector effectiveness occurs because the density of the injected air is reduced in direct proportion to the temperature while the velocity increases by the square root of the temperature.

We will now consider three applications for tip injection in compressors: (1) recovery from fully developed stall; (2) stage matching at part-speed operating conditions; and (3) recirculating casing treatment.

Stall Recovery. We now consider whether steady injection can be used to recover from stall as an alternative to standard stall recovery schemes such as vane actuation, bleed, or throttle opening. The following stall recovery tests were performed at both 70 and 100 percent speed:

1 With the injectors turned off, the compressor was throttled into stall, and the injectors were then activated with no change in throttle setting.

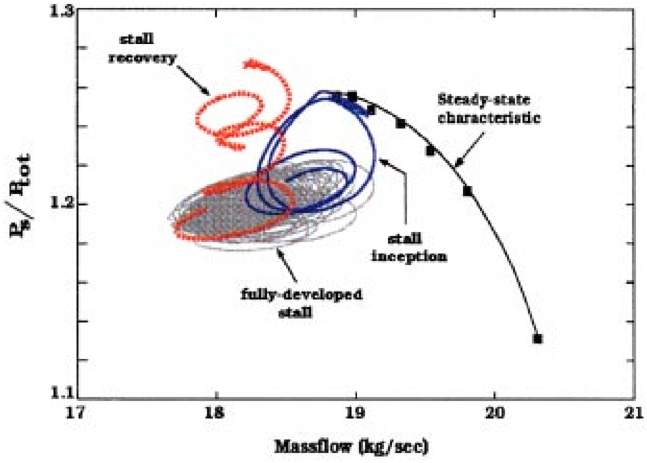

Fig. 13 Unsteady compressor operating point at design speed during stall inception and stall recovery with tip injection. Blue: stall inception; gray: fully developed stall; red: stall recovery with tip injection.

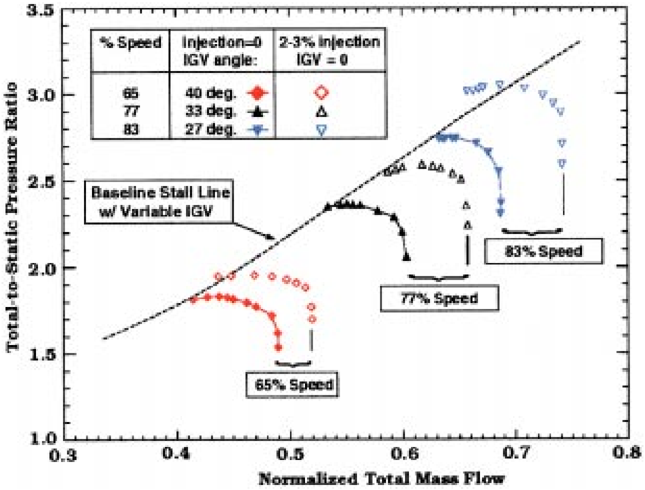

Fig. 14 Part-speed performance characteristics of a two-stage high-speed fan with and without tip injection. Solid symbols: nominal IGV schedule with no tip injection; open symbols: IGV fixed at 0 deg (axial) with tip injection.

2 With the injectors turned on, the compressor was throttled to a massflow below the noninjected stall point. With no change in throttle setting, the injectors were turned off, resulting in compressor stall, and then were turned back on.

In each case, the compressor recovered from stall at a fixed throttle setting with the aid of tip injection. The unsteady operating characteristic of the rotor was measured using high-response pressure sensors located upstream and downstream of the rotor during these tests. The sensors were low-pass filtered at 1 kHz and sampled at 3 kHz. The unsteady compressor inlet massflow was determined from a total pressure measured at midspan upstream of the injectors (7.5 chords upstream of the rotor) and a wall static pressure measured at the same axial location. The unsteady total-to-static pressure ratio was determined using a wall static pressure measured downstream of the rotor and the upstream midspan total pressure.

The results of a stall recovery test of type 1 listed above at design speed are shown in Fig. 13, where the unsteady pressure and massflow are superimposed on the steady operating characteristic. Four injectors were used with a total injected massflow equal to 1.3 percent of the annulus flow. The blue trace denotes the operating point during the beginning of throttle closure and the initial drop into stall. The gray traces denote the operating point during an additional throttle closure that occurred over the next 1200 rotor revolutions. The dashed red trace denotes the recovery from stall that occurred during 90 rotor revolutions after the injectors were activated by opening a fast-acting valve, which pressurized the injector supply torus. Tip injection not only recovers the compressor from stall, but also restores the compressor to its pre-stall level of pumping.

Stage Matching. Variable geometry vanes are typically used in the front stages of multistage compressors to control blade loading during part-speed operation. The required vane actuation mechanisms are complex and costly to produce and maintain. We therefore explored whether discrete tip injection can be used as an alternative to variable geometry for stabilizing a multistage compressor at part speed. Employing tip injection in a turbofan engine may be practical since the engine spends only a small percentage of its operating time at low speed. However, for compressors that operate at part speed for extended periods of time, tip injection will not be a viable alternative to variable geometry from an aerodynamic performance perspective, due to the efficiency penalty incurred using tip injection.

An initial demonstration of this concept was performed on a two-stage low-aspect-ratio fan. The fan has a design tip speed of 490 m/s and features a variable IGV and first-stage stator for stage matching at part-speed conditions. Design details are given by Manwaring et al. [28]. Fourteen injectors were arranged around the circumference in a spool piece inserted between the IGV and first rotor. Injected air was supplied from an external source, the injectors were operated in their choked condition at a total flow rate equal to 2–3 percent of the annulus flow, and the first-stage stator was fixed at its design-speed setting angle. At part speed, the compressor stalls when the IGV is opened from its nominal setting to the axial (IGV=0 deg setting) direction with air injection turned off.

Overall total-to-static pressure ratio characteristics for part-speed operation are shown in Fig. 14, where the total massflow is normalized by the design-point flow. Pressure ratio characteristics for the nominal IGV schedule with no air injection are denoted by solid symbols. Pressure ratio characteristics measured with the IGV fixed at its full-open position (0 deg) with air injection are denoted by open symbols. The results show that air injection enabled the nominal surge line to be met or exceeded without the need for variable geometry.

Casing Treatment. Recirculating casing treatments [29,30] have several disadvantages: They are geometrically complex; they recirculate flow several times through the rotor tip region raising case temperatures and reducing efficiency; they are difficult to deactivate during those parts of a mission for which augmented stability is not required. Most importantly, these treatments feature an annular intake over the rear of the rotor and an annular exhaust upstream of the rotor tip. The present results indicate that further improvement in stable operating range would be expected if the recirculated fluid were injected through discrete rather than full-annular slots, thus raising its velocity.

We have demonstrated that significant range extension can be achieved using only four injectors spaced randomly about the circumference injecting less than 1 percent of the annulus flow. Therefore, it is reasonable to consider a ‘‘discrete casing treatment’’ consisting of a recirculating system that would bleed high-pressure air from the rear of a blade and use it to supply discrete injectors upstream of the blade. By bleeding and injecting from different portions of the circumference, multiple recirculation of fluid can be avoided. With a shut-off valve in the recirculation line, this treatment can be turned off when not required, eliminating its inherent efficiency penalty. Such a treatment can also be activated ‘‘on-demand’’ to recover from a fully developed stall.

Future Work. Herein we have demonstrated the effectiveness of tip injection to enhance stability in a single-stage transonic compressor using an external air supply. Stability enhancement and stall recovery would be more difficult in a multistage compressor where stage loading and therefore the stalling stage varies with operating condition. Our experiences using tip injection in multistage compressors (not reported) indicate that injection in a given blade row also impacts the performance of downstream blade rows. Based on these experiences and the results presented by Freeman et al. [11], we believe that incorporating injection in an inlet and middle stage would be sufficient to enhance stability in a multistage compressor. In addition, cycle and mission analysis studies need to be performed to: (1) assess the efficiency penalty incurred by extracting air from downstream blade rows and re-injecting at upstream blade rows, and (2) evaluate the trade-offs for using air injection (efficiency penalty) as a replacement for variable geometry (added mechanical complexity and weight). In addition, the true benefits of using tip injection cannot be assessed until a compressor design incorporates the impact of tip injection on stage matching. Clearly, there is more work to be done before injection can be applied to inservice compressors. However, we and others [7,11,31,9,10,8] have demonstrated there are substantial benefits to using injection in compression systems.

Conclusions

Numerical simulations and experimental measurements have shown that range extension can be achieved by injecting air through discrete wall jets upstream of a tip-critical transonic compressor rotor operating in isolation. Tip injection has also been demonstrated as an effective tool for recovering a compressor from fully developed stall and as an effective alternative to inlet guide vanes for providing adequate stall margin during part-speed operation of a two-stage transonic fan.

The following conclusions can be drawn from this investigation:

- Tip injection decreases incidence and blade loading at the tip, allowing increased loading at lower blade spans before the blade stalls. With tip injection present, the blade stalls when the loading at the tip reaches the level equal to that for which the blade stalls with no injection.
- Range extension is correlated with the increase in mass-averaged axial velocity at the tip due to injection. Maximum range extension is achieved when the injectors are choked.
- Range extension is related to the total circumferential extent of injection but is not related to the circumferential arrangement of injection locations.
    - For a fixed number of injectors, a sixfold change in reduced frequency yields the same range extension.
    - When the number of injectors used is reduced, the ability to increase the mass-averaged axial velocity at the tip begins to diminish due to the reduced circumferential extent of the injection. For a given injected massflow, the axial velocity and range extension can be further increased by using more injectors with a reduced exit area.
- For a given injected massflow, injection effectiveness is maximized by reducing the number of injectors in order to increase the injector exit flow velocity. This result implies that recirculating casing treatments, which inject air along the full compressor annulus, would be more effective if the recirculated air were to be injected over a smaller area at a higher velocity.

Acknowledgments

The authors would like to thank Dr. Doug Rabe, Dr. Tony DiPietro, and the staff of the Compressor Research Facility at Wright Paterson Air Force Base for their support during testing of the two-stage transonic fan. We also acknowledge the support of Mr. Dave Williams, Mr. Randy Thomas, Mr. Helmi Abulaban, and Mr. Hal Weaver at NASA Glenn Research Center for their support during testing of NASA Rotor 35. Finally, we would like to acknowledge Dr. Edward Greitzer, Dr. Nick Cumpsty, Dr. Choon Tan, Mr. Pete Tramm, and Dr. John Adamczyk, whose insight and comments have added measurably to this work.

Appendix

Circumferential Arrangement of Injectors. The compressor case was designed with penetrations for injectors spaced every 30 deg around the annulus. The table below shows the circumferential arrangements investigated for each number of injectors, *N*.

N	Injector circumferential location, degrees											
	0	30	60	90	120	150	180	210	240	270	300	330
	1/rev Injector Configurations											
8	X	X	X	X	X	X	X	X				
6	X	X	X	X	X	X						
4	X	X	X	X								
3	X	X	X									
2	X	X										
1	X											
	2/rev Injector Configurations											
8	X	X	X	X			X	X	X	X		
6	X	X	X				X	X	X			
4	X	X					X	X				
2	X						X					
	3/rev Injector Configurations											
6	X	X			X	X			X	X		
3	X				X				X			
	4/rev Injector Configurations											
8	X	X		X	X		X	X		X	X	
4	X			X			X			X		
	6/rev Injector Configuration											
6	X		X		X		X		X		X	

References

[1] Prince, D. C., Jr., Wisler, D. D., and Hivers, D. E., 1974, ''Study of Casing Treatment Stall Margin Improvement,'' NASA CR-134552.

[2] Takata, H., and Tsukuda, Y., 1977, ''Stall Margin Improvement by Casing Treatment—Its Mechanism and Effectiveness,'' ASME J. Eng. Power, **99**, pp. 121–133.

[3] Crook, A. J., Greitzer, E. M., Tan, C. S., and Adamczyk, J. J., 1993, ''Numerical Simulation of Compressor Endwall and Casing Treatment Flow Phenomena,'' ASME J. Turbomach., **115**, pp. 501–512.

[4] Paduano, J. D., Epstein, A. H., Valavani, L., Longley, J. P., Greitzer, E. M., and Guenette, G. R., 1993, ''Active Control of Rotating Stall in a Low Speed Axial Compressor Rotor,'' ASME J. Turbomach., **115**, pp. 48–56.

[5] van Schalkwyk, C. M., Paduano, J. D., Greitzer, E. M., and Epstein, A. H., 1998, ''Active Stabilization of Axial Compressors With Circumferential Inlet Distortion,'' ASME J. Turbomach., **120**, pp. 431–439.

[6] Eveker, K. M., Gysling, D. L., Nett, C. N., and Sharma, O. P., 1998, ''Integrated Control of Rotating Stall and Surge in High-Speed Multistage Compression Systems,'' ASME J. Turbomach., **120**, pp. 440–445.

[7] Behnken, R. L., Leung, M., and Murray, R. M., 1997, ''Characterizing the Effects of Air Injection on Compressor Performance for Use in Active Control of Rotating Stall,'' ASME Paper No. 97-GT-316.

[8] Weigl, H. J., Paduano, J. D., Frechette, L. G., Epstein, A. H., Greitzer, E. M., Bright, M. M., and Strazisar, A. J., 1998, ''Active Stabilization of Rotating Stall and Surge in a Transonic Single Stage Axial Compressor,'' ASME J. Turbomach., **120**, pp. 625–636.

[9] Spakovszky, Z. S., Weigl, H. J., Paduano, J. D., van Schalkwyk, C. M., Suder, K. L., Bright, M. M., 1999, ''Rotating Stall Control in a High-Speed Stage With Inlet Distortion: Part I—Radial Distortion,'' ASME J. Turbomach., **121**, pp. 510–516.

[10] Spakovszky, Z. S., van Schalkwyk, C. M., Weigl, H. J., Paduano, J. D., Suder, K. L., and Bright, M. M., 1999, ''Rotating Stall Control in a High-Speed Stage with Inlet Distortion: Part II—Circumferential Distortion,'' ASME J. Turbomach., **121**, pp 517–524.

[11] Freeman, C., Wilson, A. G., Day, I. J., and Swinbanks, M. A., 1998, ''Experiments in Active Control of Stall on an Aeroengine Gas Turbine,'' ASME J. Turbomach., **120**, No. 4, pp. 637–647.

[12] Camp, T. R., and Day, I. J., 1998, ''A Study of Spike and Modal Stall Phenomena in a Low-Speed Axial Compressor,'' ASME J. Turbomach., **120**, pp. 393–401.

[13] Koch, C. C., and Smith, L. H., Jr., 1968, ''Experimental Evaluation of Outer Casing Blowing or Bleeding of Single Stage Axial Flow Compressor, Part IV–Performance of Bleed Insert Configuration No. 3,'' NASA CR-54590.

[14] Lee, N. K. W., and Greitzer, E. M., 1990, ''Effects of Endwall Suction and Blowing on Compressor Stability Enhancement,'' ASME J. Turbomach., **112**, pp. 133–144.

[15] Reid, L., and Moore, R. D., 1978, ''Performance of Single-Stage Axial-Flow Transonic Compressor With Rotor and Stator Aspect Ratios of 1.19 and 1.26, Respectively, and With Design Pressure Ratio of 1.82,'' NASA TP 1338.

[16] Berndt, R. G., Weigl, H. J., Paduano, J. D., and Epstein, A. H., 1995, ''Experimental Techniques for Actuation, Sensing, and Measurement of Rotating Stall Dynamics in High Speed Engines,'' J. Soc. Photo-Opt. Instrum. Eng., **2494**, pp. 124–136.

[17] Adamczyk, J. J., 1985, ''Model Equation for Simulating Flows in Multistage Turbomachinery,'' ASME Paper No. 85-GT-226.

[18] Turner, M. G., and Saedi, S., 1997, ''Average Passage Code Development and Validation,'' Contract No. NASA-26617, Task No. 57.

[19] Hathaway, M. D., and Strazisar, A. J., 1998, ''Impact of Discrete Tip Injection on Stabilization of a Transonic Compressor Rotor,'' *Proc. 21st Army Science Conference*, June 13–15, Norfolk, VA.

[20] Koch, C. C., and Smith, L. H., Jr., 1976, ''Loss Sources and Magnitudes in Axial Flow Compressors,'' ASME J. Eng. Power, **98**, pp. 411–424.

[21] Koch, C. C., 1981, ''Stalling Pressure Rise Capability of Axial Flow Compressor Stages,'' ASME J. Eng. Power, **103**, pp. 645–656.

[22] Adamczyk, J. J., Celestina, M. L., and Greitzer, E. M., 1993, ''The Role of Tip Clearance in High Speed Fan Stall,'' ASME J. Turbomach., **115**, No. 1, pp. 28–39.

[23] Suder, K. L., 1998, ''Blockage Development in a Transonic, Axial Compressor Rotor,'' ASME J. Turbomach., **120**, pp. 465–476.

[24] Suder, K. L., and Celestina, M. L., 1996, ''Experimental and Computational Investigation of the Tip Clearance Flow in a Transonic Axial Compressor Rotor,'' ASME J. Turbomach., **118**, pp. 218–229.

[25] Day, I. J., 1993, ''Stall Inception in Axial Flow Compressors,'' ASME J. Turbomach., **155**, pp. 1–9.

[26] Graf, M. B., Wong, T. S., Greitzer, E. M., Marble, F. E., Tan, C. S., Shin, H. W., and Wisler, D. C., 1997, ''Effects of Non-Axisymmetric Tip Clearance on Axial Compressor Performance and Stability,'' ASME J. Turbomach., **120**, pp. 648–661.

[27] Cumpsty, N. A., 1989, ''Part-Circumference Casing Treatment and the Effect on Compressor Stall,'' ASME Paper No. 89-GT-312.

[28] Manwaring, S. R., Rabe, D. C., Lorence, C. B., and Wadia, A. R., 1997, ''Inlet Distortion Generated Forced Response of a Low-Aspect-Ratio Transonic Fan,'' ASME J. Turbomach., **119**, pp. 665–676.

[29] Kang, C. S., McKenzie, A. B., and Elder, R. L., 1995, ''Recessed Casing Treatment Effects on Fan Performance and Flow Field,'' ASME Paper No. 95-GT-197.

[30] Koff, S. G., Nikkanen, J. P., and Mazzawy, R. S., 1994, ''Rotor Casing Treatment,'' U.S. Patent Application, U.S. Serial Number 005308225A.

[31] Koch, C. C., and Smith, L. H., Jr., 1968, ''Experimental Evaluation of Outer Casing Blowing or Bleeding of Single Stage Axial Flow Compressor, Part IV—Performance of Blowing Insert Configuration No. 1,'' NASA CR-54589.

Comparative Studies on Short and Long Length-Scale Stall Cell Propagating in an Axial Compressor Rotor

M. Inoue

M. Kuroumaru

T. Tanino

S. Yoshida

M. Furukawa

Department of Energy
and Mechanical Engineering,
Kyushu University,
Fukuoka, Japan

In a low-speed compressor test rig at Kyushu University, multiple short length-scale stall cells appeared under a mild stall condition and turned into a long length-scale cell under a deep stall condition. Then, for the two types of stall cell, the pressure distribution on the casing wall and the velocity distributions upstream and downstream of the rotor have been measured by high-response pressure transducers and a slanted hot-wire, respectively. The time-dependent ensemble-averages of these distributions have been obtained phase-locked to both the rotor and the stall cell rotation using a ''double phase-locked averaging technique'' developed by the authors. The structures of the two stall cells are compared: The short length-scale stall cell is characterized by a concentrated vortex spanning from the casing wall ahead of the rotor to the blade suction surface. In the long length-scale stall cell, the separation vortices go upstream irregularly when blade separation develops in the front half of the cell, and re-enter the rotor on the hub side in the rear half of it. The unsteady aerodynamic force and torsional moment acting on the blade tip section have been evaluated from the time-dependent ensemble-averages of the casing wall pressure distribution. The force fluctuation due to the short length-scale cells is somewhat smaller than that for the long length-scale cell. The blade suffers two peaks of the force during a period of the short length-scale cells passing through it. The moment fluctuation for the short length-scale cells is considerably larger than that for the long length-scale cell. [DOI: 10.1115/1.1326085]

1 Introduction

In ordinary rotating stall in axial compressors, a single or a couple of long length-scale stall cells rotate at 30 to 50 percent of rotor speed. Occasionally, however, many short length-scale stall cells happen to appear before the compressor falls into deep stall. One cell covers only a couple of blades. They appear at intervals of 4.5 to 5 times a blade spacing. They rotate at 70 to 80 percent of rotor speed.

So far, occurrence of the multiple short length-scale stall cells has been reported in the low speed compressor test rigs [1,2]. Recently, however, Day et al. [3] suggested that they could occur in a phenomenon designated high-frequency stall inception of aero-engine type compressors operating at full speed. In a multistage compressor under a mismatched condition, they exist only in a stage and do little harm to the overall performance, since the pressure drop of the stage is small [2]. Therefore, compressors might be operated without knowing the occurrence of them. There seems to be a practical need for a better understanding of the multiple short length-scale stall cells because it is feared that blades might suffer damage from them.

In a low-speed compressor test rig at Kyushu University, the multiple short length-scale stall cells appeared under a mild stall condition and turned into a long length-scale cell under a deep stall condition. Then, the structure of the short length-scale cell was investigated by a ''double phase-locked averaging'' (DPLA) technique developed by the authors, with which the time-dependent ensemble-averages of the three-dimensional flow upstream and downstream of the rotor and the pressure distributions on the casing wall were obtained. As a result, a tornado-like vortex model was proposed for the short length-scale stall cell [4].

In this paper, comparative studies between the short length-scale stall cell (SLSC) and the long length-scale stall cell (LLSC) have been made for a better understanding of the SLSC.

2 Experimental Facility and Instrumentation

The measurements reported herein were performed in a low-speed research compressor at Kyushu University. A schematic view of the test section is shown in Fig. 1. It consists of a test rotor, an upstream and a downstream stator with the same geometries, an inlet guide vane row with the same exit flow angle as the rotor, and an outlet guide vane row with an axial outlet flow condition. The diameter, the hub/tip ratio, the number of blades, and the tip clearance of the rotor are 449 mm, 0.7, 24, and 0.5 mm, respectively. The two stators have 22 cantilevered blades with tip clearance of 0.5 mm. The compressor stage is designed for a constant whirl angle of absolute flow at the rotor inlet (stator exit) and 0.5 reaction at the mid span. The details for the design specifications and the bladings are shown in Inoue et al. [4].

The stage performance is evaluated for the combination of the rotor and the downstream stator. A reference pressure transducer is mounted on the casing wall near the rotor leading edge to observe inception and evolution of stall cells. The reference pressure trace for the stall cells is obtained by removing the blade passing frequency through a low-pass filter.

Surveys of the flow field were made by a single slanted hot-wire at locations 1, 2, and 3 upstream of the rotor and at location 4 downstream of the rotor, as shown in Fig. 1. The survey line 1 is in the radial direction 25.6 mm upstream of the rotor leading edge at the blade tip, lines 2 and 3 are along the rotor leading edge at 14.2 and 8 mm upstream of it, and line 4 is along the rotor trailing edge at 8 mm downstream of it. The casing wall pressure distributions were measured by 14 pressure transducers (Kulite XCS-062), which were mounted on the casing wall to cover the measuring points from 24.6 mm upstream of the rotor leading edge to 20.4 mm downstream of the rotor trailing edge.

Contributed by the International Gas Turbine Institute and presented at the 45th International Gas Turbine and Aeroengine Congress and Exhibition, Munich, Germany, May 8–11, 2000. Manuscript received by the International Gas Turbine Institute February 2000. Paper No. 2000-GT-425. Review Chair: D. Ballal.

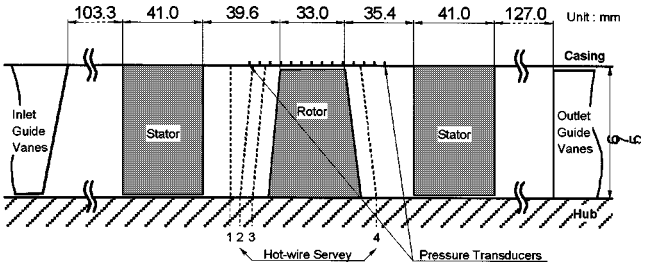

Fig. 1 Schematic view of test section and measuring locations

At each fixed location of the hot-wire sensor and the pressure transducers, the data acquisition was made for 600 circumferential sampling points per one rotor rotation, during 800 rotations by a phase-locking sampling system. At the same time, the low-pass filtered reference pressure was acquired to obtain the reference position of a stall cell relative to a blade. The DPLA technique was applied to these data to get the time-dependent average phase-locked to both the rotor and the cell rotation. That is, these data were divided into 25 groups corresponding to relative circumferential positions of the stall cell in a blade spacing. Thus, conditional sampling and averaging were made synchronously with the rotor and the cell rotation. Details of the DPLA technique are described in Inoue et al. [4].

3 Experimental Results and Discussion

3.1 Characteristics of Test Compressor Stage. Figure 2 shows the pressure-rise characteristics of the test compressor stage. When the flow rate is reduced, stall inception of the rotor is detected in the low-pass filtered reference pressure trace at point *A*, where the flow rate decreases by itself to point *B* without any throttling. In the flow range *BC*, the compressor can run at a fixed flow rate if the throttle is closed carefully. The multiple SLSCs occur in this range. This condition is called ''mild stall'' in the present paper. When the throttle is closed to point *C*, the flow rate jumps suddenly to point D and the compressor falls into a deep stall condition with a LLSC.

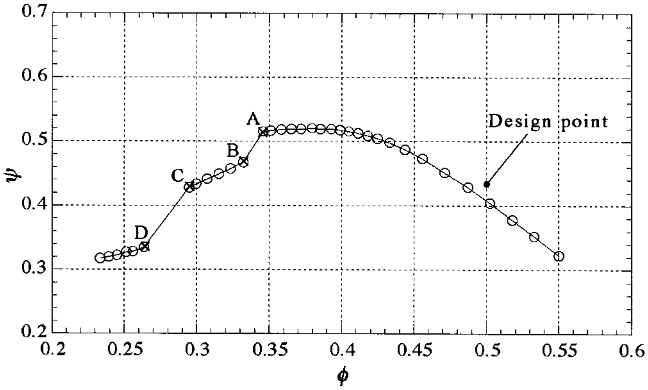

Fig. 2 Pressure-rise characteristics of compressor stage tested

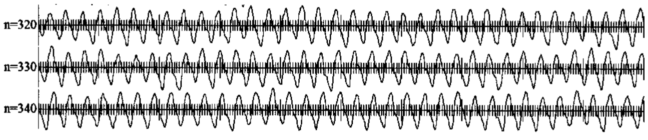

(a) mild stall condition

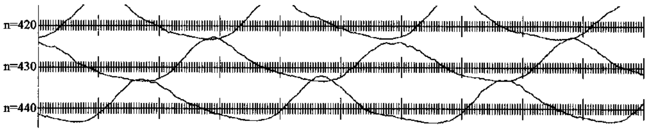

(b) deep stall condition

Fig. 3 Low pass filtered pressure traces near the rotor leading edge

3.2 Low-Pass Filtered Pressure Traces. Figures 3(*a*) and 3(*b*) show the reference pressure traces near the rotor leading edge under the mild and deep stall conditions. The short and long vertical lines on each horizontal line represent blade passing and rotor rotations, respectively, and *n* represents the rotor rotation corresponding to the left vertical line. The periodic short and long waves observed in Figs. 3(*a*) and 3(*b*) are caused by the SLSC and LLSC, respectively. The wave shape of SLSC is spiky in comparison with the LLSC. The period of the wave is evaluated by

$$t_c/t_R = 1/(\lambda Z_c) \tag{1}$$

where λ is a fraction of the cell speed to the rotor speed, Z_c is the number of cells, and t_R is a period of rotor rotation. Since the five cells rotate at 72.2 percent of the rotor speed in mild stall and a single cell rotates at 29.3 percent of rotor speed in deep stall [4], t_c/t_R is 0.277 for the SLSC and 3.41 for the LLSC, respectively.

According to the existing reports [1–4], the multiple SLSCs appear at intervals of 4.5~5 times a blade spacing and rotate at 70~80 percent of rotor speed. Then, for the rotor with the number of blades being Z_b, the following equation will be useful to discriminate the multiple SLSCs in the low-pass filtered pressure trace.

$$t_c/t_R \approx (6\sim 7)/Z_b \tag{2}$$

3.3 Flow Fields Phase-Locked to Stall Cells. So far, the flow structure of rotating stall cells has been investigated based on the ensemble-averaged data phase-locked to the cell rotation [5–8]. Such phase-locked averaging can be made by taking averages synchronously with the periodic waves shown in Fig. 3.

Figures 4 and 5 show the phase-locked averages of the flow field for the SLSC at $\phi = 0.31$ and the LLSC at $\phi = 0.25$, respectively. In both figures, the upper and lower frames show the contour maps of the upstream and downstream axial velocity component at measuring locations 3 and 4, respectively. The top and bottom horizontal lines in these frames correspond to the casing and hub walls. The axial velocity component normalized by the blade tip speed is indicated by a color scale. The solid contour lines represent an axial velocity of 0. A number is assigned to the top horizontal line at intervals of a blade spacing to identify the circumferential location. The vertical dotted line denotes the reference position of stall cell, at which the pressure trace crosses the horizontal line from bottom to top in Fig. 3.

The middle frame shows the pressure distribution on the casing wall. The casing wall pressure is represented by the pressure coefficient, defined as

$$C_p = (P_w - P_{oi})/(\rho u_t^2/2) \tag{3}$$

where P_{oi} and ρ are the pressure and the air density of the inlet chamber, and u_t is the blade tip speed. The circumferential location of blades drawn on the picture is arbitrary since this map is not phase-locked to the rotor rotation. The axial locations of the hot-wire survey are indicated by arrows 3 and 4.

Looking at the axial velocity distributions upstream and downstream of the rotor in Figs. 4 and 5, a type of stall cell seems to be part-span for both the SLSC and LLSC. There seems to be no substantial difference between the SLSC and LLSC except circumferential length occupied by a reverse flow. However, a region of considerably higher axial velocity appears immediately to the left of the SLSC upstream of the rotor in Fig. 4, while a high axial velocity region is located near the hub side away from the LLSC in Fig. 5.

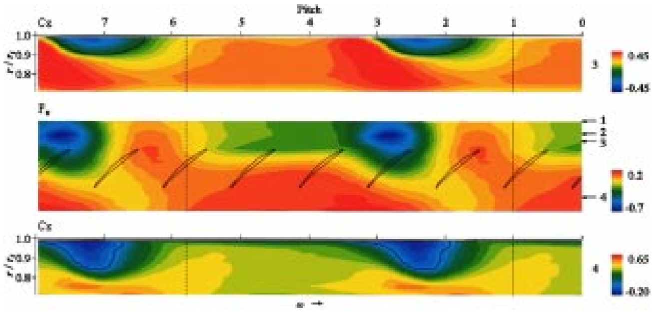

Fig. 4 Contour maps of upstream and downstream axial velocity components and casing wall pressure phase-locked to SLSC under mild stall conditions

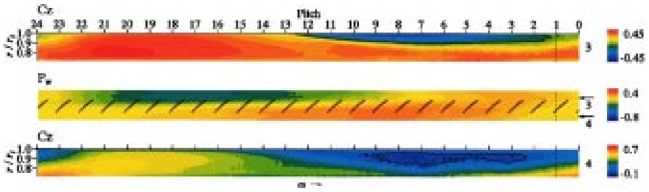

Fig. 5 Contour maps of upstream and downstream axial velocity components and casing wall pressure phase-locked to LLSC under deep stall condition

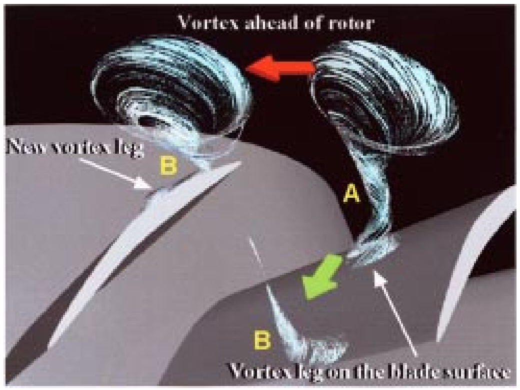

Fig. 6 Illustration of a flow model for SLSC

The most substantial difference between the SLSC and LLSC is observed in the pressure distributions on the casing wall. In the case of the LLSC (Fig. 5), the static pressures upstream and downstream of the rotor in the unstalled range (circumferential location from 16 to 21 in the number assigned on the top) are lower than those in the stalled range (from 2 to 12). The pressure changes gradually from the unstalled range to the stall range. This tendency is consistent with the data measured by Day and Cumpsty [5]. In the case of the SLSC (Fig. 4), however, the bubblelike region with significantly lower pressure is observed just upstream of the rotor. It lies between the reverse flow region and the considerably higher axial velocity region upstream of the rotor. Obviously, the structure of the SLSC is different from the LLSC.

3.4 Time-Dependent Ensemble-Averaged Flow Fields

3.4.1 Structure of SLSC. In the previous paper [4], the present authors developed the double phase-locked averaging (DPLA) technique, with which the time-dependent ensemble-averages of a flow field could be obtained phase-locking to both the rotor and the stall cell rotation. By applying this technique to the measured data on the casing wall pressure and the velocities at the measuring locations 1 and 4, animations were made from the 25 time-dependent ensemble-averages to observe flow behavior of the SLSC. As a result, a model for the SLSC was proposed, in which the bubble of significantly lower pressure shown in Fig. 4 results from a vortex having a leg on the blade suction surface as shown in Fig. 6.

A physical interpretation for this model was as follows: According to vortex theory, bound vortices are distributed on an unstalled blade surface, which bring about a blade circulation (lift force). When leading edge separation occurs, the separation vortex is released from the blade suction surface to reduce the blade circulation. In the case of part-span stall, the separation vortex appears only near the casing while the vortex lines are attached to the blade surface in the hub region. According to continuity of the vortex lines, they must separate from the blade suction surface to link to the separation vortex near the casing. The vortex tube consisting of these separated vortex lines therefore spans from the blade suction surface to the casing wall. The casing-side end of the vortex tube moves ahead of the rotor to form the low pressure bubble and travels in the circumferential direction due to interaction with the blades. Thus, the vortex bubble with a leg is generated as indicated by *A* in Fig. 6. As it travels, the vortex leg is stretched and finally broken (*B* in Fig. 6). The broken vortex leg flows downstream of the rotor to generate a reverse flow region at the rotor exit. On the other hand, a local separation occurs on the next (left) blade suction surface near the leading edge due to increase in the angle of attack, from where vortex lines are released

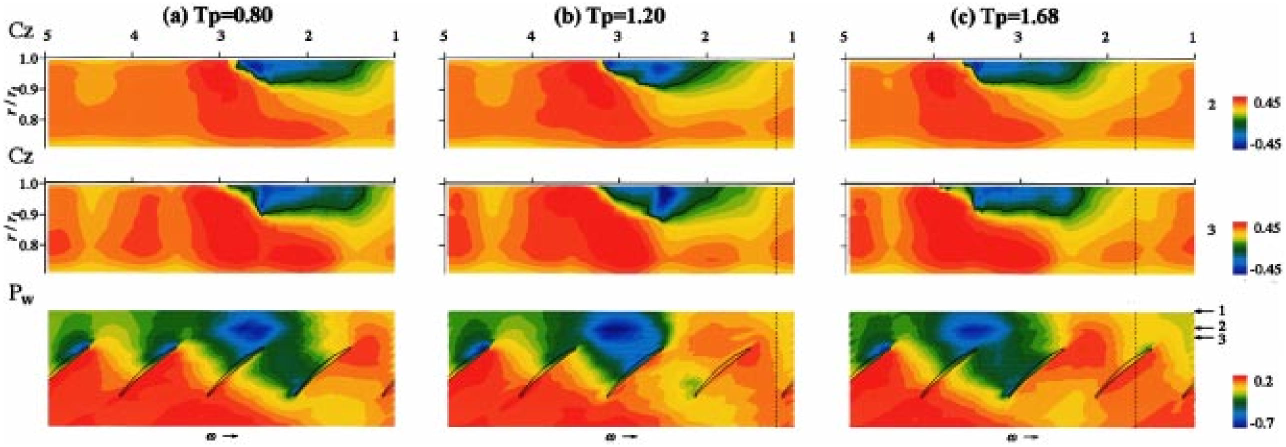
(a) Tp=0.80 (b) Tp=1.20 (c) Tp=1.68

Fig. 7 Time-dependent ensemble-averages of axial velocity distributions upstream and downstream of rotor, and casing wall pressure distribution for SLSC

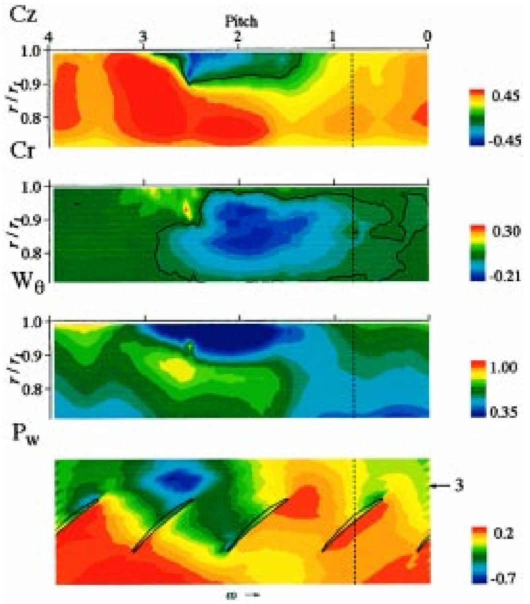

Fig. 8 Time-dependent ensemble-averages of three velocity components 8 mm upstream of rotor

in the flow. When the vortex bubble approaches the blade after the vortex leg is broken, these vortex lines are swallowed into the bubble. The separation grows to a large focus type separation similar to a tornado, and a new vortex leg is generated (*B* in Fig. 6).

To verify this model, additional measurements were made at measuring locations 2 and 3, which correspond to the center of vortex bubble and to a location between the vortex bubble center and the rotor leading edge, respectively. In Figs. 7(*a–c*), the time-dependent ensemble-averages of the axial velocity distributions at the two upstream locations 2 and 3 are shown above the casing wall pressure distributions for three different positions of the stall cell relative to a blade. T_p denotes the relative circumferential position of the stall cell, which is represented by a vertical dotted line in the figures for $T_p = 1.20$ and 1.68.

For $T_p = 0.80$, the velocity distribution near the vortex center is revealed by a strong reverse flow located on the right-hand side of the axial velocity deficit region and a high axial flow immediately to the left of it at measuring location 2 in Fig. 7(*a*). A strong reverse flow induced by the vortex leg can be observed clearly in the axial velocity distribution at measuring location 3. The vortex immerses its leg near the midspan. When the vortex bubble travels with its leg stretching ($T_p = 1.20$), a strong reverse flow region splits into two pieces at the measuring location 2 as shown in Fig. 7(*b*): The one on the left-hand side travels with the vortex bubble, while the one on the right-hand side stays at the same circumferential location. The former is associated with the vortex center and the latter is induced by the vortex leg. The reverse flow becomes stronger at measuring location 3 because of stretch of the vortex leg. When the vortex leg is broken and flows downstream, the induced reverse flow becomes weaker at measuring locations 2 and 3 in Fig. 7(*c*). A new vortex leg stretching to the next blade leading edge can be seen at measuring location 3 for $T_p = 1.68$.

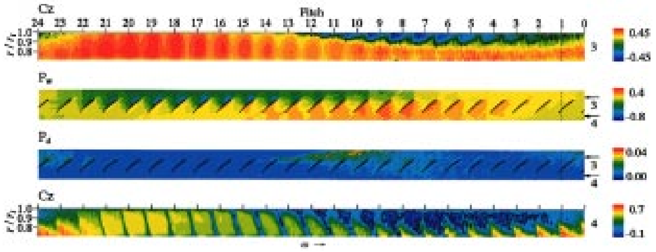

Fig. 9 Ensemble-averaged axial velocity distributions upstream and downstream of rotor as well as distributions of ensemble-averaged pressure and pressure fluctuation on the casing wall for LLSC

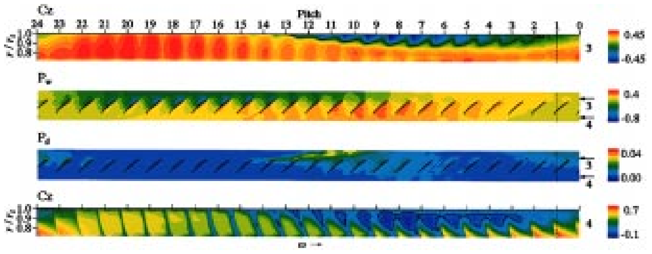

Fig. 10 Time-independent ensemble-averages of axial velocity component upstream and downstream of rotor as well as distributions of ensemble-averaged pressure and pressure fluctuation on the casing wall for LLSC

Figure 8 shows the distributions of three velocity components at the location 3 for $T_p = 0.80$. The velocity components normalized by the blade tip speed are indicated by the color scale. The relative tangential velocity is taken as positive when it is in the opposite direction of the rotor rotation. As shown in the radial and tangential velocity distribution, a vortical flow can be seen around the vortex leg.

The above-mentioned behavior can be seen more clearly in the animations (http://fe.mech.kyushu-u.ac.jp/kaiten/kaiten.html). They are consistent with the model shown in Fig. 6.

Hoying et al. [9] observed a similar vortex ahead of a rotor in their numerical simulation for spiketype stall inception, and found that it was caused by a tip clearance vortex spilling upstream of the rotor. This fact does not conflict with the model described above. The multiple SLSCs are in a developed state, while the stall inception is a transient event. Although the vortex immersed its leg near midspan in the present experiment, the leg might be located near the tip at the onset. It could be located at blade tip surface when the tip clearance is large. According to the vortex theory, the tip clearance vortex is nothing but a kind of separation vortex, which consists of vortex lines separated from blade tip instead of suction surface.

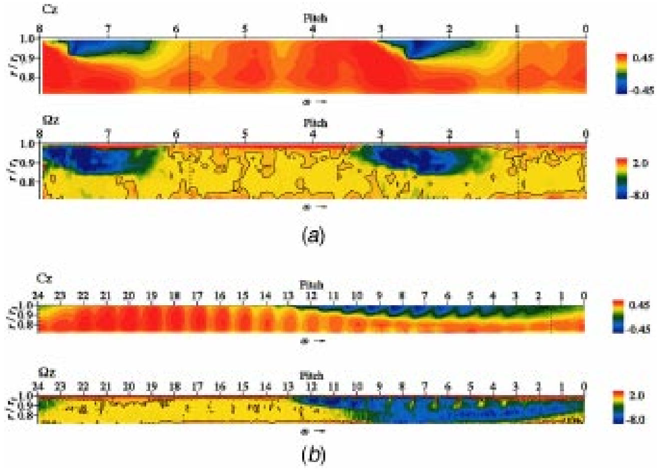

Fig. 11 Distributions of axial vorticity and velocity components upstream of rotor for: (*a*) SLSC; (*b*) LLSC

3.4.2 Structure of LLSC. Although the LLSC extends in the axial direction through the upstream and downstream stator under the deep stall condition, the discussion in the present paper is restricted to the measurement data of the velocities upstream and downstream of the rotor, and of the casing wall pressure. The DPLA technique has been also applied to these measurement data. Figure 9 shows the distributions of the ensemble-averaged axial velocity component upstream and downstream of the rotor as well as the distributions of the ensemble-averaged pressure and the pressure fluctuation on the casing wall for $T_p = 1.0$ at the flow coefficient of $\phi = 0.25$. The pressure fluctuation has been evaluated by

$$\overline{p'^2} = (\rho u_t^2/2)$$

where p' is the deviation from the ensemble-averaged pressure at each measuring point. Comparing with Fig. 5, this figure gives information on a flow field around each blade. Unstalled blades (from 16 to 21 in the number assigned on the top) and stalled blades can be easily distinguished. However, the contour lines are very jagged because the number of data at each measuring point is insufficient (only about 20) due to an overly long period of the LLSC (about 12 times of the SLSC) for the limitation of measuring time and data logging capacity. It was difficult to find substantial change in the time-dependent ensemble-averaged flow fields with various values of T_p (refer to the animation at http://fe.mech.kyushu-u.ac.jp/kaiten/kaiten.html). This fact suggested that, within accuracy of the experiments, the structure of LLSC was hardly affected by the circumferential location of the stall cell relative to a blade.

Then, the ensemble-averaging was done by phase-locking to the rotor blade for $T_p = 0.0 \sim 1.0$ to obtain smoother contour maps. The cell location is loosely phase-locked to one blade spacing. The results are shown in Fig. 10. These distributions are time-independent averages because we ignored effect of the relative location of the stall cell in a blade spacing, but still give useful information on the flow field around each blade. There is no substantial difference between Figs. 9 and 10. The variation of the flow field around a blade with time can be seen by looking at the blades from left to right in order.

In the unstalled blades in Fig. 10, a low-pressure region near the leading edge of the suction surface of each blade grows and the blade wake becomes thicker as the stall cell approaches, due to increase in angle of attack (from 21 to 16). Occurrence of local separation on a blade suction surface can be recognized by reduction of the low-pressure region near the blade leading edge and appearance of a reverse flow in each blade wake (from 15 to 13). Then, the reverse flow develops gradually downstream of the rotor in the corner between the casing and the blade suction surface in the front (left) half of the stall cell (from 13 to 7). In this range, the casing wall pressure at the rotor exit increases and the reverse flow region upstream of the rotor enlarges. At the center of cell (7) the reverse flow region in the wake reaches near the blade root, and it is hard to say that the LLSC is part-span. In the rear (right) half of the stall cell (from 7 to 1), the reverse flow regions upstream and downstream of the rotor diminish gradually, and the casing wall pressure at the rotor inlet increases. The pressure increases little through the rotor in this range.

Unlike the SLSC, there is no significantly low-pressure bubble ahead of the rotor. Instead, a strong pressure fluctuation region can be observed ahead of the rotor when the blades enter stall (from 13 to 8). It moves upstream as the low pressure region near the leading edge diminishes. According to a recent unsteady two-dimensional numerical simulation of rotating stall with long length-scale [10], the pressure fluctuation ahead of the rotor is associated with generation of multiple vortices with relatively short length-scale. Similar vortices are shown in an instantaneous flow field calculated by Saxer-Felici et al. [11]. These must be separation vortices to reduce blade circulation according to the vortex theory, and should occur in the experiments. In the case of LLSC, the vortices may be generated irregularly to cause the strong pressure fluctuation. Looking at Fig. 10, the locally lowest pressure region near the rotor leading edge separates from a blade suction surface and shifts upstream (from 11 to 7). This phenomenon seems to correspond to these separation vortices. However, they may not form a concentrated vortex like the SLSC, so that the low-pressure bubble cannot be observed in the ensemble-averaged pressure distribution on the casing. Existence of irregular short length-scale vortices will be discussed in the following section.

As mentioned above, the flow field around a blade changes gradually when the blade enters and goes out of stall in the ensemble-averaged distribution. The stall extends in the spanwise direction gradually in the front part of the cell, and shrinks in the rear part. In other words, the stall is full-span in the cell center while it is part-span on both sides of cell in the case of relatively low hub/tip ratio (=0.7)

In the present experiment, the lower the flow rate, the larger part of the circumference the LLSC occupied (the figures are omitted). The number of blades with full-span stall increased as the flow rate was reduced. When the flow rate was reduced further ($\phi = 0.15 \sim 0.07$), a signal of rotating stall disappeared in the low-pass filtered reference pressure. In this range, the whole circumference was covered by part-span stall near the casing and positive axial velocity was observed near the hub both upstream and downstream of the rotor. With further throttling, reverse flows occurred near the casing at the rotor inlet and near the hub at the rotor exit: namely the air entered from the hub side and discharged from the casing side of the rotor.

3.4.3 Vortices Upstream of Rotor. Figures 11(*a*) and (*b*) show the distributions of axial vorticity component upstream of the rotor for the SLSC and the LLSC together with axial velocity distributions. The axial vorticity component is evaluated based on the smooth time-independent velocity distribution, and normalized based on the rotor speed and the chord length at the blade tip:

$$\Omega_z = \frac{l_t}{u_t r}\left[\frac{\partial(rc_\theta)}{\partial r} - \frac{\partial(c_r)}{\partial r}\right] \tag{4}$$

where r and θ are the radial and tangential coordinates, and c_r and c_θ are the radial and tangential components of absolute velocity. In both figures, the high positive (anticlockwise) vorticity can be seen in the casing wall boundary layer, and the negative (clockwise) vorticity in the part-span stall cell. In the case of SLSC, a region of highly negative vorticity is restricted within the reverse flow region and near the vortex leg. Negative vorticity is hardly observed in the incoming flow. This phenomenon suggests that the separated vortex lines from the blade surface form the concentrated standing vortex ahead of the rotor. In the case of LLSC, the reverse flow has highly negative vorticity, especially when blade separation is developed in the front half of the stall cell (from 9 to 12). Highly negative vorticity can be seen also in the incoming flow on the hub side of the rear half (from 1 to 8). This fact suggests that the separated vortices move upstream with the reverse flow near the casing and re-enter the rotor from the hub side to form a large scale stall cell.

If the irregular short length-scale vortices are included in the highly negative vorticity region, some evidence should be found by a wavelet transform of the casing wall pressure trace upstream of the rotor, because it gives useful information of instantaneous disturbances [12]. The wavelet transform of a pressure signal is defined by

$$W(a,b) = \frac{1}{\sqrt{a}}\int \Psi(T)p(T)dt \tag{5}$$

where $\Psi(T)$ is a wavelet function, a and b are the scaling and translation parameters, and $T = (t-b)/a$. When an appropriate function is chosen as $\Psi(T)$, a large value of $W(a,b)$ implies that

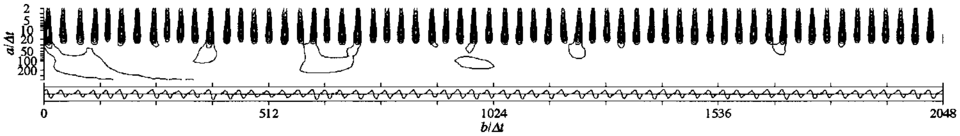

(a) mild stall condition.

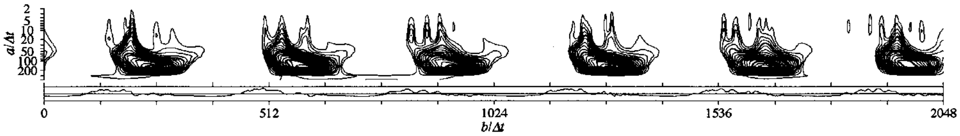

(b) deep stall condition.

Fig. 12 Wavelet transform for low-pass filtered pressure trace upstream of rotor

the disturbance with scale a exists locally around b. In the present study, $\Psi(T)=-\sin(2T)\exp(-T^2)$ was used for a spiky low-pass filtered pressure signal of a vortex.

Figures 12(a) and 12(b) show the contour maps of $W(a,b)$ for the SLSC and LLSC. The abscissa is $b/\Delta t$ and the ordinate is a logarithmic scale of $a/\Delta t$ in the opposite direction, where Δt corresponds to 1/120 of a rotor rotation. For the SLSC, the maximum values of $W(a,b)$ are located at $a/\Delta t=10$ at equal intervals of $b/\Delta t\approx 33$. This means that the size of SLSC is on the order of two blade spacings since the rotors have 24 blades ($a\approx 10\Delta t=1/12$ of a rotor rotation) and they appear at intervals of about 0.28 of a rotor rotation ($b\approx 33\Delta t=0.2175$). For the LLSC, the maximum values of $W(a,b)$ are located at $a/\Delta t\approx 100$ at equal intervals of $b/\Delta t\approx 410$. This means that the size of LLSC is on the order of the rotor circumference and they appear at intervals of about 3.4 rotor rotations. One should notice that notched disturbances are overlapped on the large-scale disturbance at $a/\Delta t\approx 10\sim 20$. Their size and the intervals are irregular. They appear much more when the blades enter stall. These disturbances are considered to be caused by the irregular short length-scale vortices moving upstream.

3.5 Force and Moment Acting on a Blade at Tip. A rotor blade suffers repeated fluctuating load associated with rotating stall propagation. The frequency of the stall cells passing through a rotor blade is

$$f_c=(1-\lambda)Z_cN_R \qquad (6)$$

where λ is a fraction of the rotating cell speed to the rotor speed, Z_c is the number of cells, and N_R is the rotor speed.

The unsteady aerodynamic force and the torsional moment acting on the blade tip section have been evaluated from the time-dependent ensemble-averages of the casing wall pressure distribution in the mild stall condition ($\phi=0.31$) and the deep stall condition ($\phi=0.25$). Figure 13 shows the variations of the aerodynamic force normal to the blade chord with time. The aerodynamic force is represented in dimensionless form based on the chord length and the equivalent dynamic pressure for the blade tip speed. The abscissa is the dimensionless time normalized by a period of rotor rotation. Estimating the periods of the multiple SLSCs and the single LLSC based on Eq. (6), they correspond to 0.72 and 1.41, respectively, in the abscissa.

Under the deep stall condition, the aerodynamic force increases in the unstalled range as the LLSC approaches ($t/t_R=0.2-0.5$ in Fig. 13). Then, it decreases in the range of $t/t_R=0.5-0.8$ due to development of local separation on the blade suction surface (refer to circumferential locations 15 to 11 in Fig. 10) and becomes flat in the range of $t/t_R=0.8-1.0$ when the reverse flow develops upstream of the rotor (11 to 7 in Fig. 10). In the rear half of the LLSC, it decreases again ($t/t_R=1.0-1.4$) and becomes negative ($t/t_R=0-0.1$: corresponding nearly to 2 to 1 in Fig. 10).

Under the mild stall condition, it is interesting that the blade suffers two peaks of the force during a period of the multiple SLSCs. The first peak (at $t/t_R\approx 0.3$ or 1.0 in Fig. 13) acts on the unstalled blade and the second sharp peak (at $t/t_R\approx 0.6$ or 1.3) is associated with the vortex leg standing on the blade suction surface. The maximum force due to the SLSC is almost the same as that in the deep stall. Positive force acts on the blade at all times in the mild stall, while negative force acts for a short time in the deep stall. The amplitude of the fluctuation force due to SLSC is about 70 percent of that for LLSC.

Figure 14 shows the variations of the torsional moment around a geometric center of the blade tip section. The ordinate is the dimensionless moment based on the chord length and the equivalent dynamic pressure for the blade tip speed. The features of the variation are quite different between the mild and the deep stall. In the deep stall, the blade suffers a peak of the negative (anticlockwise) moment when the separation on the blade suction surface develops and the reverse flow occurs upstream of the blade (near $t/t_R=0.7$). The torsional moment varies from -0.05 to 0.02 in the LLSC. On the other hand, in the case of mild stall, the blade suffers a sharp peak of positive (clockwise) moment in the cell when the vortex leg is located on the blade suction surface near the trailing edge. The maximum absolute value is about one and half as high as that suffered in the deep stall.

In deep stall with a single LLSC, the frequency of the fluctuating force and moment acting on a blade is $f_{c,\mathrm{LLSC}}\approx(0.5\sim 0.7)N_R$ since it rotates at 30 to 50 percent of rotor speed ($\lambda\approx 0.3-0.5$). On the other hand, the multiple SLSCs appear at intervals of 4.5 to 5 times of a blade spacing and rotate at 70 to 80 percent of rotor speed in the mild stall. Denoting the number of rotor blades by Z_b, the frequency of the fluctuating moment becomes $f_{c,\mathrm{LLSC}}\approx(0.5\sim 0.7)N_RZ_R$ since $Z_c\approx Z_b/(4.5\sim 5)$ and 1 $\approx 0.7\sim 0.8$ in Eq. (6). The frequency of fluctuating force is twice

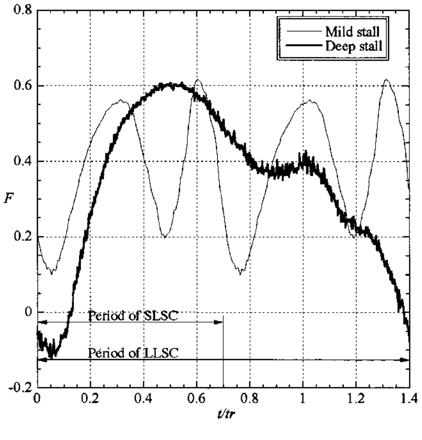

Fig. 13 Fluctuating force acting on a blade tip section

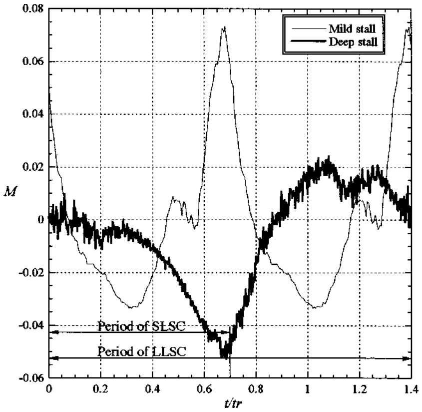

Fig. 14 Fluctuating moment acting on a blade tip section

as high as the moment. These frequencies may coincide with a natural blade frequency, if multiple SLSCs happen to occur.

A compressor is never operated for hours under a deep stall condition where the long length-scale cell is rotating. However, it is feared that it might be operated without knowledge of the occurrence of multiple short length-scale stall cells in one of the stages, because the overall pressure does not decrease in many cases (especially in a mismatched condition). A warning for occurrence of the multiple short length-scale cells should be emphasized.

4 Conclusions

So far rotating stall with multiple short length-scale cells was considered to be a phenomenon that happened only in low-speed axial compressor test rigs. However, the high-frequency stall inception in two aero-engine type compressors operating at full speed [3] suggested that these phenomena might occur in high-speed compressors. It was thought to be necessary to clarify their nature.

In a low-speed compressor test rig at Kyushu University, multiple short length-scale stall cells appeared under a mild stall condition and developed into a long length-scale cell under a deep stall condition. Then comparative studies between short and long length-scale stall cells were made for a better understanding of the short length-scale stall cell. The results are summarized as follows:

1 Occurrence of the multiple short length-scale stall cells can be detected by the low-pass filtered pressure trace on the casing wall near the rotor leading edge. The shape is spiky and the period is short in comparison with the long length-scale stall cell. The period can be roughly estimated by Eq. (2).

2 In the ensemble-averaged pressure distribution phase-locked to the rotating stall cell, the short length-scale stall cell is characterized by a bubble of significantly lower pressure traveling ahead of the rotor. On the other hand, in the case of the long length-scale stall cell, the static pressures upstream and downstream of the rotor in the stalled range are higher than those in the unstalled region. The pressure changes gradually from the unstalled range to the stall range.

3 The short length-scale stall cell consists of a tornado-like separation vortex, which spans from the casing wall ahead of the rotor to the blade suction surface.

4 In the long length-scale stall cell, the blades enter and exit stall gradually. The separation vortices, which should be generated from the blades, are considered to move upstream with the reverse flow and reenter the rotor to form a large scale stall cell.

5 The unsteady aerodynamic force and torsional moment acting on the blade tip section have been evaluated from the time-dependent ensemble-averages of the casing wall pressure distribution. The force fluctuation due to the short length-scale cells is somewhat smaller than that for the large length-scale cell. The blade suffers two peaks of force during a period of the short length-scale cells. The moment fluctuation for the short length-scale cells is considerably larger than that for the large length-scale cell.

Nomenclature

c_r = radial velocity component
c_z = axial velocity component
c_θ = tangential velocity component
C_p = pressure coefficient
f_c = frequency of fluctuating blade force or moment
F = dimensionless force normal to blade chord
l_t = chord length at blade tip
M = dimensionless torsional moment around geometric center of blade section
n = rotor rotation
p_{0i} = stagnation pressure at inlet
p_w = casing wall pressure
p' = deviation of pressure from ensemble-average
r = radius
t = time
t_c = period of rotating stall cell
t_R = period of rotor rotation
T_p = dimensionless circumferential position of stall cell relative to a blade
u_t = blade tip speed
$W(a,b)$ = wavelet transform, where a and b are scaling and translation parameters
Δt = reference time scale in wavelet analysis
ϕ = flow rate coefficient
ψ = pressure coefficient
ρ = air density of air
Ω_z = axial vorticity component
θ = tangential component

References

[1] Mathioudakis, K., and Breugelmans, F. A. E., 1985, ''Development of Small Rotating Stall in a Single Stage Axial Compressor,'' ASME Paper No. 85-GT-227.

[2] Silkowski, P. D., 1995, ''Measurement of Rotor Stalling in a Matched and a Mismatched Multistage Compressor,'' GTL Report, No. 221, Gas Turbine Laboratory, Massachusetts Institute of Technology.

[3] Day, I. J., Breuer, T., Escuret, J., Cherrett, M., and Wilson, A., 1999, ''Stall Inception and the Prospects for Active Control in Four High Speed Compressors,'' ASME J. Turbomach., **121**, pp. 18–27.

[4] Inoue, M., Kuroumaru, M., Tanino, T., and Furukawa, M., 2000, ''Propagation of Multiple Short Length-Scale Stall Cells in an Axial Compressor Rotor,'' ASME J. Turbomach., **122**, pp. 45–53.

[5] Day, I. J., and Cumpsty, N. A., 1978, ''The Measurement and Interpretation of Flow Within Rotating Stall Cells in Axial Compressors,'' J. Mech. Eng. Sci., **20**, pp. 101–114.

[6] Das, D. K., and Jiang, H. K., 1984, ''An Experimental Study of Rotating Stall in a Multistage Axial-Flow Compressor,'' ASME J. Eng. Gas Turbines Power, **106**, pp. 542–551.

[7] Poensgen, C. A., and Gallus, H. E., 1996, ''Rotating Stall in a Single-Stage Axial Flow Compressor,'' ASME J. Turbomach., **118**, pp. 189–196.

[8] Palomba, C., Puddu, P., and Nurzia, F., 1998, ''3D Flow Field Measurement Around a Rotating Stall Cell,'' ASME Paper No. 98-GT-594.

[9] Hoying, D. A., Tan, C. S., Huu, Duc Vo, and Greitzer, E. M., 1999, ''Role of Blade Passage Flow Structures in Axial Compressor Rotating Stall Inception,'' ASME J. Turbomach., **121**, pp. 735–742.

[10] Outa, E., and Kato, D., 1998, ''N-S and Experimental Aspects of a Developed Part-Span Stall in an Axial Stage of a Rotor and Stator Cascades,'' Proc. US-Japan Seminar, Abnormal Flow Phenomena in Turbomachinery, Osaka.

[11] Saxer-Felici, H. M., Saxer, A., Inderbitzin, A., and Gyarmathy, G., 1999, ''Prediction and Measurement of Rotating Stall Cells in an Axial Compressor,'' ASME J. Turbomach., **121**, pp. 365–375.

[12] Farge, M., 1992, ''Wavelet Transforms and Their Applications to Turbulence,'' Annu. Rev. Fluid Mech., **24**, pp. 395–457.

Discussion: ‘‘Comparative Studies on Short and Long Length-Scale Stall Cell Propagating in an Axial Compressor Rotor’’ (Inoue, M., Kuroumaru, M., Tanino, T., Yoshida, S., and Furukawa, M., 2001, ASME J. Turbomach., 123, pp. 24–30)

N. A. Cumpsty

One is always pleased to see another paper from the compressor facility in Kyushu and the authors are to be congratulated on the meticulous measurements they have made. There are a few points I would like to make relating to their findings.

First, for clarity, I would like to address part-span stall and stall inception. In the introduction to the present paper it is stated that Day et al. [1] suggested that high-frequency stall inception was the same occurrence as part-span stall. I am sure that this must be incorrect. High-frequency inception (often known as spikes) can lead to part-span or full-span stall, or even to surge, depending on the nature of the compression system. However, the spikes are part of a transient phenomenon of inception, whereas the stall cells are a nominally steady pattern.

Part-span stall is actually the most common type of rotating stall. It occurs in most high-speed multistage compressors when they are run at speeds below the design value because of the mismatching from front to back that occurs at this condition. At reduced rotational speeds the front stages are forced to pass too little volume flow, and therefore stall, but the rear stages are forced to pass flow above the design value and are therefore very stable. When only the first few stages are stalled, the stall cells in the front stages must therefore die out before the rear stages, and this puts constraints on the type of stall that can form. In fact it requires that the stall be part-span with a relatively large number of cells. The large number of cells (more specifically the short wavelength in the circumferential direction) makes the potential effects decay rapidly in the axial direction; it also facilitates circumferential mixing to uniform of the vortical part of the cell structure. The part-span nature means that the blocked region behind each cell can relax to fill the whole height of the annulus downstream of the stall cell. This means that some flow can pass through the stalled blade passages so that at the same circumferential position there can be stalled flow in the front stages and unstalled flow in the rear stages. Multistage compressors designed for experiments at low speed tend to behave differently, since compressibilty is largely absent, and if the stages are identical all the stages stall more or less simultaneously. As a result, low-speed multistage research compressors normally stall as full-span cells, with only one or two cells around the circumference. In low-speed single stages or isolated rotors the stalling behavior is not the same as multistage machines; part-span stall is more common, a difference that was brought out by Day [2].

The pressure field associated with a short-length stall cell is evident in Figs. 5 and 7, while for a long-length stall cell it is shown in Fig. 10. It is to be expected that the amplitude of the pressure perturbations will be larger for the short-length cell because the changes between unstalled and stalled have to take place over a shorter circumferential length. The nature of the pressure disturbances, and their association with the flow in the stall cell, was explored by Cumpsty and Greitzer [3].

Turning to the specific findings of the present paper concerning vortices, I do have some concern about the deduction of flow structure from ensemble averages. It is on the basis of ensemble averages that the authors have deduced that close to stall there is a vortex extending ahead of the rotor blade to intersect with the casing. This is, I suspect, an artifact of the averaging process. (A similar false structure with a large single vortex was deduced from ensemble averages of turbulent spots developing during the transition of laminar boundary layers into turbulent ones; the reality was many random turbulent vortical structures, but no single vortex.) It also needs to be borne in mind that presence of vorticity in Fig. 11 does not indicate the presence of a vortex. In sections 3.4.1, 3.4.2, and 3.4.3 statements are made about the way the vortices are behaving. I would suggest that these should be regarded as conjecture and not as firmly established; the same is true of conclusion number 3.

References

[1] Day, I. J., Breuer, T., Escuret, J., Cherrett, M., and Wilson, A., 1999, ‘‘Stall Inception and the Prospects for Active Control in Four High-Speed Compressors,’’ ASME J. Turbomach., **121**, pp. 18–27.

[2] Day, I. J., 1976, ‘‘Axial Compressor Stall,’’ PhD Dissertation, University of Cambridge, United Kingdom.

[3] Cumpsty, N. A., and Greitzer, E. M., 1982, ‘‘A Simple Model for Rotating Stall Propagation,’’ ASME J. Eng. Power, **104**, pp. 170–176.

Closure to ‘‘Discussion of ‘Comparative Studies on Short and Long Length-Scale Stall Cell Propagating in an Axial Compressor Rotor’ ’’ (2001, ASME J. Turbomach., 123, p. 31)

M. Inoue
e-mail: ino@mech.kyushu-u.ac.jp

M. Kuroumaru

T. Tanino

S. Yoshida

M. Furukawa

Department of Mechanical Engineering, Kyushu
University 6-10-1, Hakozaki, Higashi-Ku, Fukuoka, 812-
8581, Japan

The authors are puzzled by a somewhat spiteful discussion from Professor Cumpsty.

This paper does not describe a transient phenomenon of stall inception, but rather the occurrence of the short length-scale stall cells in a mild stall condition. Regarding the inception process of this type of stall, we made another experiment motivated by his discussion for our previous paper. We are preparing a paper, in which difference of behavior will be elucidated between the multiple short length-scale part-span stall cells in the mild stall and the high-frequency waves leading to a deep stall.

We agree with the explanation of part-span stall that occurs in most multistage compressors operating at speeds below the design values and is sometimes called as ‘‘multi-cell front-end stall.’’ However, the part-span stall cells in this condition seem not always to have the same structure and scale as the SLSC described in this paper. In many cases the scale is larger than the SLSC.

The amplitude of pressure disturbance does not depend mainly on the circumferential length of stalled and unstalled range. One should notice the bubble-shaped significantly low pressure areas following the relatively high pressure areas of stalled blades upstream of the rotor in Figs. 4 and 7, while there is no low pressure bubble between stalled and unstalled area in Figs. 5 and 10. The spiky wave of the SLSC is characterized by the rapid increase followed by rapid decrease in the pressure.

The tornado-like structure of the SLSC was deduced from the ensemble averages of the casing wall pressure and the three-dimensional velocity components upstream and down stream of the rotor by using the DPLA technique. In this technique, we can get a pressure field trace on the casing wall by using 14 pressure transducers (Kulite SCS-062). The significantly low pressure areas can be observed at nearly equal intervals, although their shape changes considerably. The change in the shape is not surprising, because a tornado is fluctuating violently in general. Recently, we measured the pressure traces at eight circumferential locations on the casing wall near the rotor leading edge. From observation of the raw pressure traces and the low-pass filtered pressure traces, it was found the waves were rotating nearly 70 percent of the rotor speed without disappearing. Generation of the vortices is not random unlike in a turbulent spot. More recently, we made a powerful numerical simulation of unsteady three-dimensional viscous flow in the whole annulus area of an axial rotor operating at a low flow-rate, and found the presence of a vortex spanning from the blade suction surface to the casing wall ahead of the rotor. The result will be described in a future paper.

The authors believe that the SLSCs have the vortical structure, although they may fluctuate violently.

A. Tsalavoutas
Research Assistant.

K. Mathioudakis
Associate Professor.

A. Stamatis
Research Associate.

Laboratory of Thermal Turbomachines,
National Technical University of Athens,
P.O. Box 64069,
Athens 15710, Greece

M. Smith
Principal Engineer,
ABB Alstom Power UK Ltd.,
United Kingdom

Identifying Faults in the Variable Geometry System of a Gas Turbine Compressor

The influence of faults in the variable geometry (variable stator vanes) system of a multistage axial compressor on the performance of an industrial gas turbine is investigated. An experimental investigation has been conducted, by implanting such faults into an operating gas turbine. The faults examined are individual stator vane mistunings of different magnitudes and located at different stages. Fault identification is based on the aerothermodynamic measurement data and is achieved by employing two different techniques, namely adaptive performance modeling and monitoring the circumferential distribution of the turbine exit temperature. It is observed that the deviations of the health indices produced by an adaptive performance model form patterns that can be used to identify the faults. The patterns characterize both the kind and the magnitude of the fault. On the other hand, the turbine exit temperature profile is also influenced and its change can be used as additional information, to increase the confidence level of the diagnosis (contrary to customary practice, which expects temperatures profiles to reflect only burner or turbine malfunctions). [DOI: 10.1115/1.1330267]

1 Introduction

Incorporating variable geometry into the stages of axial compressors is a practice followed by engine manufacturers, in order to improve operational behavior and efficiency of modern gas turbines. The operation of the systems incorporating the variable geometry is susceptible, however, to a number of faults that could lead to maladjustments of one or more vanes. The occurrence of such faults could lead to a decrease of engine efficiency or even to compressor surge during start-up or shutdown. It is thus very useful to establish ways to monitor the operation of the variable geometry system.

Works related to the monitoring of gas turbines with variable geometry compressors have been appearing in the open literature for a while. For example, a method for predicting the influence of variable geometry on compressor and engine performance has been presented by Muir et al. [1], implementing the stage stacking method for prediction of compressor performance, in conjunction with an engine performance model. An experimental investigation of the effects of possible variable guide vane faults on the performance of a gas turbine used for propulsion of a military combat aircraft has been conducted by Eustace et al. [2]. The work was focused in the extraction of characteristic fault signatures from both steady-state and transient engine data. A model-based technique that can be used for the detection of performance faults of a military turbofan engine, including variable geometry malfunctions, was presented by Merrington et al. [3].

Individual vane mistuning for one particular stator of a gas turbine was also examined by Stamatis et al. [4]. It was found that this particular fault can be clearly identified by applying the technique of adaptive modeling. The present paper presents some further work carried out, with the purpose of examining how variable geometry vane faults can be identified, when they occur at different stages and have different characteristics. The particular new feature of this experimental investigation is that different numbers of vanes were mistuned at different stages and by differing amounts, to explore a range of different fault characteristics. A further innovative aspect lies in the approach followed, which is based on a combination of monitoring overall performance changes and local changes in hot gas temperature profiles.

2 Variable Guide Vanes and Related Malfunctions

In most new technology gas turbines, variable geometry guide vanes are employed in one or more of the front stages of axial compressors and are usually scheduled versus the compressor rotational speed. They are closed at low speed to reduce the mass flow passed by the front stages for that given speed.

The variable geometry vanes are controlled by a number of linkages, which are actuated by the engine controller. A typical layout of such a mechanism is presented in Fig. 1. The knowledge of the actuator position gives the possibility to establish the position (angle) of each vane, based on the geometry of the system.

Considering now the system operation, a usual problem that arises is that the employed linkages undergo progressive wear and can drift from their calibration or schedule, which can result not only in efficiency reduction but also potential compressor surging, especially at start-up.

In order to avoid such problems, the user would have to examine the position of every vane, which is practically impossible. The procedure usually followed is to check that the main actuator position is in accordance with the predefined schedule and remains within accepted bounds, based on the assumption that the vanes will follow the actuator movement according to the system

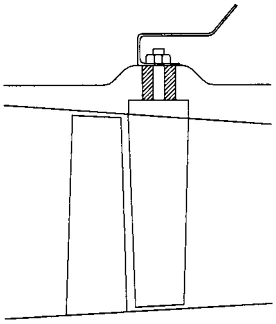

Fig. 1 Schematic of a typical linkage of a variable geometry vane

---

Contributed by the International Gas Turbine Institute and presented at the 45th International Gas Turbine and Aeroengine Congress and Exhibition, Munich, Germany, May 8–11, 2000. Manuscript received by the International Gas Turbine Institute February 2000. Paper No. 2000-GT-33. Review Chair: D. Ballal.

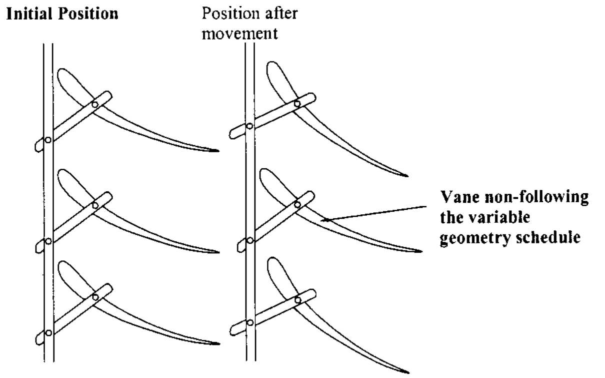

Fig. 2 Schematic representation of individual vane mistuning

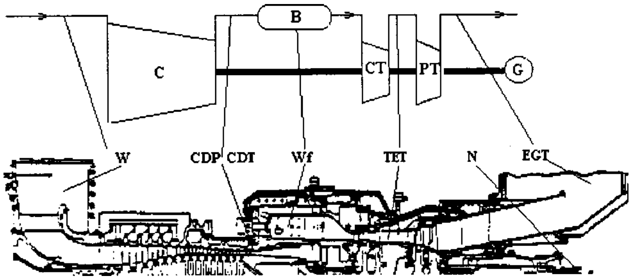

Fig. 3 Engine layout and measured quantities

design. The limitations of this approach are obvious since it cannot detect problems related to the positioning mechanism of one or more individual vanes. A loose bolt or stacked vane can cause such a problem for example, as schematically presented in Fig. 2.

However, the presence of even such small faults will alter the aerodynamic behavior of the affected compressor stage. This alteration will cause, in turn, a systematic change to the operation of the stages that follow. Adding together all these changes, the final result will be a change of the compressor and thus engine performance. Therefore, it would be desirable to check the presence of such faults in conjunction with methods capable of identifying performance changes of compressor and engine.

When a set of measurement data from an operating gas turbine is available it is possible to have a first idea of the condition of the engine by simply comparing those data to reference values. However, this approach has the disadvantage that it gives information about the nature of the fault only if previous experience on fault symptoms exists.

A method that has been shown to be powerful for diagnosing component malfunctions in gas turbines is the method of Adaptive Modeling [5]. The method employs the values of measured quantities in order to determine parameters characteristic to the performance of each component, which can be used to assess its health. It has the advantage that it provides a unified treatment for cases in which different data are available, it gives additional flexibility as to estimating the condition of different components, while it provides information easily interpretable.

In order to investigate the effects of different possible variable guide vane faults on overall engine performance and to establish resulting fault signatures, an experimental investigation was performed. Various faults were implanted in the variable guide vane system of a multistage axial compressor of an industrial gas turbine. The effects of the examined faults as well as the diagnostic possibilities offered by different methods are discussed in the following.

3 Engine Test Program

The TORNADO gas turbine, described by Wood [6] and Charchedi and Wood [7], was the engine used as the test vehicle. The engine consists of four main modules, a compressor, a combustor, a core turbine, and a power turbine. The two turbines can either be interconnected for single shaft operation, or not connected, for twin shaft operation. In the current series of tests the engine was operated in the single shaft mode.

The compressor uses variable IGVs followed by four rows of variable stators to achieve a pressure ratio of 12:1. The design speed of the compressor is 11,085 rpm; at speeds below 10,000 rpm the stators start to close progressively, until they are in the fully closed position for all speeds below 8000 rpm.

The test program was performed on an engine development test bed. For the aerothermodynamic performance measurements, the standard instrumentation of the test bed was used. The data have been acquired with the engine data logging system. Locations at which measurements were performed are shown in Fig. 3.

Test Procedure. To establish engine performance changes caused by the implanted faults, a number of tests were performed with the engine in both healthy and faulty condition. The test sequence commenced with establishing the performance of the engine in the nominal condition. This step is necessary when the method is applied, as it ensures that the reference condition is adapted to the particular engine tested. This feature of adaptive modeling allows elimination of the uncertainty caused by engine-to-engine variability and gives more reliable component condition indices [5]. Following this, the test schedules were repeated for each fault condition in turn. The engine was operated at each one of the examined fault cases for a short time period in order to avoid any possible harmful effects. Every time, a number of measurements were obtained from the engine data logging system, thus establishing a library of measurements sets.

Implanted Faults. Several variable guide vane faults were implanted into the engine by making adjustments to the linkages of one or more vanes. The adjustments performed were restricted in magnitude to be within operational limits. The faults implanted were thus not representative of an unserviceable engine but were of sufficient magnitude to examine the effects of even small faults on engine performance and verify the effectiveness of the fault diagnostic techniques.

The location and the magnitude of the implanted fault was selected in such a way that the tests performed are representative of faulty cases that were either reported by engine users or are very possible to occur. A list of the performed tests is given in Table 1.

All tests were performed for the same compressor mechanical speed, which was kept equal to nominal. Thus, the whole set of measurements refers to almost the same engine operating conditions (small variations of ambient conditions were observed during the test sequence).

Table 1 List of performed tests

Test Number	Description	Details
1	Datum Test	Healthy Engine
2	IGV Fault	One vane mistuned by 10^0
3	Stage-1 Fault	One vane mistuned by 5^0
4	- //-	One vane mistuned by 10^0
5	- //-	One vane mistune by 15^0
6	- //-	Three vanes mistuned by 5^0
7	- //-	Three vanes mistuned by 10^0
8	- //-	Three vanes mistuned by 15^0
9	Stage-4 Fault	One vane mistuned by 10^0
10	- //-	Two vanes mistuned by 10^0
11	Datum Test	Healthy Engine

4 Fault Effects on Performance Parameters

In order to have a first idea on the effect of the different faults on engine performance, the measured parameters were compared for the different mechanical conditions. The reference baseline was established by the analysis of datum test measurements. We note here that both the measurement sets of healthy and faulty conditions were corrected to standard day conditions.

The investigated VGV fault effects on engine performance parameters are presented in Fig. 4. As we can see, the occurrence of each one of the investigated faults has a significant effect on engine performance. In all cases, the fault occurrence will result in a significant decrease of the engine load and fuel flow rate for a given controller set point, while a proportional decrease is also observed in other parameters (air flow rate, compressor delivery pressure and temperature and turbine exhaust temperature). Noteworthy is the fact that the observed deviations demonstrate, in all cases, the same pattern.

Considering now the magnitude of deviations, our observations can be summarized as follows:

- For the case that the fault is restricted to the vanes of a single stage, as we can see in Figs. 4(*a*) and 4(*b*), the magnitude of deviations appears to be related to the degree of the vane mistuning.
- As we can see from Figs. 4(*a*), 4(*b*) and 4(*c*), VGV faults of the first stages have a greater impact on engine performance, as the deviations produced are of larger magnitude.

Based on these observations, we can state that the occurrence of even a small fault on engine variable geometry system has a noticeable impact on engine performance. Thus, we can state that by monitoring a number of performance parameters, one can detect the presence of a fault.

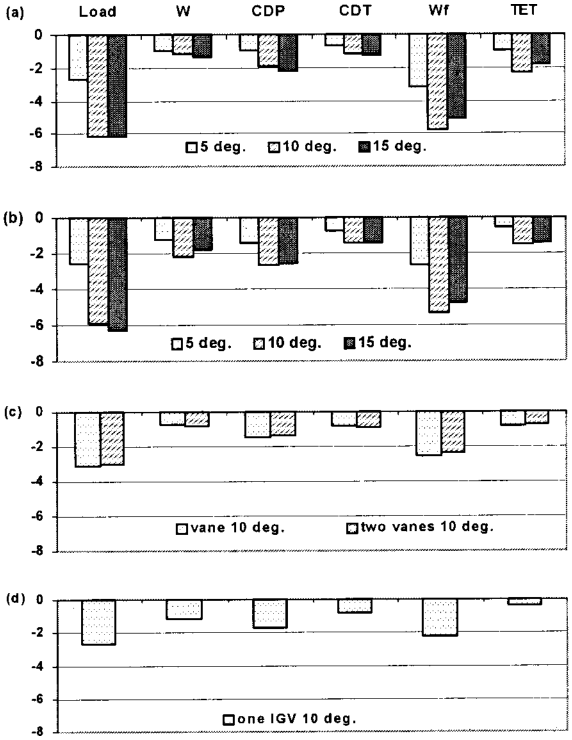

Fig. 4 VGV fault effects on engine performance: (*a*) Stage 1, one-vane faults, (*b*) Stage 1, three vane faults, (*c*) Stage 4 faults, and (*d*) IGV faults

5 Fault Signatures From an Adaptive Performance Model

A further analysis of the measurement sets obtained was performed by employing the adaptive performance modeling method. The aim was the derivation of fault signatures that can be used in future for fault detection and identification.

An adaptive performance model capable of simulating the operation of a typical TORNADO engine has been developed in the past by Stamatis et al. [4,5]. This model utilizes a set of eight modification factors that characterize the performance of engine components. However, in the case that the engine operates at single shaft mode, as in the present experimental campaign, the number of modification factors can be decreased to six. This is achieved by combining the operation of the two turbines (core and power) into one that performs the same function. The introduced modification factors are the following:

$$\text{Compressor:}\quad f_1 = q_c / q_{c,\text{ref}} \quad f_2 = \eta_{pc} / \eta_{pc,\text{ref}} \tag{1}$$

$$\text{Burner:}\quad f_3 = \text{BPL}/\text{BPL}_{\text{ref}} \quad f_4 = \eta_b / \eta_{b,\text{ref}} \tag{2}$$

$$\text{Turbine:}\quad f_5 = q_T / q_{T,\text{ref}} \quad f_6 = \eta_{is,T} / \eta_{isT,\text{ref}} \tag{3}$$

The first step for the application of the adaptive performance method on the examined cases is the selection of the modification factors that will be evaluated and monitored. Their selection is based on the number and type of available measurements, which in this case are the following five: air flow rate, compressor delivery pressure and temperature, fuel flow rate, and exhaust gas temperature. Compressor speed and engine load defines the engine operating point. From these five measurements, following the procedure described by Stamatis et al. [8], the modification factors that can be evaluated with the maximum accuracy, and are more likely to change in correspondence to engine condition modifications, were found to be the factors $f1$, $f2$, $f4$, $f5$, and $f6$.

Having selected a set of modification factors, the next step was the establishment of the baseline. This was achieved by analyzing the measurements of the datum test where the engine was intact (healthy condition). The analysis provided a set of reference performance characteristics capable of an accurate reproduction of operation of the particular TORNADO engine used for the tests and the limits of modification factors deviations that correspond to the ''healthy'' engine. These limits were estimated to be equal to ±0.5 percent.

The next step was the implementation of the adaptive engine model to data from the examined faulty cases. For each one of these cases, a set of modification factors percentage deviations was evaluated from the corresponding set of measurements. The averages of these deviations are presented in Fig. 5.

As we can see, in all cases a systematic change of factor $f1$ is observed. Although a trend of larger deviations for more severe faults is observed, it cannot be clearly stated that deviation magnitude is in proportion to fault severity. The limited amount of test data available implies that statistical dispersion is not small enough to lead to more specific conclusion about severity-deviation correlation. The other factors don't exhibit any systematic change, while their deviations lie within healthy limits. Only the factor $f5$, in three test cases, exhibits deviations that slightly exceed these limits (Figs. 5(*a*) and 5(*b*)).

Diagnosis of a fault existence and possible identification of its kind is facilitated if factors $f1$ and $f2$ are cross-plotted on compressor diagnostic plane (plane that characterizes the compressor condition). A cross plot of the evaluated deviations of factors $f1$ and $f2$ is given on Fig. 6. All points move in the same direction away from the nominal point (point [0,0]), while the distance from the origin reflects the fault severity. All faults are manifested as a decrease in pumping capacity of the compressor, while its efficiency remains practically unaltered. Looking at the turbine diag-

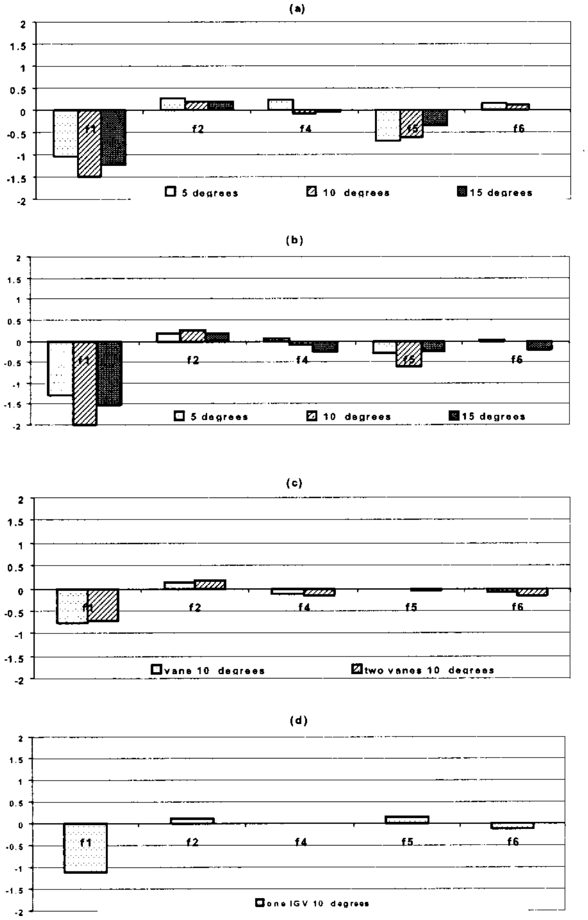

Fig. 5 Modification factors percentage deviations: (*a*) Stage 1, one-vane faults, (*b*) Stage 1, three vane faults, (*c*) Stage 4 faults, and (*d*) IGV faults

nostic plane presented in Fig. 7, we can see that the points are much closer to the origin while there is no visible trend of displacements.

Thus we can state that in all test cases there is a clear fault signature that can be used for fault identification. It is difficult, however, to distinguish the particular faulty vane configuration. The implanted faults belong to the class of compressor fault and thus, as it was expected only the compressor modification factors exhibit a systematic change.

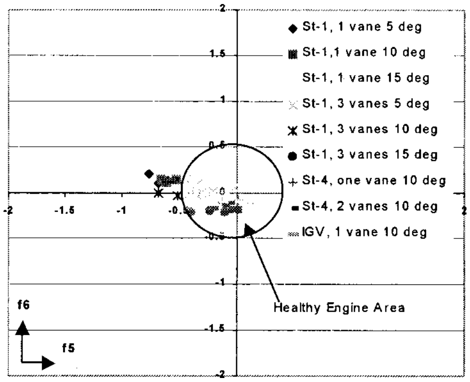

Fig. 7 Turbine diagnostic plane

6 Additional Information From Temperature Patterns

Within a gas turbine engine, the flow field issuing from the compressor is nonuniform containing circumferential and radial variations. The pattern of these variations, for certain operating conditions, is related to the compressor blade design. A change in the compressor blading, as in the case of mistuned guide vanes, should be expected to result in an alteration of the flow field at the compressor exit. (Recent studies performed by Barker et al. [9] revealed that nonuniformities in the flow that enters the combustor can affect the mixing performed within the combustor and thus the flow field at the combustor exit.) It should be remembered that the hot gasses from the combustion chamber enter the turbine and have to pass through one or more stages. The turbine blade rows will act as filters on circumferential nonuniformities, and the question is whether nonuniformities will persist and can thus be observable at the turbine exit.

On the basis of this reasoning, it was examined whether the modifications of the flow field produced by the variable geometry faults can be identified from the gas temperature circumferential distribution. A sample result of measured temperature distributions is illustrated in Fig. 8. The corrected temperature profiles downstream of the core turbine for the engine in the reference condition, and for the case in which three vanes of the first stage were mistuned by 15 deg, are presented.

The reference temperature profile is established from the obtained measurements database. From profiles at discrete operating points, the profile at any intermediate load is produced by interpolation. This way we obtain a reference temperature profile that corresponds to the same operating conditions.

As we can see, a modification of the temperature pattern is

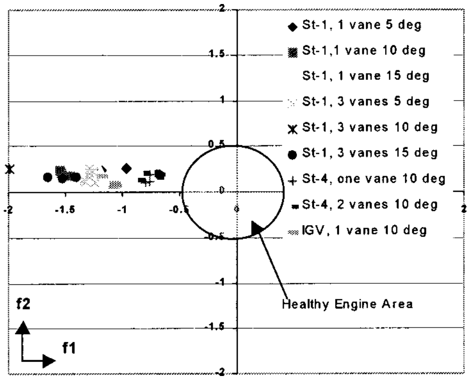

Fig. 6 Compressor diagnostic plane

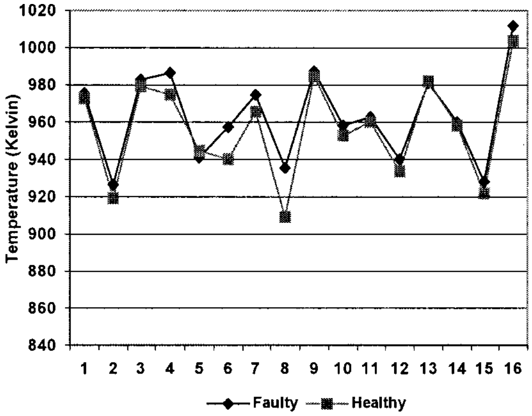

Fig. 8 Temperature pattern at core turbine outlet for two cases

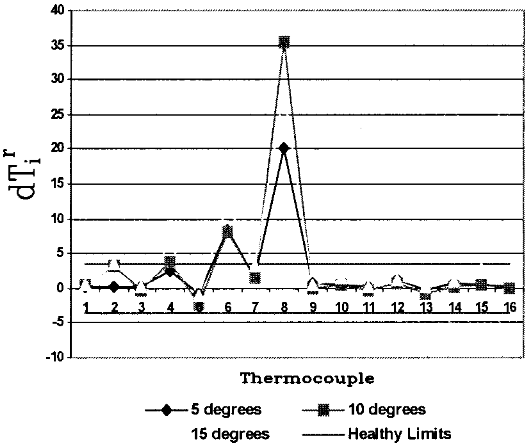

Fig. 9 Reduced temperature deviations for the case that three vanes of Stage 1 are mistuned

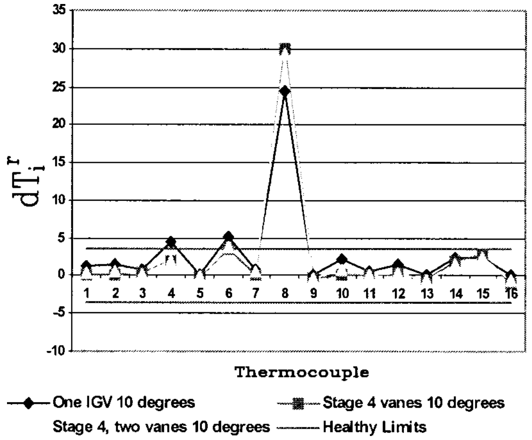

Fig. 11 Reduced temperature deviations for different faults

noticed. This modification consists of an increase in the temperature registered by a number of thermocouples, while the rest of the readings do not exhibit significant deviations.

In order to investigate the possibility of extracting additional diagnostic information from a possible systematic change of the temperature profile at the turbine outlet, the obtained patterns were compared by evaluating the reduced temperature deviations (introduced by Tsalavoutas et al. [10]), defined as

$$dT_i^r = dT_i \frac{|dT_i|}{dT_s} \frac{1}{dT_{\text{av}}} \tag{4}$$

where dT_i is the difference between the current and reference temperature,

$$dT_i = T_i - T_{i,\text{ref}} \tag{5}$$

dT_{av} is the average absolute temperature deviation

$$dT_{\text{av}} = \frac{\Sigma_{i=1}^{N} |dT_i|}{N} \tag{6}$$

and dT_s is a measure of the maximum expected temperature deviation due to the presence of random error in the measurements.

The effectiveness of this method for identifying even small alterations of temperature profiles and extracting diagnostic information, has been presented by the group of authors [10]. The evaluated reduced temperature deviations for the case in which three vanes of stage 1 are mistuned by different degrees is presented in Fig. 9.

It is shown that the evaluated reduced deviations for a number of thermocouples exceed the threshold, while its magnitude is proportional to the fault severity. The deviations of the remaining thermocouples are of smaller magnitude and in all cases, lie within the healthy limits. The same observations can be made also for the patterns of reduced deviations for the other examined cases, presented in Figs. 10 and 11.

It is noticeable that in all test cases the same thermocouple exhibits the maximum reduced deviation. This can be attributed to the fact that in the examined faulty cases, the affected vanes were located at the same circumferential region. On the other hand, the pattern of the deviations has a similar form for all the different vane faults. We can therefore state that the occurrence of a fault in the variable guide vanes will give a characteristic pattern of reduced temperature deviations. However, the diagnostic possibilities offered by its usage are directly related to its differentiation from corresponding patterns given by other kind of faults.

In this respect, the pattern of reduced temperature deviations for different burner faults that were implanted in the same engine is given in Fig. 12 (details about these particular faults were presented by Tsalavoutas et al. [10]).

In this case, the deviations of two adjacent thermocouples are negative and lower than the threshold while the rest of the deviations are positive, and in more severe cases, lie outside the healthy limits. The clear differentiation between the two fault signatures (variable guide vane and burner fault) is therefore obvious. It could be argued that even if the burner faults were in the opposite direction, the form of the pattern is different and therefore distinguishable from the vane faults.

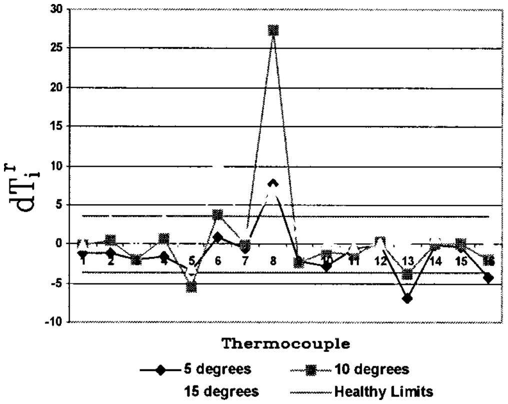

Fig. 10 Reduced temperature deviations for the case in which one vane of the first stage was mistuned

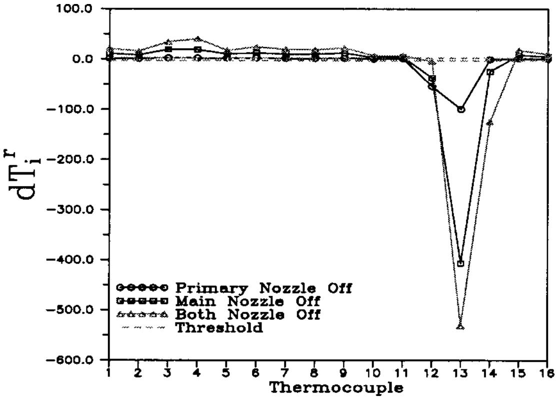

Fig. 12 Reduced temperature deviations for different burner faults [10]

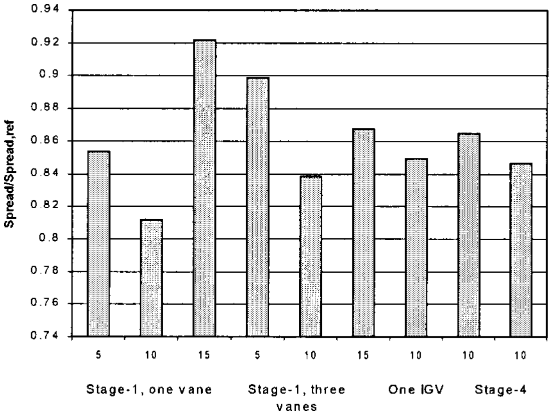

Fig. 13 Temperature spread for the examined cases (healthy and faulty)

Besides the observed reduced temperature deviations, a considerable alteration is also noticed in the temperature spread, as illustrated in Fig. 13. The ratio of the temperature spread of measured pattern for faulty operation to the spread of the reference pattern that corresponds to the same operating conditions is given. In all cases, a decrease of the temperature spread is noticed, contrary to the usual experience where fault occurrence is always connected to an increase of the temperature spread. Inspection of Fig. 8 explains why the spread is reduced with a vane fault. The significant observation here is that although spread reduction is a favorable condition for the hot part of the engine, it can nevertheless be linked to an engine malfunction.

7 Discussion

The results of the experimental investigation presented above have shown that compressor variable geometry vane faults can be identified by first observing their effect on overall engine performance parameters. Employing component-oriented diagnostic procedures such as the technique of the adaptive modeling provides a clearer picture. Further confidence in such a diagnosis can be provided by information extracted from temperature profiles downstream of the turbine. The confidence increase is a result of the fact that the information used (namely temperature distribution) is additional to the one used for performance evaluation purposes, where mean values only are of interest. A prerequisite for having this second possibility is the application of a method, which is sensitive enough to characterize profile form changes.

The present study has examined faults affecting vanes of different stages in different ways. A conclusion that can be drawn from the results presented is that the symptoms obtained by applying either adaptive modeling or the pattern analysis technique are similar for the different fault cases. Therefore, these symptoms can be considered to be typical for this type of fault, that is, they could be used as fault signatures.

A question that can be posed is how these symptoms are related to the symptoms of the entire row of vanes being mispositioned (''misrigging''). In tests that were performed on an engine of the same type, reported by Baligand et al. [11], misrigging was found also to produce a change mainly in factor $f1$. Temperature profiles were not found to exhibit a systematic change as in the cases discussed in the present paper. This feature could be useful in order to distinguish misrigging from individual vane mistuning.

On the other hand, the pattern of modification factor deviations is different from patterns of other compressor malfunctions, such as fouling. The mistuning of variable geometry vanes results mainly in a change of compressor flow capacity, observed on factor $f1$, while compressor fouling results in both flow capacity and efficiency reduction, as for example discussed by Tarabrin et al. [12]. The fact that fouling causes a systematic change of compressor efficiency, observed on factor $f2$, has also been demonstrated from test data by Mathioudakis et al. [13]. Therefore, these two types of faulty operation are distinguishable.

The confidence level of the fault detection and identification can be further increased by employing additional independent methods, based on measurements of unsteady pressure, sound, and vibration, as presented by Loukis et al. [14]. Finally, the previously discussed observations can be easily realized in an expert system, assigned the task of the supervision of contemporary engines. Such an implementation has been undertaken with the contribution of the present authors, and successful on-line application to an operating engine was demonstrated [11].

8 Conclusions

The effects of faults on the variable guide vane system of a multistage axial compressor on engine performance were experimentally investigated. Faults located at different stages and having different characteristics were examined. It was shown that the presence of these faults can cause considerable deviations of performance parameters.

Ways of exploiting typically available measurements for extracting diagnostic information that could lead to fault detection and identification were presented. Implementation of an adaptive performance model was shown to give a certain type of ''signature'' characterizing this type of faults, in the form of characteristic patterns, which can be used for fault detection and identification.

Turbine exit temperature distributions were found to be affected by the presence of compressor faults, a finding that is for the first time reported in this paper, contrary to the usual belief that temperature patterns are related to turbine or combustor faults. Moreover, the reduced deviations of the temperature pattern were shown to form a distinct pattern that can be used as additional diagnostic information, to increase the confidence of the diagnosis of variable geometry vane faults.

Acknowledgments

The work described in this paper has been performed within the framework of research contract BREU-506-Project BE-4192. The authors express their thanks to the European Communities for their financial support.

Nomenclature

BPL = burner pressure loss
CDP = compressor delivery pressure, bar
CDT = compressor delivery temperature, K
EGT = exhaust gas temperature, K
$f_1 - f_6$ = engine's components performance modification factors (Eqs. (1)–(3))
η_{pc} = compressor polytropic efficiency
η_{tis} = turbine isentropic efficiency
η_b = burner efficiency
N = compressor rotational speed
q_c = corrected compressor air flow rate, kg/s
q_t = corrected turbine flow rate, kg/s
TET = core turbine exit temperature, K (Fig. 3)
W = airflow rate, kg/s
W_f = fuel flow rate, kg/s

Subscript

ref = reference value of performance parameter

References

[1] Muir, D. E., Saravanamuttoo, H. I. H., and Marshall, D. J., 1989, ''Health Monitoring of Variable Geometry Gas Turbines for the Canadian Navy,'' ASME J. Eng. Gas Turbines Power, **111**, pp. 244–250.

[2] Eustace, R. W., Woodyatt, B. A., Merrington, G. L., and Runacres, A., 1994, ''Fault Signatures Obtained From Fault Implant Tests on an F404 Engine,'' ASME J. Eng. Gas Turbines Power, **116**, pp. 178–183.

[3] Merrington, G. L., 1994, ''Fault Diagnosis in Gas Turbines Using a Model-Based Technique,'' ASME J. Eng. Gas Turbines Power, **116**, pp. 374–380.

[4] Stamatis, A., Mathioudakis, K., Smith, M., and Papailiou, K., 1990, ''Gas Turbine Component Fault Identification by Means of Adaptive Performance Modeling,'' ASME Paper No. 90-GT-376.

[5] Stamatis, A., Mathioudakis, K., and Papailiou, K., 1990, ''Adaptive Simulation of Gas Turbine Performance,'' ASME J. Eng. Gas Turbines Power, **112**, pp. 168–175.

[6] Wood, G. R., 1981, ''The Ruston TORNADO: A 6 MW Gas Turbine for Industrial Applications,'' ASME Paper No. 81-GT-17.

[7] Carchedi, F., and Wood, G. R., 1982, ''Design and Development of a 12:1 Pressure Ration Compressor for the RUSTON 6-MW Gas Turbine,'' ASME J. Eng. Power, **104**, pp. 823–831.

[8] Stamatis, A., Mathioudakis, K., and Papailiou, K., 1992, ''Optimal Selection and Health Index Selection for Gas Turbine Performance Status and Fault Diagnosis,'' ASME J. Eng. Gas Turbines Power, **114**, pp. 209–216.

[9] Barker, A. G., and Carrotte, J. F., 1999, ''Compressor Exit Conditions and Their Impact on Flame Tube Fuel Injector Flows,'' ASME Paper No. 99-GT-238.

[10] Tsalavoutas, A., Mathioudakis, K., and Smith, M. K., 1996, ''Processing of Circumferential Temperature Distribution for the Detection of Gas Turbine Burner Malfunctions,'' ASME Paper No. 96-GT-103.

[11] Baligand, B., Garnier, B., Mathioudakis, K., and Smith, M., 1995, ''Gas Turbine Health Monitoring Demonstrator,'' *Proc. 2nd Int. Conf. on Acoustical and Vibratory Surveillance Methods and Diagnostic Techniques*, SFM/IMEKO/SFA-SEMLIS, Oct. 10–12, pp. 521–531.

[12] Tarabrin, A. P., Bodrov, A. I., Schurovsky, V. A., and Stalder, J.-P., 1998, ''Influence of Axial Compressor Fouling on Gas Turbine Unit Performance Based on Different Schemes and With Different Initial Parameters,'' ASME Paper No. 98-GT-416.

[13] Mathioudakis, K., Stamatis, A., Tsalavoutas, A., and Aretakis, N., 1999, ''Performance Analysis of Industrial Gas Turbines for Engine Condition Monitoring,'' presented at First International Conference on Engineering Thermophysics, Beijing, Aug. 18–21.

[14] Loukis, E., Wetta, P., Mathioudakis, K., Papathanasiou, A., and Papailiou, K., 1991, ''Combination of Different Unsteady Quantity Measurements for Gas Turbine Blade Fault Diagnosis,'' ASME Paper No. 91-GT-201.

Using Sweep and Dihedral to Control Three-Dimensional Flow in Transonic Stators of Axial Compressors

V. Gümmer

U. Wenger

Compressor Engineering,
Rolls-Royce Deutschland Ltd. & Co. KG,
Eschenweg 11,
D-15827 Dahlewitz, Germany

H.-P. Kau

Chair of Flight Propulsion,
University of Technology Munich,
Boltzmannstraße 15,
D-85747 Munich, Germany

The paper describes an advanced three-dimensional blading concept for highly loaded transonic compressor stators. The concept takes advantage of the aerodynamic effects of sweep and dihedral. To the knowledge of the authors this is the first approach reported in the open literature that combines those two basic types of lean in an engine-worthy aerofoil design. The paper makes a contribution to the understanding of the endwall effect of both features with special emphasis put on sweep. The advanced three-dimensional blading concept was applied to an Engine Section Stator (ESS) of an aero-engine fan. In order to demonstrate how three-dimensional flow can be controlled, numerical analysis of the flow structure in a conventional and an advanced stator configuration was performed using a three-dimensional Navier–Stokes solver. The numerical analysis showed the advanced blade improving both radial loading distribution and the three-dimensional endwall boundary layer development. In particular, a strong hub corner stall could be largely alleviated. High-speed rig testing of the advanced ESS confirmed the concept and showed good qualitative agreement between measurement and prediction. The work presented was closely linked to the development of the BR710 engine on which the advanced ESS is in service today. [DOI: 10.1115/1.1330268]

Introduction

The compression system takes a central role in weight and cost reduction of aero-engines. In order to reduce parts count and improve performance, stage loading must rise and the boundary layers on the aerofoils and the endwalls have to be well controlled. The introduction and refinement of custom-tailored aerofoils, as reported by Hobbs and Weingold [1], focused on the profile boundary layers. The first approach of accounting for flow features near the endwalls were end bend concepts as given by Behlke [2] and Robinson [3]. The early end bend concepts were based on a two-dimensional way of thinking although aimed at a three-dimensional flow problem. The incorporation of end bends involves a certain degree of local aerofoil lean, which also contributes to the net result.

During the last few years the deliberate use of local aerofoil lean in compressors has generated more and more interest and is believed to give another step change in compressor performance. LeJambre et al. [4] demonstrated a 2 percent rise of polytropic efficiency on a multistage HP-compressor, which featured stators with bowed stacking lines. Nevertheless, there appears to be no common understanding of how local blade lean can be used to control the three-dimensional flow and reduce the endwall losses in axial compressors. The problem of lean can be described by *sweep* and *dihedral*, both terms having their roots in aircraft wing aerodynamics. The implications of sweep and dihedral are twofold. There is a well-known two-dimensional flow effect, and there is a three-dimensional effect at the endwall, which is much more complicated and not fully understood. In order to help in closing this gap, the first part of this paper describes the basic flow mechanisms related to sweep and dihedral in the endwall region and identifies causal links between blade stacking and the flow behavior induced. With particular focus on endwall effects of sweep, the second and main part of the paper deals with the application of the tailored stacking concept to an engine section stator (ESS) of a transonic fan.

Endwall Flow Mechanisms Induced by Sweep and Dihedral

First of all a geometric definition of sweep and dihedral is given (see Fig. 1). The orientation of the aerofoil stacking axis is set in relationship to the flow field. The stacking axis is defined as passing through the center of gravity of each aerofoil section. As the blade has stagger an axial lean as well as a circumferential lean leads to a combination of sweep and dihedral. This is difficult to capture by the angles ξ and η given in the meridional and axial planes. The aerofoil is represented by a surface formed by the chord of the individual aerofoil sections. That surface also represents the main flow direction at specific positions along the span. The flow around the blade is given on an axisymmetric conical stream surface.

The sweep angle φ and the dihedral angle ν are defined using the coordinate system x_P, y_P, z_P positioned at the pinch point P of the stacking axis and the stream surface. The x_P axis is positioned on the line formed by the intersection of the stream and blade surfaces. The y_P axis is normal to the blade surface and the z_P axis is tangential to the blade surface. The sweep angle φ is given between stacking and the z_P axis. The dihedral angle ν is given between the y_P axis and its projection onto the stream surface. The angles φ and ν can be expressed through the stagger angle λ, the stream surface cone angle σ, the axial lean angle ξ, and the tangential lean angle η using the trigonometric functions derived by Smith and Yeh [5]. *Positive sweep* is obtained by moving the endwall sections parallel to the chordline toward the approaching flow. Moving endwall sections perpendicular to the chordline into the direction of lift gives *positive dihedral*. The physical implications of sweep and dihedral in the endwall region have been covered in detail by Gümmer and Wenger [6]. A summary of the key points is given here.

Contributed by the International Gas Turbine Institute and presented at the 45th International Gas Turbine and Aeroengine Congress and Exhibition, Munich, Germany, May 8–11, 2000. Manuscript received by the International Gas Turbine Institute February 2000. Paper No. 2000-GT-491. Review Chair: D. Ballal.

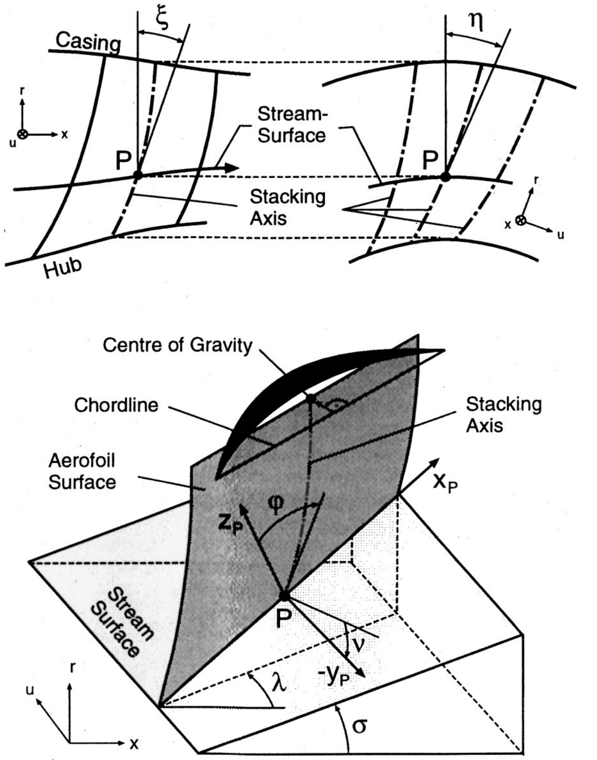

Fig. 1 Definition of sweep and dihedral on a compressor aerofoil

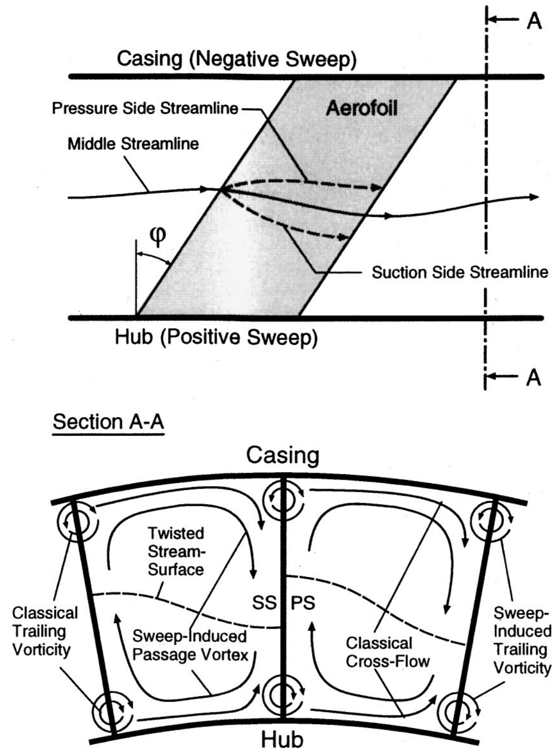

Fig. 2 Classical and sweep-induced secondary flow components

Endwall Effects of Sweep. The two-dimensional effect is well-known and similar to that on wings. As demonstrated by Stark [7] in compressor cascades, the critical Mach number is inversely proportional to the cosine of the sweep angle. Sweep reduces shock-induced boundary layer separation and the related loss. A compressor blade row of uniform sweep (i.e., positive sweep at the hub and negative sweep at the casing) and the secondary flow components generated is shown in Fig. 2. A streamline offset that begins at midpassage height at the blade leading edge and increases in the flow direction is induced by the sweep. This results in a stream surface that is twisted and nonaxisymmetric. The stream surface twist at midheight creates a large secondary flow vortex covering the full blade passage. The sweep-induced passage vortex is counteractive to the classical cross-passage flow at the hub and supports the cross-passage flow at the casing. Close to the endwalls, the streamline offset is suppressed and sweep-induced vortices are shed from the trailing edge. Those have the same sense of rotation as the classical trailing vortices at the hub and opposite direction at the casing. Therefore, the secondary flow pattern has a much higher level of complexity in swept than conventionally stacked blade rows.

A key function is taken over by the *endwall potential effect* already observed by Stark [7] and Stark and Gotthardt [8]. To explain that effect, the endwall can be replaced by a mirror image of the aerofoil. Then the endwall section can be discussed as the center section of a swept wing. According to swept wing theory, a compressor blade row of positive sweep changes the chordwise loading along the span, with the tendency of the lift force moving rearward when approaching the endwall. The trailing vortices shed from the wall sections are known to reduce lift, although they induce an upwash and increased incidence in the approaching flow. Effectively, peak diffusion shifts toward the rear part of the blade passage while overall diffusion is reduced. However, the incidence close to the contour (effective incidence) is lower.

There are mechanisms beyond the basic endwall potential effect that are related to the swirling flow within the compressor. In the case of a positively swept blade end, the metal blockage effect increases the endwall streamtube height ahead of the blade row and results in a higher inlet flow angle and lower inlet Mach number. This effect in isolation already improves choke and stall margin of the endwall sections at a fixed specific inlet mass flow and blading philosophy.

The total of the individual sweep effects gives a more favorable profile pressure distribution in the wall sections. As the profile loading distribution sets pressure gradients across the blade passage, not only can profile boundary layers profit from sweep, but secondary flow also can be managed. Early evidence in this respect is given by the work of Stark and Barsun [9]. In a compressor cascade of uniform sweep, they found lower secondary losses at the positively swept end of the blade. Much later Peng et al. [10] reported positive sweep at the blade ends improved endwall losses in linear cascades at high incidence settings. However, first contributions to a more detailed understanding of the sweep impact on secondary flow behavior were only given recently by Place [11] and Sasaki and Breugelmans [12]. Both publications looked at sweep of the blade ends and found positive sweep clearly having a beneficial effect on the three-dimensional endwall flow. The cross-passage flow and the corner stall could be reduced, resulting in improved endwall flow conditions and loss over at least a part of the blade row operating range. At the kink-point sections (transition from swept end to radial blade portion), however, increased loading and loss were observed. Improved performance over the entire operating range was achieved by Baumgarten [13] using positive sweep in the hub of a highly loaded stator of a low-speed fan.

Endwall Effects of Dihedral. In aeronautics dihedral mainly impacts the stability and flight characteristics of the aircraft. In compressors the prime driver for using dihedral is to add a radial blade force to the radial equilibrium of the flow between hub and casing. This effect is already incorporated in throughflow modeling. Streamtube height and static pressure change their radial profile when dihedral is introduced. The magnitude of change is largely dependent on the blade aspect ratio. On a blade end of positive dihedral the streamtube diverges in the front part and converges in the rear part of the blade row. Consequently the inlet flow angle increases, but the endwall diffusion is alleviated by the favorable streamtube distribution. Thinking in terms of a vortex line representing the blade, there is a component of vorticity introduced in the meridional plane [14] supporting the above-described streamtube change. These mechanisms are based on the existence of an endwall in the sense of setting the radial equilibrium, but do not include the endwall potential effect.

Taking an approach similar to that used in the case of sweep, the endwall potential effect of dihedral can be assessed by replacing the endwall by a mirror image of the aerofoil and looking at velocities induced by a single vortex line representing that configuration. Looking at a midchord position of the endwall section, it can be concluded that positive dihedral reduces induced velocities on the suction surface and increases them on the pressure surface. Due to the opposite direction of induced velocities on the two surfaces, the static pressure level increases all around the section. The net result is a reduction of peak Mach number and suction side diffusion. In contrast to sweep, an endwall section featuring dihedral maintains the style of its static pressure distribution.

Dihedral also does not introduce additional large-scale vortices and therefore has little impact on the qualitative pattern of classical secondary flow. As proposed by the investigations of Shang et al. [15], Place [11], and Sasaki and Breugelmans [12] there is a limited but not unique reaction of cross-passage flow to positive dihedral. However, in those blade rows dominated by three-dimensional endwall boundary layer separations rather than classical secondary flows, the off-loading effect of dihedral could significantly reduce the extent of three-dimensional separations and redistribute the flow within the passage.

Benefits of Sweep and Dihedral. With focus on the endwall potential effect, the previous sections have shown the potential of positive sweep and positive dihedral to control local pressure gradients within the passage. This gives the opportunity to focus on the improvement of the three-dimensional endwall flow. While sweep largely controls the chordwise loading distribution and to some degree spanwise loading, dihedral primarily can be used to impact the radial pressure field. Regions of sharp transition between the leaned endwall portion (positive sweep or positive dihedral) and the conventionally stacked portion of the blade are to be avoided as they are similar to configurations of negative sweep or dihedral, which generally produce increased aerodynamic loading and loss.

Advanced Aerofoil Design

In the past, work was limited to investigations of either sweep or dihedral in low-speed cascades or machines. To the knowledge of the authors, the advanced three-dimensional blading concept presented here is unique in open literature for two particular reasons. First, the concept combines the two-dimensional and endwall effects of sweep with those of dihedral to give local flow control. Second, the concept was successfully applied to a transonic stator of a real aero-engine.

The blade row concerned is the BR710 Engine Section Stator (ESS), which was certified in mid-1996. To demonstrate the aerodynamic performance impact of the three-dimensional blading concept, two variants of the ESS have been numerically assessed with regard to sectional loading and secondary flow generation. A conventional aerofoil featuring radial stacking serves as a reference when looking at advantages of the advanced aerofoil, as shown in Fig. 3. Due to the promising numerical results, only the advanced ESS configuration was tested on a high-speed fan rig. Major results of the numerical and the experimental investigations are reported in this paper.

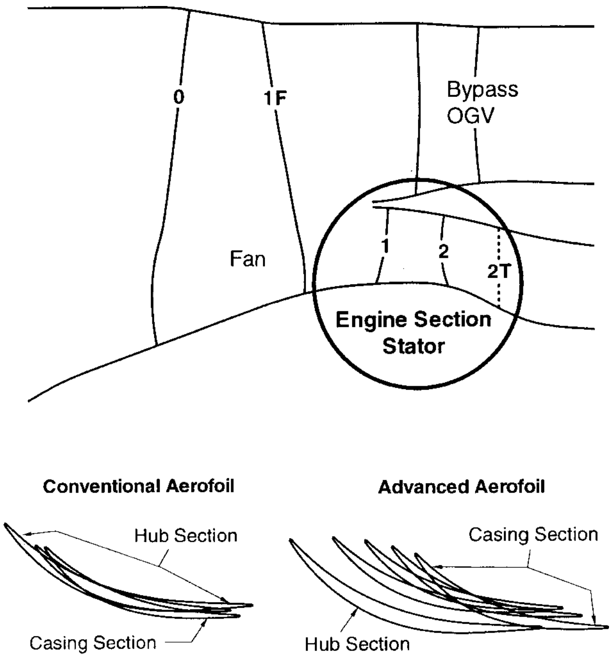

Fig. 3 Engine Section Stator (ESS) using conventional and advanced aerofoils

The Blading Concept. The aerodynamics of the ESS involve Mach numbers of just below unity and flow turning of beyond 50 deg in the hub region. The advanced aerofoil features strong sweep and dihedral in the bottom half of the blade height. The conventional and the advanced ESS are shrouded and were designed to the same effective inlet and exit annulus areas. The stacking of both aerofoils is shown as top view in Fig. 3. The two aerofoils have identical space–chord and thickness–chord ratios. Both use CDA-style profiles of equivalent camber and thickness distribution. The metal angles of the two aerofoil variants are chosen on the basis of identical incidence and exit flow angle calculated in Q3D modeling, i.e., radial equilibrium and metal blockage effects are included. The maximum inlet metal angle difference between the two aerofoils was 2 deg at the hub.

The application of positive sweep and positive dihedral to the ESS was focused on the area of highest aerodynamic distress, the hub region. The stacking chosen addresses the radial Mach number and turning distribution as well as the fact that a boundary layer of significant thickness enters the blade row on the inner wall. For that reason secondary flow and three-dimensional separations tend to be more severe in the lower than in the upper part of the ESS passage. Dihedral was primarily used to produce a more even loading across the blade height. In effect it also gives additional ''off-load'' to the hub as well as the casing section due to the endwall potential effect. Sweep was introduced in the hub region to gain choke margin and drop diffusion along the inner wall, thereby increasing blade section operating range, while reducing drivers for secondary flow and endwall separation.

Numerical Results. Similar to the problem of three-dimensional relief found by Wadia and Beacher [16], the setting of incidence near the wall becomes a critical issue with blades featuring strong sweep and dihedral. Therefore, the numerical assessment of the flow field in the ESS was performed using a three-dimensional Navier–Stokes solver. The code used for the present investigations is an in-house product that is based on the BTOB3D code of Dawes [17–19] and includes further improvements to the basic version. Among other changes the time step-

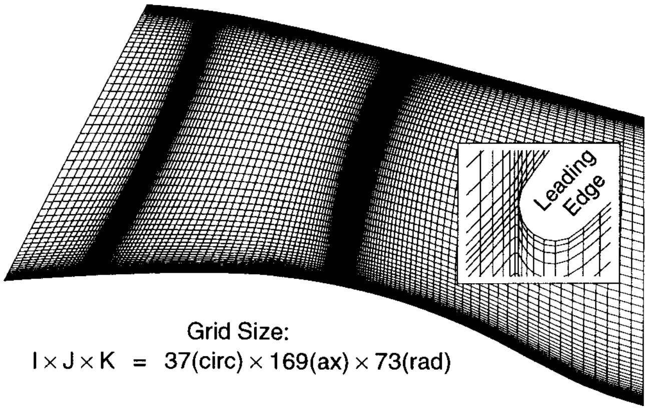

Fig. 4 Grid of the advanced ESS configuration

ping scheme, the multigrid function and the implementation of the turbulence model have been addressed. The code still uses a single-block **H**-type mesh.

All calculations were performed using the Baldwin–Lomax turbulence model and were run in multigrid mode. The grid size was 460,000 points. For the advanced ESS configuration the grid in the meridional plane and around the leading edge is shown in Fig. 4. Both ESS configurations were modeled using identical relative mesh spacing functions chosen for sufficient resolution of the flow close to the surfaces. Low grid stretching factors were used in all dimensions (1.2 axially, 1.2 radially, and 1.3 circumferentially). In the absolute flow direction the entry of the calculation domain is about 2/3 chord ahead of the leading edge. To achieve this, the grid was slightly extended upstream beyond the end of the radial flow splitter. The calculation domain ends 1.5 chords downstream of the trailing edge and includes the rig traverse plane 2T.

The inlet boundary conditions of the ESS were provided by a Q3D model based on a streamline curvature analysis of test data taken on an earlier rig build incorporating the same fan blade. Total temperatures and absolute whirl angles were taken from that Q3D model with no modification. The total pressure profile was modified at the hub to reflect a turbulent inlet boundary layer. All the results presented are based on a boundary layer thickness of 2.5 percent of ESS height. As shown in Fig. 5, for the design point, the measurements acquired in the advanced ESS rig confirm the assumptions made. The measured inlet total pressure profile is virtually identical to the one modeled. The whirl angle distribution indicated by a wedge probe measurement shows agreement within 1.5 deg. The procedure of setting inlet conditions for the ESS single row calculation was consistently used for all of the three operating points (design, near stall, near choke) discussed in this paper. Therefore, the boundary conditions used in the numerical assessment of the ESS are known to a sufficient degree of accuracy. They represent a good basis for the comparison to experi-

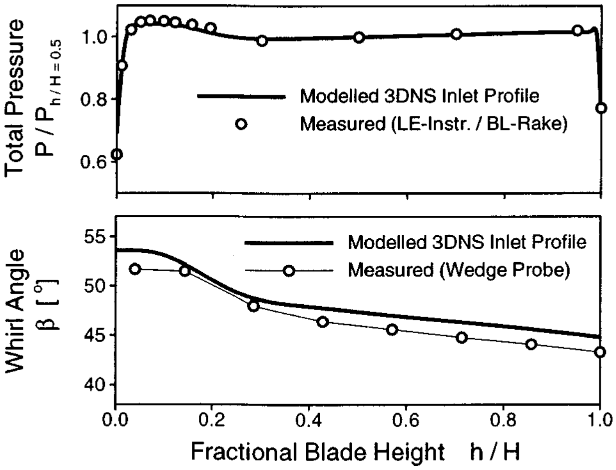

Fig. 5 ESS inlet conditions at the design point, 3DNS modeling and rig measurement

Table 1 Operating points considered

Operating Point (On Design Characteristic)	Near Choke	Design Point	Near Stall
Flow Function (normalised using design value)	1.042	1.000	0.925

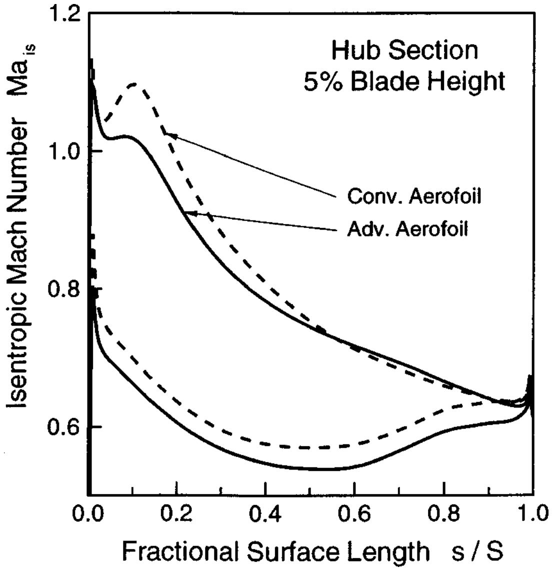

Fig. 6 ESS loading distribution at 5 percent blade height, 3DNS prediction, design point

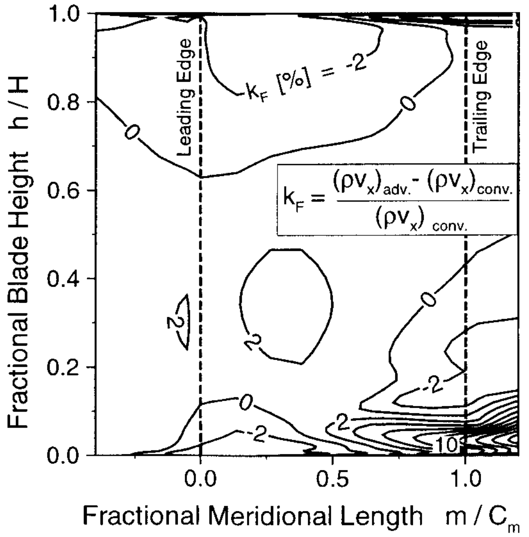

Fig. 7 Relation of circumferentially averaged local flow (axial velocity × density) of the conventional and the advanced ESS, 3DNS prediction, design point

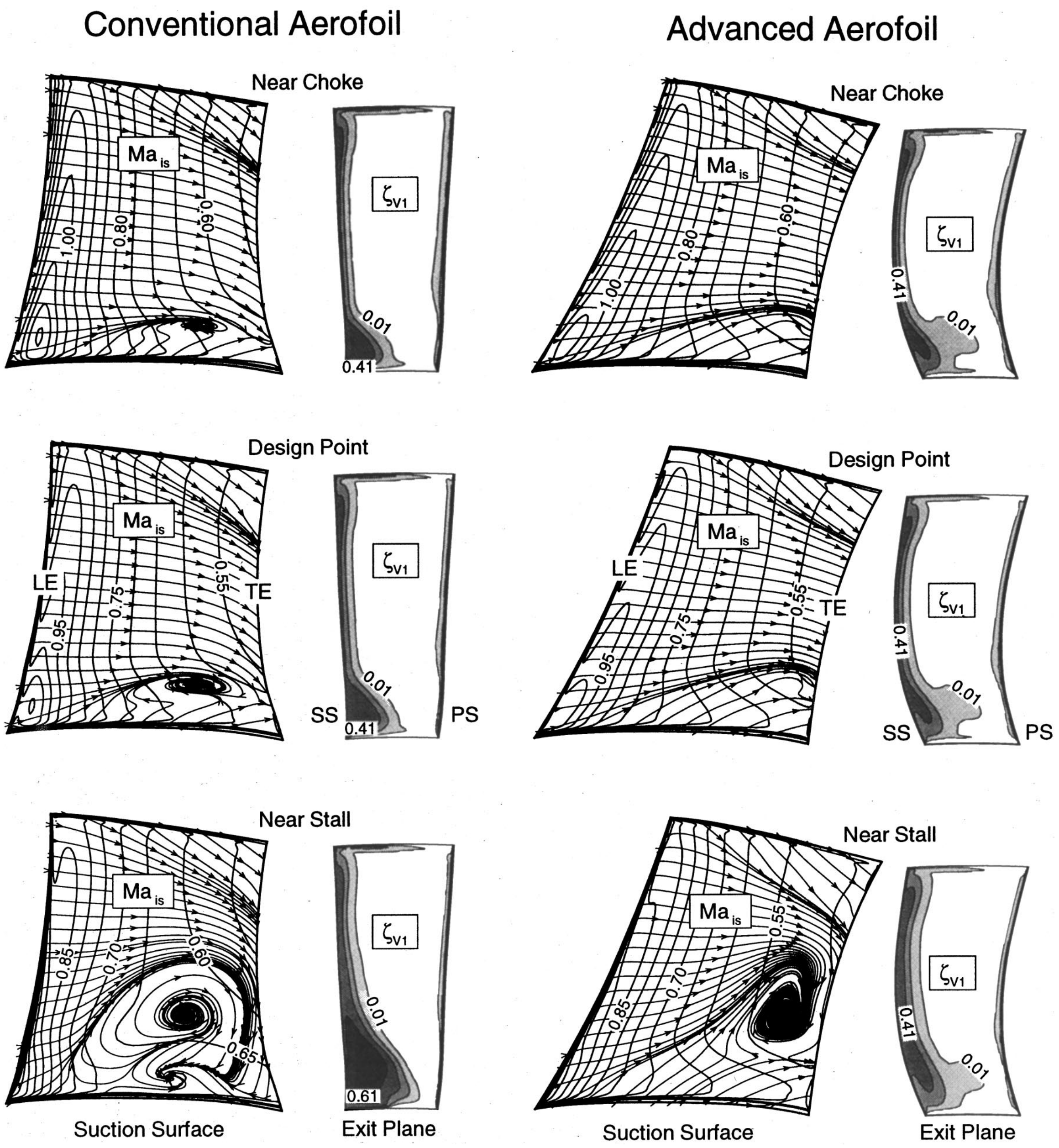

Fig. 8 **Isentropic Mach number distribution and streamlines on the suction surface, loss distribution at the trailing edge plane, conventional and advanced ESS configuration, 3DNS prediction at near choke, design and near-stall condition**

mental results obtained from the advanced ESS rig test. The flow rates corresponding to the three operating points considered are listed in Table 1.

As the degree of sweep and dihedral, and therefore the resulting flow effect, is strongest in the hub region of the aerofoil, discussion is focused on that area. Figure 6 compares the isentropic Mach number distribution on the aerofoil obtained from three-dimensional Navier–Stokes (3DNS) analysis in a section at 5 percent blade height of the conventional and the advanced ESS configuration. There is a significant reduction of the peak suction surface Mach number achieved on the advanced aerofoil. This is mainly caused by the two-dimensional and endwall potential effect of positive sweep. Streamtube effects and the endwall potential effect of dihedral also contribute to the net result. In particular, the endwall potential effect of positive sweep can be identified when comparing the distribution of chordwise loading (difference between suction and pressure side Mach number) of the two aerofoil designs. The hub section of the advanced blade shows a loading reduction in the front portion and a loading increase in the rear portion of the chord, with suction side total diffusion being much more favorable on the advanced aerofoil.

The modified static pressure field of the advanced design blade passage changes the behavior of the profile and endwall boundary layers as well as the magnitude of blockage produced by boundary layer separation in the near-endwall region. As detailed later, endwall separations and the large hub corner stall dominating the flow pattern at the lower flow path was significantly reduced in the advanced ESS configuration. The massflow was redistributed in the passage and also in the near field ahead of it. This is illustrated in Fig. 7, which shows the relative difference of the local circumferentially averaged massflow (expressed through the product of axial velocity and density) between the advanced and the conventional blade plotted as contours in the plane of relative meridional length and relative blade height. The comparison is made on the basis of the same overall entry flow to both ESS configurations. The $k_F=0$-contour identifies locations of identical local massflow in the two ESS's. The figure shows that at blade row entry the advanced configuration passes about 2 percent less flow near the hub and casing and 2 percent more flow in the middle of the flow path. With the degree and sign of the sweep and dihedral used and based on statements made in the paragraphs above, a flow deficit at the blade row entry would be expected at the hub, but not at the casing. However, there are additional flow mechanisms that are important. The strong reduction of the corner stall size at the hub of the advanced ESS configuration (visible as quite a large flow excess over the conventional stator in the hub-trailing edge region) leads to less flow passing the upper portion of the flowpath, which also affects the casing leading edge region. As demonstrated here, in highly loaded blade rows, flow redistribution is very much controlled by the viscous three-dimensional endwall boundary layer behavior that occurs as a reaction to phenomena qualitatively explainable with inviscid theory.

Major advantages of the advanced ESS configuration are found in terms of design point and off-design performance. Figure 8 shows the predicted 3DNS flow field of the conventional and the advanced blade compared at three stage operating points: near choke, design, and near stall. There are isentropic Mach number contours and streamlines plotted along the suction surface of the aerofoil and the calculated loss distribution plotted in the blade row exit plane.

A primary flow feature of both ESS configurations is a corner stall flow pattern present at both blade ends but more evident at the hub. Corner stall is basically a result of the cross-passage flow driving the well-known classical passage vortex and washing up endwall boundary layer material up the suction surface. Corner stall is linked to the presence of at least one three-dimensional separation line, at which the profile and endwall boundary layer interact and separate from the suction surface. This does not necessarily require reverse flow. When the corner stall grows and gets more severe, a complicated pattern of three-dimensional separation lines, attachment lines, and foci can occur. Reverse flow is likely to be involved in these cases.

The flow field of the conventional ESS features a large hub corner stall that grows into a more salient feature of the flow pattern as the stage is throttled. At any condition the corner stall structure in the conventional ESS is more complex than in the advanced ESS and the blade row performance is clearly limited by a flow phenomenon occurring in the hub region. As a result of the blockage of the corner stall, the casing sections remain moderately loaded. Looking at the corner stall pattern on the advanced aerofoil configuration, there is less tendency of the hub boundary layer material washing up the suction surface in the front portion of the aerofoil where the sweep-induced passage vortex delays cross-passage flow. There is stronger radial migration of endwall boundary layer fluid in the rear portion of the aerofoil, where cross-passage pressure gradients are increased through the loading shift induced by the endwall potential effect of sweep. This is indicated by the slope of the three-dimensional separation line along the suction side in Fig. 8.

In particular, toward stall the topology of the corner stall shows a complex structure including more than one three-dimensional separation/attachment line and a number of singular points (see Tobak and Peake [20] and Perry and Chong [21]). An in-depth discussion of these phenomena is not within the scope of this paper. However, it is important to mention that in the conventional blade row the separation line that represents the envelope of the corner stall region builds a barrier to the approaching flow (involving significant local reverse flow). In contrast, the advanced blade row separation lines are more in line with the main flow direction and therefore produce drastically less blockage. The losses in the exit plane of the advanced ESS indicate a hub corner stall region, which is much flatter but moved radially toward midspan. Loss distributions remain uniform across the span when approaching the stall regime, although the corner stall region reaches midheight.

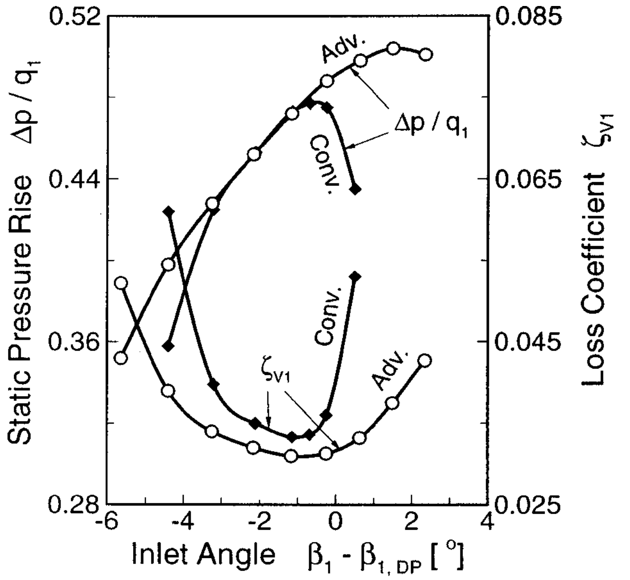

Fig. 9 Total averaged static pressure rise and loss coefficient, conventional and advanced ESS, high flow constant mean Mach number loop, 3DNS prediction

In order to assess more of the operation range of the two ESS configurations, an inlet angle variation was performed. The variation was centered around a working line operating point at 105 percent of design speed. ESS inlet conditions were again obtained from a Q3D model matched to test data. The variation of the operating point was achieved by applying a radially constant offset to the inlet angle distribution and setting exit static pressure to maintain mean inlet Mach number. This investigation considers performance changes along a constant mean Mach number loop rather than along the stage characteristic.

The resulting total averaged values of the static pressure rise coefficient $\Delta p / q_1$ and the total pressure loss coefficient ζ_{V1} are plotted in Fig. 9. The loss loop of the advanced stator is lower at design inlet flow angle and significantly wider than calculated for the conventional stator. In the high power range the advanced ESS has advantages over the conventional ESS in terms of efficiency and operating range. Through observation of the left-hand side of the graph one concludes that the pressure rise characteristic drops off rapidly as choke is approached. Based on a loss of 5 percent, the advanced blade gained an additional choke margin of 2 deg of inlet angle. Also, on the stall side of the operating range, the loss of the advanced stator stays far below that of the conventional stator and its static pressure rise characteristic rolls over at a higher mean inlet flow angle. Assuming stall at peak static pressure rise, there are another 2 deg of operating range gained by the tailored stacking of the advanced aerofoil configuration.

Comparison to Experimental Results. The flow field of the advanced ESS configuration was investigated on a fan rig facility allowing surface pressure measurements at various blade heights and area traverses at about one chord length downstream of the trailing edge (see plane 2T in Fig. 3). The surface static pressures have been converted into a static pressure coefficient using ESS inlet reference pressures. The inlet total pressure distribution was measured at the leading edge. Pressure tappings on the two endwalls provided an inlet static pressure distribution (assumed linear). When plotting the difference of suction and pressure side pressure coefficient Δc_{p1} rather than the absolute quantities, differences in chordwise loading distributions can be observed. This

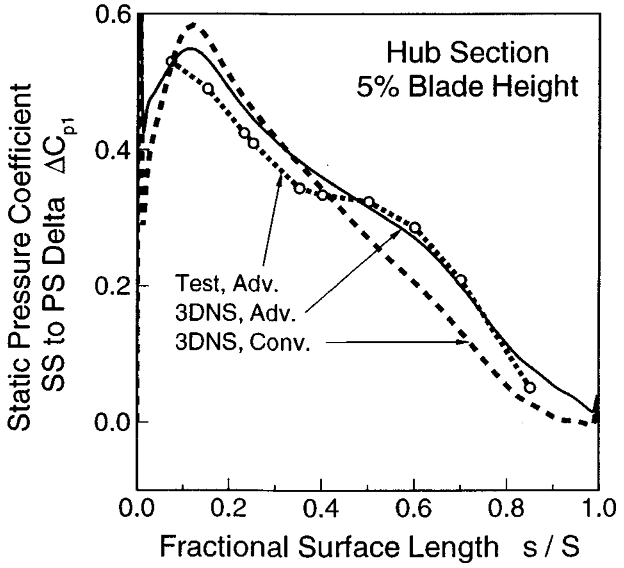

Fig. 10 ESS loading distribution at 5 percent blade height, 3DNS prediction and measurement, design point

exercise was done for the 3DNS results of the two ESS variants and the test result of the advanced aerofoil. Figure 10 looks again at the design point and 5 percent ESS blade height. There is relatively good agreement between the measured and calculated pressure distribution of the advanced aerofoil. The predicted rearward movement of the loading due to the endwall potential effect in sections of positive sweep is confirmed by the test results. The measurements also show that the effect is even more pronounced than that predicted.

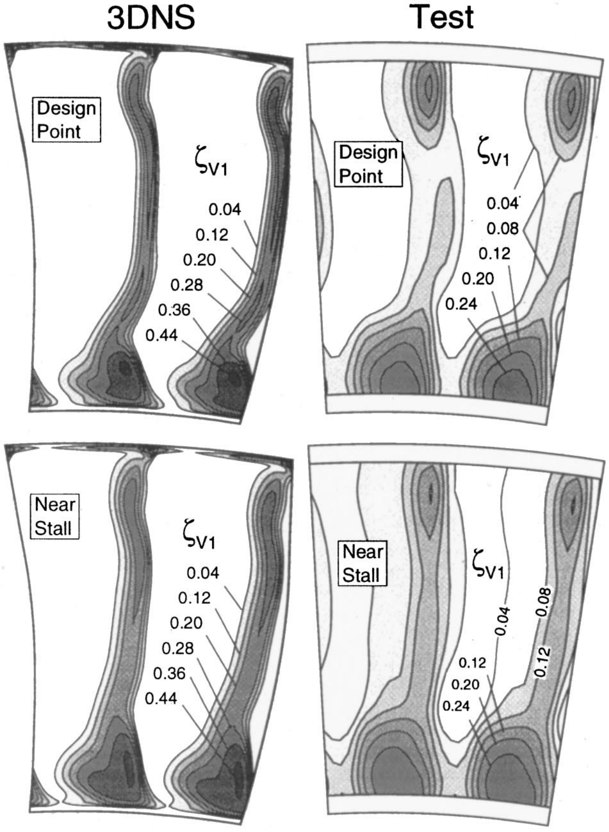

Fig. 11 Loss coefficients in plane 2*T*, advanced ESS, 3DNS prediction and measurement, design point and near-stall condition

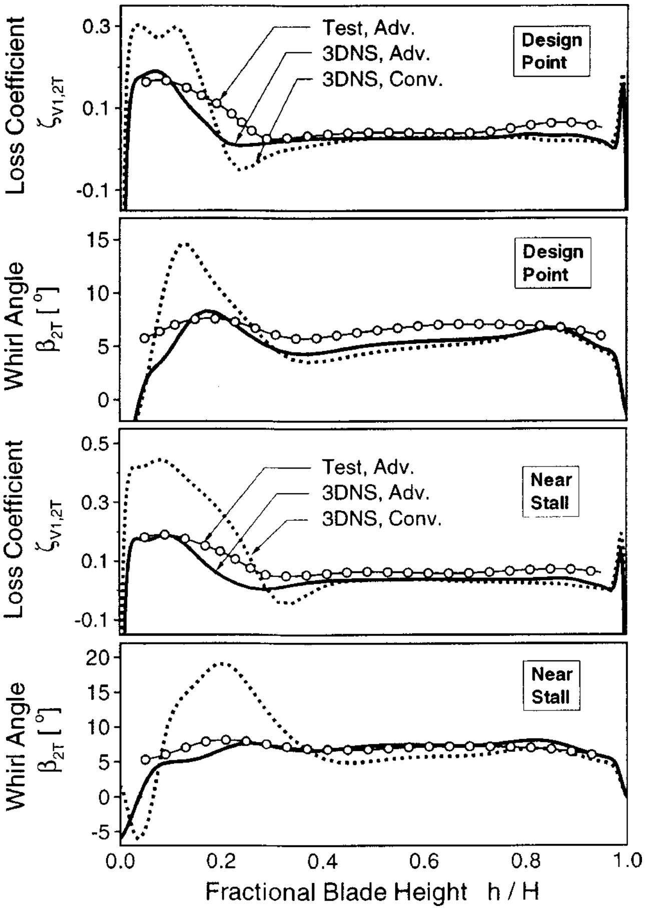

Fig. 12 Circumferentially averaged whirl angle and loss distribution in plane 2*T*, advanced ESS, 3DNS prediction and measurement, design point and near-stall condition

Pneumatic five-hole probe measurements taken at plane 2T revealed that the actual flow pattern is similar to the predicted flow pattern but with evidence of some clearly defined local differences (see Fig. 11). A contribution to this quantitative disagreement of the measured and predicted flow pattern was found to be an unsteady rotor–stator interaction, which is generally present but not always considered when taking pneumatic measurements in turbomachinery. In the present case fast response probe traverses revealed inlet flow angle and pressure fluctuations that caused cyclic changes of the ESS wake pattern.

The time-averaged flow pattern seen by the pneumatic probe is a smeared picture of the time-dependent flow pattern. This is true at the design point and even more pronounced at the near stall condition. Figure 11 shows the predicted and the measured distributions of total pressure loss at plane 2T for these two operating points. Although the overall appearance of the loss pattern is similar for 3DNS prediction and measurement, the measured trailing edge wake of the aerofoil is much wider and not as sharp as predicted. The corner stall regions measured at the hub and the casing are more extended in the circumferential as well as the radial direction than they are in the 3DNS prediction. On the other hand, the measured peak loss values are significantly lower than predicted. This proved to be just partly an unsteadiness effect, as the time-accurate passage flow (not presented) still showed stronger corner stall and blockage than the 3DNS prediction. Consistent with that observation, generally higher surface Mach numbers were measured.

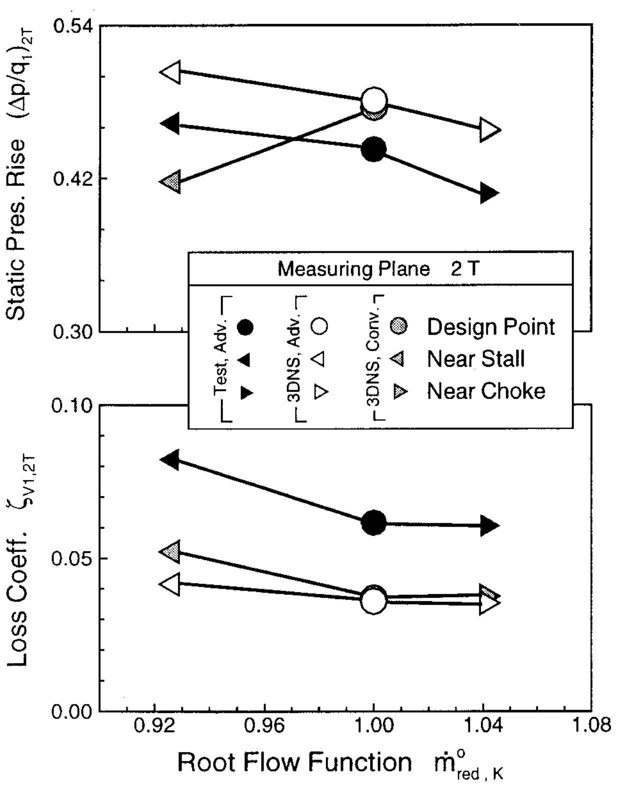

Fig. 13 Total averaged static pressure rise and loss in plane 2*T*, advanced ESS, 3DNS prediction and measurement

Nevertheless, when looking at the reaction of the flow field to changing the operating point from design to near stall, agreement between 3DNS and measurement becomes evident. There occurs a radial straightening and a balanced growing of the overall wake structure. The profile boundary layer in the midportion of the aerofoil and the corner stall regions at the hub and casing both slowly grow. This was one of the goals of the stacking concept of the advanced ESS.

Qualitative agreement of 3DNS prediction and measurement is also revealed by circumferentially averaged performance parameters. For the 3DNS as well as the test results mass-averaging was applied. In Fig. 12 the radial profiles of measured and predicted loss and whirl angle are plotted for the design point and the near-stall condition. The distributions obtained from 3DNS analysis of the conventional aerofoil are also shown for better assessment of the advanced aerofoil results. At both operating points the 3DNS prediction shows a flat loss and whirl angle profile across the inner 60 percent of the blade height. In the portion at about 15 percent from the endwalls, higher loss and underturning is found due to secondary flow and the associated corner stall occurring in this region. Directly at the endwalls, negative loss and overturning can be observed since high-momentum fluid replaced the low-momentum inlet wall boundary layer. The measured profiles qualitatively agree with the predicted radial trend, but the measured loss is at a slightly higher level with endwall losses extending further toward midspan. The measured exit swirl angle profile is mainly higher and flatter than predicted. Both loss and whirl angle show significant differences between the measurement on the advanced blade and the 3DNS prediction on the conventional blade in the lower 30 percent of blade height.

Measurement and 3DNS prediction show the same flow field response of the advanced aerofoil when going to the near stall operating condition. Moderately rising endwall losses and evenly increasing loss and whirl angle in the middle portion of blade height can be observed in both results. In addition, the agreement of measured and predicted distributions is better at the near stall condition, especially in terms of whirl angle.

In Fig. 13 total averaged loss and static pressure rise are plotted versus normalized fan core stream flow function. Again mass-averaging was used. The measurement on the advanced aerofoil shows significantly higher losses and less static pressure rise all across the operating range. The measured losses rise more rapidly as stall is approached, but the pressure rise characteristic is nearly at the same slope as the one predicted. In contrast to the 3DNS results for the conventional aerofoil, the measured as well as the predicted pressure rise characteristic for the advanced aerofoil has not rolled over at the near stall condition. As emphasized earlier, this was one of the objectives when introducing sweep and dihedral to the advanced aerofoil. In addition the total averaged quantities, and in particular the losses, do not adequately highlight the deficits of the conventional aerofoil as the axial velocity profile used for mass-averaging is strongly degraded in the hub region.

Nevertheless, these results suggest that the integrated parameters predicted by the 3DNS code on the conventional and the advanced ESS give the right trend but do not reliably indicate absolute levels.

Conclusions

The aerodynamic endwall effects of sweep and dihedral were described. A summary description of the range of mechanisms involved in these two features was presented. Positive sweep and positive dihedral reduce endwall losses and increase the operating range on compressors stators.

To the knowledge of the authors, this is the first time sweep and dihedral have been combined in an advanced blading concept for transonic compressor stators and the results published. The concept was applied to the engine section stator of the BR710 engine, leading to an engine-worthy design, which is in service today.

A three-dimensional Navier–Stokes code was used for the numerical assessment of the new blading concept. A conventional and an advanced aerofoil were compared with respect to the detailed flow field and the resulting performance parameters. Those flow features limiting the performance of the conventional blade row—the most important of them being a large hub corner stall—were identified and could be alleviated in the advanced design.

Despite the qualitative rather than quantitative nature of the 3DNS assessment, relative comparison of the numerical results allowed a concept for three-dimensional flow control in the blade passage to be set up and indicated significant advantages of the advanced aerofoil in terms of local flow structure and overall performance at design and off-design conditions. The numerical analysis showed that the advanced blade improved the radial distribution of loading and the development of the three-dimensional endwall boundary layers. As a result of positive sweep, the endwall low-energy fluid tends to be transported farther toward midspan, enhancing the radial mixing process.

High-speed rig testing of the advanced ESS confirmed the new blading concept. Qualitative agreement between measurement and 3DNS prediction was found with respect to the local flow pattern, the radial distribution of circumferentially averaged parameters, and the overall pressure rise characteristic. Good qualitative agreement was found in terms of local flow field changes occurring when the stall regime is approached. In quantitative terms, however, some well-defined differences were present, which are partly due to the tendency of the 3DNS code to underpredict loss, and partly caused by unsteady rotor–stator interaction found in the machine.

Acknowledgments

The authors would like to thank the Fluid Mechanics Institute of Braunschweig, in particular Professor U. Stark, for valuable advice and discussion on many issues related to the work presented here. Sincere gratitude is also offered to A. J. Rae and P. Creasey of Rolls-Royce plc Compressor Engineering for supporting and conducting the rig testing at Derby. As the overall work was conducted under the Rolls-Royce Deutschland Ltd. & Co. KG research and development program, the management is gratefully acknowledged for supporting this research and permitting the presentation of results.

Nomenclature

C_m = meridional chord, m
$c_{p1}(p-p_1)/(P_1-p_1)$ = static pressure coefficient
c_a = lift coefficient
H = blade height, m
h = blade height coordinate, m
I, J, K = grid dimensions
k_F = Adv. to Conv. flow factor
Ma = Mach number
m = meridional coordinate, m
$\dot{m}^{o}_{red,K}$ = normalized flow function
P = total pressure, Nm^{-2}
p = static pressure, Nm^{-2}
q = dynamic head, Nm^{-2}
r = radial coordinate, m
S = profile surface length, m
s = profile surface coordinate, m
u = circumferential coordinate, m
w_x = velocity, ms^{-1}
x = axial coordinate, m
x_p , y_p , z_p = blade coordinate system, m
α = angle of attack, deg
β = absolute swirl angle, deg
η = tangential lean angle, deg
φ = sweep angle, deg
λ = blade stagger angle, deg
ν = dihedral angle, deg
ξ = axial lean angle, deg
ρ = density, kgm^{-3}
σ = stream surface cone angle, deg
ζ_V = total pressure loss coefficient

Subscripts

DP = design point
is = isentropic
1 = ESS entry plane
2 = ESS exit plane
$2T$ = traverse plane

Abbreviations

Adv. = advanced aerofoil
BL = boundary layer
Conv. = conventional aerofoil
DP = design point
ESS = engine section stator
LE = leading edge
NS = Navier–Stokes
Q3D = quasi-three-dimensional method
PS = pressure surface
SS = suction surface
TE = trailing edge

References

[1] Hobbs, D. E., and Weingold, H. D., 1984, ''Development of Controlled Diffusion Airfoils for Multistage Compressor Application,'' ASME J. Eng. Gas Turbines Power, **106**, pp. 271–278.
[2] Behlke, R. F., 1986, ''The Development of a Second Generation of Controlled Diffusion Airfoils for Multistage Compressors,'' ASME J. Turbomach. **108**, pp. 32–41.
[3] Robinson, C. J., 1991, ''End-Wall Flows and Blading Design of Axial Flow Compressors,'' Ph.D. Thesis, Cranfield Institute of Technology, England.
[4] LeJambre, C. R., Zacharias, R. M., Biederman, A. J., Gleixner, B. P., and Yetka, C., 1995, ''Development and Application of a Multistage Navier–Stokes Flow Solver: Part II—Application to a High-Pressure Compressor Design,'' ASME J. Turbomach., **120**, pp. 215–223.
[5] Smith, L. H., and Yeh, H., 1963, ''Sweep and Dihedral Effects in Axial-Flow Turbomachinery,'' ASME J. Basic Eng., **85**, pp. 401–416.
[6] Gümmer, V., and Wenger, U., 2000, ''The Impact of Sweep and Dihedral on Axial Compressor Endwall Aerodynamics,'' *Proc. 8th International Symposium on Transport Phenomena and Dynamics of Rotating Machinery* (ISROMAC-8), Mar. 26–30, Honolulu, HI.
[7] Stark, U., 1967, ''Strömungsuntersuchungen an gepfeilten Verdichtergittern bei kompressibler Unterschallströmung,'' DFL-Forschungsbericht 67–09.
[8] Stark, U., and Gotthardt, H., 1978, ''Theoretische und experimentelle Untersuchungen an konischen Turbinengittern. Teil 1: Potentialtheoretische Untersuchungen an gepfeilten Verdichter-und konischen Turbinengittern,'' Bericht 78/2, Institut für Strömungsmechanik, Technische Universität Braunschweig.
[9] Stark, U., and Barsun, K., 1969, ''Untersuchungen über den Einfluß der Machzahl und der Pfeilung auf die Sekundärverluste in Verdichtergittern bei hohen Unterschallgeschwindigkeiten,'' DFL-Forschungsbericht 69-55.
[10] Peng, Z., Wu, G., Yan, M., and Ren, L., 1991, ''An Experimental Investigation of Technologies of Endwall Flow Control in a Compressor Plane Cascade,'' AIAA Paper No. 91–2005.
[11] Place, J. M. M., 1997, ''Three-Dimensional Flow in Core Compressors,'' Ph.D. Thesis, Department of Engineering, University of Cambridge.
[12] Sasaki, T., and Breugelmans, F., 1998, ''Comparison of Sweep and Dihedral Effects on Compressor Cascade Performance,'' ASME J. Turbomach., **120**, pp. 454–464.
[13] Baumgarten, S., 1998, ''Untersuchungen zur Auslegung von unprofilierten Nachleitradbeschaufelungen bei hochbelasteten Axialventilatoren,'' Dissertation, Technische Universität Braunschweig.
[14] Weingold, H. D., Neubert, R. J., Behlke, R. F., and Potter, G. E., 1995, ''Reduction of Compressor Stator Endwall Losses Through the Use of Bowed Stators,'' ASME Paper No. 95-GT-380.
[15] Shang, E., Wang, Z. Q., and Su, J. X., 1993, ''The Experimental Investigation on the Compressor Cascades With Leaned and Curved Blade,'' ASME Paper No. 93-GT-50.
[16] Wadia, A. R., and Beacher, B. F., 1989, ''Three-Dimensional Relief in Turbomachinery Blading,'' ASME Paper No. 89-GT-151.
[17] Dawes, W. N., 1988, ''Development of a Three-Dimensional Navier–Stokes Solver for Application to All Types of Turbomachinery,'' ASME Paper No. 88-GT-70.
[18] Dawes, W. N., 1992, ''Towards Improved Throughflow Capability: The Use of Three-Dimensional Viscous Flow Solvers in a Multistage Environment,'' ASME J. Turbomach., **114**, pp. 8–17.
[19] Dawes, W. N., 1991, ''Multi-Blade Row Navier–Stokes Simulations of Fan-Bypass Configurations,'' ASME Paper No. 91-GT-148.
[20] Tobak, M., and Peake, D. J., 1982, ''Topology of Three-Dimensional Separated Flow,'' Annu. Rev. Fluid Mech., **14**, pp. 61–85.
[21] Perry, A. E., and Chong, M. S, 1987, ''A Description of Eddying Motions and Flow Patterns Using Critical-Point Concepts,'' Annu. Rev. Fluid Mech., **19**, pp. 125–155.

Xavier Ottavy
Isabelle Trébinjac
André Vouillarmet

Ecole Centrale de Lyon,
Laboratoire de Mécanique des
Fluides et d'Acoustique,
UMR CNRS 5509/ECL/UCB Lyon I,
69131 Ecully Cedex, France

Analysis of the Interrow Flow Field Within a Transonic Axial Compressor: Part 1—Experimental Investigation

This paper relates to two-dimensional laser two-focus (L2F) anemometry measurements, conducted in a transonic research high-pressure compressor. Curved glass, which conforms to the shroud contour, was used. The resulting optical distortions of the control volume were corrected using an original and inexpensive optical assembly. Synchronized measurements were performed on two surfaces of the IGV–rotor interrow region. Particular care was taken in evaluating the capabilities of our L2F technique to accurately describe a flow field with strong gradient. The results presented show that the flow field is dominated by the moving oblique shock and its interaction with the IGV wake.
[DOI: 10.1115/1.1328085]

Introduction

At the present time, the high-speed multistage compressor is the most crucial component with regard to the performance of a turbojet of the new generation. However, the strong nonstationary phenomena occurring in such a machine are not still fully understood, and thus are often neglected in the design procedures. If time-accurate three-dimensional numerical codes are promising, in such configurations they are more often than not restricted to a nonviscous version. A classic multiblade row calculation method consists of coupling the results of stationary calculations applied to isolated adjacent blade rows, with assumptions being made for the coupling. But the transport of secondary flows (passage and tip vortices, wakes and shock waves, etc.) with change of frame, is not well known and has an effect upon the whole flow structure, particularly in transonic flows [1–3]. Thus, detailed and reliable fast response measurements are needed to qualify and to calibrate the numerical codes. Three-dimensional laser anemometry [4,5] is now operational, but it leads to real problems with regard to access to the flow channel of real high-speed, small-scale compressors. Global nonintrusive techniques like Particle Image Velocimetry [6,7] and Doppler Global Velocimetry [8], are very attractive, but at the moment, in addition to access restraint, they are not so accurate. Therefore, two-dimensional laser anemometry still remains the most suited technique.

A research program devoted to detailed measurements within an axial transonic research compressor, representative of the first stage of a high-pressure ratio compressor, has been undertaken jointly by SNECMA and the LMFA. This compressor is composed of an inlet guide vane (IGV), a rotor, and a stator. The laser two-focus anemometer used in this study was designed in the Laboratory to reduce acquisition time without sacrificing accuracy. Particular care was also given to estimating the measurement accuracy, especially in terms of time-discretization and of the capability of the seeding particles to follow the flow, which is subjected to strong deceleration through the shock waves.

Small, thin, flat glass windows typically provide optical access to the compressor flow field. This results in a mismatch between the window surface and the casing, which can induce perturbations. Even if these are very local, they can lead to substantial aerodynamic effects on the global flow field, especially in transonic or supersonic fields [9]. In the case of measurements in the vicinity of the blade tip clearance, the disturbance can be of the same order of magnitude as the phenomena under investigation. Therefore, curved glass windows, which conform to the outer flow path contour, are preferable. However, the curvature leads to optical distortions of the laser beams passing through the windows. In the case of LDA, these distortions increase measurement uncertainties, caused both by the deformation of the measurement volume and by changes in measurement location [10,11]. Durett et al. [12] have designed a lens to correct these aberrations. In the case of L2F anemometry, the problem is rather different and the effects are more severe. The distortions created by curved windows hinder the creation of acceptably focused spots in the control volume and could even prevent the acquisition of any data at all. These distortions have been studied by Ottavy et al. [13], and a simple and inexpensive optical assembly to restore acceptable foci was proposed and adapted to the investigated compressor.

Measurements, synchronized with the rotation of the rotor, were performed in the IGV-rotor interrow region. A section A, normal to the free-stream direction, and a blade-to-blade surface B, at 50 percent section height, were explored. This investigation is presented in two parts. The first part of this paper relates the experimental arrangement. Then the results are presented, including an evaluation of the measuring capabilities of the L2F system in the shock wave region. In Part II of this paper, the evolution of the IGV wakes, the shape and the location of the oblique shock wave emanating from the leading edge of the rotor blades and their interaction, are studied. Furthermore, the flow field is analyzed using decompositions in terms of temporal and spatial average values and fluctuating components.

Experimental Facility and Instrumentation

The Investigated Compressor. The investigated compressor, called ECL4, designed and built by SNECMA, is composed of an inlet guide vane, a rotor, and a stator. It is characterized by very high aerodynamic loading. At the design point, the pressure ratio is 2.25 and the specific values of the mass flow and the rotating speed are, respectively:

$$\dot{m}_{\mathrm{red}} = \frac{\dot{m}\sqrt{\gamma r T_{o_o}}}{p_{o_o} D^2} = 0.25 \quad (1)$$

Contributed by the International Gas Turbine Institute and presented at the 45th International Gas Turbine and Aeroengine Congress and Exhibition, Munich, Germany, May 8–11, 2000. Manuscript received by the International Gas Turbine Institute February 2000. Paper No. 2000-GT-496. Review Chair: D. Ballal.

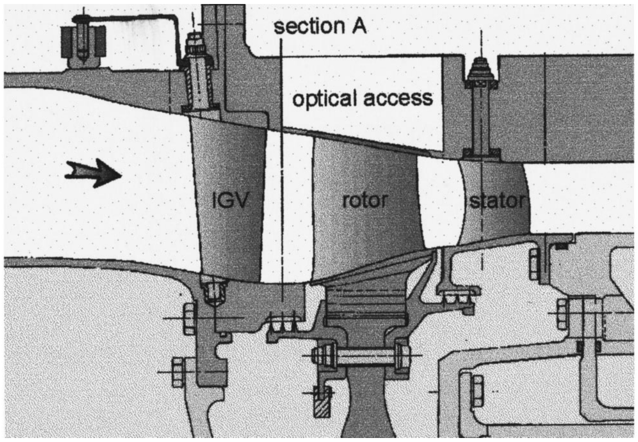

Fig. 1 Sketch of ECL4 compressor stage

$$N_{\mathrm{red}}=\frac{ND}{\sqrt{\gamma r T_{o_o}}}=0.36 \tag{2}$$

The inlet guide vane introduces an inlet counterswirl to the rotor at design speed, in order to increase the work capacity of the stage. The rotor blades are characterized by a very low aspect ratio (<0.9) and high solidity. The variable-stagger stator vanes are characterized by more conventional values of aspect ratio (about 1.3) and solidity (1.65 at midheight) than those of rotor blades. The ECL4 flow path is represented in Fig. 1.

The L2F Anemometer. The laser two-focus anemometer used in this study (Fig. 2) was designed in the laboratory, based on the work of Schodl [14]. The two spots constituting the measurement volume are created by two light cones, with parallel axes and optical angles of ±5 deg, which are focused by the frontal lens of the optical system (focal length 270 mm). These essentially ellipsoidal spots have a diameter of about 10 μm and are separated by a distance δ of 0.5 mm. The light scattered by the particles convected by the flow is collected inside cones with an apex angle of ±10 deg surrounding the incident light cones. Due to the required high power, which leads to high experimental costs, improved data acquisition procedures have been developed in order to reduce acquisition time [15]. First, a statistical analysis based on a hypothesis of noncorrelated variables, applied in a weak form, is used. Second, to synchronize measurements in rotating blade passages, an optimal blade pitch partition is realized by predicting the areas where no measurement is possible due to the blade twist and light reflections on the blade surfaces. Once all the quantifiable uncertainties have been taken into account, flow angle detection is generally found to be accurate to within ±0.5 deg in this experimented configuration, and mean velocity measurement error does not exceed ±1.5 percent. The case of the regions of strongly decelerated flows (where the lag of the particle is more severe) will be considered below.

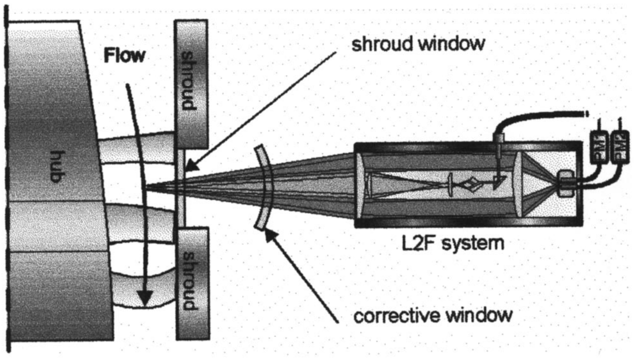

Fig. 2 Schematic arrangement of optical setup

Optical Access With Curved Windows. The need to have large optical access without introducing any mismatch between the window and the shroud contour led us to provide a curved window. Due to the geometric and pressure characteristics of the compressor, the radius and the thickness of the curved glass used are $R_s=253$ mm and $e_s=2.9$ mm. This window, called hereafter the ‘‘shroud window,’’ induces an optical distortion of the laser beam passing through it. This distortion is increased if a nonzero angle is present between the axis of the L2F system and the local vector normal to the window surface (angles Φ_s in the meridional section and η_s in the azimuthal section). As the principle of the L2F two-dimensional anemometry technique consists in measuring the time-of-flight of particles between two spotlights created by two tightly focused parallel laser beams resembling light cones, it is evident that the size of the focus volume has to be minimized in order to maintain good measurement accuracy and high light intensity. Moreover, the geometric characteristics of the control volume (distance between the two spots and their angular position) have to be known exactly. So, these distortions were studied [13], and an optical assembly, whose principle is presented below, was adapted to the investigated compressor to restore acceptable foci. If we consider the reference case in which the light beams do not pass through any glass window, each focus is assumed to be a geometric point F_{ref} (Fig. 3(*a*)). The $S1$ and $S2$ light surfaces are perpendicular to the (x,y) plane, within the light cone. In Fig. 3(*b*) a plane window is inserted, perpendicular to the axis of the light cone, between the focus and the frontal lens. The focused spot F has shifted slightly but, as the light cone angle remains small (around 5 deg), it is still very similar to a geometric point. Let us now replace the plane window by a curved glass window that is shaped on a cylinder whose axis is parallel to the $(0, z)$ direction, as shown in Fig. 3(*c*). On the one hand, the light surfaces $(S1, S2)$ focus on $[F2F2']$ (where F is the midpoint) but, because of the window curvature, they do not intersect one another at their foci but at $[F1F1']$. On the other hand, the light surfaces perpendicular to the $(0, z)$ direction focus on $[F1F1']$ and intersect one another at $[F2F2']$. This results in two concentrated light zones $[F1F1']$ and $[F2F2']$, which diverge when the radius of curvature of the glass decreases and when the thickness increases. In order to restore a sole focused spot, a second curved window (called the ‘‘corrective window’’), shaped on a cylinder whose axis is parallel to the $(0, y)$ direction, is inserted between the shroud window and the frontal lens (Fig. 3(*d*)). This second window induces similar distortions in the (x, z) plane as the shroud window in the (x, y) plane. By optimally adjusting (as described below) the radius R_c and thickness e_c of the glass and distance d between the two windows, a focus comparable to a point $F3$ is obtained.

The focus error was analyzed by using two particular beams within the light cone. This calculation was restricted to the configuration where the axis of the cone is perpendicular to the windows. By simply minimizing the focus error, expressed as a function of the characteristics and of distance d between the shroud and the corrective windows, and of the maximum immersion $FI_{\max}$ of the focus volume in the compressor channel, the radius of the corrective window R_c and the optimized distance d between the two windows could be estimated very well.

However, taking into account angles Φ_s and η_s would complicate the calculation. Furthermore, we have to distinguish the two focusing light cones, which create the two light spots, in order to foresee the changes in the actual characteristics of the probe volume (angular position and distance between the two spots). Thus, a numerical simulation, using a discretization of the laser cone

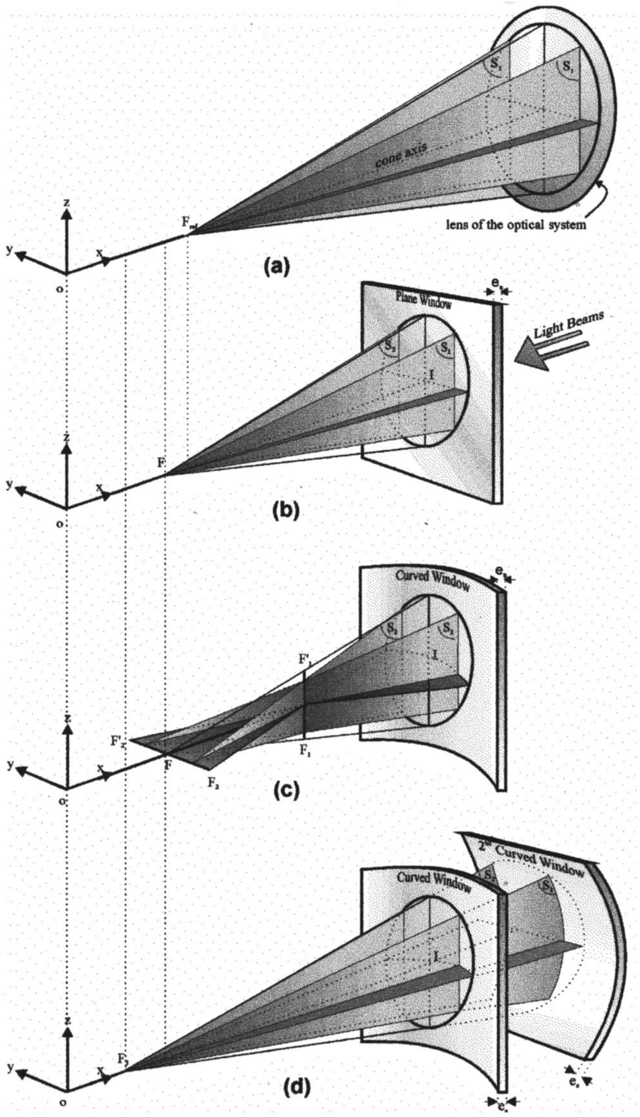

Fig. 3 Optical distortions of a laser cone passing through windows

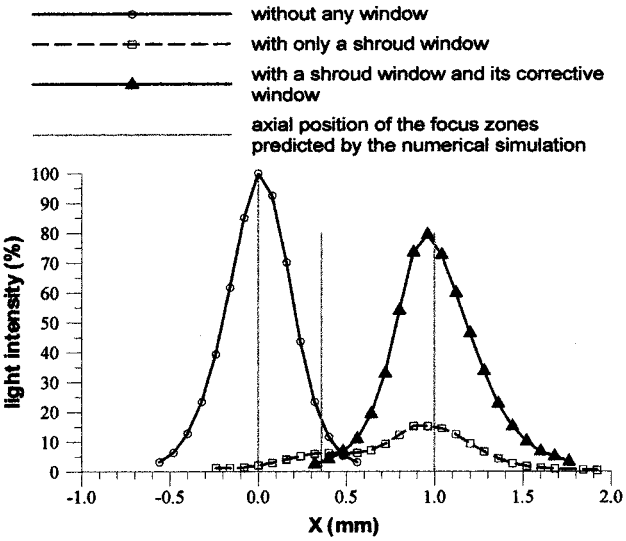

Fig. 4 Comparison of measured optical depths of field of anemometer with and without windows

and initialized with the corrective window characteristics deduced from the previous analytical solution, was developed to predict the four free parameters, which characterize the corrective window (R_c, e_c, η_c, and Φ_c), distance d between the two windows for each immersion *FI*, and the actual characteristics of the control volume.

By applying this study to the tested compressor, a suitable corrective window was determined, with a thickness $e_c = 1.9$ mm, a radius $R_c = 470$ mm, and a maximal distance between the two panes of glass $d_{\max}$ equal to 190 mm (for the maximum immersion $FI_{\max}$ of 80 mm). The improvement of the shape of the focus volume can be highlighted by considering the case where the cone passes through the shroud window of the compressor, without any corrective window, with $\Phi_s = 10$ deg, $\eta_s = 0$ deg, and $FI = 75$ mm. The numerical evaluation of the longitudinal characteristic size of the focus volume gives $l = 260$ μm. The minimal value is reached with the use of a corrective window with $\Phi_c = -29.8$ deg, $\eta_c = 0$ deg, and $d = 95$ mm. In that case, the longitudinal size l is only 5 μm. This value is approximately three times lower than for the case where the light cone passes through a single plane glass window of an equal thickness. Furthermore, a setup was realized to control the spatial resolution (longitudinal depth of field) of the anemometer experimentally if using a curved window. The immersion choice is 100 mm and the optimized distance between the two panes of glass is $d = 305$ mm. In Fig. 4 the measured spatial resolution curves in three different cases are plotted. In the first case, which was obtained without any window, the evolution of the reduced scattered light intensity looks like a Gaussian curve and leads to an optical depth of field (defined at the $1/e^2$ intensity point) of 0.8 mm. The second case, where only the shroud window is introduced, leads to a bad result: The obtained signal is very low and the depth of field is two times greater. Moreover, we can notice two maximum values corresponding to the two focus zones described in Fig. 3(*c*). In the third case, where the optimized corrective window is introduced, a good result is restored: a high level, Gaussian-shaped signal, leading to a depth of field of 1.0 mm. We can observe that the numerical simulation predicts the different positions of the focus zones very well.

Last, it should then be noted that, when the L2F optical system rotates, the control volume becomes unaligned with the shroud window axis ($\gamma \neq 0$ deg). This leads to insignificant errors regarding its characteristics: 0.3 percent for the distance δ between the two spots and 0.1 deg for the angular position of the measurement volume, when the angular position γ moves from 0 to 90 deg (for the case with $\Phi_s = 10$ deg, $\eta_s = 0$ deg, and $FI = 75$ mm).

Seeding. The compressor was seeded with a polydisperse aerosol of paraffin oil, through a movable smoke probe (3 mm in diameter) located 50 diameters upstream of the measurement point. The liquid droplet size distribution was measured with a PDA technique to be between 0.5 and 2 μm (the mean value is approximately 1 μm). We have checked that, in our case, the effects of the centrifugal forces on the particle trajectory is quite negligible. But the recovery distance, for particles crossing an oblique shock, increases rapidly with particle diameter. A calculation, based on the works of Melling [16], has been made for a flow with an upstream Mach number of 1.25, deflected with an angle of 4.5 deg. It shows that, for paraffin oil particles, whose mean diameter is less than 1 μm, the distance to reach the flow velocity downstream of the shock is approximately 6 mm. This bias will be discussed below.

Results

Measurement Location. A section normal to the free-stream direction (called *A*) and a blade-to-blade surface at 50 percent

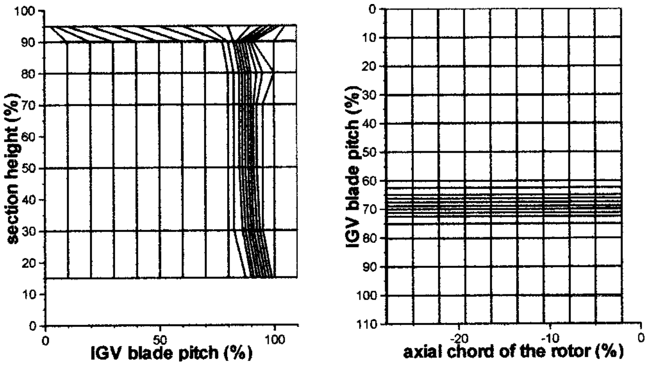

Fig. 5 Experimental mesh of surfaces *A* and *B*

section height (called *B*) have been explored. By using 20 different azimuthal locations, 110 percent of the IGV pitch is covered and the IGV wake is captured with around ten azimuthal positions, so it is well described in the absolute frame. The acquisition of data was synchronized with the rotation of the rotor. The time between the passage of two rotor blades was discretized into ten intervals, which correspond to ten spatial positions in the relative frame.

At midspan, section *A* is located at 31 percent of the IGV chord, downstream of the IGV trailing edge, and at 28 percent of the rotor chord, upstream of the rotor leading edge. Measurements were taken from 15 to 95 percent section height. The blade-to-blade surface *B* is described from section *A* up to the rotor leading edge region. The experimental mesh of the two measurement surfaces is shown in Fig. 5.

Due to the axial thrust and thermal dilatations of the machine, a procedure was defined for positioning the L2F control volume during compressor operation. The uncertainty of the axial and radial locations of any measurement point is then estimated to be ±0.15 mm.

Flow Field Description in Section *A* Normal to the Free-Stream Direction. The results shown hereafter deal with the flow field in section *A* normal to the free-stream direction, expressed in the absolute frame, i.e., relative to the IGV. Therefore, the location of the rotor blades is time dependent. The results are presented through iso-value maps in which the abscissa is the angular position normalized by the IGV pitch and the ordinate is the radius expressed as a percentage of the section height.

The contour maps of the mean absolute velocity V, the mean absolute angle α, and the velocity standard deviation σ_V are respectively presented in Figs. 6, 7, and 8 for four different positions of the rotor blade row (expressed as a percentage of the rotor pitch time T_r). The IGV wake, characterized by a deficit in velocity (Fig. 6) is clearly visible at around 90 percent of the IGV pitch. Its slight change in location and the hub-to-tip evolution of the

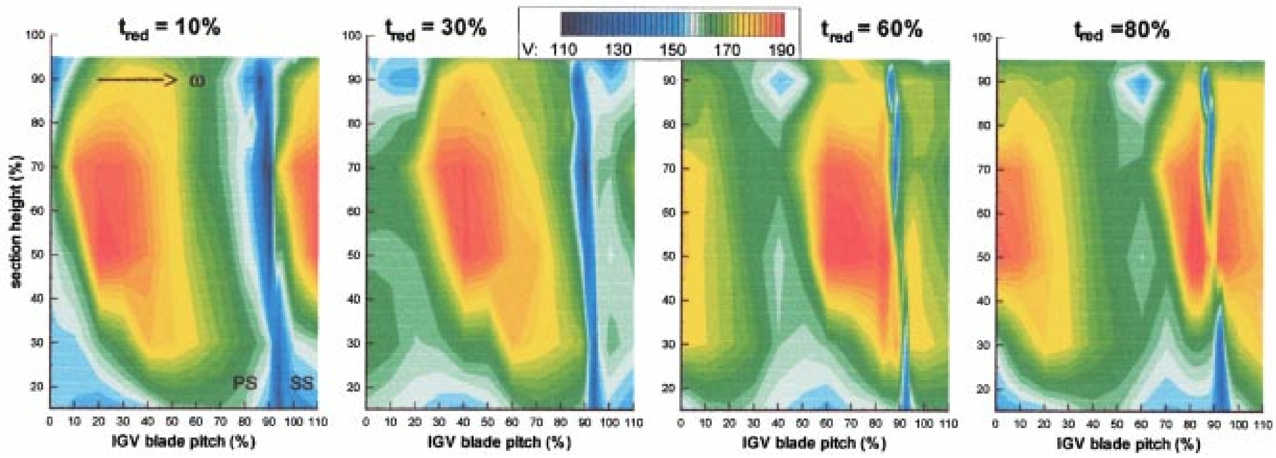

Fig. 6 Contour maps in section *A* of the absolute velocity *V* for four different positions of rotor blade row

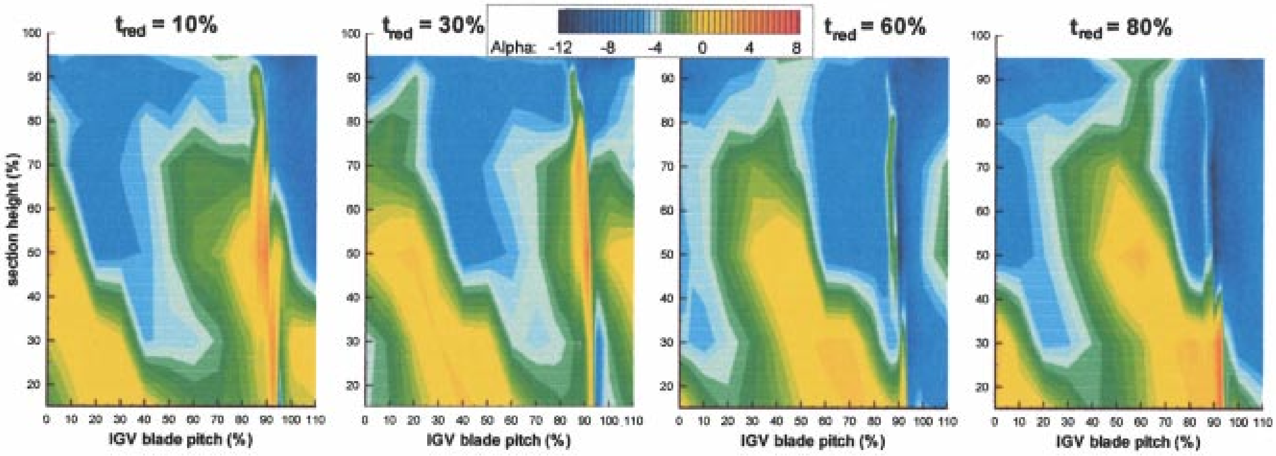

Fig. 7 Contour maps in section *A* of absolute angle α for four different positions of rotor blade row

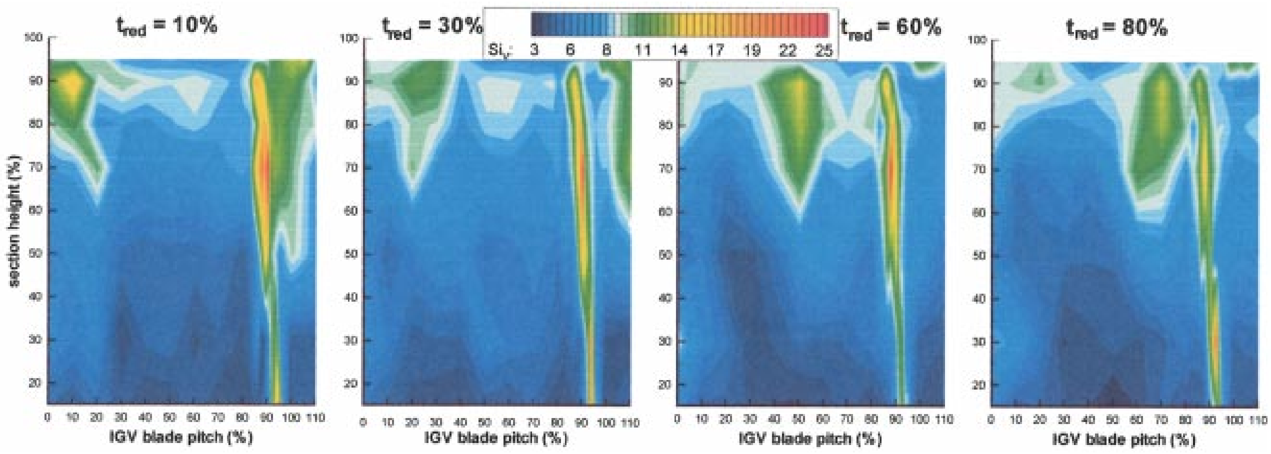

Fig. 8 Contour maps in section *A* of velocity standard deviation σ_V for four different positions of rotor blade row

flow angle observed in Fig. 7, arise from the radial twisting of the trailing edge of the IGV. Outside the wake, the velocity distributions present oscillations in the circumferential direction resulting from the oblique shock emanating from the rotor leading edge and from the expansion waves due to the convex suction side of the rotor blades. As the rotor moves in the same direction as the increasing IGV angular values, the shock is located at the left of the high-velocity pocket. Thus, the four relative positions of the rotor presented in the figures correspond to a time when the shock has just crossed the wake ($t_{\mathrm{red}}=10$ percent, where $t_{\mathrm{red}}=(t-t_{\mathrm{ref}})/T_r$), a time when the wake is within the expansion zone, just before the passing of the shock ($t_{\mathrm{red}}=80$ percent) and two intermediate times ($t_{\mathrm{red}}=30$ and 60 percent). We can observe that the strength of the shock is greatest at midheight and its shape is fully three dimensional. The wake tends to disappear in the expansion zone, whereas it deepens after the shock. This is all the more noticeable as the shock is strong (at around 60 percent of section height). Regarding the absolute angle in Fig. 7, we observe high positive values within the wake just after the passing of the shock and negative values when the wake is in the expansion zone. As the IGV outlet blade angle is negative, this means the expansion overturns the wake, whereas the shock turns it in the rotor speed direction. Moreover, at any given time, the flow is underturned on the pressure side of the wake and overturned on the suction side. For instance, if looking at the map at $t_{\mathrm{red}}=80$ percent, the flow angle is -5 deg on the pressure side of the wake at 60 percent of section height and reaches -12 deg on the suction side. We can observe in Fig. 8 that, as expected, the highest levels of velocity standard deviation are located within the wake (the same is true of the angle standard deviation, not shown here). A pocket of high-velocity fluctuations is moreover notable near the casing (centered at 90 percent of section height). It moves with the shock and probably results from the shock/wall boundary layer interaction.

The time-averaged absolute angle and velocity fields calculated from the L2F results are compared with those obtained with a three-hole mean pressure probe in Figs. 9 and 10 [9]. This probe is composed of three joined tubes with 0.7 mm diameter. In spite of a poorer spatial resolution of the probe measurements, we observe a rather good agreement, especially for the angle evolutions. The global difference observed on the velocity levels is probably due to the poor reliability of the pressure tap of the probe in such a flow field, the probe size being around half the wake width. A secondary flow zone, characterized by an over deviation and an under velocity, is clearly visible in the wake suction side/shroud corner.

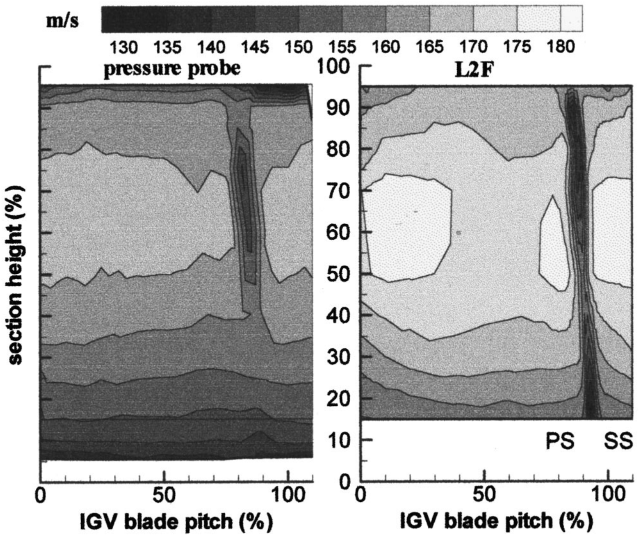

Fig. 9 Comparison of time-averaged absolute velocity fields obtained in section *A* with L2F and "three-hole" pressure probe

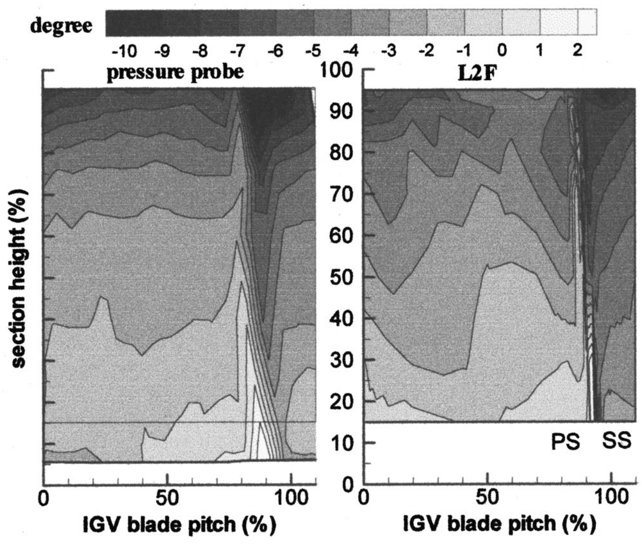

Fig. 10 Comparison of time-averaged absolute angle fields obtained in section *A* with L2F and "three-hole" pressure probe

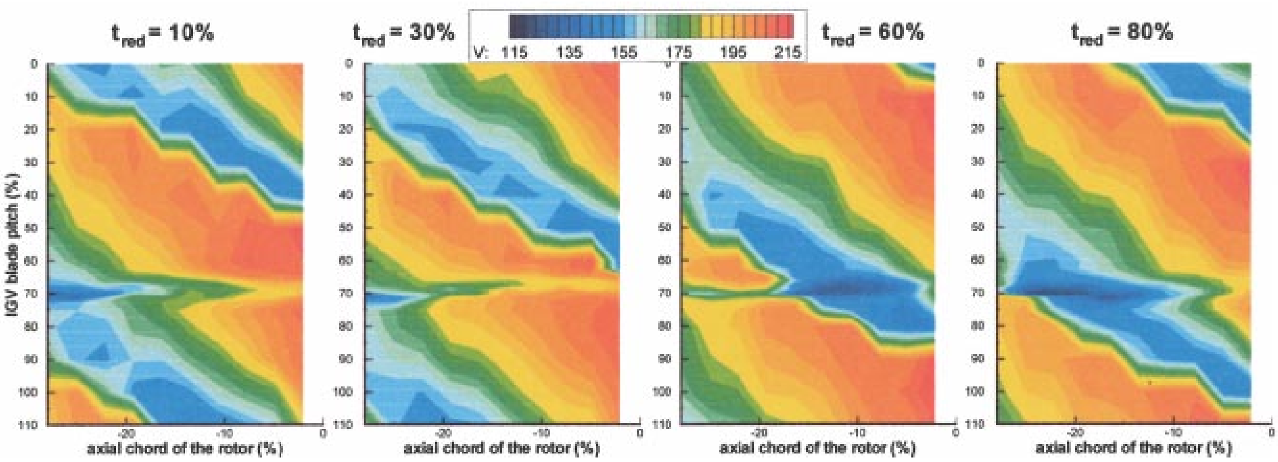

Fig. 11 Contour maps on surface *B* of the absolute velocity *V* for four different relative positions of rotor blade row

Flow Field Description on the Blade-to-Blade Surface *B* at 50 Percent Section Height. The results obtained on the blade-to-blade surface B located at 50 percent section height are presented through iso-value maps in which the abscissa is the axial distance expressed as a percentage of the rotor blade chord, and the ordinate is the angular position normalized by the IGV pitch. As above, four times ($t_{\mathrm{red}}=10$, 30, 60, and 80 percent) are extracted from the ten acquired times. The contour maps of the absolute velocity V, the absolute angle α, and the velocity standard deviation σ_V are, respectively, shown in Figs. 11, 12, and 13. The IGV wake, the oblique shock wave emanating from the leading edge of the rotor blades, and the expansion zone are clearly visible. On the whole, the same conclusions regarding the behavior of the wake through the moving shock, as those deduced from the results obtained in section A, can be stated.

The interrow flow field is dominated by the moving oblique shock and the interactions that it generates. Therefore, before analyzing each of the structures as well as their interactions, it seems to be very important to evaluate the capabilities of our L2F technique to describe a flow field with strong gradients accurately.

Evaluation of the Measuring Capabilities in the Shock Wave Region. Among the various causes, the discretization of the rotor blade pitch and the behavior of the seeding particles play a great part in the measurement uncertainties registered in the shock wave region. Series of measurements were made in a wake-free point of section A, with various numbers N_w of rotor blade pitch intervals (also called measurement windows). It is seen in Fig. 14 that the deceleration through the shock spreads out 20 percent of the blade pitch width. This gradient distance, observed at whatever blade pitch partition is set, corresponds to the previously estimated recovery distance of particles (6 mm). Nevertheless, we have checked that flow parameters downstream of the shock (deceleration level and deviation angle) are well restored, even if it is with some delay. Moreover, the difference in the time average velocity for the 10 and 20 window cases is less than 0.03 percent. Therefore, if seeding with 1 μm particles, it is pointless to overrefine the blade pitch cutout. On the contrary, the accuracy of the determination of the shock location (assumed to be at the beginning of the deceleration) is directly connected with the width of the measurement window enclosing it. Furthermore, the gradient downstream of the shock can spread out two or three adjacent windows wide, depending on the position of the shock inside the first window.

In strong gradient regions, the spatial variation of the velocity inside a measurement window leads to a bias in the measured standard deviations. For instance, if considering a laminar flow field with linear variation of the velocity from V_1 to V_2 within a window, a simple calculation leads to a velocity standard deviation such as:

$$\sigma_V=\frac{|V_1-V_2|}{2\sqrt{3}} \tag{3}$$

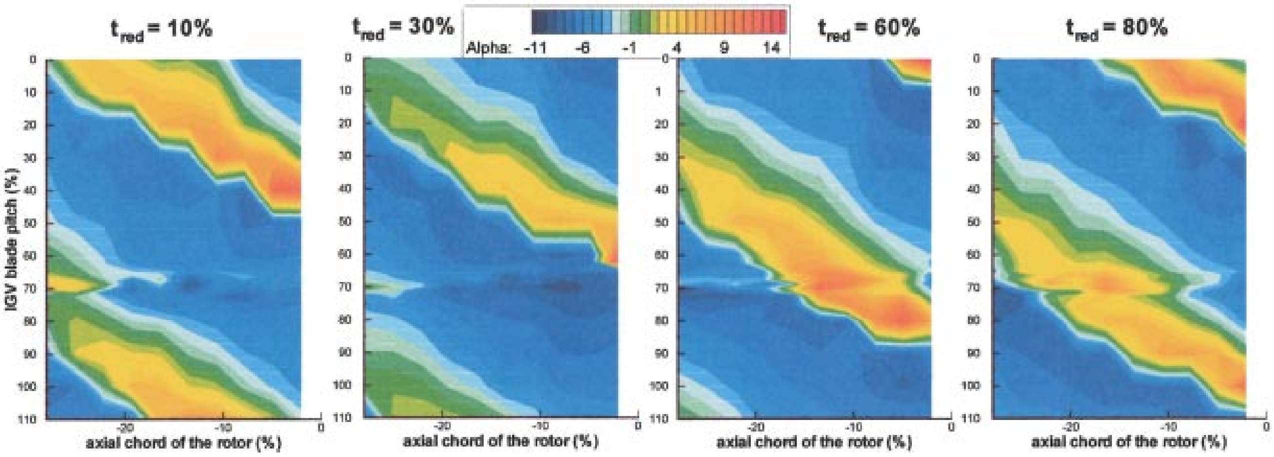

Fig. 12 Contour maps on surface *B* of the absolute angle α for four different relative positions of rotor blade row

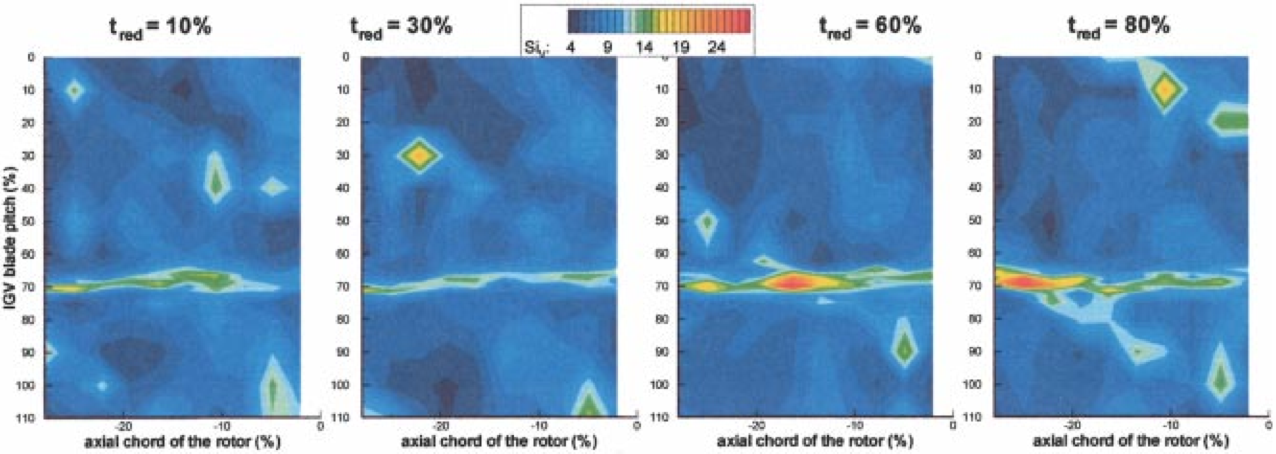

Fig. 13 Contour maps on surface *B* of the standard deviation σ_V for four different relative positions of rotor blade row

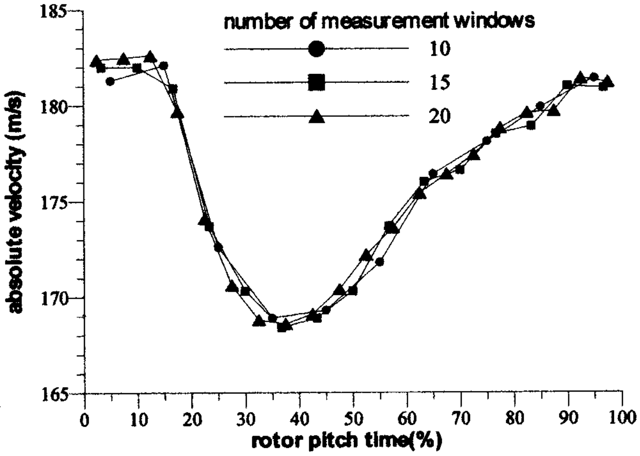

Fig. 14 Flow deceleration through shock in section *A*, for different blade pitch partitions

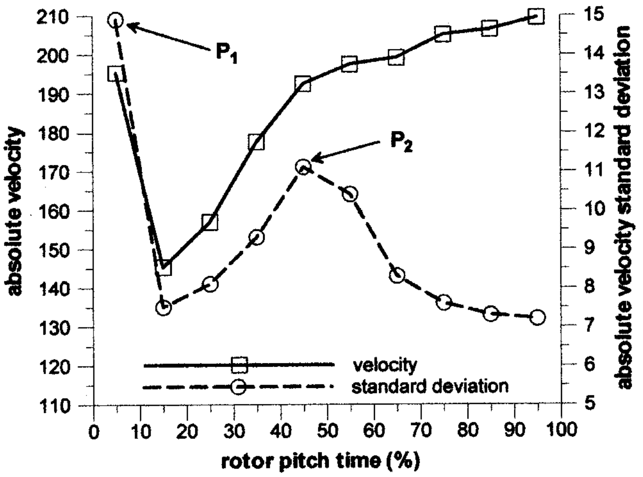

Fig. 15 Time evolutions of mean absolute velocity and standard deviation at a point located on surface *B*, in a wake-free region, 5 percent of rotor chord upstream of leading edge of rotor

The measured standard deviation in a strong gradient region can thus be decomposed into a real part and a fictitious part only due to the spatial variation of the velocity inside the window. The time evolutions of the absolute velocity and the associated standard deviation at a point located on surface *B*, in a wake-free region, 5 percent of the rotor chord upstream of the leading edge of the rotor, are presented in Fig. 15. The highest levels of the standard deviation σ_V are observed in the shock region (point $P1$) and in the expansion zone (point $P2$). The values, measured at any point P, result from the integration of the flow parameters within the measurement window, centered on point P, and whose width is 10 percent of the rotor pitch. In accordance with the previous expression, Eq. (3), the fictitious standard deviation reaches about 9 m/s at point $P1$ and 3 m/s at point $P2$. Therefore, at both points, the real standard deviation reaches about 7 m/s, i.e., the level of the standard deviation measured outside the strong gradient zones. The measured values of the standard deviations in regions of high-velocity gradients have thus to be considered with great care because they are biased. By overrefining the blade pitch cutout, the fictitious part of the standard deviation would decrease. But, as seen above, this refinement is actually of interest only if efforts are made as to the size and the monodisperse character of the seeding particles.

Conclusion

L2F measurements have been performed in the interrow region of the transonic compressor, provided with large curved windows. The induced optical distortions have been fully prevented by using an original and inexpensive optical assembly. The data obtained show that the flow field is dominated by the moving shock emanating from the rotor, and its influence on the IGV wake. The accuracy of the measurements is evaluated, especially in the strong gradient regions of the flow. It is seen that the deceleration level and the deviation angle are well restored but with some delay, mainly due to the size and the polydisperse character of the seeding particles. It can be concluded that, with care, the data bank obtained is reliable for analyzing the structures present in the flow field, and their interactions.

Acknowledgments

We would like to thank SNECMA, which placed the investigated compressor at our disposal and supported this work.

Nomenclature

D = characteristic linear dimension of compressor
F = focused spot location

FI = immersion (distance between probe volume and outer surface of shroud window)
N = rotating speed
N_w = number of measurement windows
P = measurement point location
R = radius of curvature of the glass window
$S1$, $S2$ = light surfaces
T = temporal period
T_0 = stagnation temperature
V = absolute velocity modulus
d = distance between outer surfaces of two curved windows
e = thickness of glass window
l = longitudinal length of measurement volume
$\dot{m}$ = mass flow
p_0 = stagnation pressure
r = specific gas constant
t = time
x, y, z = Cartesian coordinates
Φ = angle between axis of L2F optical system and normal to glass window, in meridional section
α = absolute velocity angle
γ = ratio of specific heats
γ = angle between direction defined by two foci and axis of curved shroud window, in perpendicular plane of L2F optical system axis
δ = distance between two light spots
ν = angle between axis of L2F optical system and normal to glass window, in azimuthal section
σ = standard deviation

Subscripts

c = corrective window
max = maximum value
r = rotor
s = shroud window
V, α = polar components of the velocity vector
red = reduced value
ref = reference value
0 = inlet conditions

References

[1] Burnes, T., Ottenberger, D. B., and Elliot, M., 1998, ''F/A-18 E/F Aircraft Engine (F414-GE-400),'' in: *Blade Row Interference Effects in Axial Turbomachinery Stages*, Von Karman Institute for Fluid Dynamics, LS 1998-02.
[2] Fritsch, G., and Giles, M. B., 1995, ''An Asymptotic Analysis of Mixing Loss,'' ASME J. Turbomach., **117**, pp. 367–374.
[3] Wisler, D. C., 1998, ''The Technical and Economic Relevance of Understanding Blade Row Interaction Effects in Turbomachinery,'' in: *Blade Row Interference Effects in Axial Turbomachinery Stages*, Von Karman Institute for Fluid Dynamics, LS 1998-02.
[4] Beversdorff, M., Matziol, L., and Blaha, C., 1998, ''Application of 3D-Laser Two Focus Velocimetry in Turbomachine Investigations,'' AGARD Conf. Proc., **598**, pp. 13.1–13.7.
[5] Förster, W., Schodl, R., and Rijmenants, E., 1990, ''Design and Experimental Verification of the 3D Velocimeters Based on the L2F Technique,'' *Proc. 5th International Symposium on Application of Laser Anemometry to Fluid Mechanics*, Lisbon.
[6] Tisserand, D., and Breugelmans, F. A. E., 1997, ''Rotor Blade-to-Blade Measurements Using Particle Image Velocimetry,'' ASME J. Turbomach., **119**, pp. 176–181.
[7] Wernet, M. P., 1998, ''Demonstration of PIV in a Transonic Compressor,'' AGARD Conf. Proc., **598**, pp. 51.1–51.13.
[8] Roehle, I., and Schodl, R., 1998, ''Applications of Three Dimensional Doppler Global Velocimetry to Turbo Machinery and Wind Tunnel Flows,'' AGARD Conf. Proc., **598**, pp. 52.1–52.10.
[9] Escuret, J. F., Veysseyre, P., Villain, M., Savarese, S., Bois, G., and Navière, H., 1997, ''Effect of a Mismatch Between the Buttons of Variable Stator Vanes and the Flow Path in a Highly Loaded Transonic Compressor Stage,'' ASME Paper No. 97-GT-471.
[10] Hathaway, M. D., Chriss, R. M., Wood, J. R., and Strazisar, A. J., 1993, ''Experimental and Computational Investigation of the NASA Low Speed Centrifugal Compressor Flow Field,'' ASME J. Turbomach., **115**, pp. 527–542.
[11] Doukelis, A., Founti, M., Mathioudakis K., and Papailiou, K., 1996, ''Evaluation of Beam Refraction Effects in a 3D Laser Doppler Anemometry System for Turbomachinery Applications,'' in: *Measurement Science and Technology*, Vol. 7, pp. 922–931.
[12] Durrett, R. P., Gould, R. D., Stevenson, W. H., and Thompson, H. D., 1985, ''A Correction Lens for Laser Doppler Velocimeter Measurements in a Cylindrical Tube,'' AIAA J., **23**, No. 9, pp. 1387–1391.
[13] Ottavy, X., Trébinjac, I., and Vouillarmet, A., 1998, ''Treatment of L2F Anemometer Measurement Volume Distortions Created by Curved Windows for Turbomachinery Application,'' Meas. Sci. Technol., **9**, pp. 1511–1521.
[14] Schodl, R., 1986, ''Laser Two Focus Velocimetry,'' AGARD CP 399 Paper.
[15] Vouillarmet, A., and Trébinjac, I., 1998, ''Improvement in L2F Anemometry Technique for Inter-Blade Investigations in High-Speed Turbomachinery,'' ASME Paper No. 98-GT-157.
[16] Melling, A., 1986, ''Seeding Gas Flows for Laser Anemometry,'' AGARD CP 399.

Xavier Ottavy
Isabelle Trébinjac
André Vouillarmet

Ecole Centrale de Lyon,
Laboratoire de Mécanique des
Fluides et d'Acoustique,
UMR CNRS 5509/ECL/UCB Lyon I,
69131 Ecully Cedex, France

Analysis of the Interrow Flow Field Within a Transonic Axial Compressor: Part 2—Unsteady Flow Analysis

An analysis of the experimental data, obtained by laser two-focus anemometry in the IGV-rotor interrow region of a transonic axial compressor, is presented with the aim of improving the understanding of the unsteady flow phenomena. A study of the IGV wakes and of the shock waves emanating from the leading edge of the rotor blades is proposed. Their interaction reveals the increase in magnitude of the wake passing through the moving shock. This result is highlighted by the streamwise evolution of the wake vorticity. Moreover, the results are analyzed in terms of a time-averaging procedure and the purely time-dependent velocity fluctuations that occur are quantified. It may be concluded that they are of the same order of magnitude as the spatial terms for the inlet rotor flow field. That shows that the temporal fluctuations should be considered for the three-dimensional rotor time-averaged simulations. [DOI: 10.1115/1.1328086]

Introduction

A critical issue for the turbomachinery industry remains the time-averaged simulation of multistage turbomachinery. Classical three-dimensional multiblade row simulation methods consist in connecting results of stationary calculations applied to isolated adjacent blade rows, the information between the rows usually being exchanged through mixing planes. A circumferential averaging procedure yields time-averaged conditions along these interrow planes. Nevertheless, unsteady blade-row interaction has repercussions on the time-averaged flow [1–3]. Bardoux et al. [4] provide an interesting review of numerical results using mixing-plane methods and more complex approaches using deterministic correlation models. The authors highlight the shortcomings of such methods, which are mainly due to the fact that only spatial correlations are modeled. From time-dependent numerical results in a transonic turbine stage, they perform a direct computation of all the correlations in order to evaluate their influence on the time-averaged flow field. Regarding the experimental results available in the literature, few can be used to calculate these deterministic correlations. Thus, from the data bank obtained from the measurements performed in the interrow region of a transonic compressor, our main subject of interest is the evaluation of the temporal correlations, which represent the unsteadiness of the flow. Without claiming to build any model for the computation of these correlations, we propose to give some clues to the orders of magnitude of the temporal correlations relative to the spatial correlations.

In the first part of this paper, the results of laser two-focus (L2F) measurements performed in the IGV-rotor interrow region of a highpressure ratio compressor were presented. They provide a detailed data bank for a comprehensive description of the interrow flow field and for a validation of numerical simulations. It is pointed out that the flow field is dominated by the moving oblique shock emanating from the rotor blade leading edge and its interaction with the IGV wake.

In this Part 2 of the paper, the experimental data in the compressor are further discussed, with special attention to the evolution of the IGV wakes, the shape and the location of the oblique shock wave emanating from the leading edge of the rotor blades and their interaction. If the 20 investigated azimuthal locations cover 110 percent of the IGV pitch and allow a good description of the IGV wakes in the absolute frame, they make up a field that is not wide enough to restore the whole flow field in the relative frame. Therefore, the spatial–temporal (chorochronic) periodicity [5,6] is experimentally checked and applied to the data. Furthermore, the flow field is analyzed, in terms of temporally and spatially averaged values and fluctuating components, using the decomposition developed by Adamczyk et al. [7]. The purely time-dependent velocity fluctuations especially are quantified.

IGV Wake and Rotor Oblique Shock

Measurement Location. The data were collected in section *A* normal to the free-stream direction, and on a blade-to-blade surface *B* at 50 percent section height. At midspan, section *A* is located at 31 percent of the IGV chord, downstream of the IGV trailing edge, and at 28 percent of the rotor chord, upstream of the rotor leading edge. The blade-to-blade surface *B* is described from section *A* up to the rotor leading edge region. The data location is given in Fig. 1.

Flow Field Decomposition. In addition to three-dimensional, turbulent, and viscous effects, nonuniformities and unsteadiness due to the rotor–stator interaction introduce major complexity in the analysis of the flow field. This problem can be simplified by decomposing any flow variable $X(r,z,\theta,t)$ into averaged $\overline{X}$ and fluctuating X' components. Such decomposition can be applied either in the absolute frame or in the frame relative to the rotor. A first decomposition stage consists in writing:

$$X(r,z,\theta,t)=\overline{X}(r,z,\theta)+X'(r,z,\theta,t) \tag{1}$$

$$\overline{X}(r,z,\theta)=\bar{\bar{\tilde{X}}}(r,z)+\overline{X^*}(r,z,\theta) \tag{2}$$

with

$X(r,z,\theta,t)$=instantaneous value at any given location
$\bar{\bar{\tilde{X}}}(r,z,)$=time and blade-to-blade averaged value (or axisymmetric value)
$\overline{X^*}(r,z,\theta)$=blade-to-blade fluctuating component of time-averaged value

---

Contributed by the International Gas Turbine Institute and presented at the 45th International Gas Turbine and Aeroengine Congress and Exhibition, Munich, Germany, May 8-11, 2000. Manuscript received by the International Gas Turbine Institute February 2000. Paper No. 2000-GT-497. Review Chair: D. Ballal.

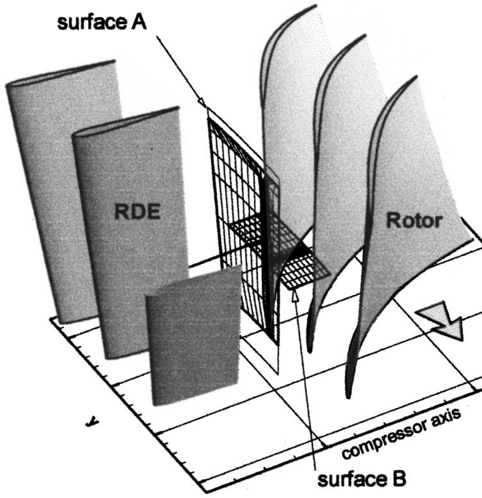

Fig. 1 Data location

$X'(r,z,\theta,t)$=periodic temporal fluctuating component, clocked with rotor frequency.

The fluctuating components are exclusively periodic because the L2F data acquired in each rotor blade channel are superimposed. Note that all the mean values are obtained with an arithmetic averaging process.

A further decomposition can be applied to this last term and will be expressed later.

IGV Wake. The measurements have been realized in the absolute frame and the investigated azimuthal locations, covering 110 percent of the IGV pitch, allow a good description of the IGV wakes. The measurements performed in section *A* lead to a description of the radial evolution of the stator wake. The feature of the wake is described by the blade-to-blade periodic fluctuating components of the time-averaged velocity in the absolute frame, $\overline{V}^*(r,z,\theta)$, and angle, $\overline{\alpha}^*(r,z,\theta)$. These components are shown in Fig. 2, versus the angular position normalized by the IGV pitch, for four immersion values. The wake width at 50 percent section height is about 10 percent of the stator blade pitch and, except at 95 percent of span, it remains more or less constant along the section. The maximum defect in velocity at 50 percent section height is 23 m/s (i.e., 13 percent of the free-stream velocity), whereas it reaches 40 m/s (i.e., 24 percent of the free-stream velocity) at 90 percent. From 15 to 90 percent of span, the angle evolutions indicate that the flow is overturned (higher negative values) on the suction side and underturned on the pressure side of the wake. This is consistent with the wake feature of an isolated blade row. In the end-wall region (95 percent of span), the wake width is very large, which is probably partly due to the radial migration of low-momentum stator blade boundary layer flow toward the shroud.

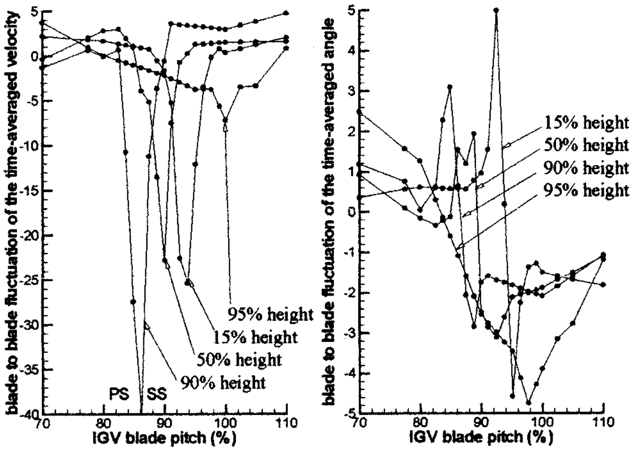

Fig. 2 Blade-to-blade fluctuating components of the time-averaged velocity and angle, versus the angular position normalized by the IGV pitch, for four immersion values

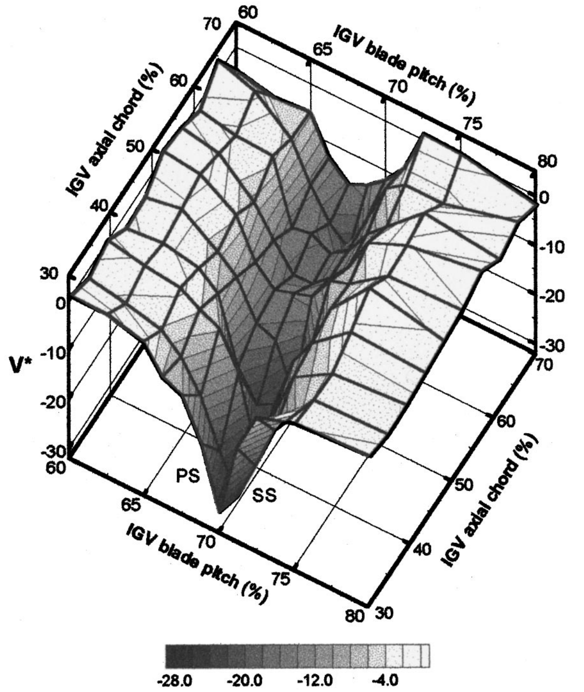

Fig. 3 Streamwise evolution of the stator wake blade-to-blade fluctuating component of the time-averaged velocity at 50 percent of span

The streamwise evolution of the stator wake blade-to-blade fluctuating component of the time-averaged velocity, from section *A* up to the rotor leading edge, is drawn in Fig. 3, from the measurements performed at 50 percent of span (surface *B*). Along this distance (from 30 to 70 percent of the IGV axial chord, downstream of the trailing edge) the wake width increases slightly, whereas the maximum defect in velocity decreases to half the value obtained in section *A*.

Rotor Leading Edge Shock. In order to analyze the oblique shock wave emanating from the leading edge of the rotor blades, it is more suitable to make a transcription of the data obtained, in the frame relative to the rotating blade row. However, the field that has been investigated is not wide enough in the circumferential direction to restore the whole flow field in the relative frame, so it is necessary to hypothesize spatial–temporal (chorochronic) periodicity. Such a procedure, which excludes distortions moving in the circumferential direction at a fraction of the rotor speed (rotating stall, for instance) and requires an axisymmetric upstream flow field, is usually applied in numerical simulations where the calculations are performed in one channel only. It has been experimentally checked and applied to the obtained data.

Let us consider the IGV (stator) with N_s blades, and the rotor with N_r blades, of the investigated compressor. The time variations of any aerodynamic parameter $X_{\theta 1}(t)$ at a fixed point $P_{\theta 1}$ of the stator–rotor interrow region are assumed to result from the perturbations arising from the rotor blades moving downstream (Fig. 4). Thus, the temporal period T_s of the measured signal X is connected to the spatial period of the rotor blade passage (blade pitch Θ_r) by its rotating speed ω $(\Theta_r=\omega\cdot T_s)$. Let us now con-

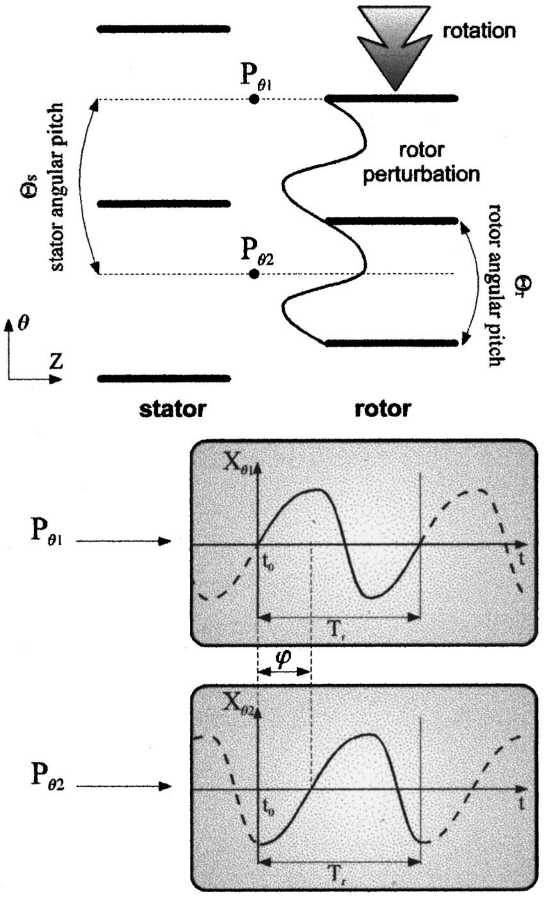

Fig. 4 Illustration of the spatial-temporal periodicity

sider another point $P_{\theta 2}$ located at the azimuthal coordinate θ_2 such that $\theta_2 = \theta_1 - \Theta_s$ (where Θ_s is the stator angular pitch). Points $P_{\theta 1}$ and $P_{\theta 2}$ are defined as homologous. At $P_{\theta 2}$, signal $X_{\theta 2}(t)$ is under the same rotor perturbations, but phase-shifted:

$$X_{\theta 2}(t) = X_{\theta 1}(t - \varphi) \tag{3}$$

So the hypothesis of the spatial–temporal periodicity consists in linearly linking the time and the circumferential distance. The phase shift φ is expressed by:

$$\varphi = \left(1 - \frac{N_r}{N_s}\right) \frac{\Theta_r}{\omega} \tag{4}$$

The phase shift has been experimentally checked for two pairs of homologous points (located at 0–100 percent and 10–110 percent of the IGV pitch), and for each of the ten axial locations investigated on surface B. That leads to an estimated mean value of φ (expressed as a percentage of the rotor temporal period T_r) of 17.5 percent. The theoretical value of φ calculated with Eq. (4), is 19 percent. The small disparity observed between these two values can be attributed to the differences in shape of the signals resulting from the measurement uncertainties. We can therefore assume that the spatial–temporal periodicity is well verified.

Thus, by transcribing the L2F data in the relative frame, using this hypothesis of spatial–temporal periodicity, and by time-averaging the values in the relative frame, the mean inlet relative flow is restored. The contour map of the relative Mach number M_R at 50 percent of span (surface B) is presented in Fig. 5, where the abscissa is the axial distance expressed as a percentage of the rotor blade chord and the ordinate is the angular position normalized by the rotor pitch. The strong deceleration through the shock as well as the acceleration due to the expansion waves are clearly visible. The shock is nearly normal around the leading edge and turns oblique upstream.

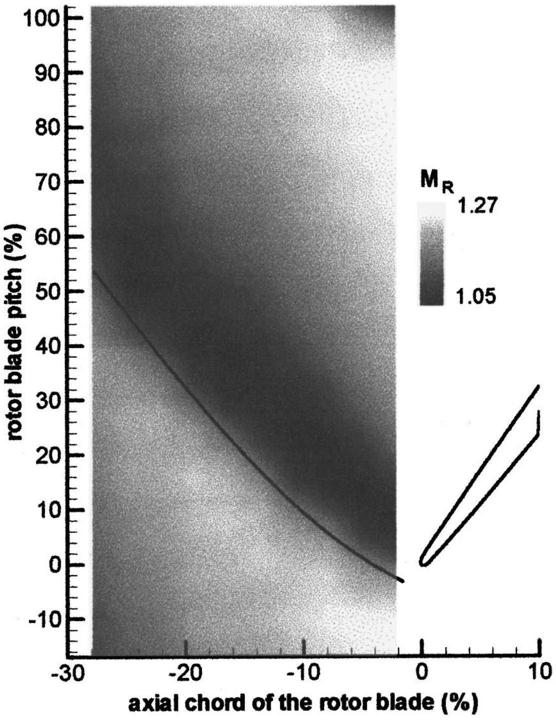

Fig. 5 Contour map of the relative time-averaged Mach number at midspan and analytical shock location

An analysis of the shock pattern is proposed by means of the calculation of the ‘‘unique incidence condition,’’ assuming a two-dimensional cascade flow with an axial subsonic velocity component. This calculation, which is valid for a started supersonic cascade with sharp blades, is extended to include the effects of detached shock waves in the case of a blunt leading edge [8]. The total pressure losses, leading to a blockage factor, are obtained by integration along a pitch, assuming the shock wave degenerates to one Mach line upstream of the adjacent blade. The axial stream contraction is taken into account by means of an additional blockage factor, calculated from the geometric convergence of the channel. This procedure yields the inlet flow angle and the shape of the detached shock wave at a prescribed inlet flow Mach number. In the present case, the conditions upstream of the bow wave are not constant. The value of M_{R1} is therefore not known and is calculated by time-averaging the Mach number at a point located in the wake-free region of section A. This way of determining the relative inlet flow Mach number has been validated by Trébinjac and Claudin [9]. It leads in the present case to $M_{R1} = 1.14$. The calculation of the inlet flow angle leads then to $\beta_{\mathrm{cal}} - \beta_{\mathrm{mes}} = 0.3$ deg. The agreement is all the better as the difference value is within the measurement errors. The predicted shape of the shock wave is superimposed onto the experimental results in Fig. 5. The calculated detachment distance is 0.8 mm, whereas it is experimentally estimated to be 0.7 mm. All these analytical results are very satisfactory in spite of the simplifying assumptions. Moreover, such a simple integral method is a useful tool for predicting the flow zones, which require an overrefinement of the mesh, experimentally and numerically speaking.

IGV Wake and Oblique Shock Interaction. The time-dependent behavior of the IGV wake, interacting with the shock, is presented in Part 1 of the paper and is briefly illustrated in Fig. 6, by comparing the azimuthal evolutions of the instantaneous

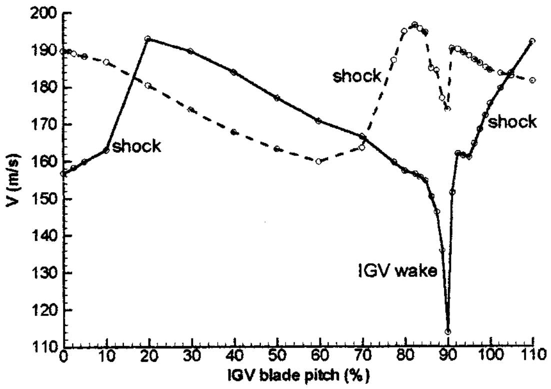

Fig. 6 Two azimuthal evolutions of the absolute velocity at midspan, for two different times

velocity for two times (i.e., positions of the rotor row relative to the IGV). In this example, the axial location of the data is very close to section A.

The time-averaging process described above isolates the wake (by averaging in the absolute frame of reference) or the shock (by averaging in the relative frame). The effects of the shock/wake interaction are now evaluated by quantifying the temporal fluctuating components of the velocity and the angle. If the temporal fluctuations are calculated in the absolute frame, the effect of the moving shock on the wake feature can be quantified. Among all the results obtained on surface B for ten positions of the rotor blade row, two contour maps of the temporal fluctuating components of the velocity, $V'(r,z,\theta,t)$, and angle, $\alpha'(r,z,\theta,t)$, are extracted for two times (i.e., two positions of the row) highlighting the shock/wake interaction. These maps are presented in Figs. 7 and 8, where the abscissa is the axial distance expressed as a percentage of the rotor blade chord and the ordinate is the angular position normalized by the IGV pitch. In both figures, regarding

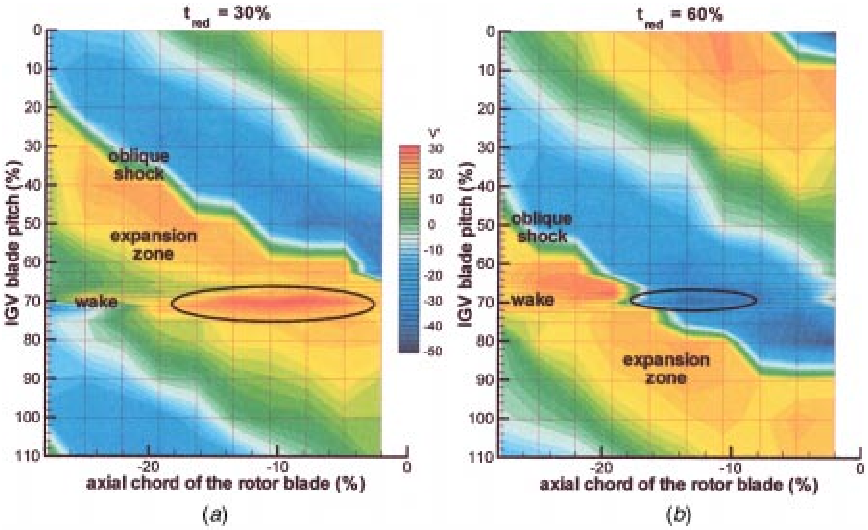

(*a*) (*b*)

Fig. 7 Contour map on surface B of the temporal fluctuating component of the velocity for two different times

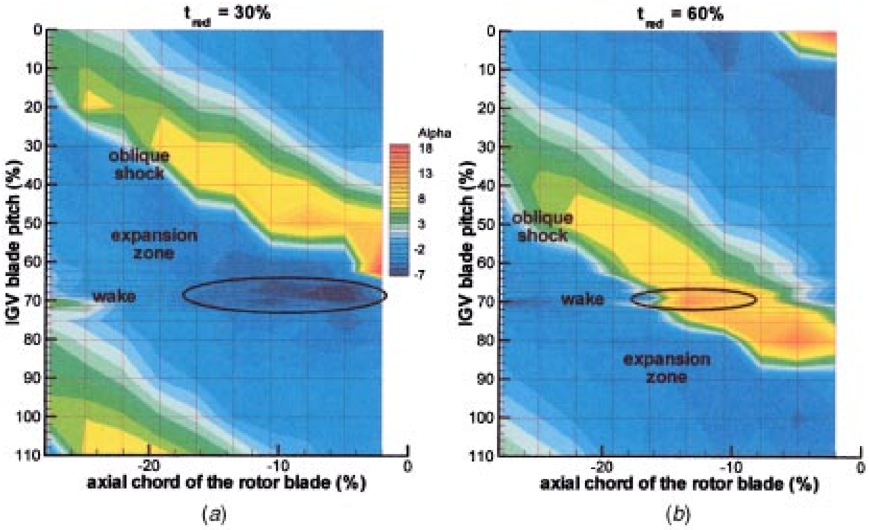

(*a*) (*b*)

Fig. 8 Contour map on surface B of the temporal fluctuating component of the angle for two different times

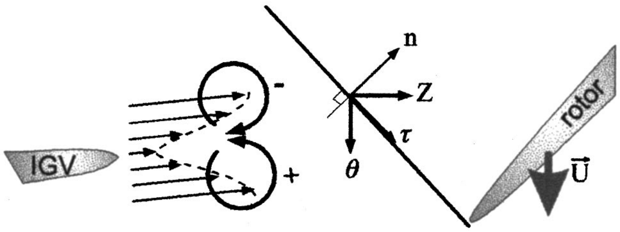

Fig. 9 Schematic description of a moving shock wave interacting with the vorticity linked with a wake

the encircled zone, case (a) corresponds to a time before the shock has crossed the wake $(t_{\mathrm{red}}=(t-t_{\mathrm{ref}})/T_r=30$ percent) whereas case (b) corresponds to a time just after the passage of the shock ($t_{\mathrm{red}}=60$ percent). In case (a), the wake is mainly in the expansion region and fluctuations V' reach high positive values. This means that the wake is accelerated more by the expansion waves than is the wake-free flow, and the magnitude of the wake will decrease before passing through the shock. In case (b), fluctuations V' in the wake reach high negative values after passing through the shock, so the wake deepens below the shock. Regarding fluctuations α' (Fig. 8), the flow within the wake comes under higher deviations than the free-wake flow (higher negative values of α' before the shock and greater positive values after the shock).

Moving downstream, the level of the fluctuations, averaged in the wake, increases globally by 50 percent. However, that does not mean the interaction is stronger because, a great part of the fluctuations arises from the increasing strength of the shock when approaching the leading edge of the rotor blades. By decomposing these fluctuations, as proposed below, the part due to the shock can be separated from the part due to the interaction proper.

Thus, the shock wave modifies the wake, which is a low-momentum fluid zone, much more than the wake-free flow. Such behavior is corroborated by analyzing the evolution of the stationary wake vorticity through the moving oblique shock. The vorticity transport equation, for compressible viscous flow, derives from the application of the rotational operator on the momentum equation. In the absolute frame, it is written as follows:

$$\frac{\partial\vec{\Omega}}{\partial t}+(\vec{V}\cdot\overrightarrow{grad})\vec{\Omega}-(\vec{\Omega}\cdot\overrightarrow{grad})\vec{V}=\frac{\vec{\Omega}}{\rho}\cdot\frac{d\rho}{dt}-\overrightarrow{grad}\frac{1}{\rho}\wedge\overrightarrow{grad}\,p+\overrightarrow{rot}\left(\frac{1}{\rho}\cdot\mathrm{div}(\bar{\bar{\tau}})\right)+\overrightarrow{rot}\,\vec{f} \quad (5)$$

where

$$\frac{d\rho}{dt}=\frac{\partial\rho}{\partial t}+\vec{V}\cdot\overrightarrow{grad}\,\rho \quad (6)$$

In order to quantify the effect of the oblique shock on the vorticity of the wake, the most convenient coordinate system is coordinate system $(\vec{n},\ \vec{r},\ \vec{\tau})$ where $\vec{n}$ and $\vec{\tau}$ are, respectively, the unit direction vectors normal and tangent to the shock (Fig. 9). The pattern of the oblique shock, emanating from the rotor blade leading edge and extending upstream of it, is assumed to be imposed by the wake-free incoming supersonic flow. Its moving in the circumferential direction is taken into account by the time derivative of the fluid density in the absolute frame. This time fluctuation is clocked with the rotor blade-passing frequency and can thus be written as:

$$\frac{\partial\rho}{\partial t}=\frac{\delta\rho}{\delta t}-\vec{U}\cdot\overrightarrow{grad}\rho \quad (7)$$

with $\delta\rho/\delta t$ the time derivative of the density in the relative frame.

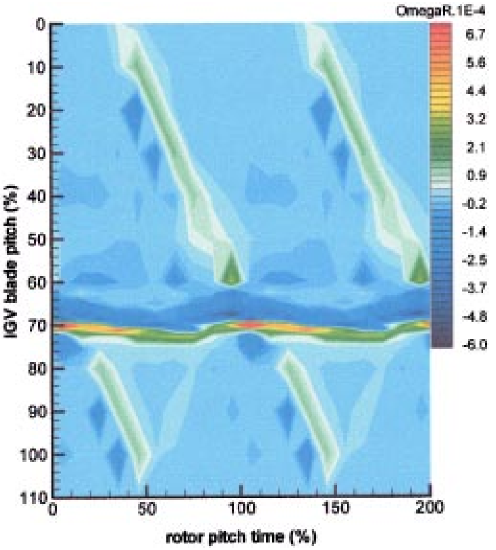

Fig. 10 Contour map of the radial component Ω_r of the vorticity calculated from the experimental data

If the wake is assumed to be two dimensional, its velocity field is described in the $(\vec{n},\ \vec{r},\ \vec{\tau})$ coordinate system by two components, $V_n(n,\tau)$ and $V_\tau(n,\tau)$. The associated component of the vorticity is:

$$\Omega_r=-\frac{\partial V_\tau}{\partial n}+\frac{\partial V_n}{\partial\tau} \quad (8)$$

Using this model and neglecting the terms representative of the nonstationarity of the density field in the relative frame, the external forces, and the turbulent and viscous stress tensor in the basic equation, the change in Ω_r can be written as:

$$\frac{d\Omega_r}{dt}=-\frac{1}{\rho}\cdot\frac{\partial V_n}{\partial\tau}\cdot\frac{\partial V_n}{\partial n}(U_n+V_n) \quad (9)$$

It is clear from this equation that the change in Ω_r is brought by a stationary term and a nonstationary term by the normal component of rotor speed U_n. These two effects are cumulative and lead to an increase in the magnitude of vorticity Ω_r, whatever its sign.

Figure 10 shows the contour map of the radial component Ω_r of the vorticity, calculated from the experimental data. The ordinate is the angular position normalized by the IGV pitch and the abscissa is the time expressed as a percentage of the rotor pitch time, but two periods are placed side by side to make it clearer. The shock region is marked off by low positive values of the magnitude of Ω_r, whereas the wake boundaries are characterized by high values. The increase in magnitude of Ω_r in the interaction zone of the wake with the moving oblique shock is clearly visible. This corroborates, as mentioned above, that the wake deepens below the shock.

Purely Time-Dependent Velocity Fluctuations

Adamczyk Decomposition. As mentioned above, a discriminating decomposition of the periodic temporal fluctuating component in the absolute frame, $X'(r,z,\theta,t)$, is achieved in order to extract the effect of the shock/wake interaction proper. This decomposition was proposed by Adamczyk et al. [7]:

$$X'(r,z,\theta,t)=\overline{X}^{*}_{rel}(r,z,\theta)+X''(r,z,\theta,t) \quad (10)$$

Then:

$$X(r,z,\theta,t)=\bar{\bar{X}}(r,z)+\overline{X}^{*}(r,z,\theta)+\overline{X}^{*}_{rel}(r,z,\theta)+X''(r,z,\theta,t) \quad (11)$$

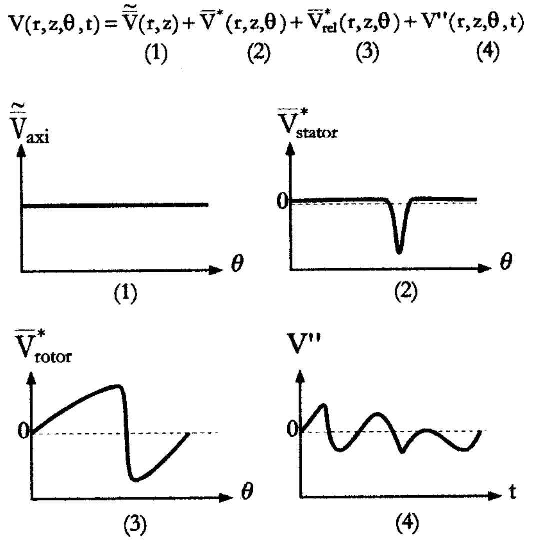

Fig. 11 Comprehensive sketch of the Adamczyk decomposition of the velocity

The first two terms are those resulting from the previous stage of the decomposition (2), in the absolute frame. $\overline{X}^{*}_{rel}(r,z,\theta)$ is the spatial fluctuation of the time-averaged flow in the frame relative to the rotor. $X''(r,z,\theta,t)$ is a purely time-dependent fluctuation that arises from the interaction of phenomena occurring in different frames. This term is also called ''deterministic fluctuation,'' as opposed to the random (or nondeterministic) fluctuation that arises from the turbulence and other phenomena not clocked with the rotor frequency. In the present decomposition applied to the experimental values, the random part is excluded because it is already averaged by the acquisition and reduction procedures that lead to the mean values of the modulus and angle of the velocity vector. Nevertheless, it is taken into account in the values of the standard deviation. Regarding the numerical approaches using such a decomposition, this random part is also excluded because it is assumed to be modeled by a turbulence model. A comprehensive sketch of the decomposition of the instantaneous velocity modulus is proposed in Fig. 11, in order to illustrate the different physical meanings of each term.

The time-dependent L2F data enable the calculation of each of the four terms of the decomposition of the modulus and angle of the velocity vector. From the periodic temporal fluctuating component of the velocity in the absolute frame, $V'(r,z,\theta,t)$, the stator deterministic correlation, which represents the averaged consequence of unsteady phenomena, can be calculated. This correlation can be decomposed into a purely spatial part, two spatial-temporal parts, and a purely unsteady part:

$$\begin{aligned}\overline{V'(r,z,\theta,t)\cdot V'(r,z,\theta,t)} &= \overline{\overline{V}^{*}_{rel}(r,z,\theta)\cdot\overline{V}^{*}_{rel}(r,z,\theta)}\\ &+\overline{\overline{V}^{*}_{rel}(r,z,\theta)\cdot V''(r,z,\theta,t)}\\ &+\overline{V''(r,z,\theta,t)\cdot\overline{V}^{*}_{rel}(r,z,\theta)}\\ &+\overline{V''(r,z,\theta,t)\cdot V''(r,z,\theta,t)} \qquad (12)\end{aligned}$$

Let us mention that, in the various models that handle the interaction between blade rows, all the correlations, except the purely spatial one, are usually neglected.

Results

The purely time-dependent correlation $\overline{V''(r,z,\theta,t)\cdot V''(r,z,\theta,t)}$ has been calculated from the L2F results on surface B. The values obtained are normalized by the spatial correlation $\overline{\overline{V}^{*}_{rel}(r,z,\theta)\cdot\overline{V}^{*}_{rel}(r,z,\theta)}$ induced by the shock wave in section A, which is about $122\,\mathrm{m^2/s^2}$. The contour map of the normalized unsteady correlation is shown in Fig. 12, where the abscissa is the axial distance expressed as a percentage of the rotor blade chord and the ordinate is the angular position normalized by the IGV pitch. As expected, the high levels are located within the wake, where the unsteady correlation reaches 80 percent of the maximum spatial correlation. It remains more or less constant from section A up to the leading edge of the rotor blades. That means the increase in the temporal fluctuations, $V'(r,z,\theta,t)$ mentioned above, when moving downstream, is mainly due to the increase of the spatial velocity fluctuation of the rotor time-averaged flow ($\overline{V}^{*}_{rel}(r,z,\theta)$), which is only due to the increase of the strength of the shock when approaching the leading edge of the rotor blades, and not of the interaction proper (i.e., the unsteady fluctuations).

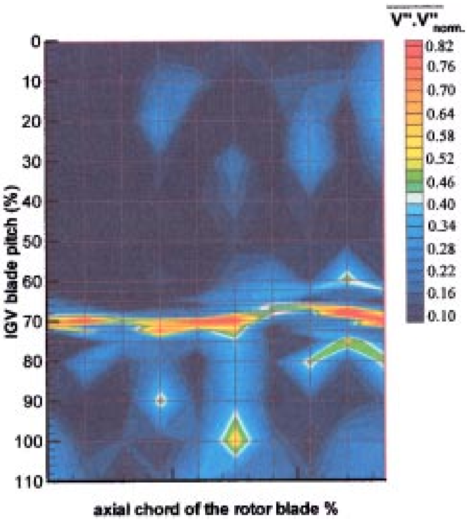

Fig. 12 Contour map of the normalized unsteady correlations

These results show that the purely unsteady part of the deterministic correlations is of the same order of magnitude as the spatial part. But the relative strengths of the various parts of the deterministic correlations have been quantified only in the inlet rotor flow field. In this region, the sources of unsteadiness are certainly of less importance than within the rotor blade row (unsteadiness due to the normal passage shock, the blade boundary layers, the secondary flows, and all the interactions). Then, the temporal correlations may be assumed to increase still further within the rotor, and should not be neglected in the three-dimensional rotor time-averaged simulations. A numerical study of the time-averaged flow in a transonic single-stage turbine, realized by Bardoux et al. [10], led to similar conclusions. The authors demonstrate that the temporal correlations are of a greater order of magnitude than the spatial correlations inside the rotor. These temporal correlations illustrate the oscillation of the rotor passage vortices and the chopping of the stator wakes. To return to the present investigation in the compressor, future work should include measurements within the rotor and the analysis of a three-dimensional unsteady simulation, thus confirming the significant role of temporal correlations compared to spatial correlations.

Conclusion

By analyzing the time-dependent L2F results obtained in the interrow flow field of a transonic compressor stage, the effects of the rotor leading edge shock wave/IGV wake interaction can be evaluated. This analysis is performed by implementing tools usually used in numerical works, to reduce the experimental data.

A comprehensive description of both the IGV wake and the shock emanating from the leading edge of the rotor is made. The experimental shock pattern is compared with the shock pattern deduced by an integral method. The very good agreement means the analytical calculation can be considered as an easy and quick tool for giving information, useful for the initialization of numerical simulations.

The effect of the shock/wake interaction proper is quantified by calculating the purely time-dependent correlation occurring in the Adamczyk decomposition. This temporal correlation proves to be of the same order of magnitude as the spatial correlation. That tends to prove that temporal correlations should be considered in the three-dimensional rotor time-averaged simulations, so as they will probably increase inside the rotor.

Nomenclature

M_R = relative Mach number
N = number of blades
P = measurement point location
T = temporal period
$\vec{U}$, U = rotor velocity vector, modulus
$\vec{V}$, V = velocity vector, modulus
X = flow parameter
$\vec{f}$ = external forces
n = coordinate normal to the shock
p = pressure
r = radial coordinate
t = time
z = axial coordinate
$\vec{\Omega}$, Ω = vorticity vector, modulus
Θ = angular blade pitch
α = absolute velocity angle
φ = phase shift
ω = rotation speed (rad/s)
θ = azimuthal coordinate
ρ = fluid density
$\bar{\bar{\tau}}$ = turbulent and viscous stress tensor
τ = coordinate tangent to the shock

Superscripts

— = time-averaged value
~ = spatially averaged value
$'$ = time-fluctuating value in the absolute frame
$*$ = spatial fluctuating value
$''$ = purely time-dependent fluctuating value

Subscripts

R = relative to the rotor
n = component normal to the shock
r = radial component
r = rotor
red = reduced value
ref = reference value
rel = relative to the rotor (for a time-averaged process)
s = stator
θ = azimuthal coordinate
τ = component tangent to the shock
1 = rotor inlet conditions

References

[1] Adamczyk, J. J., Celestina, M. L., and Chen, J. P., 1996, ''Wake-Induced Unsteady Flows: Their Impact on Rotor Performance and Wake Rectification,'' ASME J. Turbomach., **119**, pp. 88–95.
[2] Hall, E. J., 1997, ''Aerodynamic Modeling of Multistage Compressor Flow Fields. Part II: Modeling Deterministic Correlations,'' ASME Paper No. 97-GT-345.
[3] Rhie, C. M., Gleixner, A. J., Spear, D. A., Fischberg, C. J., Zacharias, R. M., 1998, ''Development and Application of a Multistage Navier–Stokes Solver. Part I: Multistage Modeling Using Bodyforces and Deterministic Stresses,'' ASME J. Turbomach., **120**, pp. 205–214.
[4] Bardoux, F., Dano, C., Leboeuf, F., and Toussaint, C., 1998, ''Characterization of Deterministic Stresses for a Turbine Stage—Part 1: Steady Flow Analysis,'' ASME Paper No. 99-GT-100.
[5] Erdos, J. I., Alzner, E., and McNally, W., 1977, ''Numerical Solution of Periodic Transonic Flow Through a Fan Stage,'' AIAA J., **15**, pp. 1559–1568.
[6] Gerolymos, G. A., and Chapin, V., 1991, ''Generalized Expression of Chorochronic Periodicity in Turbomachinery Blade Row Interaction,'' La Recherche Aerospatiale, **5**, pp. 69–73.
[7] Adamczyk, J. J., Mulac, R. A., and Celestina, M. L., 1986, ''A Model for Closing the Inviscid Form of the Average-Passage Equation System,'' ASME Paper No. 86-GT-227.
[8] Lichtfuss, H. J., and Starken, H., 1974, ''Supersonic Cascade Flow,'' Progress in Aerospace Sciences, **15**, D. Küchemann, ed., Pergamon Press, Oxford, New York, pp. 37–150.
[9] Trébinjac, I., and Claudin, I., 1997, ''Results and Analysis of a L2F Flow Field Investigation Within a High-Speed High-Pressure Centrifugal Compressor,'' Int. J. Thermal Fluid Sciences, **6**, No. 3, pp. 155–163.
[10] Bardoux, F., Dano, C., Leboeuf, F., and Toussaint, C., 1998, ''Characterization of Deterministic Stresses for a Turbine Stage—Part 2: Unsteady Flow Analysis,'' ASME Paper No. 99-GT-101.

Suppression of Rotating Stall by Wall Roughness Control in Vaneless Diffusers of Centrifugal Blowers

Masahiro Ishida
e-mail: hiro@net.nagasaki-u.ac.jp

Daisaku Sakaguchi

Hironobu Ueki

Department of Mechanical Systems Engineering,
Nagasaki University,
Nagasaki 852-8521, Japan

By positioning the completely rough wall locally on the hub side diffuser wall alone in the vaneless diffuser, the flow rate of rotating stall inception was decreased by 42 percent at a small pressure drop of less than 1 percent. This is based on the fact that the local reverse flow occurs first in the hub side in most centrifugal blowers with a backswept blade impeller. The three-dimensional boundary layer calculation shows that the increase in wall shear component normal to the main-flow direction markedly decreases the skewed angle of the three-dimensional boundary layer, and results in suppression of the three-dimensional separation. It is also clarified theoretically that the diffuser pressure recovery is hardly deteriorated by the rough wall positioned downstream of $R = l.2$ *because the increase in the radial momentum change, resulting from reduction in the skewed angle of the three-dimensional boundary layer, supports the adverse pressure gradient.* [DOI: 10.1115/1.1328084]

Keywords: Centrifugal Blower, Vaneless Diffuser, Rotating Stall, Three-Dimensional Boundary Layer, Separation Control, Rough Wall

Introduction

Suppression of unstable flow, such as rotating stall and surge, is one of the key issues of turbomachinery. In centrifugal blowers with radial blade impellers, unstable flow is mainly caused by inducer stall, while in centrifugal blowers with backswept blade impellers, it is mainly due to diffuser stall, according to the results reviewed by Fukushima et al. [1]. Whether it is due to inducer stall or diffuser stall seems to be dependent on the diffuser inlet core-flow velocity distortion between hub and shroud. The objective of this study is to suppress the rotating stall observed in the vaneless diffuser of the latter type blower without deteriorating blower performance.

Rotating stall in the vaneless diffuser is caused, in most cases, by reverse flow based on three-dimensional separation of the boundary layer. In order to suppress the rotating stall inception, many researchers investigated the effect of various devices: throttling at the diffuser exit [2], reduction of diffuser inlet width [1], circular cascade diffuser with a low solidity [3], and variable diffuser guide vane with a low solidity in combination with the impeller inlet guide vane [4]. The low solidity cascade could successfully suppress the boundary layer separation on the diffuser wall because the secondary flow induced by the cascade might sweep the low-energy fluid out of the cascade blade surface and the diffuser wall, and a combination of the low-solidity cascade and the inlet guide vane resulted in complete suppression of rotating stall. Recently, a new device for complete suppression of rotating stall was proposed by Kurokawa et al. [5], which is the swirl breaker consisting of many shallow radial grooves distributed properly on the diffuser walls. In this case, the tangential component of velocity is decreased markedly by the radial grooves, and the three-dimensional separation is suppressed because the flow angle approaches the radial direction. This device, however, may result in a remarkable pressure drop because the angular momentum dissipates markedly. Another device was proposed by Tsurusaki et al. [6], in which jets were injected in the counter-direction of impeller rotation, and almost complete suppression of rotating stall was obtained; however, this device requires an additional energy for injecting jets. The counter-jets and the swirl breaker play the role of decreasing the tangential component of velocity, that is, increasing the tangential shear stress. The almost equivalent effect must be obtained by an increase in wall friction.

The flow in vaneless diffusers is skewed and, in the case of small flow rates, a reverse flow occurs locally along the diffuser walls and rotating stall results. The skewed boundary layer in the vaneless diffuser was analyzed first by Jansen [7] assuming that the flow is symmetric with respect to the diffuser depth. However, this assumption is not satisfactory in the practical cases because, as the flow rate is decreased in most low specific speed type centrifugal impellers having backswept blade [8,9], the local reverse flow occurs first on the hub side wall in the diffuser entry region, and the separation region transfers from the hub side to the shroud side at a downstream position. Rotating stall does not occur even when the small three-dimensional separation region exists steadily in the vaneless diffuser; therefore, the critical flow angle for the rotating stall inception is smaller than the critical flow angle for the reverse flow inception by the factor about 0.88 [10]. Senoo et al. [8,11] showed the analytical method for the asymmetric flow in the vaneless diffuser as well as the criteria on the critical inlet flow angle, in which it was assumed that, for each of the radial and the tangential components of the main-flow velocity, there is a velocity gradient with respect to the depth at the diffuser inlet.

As the flow rate decreases, the reverse flow on the hub side wall in the diffuser entrance region reaches to the impeller exit; however, this reverse flow cannot enter into the backside of the impeller disk. The inception of unstable flow seems to be triggered by an interaction between the local reverse flow on the hub side of the vaneless diffuser and the jet-wake flow discharged from the impeller. Ishida et al. [12] showed this result by analyzing the correlation coefficient between the radial and tangential components of velocity fluctuation. On the other hand, according to the visualization work of the separation ring formed on the shroud

---

Contributed by the International Gas Turbine Institute and presented at the 45th International Gas Turbine and Aeroengine Congress and Exhibition, Munich, Germany, May 8–11, 2000. Manuscript received by the International Gas Turbine Institute February 2000. Paper No. 2000-GT-461. Review Chair: D. Ballal.

casing wall in a centrifugal blower with the unshrouded radial blade impeller [13], the rotating stall was not initiated by the reverse flow on the shroud wall, but the unstable flow finally occurred by the inducer stall as the flow rate was decreased further. In this case, the reverse flow on the shroud diffuser wall enters smoothly into the tip clearance space and moves upstream along the shroud casing wall toward the separation ring position, then flows into the blade passage again. In other words, it is not the cause of unstable flow if the reverse flow forms a stable recirculation flow at the shroud side in the meridional space. Judging from these two results, the rotating stall in the vaneless diffuser seems to be caused by the three-dimensional flow separation not on the shroud wall but on the hub wall. It is a key point, therefore, to suppress the reverse flow on the hub side.

In the present study, the authors have analyzed theoretically the effect of wall friction on the wall-limiting streamline flow angle of the skewed boundary layer as well as on the diffuser pressure recovery by using the three-dimensional boundary layer calculation code based on the momentum integral method [8]. Calculations are conducted especially under the condition that the inlet core-flow velocity is asymmetric with respect to the diffuser depth in which the tangential component of inlet main-flow velocity is lower at the hub side than at the shroud-side. According to the analysis, the three-dimensional separation zone on the hub side wall decreases markedly in both length and height by an increase in the wall friction coefficient, and it disappears if the friction coefficient is about twice of the smooth wall. In order to avoid a large pressure loss due to an increase in wall friction, the rough wall is positioned locally on the hub side wall alone. It is verified experimentally as well as theoretically that the locally rough wall has a marked effect on the diffuser stall suppression. The optimum positioning of the rough wall is investigated experimentally for obtaining a maximum improvement in the diffuser stall limit at a minimum expense of diffuser pressure recovery. The reasons that the stall limit can be improved significantly by the locally rough wall and that only a small drop in diffuser pressure recovery can be achieved by increasing the wall friction are clarified from the view points of the direction of wall shear stress as well as the momentum balance in the radial direction.

Test Blower and Impeller Characteristics

The meridional section of test blower is shown in Fig. 1, which was used in the authors' previous study [9]. The tested unshrouded centrifugal impeller has 16 backswept blades with an exit blade angle of 45 deg; the exit diameter is 510 mm, the exit blade height is 17 mm, and its specific speed is $\sigma_s(=\phi^{1/2}\psi^{-3/4})=0.43$ at a design flow coefficient of $\phi=0.27$. The experimental setup consists of a suction plenum tank with a conical damper for the flow rate control, a test impeller, and a parallel wall vaneless diffuser. Air was axisymmetrically discharged from the blower to the atmosphere through a vaneless diffuser with an exit radius ratio of about 1.8. The axial tip clearance of the impeller shroud was changed from 0.5 mm to 2.5 mm by inserting shims at the exit position of the vaneless diffuser. In the experiment, the impeller was operated at a constant speed of 2000 rpm. The hub-to-shroud distributions of time-mean velocity and turbulence were measured by a Pitot tube and a hot wire at four radial positions, as shown in Fig. 1; their radial positions are $R=1.02$ immediately downstream of the impeller exit and $R=1.10$, 1.18, and 1.57 in the vaneless diffuser. The characteristic curves of the test impeller are shown in Fig. 2, where ψ_s denotes the static pressure coefficient measured at $R=1.02$ and the parameter ''λ'' is the tip clearance ratio. The solid marks indicate the flow range in which the periodic unstable flow was observed clearly by using the semiconductor pressure transducer. The unstable flow is seen in a wide flow range, and a small disturbance appears near the inception point of unstable flow on the characteristic curve. The flow rate of unstable flow inception seems to increase with increasing the tip clearance mainly due to increase in the diffuser depth.

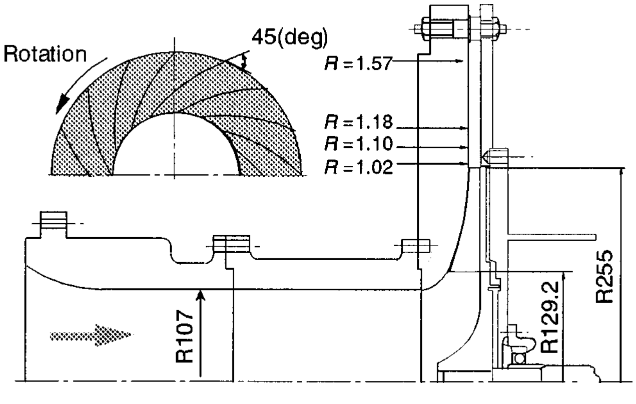

Fig. 1 Meridional section of test blower and impeller

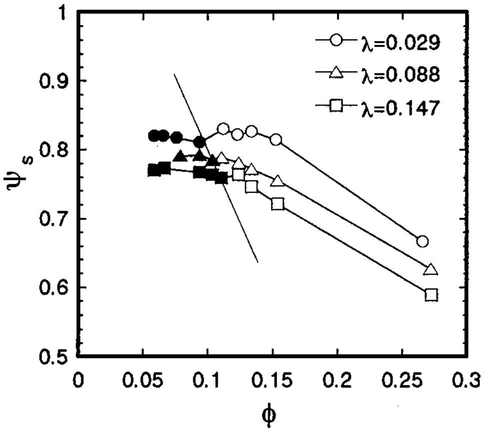

Fig. 2 Change in impeller characteristics due to tip clearance

The clear periodic phenomena of rotating stall were observed at the large tip clearance of $\lambda=0.147$ so that the measurements were conducted in detail at this tip clearance. The hub-to-shroud velocity distributions in the vaneless diffuser are shown in Figs. 3(*a*) and 3(*b*), which show the radial and tangential components of the velocity, respectively, measured at $\phi=0.131$, slightly larger than the stall inception flow rate. As shown in Fig. 3(*a*), the reverse flow does not occur at $R=1.02$, the reverse flow zone appears first on the hub side wall at $R=1.10$, and it appears on both shroud and hub walls at $R=1.18$. The three-dimensional separation on the hub

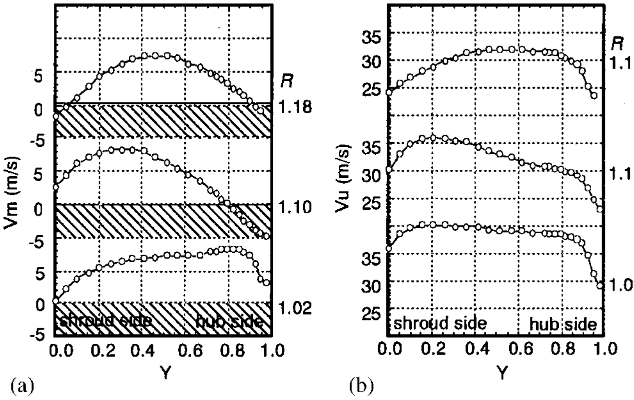

Fig. 3 Measured hub-to-shroud velocity distribution in vaneless diffuser ($\phi=0.131$, $\lambda=0.147$): (*a*) radial component; (*b*) tangential component

side wall at $R=1.10$ seems to be mainly caused by the distortion of tangential velocity component of the core-flow at the diffuser inlet; "*Vu*" is slightly lower at the hub side than at the shroud side even though the radial component is higher at the hub side. As the tangential velocity component is about five times larger than the radial one, a small difference in the tangential component between hub and shroud results in a remarkable difference in centrifugal force between them. The radial velocity near the hub side has to be decelerated remarkably to support the same adverse pressure gradient in the radial direction at both sides in the case of parallel wall diffuser. Therefore, the local reverse flow appears first at the hub side, which will be also analyzed theoretically in a later section.

Theoretical Analysis of Three-Dimensional Separation

Effect of Wall Friction on Three-Dimensional Separation and Pressure Recovery. To calculate the three-dimensional boundary layer on vaneless diffuser walls, the momentum integral method developed by Senoo et al. [8] was adopted here, in which the power law velocity profile popular in the two-dimensional boundary layer was assumed for the component of the main flow direction (*s* direction) and another power law velocity profile similar to the wall-jet one was assumed for the crossflow component normal to the main-flow streamline (*n* direction) as shown in Fig. 4. In the figure, *Ve* denotes the velocity vector at the outer edge of the boundary layer, and *u* and *w* denote the respective velocity components of the flow close to the wall. γ is the maximum skewed angle of the three-dimensional boundary layer. The wall shear stress τ_w acts in the direction opposite to the velocity vector along the wall-limiting streamline, and τ_n and τ_s are the components in the *n* and *s* directions, respectively.

As the three-dimensional separation was affected significantly by a slight distortion of the tangential velocity component of the inlet core-flow, as shown in Fig. 3, a linear velocity gradient with respect to the diffuser depth is assumed to be $\Delta Vu/Vum=\pm 0.02$ only for the tangential component, while the radial velocity distortion is assumed to be $\Delta Vm/Vmm=0$ for simplicity, as shown in Fig. 5. The model calculation shown in Figs. 5 and 6 is conducted at $\phi=0.15$ and $\lambda=0.029$ ($b/r_2=0.069$), the flow rate at which the three-dimensional separation appears. The mean flow angle of the inlet core-flow is determined by the flow rate and the slip factor recommended by Wiesner [14] using the velocity triangle relation. And the inlet boundary layer thickness is assumed to be 5 percent of the diffuser depth on both walls because the effect of the inlet boundary layer thickness on the three-dimensional separation zone was small.

Figure 5 shows the velocity contours of the radial component in the case of the smooth walls, and Fig. 6 shows the variations of the flow angle "α" measured from the circumference at the outer edge of boundary layer, and the wall-limiting stream line flow angle "α_w" measured from the circumference, or the flow angle of the flow close to the wall. The subscript 1 denotes the flow angle at the shroud side, and the subscript 2 denotes the one at the hub side. The calculated results shown in Figs. 5 and 6 are the case that $\Delta Vu/Vum$ is -0.02 at the hub side edge of the core-flow and $+0.02$ at the shroud side, respectively, while *Vm* is constant. The negative values of α_{w1} and α_{w2} in the wall-limiting streamline flow angle distribution indicate the three-dimensional separation zone. In the standard case with the uniform symmetric core-flow, $\alpha_1=\alpha_2$, $\alpha_{w1}=\alpha_{w2}$, and the three-dimensional separation appears at $R=1.075$ on both walls simultaneously and disappears at $R=1.55$. On the other hand, in the case with the asymmetric core-flow, the separation zone appears only on the hub side wall at this flow rate. A small distortion of the inlet tangential velocity distribution results in a deeper separation zone on the wall with the lower tangential velocity, and the initiation point of separation moves upstream compared with the symmetric case. As the flow rate was decreased further, not shown here, the depth of the hub side separation zone increased without extending the downstream end of the separation zone, and another separation zone appeared at a downstream position on the shroud wall at $\phi=0.14$, which was similar to the flow pattern measured at $\phi=0.131$ as shown in Fig. 3(*a*).

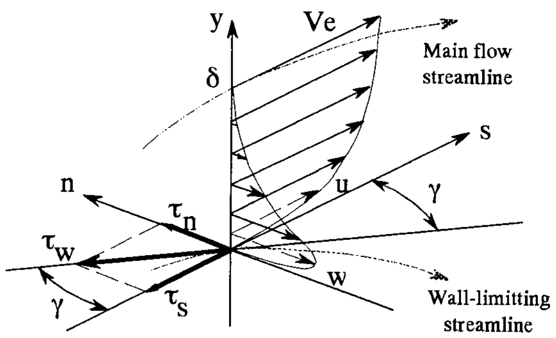

Fig. 4 Velocity component profiles in three-dimensional boundary layer

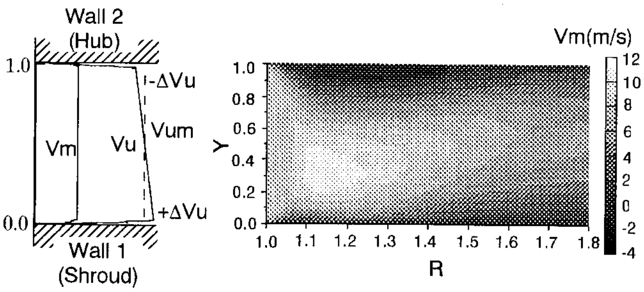

Fig. 5 Calculated radial velocity contour in vaneless diffuser under asymmetric inlet main-flow condition ($\phi=0.15$, $\lambda=0.029$, $\Delta Vu/Vum=\pm 0.02$, $\Delta Vm/Vmm=0$)

In order to clarify the effect of wall friction on the three-dimensional separation and the diffuser pressure recovery under the asymmetric core-flow condition, the wall friction coefficient defined by $C_{fu}=2\tau_s/\rho Ve^2$ is changed. In general, the wall friction coefficient varies with radius, especially in the diffuser entry region if C_{fu} is determined by the function of Reynolds number based on the boundary layer thickness. In the case of small flow rates, the boundary layers on both walls develop quickly and merge at a small radial position less than $R=1.2$ because the flow

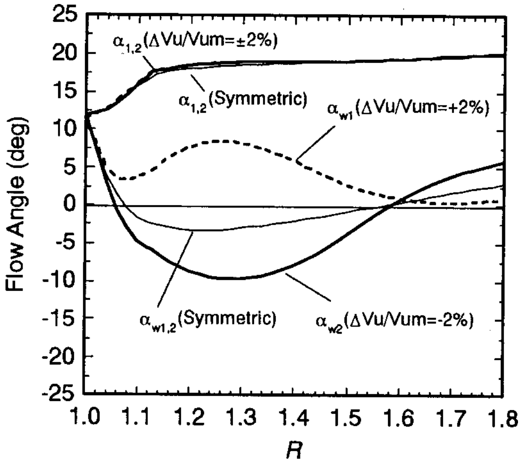

Fig. 6 Comparison of calculated wall-limiting streamline flow angles between symmetric and asymmetric main-flows ($\phi=0.15$, $\lambda=0.29$, $\Delta Vu/Vum=\pm 0.02$, $\Delta Vm/Vmm=0$ for asymmetric main-flow)

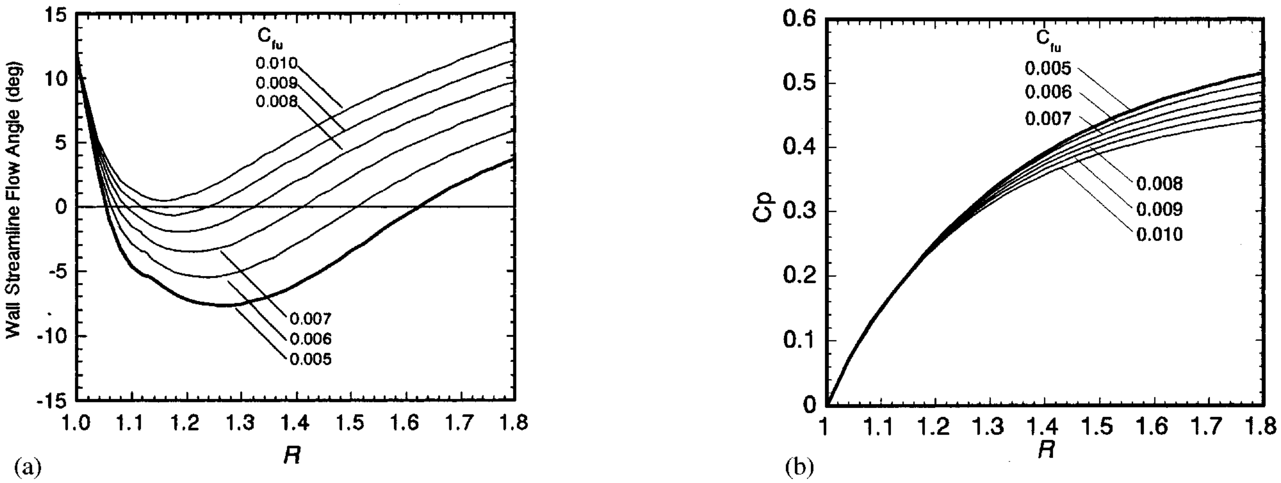

(a) (b)

Fig. 7 Effect of wall friction on three-dimensional separation and diffuser pressure recovery ($\phi=0.15$, $\lambda=0.029$, $\Delta Vu/Vum=\pm 0.02$, $\Delta Vm/Vmm=0$): (*a*) change in wall-limiting streamline flow angle at hub side; (*b*) change in diffuser pressure recovery

path becomes long due to the small flow angle. The calculated results on the three-dimensional separation zone and the diffuser pressure recovery were hardly affected by whether C_{fu} is variable or constant in the case of the smooth wall. It is reasonable to assume a constant C_{fu} from the inlet to the exit for simplicity.

Figure 7(*a*) shows a change in the wall-limiting streamline flow angle ''α_{w2}'' on the hub side wall due to the wall friction coefficient varying from 0.005 to 0.010. The three-dimensional separation zone becomes markedly narrower by increasing the wall friction coefficient, and it disappears at the friction coefficient of 0.01, which is about twice that of the smooth wall. It is suggested that the increase in wall friction shows a marked effect on suppression of the local reverse flow, resulting in rotating stall. The effect of wall friction on the diffuser pressure recovery at this flow rate is shown in Fig. 7(*b*). ''*Cp*'' denotes the pressure recovery coefficient defined by the diffuser inlet dynamic pressure. The thick solid line indicates the standard case of the smooth wall with $C_{fu}=0.005$, and the thin solid line in the lowest indicates the case of the rough wall with $C_{fu}=0.010$. By increasing C_{fu} from 0.005 to 0.010, the diffuser pressure recovery decreases by 14.3 percent at the diffuser exit. Furthermore, the pressure recovery was hardly affected by the small distortion of the inlet core-flow velocity as small as $\Delta Vu/Vum=\pm 0.02$.

It is seen in Fig. 7(*b*) that the pressure rise from $R=1.0$ to 1.2 is not affected by the increase in wall friction coefficient. This is mainly based on the fact that there is a core flow not affected directly by the wall friction in the entrance region, where the pressure rise is dominated by the centrifugal force and the deceleration of the core-flow velocity. On the other hand, the effect of wall friction on the pressure recovery seems to be concentrated in the region downstream of $R=1.2$. The reason is as follows: In the entrance region, the dynamic energy is dissipated largely in the boundary layer by a large wall friction force because of the thin boundary layer and the large tangential velocity. The dynamic energy averaged over the section around $R=1.2$ is decreased significantly by the increase in wall friction. The key issue is that the dynamic energy to be converted into pressure is small at $R=1.2$ in the case of the whole rough wall.

Effect of Locally Rough Wall on Diffuser Pressure Recovery. According to the theory by Senoo and Ishida [15], nonaxisymmetric flow at the impeller exit, such as ''jet-wake flow pattern,'' can be made uniform isentropically until $R=1.2$ in most cases; however, the excessive wall friction loss occurs in the diffuser entrance region due to this nonuniformity. To avoid a large dissipation of dynamic energy, it is obviously better not to increase the wall friction in the region upstream of $R=1.2$.

Figure 8 shows the effect of the locally rough wall on the pressure recovery coefficient. The thick solid line indicates the standard case of the smooth walls, the thin solid curve shows the case where the rough walls have a friction coefficient of 0.010, which are the same as those shown in Fig. 7(*b*). If C_{fu} is changed from 0.005 upstream of $R=1.2$ to 0.010 downstream of $R=1.2$ on both walls, indicated by the chained line, the decrement from the standard case in the pressure recovery at the diffuser exit becomes 6.2 percent. Further, if C_{fu} is changed from 0.005 to 0.010 at $R=1.2$ on the hub side wall alone, indicated by the broken line, the decrement in the diffuser pressure recovery becomes as small as 3.1 percent, which is only about one-fourth of the whole rough wall case. This pressure drop of 3.1 percent in the diffuser pressure recovery corresponds to that of 0.8 percent in the entire pressure rise because the pressure rise in the diffuser is about 25 percent of the blower.

It should be noticed that the pressure rise between $R=1.2$ and 1.4 is hardly affected by the rough wall; that is, the radial pressure gradient between $R=1.2\sim1.4$ for the locally rough wall is almost equal to the radial pressure gradient for the smooth wall. As the wall friction increases, the pressure gradient must be decreased by decreasing the centrifugal force resulting from a decrease in the tangential component of velocity. In general, the main factor to support the radial adverse pressure gradient in the diffuser is centrifugal force, and the secondary factor is a change in momentum

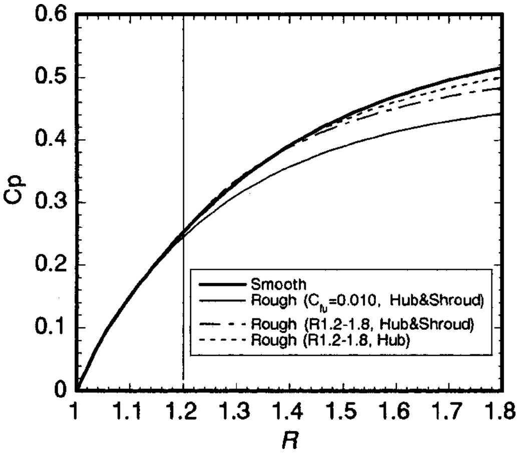

Fig. 8 Effect of locally rough wall on diffuser pressure recovery ($\phi=0.15$, $\lambda=0.029$, $\Delta Vu/Vum=\pm 0.02$, $\Delta Vm/Vmm=0$)

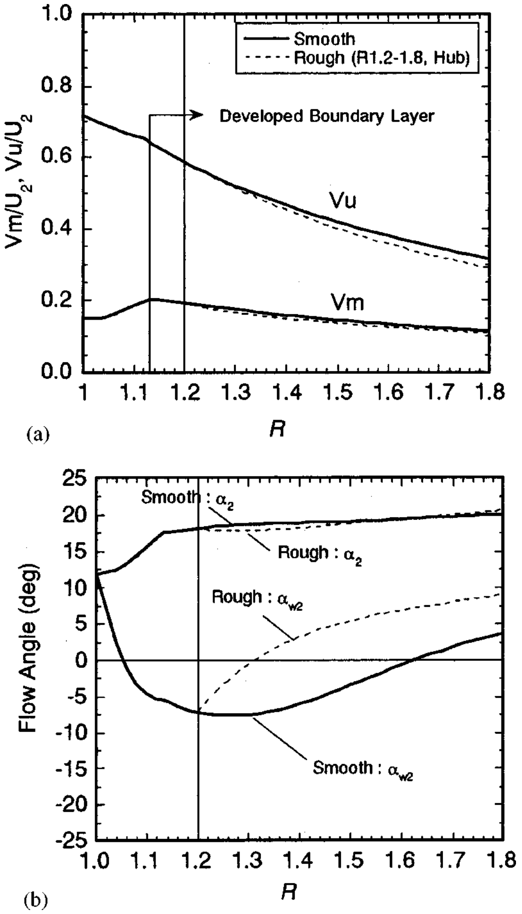

Fig. 9 Effect of locally rough wall on velocity and flow angle at hub side in case with three-dimensional boundary layer separation (ϕ=0.15, λ=0.029, $\Delta Vu/Vum=\pm 0.02$, $\Delta Vm/Vmm=0$): (*a*) tangential and radial components of velocity; (*b*) flow angles of main-flow and wall-limiting streamline

in the radial direction, resulting from the deceleration of the radial component of velocity. In order to clarify this noticeable phenomenon, the variations of the tangential and radial components of velocity and the flow angle at the outer edge of the hub side boundary layer as well as the wall-limiting streamline flow angle on the hub wall are checked. These variations in the diffuser with the smooth wall or the locally rough wall are compared in Figs. 9(*a*) and 9(*b*). As shown in Fig. 9(*a*), the core-flow not affected directly by the wall friction disappears at R=1.13, where the diffuser depth is filled with the boundary layers developed on both walls. Downstream of R=1.2, both tangential and radial components of velocity decrease more in the case of the locally rough wall than in the case of the smooth wall, as shown by the broken lines and the solid lines in Fig. 9(*a*). As shown in Fig. 9(*b*), the wall-limiting streamline flow angle ''α_{w2}''on the hub side wall increases markedly downstream of R=l.2 due to the increase in wall friction, and the three-dimensional separation disappears around R=1.3. The length of the three-dimensional separation zone of the locally rough wall case is less than half of that of the smooth wall case.

The relationship between the polar diagram of the velocity vector of the three-dimensional boundary layer and the wall shear stress vector is shown schematically in Fig. 10 in the case with the three-dimensional separation. In both Fig. 10 and Fig. 4, *Ve* denotes the main-flow velocity vector and α is its flow angle from the circumference. v denotes the velocity vector of the flow close to the wall and α_w is its flow angle from the circumference, which is called the wall-limiting streamline flow angle. γ is the skewed angle of the three-dimensional boundary layer. The wall shear stress τ_w acts in the direction opposite to the velocity vector v along the wall-limiting streamline. τ_m and τ_u are the radial and tangential components of the wall shear stress, and τ_n and τ_s are the components normal to main-flow direction and along the main-flow direction.

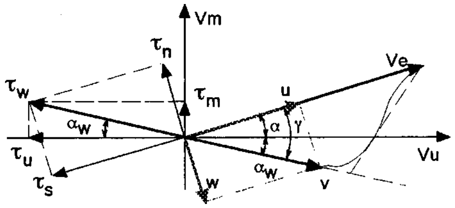

Fig. 10 Schematic relation between polar diagram of velocity vector and wall shear stress vector in case with three-dimensional separation

As seen from Figs. 4 and 10, the adverse pressure gradient normal to the main-flow direction ''*dp*/*dn*'' acts to increase the crossflow, resulting in increase of the skewed angle ''γ.'' On the other hand, the wall shear stress component ''τ_n'' normal to the main-flow direction acts to decrease the crossflow. Judging from Fig. 8, the pressure gradient ''*dp*/*dn*'' must be hardly changed between R = 1.2~1.4 by the increase in wall friction, and the crossflow momentum is small compared with the main-flow momentum as seen from Fig. 4. As a result, the increase in τ_n results in a marked decrease in the skewed angle ''γ'' as shown in Fig. 9(*b*). In other words, the three-dimensional separation zone becomes smaller, and the distortion of hub-to-shroud radial velocity distribution also becomes smaller at the downstream position; therefore, the decrement of momentum in the radial direction increases based on the larger deceleration of the radial velocity component as shown in Fig. 9(*a*).

The pressure rise based on centrifugal force is decreased by the reduction of the tangential component of velocity in the rough wall case; however, the pressure gradient almost equal to the smooth wall case is supported first by the additional increase in the radial momentum change mentioned above, and second by the positive radial component ''τ_m'' of the wall shear stress in the region between R = 1.2~1.3 where the three-dimensional separation exists.

Experimental Results and Discussion

Suppression of Rotating Stall by Means of Rough Wall. As shown in Fig. 9(*b*), the wall-limiting streamline flow angle showed the negative maximum value between R=1.2~1.4. It is desirable to position the rough wall in the region downstream of R=I.2 in order to reduce the three-dimensional separation region effectively without deteriorating the diffuser pressure recovery.

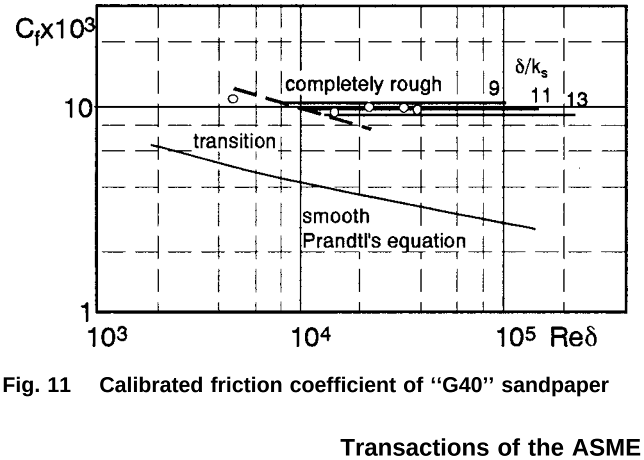

Fig. 11 Calibrated friction coefficient of ''G40'' sandpaper

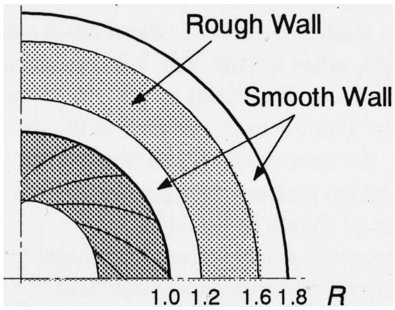

Fig. 12 Rough wall position on the vaneless diffuser wall

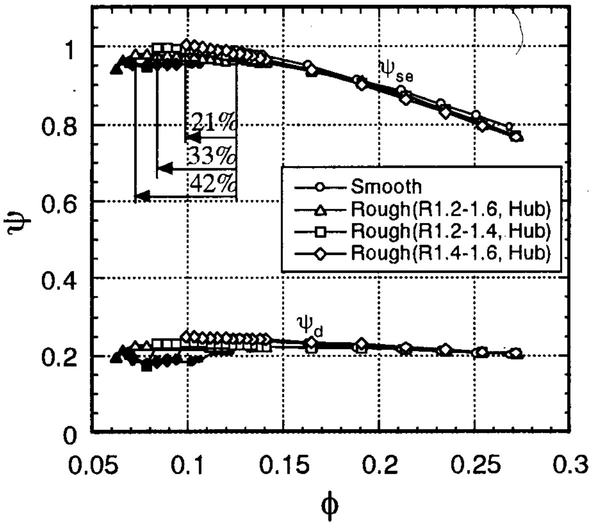

Fig. 13 Change in blower characteristics due to wall roughness control ($\lambda=0.147$)

In order to obtain about twice the friction coefficient of the smooth wall, the completely rough wall condition was checked by using ''G40'' sandpaper. According to the calibrated result shown in Fig. 11 [16], this sandpaper has the equivalent roughness of $k_s=0.55$ mm and the friction coefficient indicated by open circle marks shows about 0.01 in the Reynolds number ''Re_s'' range larger than 1.0×10^4. In the present experiment, sandpaper with a friction coefficient of $C_{fu}=0.01$ was stuck between $R=1.2\sim1.6$ first on both walls and second only on the hub side wall as shown in Fig. 12. The rough wall position on the hub side wall was further divided into two regions between $R=1.2\sim1.4$ and between $R = 1.4\sim1.6$.

Figure 13 shows the change in the blower characteristics due to the rough wall positioned locally in three positions mentioned above. The ordinate is the static pressure coefficient defined by the dynamic pressure based on the impeller peripheral velocity. ψ_{se} is the static pressure coefficient at the diffuser exit, and ψ_d is the difference between the static pressure coefficients at the diffuser exit and at $R=1.02$ immediately downstream of the impeller exit. The circle marks indicate the case of the smooth wall, the triangle marks indicate the rough wall on the hub side alone between $R=1.2\sim1.6$, the square marks denote the one between $R=1.2\sim1.4$, and the diamond marks denote the one between $R=1.4\sim1.6$. The respective solid mark indicates the flow range where the rotating stall was observed. Based on the local increase in wall roughness on the vaneless diffuser wall, the flow rate of rotating stall inception was markedly decreased from the reference inception flow rate by 42 percent for the rough wall between $R=1.2\sim1.6$, 33 percent for $R=1.2\sim1.4$, and 21 percent for $R=1.4\sim1.6$, respectively. Comparing among these three cases, the improvement in stall limit is larger if the rough wall region is wider, and the changing point to the rough wall is more upstream. Furthermore, the stall limit improvement in the ease of the rough walls at both hub and shroud sides was almost equal to the rough wall on the hub side alone. It is noticeable that the almost equal improvement in the stall limit is successfully achieved by the increase in wall roughness on the hub side alone. This is based on the fact that the three-dimensional separation occurs first on the hub side wall in most blowers with the backswept blade impeller. According to Fig. 13, within the experimental accuracy, the pressure rise ''ψ_d'' in the diffuser is almost equal in the three kinds of rough wall positioning, and they are also almost equal to the standard case at any flow rates, even at the design flow rate of $\phi=0.27$.

Change in Velocity Distribution Due to Rough Wall. The hub-to-shroud distributions of the tangential and radial components of velocity measured at $R=1.57$ are compared between the smooth wall case and the rough wall one in Fig. 14(*a*), and the corresponding calculated results are compared in Fig. 14(*b*), where $\phi=0.131$ is near the rotating stall inception point at $\lambda=0.147$ ($b/r_2=0.076$), and the rough wall is positioned between $R=1.2\sim1.6$ on the hub side wall alone. The calculated results agree well with the measured ones; by positioning the rough wall

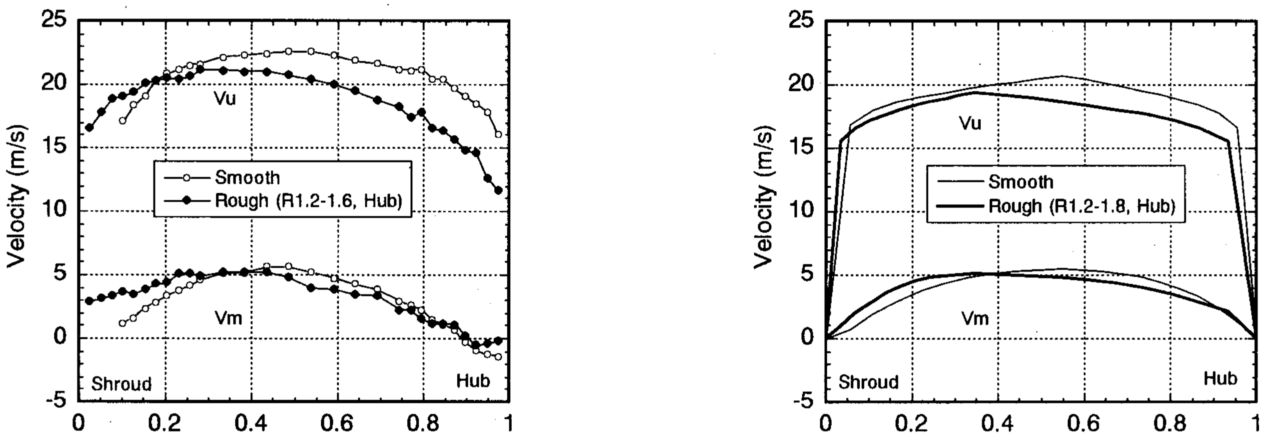

(a)

(b)

Fig. 14 Comparison of measured and calculated velocity distributions between smooth and rough walls ($\phi=0.131$, $\lambda=0.147$, $R=1.57$, $\Delta Vu/Vum=\pm0.02$, $\Delta Vm/Vmm=0$ for calculation): (*a*) measured result; (*b*) calculated result

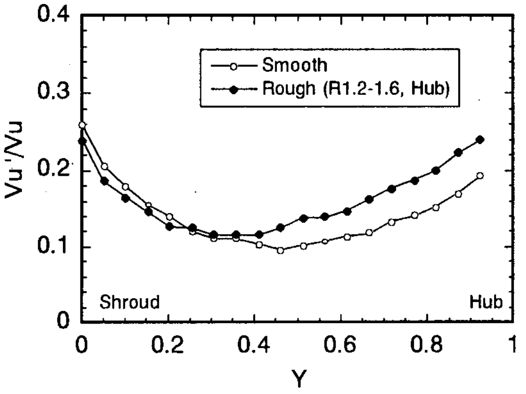

Fig. 15 **Comparison of measured turbulence intensity distribution between smooth and rough walls (ϕ=0.131, λ=0.147, R=1.57)**

on the hub side alone, the boundary layer thickness at the hub side becomes thicker than the one at the shroud side, the peak position of the velocity distribution transfers to the shroud side, and the tangential velocity is decreased remarkably in the whole section. The distortion of the radial velocity distribution becomes somewhat smaller compared with the smooth wall case, resulting in an increase in the radial momentum change, which additionally supports the radial pressure gradient. It is mainly due to a large decrease in the skewed angle of the three-dimensional boundary layer.

There is a small difference between the measured and the calculated radial velocity distributions. A small separation zone exists at the hub side in the experiment, but not in the calculation, although the separation zone becomes small by roughening.

Figure 15 shows a comparison between the smooth and rough wall cases in the hub-to-shroud distribution of turbulence intensity of the tangential velocity component measured at R=1.57 by using the single hotwire parallel to the wall. It is reasonable that the turbulence intensity in the shroud-side boundary layer is not affected by the rough wall, and the one in the hub side boundary layer is increased significantly due to the turbulence induced by the rough wall. This must be another factor that suppresses the three-dimensional separation because the fluid with high energy far from the wall transfers toward the wall. The main-flow and crossflow velocity profiles may vary from the original ones assumed in the momentum integral method.

Effect of Wall Friction on Pressure Recovery at Design Flow Rate

Figure 16 shows a comparison of the pressure distributions in the vaneless diffuser at the design flow rate of ϕ=0.27 between the cases with the smooth wall and the locally rough wall on the hub side alone. The calculated pressure recovery coefficients are indicated by the thick and thin solid lines for the smooth and rough walls, respectively, and the open and solid circles show the corresponding experimental results. The difference between the smooth wall and the locally rough wall in the pressure recovery is almost equal in both calculation and experiment; however, the measured pressure recovery is lower than the calculated one because the diffuser depth was slightly narrower downstream of R=1.2 due to the sandpaper thickness and also the flow was accelerated by the blockage effect based on the twelve circular struts for diffuser wall spacing located around R=1.65 as shown in Fig. 1. The local increase in wall roughness, which is on the hub side wall alone, results in a slight decrease, less than 1 percent of the blower pressure rise at the design flow rate, as predicted in the calculation.

It should be noticed again in Fig. 16 as well as in Fig. 8 that the radial pressure gradient between R=1.2 and 1.4 is hardly affected

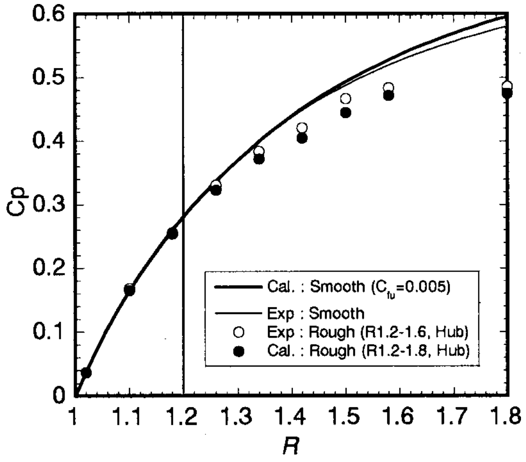

Fig. 16 **Comparison of diffuser pressure recovery between the cases with and without rough wall at design flow rate (ϕ=0.27, λ=0.147, $\Delta Vu/Vum$=±0.02, $\Delta Vm/Vmm$=0 for calculation)**

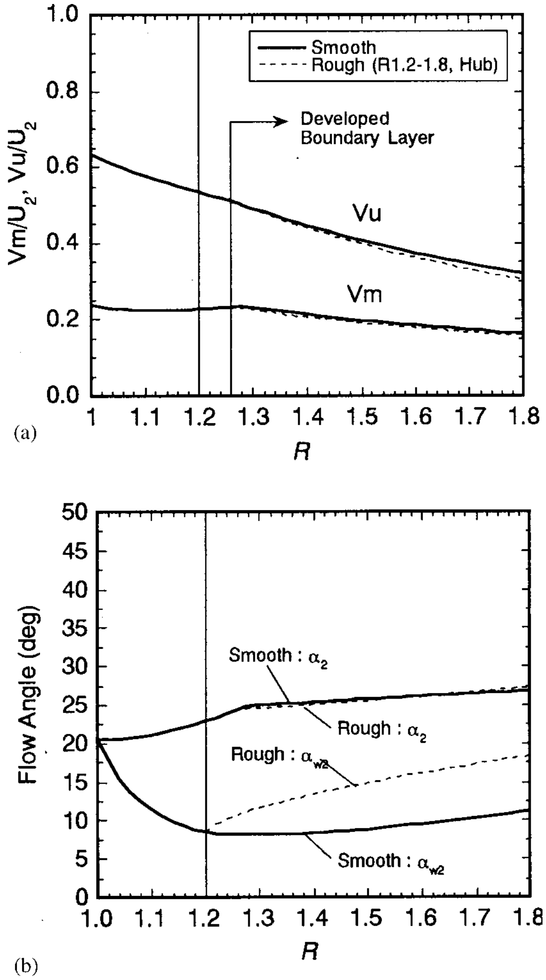

Fig. 17 **Effect of locally rough wall on velocity and flow angle at hub side in case without three-dimensional boundary layer separation (ϕ=0.27, λ=0.147, $\Delta Vu/Vum$=±0.02, $\Delta Vm/Vmm$=0): (*a*) tangential and radial components of velocity; (*b*) flow angles of main-flow and wall-limiting streamline**

by positioning the rough wall locally. The variations of the tangential and radial components of velocity and the flow angle at the outer edge of the hub side boundary layer as well as the wall-limiting streamline flow angle on the hub side wall are compared in Figs. 17(*a*) and 17(*b*) between the smooth and rough walls. As shown in Fig. 17(*a*), both tangential and radial velocities are not changed between $R=1.2\sim1.26$ by the rough wall because the core-flow exists until $R=1.26$, which results in almost no difference in the radial pressure gradient in this region between the smooth and rough walls. Downstream of $R = l.26$, they are decreased by the direct influence of wall roughness as shown by tile broken lines, As shown in Fig. 17(*b*), there is no separation region in this case; however, the wall-limiting streamline flow angle increases markedly, as is seen in Fig. 9(*b*), just downstream of $R=l.2$ due to increase in wall friction. The change in momentum in the radial direction, the first factor to support additionally the radial pressure gradient, is increased by the rough wall because the distortion of the radial velocity distribution is reduced due to a large decrease in the skewed angle of the three-dimensional boundary layer.

Conclusions

The authors have proposed a new technique that effectively suppresses the rotating stall in the vaneless diffuser of centrifugal blowers with a backswept blade impeller. In the experiment, the completely rough wall was positioned locally on the hub side alone, and the effect of an increase in wall friction on the three-dimensional boundary layer separation was investigated experimentally as well as theoretically using the three-dimensional boundary layer calculation code. It was also analyzed why the pressure gradient in the vaneless diffuser is hardly affected by the local increase in wall friction. The concluding remarks obtained are as follows:

1 The rotating stall in the vaneless diffuser of centrifugal blowers with the backswept blade impeller is caused by the three-dimensional separation on the hub side wall, not the shroud side wall, mainly depending on the distortion of tangential component of inlet main-flow velocity.

2 By positioning the completely rough wall on the hub side alone in the region between $R=1.2\sim1.6$, the stall limit was improved markedly by 42 percent, based on suppression of the three-dimensional separation.

3 The increase in the wall shear component normal to the main-flow streamline ''τ_n'' markedly decreases the skewed angle of the three-dimensional boundary layer, and results in suppression of the three-dimensional separation.

4 The turbulence intensity is increased significantly in the hub side boundary layer by the rough wall. This might be another factor that suppresses the three-dimensional separation.

5 Even though the rough wall is positioned downstream of $R=1.2$ at the hub side, diffuser pressure recovery almost equal to the smooth wall case is achieved mainly due to additional increase in the radial momentum change resulting from reduction in the distortion of the radial velocity distribution.

6 As a result, the additional pressure drop due to the locally rough wall was less than 1 percent of the entire pressure rise of the blower.

Acknowledgments

The authors wish to thank Prof. Yoshifumi Kinoshita, Naruto University of Education, for his great support in regard to the three-dimensional boundary layer calculation code, Emeritus Prof. Yasutoshi Senoo for his stimulating comment with respect to the highly turbulent shear layer, and Mr. Mizuki Inoue, a graduate student of Nagasaki University, for securing the experimental data. The authors would like to express appreciation for financial support from the Harada-Memorial Foundation. This work was also supported in part by the Grant-in-Aid from the Ministry of Education, Science, and Culture of Japan.

Nomenclature

b = diffuser depth
b_2 = blade height at impeller exit
C_{fu} = friction coefficient in the main-flow direction $=2\tau_s/\rho Ve^2$
Cp = pressure recovery coefficient
c_2 = axial tip clearance at impeller exit
R = radius ratio $=r/r_2$
r_2 = impeller exit radius
U_2 = peripheral velocity of impeller
u,w = velocity of main-flow direction and crossflow
Ve = main-flow velocity at outer edge of boundary layer
Vm = radial component of velocity
Vmm = mean radial velocity of inlet core-flow
Vu = tangential component of velocity
Vu' = tangential component of velocity turbulence
Vum = mean tangential velocity of inlet core-flow
Y = dimensionless diffuser depth $=y/b$
α_1, α_2 = flow angle at outer edge of boundary layer measured from circumference
α_{w1}, α_{w2} = wall-limiting streamline flow angle, or flow angle from circumference of the flow close to the wall
γ = skewed angle of three-dimensional boundary layer
δ = boundary layer thickness
ϕ = flow coefficient $=Vmm_2/U_2$
$\psi_d, \psi_s, \psi_{se}$ = static pressure coefficient for pressure rises in the diffuser, at the impeller exit and at the diffuser exit $=2\Delta p/\rho U_2{}^2$
τ_m, τ_u = radial and tangential components of wall shear stress
τ_n, τ_s = wall shear stress components normal to main flow and along the main flow streamline
τ_w = wall shear stress
λ = tip clearance ratio at impeller exit $=c_2/b_2$

Subscripts

1 = shroud side
2 = hub side, or impeller exit

References

[1] Fukushima, Y., Nishida, H., and Miura, H., 1989, ''Rotating Stall of Centrifugal Compressors,'' Turbomachinery, **17**, No. 3, pp 149–159 [in Japanese].
[2] Abdelhamid, A. N., 1982, ''Control of Self-excited Flow Oscillations in Vaneless Diffuser of Centrifugal Compressor System,'' ASME Paper No. 82-GT-188.
[3] Senoo, Y., Hayami, H., and Ueki, H., 1983, ''Low-Solidity Tandem-Cascade Diffusers for Wide-Flow-Range Centrifugal Blowers,'' ASME Paper No. 83-GT-3.
[4] Harada, H., 1996, ''Non-Surge Centrifugal Compressor With Variable Angle DiffuserVanes,'' Turbomachinery, **24**, No. 10, pp. 600–608 [in Japanese].
[5] Kurokawa, J., Matsui, J., Kitahora, T., and Saha, L., 1997, ''A New Passive Device to Control Rotating Stall in Vaneless and Vaned Diffusers by Radial Grooves,'' Proc. JSME Intl. Conf. on Fluid Engrg., **II**, pp. l109–1114.
[6] Tsurusaki, H., and Kinoshita, T., 1999, ''Flow Control of Rotating Stall in a Radial Vaneless Diffuser,'' Proc. of 3rd ASME/JSME Joint Fluids Engrg. Conf., Paper No. FEDSM99-7199.
[7] Jansen, W., 1964, ''Steady Fluid Flow in a Vaneless Diffuser,'' ASME J. Basic Eng., **86**, No. 3, pp. 607–619.
[8] Senoo, Y., Kinoshita, Y., and Ishida, M., 1977, ''Asymmetric Flow in Vaneless Diffusers of Centrifugal Blowers,'' ASME J. Fluids Eng., **99**, pp. 104–114.
[9] Ishida, M., Sakaguchi, D., Ueki, H., and Sun, Z., 1997, ''Relationship Between Rotating Stall Inception and Three-Dimensional Flow Separation on Vaneless Diffuser Wails in Centrifugal Blowers,'' Proc. JSME Intl. Conf. on Fluid Engrg., No. 97-203, **II**, pp. 1097–1102.
[10] Kinoshita, Y., and Senoo, Y., 1985, ''Rotating Stall Induced in Vaneless Dif-

fusers of Very Low Specific Speed Centrifugal Blowers,'' ASME J. Eng. Gas Turbines Power, **107**, pp. 514–521.
[11] Senoo, Y., and Kinoshita, Y., 1977, ''Influence of Inlet Flow Conditions and Geometries of Centrifugal Vaneless Diffusers on Critical Flow Angle for Reverse Flow,'' ASME J. Fluids Eng., **99**, 98–103.
[12] Ishida, M., Ueki, H., Sakaguchi, D., and Surana, T., 1993, ''Unstable Flow Measurement in a Centrifugal Blower by SemiconductorLaser 2-Focus Velocimeter,'' Proc. 4th Asian Intl. Conf. on Fluid Machinery, **1**, pp. 77–82
[13] Ishida, M., and Sakaguchi, D., 1997, ''Behavior of Separation Ring on Shroud Casing Wall of a Centrifugal Blower (Visualization of Separation Ring by Oil Film Technique),'' J. Visualization Society Japan, **17–64**, pp. 46–50 [in Japanese].
[14] Wiesner, F. J., 1967, ''A Review of Slip Factors for Centrifugal Impellers,'' ASME J. Eng. Power, **89**, pp. 558–572.
[15] Senoo, Y., and Ishida, M., 1975, ''Behavior of Severely Asymmetric Flow in a Vaneless Diffuser,'' ASME J. Eng. Power, **97**, No. 3, pp. 375–387.
[16] Senoo, Y., Ishida, M., and Ono, M., 1973, ''Pressure Loss of Asymmetric Flow in the Vaneless Diffuser of a Centrifugal Blower,'' Reports of Institute of Industrial Sciences, Kyushu University, No. 58, pp. 25–34 [in Japanese].

Direct Method for Optimization of a Centrifugal Compressor Vaneless Diffuser

Yu-Tai Lee
Naval Surface Warfare Center,
Carderock Division,
West Bethesda, MD 20817

Lin Luo
The Pennsylvania State University,
University Park, PA 16801

Thomas W. Bein
Naval Surface Warfare Center,
Annapolis Detachment,
Annapolis, MD 21402

A Direct Method for Optimization (DMO) is developed for investigating pressure rise and energy loss in a vaneless diffuser of a generic compressor used in shipboard air-conditioning systems. The scheme uses Reynolds-Averaged Navier–Stokes (RANS) results and evaluates gradients of a predetermined objective function. The current Direct Method for Optimization differs from the popular Inverse Design Method in the process of obtaining final configurations and in the final configurations obtained. The Direct Method for Optimization achieves a final shape from maximizing/minimizing a nonlinear function, i.e., the objective function. Both gradient and nongradient Direct Methods for Optimization are compared with respect to accuracy and efficiency. The coupled DMO/RANS optimization code is benchmarked using a plane turbulent diffuser also investigated by Zhang et al. using an adjoint method. The benchmark indicates that if a global optimum exists, the result should be independent of the methodologies or design parameters used. The DMO/RANS method is applied to redesign a three-dimensional centrifugal vaneless diffuser used in a modern generic compressor. The objective function is a composite function of the diffuser's pressure rise and total energy loss. The new optimum diffuser has a minimum width at a location far beyond the conventional diffuser pinch point. The new diffuser also provides an efficient section for pressure recovery, which takes place after the minimum width location. Test data for the new diffuser validate the current approach at the design condition. Furthermore, improved performance is also recorded experimentally at off-design conditions for the optimized diffuser.

[DOI: 10.1115/1.308571]

Introduction

Diffusers, functioning as pressure-recovery devices, are absolutely essential for good turbomachinery performance. Diffuser performance is governed by geometric and aerodynamic parameters.

Diffusers are categorized as channel, conical, and annular types [1]. The annular diffuser with radial inflow and radial outflow is also known as a vaneless diffuser. Vaneless diffusers are employed for centrifugal compressors and pumps as exemplified in Fig. 1 for an air-conditioning compressor. Although the compressor in Fig. 1 was designed using a state-of-the-art turbomachinery design tool, it still shows a large discrepancy between the predicted compressor efficiency and the measured efficiency. Further research [2] indicates that the faulty prediction occurs at the compressor's diffuser and volute. Improved computational techniques were therefore developed [3] to investigate the flow features within these components. In order to refine each component's performance further in an efficient manner, development of an optimization method is desirable.

The mathematical requirement of an optimization scheme is to maximize (or minimize) an objective (or an output) function, which represents the parameter of interest from a mathematical model of the problem. As we know, in order to determine the minimum value of a function, multidimensional mapping of the function is impractical. Thus, an optimization procedure is required that is considerably more efficient than multidimensional mapping.

Many attempts and successes exist in the literature on the topics of optimization using computational-fluid-dynamic (CFD) methods. Among these efforts, the adjoint method and the gradient-based method are the most popular approaches. The adjoint method is represented by Baysal and Eleshaky [4] and Reuther and Jameson [5] for wing shapes, and by Cabuk and Modi [6] and Zhang et al. [7] for plane diffusers. The gradient-based method is represented by Panting [8] for aeroengine optimization, Mrsa [9] for nozzle design, and Koller et al. [10] for compressor blade shaping. The adjoint method requires derivation of the adjoint equations for each new problem. Extension of the adjoint method

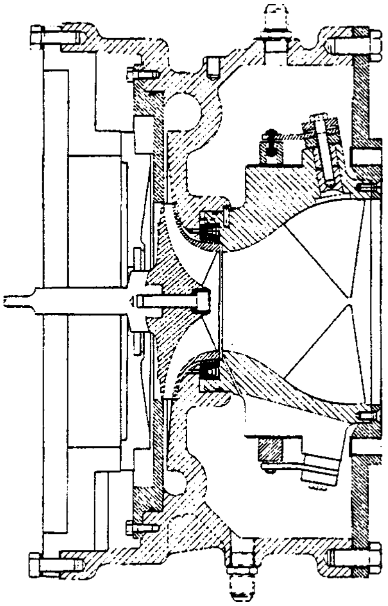

Fig. 1 Generic air-conditioning compressor

Contributed by the International Gas Turbine Institute and presented at the 45th International Gas Turbine and Aeroengine Congress and Exhibition, Munich, Germany, May 8–11, 2000. Manuscript received by the International Gas Turbine Institute February 2000. Paper No. 2000-GT-453. Review Chair: D. Ballal.

from laminar to turbulent flow is not a trivial task, and the adjoint equations for more sophisticated turbulence models can be quite challenging. Furthermore, the objective function for an adjoint method may lack uniqueness [7], which affects the final optimum solution.

In this paper we present a more heuristic approach and apply it to a general diffuser optimization. The method developed is called the Direct Method for Optimization (DMO) and is a gradient-based approach. The DMO is coupled with a CFD method and a regridding approach to iteratively march to the optimized shape.

Direct Method for Optimization

The mathematical representation of an optimization problem can be formulated as follows. Given a predetermined input vector $\vec{x}$ and an objective function (or a parameter of interest) $f(\vec{x})$ for the problem, the DMO is to find an optimal value $\vec{x}^*$ such that $f(\vec{x}^*)\leqslant f(\vec{x})$, provided the constraint $\vec{x}_{\min}\leqslant\vec{x}\leqslant\vec{x}_{\max}$.

For the stated problem, a local minimum can be found through a gradient vector,

$$g_i=\frac{\partial f(\vec{x})}{\partial x_i} \tag{1}$$

where $\vec{x}=(x_i)$ and $\vec{g}=(g_i)$, $i=1,\ldots,n$ and n is the dimension of the problem. The general objective function $f(\vec{x})$ can be approximated as a multidimensional quadratic function,

$$f(\vec{x})\approx\frac{1}{2}\vec{x}\cdot[A]\cdot\vec{x}-\vec{b}\cdot\vec{x}+c \tag{2}$$

where $[A]$ is the second partial derivative (or the Hessian) matrix of f. In order to convert the multidimensional function to a one-dimensional problem and use a line-minimization scheme, an optimal direction must be determined. This direction has been proven [11] to be one of a conjugate pair, called a conjugate set, which are the bases for selecting the marching direction in the direction set method [11]. For functions that are not exactly quadratic forms, as shown in Eq. (2), repeated use of the mutually conjugate line-minimization directions will, in due course, converge quadratically to the desired minimum.

Furthermore, if the direction of the line-minimization is constructed to be conjugate to the direction used in the previous iteration or to all directions traversed in all previous iterations, the conjugate gradient algorithm is obtained. In this paper, the Polak–Ribiere conjugate gradient scheme [12] is adapted. If $\vec{u}$ is such a conjugate direction, the Polak–Ribiere scheme is given as

$$\begin{gathered}\vec{u}_1=-\vec{g}(\vec{x}_1)\\ \vec{u}_{k+1}=-\vec{g}(\vec{x}_{k+1})-\gamma_{k+1}\vec{g}(\vec{x}_k)\\ \gamma_{k+1}=\frac{\vec{g}(\vec{x}_{k+1})\cdot\{\vec{g}(\vec{x}_{k+1})-\vec{g}(\vec{x}_k)\}}{\vec{g}(\vec{x}_k)\cdot\vec{g}(\vec{x}_k)}\end{gathered} \tag{3}$$

where the subscript represents the iteration number.

DMO on Vaneless Diffuser

Using the aforementioned Polak–Ribiere conjugate gradient scheme (Eq. (3)), the geometric and flow constraints of the vaneless diffuser of the given compressor are depicted in Fig. 2. The inlet condition is fixed by a constant mass flow rate and a constant inflow angle. The shape of the diffuser shroud is represented by a cubic spline. The number of design stations, which correspond to the dimension n of the current optimization problem, is flexible. In this paper, we use 3 and 6 points to demonstrate the robustness of the methodology. Figure 2 shows the six-point design stations. Segment S0 of the shroud curve in Fig. 2 is fixed as an inlet-shape constraint. All the other shroud locations, including the one at the diffuser exit, are to be optimized.

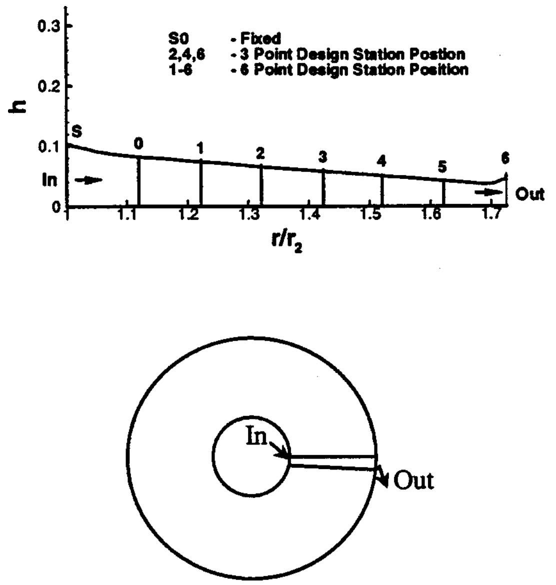

Fig. 2 Schematics of the vaneless diffuser geometry

For the current diffuser problem, the objective function f is defined as

$$f(\vec{h})=\beta\omega-\alpha C_p$$

$$\omega=\frac{p_{t3}-p_{t2}}{1/2\rho_2U_2^2};\quad C_p=\frac{p_{s3}-p_{s2}}{1/2\rho_2U_2^2} \tag{4}$$

where $\vec{h}=(h_i)$, $i=1,\ldots,n$ represents the diffuser width vector at the design stations and is normalized by the impeller radius, ω is the total pressure loss coefficient, C_p is the static pressure rise coefficient, p_{s2} and p_{s3} are the inlet and outlet mass-averaged static pressures, p_{t2} and p_{t3} are the mass-averaged inlet and outlet total pressures, α and β are weighting coefficients, and ρ_2 and U_2 are inlet density and velocity. Equation (4) indicates that the objective function f is a composite function of the diffuser static pressure rise and the total pressure loss and is weighted by the coefficients α and β. All the parameters studied are nonlinear functions of $\vec{h}$. The static and total pressure distributions are obtained by solving the RANS equations.

The complete optimization procedure is described as follows:

1 Problem definition: including input vector $\vec{h}$, constraints, and objective function $f(\vec{h})$;
2 Initialization of optimization calculation: including normalization of $\vec{h}$ and variable limitation;
3 Flow prediction: including solving the RANS equations with an initial grid and calculating relevant $f(\vec{h})$;
4 Preparation of optimization calculation: including evaluation of gradient vector $\vec{g}$ and determination of mutually conjugate directions;
5 Optimization calculation: including bracketing the minimum, conducting the line minimization and optimization iteration;
6 Convergence check: checking the convergence of the design variables. If the design requirements are met, the process is complete. Otherwise, the calculation continues to the next step.
7 CFD regridding: including defining the new boundary surfaces and their smoothing, and interior grid movement. Return to step (3) for another gradient iteration.

The gradient vector $g(\vec{h})$ is obtained by

$$g(h_i)=\frac{f(h_i+\Delta h_i)-f(h_i)}{\Delta h_i},\quad (i=1,\ldots,n) \tag{5}$$

Evaluating these gradients takes enormous computational effort. Thus, in this paper, two other nonlinear non-gradient-based optimization schemes are also examined for the present vaneless diffuser case. These are the downhill simplex method [13] and the Powell method [14]. Although there is no requirement to evaluate the gradient of the objective function f for these latter schemes, the total number of iteration cycles needed to obtain a minimum may be large. If, however, the function f does not lead to quadratic convergence, these nongradient, more heuristic schemes become more competitive in terms of computational effort and accuracy. A numerical illustration of the aforementioned procedure is given in the appendix for a two-dimensional plane diffuser optimization discussed in the Prediction Results section.

RANS Solution Method

Computational Scheme. The governing equations, including the continuity, momentum, and energy equations, for compressible flow are solved with a two-equation $k-\varepsilon$ turbulence model for the diffuser flow. The governing equations in curvilinear coordinates are written as:

$$\frac{1}{J}\frac{\partial}{\partial t}(\rho q)=\frac{\partial}{\partial \xi_i}\left(-\rho U_i q+\mu_{\mathrm{eff}} G_{ij}\frac{\partial q}{\partial \xi_i}\right)+S_q \qquad (6)$$

where $q=[1,u_{\mathrm{x}},u_{\mathrm{y}},u_{\mathrm{z}},h,k,\varepsilon]$ and ρ,J,U_i,G_{ij} represent fluid density, the Jacobian of the coordinate transformation, transformed velocities, and diffusion metrics, respectively. The effective viscosity μ_{eff} represents a sum of the laminar viscosity μ and the turbulent eddy viscosity μ_t, re-scaled by a turbulence Prandtl number or Schmidt number. The turbulent eddy viscosity $\mu_t=\rho C_\mu k^2/\varepsilon$ and $C_\mu=0.09$.

Finite-difference approximations are used to discretize the transport equations on nonstaggered grid systems. An upwind scheme is used to model the convective terms and a central differencing formula is used for the viscous and source terms of Eq. (6). For turbulence quantities, the convection process is modeled by an upwind scheme. A pressure-based predictor/corrector solution procedure [15] is employed to achieve velocity-pressure coupling. The discretized systems are solved by an implicit Euler time-marching scheme. The numerical solutions are considered converged when the residuals of each discretized equation have dropped by five orders of magnitude from their initial values. The computational technique and results for a centrifugal compressor's vaneless diffuser and volute have been demonstrated in Lee and Bein [3]. In order to minimize the RANS computational effort for the present vaneless diffuser optimization, axisymmetric calculations are performed with a prescribed inflow angle, total pressure, total temperature, and a diffuser exit pressure. The diffuser exit pressure prescribed at the exit mid-width is obtained through iteration until the design mass flow rate is maintained.

Grid Movement. Regridding en route to the optimized shape is completed using an algebraic grid movement strategy. After a new shroud shape is generated by the DMO, the points on the shroud boundary are moved to the new shape, and interior grid points are moved proportionally based on the original grid distribution. Grid smoothing is employed to compensate for large boundary movement and inadvertent grid-line crossing.

Prediction Results From Optimization Calculations

Plane Diffusers in Turbulent Flow. Cabuk and Modi [6] and Zhang et al. [7] have studied plane diffuser optimization for laminar and turbulent flows using the adjoint method. They use an objective function of the flow-weighted static-pressure rise between the diffuser inlet and outlet. For the turbulent plane diffuser, Zhang studied a geometry with a ratio of diffuser length to inlet width equal to 6. As Fig. 3 shows, a head-pipe and a tail-pipe with lengths equal to the inlet width were added to the entrance and exit. The grid shown in Fig. 3, with dimensions of 40×30, was used for the incompressible turbulent-flow computations in this paper and is comparable to the grid used by Zhang. The Reynolds number is 10,000 based on the mean inlet velocity and inlet width. The inflow is assumed to have a fully developed power-law velocity distribution. The initial diffuser shape, a constant width channel, differs from that used by Zhang, a cosine type with an amplitude of 0.33. In order to compare the current approach to Zhang's, α is set to unity and β to zero in Eq. (4). Zhang shows results based on two different design functions in his adjoint representation of the objective function: a product form,

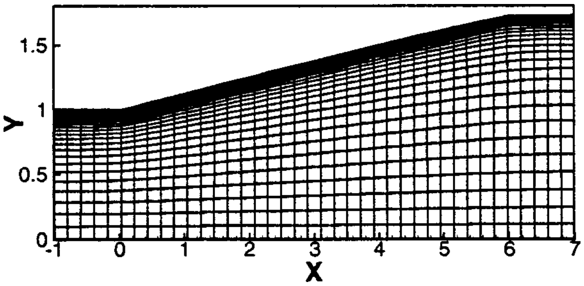

Fig. 3 Typical computational grid for turbulent plane diffuser

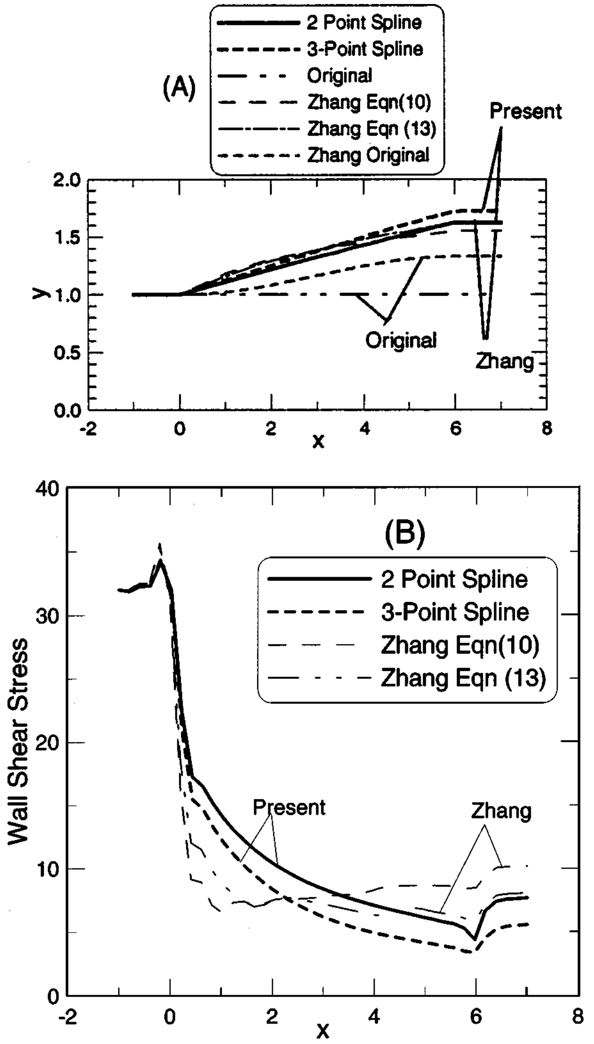

Fig. 4 Optimization of plane diffuser and comparison with [7]: (*A*) diffuser shapes; (*B*) wall shear stress

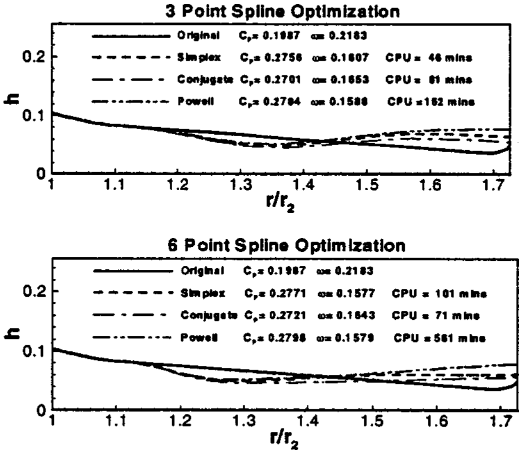

Fig. 5 Optimization of vaneless diffuser: (*A*) three-point spline; (*B*) six-point spline (C_p=static pressure rise, ω=total pressure loss)

and a shear ratio form (identified as Eq. (10) and Eq. (13), respectively, in his paper). The choice of the different design functions is due to the nonuniqueness of the problem.

Prediction results based on the present DMO/RANS calculation are shown in Fig. 4 and compared to Zhang's results. A two-point spline calculation and a three-point spline calculation were used with the current approach. The design locations are at $x=3$ and 6 for the two-point spline and at $x=2$, 4, and 6 for the three-point spline. The final diffuser curves are plotted in Fig. 4(*a*) and the wall shear distributions are depicted in Fig. 4(*b*). The variation of the objective function between successive iterations is monitored and compared to a prescribed tolerance. For the plane diffuser, the tolerance is set to 10^{-5}. The complete optimization calculation for the two-point spline takes 110 iterations and 5 gradient cycles. Although the two-point spline agrees better with Zhang's shear form result, the three-point spline produces a slightly larger exit area, higher pressure recovery and lower wall shear. The abrupt drop in shear stress at the end of the inlet head-pipe, which exists in all the solutions, is associated with a discontinuity in wall slope and a divergence of the wall shape at that location. Limited by the solution accuracy of each optimization approach and their constraints, the present comparison indicates that different methods or different design parameters lead to similar final global optimum shapes, as they should if indeed a unique optimum exists.

Vaneless Diffuser of the Generic Compressor. The vaneless diffuser of the generic compressor, as shown in Figs. 1 and 2, starts at the impeller exit radius of $r_2=12.24$ cm (4.82 in). The diffuser inlet velocity is 128 m/s (420 ft/s) and the mass flow at the design condition is 4 kg/s (8.8 lbm/s). The diffuser inflow Mach number is 1.05 and the flow angle is estimated to be 79.5 deg from radial. The Reynolds number based on r_2 and the diffuser inlet velocity is 3.1×10^7. The diffuser has a length of $r_3/r_2=1.725$ and an inlet width of $h_2=0.104$. The original diffuser has a flat hub (front plate) and a curved shroud (back plate). The current optimization design is performed at the design condition with the following geometrical constraints: The diffuser length and the inlet width are kept constant; and the initial section of the shroud curve, i.e., the segment S0 in Fig. 2, is fixed. Station 0 is close to the conventional pinch location. In order to minimize the modification of the compressor front plate where the transmission and the motor are located, the diffuser hub surface is maintained as a fixed flat surface.

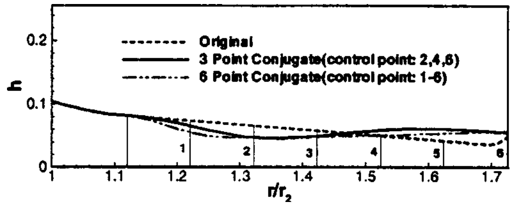

Fig. 6 Comparison of three-point and six-point spline shapes

The optimization results for the vaneless diffuser are shown in Figs. 5–11. Figure 5 compares the original and final shroud curves obtained from the conjugate gradient method and the non-gradient downhill simplex and Powell methods with both weighting functions α and β equal to unity. Both the three-point spline and six-point spline are used to study the impact of the number of design dimensions. The curve obtained from the three-point conjugate method is plotted against that from the six-point conjugate method in Fig. 6. The additional design stations at locations 1, 3, and 5 provide an extra level of control for reaching the final optimum shroud curve. Since the simplex and the Powell methods treat the conditions at the endpoint (i.e., the diffuser exit) somewhat differently than the conjugate gradient method, they produce a larger exit width. Because of the smaller exit width produced by the conjugate gradient method, the compressor test for a new diffuser adopts the resultant curve obtained from the conjugate gradient calculation without changing the volute configuration. The static pressure rise C_p, total pressure loss ω, and total CPU time used (in minutes) for each calculation are also shown in Fig. 5. The variations of the predicted flow parameters for all cases studied here are within 3.5 percent for C_p and 4.7 percent for ω. The computational time indicates that the conjugate gradient method is a more efficient scheme for the six-point optimization.

The weighting coefficients α and β in Eq. (4) are factors for controlling the importance of C_p and ω to the final optimum result. Separate calculations using the conjugate gradient method were carried out by setting (*i*) $\alpha=1$ and $\beta=1$; (*ii*) $\alpha=1$ and $\beta=3$; and (*iii*) $\alpha=3$ and $\beta=1$. The optimum shroud curves from these calculations, shown in Fig. 7, indicate that the equal-weight approach is as good as other weights for C_p and ω. Therefore α and β are chosen to be unity in all other calculations.

Figure 8 shows the grids used for the original and modified

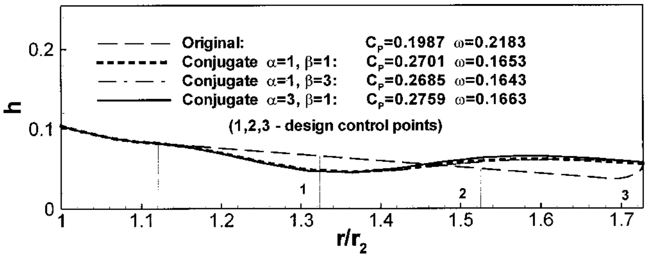

Fig. 7 Impact of the weighting coefficients in Eq. (4)

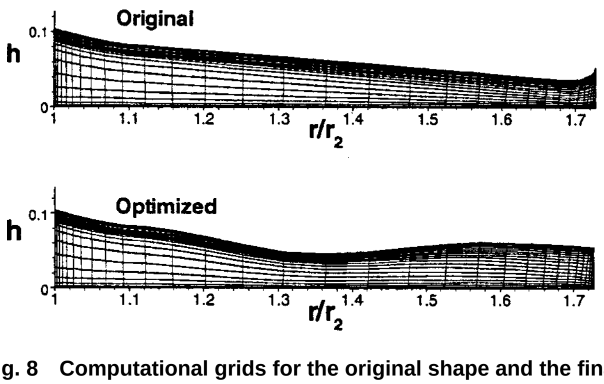

Fig. 8 Computational grids for the original shape and the final shape using conjugate gradient method

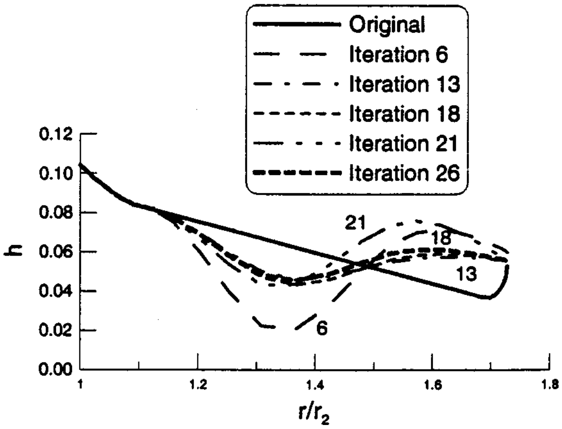

Fig. 9 Selected intermediate shroud shapes through 26 iterations from the original curve

diffusers based on the six-point gradient calculation. The grids have dimensions of 21×31×3 (in the h, r, and θ directions). A clustered grid is used near the shroud surface.

Figure 9 shows variations of the shroud curves at intermediate steps during the conjugate gradient calculation. The complete optimization is completed in 26 iterations and 2 gradient cycles with a tolerance equal to 10^{-3}. Although the plotting scale of the ordinate has been magnified, Fig. 9 shows the robustness of the current scheme, which is capable of correctly steering the prediction after overshooting the final result.

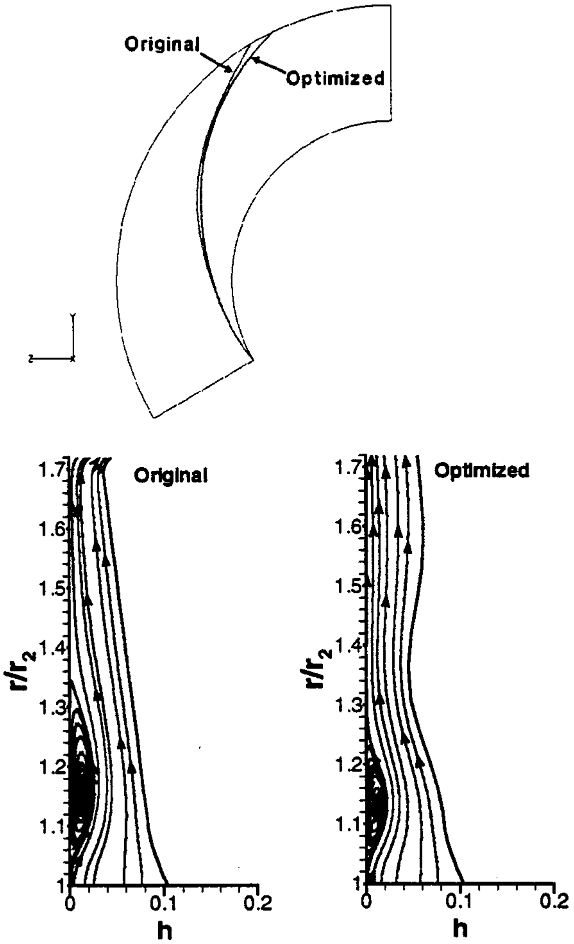

Fig. 10 Predicted flow path: (*A*) on the front plate; (*B*) on a radial section

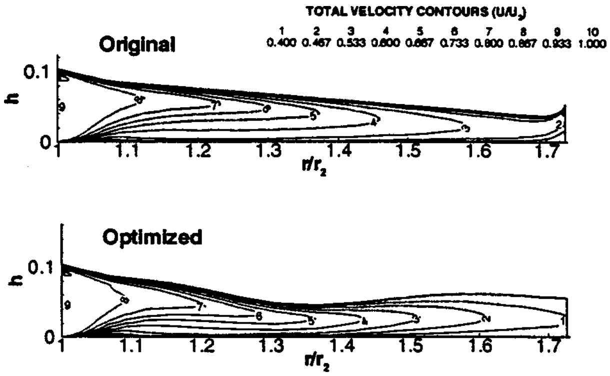

Fig. 11 Predicted total velocity contours

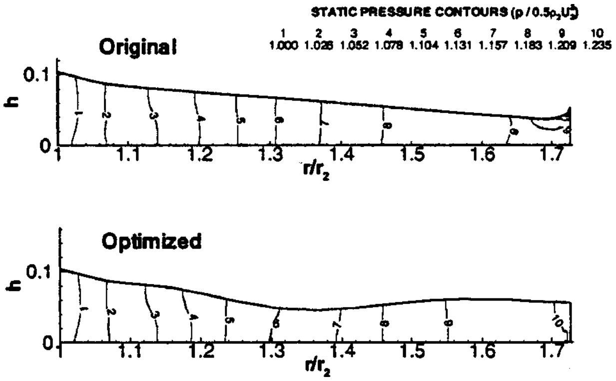

Fig. 12 Predicted static pressure contours

The flow path near the flat hub surface is drawn in Fig. 10(*a*) for the original diffuser and for the modified diffuser from the six-point conjugate gradient calculation. The primary differences in flow angle between the two cases occur near $r/r_2=1.25$ and in the exit area. A view of the flow in a radial section is shown in Fig. 10(*b*). For the original diffuser, the flow separates near the inner radius. Although the flow also separates for the optimized diffuser, the separation region is reduced in size due to the converging shroud curve. The optimization does not completely eliminate the flow separation due to the geometric constraint of the shroud inlet curve, i.e., the section S0 in Fig. 2. A dramatic change in flow angle occurs near the diffuser exit, as shown in Fig. 10(*a*). The optimized shape directs the flow into the volute in a much smoother pattern due to the reduced flow angle.

The velocity and static-pressure distributions along the original and optimized diffusers are shown in Figs. 11 and 12. The convergence of the shroud up to $r/r_2=1.3$ differs from the conventional concept of locating the vaneless diffuser's pinch point within $r/r_2=1.10$ to 1.15. The flow in the optimized diffuser decelerates slower in the radial direction decreasing the effect of the flow separation (Fig. 10(*b*)). The optimized diffuser, however, decelerates the flow faster overall (Fig. 11). This efficient decelerating flow within the diverging shroud (between $r/r_2=1.3$ and 1.7) of the optimized diffuser provides a more efficient mechanism for pressure recovery as shown in the static pressure contours of Fig. 12. The averaged exit Mach number for both diffusers is 0.45.

Experimental Results of the Generic Compressor. Compressor tests were conducted using the original diffuser and the optimum diffuser obtained from the six-point conjugate gradient calculation. The compressor is installed in a shipboard air-

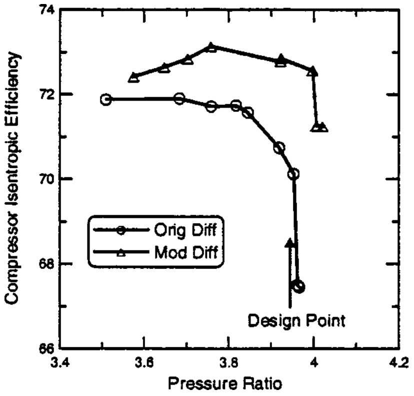

Fig. 13 Measured compressor efficiency for the original and the modified diffusers

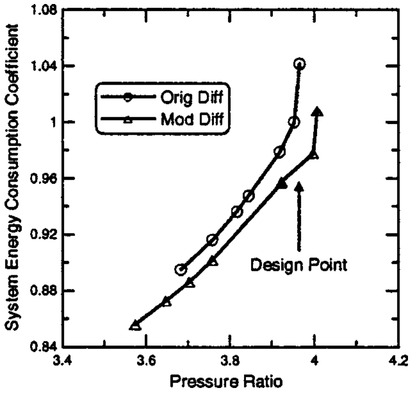

Fig. 14 Measured system energy consumption for the original and the modified diffusers

conditioning system. The compressor performance map was obtained by fixing the impeller speed at 15,160 rpm, the suction conditions and the inlet guide vane positions (fully open), and varying the condensing conditions. Measured data are shown in Figs. 13 and 14 for compressor isentropic efficiency and system energy consumption coefficient versus the ratio of the discharge pressure to the suction pressure. The system energy consumption coefficient is a ratio of the total system energy consumed at various conditions to the consumed energy at the design point for the original diffuser. Due to the current diffuser modification, the compressor efficiency is increased by 2 to 3 percent at the design point and by 1 to 5 percent at off-design conditions. Since the inefficient volute flow remains, the overall compressor efficiency stays relatively low even with the modified diffuser. System energy consumption is reduced by 3 percent at the design point and by 1–7 percent at off-design conditions. These test data support the present optimization results for the vaneless diffuser.

Conclusions

A nonlinear Direct Method for Optimization (DMO) is developed for two-dimensional plane diffusers and three-dimensional vaneless diffusers. The method, coupled with a Reynolds-Averaged Navier–Stokes (RANS) solution method, optimizes a composite objective function of flow parameters which include the diffuser's static-pressure rise and total-pressure loss.

The developed DMO is validated by comparing results to those obtained from an adjoint approach for a plane turbulent diffuser. Limited by the solution accuracy of each optimization approach and their constraints, the comparison between the current solutions and the solutions obtained from the adjoint method indicates that different methods and different design parameters in the objective function lead to similar final optimum shapes.

The current DMO/RANS method is also used to redesign a three-dimensional vaneless diffuser whose original shape was obtained using a state-of-the-art turbomachinery design tool. The final optimum shape from a six-point conjugate gradient calculation shows a converging–diverging shroud. The minimum width occurs at a location far beyond the conventional pinch point. The iteration cycle of the DMO/RANS coupling proceeds along conjugate directions, not only to minimize the objection function, but also to improve the general flow features through a correct selection of the objective function. The theoretically predicted optimum diffuser shape was validated by experiments, both at the design and off-design conditions, to be superior to the original diffuser shape.

Acknowledgments

This work was sponsored by the Shipboard Energy Conservation Program administrated at the Annapolis Laboratory of the Naval Surface Warfare Center. The program manager at the Chief of Naval Operations, Code N420C, is Mr. H. Hodgkins. The program manager at the Carderock Division, Naval Surface Warfare Center is Mr. W. Stoffel. Partial support was provided by the Office of Naval Research (Program Element PE 602121) under the Machinery Systems Task. The program monitor is LCDR F. Novak. The authors are indebted to Messrs. M. Tse, C. Engstrom, and J. M. Loellbach for their help in preparing the final manuscript. Comments from the reviewers and Dr. M. J. Miller are also greatly appreciated.

Nomenclature

$[A]$ = Hessian matrix
$\vec{b}$ = coefficient vector
c, C_μ = constant coefficients
C_p = static pressure rise coefficient
f = objective function
$\vec{g}$ = gradient vector
G_{ij} = diffusion matrix
$\vec{h}$ = diffuser width vector, normalized by r_2
J = Jacobian of coordinate transformation
k = turbulent kinetic energy
n = vector length or dimension
p, p_s = static pressure
p_t = total pressure
q = dependent variable matrix
r = radius
S_q = source term
t = time
$\vec{u}$ = vector representing optimization direction
U_i = velocity components
x, y = coordinates
$\vec{x}, \vec{x}^*$ = input vector and optimum value of $\vec{x}$
α, β, γ = coefficients
ε = turbulence dissipation
λ = line minimization coefficient
$\mu, \mu_t, \mu_{\text{eff}}$ = laminar, turbulent and effective viscosities
θ = tangential
ρ = density and inlet density
ω = total pressure loss coefficient
ξ_i = transformed coordinates

Subscripts

2 = impeller exit
3 = dffuser exit
k = iteration

Appendix

Numerical Illustration of DMO for Plane Diffusers. In order to illustrate the DMO procedure, a numerical example for a complete gradient iteration is depicted as follows for the plane diffuser (shown in Fig. 3). As described in the Prediction Results section for the plane diffusers, Eq. (4) is simplified to $f(\vec{h}) = -C_p$. For the two-point spline calculation shown in Fig. 4, there are two design stations located at $\vec{x}=(3,6)$ and $n=2$. Results from the seven-step optimization procedure (mentioned right before Eq. (5)) after the first gradient cycle are as follows.

1 Initialize input vector or diffuser half width vector $\vec{h}=(1.0,1.0)$. After the first gradient cycle the half width vector is $\vec{h}=(1.0385,1.5895)$ and Fig. 15 shows its spline-fitted shape;

2 Constraint is set to be $0 \leqslant h_i \leqslant 3h_0$, where h_0 is the half width at $x=0$;

3 Flow prediction is performed based on the grid shown in Fig. 15. The predicted $f(\vec{h})=0.1884$;

4 Gradient vector $\vec{g}$ is calculated using Eq. (5) by perturbing the local diffuser half width using $\Delta h=0.1$. Figure 16 shows two perturbed diffuser shapes with their computational grids for evaluations of each component of $\vec{g}$. The predicted gradient vector is $\vec{g}=(0.2229,0.1789)$;

5 Equation (3) calculates the conjugate direction from the predicted $\vec{g}$ of step 4. The line minimization locates $\vec{h}_{k+1}=\vec{h}_k+\lambda_k\vec{u}_k$ for minimum $f(\vec{h}_{k+1})$, where k is an iteration number and λ is a line minimization coefficient [11]. After the first gradient cycle, $\vec{h}_k=(1.0385,1.5895)$, $\vec{u}_k=(0.3601,0.1233)$, $\lambda_k=1.1209$ and $\vec{h}_{k+1}=(1.4421,1.7276)$ and $f(\vec{h}_{k+1})=0.2679$;

6 Check the constraint condition specified in step 2. If the condition is satisfied, continue to next step. Otherwise, reset $f(\vec{h})$ to be a large value and continue to next step;

7 Check the convergence for the CFD solution. If $|(f(\vec{h}_{k+1})-f(\vec{h}_k))/f(\vec{h}_{k+1})| \leqslant \varepsilon$, the calculation is complete. Otherwise, use $\vec{h}_{k+1}$ as the initial value and return to step 3. In the present gradient cycle, $\varepsilon=0.01$ and $|(f(\vec{h}_{k+1})-f(\vec{h}_k))/f(\vec{h}_{k+1})|=0.297 > \varepsilon$. The iteration continues from step 3.

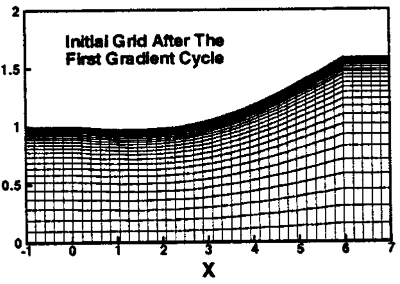

Fig. 15 Initial diffuser shape and grid after the first gradient cycle

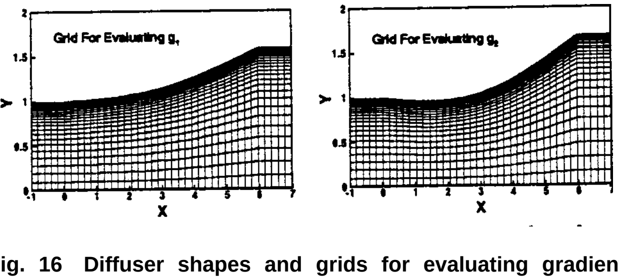

Fig. 16 Diffuser shapes and grids for evaluating gradient vector

References

[1] Japikse, D., and Baines, N. C., 1998, *Diffuser Design Technology*, Concepts ETI, Inc.
[2] Bein, T. W., and Lee, Y. T., 1999, ''Performance Evaluation of an Air-Conditioning Compressor, Part I: Measurement and Design Modeling,'' International J. of Rotating Machinery, **5**, No. 4, pp. 231–240.
[3] Lee, Y. T., and Bein, T. W., 1999, ''Performance Evaluation of an Air-Conditioning Compressor, Part II: Volute Flow Predictions,'' International J. of Rotating Machinery, **5**, No. 4, pp. 241–250.
[4] Baysal, O., and Eleshaky, M. E., 1991, ''Aerodynamic Sensitivity Analysis Methods for the Compressible Euler Equations,'' ASME J. Fluids Eng., **113**, pp. 681–688.
[5] Reuther, J., and Jameson, A., 1995, ''Supersonic Wing and Wing-Body Shape Optimization using an Adjoint Formulation,'' *CFD for Design and Optimization*, ASME FED-Vol. 232, pp. 45–52.
[6] Cabuk, H., and Modi, V., 1992, ''Optimum Plane Diffusers in Laminar Flow,'' J. Fluid Mech., **237**, pp. 373–393.
[7] Zhang, J., Chu, C. K., and Modi, V., 1995, ''Design of Plane Diffusers in Turbulent Flow,'' *Inverse Problems in Engineering*, **2**, Overseas Publishers Association, pp. 85–102.
[8] Panting, J. R., 1998, *Optimizing the Super-turbocharged Aeroengine*, Professional Engineering Publishing Limited, London.
[9] Mrsa, Z., 1998, ''A Turbulent Flow Shape Optimization Method for Nozzle Design,'' Computational Technologies for Fluid/Thermal/Structural/Chemical Systems With Industrial Applications, Vol. II, ASME PVP-Vol. 377-2, pp. 87–92.
[10] Koller, U., Monig, R., Kusters, B., and Schreiber, H., 2000, ''Development of Advanced Compressor Airfoils for Heavy-Duty Gas Turbines, Part I: Design and Optimization,'' ASME J. Turbomach., **122**, pp. 397–405.
[11] Press, W. H., Flammery, B. P., Teukolsky, S. A., and Vetterling, W. T., 1989, *Numerical Recipes, The Art of Scientific Computing*, Cambridge University Press.
[12] Polak, E., 1971, *Computational Methods in Optimization*, Academic Press, New York, Sec. 2.3.
[13] Nelder, J. A., and Mead, R., 1965, ''A Simplex Method for Function Minimization,'' Comput. J. (UK), **7**, pp. 308–313.
[14] Acton, F.S., 1973, *Algorithms for Minimization Without Derivatives*, Prentice-Hall, Englewood Cliffs, NJ, Chap. 7.
[15] Chen, Y. S., 1989, ''Compressible and Incompressible Flow Computations With a Pressure Based Method,'' Paper No. AIAA-89-0286.

Discussion: ''Direct Method for Optimization of a Centrifugal Compressor Vaneless Diffuser'' (Lee, Y.-T., Luo, L., and Bein, T. W., 2001, ASME J. Turbomach., 123, pp. 73–79)

N. A. Cumpsty
Chief Technologist, Rolls-Royce plc, PO Box 31, Derby DE24 8BJ, United Kingdom

I found this an interesting and original paper. Although I do not pretend to understand the details of the optimization procedure, I am interested in the predictions, and one aspect of the results does surprise me. I would have expected the optimum annulus shape to be markedly different depending on whether the optimization was for minimizing loss in stagnation pressure or maximizing rise in static pressure. I am therefore surprised that the shapes of the annulus are so similar in Fig. 7 for the different optimization weightings; it does not seem to make much difference whether the static pressure rise Cp or the total pressure loss w are optimized. Similarly, I am surprised that the values of predicted static pressure rise coefficient Cp and stagnation pressure loss coefficient w are almost equal for different optimizations, though substantially better than for the datum diffuser. What does this tell us about the optimization process and about the flow that is being studied?

One of the least desirable features of the datum diffuser seems to be the sudden area increase near its exit. Is it possible that the improvement in performance of the optimized diffusers comes primarily from eliminating this feature?

We are told that the compressor volute has very poor performance; in other words the pressure rise in the volute downstream of the diffuser will contribute relatively little to the overall machine efficiency and pressure rise. In that case would it not have been more appropriate for this diffuser to have optimized only on static pressure rise and ignore the loss in the diffuser?

Closure to ''Discussion of 'Direction Method for Optimization of a Centrifugal Compressor Vaneless Diffuser' '' (2001, ASME, J. Turbomach., 123, p. 79)

Yu-Tai Lee, Lin Luo, and Thomas W. Bein

The point made by Professor Cumpsty concerning the results related to the variation of the weighting coefficients shown in Fig. 7 is well taken. We found that the figure's legend was misplaced in the pamphlet paper; we have redrawn Fig. 7. If the stagnation pressure is approximated by $p_t = p_s + 1/2\rho u^2$, the objective functions searched by the three sets of weighting coefficients shown in Fig. 7 are

$$\begin{aligned} f(h) &= \min(\Delta p_s + \Delta p_t) = \min(\Delta p_s + \Delta p_s + \Delta(1/2\rho u^2)) \\ &= \min(2\Delta p_s + \Delta(1/2\rho u^2)) \end{aligned}$$

for $\alpha=1$ and $\beta=1$, and

$$\begin{aligned} f(h) &= \min(\Delta p_s + 3\Delta p_t) = \min(\Delta p_s + 3\Delta p_s + 3\Delta(1/2\rho u^2)) \\ &= \min(4\Delta p_s + 3\Delta(1/2\rho u^2)) \end{aligned}$$

for $\alpha=1$ and $\beta=3$, and

$$\begin{aligned} f(h) &= \min(3\Delta p_s + \Delta p_t) = \min(3\Delta p_s + \Delta p_s + \Delta(1/2\rho u^2)) \\ &= \min(4\Delta p_s + \Delta(1/2\rho u^2)) \end{aligned}$$

for $\alpha=3$ and $\beta=1$. The weighting coefficients for the static pressure rise term of the last two calculations ($\alpha=1$, $\beta=3$ and $\alpha=3$, $\beta=1$) are identical, although the coefficients for the dynamic head are 3 versus 1. Similarly the dynamic-head coefficients between $\alpha=1$, $\beta=1$ and $\alpha=3$, $\beta=1$ are identical and the pressure rise coefficients are 2 versus 4. The three cases investigated in Fig. 1 have much less impact from the changes of the weighting coefficients than the limiting case with $\alpha=1$ and $\beta=0$. In addition, for the current diffuser, the gains from C_p and ω are comparable in their magnitudes between the original and the other cases. Therefore, the end configurations are less dependent on the coefficients used and very close to each other.

Certainly the original diffuser outlet shape plays some role in the final result, but it is not the sole contribution. Both Figs. 10 and 12 show that the gain in the loss reduction is mainly from the front section of the diffuser and the gain in the pressure recovery is mainly from the rear half of the diffuser, but not just from the last 5 percent of the diffuser length.

Although the attached volute of the present compressor does not perform well, the gain in pressure recovery from the diffuser shown in Fig. 1 is 35.9 percent between the original and the case with $\alpha=\beta=1$. Similarly, the loss reduction is reduced by 24.3 percent. The resultant shape will be different from the current optimized shape if the coefficients are set as $\alpha=1$ and $\beta=0$. The advantage of selecting $\alpha=1$ and $\beta=0$ is to achieve a higher pressure rise. However, the flow separation shown in Fig. 10 may become pronounced due to lack of control in loss used in the optimization calculation and eventually the stall occurs much earlier than under the original conditions.

R. Dénos
T. Arts
G. Paniagua
Von Karman Institute for Fluid Dynamics,
Rhode Saint Genèse, Belgium

V. Michelassi
Department of Mechanical
and Industrial Engineering,
University of Rome,
Tre, Italy

F. Martelli
Energetics Department "Sergio Stecco,"
University of Florence,
Florence, Italy

Investigation of the Unsteady Rotor Aerodynamics in a Transonic Turbine Stage

The paper focuses on the unsteady pressure field measured around the rotor midspan profile of the VKI Brite transonic turbine stage. The understanding of the complex unsteady flow field is supported by a quasi-three-dimensional unsteady Navier–Stokes computation using a $k-\omega$ turbulence model and a modified version of the Abu-Ghannam and Shaw correlation for the onset of transition. The agreement between computational and experimental results is satisfactory. They both reveal the dominance of the vane shock in the interaction. For this reason, it is difficult to identify the influence of vane-wake ingestion in the rotor passage from the experimental data. However, the computations allow us to draw some useful conclusions in this respect. The effect of the variation of the rotational speed, the stator–rotor spacing, and the stator trailing edge coolant flow ejection is investigated and the unsteady blade force pattern is analyzed.
[DOI: 10.1115/1.1314607]

Introduction

For low-pressure turbine applications, the blade interference has been intensively studied and considerable advances have already been achieved. The rotor–stator interaction is dominated by the vane wakes, which have a positive effect on the rotor blades boundary layer status (becalmed region following the turbulent spots). These investigations resulted in decreasing the losses while decreasing the number of blades of the rotor [1,2].

High-pressure turbines have received less attention. Very often, a transonic flow exits the vane and the interaction is a combination between direct and reflected shocks and wake, the first being predominant. The large pressure gradients associated with the shock wave affect not only the aerodynamics of the flow in the rotor passage, but also the heat transfer [3]. Blades are submitted to unsteady lift that causes vibrations while unsteady heat transfer regime increases thermal fatigue. The understanding of such complex interactions is necessary to improve the blade design and the flow field prediction as well as the evaluation of mechanical and thermal fatigue.

The experimental insight of the flow unsteadiness in stator or rotor passages became possible thanks to the miniaturization of the transducers, their extended frequency range as well as the use of wireless data transmission systems in the case of measurements on rotor blades [4]. In parallel with the success of experimental investigations, several CFD tools have been developed and used for the simulation of the compressor and turbine stator–rotor interaction [5–8]. The unsteady flow field can be resolved by the time-inclining method [9] or by enhancement of the dual time-step method [10].

A sweeping phenomenon of the vane trailing edge shock from the rotor blade crown down to the leading edge was first observed in experiments by Doorly and Oldfield [11] and Ashworth et al. [12] and confirmed by calculations of Giles [13] and Saxer and Giles [14]. Giles [13] also reported complex shock patterns like periodic stator trailing edge shock reflections on the rotor blade and periodic emergence of shocks between stator trailing edge and rotor leading edge. The measurements of the unsteady pressure field and heat transfer coefficients in highly loaded transonic stages were carried out by several researchers [7,15–17], but there are still many features to be understood. The combination of measurements, limited to end-walls in rotor blades, with unsteady computations, which provide information on the entire flow field, proved to be a very powerful tool for this purpose [7,16].

In the frame of a EEC-sponsored collaborative effort, the von Karman Institute proceeded to an extensive test program to improve the understanding of the unsteady aerothermodynamics of a transonic turbine stage, including the effects of the rotational speed, the stator trailing edge coolant ejection, and the rotor–stator spacing.

Michelassi et al. [18] compared the measured and computed steady and unsteady heat transfer around the rotor blade at midspan. Dénos et al. [19] reported the steady and unsteady rotor pressure measurements. The present paper focuses on the interpretation of the unsteady aerodynamics around the rotor midsection using both experimental results and CFD predictions.

Turbine Test Rig

The turbine stage was tested in the VKI short duration compression tube facility CT3 (Fig. 1). This facility is capable to simulate Reynolds and Mach numbers, gas/wall and gas/coolant temperature ratios of modern aero-engine HP turbines.

The rotor midsection is instrumented with 24 surface mounted miniature piezo-resistive pressure transducers (14 on the suction side and 10 on the pressure side) from Kulite, distributed over three rotor blades. The implementation of the pressure chips of 1.2×1.2 mm^2 was realized at the University of Oxford, UK. The Fast Fourier Transform of a signal delivered by one of these sensors, located in the vicinity of the rotor leading edge, reveals at least 11 harmonics of the fundamental blade passing frequency (4.6 kHz). The relative total pressure is measured by means of a standard Kulite pressure transducer placed with a small retreat in a 2 mm cylinder inserted in the rotor blade leading edge.

The data are transmitted via a 16-channel opto-electronic transmission system with a bandwidth of 80 kHz [20,21]. The signals of the transducers were corrected during the run-up of the rotor as well as during the blowdown for the centrifugal force with an in-house method and for the temperature according to a procedure developed by Ainsworth [22]. The overall uncertainty on the rotor surface pressure measurements is evaluated to be of the order of 1 percent of the relative inlet total pressure.

Contributed by the International Gas Turbine Institute and presented at the 45th International Gas Turbine and Aeroengine Congress and Exhibition, Munich, Germany, May 8–11, 2000. Manuscript received by the International Gas Turbine Institute February 2000. Paper No. 2000-GT-435. Review Chair: D. Ballal.

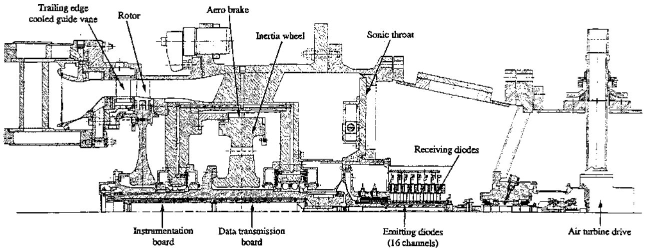

Fig. 1 Turbine test section

Full details on the turbine test rig, the turbine stage, and the instrumentation were reported by Dénos [4].

Quasi-Three-Dimensional Unsteady Navier–Stokes Solver

The implicit time marching code MDFLOS3D is designed to solve the unsteady Favré-averaged three-dimensional Navier–Stokes equations expressed in terms of conservative variables. The solver is used in a quasi-three-dimensional manner by assuming a variable stream-tube height. The equations are discretized on centered finite volumes in curvilinear coordinates, and solved by a scalar approximate factorization method. The steady-state solution is achieved by a local time step strategy, whereas time-accurate calculations are carried out by a second-order-accurate double time step approach [23] introduced in the factored solver, retaining the implicit nature of the algorithm [24].

Zero equation turbulence models, which, although often implemented, should not be used in stator–rotor interaction because of the lack of any history effect, are replaced here by a $k-\omega$ two-equation turbulence model. The excessive turbulence production in stagnation points due to normal strains, common to all turbulence models based on the Boussinesq assumption, is limited in this version of the $k-\omega$ model by introducing the realizability constraint proposed by Durbin [25]. Details can be found in Michelassi et al. [18].

The two-dimensional nature of the flow allows a transition model based on integral parameters to be used. The selected model detects transition by using the Abu-Ghannam and Shaw correlation [26], while the transition length is modeled according to Michelassi et al. [18].

The stator and rotor blade profiles are those at midspan with a variable rotor height modeled with a variable stream-tube height. Both the stator and rotor grids are of the I-type (Fig. 2) with not-point-to-point periodic boundaries. This choice ensures a nearly orthogonal grid in the wake with a reduced skewness. On the periodic boundaries and at the stator–rotor interface, the grids of adjacent blades are overlapped to ensure a C-1 continuity of the solution without altering the structure of the solver. The I-type grids for viscous calculations have 200×104 and 258×153 points for the stator and the rotor, respectively. While the real turbine stage consists in 43 vanes and 64 blades, the numerical domain is composed of 2 vanes and 3 blades.

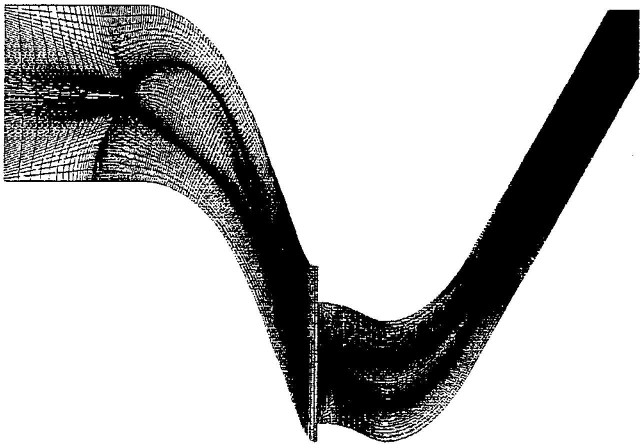

Fig. 2 Stator and rotor grids

The vane-to-blade ratios are 1.488 and 1.5, respectively. In the computations, the rotor rows was rescaled by a factor 0.9923 whereas the stator row, which controls the mass flow rate, was left unaltered.

The boundary conditions are set by specifying the stage inlet total pressure, temperature, flow angle, turbulent kinetic energy (1.6 percent) and length scale (1 percent of the stator pitch) and the stage exit static pressure. A no-slip adiabatic wall condition is set on the stator blade, whereas heat transfer is allowed on the rotor blade by imposing the ambient temperature, as is the case in the tests.

Turbine Stage

The main geometric characteristics of the turbine stage at midspan are summarized in Table 1. The vane is internally cooled ($\dot{m}_c = 3$ percent of overall mass flow) with ejection at the trailing edge on the pressure side. The rotor was designed with a meridional flow divergence of 10 percent to reduce the axial outlet velocity and to minimize the secondary losses. The inlet and outlet conditions and the main similarity parameters are reported in Table 2.

The experimental traces, originally sampled at 300 kHz (65 points per passage at 6500 rpm) will be presented as phase-locked averages of 129 vane passages (three revolutions). Due to the absence of a brake, the rotor accelerates during the test; however, this acceleration is limited by the presence of an inertia wheel (Fig. 1) to about 800 rpm/s at 6500 rpm. The time corresponding to three revolutions is about 0.03 s and the variation in the rotational speed, the rotor relative inlet angle and pressure are limited to 24 rpm, 0.5 deg, and 3 mbar, respectively. The rpm variation during the 0.03 s is taken into account in the phase-locked average.

The phase-locked averaging routine does not use any interpolation of the signal and provides high-quality statistical data composed of:

Table 1 Typical stage geometric characteristics

	Stator	Rotor
Number of blades	43	64
Chord	72.3 mm	48.4 mm
Axial chord	43.2 mm	39.6 mm
Hub radius	344.5 mm	339.4 mm (at exit)
Tip radius	395.2 mm	395.2 mm

Table 2 Stage flow conditions at design point

T_{01}	440 K	M_2	1.03
P_{01}	1.620 bar	P_{02r}	0.927 bar
P_{01}/P_{s3}	3.05	M_{2r}	0.45
$Re_{2c,s}$	10^6	M_{3r}	0.89
T_{01}/Twall		1.5	
T_{01}/Tcoolant		1.5	
Overall mass flow		10.8 kg/s	
Rotational speed		6500 RPM	
Vane passing frequency		4.6 kHz	
Stator-rotor spacing		0.35 $c_{s,ax}$	

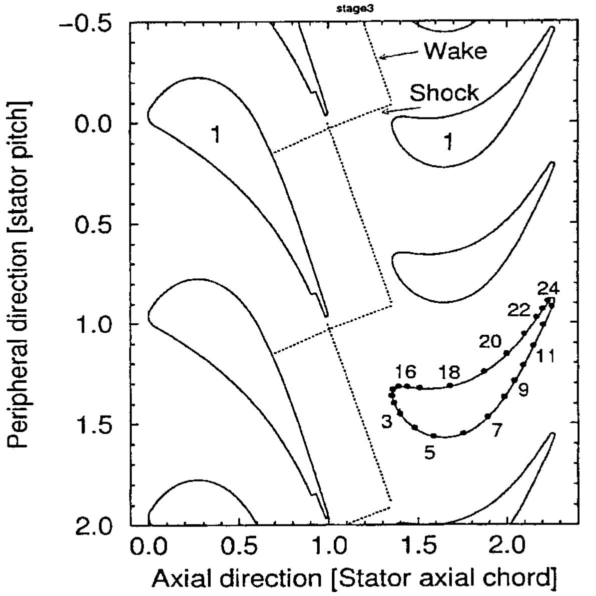

Fig. 3 Rotor/stator position at phase 0; schematic of the vane shock and wake system for a stator–rotor spacing of 0.35 $c_{s,ax}$

- the mean period across a pitch (phase-locked average),
- the minimum and maximum of the mean period,
- the rms for each point of the phase-locked average,
- a linear regression correlation coefficient between the raw and the phase-locked averaged signal.

The phase-locked averages and the results of the computations will be presented as a function of the vane reduced pitch, referred to as phase φ in the following. $\varphi=0$ when the stacking axis of the rotor blade is aligned with the one of the vane; $\varphi=1$ when the blade has completed one stator pitch traverse (Fig. 3). All signals were corrected for the phase delays induced by the instrumentation and transmission boards.

Unsteady Inlet Relative Total Pressure

The phase-locked averaged signals of the rotor relative inlet total pressure variation $\Delta P_{02r}/P_{01}$ with an axial stator–rotor distance of 0.35 $c_{s,ax}$, for 6500 rpm, with and without stator trailing edge coolant ejection, are shown in Fig. 4 together with the rms distribution. The amplitude of the total pressure fluctuations at 6500 rpm amounts to 6.5 percent of the upstream total pressure P_{01} or 11.2 percent of the design relative inlet total pressure P_{02r}.

Influence of the Shock. A sharp pressure rise associated with a peak in rms can be seen at $\varphi=0.97$. This large fluctuation can be associated with the traverse of the probe across the vane trailing edge shock. To aid interpretation, Fig. 3 shows a schematic of the vane shock and wake derived from a Schlieren picture [27] taken in a linear cascade and from vane outlet angle measurements in an annular cascade [28], both behind the vane alone and in steady flow conditions. In this simple representation, the position of the shock interference with the plane corresponding to the probe nose can be located at $\varphi=0.91$. Note that the peak in the rms does not mean that high static pressure fluctuations occur within the shock, but stems from the slight changes in the shock position, which cause an artificial fluctuation in the phase-locked averaging process.

The computations reveal that the shock is not steady but oscillates slightly around the axial direction. This can be clearly observed in Fig. 10, which reports the shock function ($S=\vec{U}/a\cdot\vec{\nabla}(p)/|\vec{\nabla}(p)|$) in the stage. This function highlights the zone of high Mach number combined with steep pressure gradients. The compression and expansion waves are represented with red and blue lines, respectively. Two vane trailing edge shock waves *B* can be identified attached to vane 1 and 2. While the first has an incidence similar to the steady representation, the second is inclined below the axial direction. This last case almost coincides with the shock reaching the rotor leading edge. This inclination of the shock is probably responsible for the small difference between the measurement ($\varphi=0.97$) and the steady case ($\varphi=0.91$). While the shocks *B* remain attached to the vane trailing edge, the origin of the expansion waves *D* moves upstream and downstream on the vane rear suction side depending on the relative position between the stator trailing edge and the rotor leading edge. As a result, the static pressure field of the vane is also affected. This effect is, however, limited to the suction part located downstream of the throat, as shown in Fig. 5, that reports the vane isentropic Mach number fluctuations distribution. This phenomenon was observed in both experiments [16] and computations [14].

Influence of the Wake. The bump in the rms distribution just to the right of the peak, with a local maximum at $\varphi=1.15$, probably points to the impact of the stator wake (Fig. 4). This interpretation is supported by the difference in the rms distribution between the pressure traces with and without trailing edge coolant flow ejection. The impact of the wake on the total pressure probe inserted at leading edge predicted by the simple steady assumption occurs at $\varphi=0.91$ instead of $\varphi=1.15$ ($\Delta\varphi=0.24$) found in the measurements.

In low-speed turbines, the wake slip effect results in a lower incidence angle and causes the wake to reach the leading edge

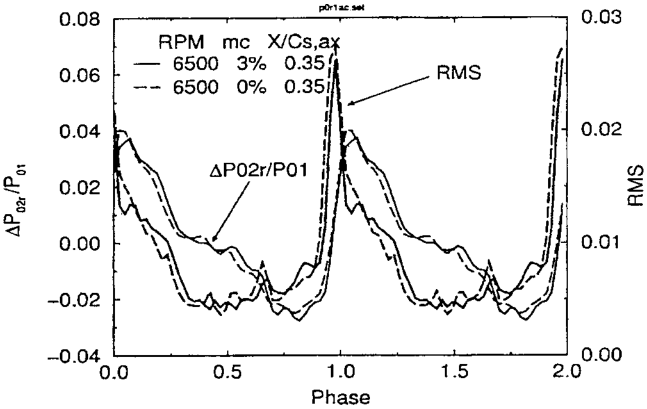

Fig. 4 Phase-locked average and rms of the measured rotor relative inlet total pressure: influence of trailing edge coolant ejection

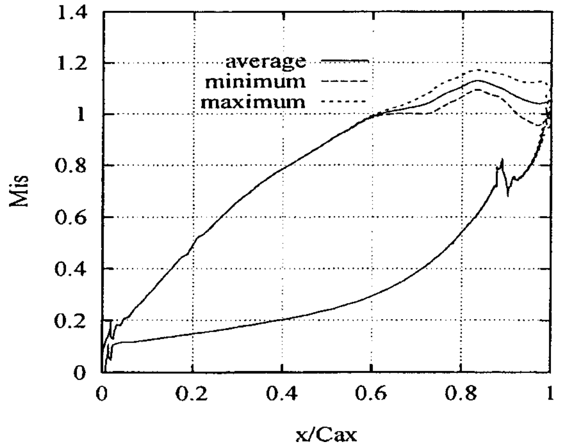

Fig. 5 Computed isentropic Mach number distribution on the vane (6500 rpm, 0.35 $c_{s,ax}$, $m_c=3$ percent)

sooner than expected. An opposite effect is observed here. In contrast with low-speed turbines, transonic turbines exhibit large pitchwise static pressure gradients downstream of the vane. If the relative flow angle inside the wake is computed in a zone of low static pressure, it can be locally higher than the mean flow angle. The wake path and the pressure discontinuity propagation line being different, the over or underdeflection of the wake would depend on how often the wake traveled in a low or high static pressure zone. As a result, it is very difficult to anticipate if the wake will hit the rotor leading edge sooner or later than expected. The situation is further complicated here by the fact that the wake and the shock probably intersect in the vicinity of the measurement plane (Fig. 3). In any case, the variation of angle caused by a total pressure drop of 8 percent with a constant pitchwise static pressure would not result in a phase difference larger than 0.03 in the present case.

The distortion of the path can be better observed in the computations. Figure 15 shows the instantaneous velocity field minus the average one. The wake can be identified in the regions where the velocity vectors are oriented upstream. The design mean inlet relative angle is approximately 45 deg. At $\varphi=0.9$, the wake, visible in the lower left corner in the region where the velocity vectors are oriented upstream, has a negative incidence. In the next step ($\varphi=0.10$) the wake incidence is close to the design incidence. This step almost coincides with the phase at which the wake influence on the total pressure probe is suspected. Proceeding further to step $\varphi=0.30$, the wake, still visible thanks to the instantaneous velocity defect, has a positive incidence in contrast to the negative incidence at $\varphi=0.9$. Figure 6 shows the computed instantaneous rotor inlet relative and absolute mass-averaged flow angles.

The computations predict a stator average exit absolute flow angle of 72.6 deg that compares well with the angle measured downstream of the isolated stator: 72.3 deg. While the computed amplitude of the absolute angle fluctuation is around 5 deg, the one of the relative angle exceeds 10 deg.

The relative inlet total pressure fluctuations are dictated by the static pressure field. The pitchwise variations of the predicted static pressure (shock) and the measured absolute total pressure (wake) downstream of the vane alone are of the order of 30 and 10 percent of their mean values, respectively. While the first variation spreads on the entire pitch, the second is limited to the wake width. If one derives the relative rotor inlet total pressure from these absolute conditions and the peripheral speed (velocity triangle), the print of the static pressure variation dominates due to the low relative Mach number (0.45) and the associated pressure ratio P_{s2}/P_{02r} (0.87). The print of the wake is one order of magnitude below. The pitchwise variations of absolute vane exit angle and total temperature make only minor contributions [4].

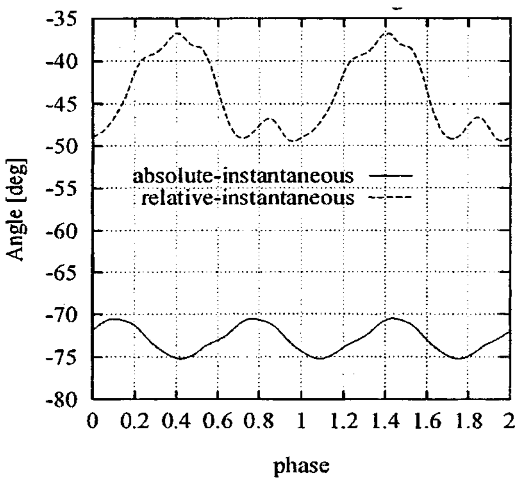

Fig. 6 Computed rotor inlet flow angle

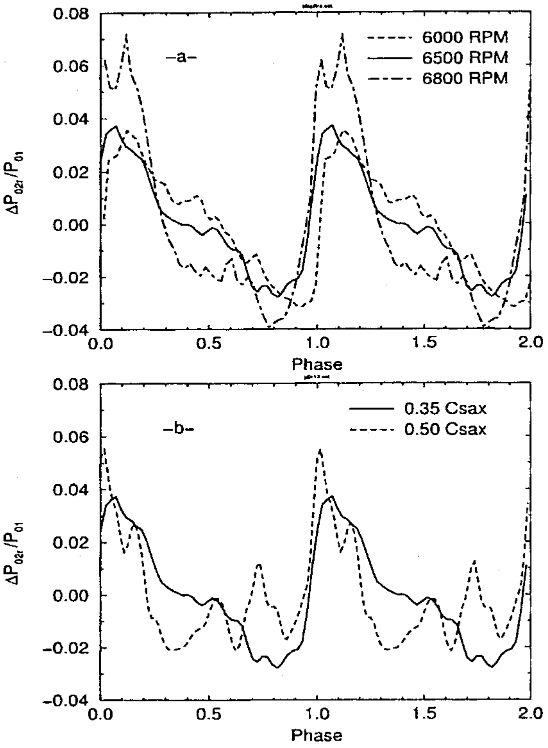

Fig. 7 Influence of: (*a*) rotational speed ($0.35\,c_{s,ax}$, $\dot{m}_c=3$ percent), and (*b*) stator–rotor spacing (6500 rpm, $m_c=3$ percent) on measured relative inlet total pressure fluctuations

Influence of the Tested Parameters. The coolant flow ejection has no significant influence on the relative inlet total pressure distribution (Fig. 4) in spite of significant differences in the trailing edge shock patterns revealed in the Schlieren photographs [27]. As far as the rms distribution is concerned, the only, but weak, effect of the trailing edge coolant ejection occurs in the region of the wake interference.

The influence of the rotational speed is shown in Fig. 7(*a*). The amplitude of the fluctuation clearly increases with the rotational speed. This can be explained by two effects:

- for fixed stator outlet conditions, the increase of the rotational speed causes a decrease in the relative inlet velocity, which reinforces the contribution of the static pressure variation (an increase of rotational speed from 6000 to 6800 rpm causes a change of 3.6 percent in P_{02r});
- the measurements of the intermediate static pressure at tip across one pitch revealed that the amplitude of its variation increases by 10 percent when the rotational speed rises from 6000 to 6800 rpm.

The second contribution is clearly dominant here.

The influence of spacing is shown in Fig. 7(*b*). The patterns are quite different with the emergence of an additional peak of not-negligible amplitude at $\varphi=0.75$. The sharp pressure gradient associated with the shock appears at the same position for both spacings suggesting that between $0.35\,c_{s,ax}$ and $0.50\,c_{s,ax}$ the stator trailing edge shock propagates nearly in the axial direction.

Unsteady Rotor Midspan Pressure

The time-averaged pressure distributions around the rotor blade from experiments and computations are compared in Fig. 8. The effect of incidence due to the change of the rotational speed ap-

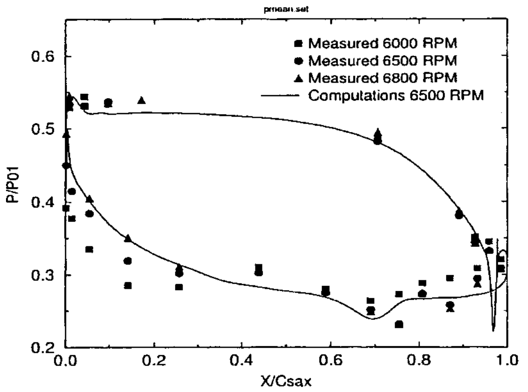

Fig. 8 Time-averaged values of measured and computed rotor blade pressure ($0.35\ c_{s,ax}$, $\dot{m}_c=3$ percent)

pears clearly in the experiments on the front suction side. The overall agreement between experiments and computations is reasonable except in the leading edge region on the suction side. A similar feature was observed when comparing the time-averaged experiments with a steady three-dimensional Navier–Stokes stage analysis. Reasons for this discrepancy are proposed by Dénos et al. [19].

The unsteady measured and computed pressure traces at each of the 24 measurement locations (6500 rpm, $0.35\ c_{s,ax}$) are presented as $(P-P_{\text{time-average}})/P_{01}$ over two pitches in Figs. 9(*a*, *b*, *c*). The mean of each trace is zero but a shift was introduced between two successive traces for clarity. A fairly good overall agreement is obtained between the measurements and the computations.

The static pressure fluctuations measured in gage 14 are very close to the measured relative inlet total pressure fluctuations, which suggests the vicinity of the stagnation point.

Influence of the Shock. The largest fluctuations are observed in the leading edge region (Fig. 9(*b*)) and the steep pressure increase can be associated with the stator trailing edge shock hitting the crown of the blade (gages 5 and 4) and sweeping the front suction side (gages 3, 2, 1) toward the leading edge (gage 14).

In Fig. 10, the shock *B*, originating from vane 1 and impinging on rotor blade 3, is represented at $\varphi=0.83$, when it passes over location 3. This coincides in Fig. 9(*b*) with a steep pressure rise. Similarly, the expansion wave *D* impinging on rotor blade 2 (presented at $\varphi=0.17$ in Fig. 10) causes the pressure decrease in location 4 at $\varphi=0.17$ in Fig. 9(*b*).

All the traces in the leading edge region exhibit a very similar pattern. First a large fluctuation per period beginning with a steep pressure rise is evident, immediately followed by a short double peak pattern. Then, after a strong decrease, a plateau is observed. While the double peak feature is present in all the measurements of Fig. 9(*b*) it can only be clearly detected in traces 1 and 2 of the computations, and marginally in trace 14. This can be attributed to a ‘‘low-pass filtering’’ effect, which is observed for certain combinations of physical time step and grid spacing in the tangential direction at the stator–rotor interface plane [24]. The same phenomenon may be responsible for the smoother pressure increase associated with the vane trailing edge shock.

The double peak pattern was observed by Dietz and Ainsworth [29]; in their case the first peak appeared within the steep pressure rise. In the experiment of Doorly and Oldfield [11], with rotating bars in front of a cascade, the Schlieren picture revealed that the instantaneous steep adverse pressure gradient, located in a zone of large time-averaged favorable pressure gradient was initiating a recirculation bubble visible only after the shock had cleared out the leading edge region. Here, the double peak feature is most probably due to a local shock or pressure discontinuity reflection. Note that in the absolute frame of reference, the flow is supersonic in this region while it is subsonic with respect to the blade wall. For this reason, it is difficult to interpret the reflection as is usually done for supersonic flow with fixed walls.

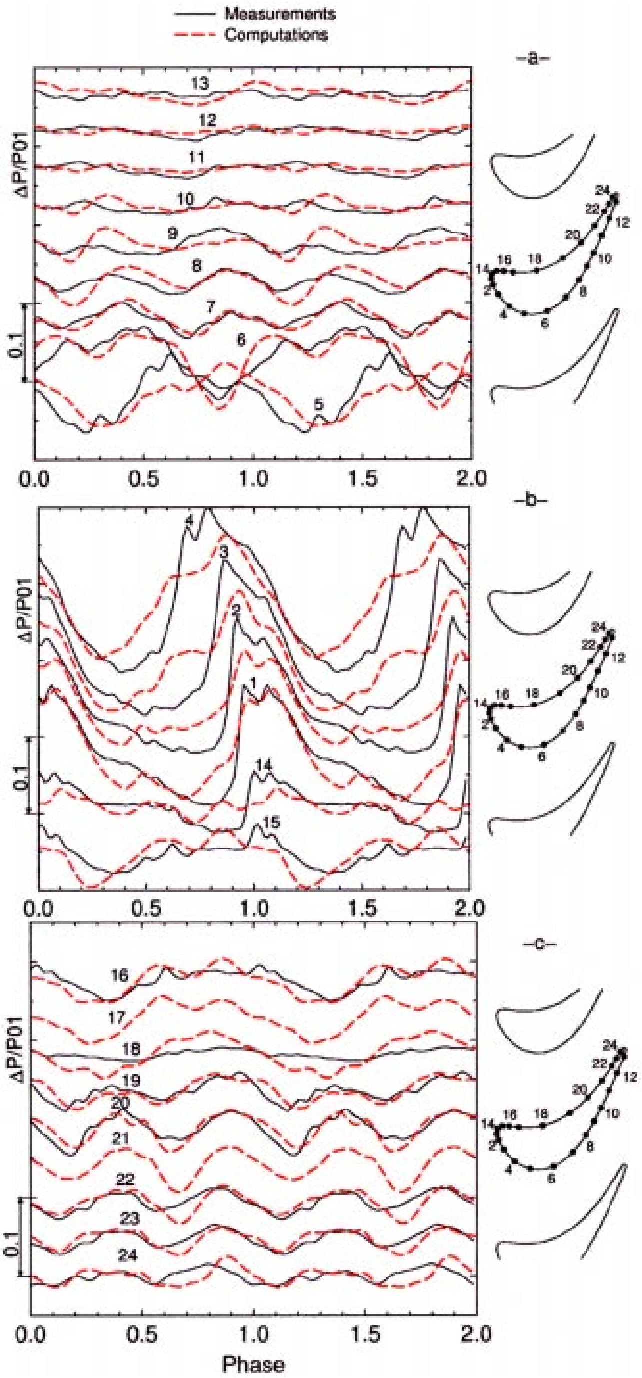

Fig. 9 Pressure fluctuations from measurements and computations (6500 rpm, $0.35\ c_{s,ax}$, $\dot{m}_c=3$ percent): (*a*) gages 5–13, (*b*) gages 15–4, (*c*) gages 24–16

Figure 9(*b*) also shows that the amplitude of the fluctuations is increasing rapidly from 8 percent of P_{01} at location 14 to 24 percent at location 4 (or 40 percent of the mean P_{02r}), which exceeds by far the predicted steady pitchwise variation of static pressure behind the stator alone (15 percent of P_{01}). A very similar feature was observed in the measurement by Rao et al. [16] for a similar stage configuration. Conversely, the calculations by Giles [13] showed an opposite trend.

Figure 11 illustrates the vane trailing edge shock impinging on

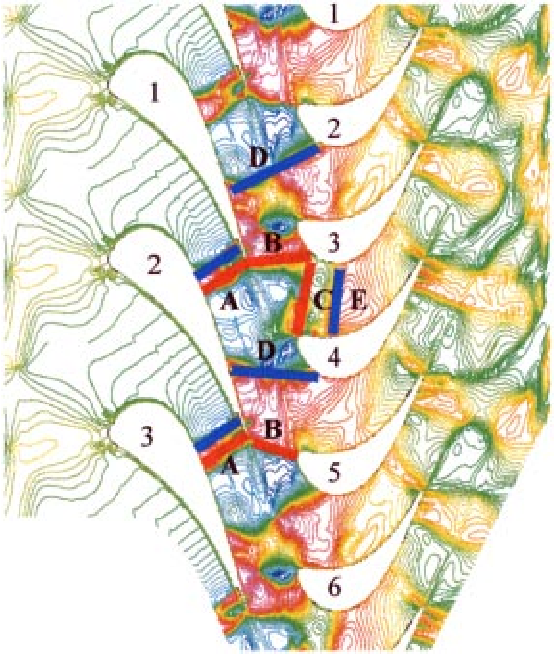

Fig. 10 Computed shock function in the stage with schematic of expansion waves (blue lines) and compression waves (red lines); the phases of rotor blades 2, 3, 4, and 5 are 0.17, 0.83, 0.49, and 0.17, respectively

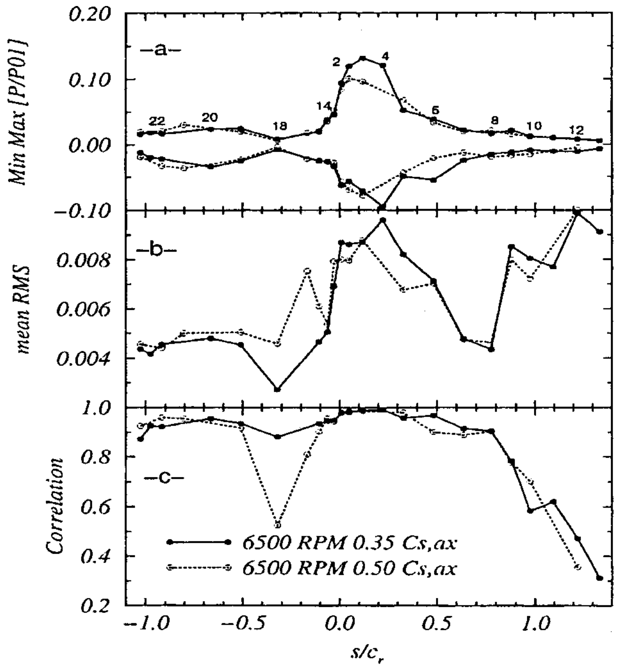

Fig. 12 (*a*) Minimum, maximum of mean period; (*b*) time-averaged rms; and (*c*) correlation coefficient of the experimental pressure traces for spacings 0.35 $c_{s,ax}$ and 0.50 $c_{s,ax}$ (6500 rpm, $\dot{m}_c=3$ percent)

the rotor suction side at three successive time steps. At time step *A*, the shock impinges the crown of the rotor blade in a region of low static pressure, i.e., supersonic flow in the absolute frame. Note that the part of the channel delimited by the dotted line (shortest distance), the vane and rotor walls and the shock line constitutes a convergent–divergent channel. At time step *B*, the divergent part is reduced and the local static pressure is higher than at *A*, which decreases the strength of the shock. It is decreased further at time step *C*. Note that the shortest distance between the vane trailing edge and the rotor leading edge also decreases from time step *A* to *C*.

The nearly axial evolution of the stator suction side shock also suggests that point 4 or 5, located on the rotor crown, are the last ones able to experience a direct effect of the shock. Note the phase opposition between traces 5 and 6, shown by both computations and experiments.

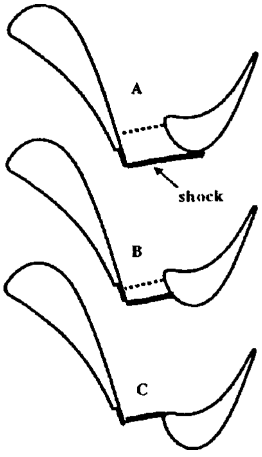

Fig. 11 Schematic showing the vane trailing edge shock as it sweeps the blade front suction side

The influence of the shock traveling inside the rotor passage can be tracked by the observation of the static pressure field in Fig. 15. The position of the stator trailing edge shock at $\varphi=0.50$ and $\varphi=0.70$ is indicated with a white bar on the left side. When sweeping from the rotor pressure side toward the suction side of the upper blade, the shock does interact with the wake, increasing locally the static pressure. This phenomenon is more evident at $\varphi=0.70$, when the static pressure grows rapidly in the entrance of the rotor passage. The local static pressure maximum follows the shock and reaches the suction side of the next rotor blade, but never manages to travel downstream of the crown.

On the front pressure side (gages 15 and 16, Figs. 9(*b*, *c*)), the overall pressure modulation is smooth except for the appearance of two small pressure peaks attributed to weak shock events. The observation of two distinct spikes at the same phase in the rms traces reinforces this conjecture (Fig. 13). While the first peak can be associated with the stator trailing edge shock, the second is probably due to the impact of a reflected shock. In Fig. 10, the shock *B*, originating from vane 1, produces a weak reflection *C* across the rotor passage, followed by an expansion wave *E* further downstream. This reflection affects location 14 of the rotor blade 4 at $\varphi\sim0.5$. A small pressure increase is observed in the computations together with the double peak in the experiments (Fig. 9(*b*). Location 14 of rotor blade 5 will be affected later by the direct impact of shock *B* from vane 2 at $\varphi\sim0.17$. This effect can also be observed in Fig. 9(*b*). Note that the shock reflection *C* as well as the expansion wave *E* appear in the rotor passage only between blades 3 and 4, i.e., that they emerge periodically. A similar feature was observed in the computation of Giles [13].

The amplitude of the pressure fluctuations becomes very small on the rear pressure and suction sides (min–max envelope in Fig. 12(*a*)). On both sides, gages 22–24 and 7–8 exhibit a double fluctuation over one period with similar amplitude and phase (Figs. 9(*a*, *c*). This suggests that a unique phenomenon simultaneously affects the entire passage in this region. A careful examination of the traces 19–24 reveals that while the first pressure wave occurs simultaneously for all traces, the phase of the second pressure wave is slightly shifted from one trace to the successive one, showing a perturbation traveling upstream. This feature is also mentioned by Giles [13].

On the rear suction side, the amplitude of the fluctuations at points 7 to 13 is much smaller than in the leading edge region (Fig. 9(*a*)). The time-averaged rms and the correlation of the raw signal with the phase-locked averaged signal (Fig. 12(*b*, *c*)) bring more information on the nature of the fluctuations. This information cannot be extracted from the computations since the solution is converged when a periodic flow field is obtained.

In these locations, the time-averaged rms is of the same order as at the leading edge but the correlation coefficient decreases dramatically down to 0.3 at the trailing edge. This means that, while the amplitude of the periodic component decreases, random fluctuations of increasing importance appear. Unlike at the leading edge, most of the fluctuations in the signal are not correlated with the shock passing events. Notice that this part of the rotor blade is hidden from a direct influence of the shock. The FFT analysis did not reveal any other frequency than the blade passing frequency meaning that the fluctuations are mostly random. This region corresponds to a small deceleration in the Mach number distribution that could cause a thickening of the boundary layer, associated with turbulent fluctuations of increasing importance.

On the rear pressure side, the rms stays at a constant low level after point 18 but with a high level of correlation. This means that most of the fluctuations are correlated with the blade passing frequency. This part of the pressure side seems accessible to the stator trailing edge shock and can probably be reached by reflected shocks.

Influence of the Wake. Two wake effects can be distinguished: the wake effect traveling at acoustic speed ($v+a$ and $v-a$) and the wake distortion effect traveling at the local convective speed. In some cases, pressure perturbations traveling close to the convective speed were observed [30,31]; in other experiments [29] pressure fluctuations traveling at acoustic speed were identified.

An attempt was made to track the propagation of the perturbations associated with a wake along the blade. This was performed assuming the injection of a perturbation at point 14 at $\varphi=1.15$, according to the observations in the rms traces of P_{02r}. Then, three propagation lines were computed: one with the local convective speed v derived from the Mach number distribution determined experimentally, the second with $v+a$, the third with $v-a$, plotted as dots on top of the rms traces in Fig. 13.

The $v-a$ trace stops at gage 4 because the local convective speed becomes almost equal to the speed of sound resulting in a zero propagation velocity. No clear correlation between the traces and the peaks in rms appear. The same dots plotted on the static pressure signals do not reveal any trend either. As mentioned earlier, the wake influence is at least one order of magnitude lower than the shock influence due to the transonic regime of the nozzle.

The distortion of the wake when approaching the leading edge region was discussed previously. At phase $\varphi=0.5$ (Fig. 15) the wake is ingested into the rotor passage. The velocity defect reaches the suction side of the next rotor blade. This migration from pressure side to suction side inside the passage was observed in both experiments [32] and computations [30] for low-speed turbines. The situation is further amplified at $\varphi=0.70$ where the wake has proceeded farther downstream. The large convection velocity difference between the rotor suction and pressure sides is responsible for the distortion of the wake. Despite the distortion, the wake is visible for quite a long time after the collision with the rotor leading edge ($\varphi=0.9$, central part of the channel).

Influence of the Tested Parameters. Most of the qualitative features described for the spacing $0.35\,c_{s,ax}$ are also encountered for the spacing $0.50\,c_{s,ax}$. The amplitude of the fluctuations is noticeably smaller in the leading edge region (gages 2, 3, and 4 in Fig. 12(*a*)) showing that the shock intensity has probably decreased strongly with increasing axial distance. Similar observations are reported by Venable et al. [33]. The absence of coolant ejection causes a small decrease in the amplitude of the fluctuations, mainly in the front suction side. When increasing the rotational speed, the amplitude of the fluctuations tends to increase slightly, similarly to the pitchwise static pressure distribution in the interblade region. The shapes of the rms curves and correlation curves are quantitatively conserved. Among the three parameters, the spacing is clearly the most influent.

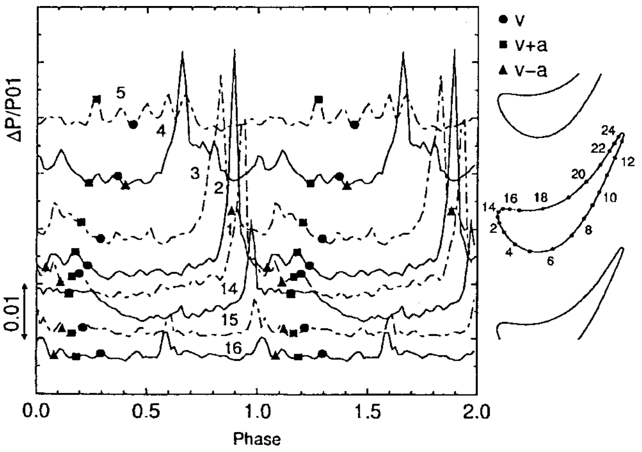

Fig. 13 The rms traces (6500 rpm, 0.35 $c_{s,ax}$, $\dot{m}_c=3$ percent) in the blade nose region; propagation directions at v, $v+a$, $v-a$ for a perturbation injected at point 14 at $\varphi=0.15$

Unsteady Blade Force

The unsteady blade force modulus and angle are shown in Fig. 14. This was obtained by integrating the pressure around the blade profile. The computations reproduce the essential features of the flow except the up-down shape of the force module between $\varphi=1.2–1.5$. Some disagreements were observed in the same phase range for the pressure traces at locations 2, 3, and 4 (Fig. 9(*b*)). At 6500 rpm, the mean blade force is directed from the pressure side toward the suction side and has an angle of 47 deg with respect to the axial direction; the fluctuation of the modulus is of the order of 11 percent of its mean value while the direction

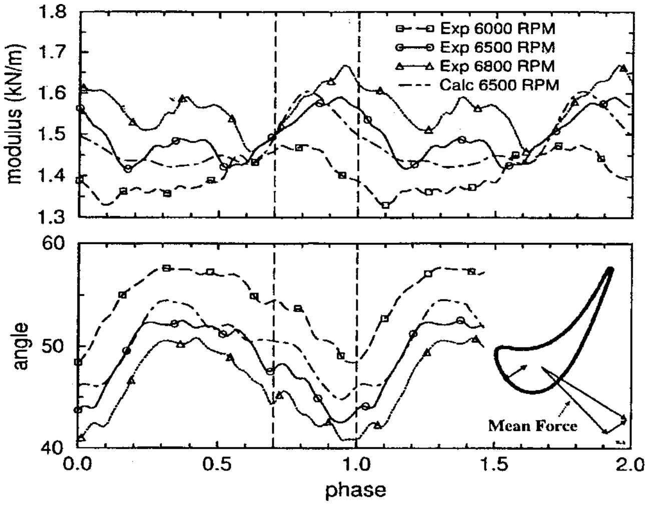

Fig. 14 Unsteady blade force modulus and angle (0.35 $c_{s,ax}$, $\dot{m}_c=3$ percent) from experiments at 6000, 6500, and 6800 rpm and computations at 6500 rpm

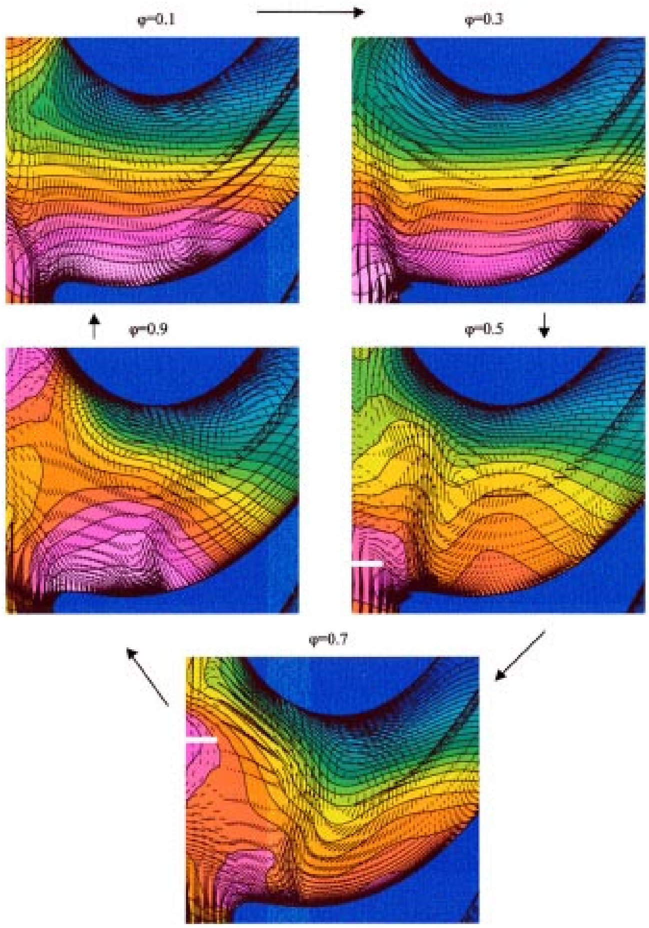

Fig. 15 Unsteady velocity and static pressure field in the rotor passage

of the force changes by 10 deg. The most striking feature is the increase of the modulus and the decrease of the angle in between the vertical dotted lines.

This region corresponds with the one in Fig. 9(*b*) where the sharp pressure rise associated with the vane trailing edge shock occurs. This higher pressure on the front suction side causes a force increase in this region, sketched by a small arrow on the left of the lower graph of Fig. 14. Combining this last with the mean force, the modulus of the unsteady force is increased and the angle inclined toward a more axial direction.

When varying the rotational speed, the blade force direction logically follows the same trend as the flow incidence (incidence increases at 6000 rpm and decreases at 6800 rpm) due to the change of the peripheral speed and the fact that the rotor relative exit angle is not very sensitive to the inlet angle. Note that the local torque computed using the mean blade force and the local radius times the blade height gives the design power of the turbine within 5 percent.

This unsteady blade force will cause an unsteady torsion of the blade. It has also repercussions on both the torque and the axial thrust. The fluctuations of the axial force and the tangential force on one blade at 6500 rpm, $0.35\,c_{s,ax}$, 3 percent coolant ejection are 29 percent and 11 percent of their mean value, respectively. If these variations occurred in phase for the 64 blades (which is not the case), there is no doubt that strong vibrations would be felt on the shaft.

Conclusions

The comparison between the measurements and the calculations is satisfactory. The computations reproduce all the main features that exist in the measurements.

The rotor relative inlet total pressure is submitted to fluctuations with an amplitude of 10 percent of its mean value. It is clear that the trailing edge shock imposes a strong static pressure discontinuity, which is largely felt in the relative total pressure. The wake has a less strong effect but the computations show how it interacts with the shock and how it is distorted.

The unsteady rotor surface pressure field is also dominated by the strong gradient imposed by the vane trailing edge shock on the front suction side. The shock-sweeping phenomenon from the crown toward the leading edge was clearly identified, associated with fluctuations up to 40 percent of the design relative total pressure. The decrease of the fluctuation amplitude from the crown to the leading edge is explained by the decreasing strength of the shock caused by the increasing local static pressure. The periodic emergence of a reflected shock was put into evidence. The amplitude of the fluctuations decreases strongly on both the rear suction side and pressure side, where the shock has no direct impact. On the first, random fluctuations of increasing amplitude appear while on the second, the fluctuations remain strongly correlated with the blade passing events. The computations reveal that the path of the wake is highly distorted, not only due to a local velocity deficit in the main stream but also due to its interaction with the shock.

While the unsteady pattern is little sensitive to the tested range of coolant ejection (0 and 3 percent) and rotational speeds (6000, 6500, and 6800 rpm), a noticeable decrease of the amplitude of the fluctuations is observed in the leading edge region when increasing the axial spacing $(0.35\,c_{s,ax}, 0.50\,c_{s,ax})$.

The unsteady blade force is dominated by the shock sweeping phenomena. At design conditions, the fluctuations of the axial and tangential forces amount to 29 and 11 percent of their mean value, respectively.

Acknowledgments

This research was carried out under contract for the European Commission as part of the BRITE EURAM AER 2-92-044 turbine project ‘‘Investigation of the Aerodynamics and Cooling of Advanced Engine Turbine Components.’’ The authors wish to acknowledge this financial support as well as the contributions of the industrial partners ALFA AVIO, FIAT, MTU, SNECMA, and TURBOMECA. The authors are grateful to Mr. Neri Bonfanti and Leonardo Florenzano for the efficient analysis of the numerical data.

Nomenclature

a = speed of sound
c = chord
k = turbulent kinetic energy
$\dot{m}$ = mass flow
M = Mach number
P = pressure
Re = Reynolds number
T = temperature
U = velocity
w = turbulence frequency
φ = phase [0-1] vane pitch
∇ = gradient

Subscripts

c = coolant
0 = total quantity
s = static quantity
1 = stator inlet
2 = stator outlet, rotor inlet
3 = rotor outlet
r = relative to the rotor frame
s = stator
r = rotor
ax = axial direction

References

[1] Halstead, D. E., Wisler, D. C., Okiishi, T. H., Walker, G. J., Hodson, H. P., and Shin, H. W., 1997, ''Boundary Layer Development in Axial Compressors and Turbines—Part 3 of 4: LP Turbines,'' ASME J. Turbomach., **119**, pp. 225–237.

[2] Harvey, N. W., Cox, J. C., Schulte, V., Howell, R., and Hodson, H. P., 1999, ''The Role of Research in the Aerodynamic Design of Advanced Low-Pressure Turbine,'' *Trans. 3rd European Conference on Turbomachinery*, pp 123–132.

[3] Garside, T., Moss, R. W., Ainsworth, R. W., Dancer, S. N., and Rose, M. G., 1994, ''Heat Transfer to Rotating Turbine Blades in a Flow Undisturbed by Wakes,'' ASME Paper No. 94-GT-94.

[4] Dénos, R., 1996, ''Investigation of the Unsteady Aerothermal Flow Field in the Rotor of a Transonic Turbine,'' Ph.D. thesis, IVK—University of Poitiers.

[5] Jung, A. R., Mayer, J. F., and Stetter, H., 1996, ''Simulation of 3D-Unsteady Stator-Rotor Interaction in Turbomachinery Stages of Arbitrary Pitch Ratio,'' ASME Paper No. 96-GT-69.

[6] Gundy-Burlet, K. L., and Dorney, D. J., 1996, ''Three-Dimensional Simulations of Hot Streak Clocking in a 1-1/2 Stage Turbine,'' presented at 32nd IAA/ASME/SAE/ASEE Joint Propulsion Conference, Lake Buena Vista, FL, July 1–3.

[7] Hilditch, M. A., Smith, G. C., and Singh, U. K., 1998 ''Unsteady Flow in a Single Turbine Stage,'' ASME Paper No. 98-GT-531.

[8] Emunds, R., Jennions, I. K., Bohn, D., and Gier, J., 1999, ''The Computation of Adjacent Blade-Row Effects in a 1.5-Stage Axial Flow Turbine,'' ASME J. Turbomach., **121**, pp. 1–10.

[9] Giles, M. B., 1991, ''UNSFLO: A Numerical Method for the Calculation of Unsteady Flow in Turbomachinery,'' GTL Rep. No. 205, MIT Gas Turbine Laboratory.

[10] DeRango, S., and Zing, D. W., 1997, ''Improvements to a Dual-Time Stepping Method for Computing Unsteady Flows,'' AIAA J., **35**, No. 9, pp. 1548–1550.

[11] Doorly, D. J., and Oldfield, M. L. G., 1985, ''Simulation of the Effect of Shock Wave Passing on a Turbine Rotor Blade,'' ASME J. Eng. Gas Turbines Power, **107**, pp. 998–1006.

[12] Ashworth, D. A., LaGraff, J. E., Shultz, D. L., and Grindrod, K. J., 1985, ''Unsteady Aerodynamic and Heat Transfer Processes in a Transonic Turbine Stage,'' ASME J. Eng. Gas Turbines Power, **107**, pp. 1022–1030.

[13] Giles, M. B., 1988, ''Stator/Rotor Interaction in a Transonic Turbine,'' AIAA Paper No. 88-3093.

[14] Saxer, A. P., and Giles, M. B., 1994, ''Predictions of Three-Dimensional Steady and Unsteady Inviscid Transonic Stator/Rotor Interaction With Inlet Radial Temperature Nonuniformity,'' ASME J. Turbomach., **116**, pp. 347–357.

[15] Moss, R. W., Sheldrake, C. D., Ainsworth, R. W., Smith A. D., and Dancer, S. N., 1996, ''Unsteady Pressure and Heat Transfer Measurements on a Rotating Blade Surface in a Transient Flow Facility,'' 85th Propulsion and Energetic Panel Symposium on Loss Mechanism and Unsteady Flows in Turbomachines, Derby, UK, AGARD CP No. 571.

[16] Rao, K. V., Delaney, R. A., and Dunn, M. G., 1994, ''Vane–Blade Interaction in a Transonic Turbine. Part 1: Aerodynamics. Part 2: Heat Transfer,'' AIAA J. Propulsion Power, **10**, No. 3, pp. 305–317.

[17] Guenette, G. R., Epstein, A. H., Giles, M. B., Haimes, R., and Norton, R. J. G., 1989, ''Fully Scaled Transonic Turbine Rotor Heat Transfer Measurements,'' ASME J. Turbomach., **111**, pp. 1–7.

[18] Michelassi, V., Martelli, F., Dénos, R., Arts, T., and Sieverding, C. H., 1999, ''Unsteady Heat Transfer in Stator–Rotor Interaction by Two Equation Turbulence Model,'' ASME J. Turbomach., **121**, pp. 436–447.

[19] Dénos, R., Sieverding, C. H., Arts, T., Brouckaert, J. F., Paniagua, G., and Michelassi, V., 1999, ''Experimental Investigation of the Unsteady Rotor Aerodynamics of a Transonic Turbine Stage,'' IMechE J. Power Energy, **23**, No A4, pp. 327–338.

[20] Sieverding, C. H., Vanhaeverbeek, C., and Schulze, G., 1992, ''An Opto-Electronic Data Transmission System for Measurements on Rotating Turbomachinery Components,'' ASME Paper No. 92-GT-337.

[21] Byrne, C. M., and Davies, M. R. D., 1996, ''Data Transmission Systems for a Transient Gas Turbine Rotor,'' ASME Paper No. 96-GT-514.

[22] Ainsworth, R., 1995, ''Recent Development in Fast Response Aerodynamic Technology,'' Von Karman Institute Lecture Series 1995-01 on Measurement Techniques.

[23] Jameson, A., 1991, ''Time Dependent Calculations Using a Multigrid With Applications to Unsteady Flows Past Airfoils and Wings,'' AIAA Paper No. 91-1596.

[24] Michelassi, V., and Martelli, F., 1998, ''Modeling of Unsteady-Heat Transfer in a Transonic Turbine Stage,'' AIAA Paper No. 98-2555.

[25] Durbin, P. A., 1996, ''On the $k-\varepsilon$ Stagnation Point Anomaly,'' Int. J. Heat Fluid Flow, **17**, pp. 89–90.

[26] Abu-Ghannam, B. J., and Shaw, R., 1980, ''Natural Transition of Boundary Layers—The Effects of Turbulence, Pressure Gradient, and Flow History,'' J. Mech. Eng. Sci., **22**, No. 5, pp. 213–228.

[27] Kapteijn, C., Amecke, J., and Michelassi, V., 1996, ''Aerodynamic Performance of a Transonic Turbine Guide Vane With Trailing Edge Coolant Ejection: Part 1—Experimental Approach,'' ASME J. Turbomach., **118**, pp. 519–528.

[28] Sieverding, C. H., Arts, T., Dénos, R., and Martelli, F., 1996, ''Investigation of the Flow Field Downstream of a Turbine Trailing Edge Cooled Nozzle Guide Vane,'' ASME J. Turbomach., **118**, pp. 291–300.

[29] Dietz, A. J., and Ainsworth, R. W., 1992, ''Unsteady Pressure Measurements on the Rotor of a Model Turbine Stage in a Transient Flow Facility,'' ASME Paper No. 92-GT-156.

[30] Hodson, H. P., 1985, ''Measurements of Wake-Generated Unsteadiness in the Rotor Passages of an Axial Flow Turbine,'' ASME J. Eng. Gas Turbines Power, **107**, pp. 467–476.

[31] Hilditch, M. A., Smith, G. C., Anderson, J. S., and Chana, K. S., 1996, ''Unsteady Measurements in an Axial Flow Turbine,'' *Proc. 85th Propulsion and Energetic Panel Symposium on Loss Mechanism and Unsteady Flows in Turbomachines*, Derby, UK, AGARD CP No. 571.

[32] Hodson, H. P., 1985, ''An Inviscid Blade-to-Blade Prediction of a Wake-Generated Unsteady Flow,'' ASME J. Eng. Gas Turbines Power, **107**, pp. 337–344.

[33] Venable, B. L., Delaney, R. A., Busby, J. A., Davis, R. L., Dorney, D. J., Dunn, M. G., Haldeman, C. W., and Abhari, R. S., 1999, ''Influence of Vane-Blade Spacing on Transonic Turbine Stage Aerodynamics, Part 1: Time-Averaged Data and Analysis,'' ASME J. Turbomach., **121**, pp. 663–672.

Experimental Heat Transfer and Bulk Air Temperature Measurements for a Multipass Internal Cooling Model With Ribs and Bleed

Douglas Thurman
U.S. Army Research Laboratory,
Glenn Research Center,
Cleveland, OH 44135

Philip Poinsatte
National Aeronautics and Space Administration,
Glenn Research Center,
Cleveland, OH 44135

An experimental study was made to obtain heat transfer and air temperature data for a simple three-leg serpentine test section that simulates a turbine blade internal cooling passage with trip strips and bleed holes. The objectives were to investigate the interaction of ribs and various bleed conditions on internal cooling and to gain a better understanding of bulk air temperature in an internal passage. Steady-state heat transfer measurements were obtained using a transient technique with thermochromic liquid crystals. Trip strips were attached to one wall of the test section and were located either between or near the bleed holes. The bleed holes, used for film cooling, were metered to simulate the effect of external pressure on the turbine blade. Heat transfer enhancement was found to be greater for ribs near bleed holes compared to ribs between holes, and both configurations were affected slightly by bleed rates upstream. Air temperature measurements were taken at discrete locations along one leg of the model. Average bulk air temperatures were found to remain fairly constant along one leg of the model.

[DOI: 10.1115/1.1333090]

Introduction

With current and future jet engine designs requiring higher pressure ratios and operating temperatures, it is important for the engine materials to withstand these extreme conditions. One method of keeping turbine blade temperatures below the critical metal temperature level is to cool the blade by routing cooling air from the compressor through turbulated serpentine passages in the blades. Small amounts of this coolant can then be bled into the external boundary layer flow through discrete holes on the surface of the blade, forming an insulating layer of cool air between the blade and the hot combustion gas. Predicting the metal temperatures correctly requires quality experimental data, especially to validate turbomachinery CFD codes often used in the design of engine components.

Many experimental studies have considered the effects of Reynolds number and different rib geometries on the heat transfer of internal cooling channels, such as Lau et al. [1], Han [2], Chyu [3], Zhang et al. [4], Wang [5], and Taslim et al. [6]. Recently there have been experimental studies on the combination of internal cooling with ribs and bleed. Taslim et al. [7] studied the effects of bleed holes on heat transfer on a trapezoidal internal cooling channel. Shen et al. [8] reported on heat transfer enhancement in a converging straight internal cooling channel with ribs and staggered bleed holes. Ekkad et al. [9] studied heat transfer in a turbulated two-pass channel with ribs between bleed holes. Rigby et al. [10], Stephens et al. [11], Bonhoff et al. [12], and McDonough et al. [13] have used these experimental studies to validate numerical predictions for complicated internal cooling geometries. However, in a typical turbine blade passage, bleed holes may not be spaced equidistant between ribs. Also the varying pressure gradient on the external surface of a blade may affect the flow bled from the internal cooling channel, resulting in nonuniform bleed flow rates. The present study focuses on varying bleed rates and rib placement relative to hole locations.

This report provides experimental heat transfer data for the first leg of a serpentine internal cooling channel with trip strips and bleed holes. A transient liquid crystal technique, as described by Hippensteele [14], was used to determine the surface heat transfer coefficients. Ribs were placed at two locations relative to the bleed holes. One case had ribs spaced equidistant between the holes; the other case had ribs just upstream of the holes. Different bleed conditions (uniform bleed flow rate, increasing bleed flow rate per hole, decreasing bleed flow rate per hole, no-bleed) were run to examine the effects of variable bleed on internal cooling. Experimental data were also obtained on bulk air temperatures in the channel.

Apparatus

The overall test facility is shown in Fig. 1. Room temperature air was drawn into the tunnel by a vacuum exhaust system. An elliptical one-dimensional aluminum bellmouth was attached to the clear acrylic plastic test section. An orifice at the exit of the test section measured the mass flow rate. Eight adjustable flow meters were attached to the bleed holes of the test section. The bleed air was collected into a manifold and flows through an orifice to determine the overall bleed mass flow rate. Tunnel flow started when a ball valve was opened downstream of the orifices. The model was enclosed in an oven covered with an automatic temperature-controlled heater blanket. Two ‘‘cool’’ HSI lamps and a color digital CCD camera were used to view the model. Video images were stored in computer memory at 1 frame/s using a commercial video frame grabber and were backed up on S-VHS videotape at 30 frames/s. A time-date generator was also used to record the time with the video data.

The test section, made of 1.91 cm (0.75 in.) thick acrylic walls, had two partitions to create a serpentine channel, as shown in Fig. 2. The first and second legs of the model were 6.67×6.67 cm (2.625×2.625 in.) cross section; the third leg was 6.67×3.3 cm

---

Contributed by the International Gas Turbine Institute and presented at the 45th International Gas Turbine and Aeroengine Congress and Exhibition, Munich, Germany, May 8–11, 2000. Manuscript received by the International Gas Turbine Institute February 2000. Paper No. 2000-GT-233. Review Chair: D. Ballal.

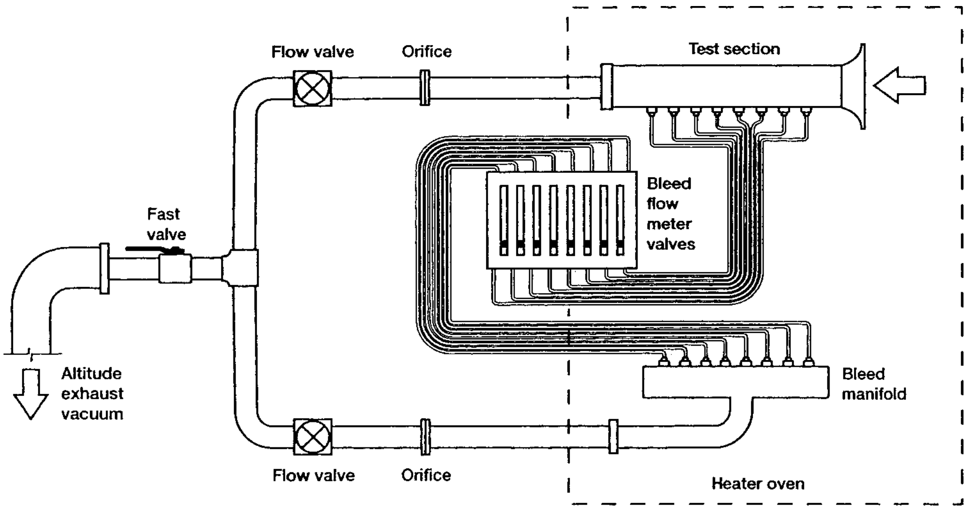

Fig. 1 Test facility

(2.625×1.3 in.). Rounded trip strips, also made of acrylic, were attached to the lower surface of the model on all three legs, spaced 5.08 cm (2 in.) apart and oriented 90° to the airflow. The rib height-to-channel height ratio (e/D) was 0.076; the rib pitch-to-height ratio (P/e) was 10. Eight 0.38 cm (0.15 in.) diameter bleed holes, spaced 5.08 cm (2 in.) apart, were drilled normal into the lower surface of the first leg only.

Liquid crystals, by virtue of their ability to change color with temperature, were used to determine surface temperature measurements. The lower surface of the model was sprayed with flat black lacquer, then with narrow-band microencapsulated chiral nematic liquid crystal paint for measuring the surface temperature to determine heat transfer. The video camera was perpendicular to the lower surface of the test section. Static pressures were measured on the lower surface of the model at the locations shown in Fig. 3(*a*). Open-ball thermocouple probes were placed in the airstream through the sidewall of the first leg and through the upper surface at the turns and ends of the channels, as shown in Figs. 3(*b*) and 3(*c*). Thin-foil surface thermocouples were attached to the lower surface for calibrating the liquid crystals. Temperature and pressure data were recorded by a PC-based data acquisition system.

Procedure

Once the mainstream and bleed flow regulators were set, the test model was heated in the oven to a uniform temperature, typically between 54.4 and 65.6°C (130 to 150°F). After the model reached the desired temperature, the cameras were turned on, and

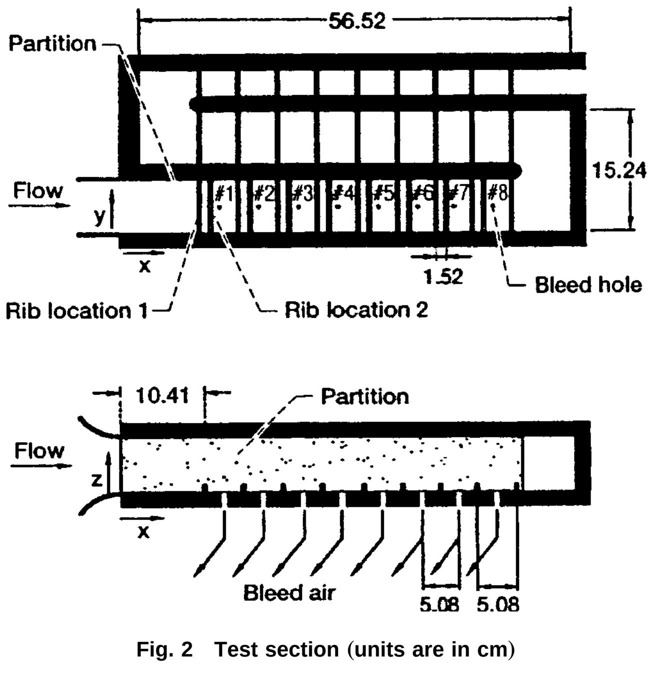

Fig. 2 Test section (units are in cm)

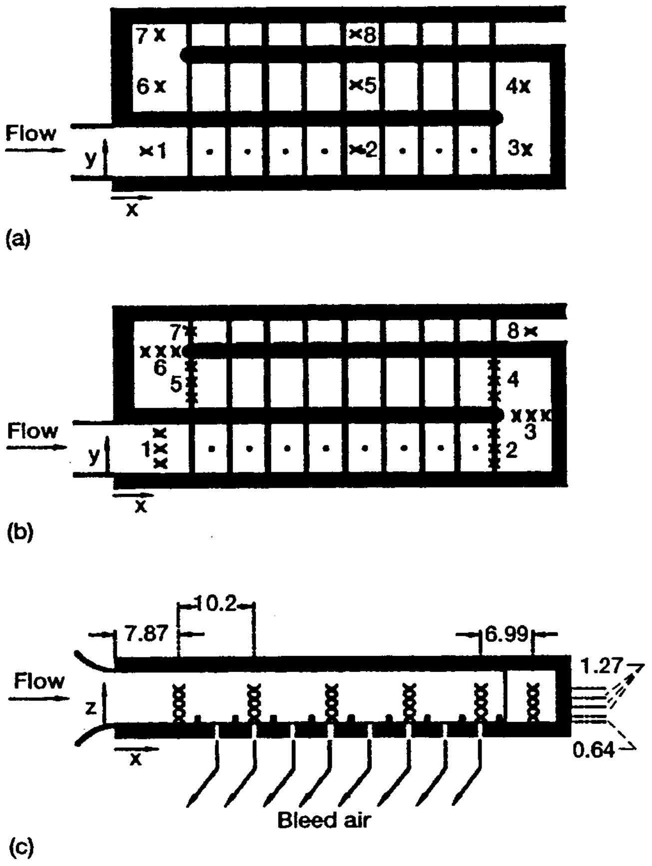

Fig. 3 (*a*) Static pressure measurement stations. (*b*) Air temperature measurement stations. (*c*) Air temperature measurement locations in first passage (units are in cm).

Table 1 Nominal percentage of total bleed flow in each hole

Hole #	Uniform bleed	Increasing bleed	Decreasing bleed	No bleed
1 Inlet	12.5	0	24.4	0
2	12.5	4.3	21.0	0
3	12.5	7.6	17.6	0
4	12.5	10.9	14.3	0
5	12.5	14.3	10.9	0
6	12.5	17.6	7.6	0
7	12.5	21.0	4.3	0
8 End of first passage	12.5	24.4	0	0

the data acquisition system and VCR were started. Then the oven was opened up and the flow valve opened, initiating airflow which suddenly cooled the model with room temperature air. The resulting liquid crystal color patterns, showing continuous surface temperature, were recorded. In the present study, only data from the first leg of the test section were examined. The yellow color band of the liquid crystal was used for calculating the heat transfer coefficients and was calibrated to be 37.8°C (100.1°F). Video images were reduced using a video frame grabbing board, employing HSI color definition, and commercial software that extracts color and therefore surface temperature. The software also allowed manual digitization of the video images where high temperature gradient regions are difficult to resolve automatically.

Assuming that lateral conduction is negligible compared to heat flow normal to the surface, surface heat transfer coefficients can be calculated using the one-dimensional transient conduction equation:

$$\theta=1-\exp(\beta^2)*\operatorname{erfc}(\beta)$$

where $\theta=(T_i-T_w)/(T_i-T_r)$, $\beta=h*(t/\rho ck)^{0.5}$, T_i is the initial surface temperature, T_w is the wall surface temperature, T_r is the bulk air recovery temperature, and t is the time from the start of the test. Note that this assumption is not actually valid near the bleed holes nor on the ribs. The local heat transfer coefficient, h, was calculated at the location of the calibrated liquid crystal color band. This isotherm also represents a uniform heat transfer coefficient when the bulk temperature is constant. Bulk temperature measurements in general showed little average increase along the passage, so the data were reduced using a single average temperature at the inlet.

Two test model configurations were employed, one with ribs equidistant between bleed holes, and one with ribs 0.51 cm (0.2 in.) upstream of bleed holes. Each configuration was run for three flow rates (nominal $\mathrm{Re}_{Dh}=31{,}000$; 61,000; and 96,000) and four bleed cases (no-bleed, uniform bleed, increasing bleed, and decreasing bleed). Reynolds numbers were based on channel hydraulic diameter, which is equal to the length of the side of the square channel. Using the present hardware, bleed flow rates of 5 to 10 percent of the main flow could be attained. Table 1 shows the nominal bleed flow rate per hole as percentages of total bleed

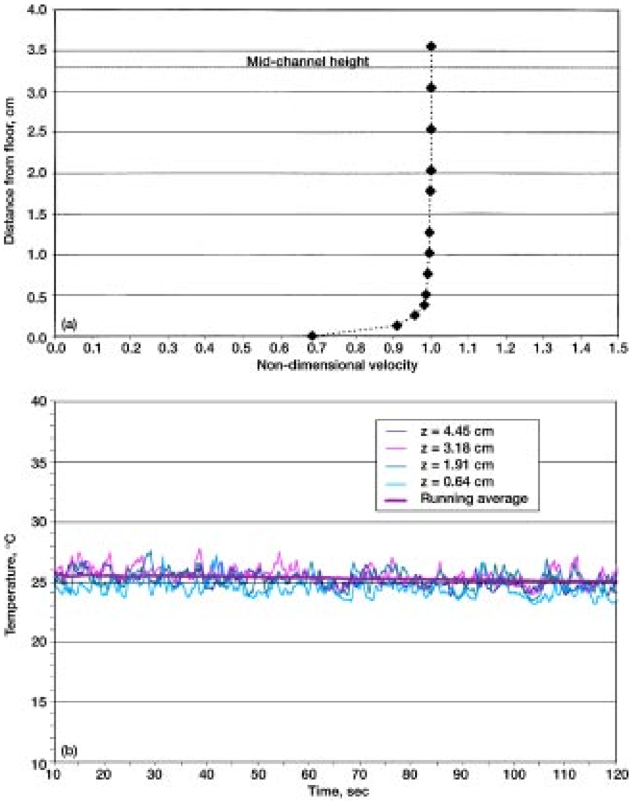

Fig. 4 (*a*) Inlet velocity profile. (*b*) Inlet airstream temperatures with uniform bleed at Re3.

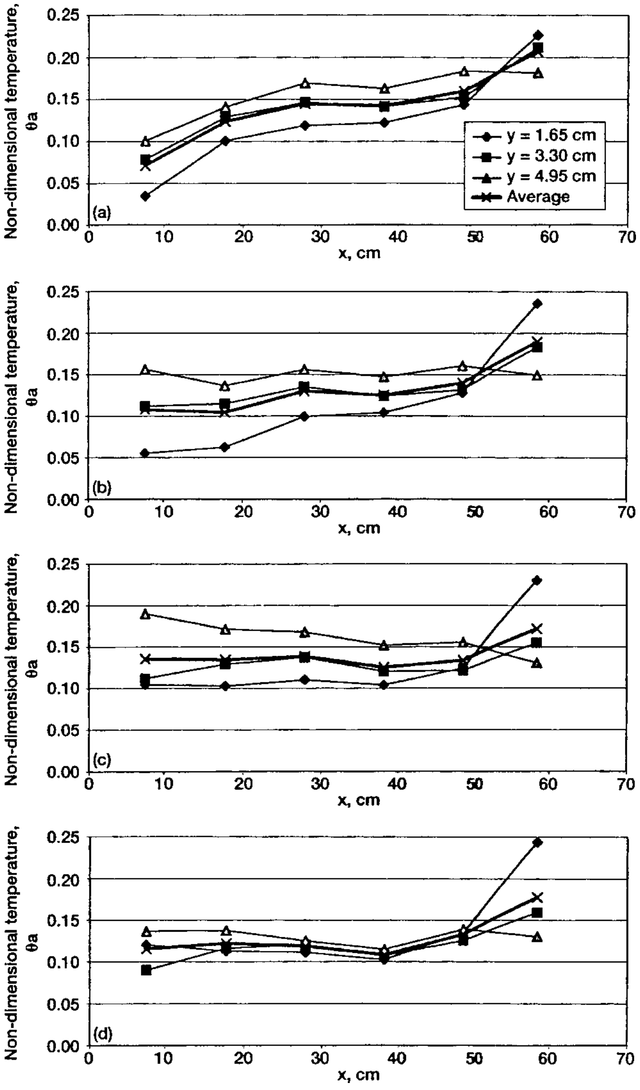

Fig. 5 Airstream temperature measurements at various heights in first channel with uniform bleed at Re3: (*a*) $z=0.64$ cm. (*b*) $z=1.91$ cm. (*c*) $z=3.18$ cm. (*d*) $z=4.45$ cm.

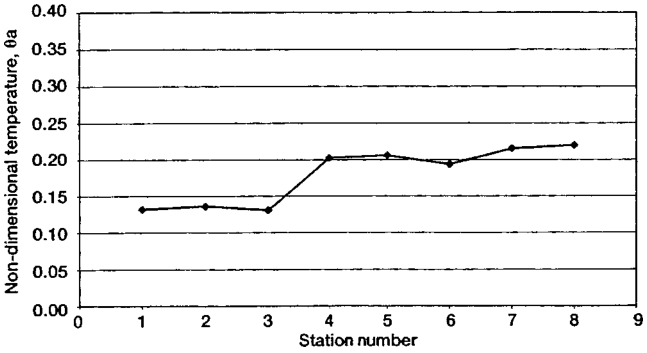

Fig. 6 Airstream temperature throughout model, averaged spanwise across channel, Re3, no-bleed, midchannel height

flow. Air temperature measurements were taken in the first leg at several cross-sectional stations as well as throughout the test section at discrete locations, as shown in Fig. 3.

An uncertainty analysis was performed following the method of Kline and McClintock [15]. Based on the following uncertainties: $T_i=\pm 0.56$°C (± 1°F), $T_w=\pm 0.28$°C (± 0.5°F), $T_r=\pm 0.83$°C (± 1.5°F), and $t=\pm 0.3$ s, the overall uncertainties in h for the multiple cases ranged from 8 to 13 percent.

Results and Discussion

The flow rate conditions referred to in the discussion below as Re1, Re2, and Re3 were run at nominal Reynolds numbers of 31,000, 61,000, and 96,000, respectively. When bleed was employed, the bleed flow rates were nominally 10, 5, and 5 percent of the inlet mass flow for Re1, Re2, and Re3, respectively. A typical inlet velocity profile (station 1) is presented in Fig. 4(*a*); inlet free-stream turbulence intensity was nominally 2 percent.

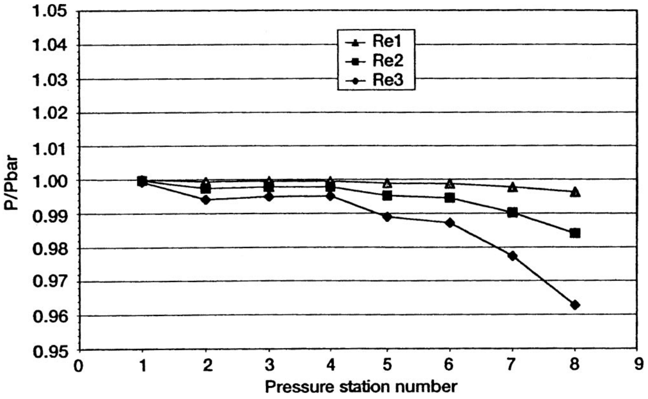

Fig. 7 Test section static pressures; uniform bleed

Bulk Air Temperatures and Static Surface Pressures. Airstream temperature measurements were taken for flow with uniform and no-bleed at various cross sections in the first passage, as shown in Fig. 3(*b*). Raw temperature versus time data from inlet temperature measurements are shown in Fig. 4(*b*) for Re3 and uniform bleed along with a running average of the four temperatures. The standard deviation of these inlet temperatures was 0.78°C (1.4°F); the fluctuations decrease moving down the channel. To examine temperature change through the duct, the fluctuations were eliminated by taking a 10 s average at 30 s after the start of the test. This is around the midpoint of typical liquid crystal data. Since room temperature and the initial heated airstream temperature could vary for each test case, a nondimensional temperature ratio was used to normalize the temperature measurements. The normalized air temperatures were calculated as

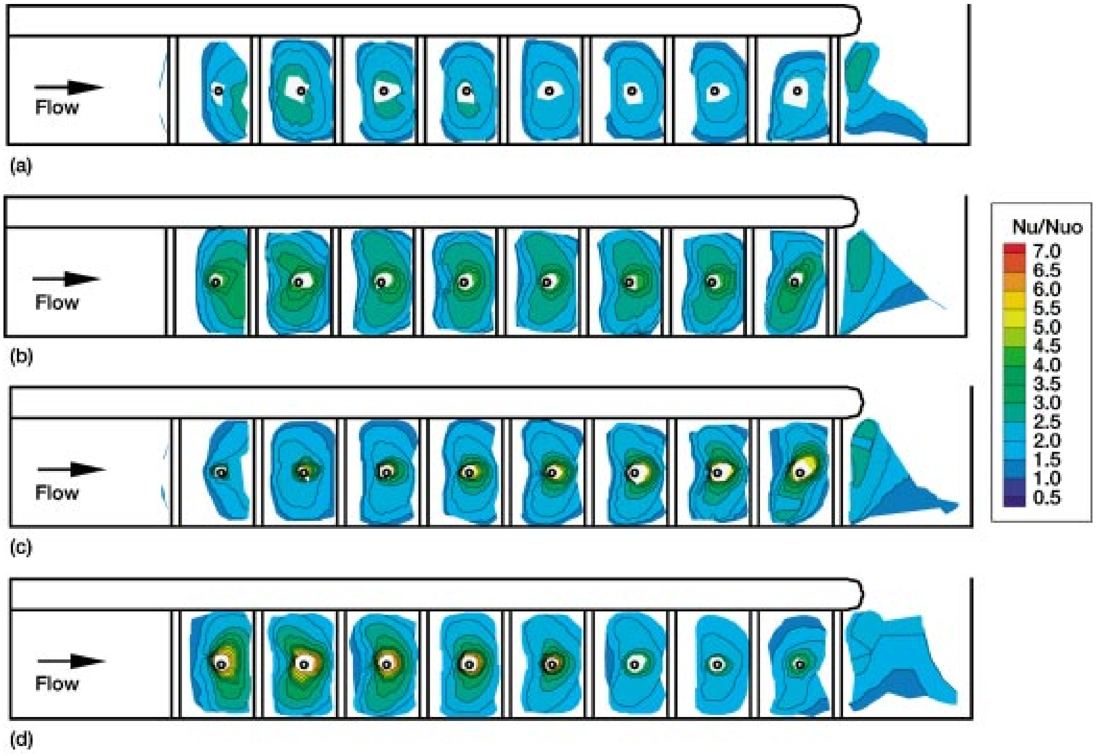

Fig. 8 Surface heat transfer Nu/Nu_o, for the case of ribs between holes: (*a*) Re1, no-bleed. (*b*) Re1, uniform-bleed. (*c*) Re1, increasing bleed. (*d*) Re1, decreasing bleed.

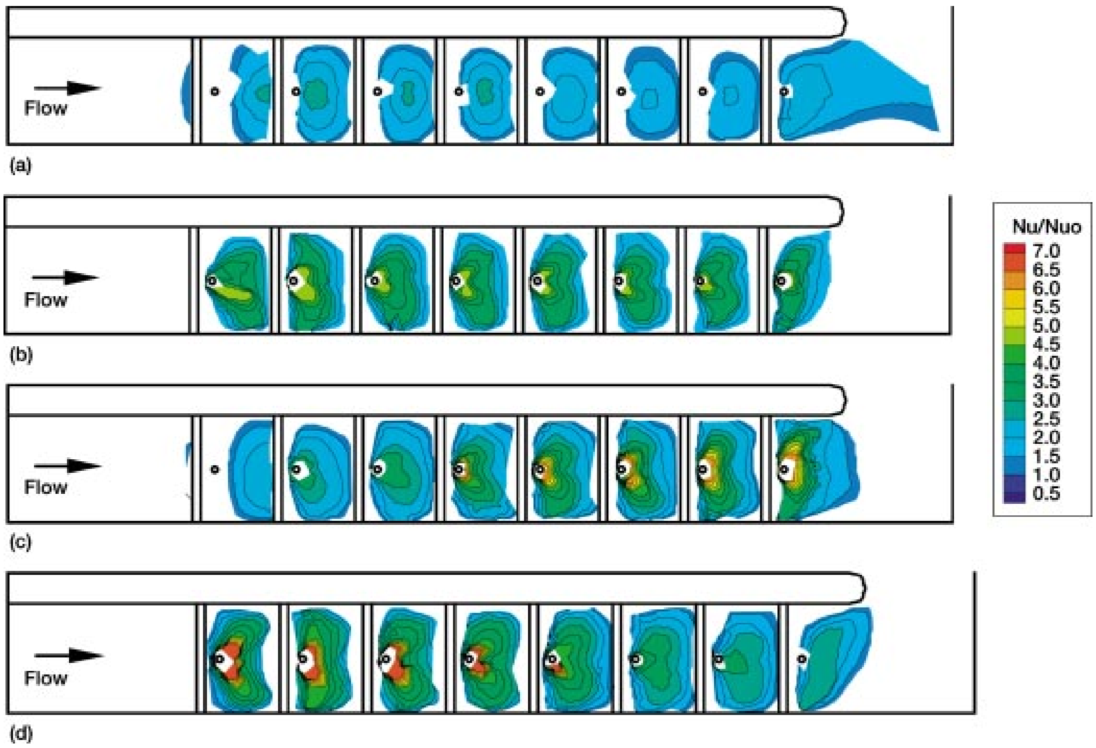

Fig. 9 Surface heat transfer, Nu/Nu_o, for the case of ribs near holes: (*a*) Re1, no-bleed. (*b*) Re1, uniform-bleed. (*c*) Re1, increasing bleed. (*d*) Re1, decreasing bleed.

$$\theta_a = (T_a - T_{\mathrm{amb}})/(T_i - T_{\mathrm{amb}})$$

Normalized airstream temperatures at Re3 with uniform bleed are presented in Fig. 5 for four different heights from the floor of the model. Note that the data points at $x = 58.4$ cm (23 in.) are actually in the first turn region. As seen in the figures, the temperature variations in the spanwise direction are generally greater than the overall temperature increase or decrease in the streamwise direction. Similar effects were seen for Re1 and Re2, with generally more temperature variation spanwise than streamwise, and spanwise variations becoming slightly greater with increasing Reynolds number. The average cross-sectional temperatures for all of the cases remained fairly constant through the channel.

Spanwise air temperature averages throughout the test section (stations shown in Fig. 3(*a*)) at midchannel height and at Re3 are shown in Fig. 6. The average temperature remains fairly constant from the inlet to station 3, the midpoint of the first turn. There is a noticeable increase between the turn and the inlet to the second leg. The average temperature stays constant from station 4 through the midpoint of the second turn, station 6, then again increases.

Static pressure measurements, shown in Fig. 7, were taken on the lower surface at the stations shown in Fig. 3(*a*). Static pressure changes little through the first passage and the first turn. The pressure then begins to decrease halfway down the second passage and decreases further as the flow speeds up through the narrower third passage.

Heat Transfer. Heat transfer is presented as the ratio of Nusselt number, $\mathrm{Nu} = hD/k$, over the Nusselt number for fully developed pipe flow, $\mathrm{Nu}_0 = 0.023(\mathrm{Re}_{\mathrm{Dh}}^{0.8})(\mathrm{Pr}^{0.4})$. Data were not generally taken on the rib surfaces since the ribs were rounded and their small size violates the one-dimensional conduction assumption. Nusselt number ratio distributions discussed below are for Re1. The trends for Re2 and Re3 are similar.

Ribs Between Holes. Heat transfer distributions for ribs between bleed holes are shown in Fig. 8. With or without bleed, it can be seen that there is very low heat transfer just downstream of the ribs where separation and reattachment of the flow occur. Figure 8(*a*) shows the no-bleed case, in which the total bleed flow was shut off, so no flow exited through the bleed holes. As seen in the figure, no effect from the holes is evident.

Having some type of bleed can greatly enhance surface heat transfer. The patterns produced by bleed with ribs between holes are backward-**C**-shaped compared to the oval shapes for the no-bleed case. These patterns are also observed in Ekkad et al. [9] and Shen [8]. For the three cases with bleed, the effect of the bleed holes can readily be seen, with higher h immediately downstream of the hole. The boundary layer is essentially bled off, and heat transfer resistance is thereby reduced. For the uniform bleed case, there is much higher heat transfer near each hole as well as away from the hole near the ribs and walls, compared to the no-bleed case. The heat transfer distributions appear to be periodic, except in the region around hole 1 due to developing flow, and around hole 8 due to the flow turning around the partition.

For the metered bleed flow cases, higher Nusselt ratios are seen near the holes with higher bleed flow rates. The ramped increasing bleed results are shown in Fig. 8(*c*). It can be seen that upstream, where the bleed flow rates are less than those for the uniform bleed case, heat transfer is similar to no-bleed. Downstream, where bleed rates are higher than uniform bleed, heat transfer is similar to the uniform-bleed case, but with slightly higher Nusselt ratios near and away from the hole. Near holes 4 and 5 where bleed rates are similar to the uniform bleed rates, heat transfer is slightly better than without bleed but not as good as with uniform bleed.

The ramped decreasing bleed results are shown in Fig. 8(*d*). Upstream, where bleed rates are higher than uniform bleed rates, heat transfer is higher near the hole and about the same as the

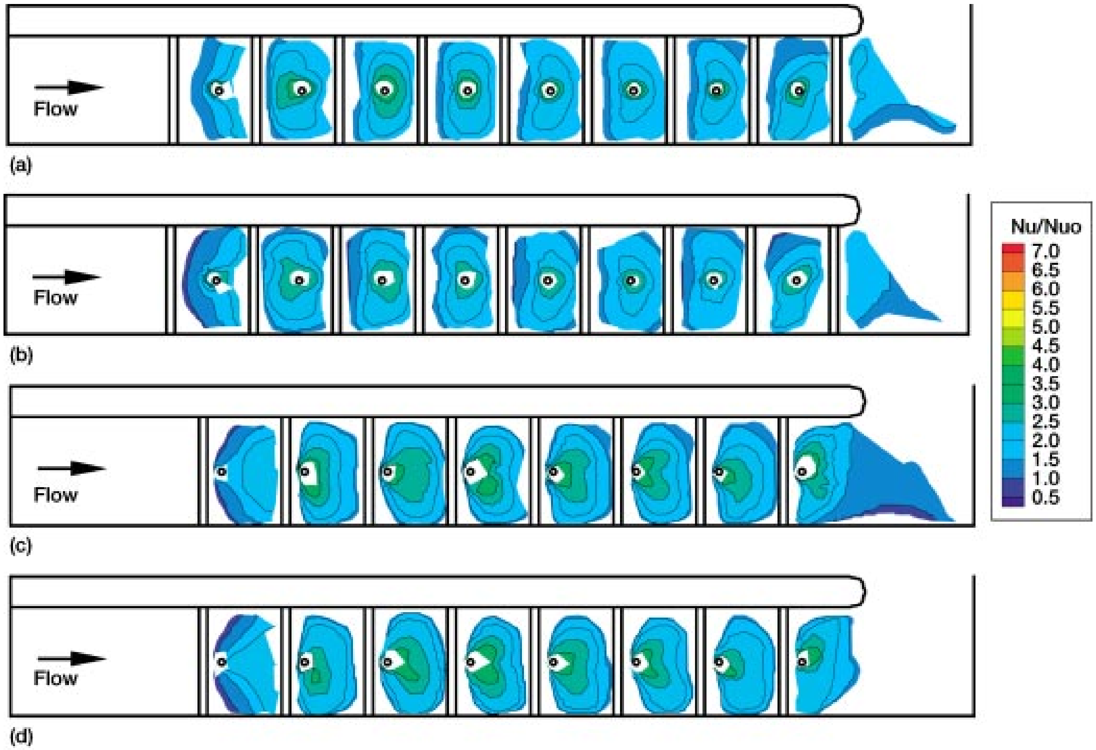

Fig. 10 Surface heat transfer, Nu/Nu$_o$: (*a*) Re2, uniform-bleed, ribs between holes. (*b*) Re3, uniform-bleed, ribs between holes. (*c*) Re2, uniform-bleed, ribs near holes. (*d*) Re3, uniform-bleed, ribs near holes.

uniform bleed case away from the hole. Heat transfer downstream is similar to the no-bleed case. Heat transfer near holes 4 and 5 is slightly better than without bleed, but not as good as with uniform bleed.

It can be seen from these cases that higher bleed rates yield higher heat transfer values near and away from the hole. By comparing the distributions near holes 4 and 5, upstream bleed conditions can be seen to have a slight effect on heat transfer down the channel. Higher or lower bleed upstream reduces the heat transfer downstream away from the hole. Uniform bleed appears to give better heat transfer enhancement overall.

Ribs Near Holes. Heat transfer distributions for ribs near bleed holes are shown in Fig. 9. Figure 9(*a*) shows that the no-bleed case is similar to Fig. 8(*a*). Figures 9(*b*)–9(*d*) show that heat transfer is greatly enhanced near the downstream edge of the ribs due to the bleeding of the stagnant separated flow behind the rib. The patterns produced by bleed are **C**-shaped, opposite that produced by the ribs-between-holes configuration.

Other than the mirrored patterns, the heat transfer trends for each case are similar to those for ribs between holes. For uniform bleed, heat transfer distributions are periodic with higher Nusselt numbers near the bleed holes. Downstream of the hole, near the upstream edge of the rib, the effect of bleed is reduced.

Heat transfer upstream for the increasing bleed case is similar to the no-bleed case; heat transfer downstream is similar to the uniform bleed case, only with slightly better enhancement away from the hole. Near holes 4 and 5 where bleed rates are about the same as those with uniform bleed, Nusselt values away from the hole are similar to those for uniform bleed and higher near the hole.

With decreasing bleed, heat transfer upstream is similar to the uniform-bleed case, with higher Nusselt values near and away from the hole. Heat transfer downstream is better than without bleed but not as good as with uniform bleed. Near holes 4 and 5, heat transfer is similar to uniform bleed away from the hole, but is higher near the hole.

By comparing the distributions near holes 4 and 5, it appears that the decreasing bleed case gives better heat transfer enhancement. When comparing to the ribs-between-holes configuration, better heat transfer enhancement is seen near and away from the hole due to the bleeding of the separated flow behind the rib, which decreases the heat transfer resistance at the surface.

Reynolds Number Effect. Overall, heat transfer enhancement tends to decrease with increasing Reynolds number. As illustrated in Fig. 10, increasing the Reynolds number for the uniform bleed case decreases the Nusselt number ratio only slightly. This is also true for all of the other cases not shown. For the cases with bleed, the heat transfer augmentation from increased mixing and boundary layer removal is less pronounced at higher Reynolds numbers. Generally for all cases with bleed, the patterns in the region around hole 1 appear to be squeezed toward the center of the channel as Reynolds number increases.

Centerline Comparison. Centerline heat transfer coefficients for the region around hole 4, between the fourth and fifth ribs, are shown in Fig. 11 for both rib-between-hole and rib-near-hole cases. The highest heat transfer can be seen to occur on the top surface of the rib and downstream of the hole; it should be noted that the data at the peaks were taken within a few seconds of the startup and thus have uncertainties substantially higher than the nominal 10 percent uncertainty reported for the more conditioned data. The lowest heat transfer occurs downstream of the rib and then gradually increases approaching the hole. Reynolds number does not appear to affect the heat transfer in this region between the rib and hole.

Conclusion

Bulk air temperature measurements taken in the first passage showed that in general, temperature variations in the spanwise direction were greater than the overall variation in the streamwise direction. The average cross-sectional temperatures remained

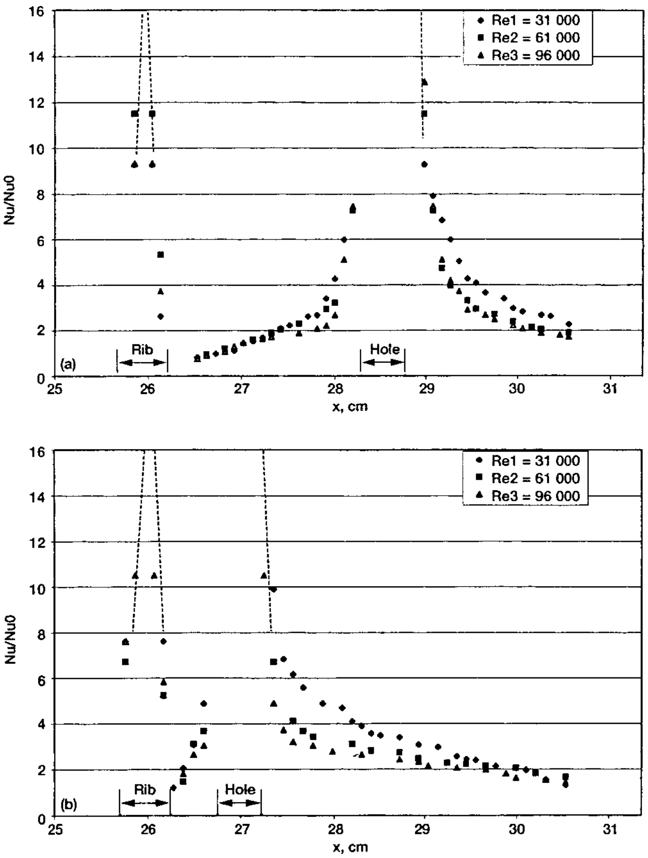

Fig. 11 Centerline heat transfer, uniform-bleed: (*a*) ribs between holes; (*b*) ribs near holes

fairly constant along the channel. Large temperature jumps occurred between the half-point around the first turn and the inlet to the second passage.

Experimental heat transfer measurements showed that any amount of bleed would enhance surface heat transfer. Placement of ribs with respect to holes had a major effect on surface heat transfer distributions. Placing ribs near bleed holes greatly enhances the heat transfer by cooling more surface area and removing the separated flow near the downstream edge of the rib. Different distribution patterns were also observed; the ribs-between-holes configuration produced backward-**C**-shaped patterns, while the ribs-near-holes configuration produced **C**-shaped patterns. By comparing the heat transfer distributions near the center of the channel where the bleed rates were similar, heat transfer enhancement was found to be affected slightly by the bleed rates upstream. Higher or lower bleed flow upstream reduced the heat transfer downstream for the ribs-between-holes configuration, while heat transfer enhancement for the ribs-near-holes configuration increases slightly with higher bleed rates upstream.

β = nondimensional time
c = specific heat of test section material
c_p = specific heat of air
D = square channel height
D_h = hydraulic diameter
e = rib height
h = heat transfer coefficient
k = thermal conductivity
m_{total} = total mass flow
Nu = local Nusselt number $=hD/k$
Nu_0 = Nusselt number from correlation for a straight channel $=0.023\text{Re}_{\text{Dh}}^{0.8}\text{Pr}^{0.4}$
P = rib pitch
Pr = Prandtl number of air $=c_p\mu/k$
Re = Reynolds number $=m_{\text{total}}/(\mu D_h)$
θ = nondimensional surface temperature
θ_a = nondimensional airstream temperature
ρ = density of test section material
T_a = air temperature in test section
T_{amb} = room temperature
T_i = initial surface temperature
T_r = bulk air recovery temperature
T_w = wall surface temperature shown by liquid crystal
t = time of liquid crystal color change
μ = viscosity of air

References

[1] Lau, S. C., McMillan, R. D., and Han, J. C., 1991, ''Heat Transfer Characteristics of Turbulent Flow in a Square Channel With Angled Discrete Ribs,'' ASME J. Turbomach., **113**, pp. 367–374.
[2] Han, J. C., 1988, ''Heat Transfer and Friction Characteristics in Rectangular Channels With Rib Turbulators,'' ASME J. Heat Transfer, **110**, pp. 321–328.
[3] Chyu, M. K., 1991, ''Regional Heat Transfer in Two-Pass and Three-Pass Passages With 180-deg Sharp Turns,'' ASME J. Heat Transfer, **113**, pp. 63–70.
[4] Zhang, Y. M., Gu, W. Z., and Han, J. C., 1994, ''Heat Transfer and Friction in Rectangular Channels With Ribbed or Ribbed-Grooved Walls,'' ASME J. Heat Transfer, **116**, pp. 58–65.
[5] Wang, Z., Ireland, P. T., Kohler, S. T., and Chew, J. W., 1998, ''Heat Transfer Measurements to a Gas Turbine Cooling Passage With Inclined Ribs,'' ASME J. Turbomach., **120**, pp. 63–69.
[6] Taslim, M. E., and Spring, S. D., 1994, ''Effects of Turbulators Profile and Spacing on Heat Transfer and Friction in a Channel,'' J. Thermophys. Heat Transfer, **8**, pp. 555–562.
[7] Taslim, M. E., Li, T., and Spring, S. D., 1995, ''Experimental Study of the Effects of Bleed Holes on Heat Transfer and Pressure Drop in Trapezoidal Passages With Tapered Turbulators,'' ASME J. Turbomach., **117**, pp. 281–289.
[8] Shen, J. R., Wang, Z., Ireland, P. T., Jones, T. V., and Byerley, A. R., 1996, ''Heat Transfer Enhancement Within a Turbine Blade Cooling Passage Using Ribs and Combinations of Ribs With Film Cooling Holes,'' ASME J. Turbomach., **118**, pp. 483–434.
[9] Ekkad, S. V., Huang, Y., and Han, J. C., 1996, ''Detailed Heat Transfer Distributions in Two-Pass Smooth and Turbulated Square Channels With Bleed Holes,'' in: *Fundamentals of Augmented Single-Phase Convection*, Proc. 1996 National Heat Transfer Conference, Vol. 8, ASME HTD-Vol. 330, pp. 133–140.
[10] Rigby, D. L., Steinthorsson, E., and Ameri, A. A., 1997, ''Numerical Prediction of Heat Transfer in a Channel With Ribs and Bleed,'' ASME Paper No. 97-GT-431.
[11] Stephens, M. A., Shih, T. I.-P., and Civinskas, K. C., 1995, ''Computation of Flow and Heat Transfer in a Rectangular Channel With Ribs,'' AIAA Paper No. 95-0180.
[12] Bonhoff, B., Tomm, U., and Johnson, B. V., 1996, ''Heat Transfer Predictions for **U**-Shaped Coolant Channels With Skewed Ribs and With Smooth Walls,'' ASME Paper No. 96-TA-7.
[13] McDonough, J. M., Garzon, V. E., and Schulte, D. E., 1999, ''Effect of Film-Cooling Hole Location on Turbulator Heat Transfer Enhancement in Turbine Blade Internal Air-Cooling Circuits,'' ASME Paper No. 99-GT-141.
[14] Hippensteele, S. A., and Poinsatte, P. E., 1993, ''Transient Liquid-Crystal Technique Used to Produce High-Resolution Convective Heat-Transfer-Coefficient Maps,'' NASA TM-106083.
[15] Kline, S. J., and McClintock, F. A., 1953, ''Describing Uncertainties in Single-Sample Experiments,'' Mech. Eng. (Am. Soc. Mech. Eng.), **75**, pp. 3–8.

S. Acharya

V. Eliades

D. E. Nikitopoulos

Mechanical Engineering Department,
Louisiana State University,
Baton Rouge, LA 70803

Heat Transfer Enhancements in Rotating Two-Pass Coolant Channels With Profiled Ribs: Part 1–Average Results

The effects of ribs with different cross-stream profiles are investigated through detailed, surface mass (heat) transfer distributions along four active walls of a square duct containing a sharp 180 deg bend. The duct simulates two passes of an internal coolant channel in a gas turbine engine with ribs mounted on two opposite walls. Mass (heat) transfer measurements, taken using the naphthalene sublimation technique, are presented for a Reynolds number of 30,000, and rotation number of 0.3. Comparisons are made with conventional ribs having a rectangular cross section. It is shown that the use of certain profiled ribs provides considerable heat transfer enhancements over conventional ribs with the same blockage ratio in the duct. These enhancements are attributed to the generation of longitudinal vorticity (or secondary flows) by the profiled ribs in the channel. [DOI: 10.1115/1.1331539]

Introduction

A major focus in the development of improved gas turbine engines is the increase in the turbine inlet temperature, and the development of improved cooling strategies. Generally, both external (film) and internal cooling are applied. Internal cooling is achieved by air circulating in multipass (serpentine) flow channels inside the body of the blade. The heat transfer in these channels is typically augmented by using turbulence promoters (rib turbulators) that are cast into the channels. The rib turbulators typically have rectangular cross sections both in the streamwise and cross-stream planes, and the majority of the reported studies have utilized rectangular ribs.

Mass transfer distributions around a 180 deg bend in two-pass, square, smooth, and ribbed channels were presented by Han et al. [1] who used the naphthalene sublimation technique. Three Reynolds numbers, two rib heights, and two rib pitches were investigated. Chyu and Wu [2] investigated the effect of rib angle of attack in square channels for a single Reynolds number, and two different pitches. Kukreja et al. [3] examined the effects of straight and **V**-shaped ribs in a square channel and presented local Sherwood number distributions for two Reynolds numbers and three different pitches. Chen et al. [4] have recently presented detailed mass transfer data on all four walls of an internally ribbed coolant channel.

These studies were reported for stationary ribbed channels where the secondary flows are induced by anisotropies in the Reynolds stresses and by centrifugal effects induced by the bend. As noted above, a number of studies have used inclined trips or **V**-shaped trips and have shown that additional secondary flows are generated by these rib orientations, and that heat transfer is enhanced by the additional secondary flows. The objective of the present paper is to explore the generation of secondary flows using profiled ribs. Several different profiled ribs ranging from simple trapezoidal profiles to saw-tooth profiles are investigated.

In rotating ribbed channels, Coriolis forces play a dominant role and generate significant secondary flows that effect the surface heat transfer. There is a large body of literature on heat transfer in rotating ribbed channels with normal or skewed trips [5–8]. Coriolis forces lead to degradation of heat transfer on one wall and enhancement on the opposite wall. Also, skewed trips [5] are shown to provide greater heat transfer than normal trips [7], and indicate that the additional secondary flows generated by the skewed trips are effective even under conditions of rotation. However, these studies are based on heat transfer measurements and provide very limited resolution (only a few points per surface). Recently a series of papers using the naphthalene sublimation technique have been presented for rotating ribbed duct flows. These include the investigations of Hibbs et al. [9], Eliades et al. [10], Park et al. [11,12], and Kukreja et al. [13]. The mass transfer measurements provide detailed surface resolution and are invaluable in providing a more complete picture of the heat/mass transfer behavior. In the present study, we investigate heat/mass transfer in profiled ribs with rotation to examine whether the secondary flows generated by the rib profiles are capable of enhancing heat transfer under conditions of rotation.

The Experiments

The experiments are performed in a test apparatus designed for the study of mass transfer (sublimation of naphthalene) in a rotating duct that simulates the coolant channels of a turbine blade. Mass transfer measurements permit the acquisition of detailed local distributions of the Sherwood number, which can then be converted to Nusselt numbers using the heat–mass transfer analogy.

Apparatus. An overall schematic of the experimental setup is shown in Fig. 1. Compressed air is used as the working fluid for all experiments in order to simulate more closely the operational parameters in a turbine engine. The air is taken from large, exterior reservoirs in order to minimize flow disturbances caused by the compressor. The compressed air is passed through a meter run where the pressure is maintained constant by a pressure regulator. A concentric bore orifice plate is used to measure the mass flow rate in the meter run. Test section and meter run pressures are measured using mechanical pressure gages that have a 17.2 kPa (2.5 psi) resolution, and are controlled independently with gate valves located downstream of both the meter run and test section. Naphthalene-laden exhaust air is directed through flexible tubing to a fume hood.

The aluminum alloy test section consists of a. 69.85 mm (2.75 in.) tapered settling chamber; a frame that supports eight removable wall frames; and a removable 180 deg bend. These major components are secured in a flange-like manner, using O-rings between all parts to prevent air leakage. When assembled, the test

---

Contributed by the International Gas Turbine Institute and presented at the 45th International Gas Turbine and Aeroengine Congress and Exhibition, Munich, Germany, May 8-11, 2000. Manuscript received by the International Gas Turbine Institute February 2000. Paper No. 2000-GT-227. Review Chair: D. Ballal.

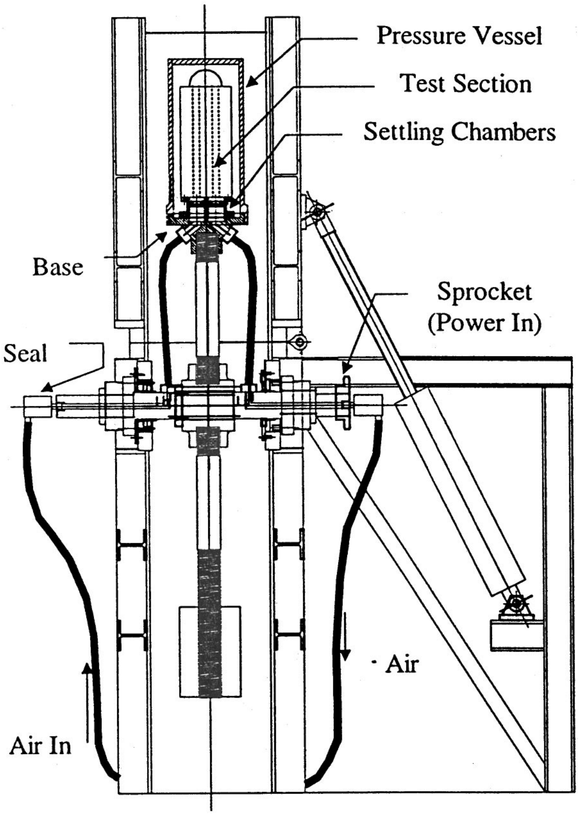

Fig. 1 Schematic of the rotating experimental facility

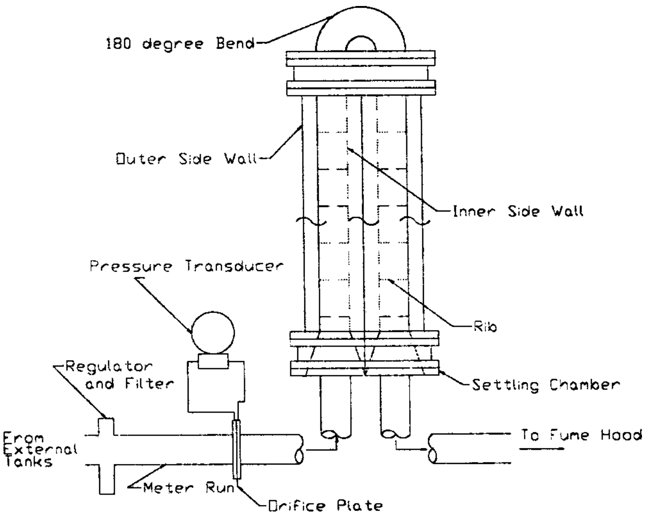

Fig. 2 Schematic of the test section

section forms 25.4×25.4×304.8 mm (1×1×12 in.) long inlet and outlet sections, 38.1 mm (1.5 in.) apart that are connected by the 180 deg 25.4×25.4 mm (0.1×1 in.) square cross-sectional bend. The first baseline rectangular-profile aluminum ribs are 2.54 ×2.54×25.4 mm (0.1×0.1×1.0 in.) long and have holes on either end for mounting (Fig. 2). The ribs are positioned to provide a baseline $P/e=10.5$. A second baseline rectangular profile ribs with higher blockage ratio and $P/e=7$ was also studied. Steel, 0.635 mm (0.025 in.) diameter music wire is inserted into these holes to secure them to the sidewalls of the test section. The ribs are mounted only on opposite walls and are not coated with naphthalene.

Detailed surface profiles of the cast surfaces are required for local mass transfer results. These profiles are obtained by moving the walls under a fixed, linear variable differential transducer (LVDT) type profilometer. A bi-directional traversing table is securely mounted to the platform of a milling machine. The plates are secured to a 15.875 mm (0.625 in.) thick tooling aluminum plate which is fixed to the traversing table. This mounting plate has been machined with an assortment of pin supports and machine screw taps to ensure the walls not only lie flat on the plate, but also are mounted in the same location for all scans. A custom written program running on a personal computer is used to control the motion of the traversing table through microstep drive motors with a 0.00127 mm (0.00005 in.) step size.

Procedure. Fresh, 99 percent pure naphthalene crystals are melted in a heavy-walled glass beaker with an electric heating element. The clean test section walls are clamped to stainless steel plates that have been polished to a mirror-like finish. Molten naphthalene is quickly poured into the hollow cavity of the plate frame to fill completely the region between the walls. The cast plates stand for at least eight hours in a fume hood to attain thermal equilibrium with the laboratory.

Each wall is then separated from the casting plate and mounted to the mounting plate for scanning. After scanning, the plates are stored in an air-tight container, saturated with naphthalene vapor, to hinder natural sublimation until the test section is assembled.

Test section assembly is begun by first inserting the two inner sidewalls and then attaching the bend. Any ribs or vortex generators are then attached to these walls and the two outer sidewalls are mounted. The alignment of all ribs is checked before the four top and bottom walls are assembled. After the experiment is over, the test section is disassembled and the walls are placed in the storage container until they are scanned again.

Data Reduction. Mass flow rate in the meter run is calculated from measurements of temperature, pressure, and differential pressure using standard equations for concentric bore orifice meters [14,15].

Naphthalene sublimation depth is calculated from the two surface profiles for each wall. Each profile is normalized with respect to a reference plane computed from three points scanned on the aluminum surface of the walls. The difference between the normalized profiles gives the local sublimation depth.

The local mass flux $\dot{m}''$ at each location is calculated from the following expression:

$$\dot{m}''=\rho_s\delta/\Delta t \tag{1}$$

where ρ_s is the density of solid naphthalene, δ is the local sublimation depth, and Δt is the duration of the experiment. Vapor pressure at the wall p_w is calculated from the following equation [16]:

$$\log_{10}(p_w)=A-B/T_w \tag{2}$$

where A and B are constants (11.884 and 6713, respectively) and T_w is the absolute wall temperature. Wall vapor density ρ_w is then calculated using the perfect gas law. Bulk vapor density of naphthalene $\rho_b(x)$ is obtained by mass conservation balances of naphthalene from the inlet $(x=0)$ to the streamwise location (x).

The local mass transfer convection coefficient h_m is then calculated as follows:

$$h_m=\dot{m}''/(\rho_w-\rho_b(x)) \tag{3}$$

The binary diffusion coefficient D_{n-a} for naphthalene sublimation in air is taken as the ratio of the kinematic viscosity of air ν to the Schmidt number for naphthalene–air (Sc=25.). The local Sherwood number is then calculated by:

$$\mathrm{Sh}=h_mD/D_{n-a}=h_mD\mathrm{Sc}/\nu \tag{4}$$

where D is the hydraulic diameter of the test section. Sherwood number results presented in this study have been scaled with the McAdams correlation for fully developed smooth wall pipe flow:

$$Sh_0 = 0.023\, Re^{0.8}\, Sc^{0.4} \tag{5}$$

where Re is the duct Reynolds number.

Comparison of heat and mass transfer results can be done through the use of the heat–mass transfer analogy [16]:

$$Nu = Sh(Pr/Sc)^{0.4} \tag{6}$$

where Nu is the Nusselt number and Pr is the Prandtl number of air. In this paper, however, we have simply presented the scaled Sherwood number ratio Sh/Sh_0, which should be interpreted as the scaled Nusselt number ratio Nu/Nu_0, where Nu_0 is the correlated fully developed Nusselt number, analogous to Sh_0.

Uncertainty. Uncertainties for all computed values are estimated using the second-power equation method [17]. The estimates for these experiments are comparable to previously reported values for both heat transfer and mass transfer studies, but are believed to be conservative.

Volume flow rate and duct Reynolds number (Re) uncertainties are estimated to be less than 10 percent for $Re > 6000$. The reported resolution of the LVDT is 0.00127 mm (0.00005 in.) while the analog-to-digital (A/D) board is reported to have an accuracy of. 0.002 mm (0.000078 in.) in a 12 kHz acquisition rate, 16-bit resolution mode. Experimental tests of accuracy and repeatability for the entire acquisition system indicate a sublimation depth uncertainty of 0.0038 mm (0.00015 in.). Sublimation depths are maintained at about 0.152 mm (0.006 in.) by varying the duration of the experiment. This target depth was selected to minimize uncertainties in both depth measurement and changes in duct cross section area. These uncertainties were found to be 1 and 3 percent, respectively. The resulting experimental duration was around 90 minutes for $Re = 30{,}000$.

Vapor density uncertainty based on measured quantities is negligible for both wall and bulk values. Overall uncertainty in Sherwood number calculation is about 8 percent and varies slightly with Reynolds number (<1 percent).

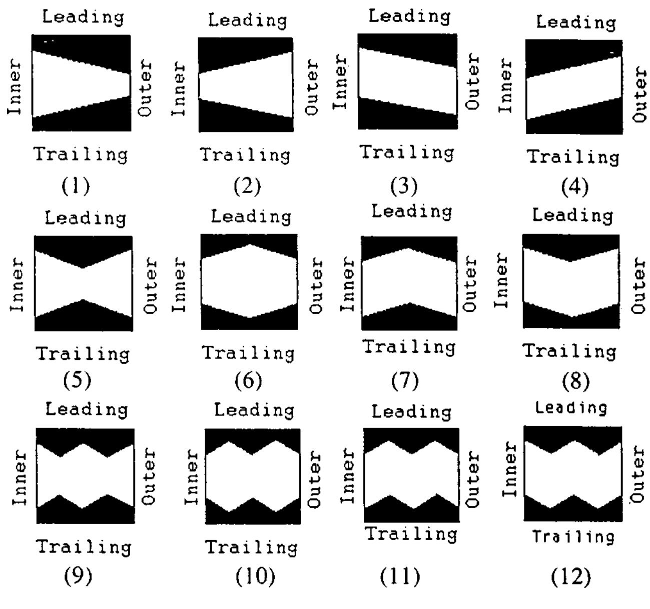

Fig. 3 Schematic of various rib profiles examined. Profiles include trapezoidal shapes (profile configurations 1, 2, 3, 4), pyramid-valley shapes (profile configurations 5, 6, 7, 8) and saw-tooth shape (profile configurations 9, 10, 11, 12).

Experimental Results

The results presented here consist of the area-averaged Sherwood numbers for each of the four active walls (top, bottom, outer side, and inner side) in the inlet and outlet square ducts of a two-pass module with a 180 deg bend. Spanwise-averaged distributions are also presented. In this paper, the spanwise direction refers to the lateral dimension corresponding to the channel width.

Experiments have been carried out for ribbed walls at Reynolds numbers of 30,000, and for rotation number of 0.3. The rib angle of attack for all cases considered was 90 deg. Two baseline (rectangular profile) rib-pitch to height (P/e) values were considered: $P/e = 10.5$ and 7. For the profiled ribs, the P/e ratio based on the minimum height is 10.5, while that based on the average height is 7. Note that the average height of the profiled ribs are selected so that it has the same blockage ratio (cross-sectional area occupied by the ribs/total cross-sectional area of the channel) as the rectangular profile rib.

Twelve different rib configurations were examined in this study and are shown in Fig. 3. These configurations were formed by combining four generic profiles: trapezoidal profiles, pyramid profiles, valley profiles, and saw-tooth profiles. The results from these

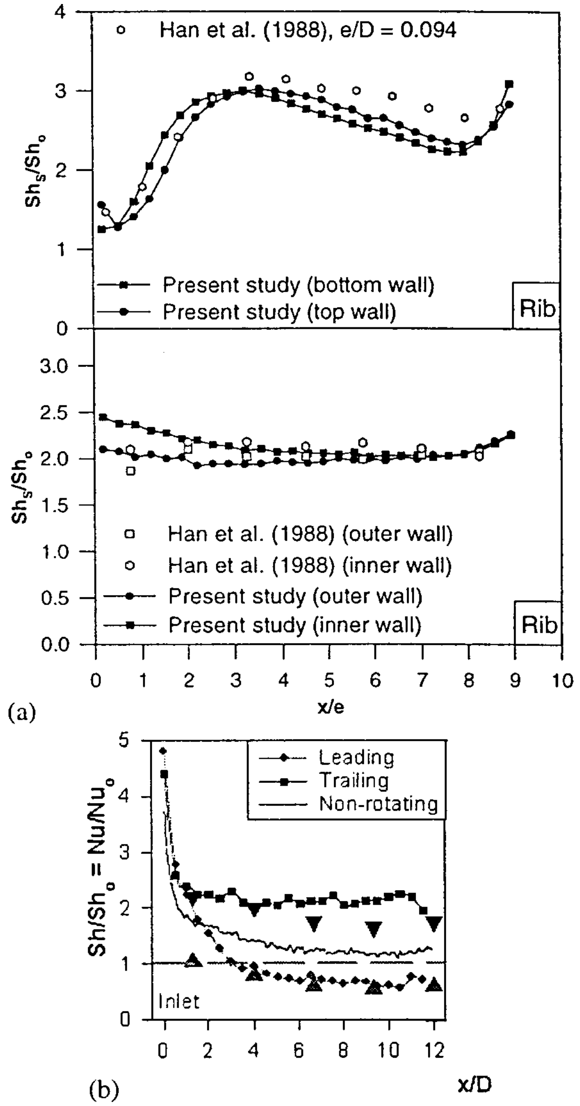

Fig. 4 Comparison of present measurements with published data: (*a*) stationary, comparisons with Han et al. [1]; (*b*) rotating, smooth inlet channel, Re=5000, Ro=0.2. Triangular symbols are data from Han et al. [20].

(a) Leading-Ribbed

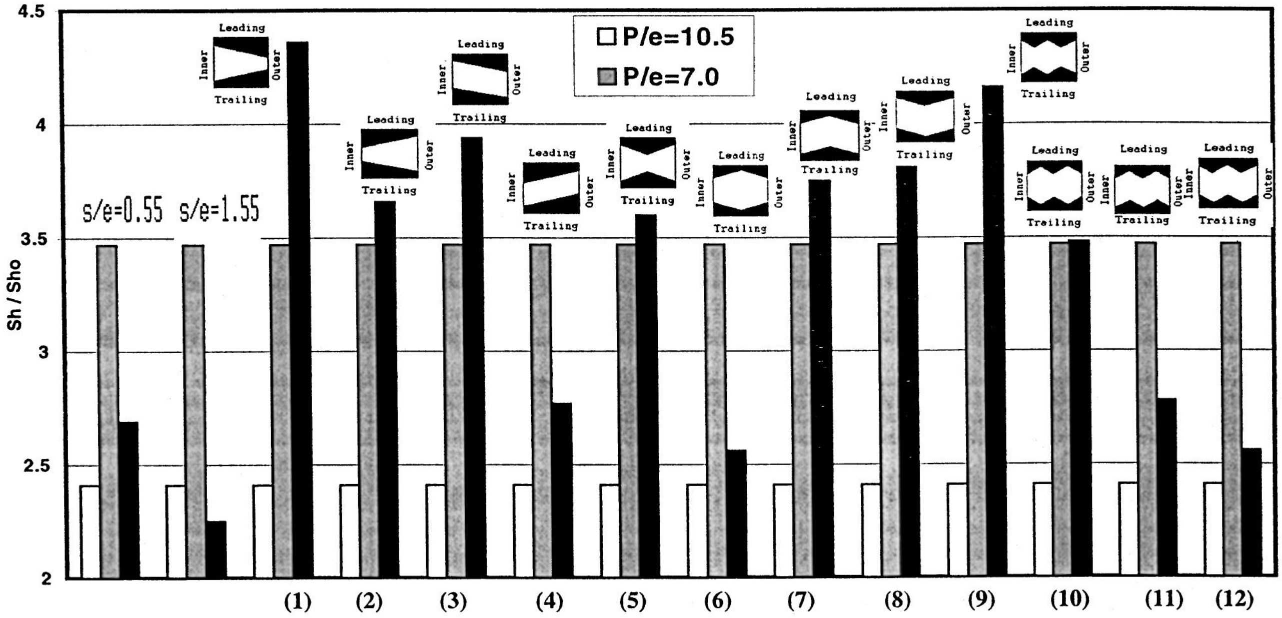

(b) Trailing Wall-Ribbed

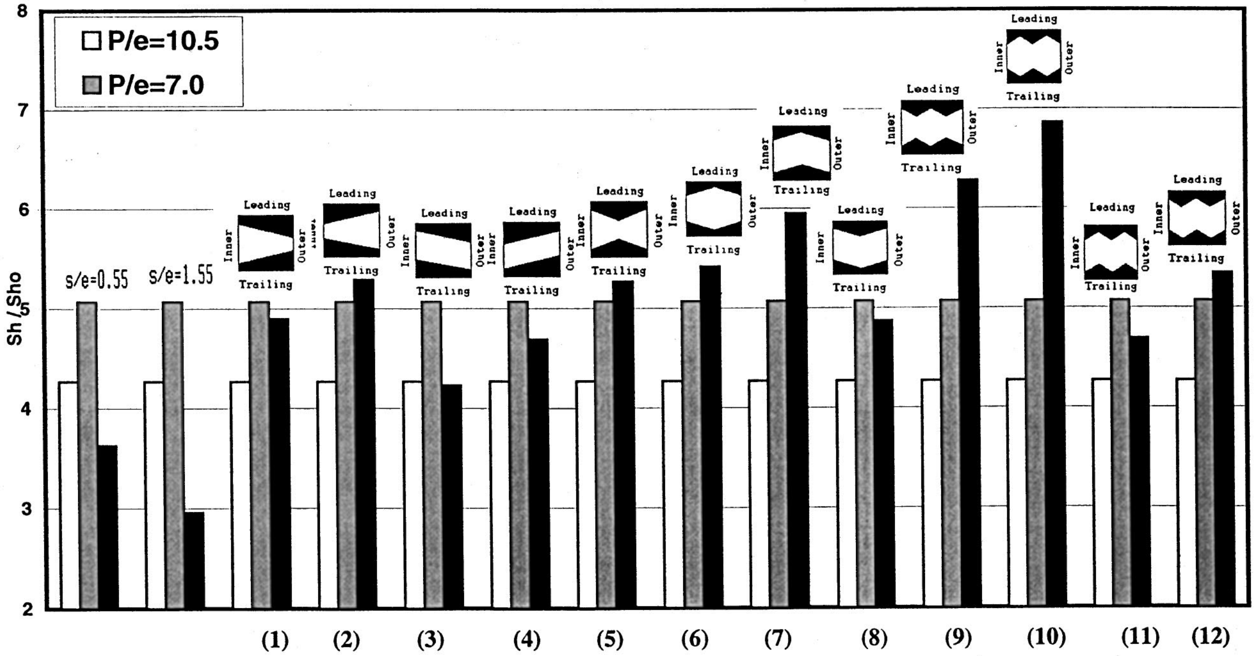

Fig. 5 Fully developed cell averages of the leading and trailing surfaces of the inlet duct at Re=30,000 and Ro=0.3. Darkest shade represents profiled ribs, intermediate shade represents rectangular ribs with $P/e=7.0$, and lightest shade represents rectangular ribs with $P/e=10.5$.

studies are also compared with those of an earlier study by Eliades et al. [10] where the effect of cylindrical vortex-generators placed above the ribs was examined for two different spacing to rib height values ($s/e=0.55$ and $s/e=1.55$).

It should be noted that buoyancy effects are known to be negligible in naphthalene sublimation experiments. Estimates of the Grashof number based on $\Delta\rho/\rho$ were found to be extremely small in the present experiments.

Comparisons With Previous Experiments. The present measurements were compared with three past mass-transfer based studies [1–3] as well as two previous heat-transfer studies [18,19] under stationary conditions. The agreement between the present measurements and all of these other studies was in general very good. The comparisons with Han et al. [1] for a single inter-rib pitch and Re=30,000 are shown in Fig. 4(*a*) in terms of the spanwise-averaged Sherwood number scaled by Sh_0, the value of the Sherwood number corresponding to fully developed pipe flow. As can be seen, the agreement is very good.

Comparisons are also made with the data of Han et al. [20] under rotating conditions (Fig. 4(*b*)). Again the overall agreement with the published data under rotating conditions is quite good, confirming the accuracy and reliability of the reported measurements.

(a) Inner Wall-Smooth

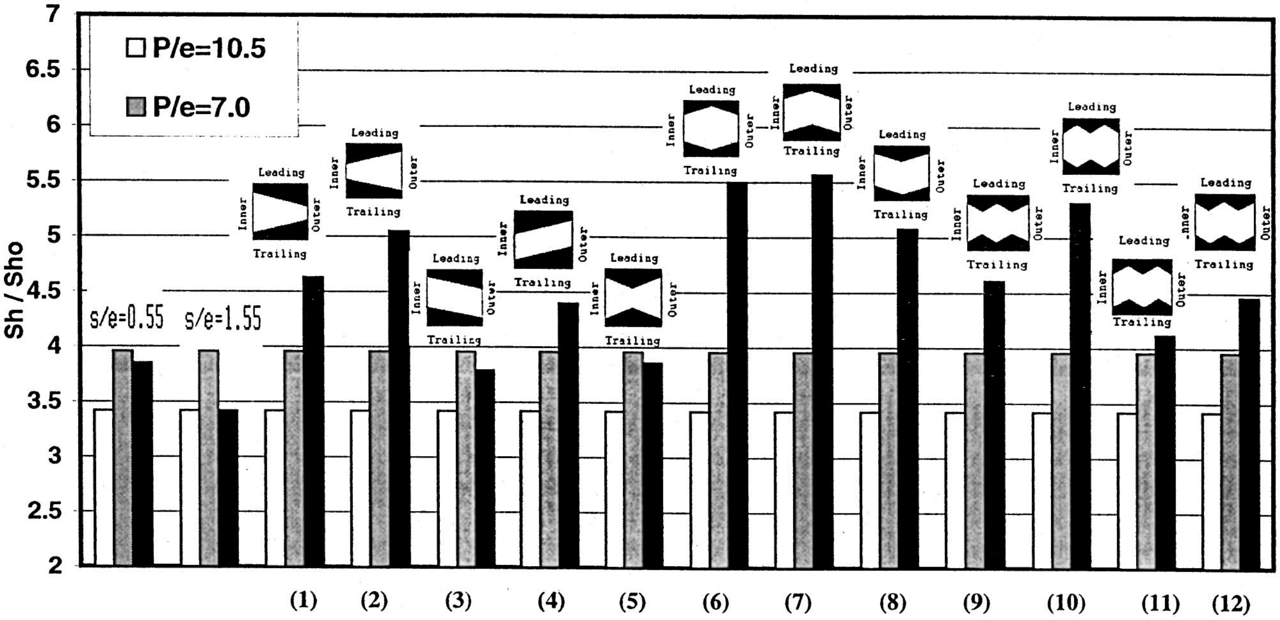

(b) Outer Wall-Smooth

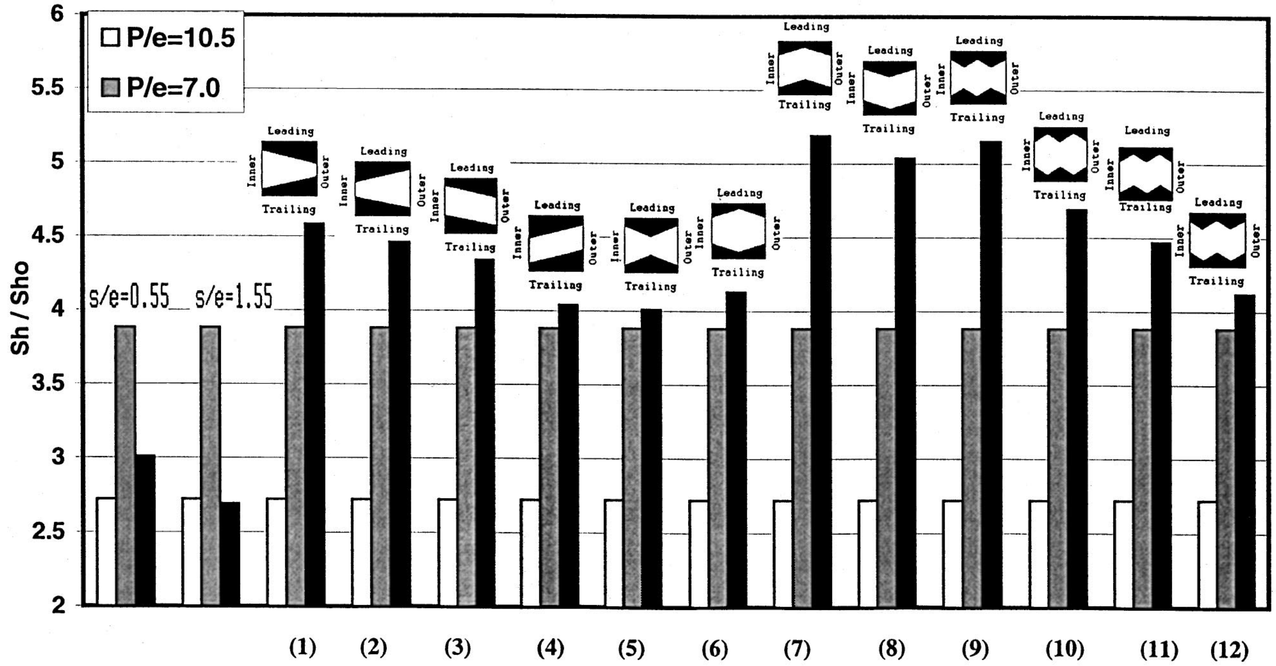

Fig. 6 Fully developed cell averages of the inner and outer wall of the inlet duct at Re=30,000 and Ro=0.3. For legends, see Fig. 5.

Results for Profiled Ribbed Channels

Cell-Averaged Sherwood Numbers. Cell averages in the periodically developed cells are presented for the inlet duct in Fig. 5 (for the ribbed leading and trailing surfaces) and in Fig. 6 (for the smooth outer and inner sidewalls). Corresponding values for the outlet duct are presented in Figs. 7 and 8. These cell averages are computed using all measured points in the spanwise (30 points) and streamwise directions (28 points) in the periodically developed cell. Thus, in computing these averages, a fairly fine grid of measurement locations was used with 840 points over a 1-in. square area. This resolution should be contrasted with thermocouple based heat transfer studies reported for rotating channels where typically one measurement point is located over a corresponding area. In Figs. 5–8, each of the twelve configurations tested is indicated by a small picture showing the rib profile, and are referred to as profile configurations 1–12 in the text. These profile configuration numbers are indicated against the profiles sketched in Fig. 3. Also shown in Figs. 5–8 are results from the rib-rod configuration of Eliades et al. [10], where a cylindrical vortex generator or rod is placed at a distance *s* over a rib of height *e*. Results shown are for two s/e values of 0.55 and 1.55. Shown against the results from the profiled ribs (darkest shade) and the rib-rod configurations are the results for the rectangular-

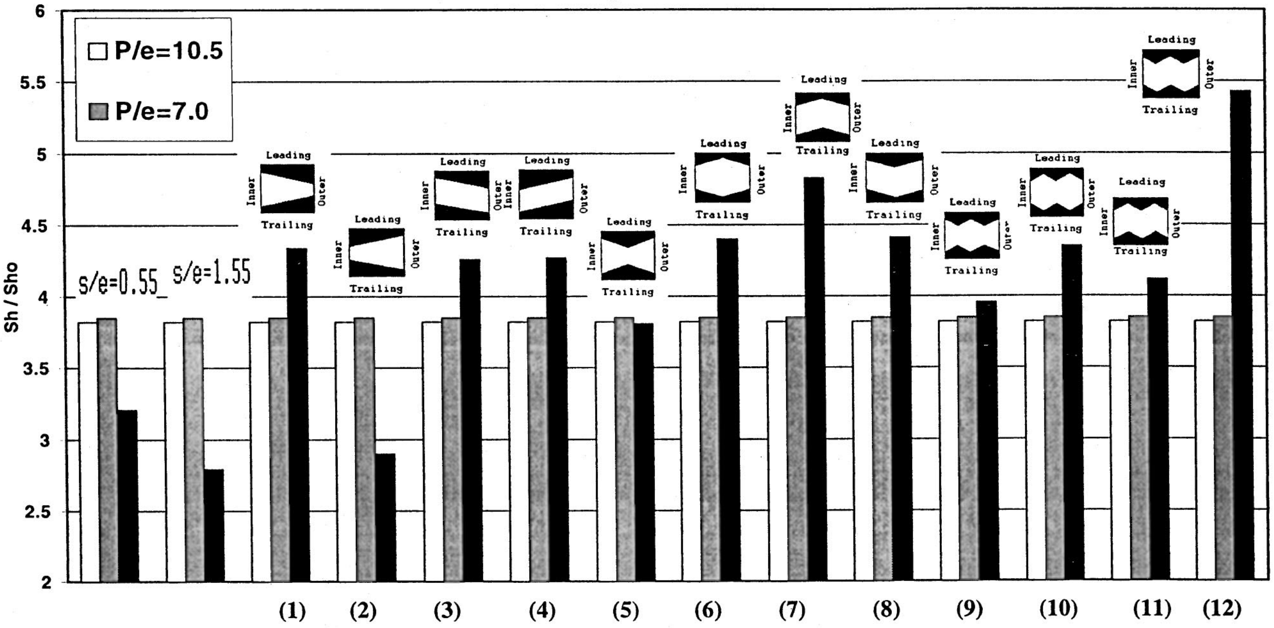
(a) Leading Wall-Ribbed

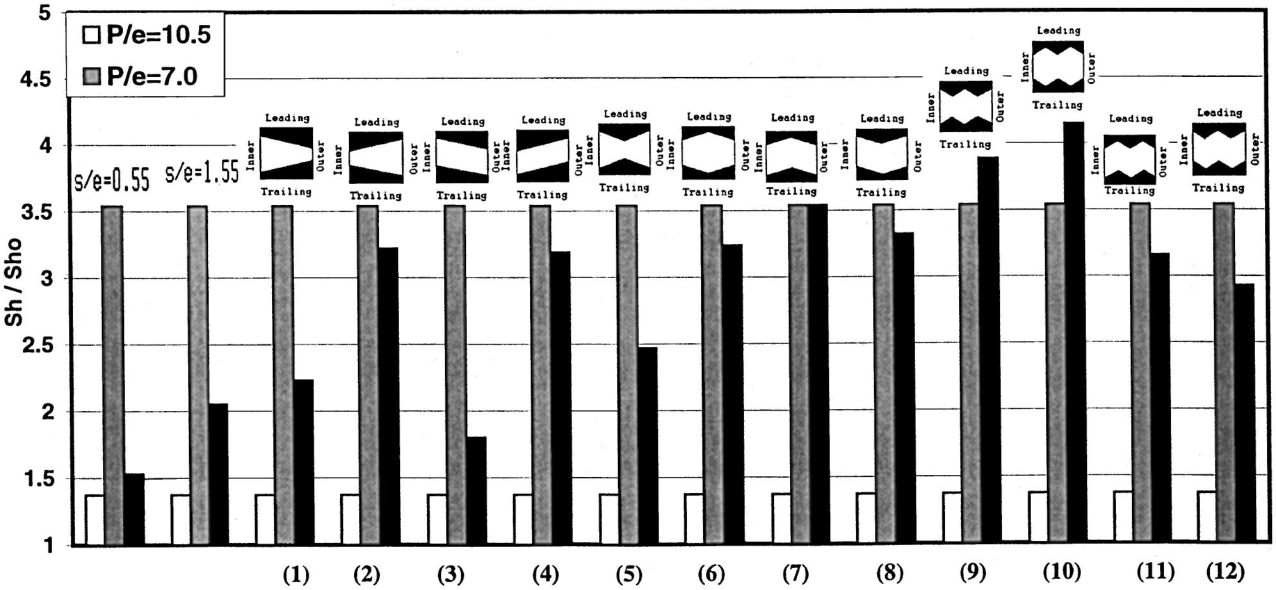
(b) Trailing Wall-Ribbed

Fig. 7 Fully developed cell averages of the leading and trailing wall of the outlet duct at Re=30,000 and Ro=0.3. For legends, see Fig. 5.

profile ribs with $P/e=7$ (intermediate shade) and $P/e=10.5$ (rectangular white shade). The $P/e=7$ represents the case where the rectangular-profile rib has the same blockage ratio as the profiled rib or the rib-rod pair, while $P/e=10.5$ corresponds to the case where the height of the rectangular rib is equal to the smallest vertical height along the profiled rib.

In the inlet duct, Figs. 5 and 6 indicate that the heat transfer enhancement induced by the profiled ribs is not uniform along all four walls, and that for a specific profile some walls show enhancement while other walls do not show any enhancement. This is due to the interaction of the rib-profile-induced secondary flows and the Coriolis forces, which generate complex secondary flows that influence each surface differently. In general, however, the smooth sidewalls show enhancement for the majority of the rib profiles, indicating that the profile-induced secondary flows improve spanwise mixing. In examining the stabilized leading ribbed surface (where rotation leads to a reduction of heat transfer), profiles 1 (trapezoidal) and 9 (saw-tooth with 2 pyramids and a valley) show the highest Sherwood numbers with 20–25 percent enhancements over the $P/e=7$ rectangular rib case (Fig. 5(*a*)). The enhancements over the $P/e=10.5$ rectangular-profile rib is considerably greater with enhancement levels exceeding 100 percent in certain cases. Along the destabilized trailing surface (where rotation leads to an increase in heat transfer), profiles 9 (saw-tooth with 2 pyramids and a valley) and 10 (saw-tooth with 1 pyramid and 2 valleys) show the highest enhancements that are respectively 22 and 36 percent over the $P/e=7$ baseline case (Fig. 5(*b*)). Note that no enhancement along the trailing surface is noted for the trapezoidal profile 1, for which approximately a 25 percent enhancement was noted along the leading surface. Such an en-

(a) Inner Wall-Smooth

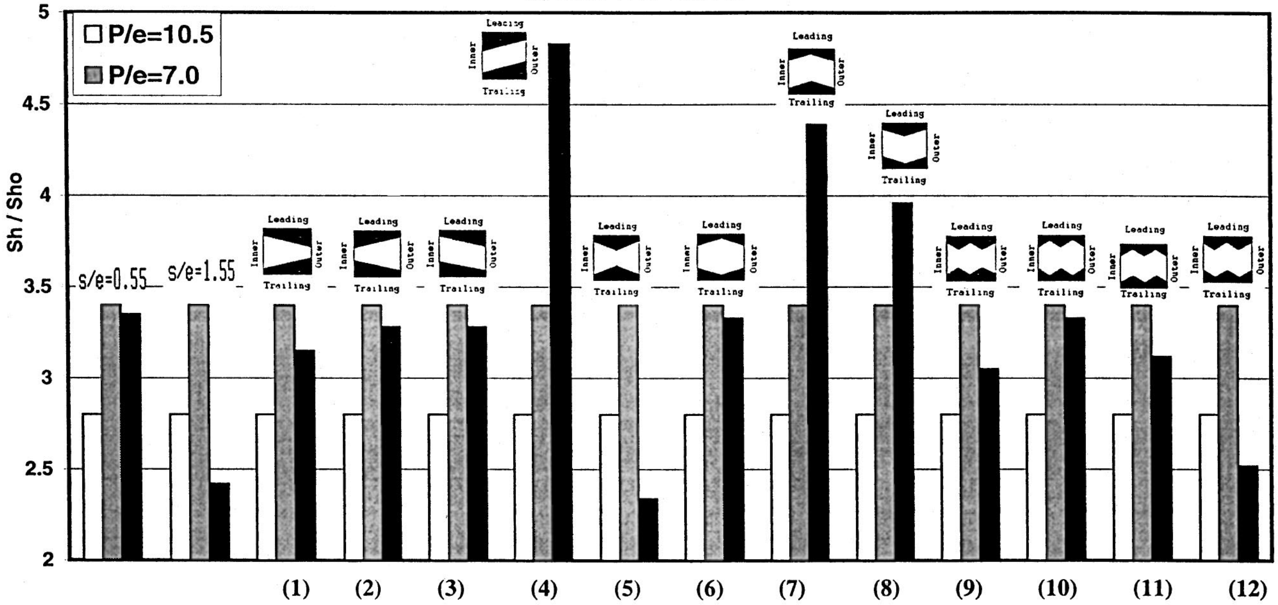

(b) Outer Wall-Smooth

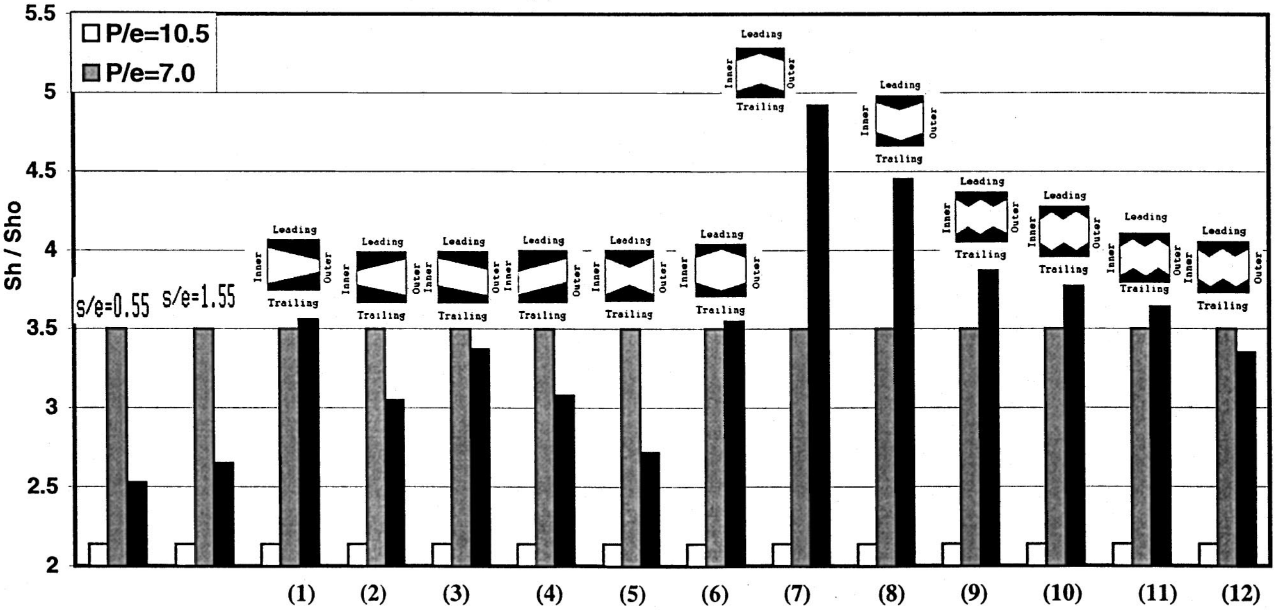

Fig. 8 Fully developed cell averages of the inner and outer wall of the outlet duct at Re=30,000 and Ro=0.3. For legends, see Fig. 5.

hancement along the stabilized surface only partially mitigates the effect of Coriolis-induced secondary flows, and leads to heat transfer values along the leading and trailing surfaces that are closer to each other than the rectangular rib case. Profile 9 shows enhancements along both the leading and trailing surfaces with an average enhancement of over 20 percent along both surfaces. For this profile, enhancements are observed along both sidewalls (Fig. 6) with the outer wall experiencing an enhancement of greater than 35 percent. Profile 10, which exhibited a strong enhancement on the trailing wall, also exhibits good enhancement along the sidewalls ranging from about 20 percent (outer wall) to over 30 percent (inner wall). As noted earlier, Fig. 6 shows that the majority of the profiles show enhancements along the sidewalls. The peak enhancement levels over the $P/e=7$ rectangular rib case are approximately 25 percent along the leading surface (profile 1), 36 percent along the trailing surface (profile 10), and over 35 percent along the sidewalls (profile 9).

Figures 5 and 6 indicate that the rod-rib combination actually degrades heat transfer compared to the $P/e=7$ baseline case. Modest enhancements can be seen compared to the $P/e=10.5$ case where the baseline rib height is equal to the height of the rib alone in the ribrod case. The $P/e=7$ baseline case represents a thicker rib with a height equal to the combined rib-rod thickness. Contrary to this behavior, the profiled ribs exhibit heat transfer rates even greater than the $P/e=7$ baseline, and appear to show potential in enhancing heat transfer along the inlet duct.

The surface heat/mass transfer along all four walls of the outlet duct are shown in Figs. 7 and 8. Focusing attention on profiles 9

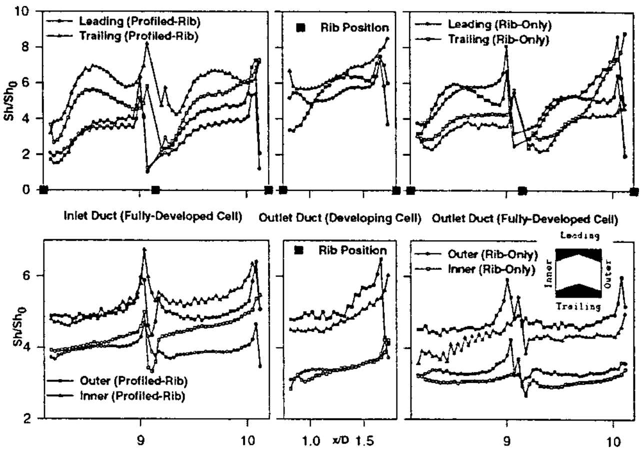

Fig. 9 Spanwise-averages in the high-resolution cells for rectangular ribs and profiled ribs: Configuration 7 (top wall–valley, bottom wall–pyramid) Re=30,000, Ro=0.3, and $P/e=7.0$

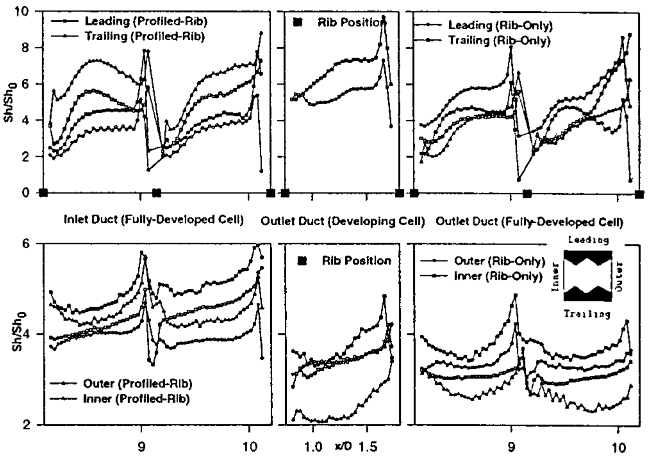

Fig. 10 Spanwise-averages in the high-resolution cells for rectangular ribs and profiled ribs: Configuration 9 (saw-tooth shaped with 2-pyramids-1-valley), Re=30,000, Ro=0.3, and $P/e=7.0$

and 10, which exhibited strong enhancements in the inlet duct, it can be observed that they also do well along the outlet duct, although the enhancements are lower than those in the inlet duct. The highest enhancement is noted along the stabilized trailing surface where profile 10 exhibits nearly a 20 percent increase in surface heat/mass transfer. The corresponding increase on the destabilized leading surface is smaller, and as a consequence, the heat transfer along the leading and trailing surfaces are observed to be closer to each other relative to the baseline rectangular rib case. While profiles 9 and 10 show the highest heat transfer on the trailing surface, profiles 7 and 12 exhibit the highest heat transfer along the leading surface, and profile 7 appears to exhibit the highest combined heat/mass transfer along the outer and inner sidewalls. The maximum enhancements on each wall are approximately 20 percent on the trailing surface (profile 10), 45 percent on the leading surface (profile 12), 36 percent on outer wall (profile 7), and 40 percent on inner wall (profile 4).

Compared to the $P/e=10.5$ baseline, significant enhancements in excess of 100 percent can be observed with the profiled ribs. As an example, profiles 9 and 10 show heat trailing surface heat transfer that are nearly 2.5 to 3 times greater than the $P/e=10.5$ baseline value.

The rib-rod configuration shows modest enhancements with respect to the $P/e=10.5$ baseline along the sidewalls and the trailing wall, but shows degradation when compared with the $P/e=7$ baseline. These observations are consistent with those in the inlet duct.

An overall assessment of the various profile shapes indicate that profiles 7, 9, and 10 provide the best performance. Attention is turned next to the spanwise-averaged Sherwood number distribution for these profiled ribs. Detailed distributions for profiled ribs 7 and 10 for both stationary and rotating conditions are given in a companion paper [21].

Spanwise-Averaged Sherwood Numbers. The spanwise-averaged Sherwood numbers are presented for profiles 7, 9, and 10 in Figs. 9, 10, and 11. The distributions are presented for two inter-rib modules in the inlet duct, the inter-rib module following the bend and two inter-rib modules in the outlet duct. The ribbed leading and trailing surface distributions are presented in the top row while the sidewalls are presented along the bottom row. The baseline $P/e=7$ case (open symbols) show the peak in the vicinity of the reattachment point and just upstream of the rib along the leading and trailing surfaces. The relative magnitudes of these peaks indicate that the peak just upstream of the rib is generally greater than the peak associated with the reattachment. Along the smooth surfaces, the Sherwood number distribution shows a peak in the vicinity of the rib induced by the increase in turbulence associated with the separated shear layer past the rib. The enhanced turbulence induced by the ribs reported by Acharya et al. [22,23] correlates well with the increased heat transfer along the sidewalls. Further, due to rotational effects, the trailing surface heat transfer exceeds that of the leading surface along the inlet duct and the leading surface heat transfer exceeds that of the trailing surface along the outlet duct.

The inner and outer wall heat transfer rates are generally comparable, with the outer wall exceeding the inner wall as the bend is approached in the inlet duct. In the first module past the bend, the dominant effect appears to be due to Coriolis forces, and bend-induced secondary flows do not appear to play a significant role.

In examining the heat transfer distributions with the profiled rib (profile 7, with a pyramid rib and a valley rib), the general trends are seen to be similar to the baseline case, except that the heat transfer rates are higher. Along the inlet duct, enhancement is usually noted along all four walls, with comparable enhancements along the trailing and side surfaces (of the order of 20–25 percent), and smaller enhancements along the leading surface. Along the outlet duct, the enhancements on the leading and trailing surfaces are either small or degradation is observed. However, the

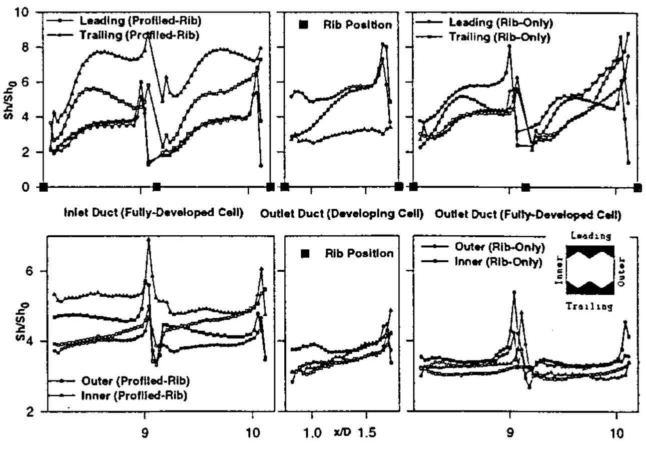

Fig. 11 Spanwise-averages in the high-resolution cells for rectangular ribs and profiled ribs: Configuration 10 (saw-tooth shaped with 1-pyramid-2-valley), Re=30,000, Ro=0.3, and $P/e=7.0$

sidewalls of the outlet duct show quite significant enhancements over the baseline rectangular rib case. The consistent enhancements along the sidewalls in the inlet and outlet duct clearly point to enhanced spanwise mixing with the profiled ribs.

The saw-tooth profiles 9 and 10 had earlier been shown to exhibit good behavior, particularly in the inlet duct. These trends are confirmed by the spanwise-averaged profiles in Figs. 10 and 11. For both profiles 9 and 10, the enhancement levels in the inlet duct are considerably higher than that for profile 7. For example, profile 10 shows local enhancement levels of the order of 40–60 percent along the sidewalls and trailing surface of the inlet duct (Fig. 11). However, the enhancement levels along the leading surface of the inlet duct and along the outlet duct are not as significant. These differences in the inlet duct, where consistent enhancements are noted, and the outlet duct, where the enhancements are more muted and even degradation is observed, indicate that in the inlet duct, the profile-induced secondary flows interact with the Coriolis induced flows in such a manner that the overall mixing and heat transfer are enhanced. Along the outlet duct, the Coriolis-induced secondary flows are directed opposite to that in the inlet duct, and their interaction with the profile-induced flows does not produce the enhancements observed in the inlet duct. Although not considered in this study, a different profile-rib pair in the outlet duct may be necessary to obtain heat transfer enhancements comparable to those in the inlet duct.

Concluding Remarks

Mass transfer studies in a two-pass coolant channel are performed under conditions of rotation ($\mathrm{Ro}=0.3$, $\mathrm{Re}=30{,}000$) with rectangular ribs (baseline case) and twelve different profiled rib configurations. Only the leading and trailing surfaces are ribbed while the sidewalls are smooth. Comparison is made with the baseline case having the same blockage ratio as the profiled rib.

It is observed that the profiled ribs generally enhance heat transfer over the baseline case. This is particularly true in the inlet duct and along the smooth sidewalls. These enhancements are caused by the generation of secondary flows and longitudinal vorticity that interact with the Coriolis induced secondary flows in the coolant channel.

Both cell-averaged and spanwise-averaged results are presented. The three profile configurations that appear to hold the greatest promise are profiles 7, 9, and 10. Profile 7 corresponds to a pyramid-shaped rib on one wall and a valley-shaped rib on the opposite wall, and shows good enhancement along the sidewalls of the inlet and outlet duct. Profiles 9 and 10 represent saw-tooth ribs on both leading and trailing surfaces, and exhibit good heat transfer enhancements along the trailing surface of the inlet duct and the sidewalls. However, considerable enhancements are not observed along the leading surface of the inlet duct and the leading and trailing surfaces of the outlet duct. The cell-averaged enhancements noted are of the order of 20–40 percent, while the spanwise-averaged enhancements are noted to have values as high as 50–60 percent.

Acknowledgments

This research was sponsored by the U. S. Department of Energy's Morgantown Energy Technology Center, under Contract No. DE-FC2192MC29061 with South Carolina Energy Research and Development Center, 386-2 College Ave., Clemson, SC, 29634-5181.

Nomenclature

D = duct hydraulic diameter, m
D_{n-a} = binary diffusion coefficient for naphthalene–air, m^2
e = rib height, m
h_m = local mass transfer convection coefficient, m/s
$\dot{m}''$ = local mass flux, kg/m^2/s
Nu = Nusselt number
Nu_0 = Nusselt number for fully developed flow
P = rib pitch, m
Pr = Prandtl number
p_w = naphthalene vapor pressure at the wall, N/m^2
Re = test section Reynolds number$=V_{av}D/\nu$
Ro = rotation number$=\Omega D/V_{av}$
Sh = Sherwood number
Sh_0 = Sherwood number for fully developed pipe flow
Sc = Schmidt number
T_w = absolute wall temperature, K
V_{av} = average streamwise component of velocity in the coolant channel
x, y, z = cross-stream coordinates, m
ρ_s = density of solid naphthalene, kg/m^3
Δt = duration of experiment, s
δ = local sublimation depth, m
ρ_w = naphthalene vapor density at the wall, kg/m^3
ν = kinematic viscosity of air, m^2/s
$\rho_b(x)$ = bulk vapor density of naphthalene, kg/m^3
Ω = rotational speed, rad/s

References

[1] Han, J. C., Chandra, P. R., and Lau, S. C., 1988, ''Local Heat/Mass Transfer Distributions Around Sharp 180° Turns in Two-Pass Smooth and Rib-Roughened Channels,'' ASME J. Heat Transfer, **110**, pp. 91–98.

[2] Chyu, M. K., and Wu, L. X., 1989, ''Combined Effects of Rib Angle-of-Attack and Pitch-to-Height Ratio on Mass Transfer From a Surface With Transverse Ribs,'' Exp. Heat Transfer, **2**, pp. 291–308.

[3] Kukreja, R. T., Lau, S. C., and McMillin, X., 1992, ''Local Heat/Mass Transfer Distribution in a Square Channel With Full and **V**-Shaped Ribs,'' Int. J. Heat Mass Transf., **36**, pp. 2013–2020.

[4] Chen, Y., Nikitopoulos, D., Hibbs, R., Acharya, S., and Myrum, T., 1999, ''Detailed Heat/Mass Transfer Distribution in a Ribbed Coolant Passage,'' Int. J. Heat Mass Transfer, in press.

[5] Johnson, B. V., Wagner, J. H., Steuber, G. D., and Yeh, F. C., 1994, ''Heat Transfer in Rotating Serpentine Passages With Trips Skewed to the Flow,'' ASME J. Turbomach., **116**, pp. 113–123.

[6] Fann, S., Yang, W. J., and Zhang, N., 1994, ''Local Heat Transfer in a Rotating Serpentine Passage With Rib-Roughened Surfaces,'' Int. J. Heat Mass Transf., **37**, pp. 217–228.

[7] Wagner, J. H., Johnson, B. V., Graziani, R. A., and Yeh, F. C., 1992, ''Heat Transfer in Rotating Serpentine Passages With Trips Normal to the Flow,'' ASME J. Turbomach., **114**, pp. 847–857.

[8] Taslim, M. E., Rahman, A., and Spring, S. D., 1991, ''An Experimental Investigation of Heat Transfer Coefficients in a Spanwise Rotating Channel With Two Opposite Rib-Roughened Walls,'' ASME J. Turbomach., **113**, pp. 75–82.

[9] Hibbs, R., Acharya, S., Chen, Y., and Nikitopoulos, D., 1996, ''Heat/Mass Transfer in a Two-Pass Rotating Smooth and Ribbed Channel,'' in: *Fundamentals of Heat Transfer With Impinging Jets*, ASME HTD-Vol. 324, p. 123.

[10] Eliades, V., Nikitopoulos, D. E., and Acharya, S., 1999, ''Detailed Mass Transfer Distribution in Rotating Two-Pass Ribbed Coolant Channels With Vortex Generators,'' ASME Paper No. 99-GT-424.

[11] Park, C. W., Lau, S. C., and Kukreja, R. T., 1998, ''Heat/Mass Transfer in a Rotating Two-Pass Channel With Transverse Ribs,'' J. Thermophys. Heat Transfer, **12**, No. 1, pp. 80–86.

[12] Park, C. W., Lau, S. C., and Kukreja, R. T., 1998, ''Heat/Mass Transfer in a Rotating Channel With Ribs of Various Sizes on Two Walls,'' J. Thermophys. Heat Transfer, **12**, No. 3, pp. 452–454.

[13] Kukreja, R. T., Park, C. W., and Lau, S. C., 1998, ''Heat (Mass) Transfer in a Rotating Two Pass Square Channel–Part II: Local Transfer Coefficient, Smooth Channel,'' Int. J. Rot. Mach., **4**, No. 1, pp. 1–15.

[14] Stearns, R. F., Johnson, R. R., Jackson, R. M., and Larson, C. A., 1951, *Flow Measurement With Orifice Meters*, D. van Nostrand Co., Toronto.

[15] Miller, R. W., 1989, *Flow Measurement Engineering Handbook*, 2nd ed., McGraw-Hill, New York.

[16] Sogin, H. H., and Providence, R. I., 1958, ''Sublimation From Disks to Air Streams Flowing Normal to Their Surfaces,'' Trans. ASME, **80**, pp. 61–69.

[17] Kline, S. J., and McClintock, F. A., 1953, ''Describing Uncertainties in Single-Sample Experiments,'' Mech. Eng. (Am. Soc. Mech. Eng.), **75**, pp. 3–8.

[18] Han, J. C., and Park, J. S., 1988, ''Developing Heat Transfer in Rectangular Channels With Rib Turbulators,'' Int. J. Heat Mass Transf., **31**, pp. 183–195.

[19] Liou, T. M., and Hwang, J. J., 1992, ''Developing Heat Transfer and Friction in a Ribbed Rectangular Duct With Flow Separation at the Inlet,'' ASME J. Heat Transfer, **114**, pp. 565–573.

[20] Han, J. C., Zhang, Y. M., and Kalkeuhler, K., 1993, ‘‘Uneven Wall Temperature Effect on Local Heat Transfer in a Rotating Two-Pass Square Channel With Smooth Walls,’’ ASME J. Heat Transfer, **115**, pp. 912–920.
[21] Nikitopoulos, D. E., Eliades, V., and Acharya, S., 2001, ‘‘Heat Transfer Enhancements in Rotating Two-Pass Coolant Channels With Profiled Ribs: Part 2 – Detailed Measurements,’’ ASME J. Turbomach., **123**, this issue, pp. 107–114.
[22] Acharya, S., Dutta, S., Myrum, T. S., and Baker, R. S., 1994, ‘‘Turbulent Flow Past a Surface Mounted Two-Dimensional Rib,’’ ASME J. Fluids Eng., **116**, pp. 238–246.
[23] Acharya, S., Dutta, S., Myrum, T. A., and Baker, R. S., 1993, ‘‘Periodically Developed Flow and Heat Transfer in a Ribbed Duct,’’ Int. J. Heat Mass Transf., **36**, pp. 2069–2082.

Heat Transfer Enhancements in Rotating Two-Pass Coolant Channels With Profiled Ribs: Part 2—Detailed Measurements

D. E. Nikitopoulos

V. Eliades

S. Acharya

Mechanical Engineering Department,
Louisiana State University,
Baton Rouge, LA 70803

Detailed heat/mass transfer distributions are presented inside a two-pass rotating ribbed coolant channel for two profiled-rib configurations. Several profiled-rib configurations have been studied (Acharya et al., 2000), and it was found that the best performance was achieved by saw-tooth ribs, and a pyramid–valley rib combination. The profiled ribs were placed directly opposite to each other on the leading and trailing surfaces. Smooth side walls were used in all the experiments. Heat transfer measurements were compared with straight ribs of equal blockage ratio. The measurements were made in a two-pass rotating facility using the naphthalene sublimation mass transfer technique, which provides highly resolved surface distributions. The results presented are for a Reynolds number of 30,000, two rotation numbers (0 and 0.3), and include average heat/mass transfer over the entire inter-rib module as well as detailed heat/mass transfer contours for two profiled-rib cases. Significant enhancement of up to 25 percent in heat/mass transfer was obtained with the pyramid–valley and saw-tooth shaped ribs under rotating conditions.

[DOI: 10.1115/1.1331538]

Introduction

Numerous studies have been performed over the years focusing upon the internal cooling of gas turbine blades with emphasis on the use of rib turbulators and different forms of vortex generators. Various geometries, experimental techniques, and test conditions have been studied. Many investigators have used heat and/or mass transfer, liquid crystal, or laser interferometry measuring techniques. Also many have incorporated rectangular or square ducts. Test conditions have been varied from Reynolds numbers of 50 to 80,000, mostly under stationary conditions. Very few investigators have reported results with rotation. The range of rotation numbers covered by previous studies has been from 0.01 to 0.4. Since the objective of this paper is to examine in some detail novel turbulator design performance under rotating conditions, we will focus our review of previous work on these areas.

A widely studied and used geometry of turbulators is that of a rib. A schematic of the typical flow structure in the area around such a rib turbulator is shown in Fig. 1. Upstream of the rib a small but vigorous corner eddy recirculation exists that causes higher heat transfer numbers as documented by Sparrow and Tao [1] and Chen et al. [2,3]. Immediately after the rib a large recirculation region forms due to flow separation leading to lower values of heat transfer rates. The flow reattaches and heat transfer peaks farther downstream at the stagnation region. The reattachment distance is affected by the Reynolds number, rotation number, rib height, distance between ribs, duct hydraulic diameter, and upstream turbulence intensity. Also flow separation is possible at the top of the rib. For a two-dimensional rib, the reattachment length typically ranges from six to ten rib heights downstream of the rib.

Several investigators have performed experiments with different types of turbulators. Han and Park [4] and Park et al. [5] reported a 300 percent increase in heat transfer for 60 and 45 deg angled ribs in a square channel. However, higher pressure drops were reported compared to rectangular channels. Han and Zhang [6] showed that 60 deg parallel ribs oriented from the inner to the outer walls gave heat transfer rates higher by as much as 30 percent compared to 60 deg parallel ribs oriented from the outer to the inner walls or 90 deg ribs. In-line ribs give better results than staggered ones. This may be due to higher effective blockage, according to Hong and Hsieh [7]. Normal, **V**-shaped, and angled ribs were tested by Kukreja et al. [8], who noted significant spanwise variation on the local mass transfer for the angled ribs. Secondary flows were introduced, causing significant changes on the smooth side walls, especially for the 45 deg angled ribs. Zhang et al. [9] reported a 36 percent increase in the heat transfer of grooved walls (60 deg groove in the wall between two regular ribs) compared to the normal rib cases.

The coolant passages of many gas turbine blades are connected together with 180 deg bends. Several researchers tested different types of bends to investigate their effect on the heat/mass transfer results. Boyle [10] tested three different types of 180 deg bends (rectangular, semi-circular, and rounded-corners) and found no significant differences in heat transfer. Han et al. [11] have reported significant increases in mass transfer immediately after the bend for both smooth wall and ribbed wall channels.

Under rotating conditions, the flow field becomes more complex. There are considerable differences between the high and low-pressure walls. This effect is due to the Coriolis force (see Fig. 2). For radially outward flow, the secondary flows induced move fluid from the leading wall toward the trailing one resulting in higher velocities and heat/mass transfer numbers on the trailing wall. The opposite phenomenon occurs for the radially inward flow. Similar Coriolis-induced secondary flows develop in a bend,

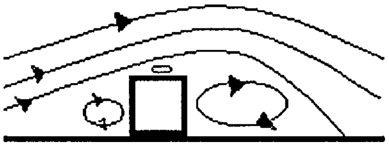

Fig. 1 Schematic of flow features around a two-dimensional rib

---

Contributed by the International Gas Turbine Institute and presented at the 45th International Gas Turbine and Aeroengine Congress and Exhibition, Munich, Germany, May 8–11, 2000. Manuscript received by the International Gas Turbine Institute February 2000. Paper No. 2000-GT-226. Review Chair: D. Ballal.

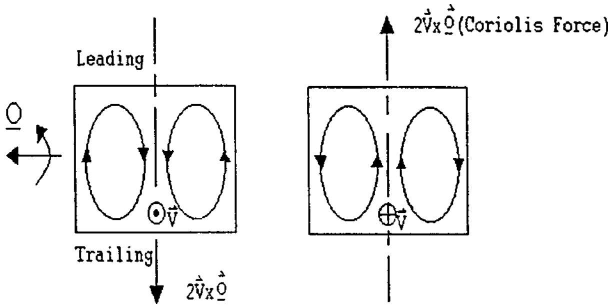

Fig. 2 Secondary flow induced by Coriolis forces in rotating channels

causing higher velocities and heat/mass transfer rates on the outside wall of the bend. In addition to the Coriolis forces, weaker secondary flows are induced by the geometry of the cross section. These geometry-induced secondary flows (Fig. 3) are overpowered by the Coriolis secondary flow patterns and do not affect, in most cases, the heat/mass transfer results under rotating conditions. For stationary cases these secondary flows induced by the cross section can be important. Wagner et al. [12] in their investigations reported that as the rotation number increases, the reattachment length decreases on the high-pressure side, resulting in higher heat transfer. The opposite occurs on the low-pressure side. This is typical of the Coriolis-induced secondary flows. The centrifugal buoyancy effect is another factor to be considered. Wagner et al. [12] suggested that buoyancy may contribute to differences between inward and outward flow. Buoyancy seems to affect strongly the high-pressure side of outward flow only. In general, they found that heat transfer ratios are about the same for smooth walls and normal trips for high rotation numbers.

Parsons et al. [13] used normal and angled ribs in their experiments. They mentioned the Coriolis effect with the resulting cross-stream flow and showed that 60 deg angled ribs give 30 percent better results than the normal ones. Skewed strips have been found to provide up to five times higher heat transfer than smooth walls, mainly due to the secondary flows induced, and also appear to have very little affect upon buoyancy. These were the major findings of Johnson et al. [14]. The effect of rib-height-to-channel hydraulic diameter, under rotating conditions, in staggered ribbed ducts was investigated by Taslim et al. [15]. The lower ratio (0.133) was found to give a 45 percent increase under rotating conditions while the higher ratio (0.333) gave only a 6 percent decrease.

Several types of vortex generators have been used to augment the performance of rib turbulators. Studies by Myrum et al. [16] and Hibbs et al. [17] have shown that cylindrical rods placed above or just downstream of traditional ribs can result in local heat transfer enhancements, particularly on the side walls, at low Reynolds numbers and smaller pitches. Similar conclusions were reached by Chen et al. [2] who also used vertical vortex generators (delta wings and cylinders placed above the ribs) and Garimella and Eibeck [18] using half delta wings. Hung and Lin [19] incorporated ribs with turbulence promoters and reported that the taller the rib and/or the turbulence promoter or the smaller the width of the duct, the better the heat transfer due to flow acceleration, but with the drawback of higher pressure drops in the duct.

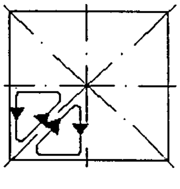

Fig. 3 Secondary flows induced by duct geometry

One of the motivations leading to the use of vortex generators in combination with rib turbulators has been the desire to introduce secondary flow structures that can interact with those in a ribbed rotating duct to enhance transport. Along this line of thought, the present study investigates the use of profiled ribs as possible heat transfer enhancement inducing geometries. We have focused on the rotating cases where the rib profile can induce three-dimensional secondary flows that may interact with those that develop due to rotation. Also, the use of profiled ribs can provide the means to control the mass/heat transfer distribution passively within the inter-rib modules. Several configurations have been examined and discussed in terms of overall performance in Acharya et al. [20]. Here we will discuss in more detail two of the most promising cases, following an overall mass transfer enhancement assessment in comparison with two relevant cases of traditional straight ribs and two cases of ribs with cylindrical vortex generators as in the case of Chen et al. [2,3].

Experimental Setup and Methods

Mass transfer measurements instead of heat transfer measurements have been performed. One of the reasons for choosing this technique, instead of direct heat transfer measurements, is the ability to collect the experimental data under rotating conditions without the use of any specialized equipment like slip rings. In addition, no heat losses, which have to be calculated precisely, are incurred with this technique. Furthermore, high resolutions, on the order of 840 points per in.^{2} in this study, are easily achieved. This would be almost impossible with direct heat transfer measurements using thermocouples. The naphthalene sublimation technique is well established and is outlined in Acharya et al. [20] together with a description of the rotating experimental facility and an uncertainty analysis for the measurements of this study. Details on the application of the naphthalene sublimation technique, reduction of raw data and the relevant uncertainty analysis can be found in Chen et al. [2,3], Hibbs et al. [17], and Eliades [21], among others. The straight ribs are made of aluminum and are machined in two sizes, 2.54×2.54×25.4 mm (0.1×0.1×1 in.) long, and 2.54×3.81×25.4 mm (0.1×0.15×1 in.). The ribs have 0.025 in. holes drilled at the two ends where straight piano wire, supported by corresponding holes on the side plate frame, is inserted to affix the ribs on the naphthalene surface, as shown in Fig. 4.

The profiled ribs are also made out of aluminum, and their width, length, and holes at the two ends are the same as for the straight ribs. The five different rib designs that have been used in this study are: trapezoidal shaped, valley shaped, pyramid shaped, saw-tooth shaped I (2-pyramids-1-valley) and saw-tooth shaped II (1-pyramid-2-valleys). A schematic of the last four designs is

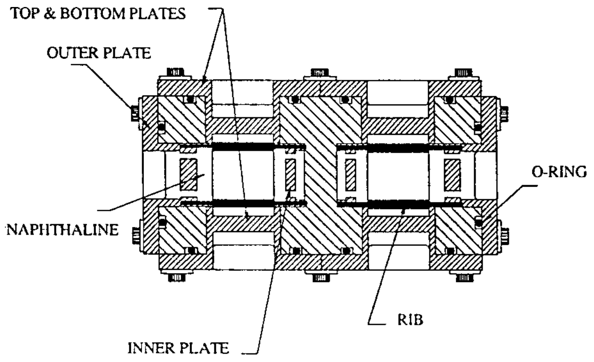

Fig. 4 Schematic of the test section

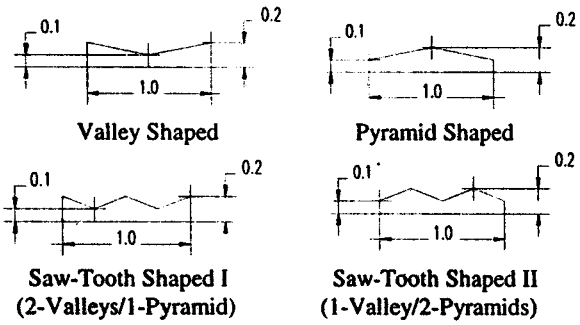

Fig. 5 Profiled ribs

shown in Fig. 5, while the various placement configurations inside the channel are described in detail in Fig. 3 of Acharya et al. [20].

Results and Discussion

The relative heat transfer performance of various profiled rib configurations examined as well as two-cylindrical vortex generator geometries are shown in the bar charts of Fig. 6 for $Re=30{,}000$ and $Ro=0.3$. The height of the bars is indicative of the average scaled Sherwood number corresponding to a fully developed inter-rib module from the inlet duct (Fig. 6(*a*)) and outlet duct (Fig. 6(*b*)). Three sets of bars are shown for each case; one corresponds to a ribbed channel with traditional straight ribs at a pitch of $P/e=7$; another corresponds to the same geometry with a pitch of $P/e=10.5$; and the last corresponds to the novel geometries we have studied. The $P/e=7$ case employed straight ribs with a height equal to the average height of the profiled ribs examined, while the $P/e=10.5$ pitch case employed ribs with a height equal to the minimum height of the profiled ribs. This was done to provide some perspective of pitch to the comparisons, since the spanwise height of the profiled ribs varies. Four geometries are identified as optimal for both the inlet and outlet ducts. These include two cases with pyramid-shaped ribs where the leading and trailing walls had ribs of complimentary shapes, and two cases of saw-tooth shaped ribs with identical geometries on the leading and trailing walls. Of these four cases we will discuss in more detail only two: the case where the rib on the leading wall has a valley and the trailing wall a pyramid (Case I) and that where both the leading and trailing wall ribs have two valleys on either side of a single, central pyramid (Case II). The first case exhibits a 25 percent mass transfer overall improvement for both the inlet and outlet ducts when compared to the $P/e=7$ reference case. The second configuration exhibits a 23 percent mass transfer improvement in the inlet duct and 9 percent improvement in the outlet when compared to the $P/e=7$ case. The fairest comparison is that with the lower pitch case because the flow blockage of the ribs is the same between the straight and profiled cases. The mass transfer results shown in Fig. 6 do not take into account mass transfer (heat/transfer) from the ribs themselves since in all cases they were inactive. In a practical setting the ribs will be active but the difference in surface area between the straight and profiled ribs under discussion is not significant (the pyramid case has 0.5 percent more area and the saw-tooth case has 2 percent more area)

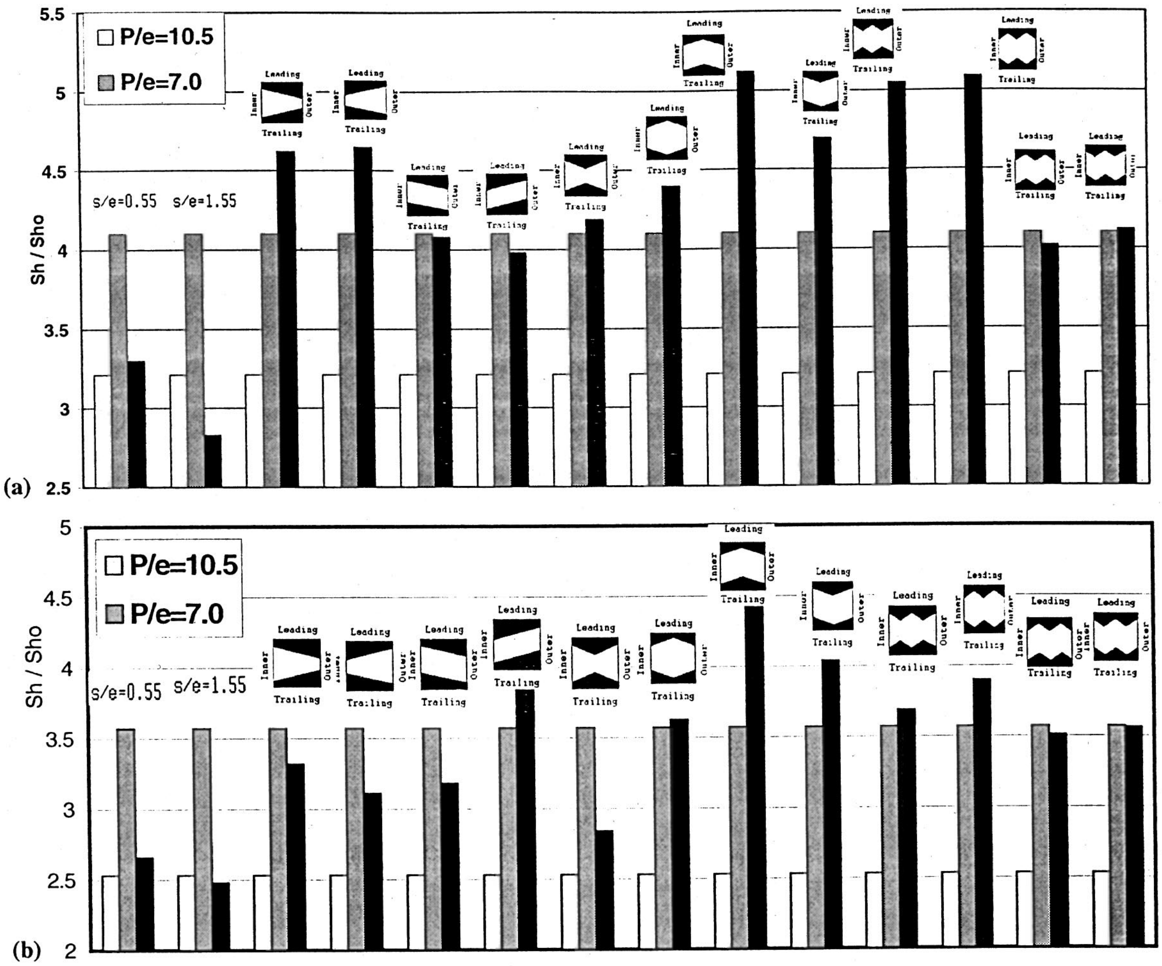

Fig. 6 Fully developed cell averages of the inlet duct (*a*) and the outlet duct (*b*) at Re=30,000 and Ro=0.3

Table 1 Fully developed cell average comparisons of $Sh_{Profiled\text{-}Rib}/Sh_{Rib\text{-}Only}$ at Ro=0.3 for Case I

Wall #	Re=30,000, P/e=7.0	Re=30,000, P/e=10.5
IL-------OL	1.08------1.25	1.56------1.26
IT-------OT	1.17------1.00	1.39------2.58
IO------OO	1.34------1.41	1.91------2.30
II--------OI	1.41------1.29	1.63------1.57

Table 2 Fully developed cell average comparisons of $Sh_{Profiled\text{-}Rib}/Sh_{Rib\text{-}Only}$ at Ro=0.3 for Case II

Wall #	Re=30,000, P/e=7.0	Re=30,000, P/e=10.5
IL-----OL	1.00------1.13	1.44------1.14
IT-----OT	1.35------1.17	1.61------3.03
IO----OO	1.21------1.08	1.72------1.76
II------OI	1.34------0.98	1.56------1.19

although in favor of the profiled ribs. It should be noted that mass transfer enhancements with profiled ribs relative to the $P/e=7$ pitch straight ribs were observed only in the rotating cases, while the nonrotating cases showed no significant differences. An average quantitative overview of the performance of the optimal profiled rib cases in this study relative to two straight rib cases are given in Tables 1 and 2.

The ratio of the profiled rib Sherwood number to a corresponding straight rib Sherwood number is shown in these tables. Given the encouraging overall and wall-by-wall mass transfer results of the two geometries mentioned previously under rotating conditions, we will proceed to examine in more detail the local features of the mass transfer on the leading, trailing, and side walls of both the inlet and outlet ducts. The nonrotating case will also be discussed as a reference and to accentuate the effects of the secondary flows due to rotation. All cases discussed are based on measurements with a resolution of 840 points per square inch.

The first case to be discussed in detail is the one that employs a valley-shaped rib on the leading walls of both inlet and outlet ducts and a pyramid shaped rib on the trailing walls. Figure 7 shows detailed mass transfer distributions for this geometry under stationary conditions (Ro=0) and Re=30,000. Results are shown in two ''fully developed'' inter-rib modules from the inlet duct, the first inter-rib module of the outlet duct after the 180 deg bend, and two fully developed inter-rib modules form the outlet duct. This is done for all four sides of the duct (leading, inner, trailing, and outer). These terms refer to the case with rotation but have been adopted for the nonrotating case as well. It should be noted that flow in the inlet duct is radially outward, while in the outlet duct it is radially inward relative of the axis of rotation of the facility. It is seen from Fig. 7 that the normalized Sherwood number distributions on the leading wall of both the inlet and outlet ducts bear the spanwise asymmetric signature of the valley shaped rib. The high mass transfer observed in the central region of the module corresponds to reattachment of the flow through the valley of the profiled rib and is located roughly five valley-rib heights downstream. Since the two ends of the valley-shaped rib near the sidewalls are progressively taller, it is reasonable to expect reattachment farther downstream relative to the central region. Indeed the trend of the Sherwood number distribution indicates exactly that. On either side of the central region, mass transfer rates are lower and higher values are observed farther downstream very close to the next rib with maxima near the two corners. In fact there is evidence that the downstream rib interferes with the reattachment of the flow from the upstream rib in this region. This is expected since the downstream is five times the maximum profiled rib height. The area immediately behind each rib is characterized by the low mass transfer rates attributed to the re-

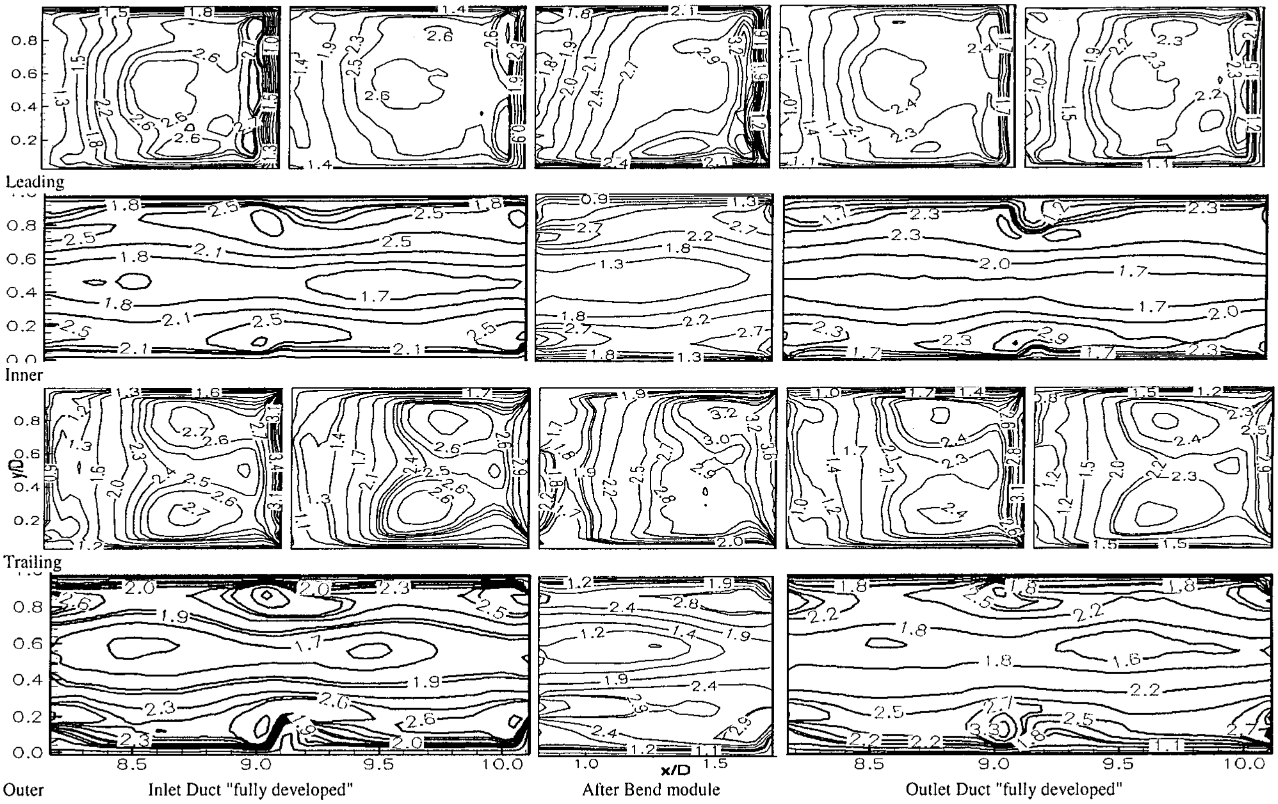

Fig. 7 Detaield Sherwood number ratio distributions Sh/Sh_o in selected developing and fully developed regions in a square duct with pyramid and valley shaped vortex generators at Re=30,000, Ro=0.0, *P/e*=7.0 (leading wall: valley, trailing wall: pyramid)

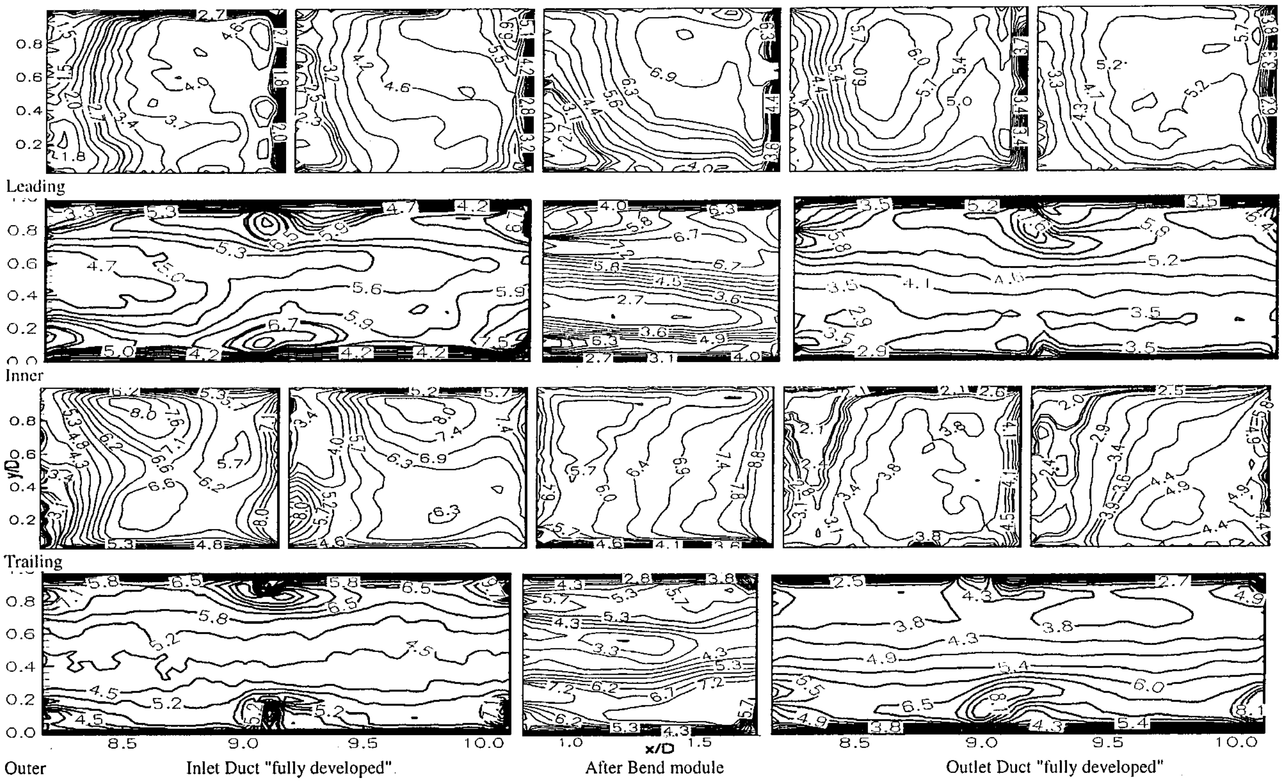

Fig. 8 Detailed Sherwood number ratio distributions Sh/Sh_0 in selected developing and fully developed regions in a square duct with pyramid and valley shaped turbulators at Re=30,000, Ro=0.3, $P/e=7.0$ (leading wall: valley, trailing wall: pyramid)

circulation region described in Fig. 1. This region is narrower behind the bottom of the valley of the rib and becomes wider as the rib profile becomes higher. The mass transfer rate decreases downstream of the reattachment point in the central region as the reattached boundary layer grows. Steep variation of the mass transfer is observed immediately upstream of each rib and is associated with the upstream recirculation region as schematically portrayed in Fig. 1.

The fully developed trailing wall details on Fig. 7 show that the normalized Sherwood number distributions of both the inlet and outlet ducts bear the spanwise asymmetric signature of the pyramid shaped rib. The low mass transfer observed in the central region of the module corresponds to the recirculation region downstream of the higher pyramid tip. Re-attachment of the flow in the central region appears very close to the downstream rib, which is located five pyramid-rib heights downstream and interferes with re-attachment. Since the two ends of the pyramid-shaped rib near the sidewalls are progressively lower, it is reasonable to expect re-attachment farther upstream relative to the central region. Indeed the trend of the Sherwood number distribution indicates exactly that with two mass transfer peaks observed closer to the walls and located roughly six valley-rib heights downstream. The area immediately behind each rib has low mass transfer rates induced by the recirculation region. This region is widest behind the tip of the pyramid of the rib and becomes narrower as the rib profile becomes lower toward the walls. The mass-transfer rate decreases downstream of the reattachment points near the walls as the reattached boundary layer grows. Steep variation of the mass transfer is again observed immediately upstream of each rib and is associated with the previously discussed upstream recirculation region.

Both sidewalls in Fig. 7 display similar characteristics typical of fully developed ribbed duct sidewalls. Lower mass transfer rates are observed in the central region shifted away from the wall with the valley profiled rib because in this case the rib height is highest near the wall. The pattern of the side walls is strongly nonuniform in the spanwise direction. The flow accelerates over the ribs and, as shown by Acharya et al. [22], high streamwise turbulence intensities are generated directly above them. These effects lead to a high mass transfer field surrounding the rib. This is initiated 1.0 to 1.5 local rib-heights upstream of the rib, where the flow accelerates and the turbulence intensity begins to increase, reaches a peak directly above or just upstream of the ribs, and then decays as it is convected and diffused downstream. A region of lower mass transfer on the sidewalls is observed near the reattachment region along the leading and trailing walls that is presumably caused by local flow deceleration. In the central region, mass transfer minima appear downstream of each profiled rib due to flow deceleration.

The bend effect does not appear to be very strong after the first profiled rib, which was placed immediately after the 180 deg bend. The leading and trailing wall distributions indicate that reattachment after the ribs occurs somewhat farther downstream of the rib on the side of the outer wall. There the velocities are higher because of the secondary flow induced by the bend, which causes higher velocities on the outer wall of the bend. No significant bend effect is observed on the inner and outer walls. The trends are the same as those observed on the fully developed modules. The weak bend effect is attributed to the strongly three-dimensional flow induced by the profiled ribs, which can disrupt the secondary and three-dimensional flow patterns induced by the bend.

The mass transfer results from the same profiled rib configuration as the one discussed above under rotating conditions, are shown in Fig. 8. The Reynolds number is also the same as in the stationary case and the rotation number is 0.3. The effect of rotation is immediately apparent and strong. The trailing wall and trailing part of the inlet duct sidewalls, as well as the leading wall and leading part of the outlet duct, display considerably higher mass transfer rates than the opposite half of the duct. This is

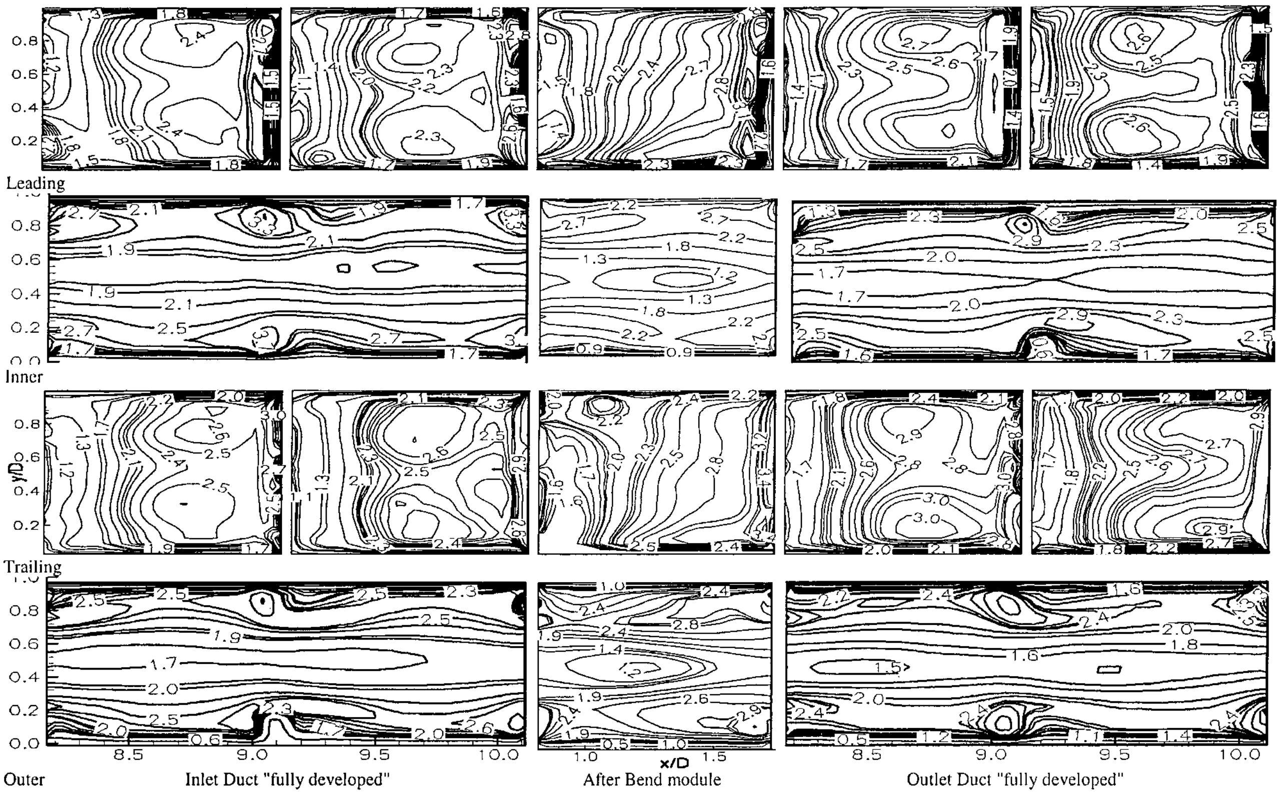

Fig. 9 Detailed Sherwood number ratio distributions Sh/Sh_o in selected developing and fully developed regions in a square duct with saw-tooth shaped vortex generators at Re=30,000, Ro=0, P/e=7.0 (1-pyramid-2-valleys)

consistent with the expected action of the Coriolis-induced secondary flows as discussed previously and indicated in Fig. 2. It should be noted that the mass transfer rates for this rotating case are overall significantly higher than those observed for the stationary case (Fig. 7). Therefore, the profiled rib effect combined with the rotational effect lead to mass transfer enhancement. The enhanced fully developed walls also consistently display the qualitative signature of the corresponding profiled ribs as they appeared in the stationary case. That is, the valley effect is clearly visible on the outlet, leading wall while the pyramid effect is visible on the inlet, trailing wall. However, the patterns on these fully developed enhanced walls are skewed toward the inner wall on the inlet duct and towards the outer wall on the outlet duct. This can be attributed to the interaction between the three-dimensionality of the flow induced by the specific and asymmetric profiled rib combination and the secondary flow induced by rotation. The fully developed sides that are less enhanced due to the effect of rotation do not display a strong signature of the corresponding profiled ribs. In general the mass transfer increase associated with reattachment is moved farther downstream on the leading wall of the inlet duct and trailing wall of the outlet duct. Higher mass transfers are skewed toward the outer wall of the inlet duct and toward the outer wall of the outlet duct. As with the enhanced walls, this can also be attributed to interaction between the three-dimensionality induced by the asymmetric profiled rib combination and that induced by rotation. The sidewalls qualitatively bare the same longitudinal trends dictated by the ribs as outlined in the stationary case. However, the low mass transfer central region is shifted away from the rotation-enhanced walls overshadowing the effect of the geometric asymmetry of the opposing profiled ribs, which was the prevailing factor in the stationary case. The bend effect manifests itself through mass transfer distributions on the leading and trailing walls, which are atypical of the rib profile. This is less so for the enhanced (leading) wall, where the high mass transfer due to reattachment from the valley part of the rib has shifted toward the outer wall, where higher velocities are expected from the combined bend and Coriolis effects. No evidence of reattachment is observed on the trailing wall after the bend. The sidewalls of the after-bend module bear the signature of the rib presence as well as that of rotation with higher mass transfer rates toward the enhanced (leading) wall. The overall higher mass transfer rates observed on the outer wall are attributed to the higher velocities developed inside the bend.

The second case where profiled ribs have displayed significant mass transfer enhancement under rotating conditions is the one where saw-tooth shaped ribs with two valleys and one central pyramid are used on both leading and trailing walls of the inlet and outlet ducts. We shall discuss the reference stationary case first. The corresponding detailed mass transfer distributions are shown in Fig. 9 for the same inter-rib modules as in the case discussed before in Figs. 7 and 8. The leading and trailing fully developed walls bear the signature of the rib profile much as in the case before. Since all ribs are the same the fully developed cells should, and indeed do, display the same qualitative features. High mass transfer regions are observed downstream of the valleys at approximately five valley-rib heights and are associated with the local reattachment regions. In the central region, behind the apex of the pyramid, the mass transfer is lower as the three-dimensional recirculation is longer due to the locally greater rib height. In fact, the mass transfer distributions indicate that reattachment in the central region has not been clearly established and probably coincides with the next rib. The inner and outer sidewalls also display the expected features. The mass transfer symmetry with respect to the central axis is within experimental uncertainty and is dictated by the geometric symmetry of the profiled ribs. Minima of mass transfer are observed in the central region, while maxima exist upstream and around the ribs for the same reasons given previously. In general the magnitudes of the local mass transfer are comparable to the previous case. Bend effects are visible in the

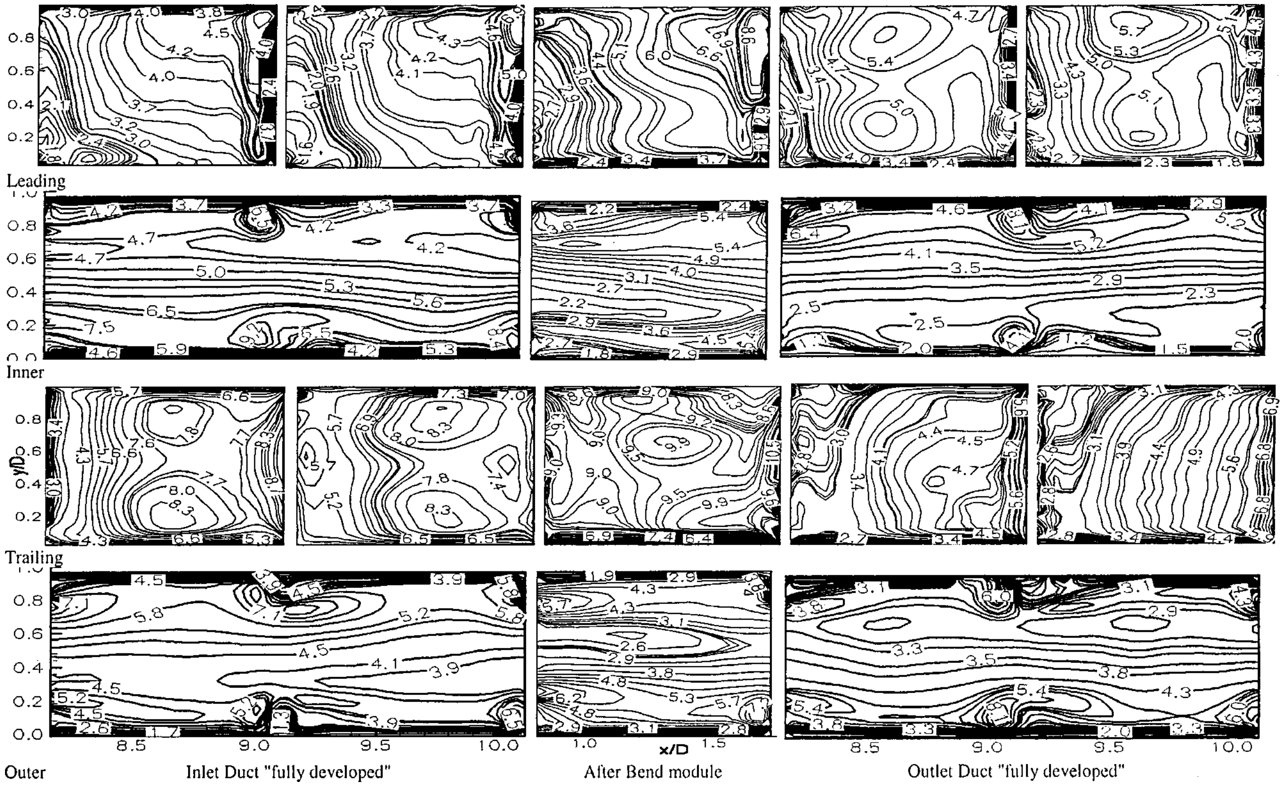

Fig. 10 Detailed Sherwood number ratio distributions Sh/Sh_0 in selected developing and fully developed regions in a square duct with saw-tooth shaped vortex generators at Re=30,000, Ro=0.3, $P/e=7.0$ (1-pyramid-2-valleys)

post-bend module. The mass transfer distribution on the leading and trailing walls after the bend are atypical of the profiled rib configuration due to the interaction between the secondary flows of the bend and the three-dimensionality introduced by the profiled rib. Higher mass transfer rates are observed nearer to the outer wall because of higher velocities induced by the bend effect. The inner and outer sidewalls of the module after the bend display the typical trends observed in the fully developed modules. However, the mass transfer rates are somewhat higher on the outer wall, which experiences higher velocities.

The mass transfer results from the saw-tooth rib configuration under rotating conditions are shown in Fig. 10. The Reynolds number is the same as in the stationary case and the rotation number is 0.3. The effect of rotation is quite strong in this case as in the valley-pyramid rib case. The trailing wall and trailing part of the inlet duct sidewalls, as well as the leading wall and leading part of the outlet duct, experience considerably higher mass transfer rates than the opposite half of the duct. This is again consistent with the Coriolis-induced secondary flow effect as depicted in Fig. 2. It should also be noted that the mass transfer rates for this rotating case are overall significantly higher than those observed for the corresponding stationary case (Fig. 9). So, once more the profiled rib effect combined with the rotational effect lead to mass transfer enhancement. The enhanced fully developed walls consistently display the qualitative signature of the profiled ribs as in the stationary case. No significantly skewed mass transfer patterns appear in this case where opposite ribs are symmetric, unlike the previous case where the opposite ribs were asymmetric. The fully developed sides, which are less enhanced due to the effect of rotation, do not display a strong signature of the corresponding profiled ribs. In general the mass transfer increase associated with reattachment is moved farther downstream on the leading wall of the inlet duct and trailing wall of the outlet duct. Higher mass transfers are skewed toward the outer wall of the inlet duct and toward the inner wall of the outlet duct. This could be attributed to interaction between the three-dimensionality induced by the profiled ribs and that induced by rotation, which may be more visible due to overall lower velocities in the main flow direction. The sidewalls qualitatively bare the same longitudinal trends dictated by the ribs as outlined in the stationary case. However, the low mass transfer central region is shifted away from the rotation-enhanced walls. The bend effect manifests itself through mass transfer distributions on the leading and trailing walls, which are not typical of the rib profile. This is less so for the enhanced (leading) wall where the high mass transfer due to reattachment from the valley part of the rib has shifted towards the outer wall where higher velocities are expected from the combined bend and Coriolis effects. No evidence of reattachment is observed on the trailing wall after the bend. The sidewalls of the after-bend module bear the signature of the rib presence as well as that of rotation with higher mass transfer rates toward the enhanced (leading) wall. The somewhat higher mass transfer rates observed on the outer wall are attributed to the higher velocities developed inside the bend.

Concluding Remarks

Detailed mass/heat transfer results have been presented for two profiled-rib configurations inside a two-pass rotating ribbed coolant channel under rotation: one case where the rib on the leading wall has a valley and the trailing wall a pyramid exhibited a 25 percent mass transfer overall improvement for both the inlet and outlet ducts when compared to the $P/e=7$ pitch reference case; the other case where both the leading and trailing wall ribs have two valleys on either side of a single, central pyramid. This case exhibited a 23 percent mass transfer overall improvement in the inlet duct and 9 percent improvement in the outlet when compared to the $P/e=7$ pitch reference case. High-resolution mass transfer measurements carried out at Re=30,000 and two rotation numbers (0 and 0.3) have revealed the local characteristics of the mass transfer rate distributions on all walls. These characteristics have been related to the geometry of the profiled ribs under both stationary and rotating conditions. The local effects of rotation, which are quite strong, have also been discussed. It has been argued on the basis of the local mass/transfer results that the combination of three-dimensional flow induced by the profiled-rib geometry and the secondary flow effects due to rotation leads to significant enhancement of mass/heat transfer. It is also shown that the spanwise mass/heat transfer distribution on the rib-bearing walls can be manipulated through the use of different rib profiles. The most significant enhancements due to the profiled ribs were observed on the walls of the two-pass duct that are rotation-enhanced, as well as the side walls. Consequently, use of profiled ribs may be a viable and effective solution to local heat transfer enhancement and/or spatial redistribution in actual rotating, ribbed multipass cooling channels for gas turbine applications.

Acknowledgments

This research was sponsored by the U. S. Department of Energy's Morgantown Energy Technology Center, under Contract No. DE-FC2192MC29061 with South Carolina Energy Research and Development Center, 386-2 College Ave., Clemson, SC 29634-5181.

References

[1] Sparrow, E., and Tao, W., 1984, ''Symmetric Vs. Asymmetric Periodic Disturbances at the Walls of a Heated Flow Passage,'' Int. J. Heat Mass Transf., **27**, 2133–2144.
[2] Chen, Y., Acharya., S., Hibbs., R., and Nikitopoulos, D. E., 1996, ''Heat/Mass Transfer in an Internally Ribbed Turbine-Blade Coolant Channel With Vortex Generators,'' ASME Paper No. 96-WA/HT-10.
[3] Chen, Y., Nikitopoulos, D. E., Hibbs, R., Acharya, S., and Myrum, T., 1996, ''Detailed Mass Transfer Distribution in a Ribbed Coolant Passage,'' ASME Paper No. 96-WA/HT-11.
[4] Han, J., and Park, J., 1988, ''Developing Heat Transfer in Rectangular Channels With Rib Turbulators,'' Int. J. Heat Mass Transf., **31**, No. 1, pp. 183–195.
[5] Park, J., Han, J., Huang, Y., Ou, S., and Boyle, R., 1992, ''Heat Transfer Performance Comparisons of Five Different Rectangular Channels With Parallel Angles Ribs,'' Int. J. Heat Mass Transf., **35**, No. 11, pp. 2891–2903.
[6] Han, J., and Zhang, P., 1991, ''Effect of Rib-Angle Orientation on Local Mass Transfer Distribution in a Three-Pass Rib-Roughened Channel,'' ASME J. Turbomach., **113**, pp. 123–130.
[7] Hong, Y., and Hsieh, S., 1993, ''Heat Transfer and Friction Factor Measurements in Ducts With Staggered and In-Line Ribs,'' ASME J. Heat Transfer, **115**, pp. 58–65.
[8] Kukreja, R., Lau, S., and McMillin, R., 1992, ''Local Heat/Mass Transfer Distribution in a Square Channel With Full and V-Shaped Ribs,'' Int. J. Heat Mass Transf., **36**, No. 8, pp. 2013–2020.
[9] Zhang, Y., Gu, W., and Han, J., 1994, ''Heat Transfer and Friction in Rectangular Channels With Ribbed or Ribbed-Grooved Walls,'' ASME J. Heat Transfer, **116**, pp. 58–65.
[10] Boyle, R., 1984, ''Heat Transfer in Serpentine Passages With Turbulence Promoters,'' NASA Tech. Memorandum 83614.
[11] Han, J., Chandra, P., and Lau, S., 1988, ''Local Heat/Mass Transfer Distributions Around Sharp 180 deg Turns in Two-Pass Smooth and Rib-Roughened Channels,'' ASME J. Heat Transfer, **110**, pp. 91–98.
[12] Wagner, J., Johnson, B., Graziani, R., and Yeh, F., 1992, ''Heat Transfer in Rotating Serpentine Passages With Trips Normal to the Flow,'' ASME J. Turbomach., **114**, pp. 847–857.
[13] Parsons, J., Han, J., and Zhang, Y., 1995, ''Effect of Model Orientation and Wall Heating Condition on Local Heat Transfer in a Rotating Two-Pass Square Channel With Rib Turbulators,'' Int. J. Heat Mass Transf., **38**, No. 7, pp. 1151–1159.
[14] Johnson, B., Wagner, J., Steuber, G., and Yeh, F., 1993, ''Heat Transfer in Rotating Serpentine Passages With Selected Model Orientation for Smooth or Skewed Trip Walls,'' NASA Tech. Memorandum 106126.
[15] Taslim, M., Rahman, A., and Spring, S., 1991, ''An Experimental Investigation of Heat Transfer Coefficients in a Spanwise Rotating Channel With Two Opposite Rib-Roughened Walls,'' ASME J. Turbomach., **113**, pp. 75–82.
[16] Myrum, T., Acharya, S., Inamdar, S., and Mehrotra, A., 1992, ''Vortex Generator Induced Heat Transfer Augmentation Past a Rib in a Heated Duct Air Flow,'' ASME J. Heat Transfer, **114**, pp. 280–284.
[17] Hibbs, R., Acharya, S., Chen, Y., Nikitopoulos, D. E., and Myrum, T., 1998, ''Heat Transfer in a Two-Pass Internally Ribbed Turbine Blade Coolant Channel With Cylindrical Vortex Generators,'' ASME J. Turbomach., **120**, pp. 589–600.
[18] Garimella, V., and Eibeck, A., 1991, ''Enhancement of Single Phase Convective Heat Transfer From Protruding Elements Using Vortex Generators,'' Int. J. Heat Mass Transf., **34**, No. 9, pp. 2431–2433.
[19] Hung, Y., and Lin, H., 1992, ''An Effective Installation of Turbulence Promoters for Heat Transfer Augmentation in a Vertical Rib-Heated Channel,'' Int. J. Heat Mass Transf., **35**, No. 1, pp. 29–42.
[20] Acharya, S., Eliades, V., and Nikitopoulos, D. E., 2001, ''Heat Transfer Enhancements in Rotating Two-Pass Coolant Channels With Profiled Ribs: Part 1–Average Results,'' ASME J. Turbomach., **123**, this issue, pp. 97–106.
[21] Eliades, V., 1998, ''Mass Transfer in Stationary and Rotating Gas Turbine Coolant Channels With Profiled Ribs and Horizontal Vortex Generators,'' M. Sc. Thesis, LSU, Baton Rouge, LA.
[22] Acharya, S., Dutta, S., Myrum, T., and Baker, R., 1993, ''Periodically Developed Flow and Heat Transfer in a Ribbed Duct,'' Int. J. Heat Mass Transf., **36**, pp. 2069–2082.

G. I. Mahmood
Graduate Student.

M. L. Hill
Graduate Student.

D. L. Nelson
Graduate Student.

P. M. Ligrani[1]
Professor.

Convective Heat Transfer Laboratory,
Department of Mechanical Engineering,
University of Utah,
Salt Lake City, UT 84112

H.-K. Moon
Consulting Engineer.

B. Glezer
Head, Turbine Cooling and Heat Transfer Analysis.

Solar Turbines, Inc.,
Turbine Cooling Design and Analysis,
San Diego, CA 92186

Local Heat Transfer and Flow Structure on and Above a Dimpled Surface in a Channel

Experimental results, measured on and above a dimpled test surface placed on one wall of a channel, are given for Reynolds numbers from 1250 to 61,500 and ratios of air inlet stagnation temperature to surface temperature ranging from 0.68 to 0.94. These include flow visualizations, surveys of time-averaged total pressure and streamwise velocity, and spatially resolved local Nusselt numbers, which are measured using infrared thermography, used in conjunction with energy balances, thermocouples, and in situ calibration procedures. The ratio of channel height to dimple print diameter is 0.5. Flow visualizations show vortical fluid and vortex pairs shed from the dimples, including a large upwash region and packets of fluid emanating from the central regions of each dimple, as well as vortex pairs and vortical fluid that form near dimple diagonals. These vortex structures augment local Nusselt numbers near the downstream rims of each dimple, both slightly within each depression, and especially on the flat surface just downstream of each dimple. Such augmentations are spread over larger surface areas and become more pronounced as the ratio of inlet stagnation temperature to local surface temperature decreases. As a result, local and spatially averaged heat transfer augmentations become larger as this temperature ratio decreases. This is due to the actions of vortical fluid in advecting cool fluid from the central parts of the channel to regions close to the hotter dimpled surface.
[DOI: 10.1115/1.1333694]

Introduction

To reduce or eliminate the need to employ film cooling, new attention has been devoted to internal cooling schemes for turbine airfoils. Internal schemes are advantageous in several respects, including smaller requirements for compressor air, and little or no aerodynamic penalties. However, the augmentation of surface heat transfer coefficients and the flow structural characteristics responsible for such augmentations must be understood for optimal internal passage design. The present investigation focuses on the use and effects of dimples in providing such augmentations. Such surface geometries have been long recognized to provide aerodynamic and flow benefits for a variety of applications [1]. Here, heat transfer and flow structure are investigated in a channel, with dimples on one surface, which models the passages used to cool turbine airfoils employed in gas turbine engines used for power generation.

Many early investigations of the effects of dimple cavities on heat transfer and flow structure are by Russian investigators. Much of this work focuses on flow and/or heat transfer either inside or downstream of single or multiple concave depressions on a wall in an internal passage. Of these studies, Gromov et al. [2] describe symmetric and nonsymmetric streamlines and flow patterns produced by such cavities with a variety of sizes. Cells of fluid motion are described in the form of tightening spirals, helical streamlines, and horse-shoe shaped vortices. Afanasyev et al. [3] describe the heat transfer enhancement mechanism for flows over walls indented with regular arrays of spherical pits. This includes the dynamic and thermal properties of the boundary layer on the smooth surface between the pits. Enhancements of 30-40 percent without appreciable pressure losses (compared to a smooth surface) are reported. Belen'kiy et al. [4] describe heat transfer intensification from a tube surface fitted with a staggered array of concave dimples on surfaces of annular internal passages. Results applicable to shell-and-tube heat exchangers show maximum relative increases in overall heat transfer for deep cavities of about 2.5, and for shallow cavities of about 2.0, compared with smooth annular internal passages. High pressure losses are also reported. Bearman and Harvey [5] investigate crossflows over dimpled cylindrical surfaces. The geometry of the dimples corresponds to the optimum concavity depth found by Kimura and Tsutahara [6] for minimum drag on cylinders. At high Reynolds numbers, significantly lower drag coefficients are present with arrays of dimples compared to smooth cylinders.

More recently, Kesarev and Kozlov [7] present distributions of local heat transfer coefficients inside a hemispherical cavity and indicate that the convective heat flux from the cavity is higher than that from the surface of a plane circle of the same diameter as the cavity diameter. The authors also describe the effects of turbulence intensity of the incident flow on the local heat flux and on the local shear stress on the cavity surface. Terekhov et al. [8] present experimental measurements of flow structure, pressure fields, and heat transfer in a channel also with a single dimple on one surface. Different magnitudes and frequencies of flow oscillations are described, along with heat transfer and pressure loss dependence on dimple geometry. From flow visualizations, Zhak [9] describes a variety of vortex structures in different shaped rectangular cavities. Schukin et al. [10] present results applicable to gas turbine cooling. Average heat transfer coefficients are reported from the measurements on a heated plate downstream of a single hemispherical cavity in a diffuser channel and in a convergent channel. The study provides data on the influences of the mainstream turbulence intensity level and the angles of divergence and convergence on heat transfer augmentation.

Other recent work by Chyu et al. [11] includes data on the influences of Reynolds number on local heat transfer coefficient distributions on surfaces imprinted with staggered arrays of two different shapes of concavities. Their measurements for H/D of 0.5, 1.5, and 3.0 show distributions of heat transfer coefficients everywhere on the surfaces that are significantly higher than val-

---

[1] Corresponding author.

Contributed by the International Gas Turbine Institute and presented at the 45th International Gas Turbine and Aeroengine Congress and Exhibition, Munich, Germany, May 8–11, 2000. Manuscript received by the International Gas Turbine Institute February 2000. Paper No. 2000-GT-230. Review Chair: D. Ballal.

ues in channels with smooth walls. Over a range of Reynolds numbers, enhancement of the overall heat transfer rate is about 2.5 times smooth surface values, and pressure losses are about half the values produced by conventional rib turbulators. Lin et al. [12] present computational simulation results of the flow structures and resulting surface heat transfer distributions for the same geometries and flow conditions. Flow streamlines and temperature distributions are presented that provide insight into flow structural characteristics produced by the dimples. Another recent investigation by Gortyshov et al. [13] employs spherical dimples, called spherical intensifiers, placed at different relative positions on the two opposite surfaces of a narrow channel. Moon et al. [14] give data for H/D from 0.37 to 1.49 that illustrate the effects of channel height on heat transfer and pressure losses on a surface with a staggered pattern of dimples. According to the investigators, improvements in heat transfer intensification and pressure losses remain at approximately constant levels over the ranges of Reynolds number and channel height investigated.

The present study is different from other investigations of the influences of dimples on flow and heat transfer because spatially resolved distributions of local Nusselt numbers, instantaneous flow structure (from flow visualizations), and distributions of total pressure and streamwise velocity are provided and interrelated to each other. Such data are presented for locations along the dimpled surface at different Reynolds numbers, and at different ratios of air inlet stagnation temperature to local surface temperature. Magnitudes of this temperature ratio include values in the range of application to gas turbine airfoil internal cooling passages. Particular attention is paid to the local flow characteristics that are responsible for augmentations of local Nusselt numbers.

Experimental Apparatus and Procedures

Channel and Test Surface for Heat Transfer Measurements. A schematic of the facility used for heat transfer measurements is shown in Figs. 1(*a*) and 1(*b*). The air used within the facility is circulated in a closed loop. One of two circuits is employed, depending upon the Reynolds number and flow rate requirements in the test section. For Reynolds numbers Re_H less than 20,000, a 102 mm pipe is connected to the intake of an ILG Industries 10P type centrifugal blower. For higher Reynolds numbers, a 203 mm pipe is employed with a New York Blower Co. 7.5 HP, size 1808 pressure blower. In each case, the air mass flow rate from the test section is measured (upstream of whichever blower is employed) using an ASME standard orifice plate and Validyne M10 digital pressure manometer. The blower then exits into a series of two plenums (0.9 m square and 0.75 m square). A Bonneville crossflow heat exchanger is located between two of these plenums, and is cooled with liquid nitrogen at a flow rate appropriate to give the desired air temperature at the exit of the heat exchanger. As the air exits the heat exchanger, it enters the second plenum, from which the air passes into a rectangular bell mouth inlet, followed by a honeycomb, two screens, and a two-dimensional 19.5:1 contraction ratio nozzle. Figure 1(*b*) shows that this nozzle leads to a rectangular cross-sectional, 411 mm by 25.4 mm inlet duct, which is 1219 mm in length. This is equivalent to 25.4 hydraulic diameters (where hydraulic diameter is 47.8 mm). A trip is employed on the bottom surface of the inlet duct, just upstream of the test section, which follows with the same cross-sectional dimensions. It exits to a 0.60 m square plenum, which is followed by two pipes, each containing an orifice plate, mentioned earlier.

Figures 2(*a*) and 2(*b*) present the geometric details of the test surface, including dimple geometry. A total of 13 rows of dimples are employed in the streamwise direction, and 9 rows are employed in the spanwise direction in a staggered array. Also identified in Fig. 2(*a*) is the test section coordinate system employed for the study. Note that the Y coordinate is normal to the test surface.

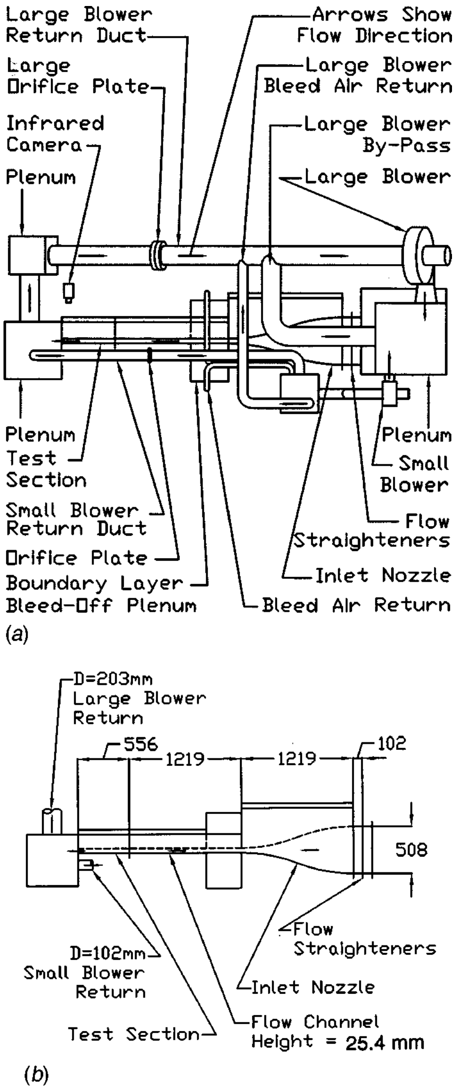

(*a*)

(*b*)

Fig. 1 Schmeatic diagrams of (*a*) the experimental apparatus, and (*b*) a side view of the experimental apparatus with dimensions. All dimensions are given in mm.

All exterior surfaces of the facility (between the heat exchanger and test section) are insulated with Styrofoam ($k=0.024$ W/mK), or two to three layers of 2.54-cm-thick, Elastomer Products black neoprene foam insulation ($k=0.038$ W/mK) to minimize heat losses. Calibrated copper-constantan thermocouples are located between the three layers of insulation located beneath the test section to determine conduction losses. Between the first layer and the 3.2-mm-thick acrylic, the dimpled test surface is a custom-made Electrofilm etched-foil heater (encapsulated between two thin layers of Kapton) to provide a constant heat flux boundary condition on the test surface. The acrylic surface contains 24 copper-constantan thermocouples, and is adjacent to the air stream. Each of these thermocouples is located 0.0508 cm just below this surface to provide measurements of local surface temperatures, after correction for thermal contact resistance and temperature drop through the 0.0508 cm thickness of acrylic. Acrylic is chosen because of its low thermal conductivity ($k=0.16$ W/mK at 20°C) to minimize streamwise and spanwise conduction along the test surface, and thus minimize ''smearing'' of spatially varying temperature gradients along the test surface. Acrylic also works well for infrared imaging because its surface emissivity ranges from 0.60 to 0.65. The power to the foil heater is controlled and regulated using a Variac power supply. Energy bal-

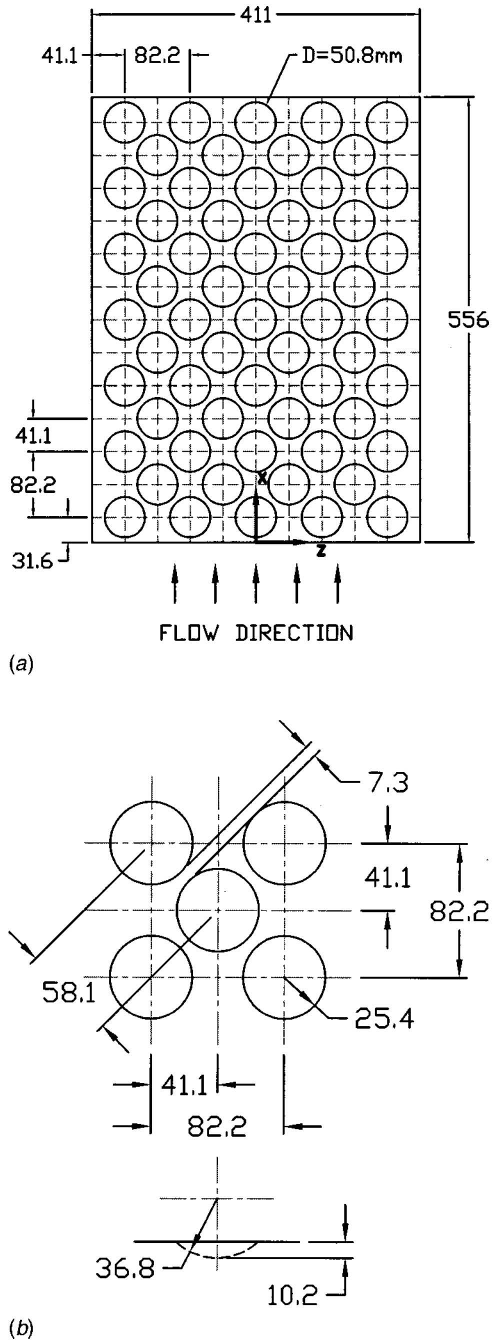

Fig. 2 Schematic diagrams of: (*a*) the entire dimpled test surface, and (*b*) individual dimple geometry details. All dimensions are given in mm.

ances, performed on the heated test surface, then allow determination of local magnitudes of the convective heat flux.

The mixed-mean temperature of the air entering the test section is measured using five calibrated copper-constantan thermocouples spread across its cross section. All measurements are obtained when the test facility at steady state, achieved when each of the temperatures from the 24 thermocouples (on the test surface) vary by less than 0.1°C over a 10 minute period.

Local Nusselt Number Measurement. To determine the surface heat flux (used to calculate heat transfer coefficients), the convective power provided by the etched foil heater is divided by the total area of the test surface (flat portions and dimples). Thus, local heat transfer coefficients and local Nusselt numbers can be considered to be based on the same area. This is a different approach than employed by Chyu et al. [11] and Moon et al. [14], who used a flat projected area to determine heat flux. As a result, heat transfer coefficients from those studies are about 16.4 percent higher than values from the present study when compared for the same geometry and flow conditions.

Spatially resolved temperature distributions along the dimpled test surface are determined using infrared imaging in conjunction with thermocouples, energy balances, digital image processing, and in situ calibration procedures. To accomplish this, the infrared radiation emitted by the heated interior surface of the channel is captured using a VideoTherm 340 Infrared Imaging Camera, which operates at infrared wavelengths from 8 μm to 14 μm. Temperatures, measured using the calibrated, copper-constantan thermocouples distributed along the test surface adjacent to the flow, are used to perform the in situ calibrations simultaneously as the radiation contours from surface temperature variations are recorded.

This is accomplished as the camera views the test surface through a custom-made, zinc-selenide window (which transmits infrared wave lengths between 6 and 17 μm) located on the top wall of the test section. Reflection and radiation from surrounding laboratory sources are minimized using an opaque shield, which covers the camera lens and the zinc selenide window. Frost build-up on the outside of the window is eliminated using a small heated air stream. The window is located just above the tenth to twelfth rows of dimples downstream from the leading edge of the test surface. Five to six thermocouple junction locations are usually present in the infrared field viewed by the camera. The exact spatial locations and pixel locations of these thermocouple junctions and the coordinates of a 12.7 cm by 12.7 cm field of view are known from calibration maps obtained prior to measurements. During this procedure, the camera is focused, and rigidly mounted and oriented relative to the test surface in the same way as when radiation contours are recorded.

With these data, gray scale values at pixel locations within videotaped images from the infrared imaging camera are readily converted to temperatures. Because such calibration data depend strongly on camera adjustment, the same brightness, contrast, and aperture camera settings are used to obtain the experimental data. The in situ calibration approach rigorously and accurately accounts for these variations.

Images from the infrared camera are recorded as 8-bit gray scale images on commercial videotape using a Panasonic AG-1960 video recorder. Images are then digitized using NIH Image vl.60 software, operated on a Power Macintosh 7500 PC computer. Subsequent software is used to convert each of 256 possible gray scale values to temperature at each pixel location using calibration data, and then determines values of local Nusselt numbers. Thermal conductivity in the Nusselt number is based on the average of the local wall temperature and the temperature of the air at the upstream inlet. Contour plots of local surface temperature and Nusselt number are prepared using DeltaGraph v4.0 software. Each individual image covers a 300 pixel by 300 pixel area. Hedlund and Ligrani [15] provide additional details on the infrared imaging and measurement procedures.

To check the repeatability and consistency of the results, infrared images from three different regions on the test surface (all located over the tenth, eleventh, and twelfth rows of dimples) are measured. Each of these regions covers the exact same area, which is the same as the center-to-center distance between four adjoining dimples in the tenth and twelfth rows. Results are identical for overlapping regions and repeatable well within uncertainty magnitudes when considered at similar locations with respect to different dimples. This indicates appropriate flow uniformity and periodicity in the test section, as well as correct test surface operation.

Time-Averaged Total Pressure, Static Pressure, and Streamwise Mean Velocity. A separate channel facility, with interior geometry identical to that in the heat transfer facility, is employed for flow visualization as well as quantitative surveys of flow structure.

A United Sensor KAA-12 1/16-in.-dia miniature Kiel total pressure probe and a separate United sensor static pressure probe are used to obtain time-averaged surveys of total pressure and static pressure, respectively. These data are then used to deduce distributions of streamwise velocity. To obtain the surveys, the probe employed is mounted on an automated two-dimensional traverse, and inserted into the test section through a slot lined with foam to prevent air leakage. The output of the probe is connected either to a Validyne DP103-06 pressure transducer (which measures differential pressures up to 2.5 mm of water), or a Celesco LCVR pressure transducer (which measures differential pressures up to 20.0 mm of water). Signals from the transducer are then processed using a Celesco CD10D Carrier-Demodulator. Voltages from the Carrier-Demodulator are acquired using a Hewlett-Packard 44422A data acquisition card installed in a Hewlett-Packard 3497A data acquisition control unit. This control unit, the Superior Electric type M092-FD310 Mitas stepping motor on the two-dimensional traverse, a Superior Electric Modulynx Mitas type PMS085-C2AR controller, and a Superior Electric Modulynx Mitas type PMS085-D050 motor drive are controlled by a Hewlett-Packard A4190A Series computer. Contour plots of measured quantities are generated using a polynomial interpolating technique (within DeltaGraph software) between data points. In each survey plane, data points are spaced 2.54 mm apart.

Flow Visualization. Flow visualization using smoke is used to identify vortex structures and other secondary flow features. Smoke from two or three horizontally oriented smoke wires is employed for this purpose. These are located 3.2 mm, 6.4 mm, and 19.1 mm from the surface over the fifth row of dimples at $X=200-210$ mm. To accomplish this, each wire is first coated with Barts Pneumatics Corp. super smoke fluid and then powered using a Hewlett-Packard 6433B DC power supply. With this arrangement, the smoke forms into single thin lines parallel to the test surface. As the smoke is advected downstream, the secondary flows that accompany vortex and secondary flow development cause the smoke to be rearranged in patterns that show the locations and distributions of these flow phenomena. Smoke patterns are illuminated in different planes using thin sheets of light provided by a Colotran ellipsoidal No. 550, 1000 watt spotlight, and light slits machined in two parallel metal plates. Images are recorded using a Dage-MTI CCD72 camera and control box with a Computar Inc. 12.5 mm, F1.8 lens, connected to a Panasonic AG-1960 type four-head, multiplex video cassette recorder. Images recorded on video tape (taken individually or in sequence) are then digitized using a Sony DCR-TRV900 digital video camera recorder. The resulting images are then further processed using a Power Macintosh 7500 PC computer, and finally printed using a Panasonic PV-PD 2000 digital photo printer.

Uncertainty Estimates

Uncertainty estimates are based on 95 percent confidence levels, and determined using procedures described by Moffat [16]. The uncertainty of temperatures measured with thermocouples is ±0.15°C. Spatial and temperature resolutions achieved with the infrared imaging are about 0.52 mm and 0.8°C, respectively. This magnitude of temperature resolution is due to uncertainty in determining the exact locations of thermocouples with respect to pixel values used for the *in situ* calibration. Local Nusselt number uncertainty is then about ±6.8 percent for $T_{0i}/T_w=0.68$. The corresponding Nusselt number ratio uncertainty is about ±0.19 (for a ratio of 2.00), or ±9.6 percent. Such $\mathrm{Nu/Nu_0}$ uncertainties then increase as T_{0i}/T_w becomes larger. Reynolds number uncertainty is about ±1.7 percent for Re_H of 10,200. The uncertainties of total pressure (relative to atmospheric pressure), static pressure (relative to atmospheric pressure), and streamwise velocity are about ±4.0, ±4.0, and ±2.5 percent, respectively.

Experimental Results and Discussion

Baseline Nusselt Numbers. Baseline Nusselt numbers are measured with a smooth test surface replacing the dimpled test surface at the same Reynolds numbers as employed in the dimpled channel. Other than the test surface, all geometric characteristics of the channel are the same as when a dimpled test surface is installed. These baseline values are used to normalize dimpled test surface values, and are thus used as a basis of comparison to dimpled test surface values. All baseline measurements are made with thermally and hydraulically fully developed channel flow, at a ratio of inlet stagnation temperature to wall temperature of 0.93-0.94.

Spatially Resolved Nusselt Number Distribution. Figure 3 presents spatially resolved Nusselt numbers measured on the dimpled test surface placed on one wall of the $H/D=0.5$ channel. The opposite channel wall is smooth, as mentioned. Reynolds number Re_H for the measurements is 10,200, and $T_{0i}/T_w=0.94$. Flow direction for the figure is from top to bottom in the direction of increasing *X/D*. The image shows dimples in the tenth to twelfth rows from the beginning of the test surface.

The locations of the circular concave depressions of the dimples correspond to circular $\mathrm{Nu/Nu_0}$ contours in Fig. 3. Lower Nusselt number ratios are located over the upstream halves of the depressions. Local Nusselt number ratios are then higher in the downstream halves. The highest values are then located near the downstream rims of each dimple, both slightly within each depression, and on the flat surface just downstream of each dimple. Consistent with the results of Kesarev and Kozlov [7] and Schukin et al. [10], most local values in the concave cavities are higher than values measured a smooth channel at the same Reynolds number and temperature ratio.

Referring to the area over *Z/D* from −0.3 to +0.3, and over *X/D* from 9.1 to 9.7, the high $\mathrm{Nu/Nu_0}$ region is spread over a region that is approximately parallel to the downstream edge of the dimple. Two fingers from this region then extend downwards in the positive *X/D* direction, which are located near the spanwise edges of adjoining dimples. These fingers continue to extend downward in the $+X/D$ direction until they connect with high $\mathrm{Nu/Nu_0}$ regions located on the flat surfaces just downstream of the adjacent dimples. With this arrangement, regions of high $\mathrm{Nu/Nu_0}$

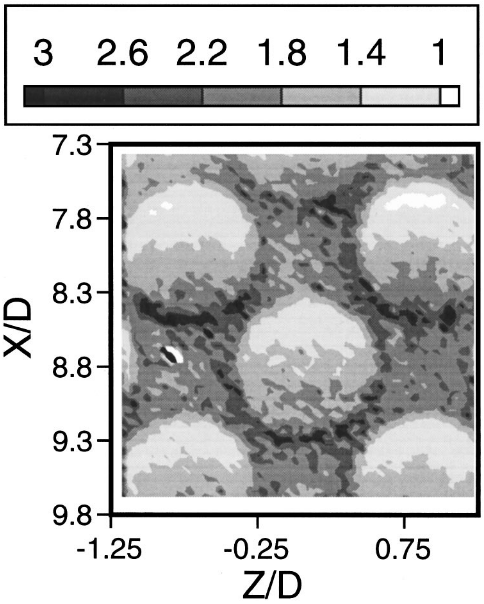

Fig. 3 Local $\mathrm{Nu/Nu_0}$ distributions measured at $\mathrm{Re}_H=10.200$ and $T_{oi}/T_w=0.94$

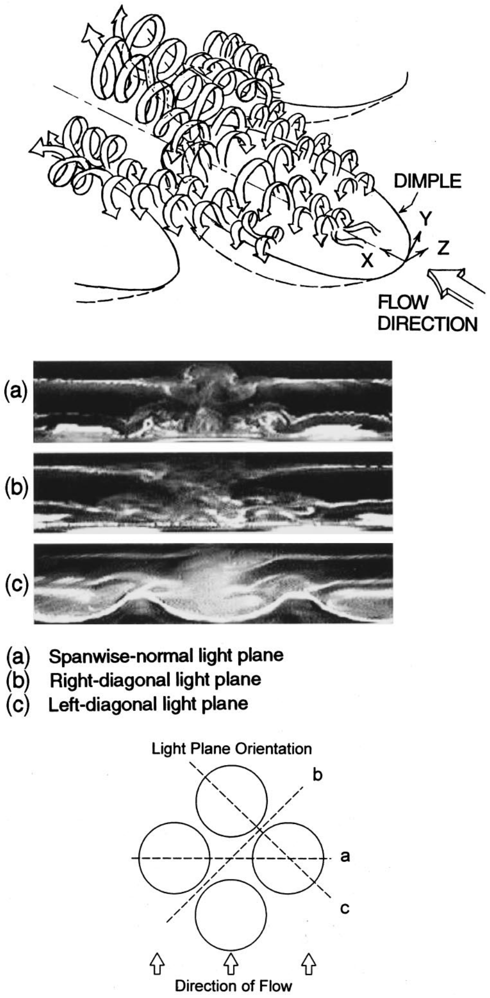

Fig. 4 Sketch of three-dimensional flow structure and flow visualization images in different light planes at dimple row 10 for $Re_H=1250$ and $H/D=0.5$

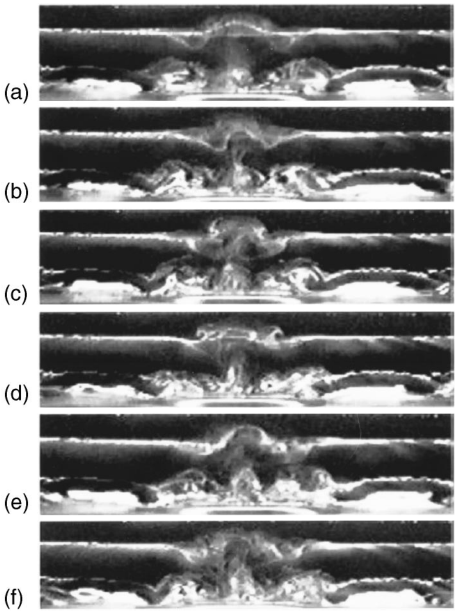

Fig. 5 Time sequence of flow visualization images in the spanwise-normal light plane at dimple row 10 for $Re_H=1250$ and $H/D=0.5$: (*a*) $t=0.0$ s, $t^*=0.0$, (*b*) $t=0.033$ s, $t^*=1.12$, (*c*) $t=0.067$ s, $t^*=2,27$, (*d*) $t=0.100$ s, $t^*=3.39$, (*d*) $t=0.133$ s, $t^*=4.50$, (*f*) $t=0.167$ s, $t^*=5.66$

are interconnected downstream of and to the sides of most dimples in the streamwise and spanwise adjacent rows.

Instantaneous Flow Structure. These regions of high local Nu/Nu_0 are the result of collections of vortex pairs and vortical fluid that is shed periodically from each dimple. The effects of this fluid on thermal transport are especially pronounced near downstream rims of dimples as well as on flat surfaces downstream of and between dimples, as mentioned. The outward shedding or ejection of fluid produces heat transfer augmentation from: (*i*) the periodicity and unsteadiness of the vortical fluid, and (*ii*) the strong secondary fluid motions of the vortical fluid and vortex pairs near the surface. A schematic drawing illustrating the character of this vortical fluid is shown in the top part of Fig. 4. Included in this figure are flow visualization images in three different planes with respect to the dimples: spanwise-normal, right-diagonal, and left-diagonal. The orientations of these planes are shown in the bottom portion of Fig. 4.

The shedding of fluid from the dimple is a key feature of the flow structure. The outward fluid motion from within the dimple (or upwash region) is present mainly at three locations with respect to each dimple. Each upwash region appears like the stem of a ''mushroom'' smoke pattern in spanwise-normal plane flow visualization images. The most prominent ''stem,'' corresponding to the strongest upwash, follows a streamwise-normal plane roughly down the centerline of each dimple. Such stems are apparent in: (*i*) streamwise views of smoke patterns illuminated in spanwise-normal planes (see Fig. 4). They are also occasionally apparent in: (*ii*) leftward-looking diagonal views of smoke patterns illuminated in right diagonal-normal planes, and (*iii*) rightward-looking diagonal views of smoke patterns illuminated in left diagonal-normal planes (again see Fig. 4). Two other stems and mushroom-shaped smoke patterns are located near the diagonal-spanwise edges of each dimple, or just downstream of these locations. Each upwash region stem leads to the ''petals'' of the ''mushroom'' located just above, at positions that are just at or just above the dimple horizon. Each ''petal'' corresponds to a vortex in the vortex pair. These vortex pairs are stretched as they are advected downstream (by the streamwise bulk flow above the dimple horizon), which causes them to become smaller in cross section and more elongated.

From a streamwise view looking downstream (spanwise-normal view in Fig. 4), the central upwash region and vortex pair are roughly symmetric with respect to a centerline-normal plane. From diagonal views (especially the right-diagonal plane in Fig. 4), the stem is elongated and bent in the downstream direction with the farthest downstream vortex elongated and somewhat distorted. This elongation is a result of viewing the vortex in a diagonal plane, and possibly a result of vortex stretching produced by the streamwise bulk flow above the dimple horizon. The axes of rotation, orientations, and structure of the vortices in these vortex pairs are about the same as they are shed from each dimple. That is, the vortices are always present temporarily at about the same locations during and after each shedding event.

At the diagonals of the dimple, the secondary flows in each vortex of each pair may impact on the flat surface adjacent to each dimple. As a result, additional smaller vortex pairs, collections of vortex pairs, or sometimes, short ''braids'' of vortical fluid are formed near dimple diagonals. This is illustrated in the schematic drawing at the top of Fig. 4, and is also apparent in the smoke patterns photographed in spanwise-normal and right- and left-diagonal planes. These pairs and packets of vortical fluid are then advected downstream as they are periodically impacted on the downstream rim of the dimpled edge and on the flat surface just downstream of the dimples. This vortical fluid is stretched further from the dimple edges (especially in dimple diagonal directions)

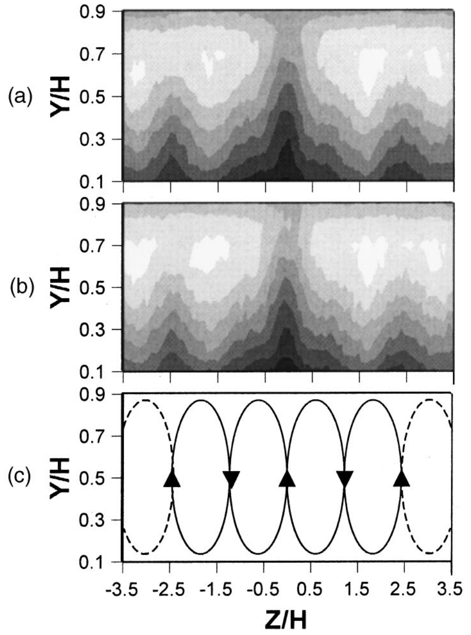

Fig. 6 Surveys of time-averaged quantities in a spanwise-normal plane at $X/D=11.88$, which is located 53.2 mm downstream of the last row of dimples on the test surface for $Re_H=9000$:(*a*) total pressure ($P_a-\bar{P}_0$), adjacent contour lines are 2.0 Pa apart; (*b*) streamwise velocity $\bar{u}$, adjacent contour lines are 0.25 m/s apart; (*c*) schematic diagram of qualitative variations of large-scale, time-averaged secondary flow vectors

as the Reynolds number increases. This causes the ''braids'' of vortical fluid to advect just above and into the dimple volumes which are located diagonal and adjacent to the dimple responsible for the initial upwash of fluid.

Another important feature of the flow structure produced by the dimpled surface is the periodicity associated with shedding of packets of vortical fluid from individual dimples. This results in a periodically varying flow structure above the dimple, which is illustrated by the time sequence of spanwise-normal flow visualization images in Fig. 5 (which are spaced 1/30 s apart from each other). Smoke patterns in the top parts of photographs (*a*), (*b*), (*e*), and (f) evidence secondary flows largely moving toward the dimple, whereas secondary flows largely move in the $+Y$ direction in the top parts of photographs (*c*) and (*d*). The small vortex pairs near dimple diagonals then oscillate to the left and right (as flow moves into and out of the side parts of the dimples) roughly in phase with the larger-scale motion. These events coincide with larger-scale inrush of flow to the dimple (photos (*a*) and (*b*) in Fig. 5), shedding of packets of vortical fluid from the dimple (photos (*c*) and (*d*)), and then another inrush event (photos (*e*) and (*f*)). This periodic sequence thus occurs continually such that the two types of events are not necessarily distinct or separate from each other. This means that some of the inward advection occurs as the shedding of fluid from the dimple is taking place, and vice versa.

Observations of videotaped flow visualization images show that the vortical fluid seems to be shed simultaneously with fluid shed from other dimples in the same spanwise row, but out of phase with the packets of fluid shed from dimples in an adjacent upstream or downstream dimple row. The inward advection and outward shedding must both take place (either simultaneously or alternatively) if continuity is to be satisfied for the flow near the dimpled surface.

Time-Averaged Surveys of Total Pressure, Streamwise Velocity, and Secondary Flow Vectors. Figure 6 presents data measured at $X/D=11.88$, which is a location about 53.2 mm downstream of the last row of dimples on the test surface. The data are time-averaged, and as such, illustrate flow characteristics which are different from, but complementary to, the flow visualization data. Each survey extends over the middle 80 percent of the height of the channel, and over Z from $-1.75D$ to $+1.75D$ (or $-3.5H$ to $+3.5H$) on each side of the spanwise centerline of the test surface. The surveys are thus located just downstream of the centerline dimple in the 13th row as well as small portions of the dimples located on either side in the same streamwise row. The surveys are then also located just downstream of two other dimples, located in the twelfth row diagonally with respect to the dimples in the thirteenth row. The data in Fig. 6 are measured at a Reynolds number Re of 9000.

Apparent in the distributions of total pressure (part (*a*)) and streamwise velocity (part (*b*)) in Fig. 6 are important deficits near the dimpled surface. Each of these is shaped roughly like an inverted ''**V**'' and is located just downstream of a dimple cavity. Note that the deficits downstream of the dimples in the 13th row (at Z/H of 0, for example) are larger and more pronounced than the deficits downstream of the dimples in the 12th row (at Z/H of $+2.5$, -2.5). Each deficit results from upwash of packets of fluid away from dimples in the positive Y direction.

Such upwash regions in the secondary flow field are shown schematically in part (*c*) of Fig. 6. These produce deficits in (P_0-P[overbar]$_0$) and u[overbar] by advecting relatively low-velocity/low total pressure fluid away from dimpled surfaces and away from the dimple horizon. Because of continuity and the boundary conditions imposed by the top and bottom walls of the channel, one downwash region is located between two adjacent upwash regions. As a result, Fig. 6(*c*) shows that two pairs of counterrotating secondary flow zones (or four total zones of rotating fluid) are present in the time-averaged flow field between the spanwise centerlines of two adjacent dimples in the same streamwise row. This is consistent with the upwash and downwash regions apparent in the flow visualization images in Figs. 4 and 5. However, upwash regions just above the dimples (where the flow visualization results are obtained) are more angled with respect to the dimple horizon at the dimple diagonals than the normally oriented upwash vectors shown in Fig. 6(*c*).

Because of the staggered arrangement of dimples in different streamwise rows, such time-averaged secondary flows are continually rearranged as flow advects over different streamwise rows of dimples. The downwash regions shown in Fig. 6(*c*) resulting from such activities advect fluid from the center portions of the channel to regions near $Y/D=0$. This and the resulting thinning of the shear layers near the dimpled surface aids the augmentation of

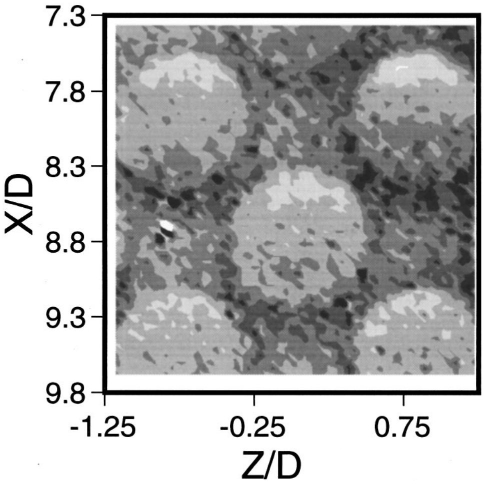

Fig. 7 Local Nu/Nu_0 distributions measured at $Re_H=61{,}500$ and $T_{oi}/T_w=0.92$. Contour plot scale is given with Fig. 3.

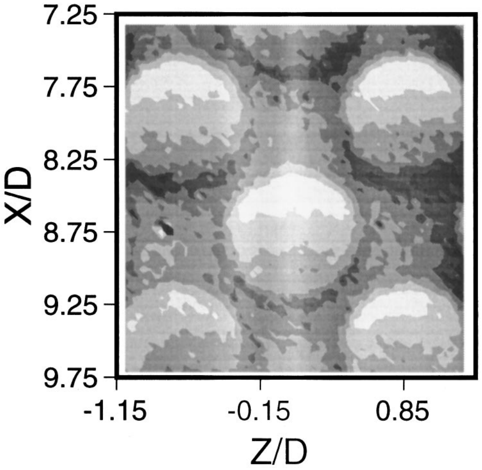

Fig. 8 Local Nu/Nu$_0$ distributions measured at Re$_H$=13,300 and T_{oi}/T_w=0.83. Contour plot scale is given with Fig. 3.

local Nusselt numbers, particularly the fingers of high Nu/Nu$_0$ in Fig. 3. As mentioned, these surface fingers extend downward in the positive *X/D* direction from the downstream edge of each dimple, and are located near the spanwise edges of adjoining dimples.

Effects of Vortex Structures on Local Nusselt Numbers at Different Reynolds Numbers and Temperature Ratios. Contour plots of local Nusselt number ratio distributions Nu/Nu$_0$ are presented in Figs. 7, 8, and 9. The data are presented for the same part of the test surface as employed to obtain the results in Fig. 3, but at different Re$_H$ or different T_{0i}/T_w compared to the data in Fig. 3. Note that the Nu/Nu$_0$ scales in all four figures are the same.

Comparing the results in Fig. 7 for Re$_H$=61,500 and $T_{0i}/T_w = 0.92$ to the results in Fig. 3 for Re$_H$=10,200 and $T_{0i}/T_w = 0.94$ illustrates the influences of Reynolds number on local Nusselt number distributions. Qualitative and quantitative variations of Nu/Nu$_0$ are very similar in these two figures. Only slight differences are apparent in the bottom portions of the dimple cavities, where crescent-shaped contours of low magnitude are slightly larger at the lower Reynolds number. In contrast, on the flat parts of the surface, Nusselt number variations are a direct result of the three-dimensional unsteady secondary flows from the dimples. Here, the similarities of local Nu/Nu$_0$ variations in Figs. 3 and 7 evidence similar vortical and secondary flow structures at the different Re$_H$ investigated.

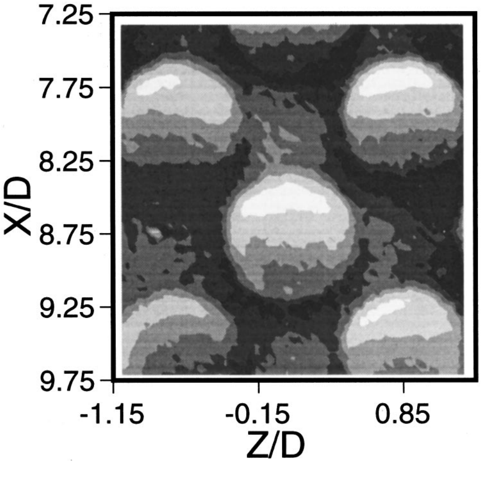

Fig. 9 Local Nu/Nu$_0$ distributions measured at Re$_H$=12,800 and T_{oi}/T_w=0.68. Contour plot scale is given with Fig. 3.

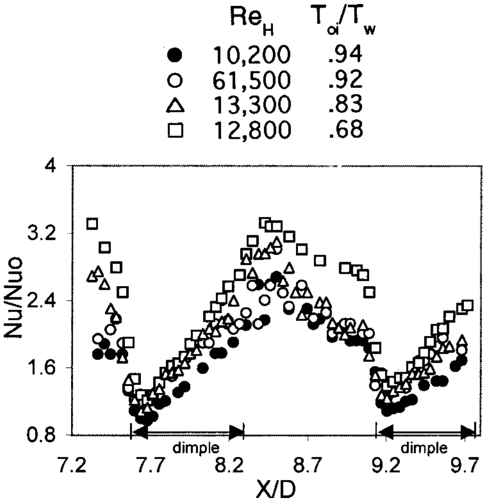

Fig. 10 Local Nu/Nu$_0$ as dependent upon *X/D*, measured at different Re$_H$ and T_{oi}/T_w at the eleventh row of dimples along a line of constant *Z/D* of 0.89

The Nusselt number ratio distributions in Figs. 8 and 9 are for T_{0i}/T_w of 0.83 and 0.68, respectively, compared to $T_{0i}/T_w = 0.94$ for Fig. 3. The Reynolds numbers for all three datasets range from 10,200 to 13,300, and thus, are all about the same. Comparing these three contour plots shows that as the ratio of inlet to wall temperature ratio decreases, the coolest part of the test surface, which corresponds to the highest values of Nu/Nu$_0$, intensifies, broadens, and extends farther away from the downstream rims of the dimples. This becomes more significant as the temperature ratio T_{0i}/T_w decreases because vortex pairs and vortical fluid in the channel bring larger amounts of colder fluid from the central parts of the channel to regions near the dimpled surface. Larger-scale secondary flows, especially downwash regions, such as those evident in the time-averaged surveys of Fig. 6, also aid this process.

The effects of varying temperature ratio and Reynolds number are further illustrated by the results presented in Figs. 10 and 11. In each case, local Nu/Nu$_0$ values are given along one line along the test surface. For Fig. 10, variations with *X/D* are given along a line corresponding to *Z/D*=0.89. This corresponds approximately with the spanwise-centerline of a dimple in the eleventh row. In Fig. 11, Nu/Nu$_0$ data are presented as they vary with *Z/D*, along a line corresponding to *X/D*=8.46. This particular streamwise location is chosen because it corresponds with the largest variations of Nu/Nu$_0$ with *Z/D*. In each case, important increases of local Nusselt numbers are evident as the temperature ratio T_{0i}/T_w decreases These are especially evident to the sides of the dimple at

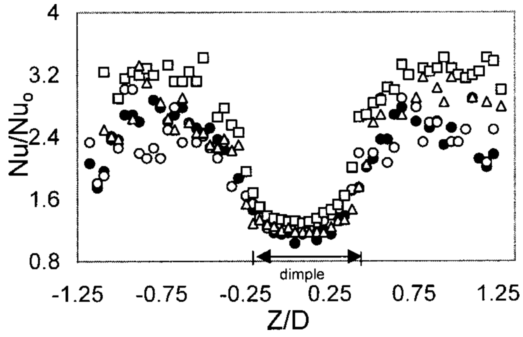

Fig. 11 Local Nu/Nu$_0$ as dependent upon *Z/D*, measured at different Re$_H$ and T_{oi}/T_w at the eleventh row of dimples along a line of constant *X/D* of 8.46. Symbols defined in Fig. 10.

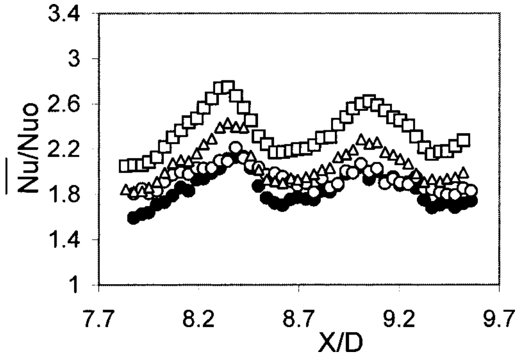

Fig. 12 Spanwise-averaged $\overline{\text{Nu}}/\text{Nu}_0$ as dependent upon *X/D*, measured at different Re_H and T_{oi}/T_w at the eleventh and twelfth rows of dimples. Symbols defined in Fig. 10.

Z/D from −1.0 to −0.5 and from +0.5 to +1.0 in Fig. 11, and downstream of a dimple in Fig. 10 at *X/D* from 8.2 to 9.0. Changes with Reynolds number are much less significant in these two figures, as expected. In each case, low Nusselt number ratios correspond with upstream portions of the dimple cavities, and the highest ratios are from locations near the rims or near the downstream edges of the dimples.

Spatially Averaged Nusselt Number Behavior. Spatially averaged Nusselt number data in Figs. 12, 13, and 14 further illustrate the influences of flow structure as the temperature ratio T_{0i}/T_w, and Reynolds number Re_H are varied. In each case, spatial averages are obtained over a rectangular area from the center to center of adjacent dimples in the tenth and twelfth rows. This gives spatial averages representative of one complete period of dimple surface geometry.

Spanwise-averaged $\overline{\text{Nu}}/\text{Nu}_0$ versus *X/D* in Fig. 12, and streamwise-averaged $\overline{\text{Nu}}/\text{Nu}_0$ versus *Z/D* in Fig. 13 both show only small changes as Reynolds number increases from 10,200 to 61,500 and T_{0i}/T_w is approximately constant. In contrast, $\overline{\text{Nu}}/\text{Nu}_0$ values increase significantly at each *X/D* or *Z/D* as temperature ratio decreases from 0.94 to 0.68 (and Re_H is approximately constant). Such variations are consistent with local data, and provide further evidence of the important influences of the vortical fluid packets produced by the dimples. High local $\overline{\text{Nu}}/\text{Nu}_0$ values are thus mostly due to higher local values just downstream of and to the sides of the dimples, whereas troughs in $\overline{\text{Nu}}/\text{Nu}_0$ distributions are generally tied to low local Nusselt numbers within dimple cavities.

The globally averaged Nusselt number data in Fig. 14 are obtained by averaging local data in both the spanwise and streamwise directions. Only small changes with Re_H are apparent. For constant T_{0i}/T_w, $\overline{\overline{\text{Nu}}}/\text{Nu}_0$ is proportional to $\text{Re}_H^{0.023}$. Such variations are qualitatively and quantitatively similar to ones measured by Chyu et al. [11] (after considering the different approaches for determination of heat transfer coefficients employed).

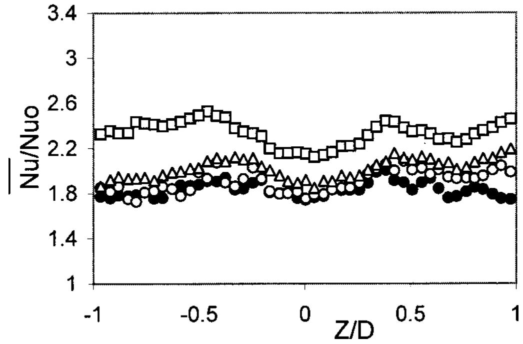

Fig. 13 Streamwise-averaged $\overline{\text{Nu}}/\text{Nu}_0$ as dependent upon *Z/D*, measured at different Re_H and T_{oi}/T_w at the eleventh and twelfth rows of dimples. Symbols defined in Fig. 10.

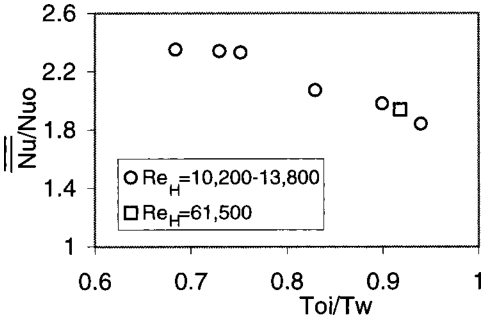

Fig. 14 Globally averaged $\overline{\overline{\text{Nu}}}/\text{Nu}_0$ as dependent upon temperature ratio T_{oi}/T_w, measured at different Re_H at the eleventh and twelfth rows of dimples

$\overline{\overline{\text{Nu}}}/\text{Nu}_0$ values shown in Fig. 14 increase by about 30 percent as the temperature ratio T_{0i}/T_w, decreases from 0.94 to 0.68 (and Reynolds number is approximately constant). This corresponds to a continual change of $\overline{\overline{\text{Nu}}}/\text{Nu}_0$ from 1.8 to about 2.4. Here, baseline Nusselt numbers Nu_0 (used for normalization) are measured at $T_{0i}/T_w = 0.93\text{-}0.94$.

According to Kays and Crawford [17], the variable property correction for such internal turbulent flows with wall heating and smooth (undimpled) surfaces is $(T_x/T_m)^{-0.5}$. This gives a decrease of variable-property, baseline Nu_0 of about 14 percent (compared to constant property values) as T_{0i}/T_w, decreases from 0.94 to 0.68. Nu_0 values determined using the Kays and Crawford [17] variable property correction can then be used to normalize dimple $\overline{\overline{\text{Nu}}}$ data at the same T_{0i}/T_w. With this approach, $\overline{\overline{\text{Nu}}}/\text{Nu}_0$ then ranges from 1.85 to about 2.89 as T_{0i}/T_w, decreases from 0.94 to 0.68.

Coolant passage friction factors are also important to designers of turbomachinery components. For Re_H from 10,200 to 13,800, ratios of dimple surface friction factor to smooth surface friction factor are 1.51–1.55. Such values, along with heat transfer augmentations at the same Reynolds numbers, provide further evidence of the feasibility of dimpled passages for internal turbine airfoil cooling.

Summary and Conclusions

Experimental results measured on and above a dimpled test surface placed on one wall of a channel are presented. Channel height *H* is 2.54 cm, and dimple print diameter *D* is 5.08 cm, giving $H/D = 0.5$. Flow structural characteristics and surface Nusselt numbers are given for Reynolds numbers Re_H from 1250 to 61,500 and temperature ratios T_{0i}/T_w, ranging from 0.68 to 0.94. Flow visualizations show vortical fluid and vortex pairs shed from the dimples. These include a large upwash region and packets of fluid emanating from the central regions of each dimple, as well as vortex pairs and vortical fluid, which form near dimple diagonals. These help to augment surface heat transfer levels as they periodically impact the test surface and periodically produce an influx of bulk fluid. This occurs as the vortices and vortical fluid act to ''pump'' fluid to and away from the surface over different length scales, which helps to augment transport of different sized packets of fluid (with different temperatures) to and away from the surface. The periodic nature of the shedding of vortical fluid from the dimples also aids the heat transfer augmentation process.

The effects of the vortex structures are particularly pronounced near the downstream rims of each dimple, both slightly within each depression, and on the flat surface just downstream of each dimple. The resulting high local Nusselt number region on the flat surface is spread over a region that is approximately parallel to the downstream edge of each dimple, and along two strips of flat surface located near the spanwise edges of downstream-diagonal, adjoining dimples.

Such augmentations are spread over larger surface areas and become more pronounced as the ratio of inlet stagnation temperature to local surface temperature decreases. This is due to the actions of different-sized vortex pairs and secondary flows in effectively advecting cool fluid from the central parts of the channel to regions close to the hotter dimpled surface. Downwash regions from the vortex pair emanating from the central part of each dimple, from the vortex pairs generated along dimple diagonals, and from rotating secondary flows spread over the entire channel cross section all make contributions to this process. As a result, local and spatially averaged heat transfer augmentations become larger as the T_{0i}/T_w, temperature ratio decreases.

Acknowledgments

The work presented in this paper was performed as a part of the Advanced Turbine System Technology Development Project, sponsored both by the U.S. Department of Energy and Solar Turbines, Inc.

Nomenclature

D = dimple print diameter
D_H = channel hydraulic diameter
H = channel height
h = heat transfer coefficient based on total surface area (dimples and flat) $= q''/(T_w - T_m)$
k = thermal conductivity
Nu = Nusselt number$=hD_H/k$
Nu_0 = baseline Nusselt number in a channel with smooth surfaces and no dimples
P = pressure
q'' = surface heat flux
Re_H = Reynolds number based on channel height $= H\overline{U}/\nu$
t = time
t^* = normalized time$=t\overline{U}/H$
T = temperature
$\overline{U}$ = streamwise bulk velocity averaged over the channel cross section
$\overline{u}$ = time-averaged local streamwise velocity
X = axial coordinate measured from test section inlet
Y = normal coordinate measured from test section dimple horizon
Z = spanwise coordinate measured from test section centerline
ν = kinematic viscosity
ρ = density

Subscripts

a = ambient value
i = time-averaged, test section inlet value
m = time-averaged, local mixed-mean value
0 = total or stagnation value
w = local wall value

Superscripts

— = spanwise- or streamwise-averaged
= = globally averaged

References

[1] Bearman, P. W., and Harvey J. K., 1976, ‘‘Golf Ball Aerodynamics,’’ Aeronautical Q., pp. 112–122.
[2] Gromov, P. R., Zobnin, A. B., Rabinovich, M. I., and Sushchik, M. M., 1986, ‘‘Creation of Solitary Vortices in a Flow Around Shallow Spherical Depressions,’’ Sov. Tech. Phys. Lett., **12**, No. 11, pp. 1323–1328.
[3] Afanasyev, V. N., Chudnovsky, Y. P., Leontiev, A. I., and Roganov, P. S., 1993, ‘‘Turbulent Flow Friction and Heat Transfer Characteristics for Spherical Cavities on a Flat Plate,’’ Exp. Therm. Fluid Sci., **7**, pp. 1–8.
[4] Belen’kiy, M. Y., Gotovskiy, M. A., Lekakh, B. M., Fokin, B. S., and Dolgushin, K. S., 1994, ‘‘Heat Transfer Augmentation Using Surfaces Formed by a System of Spherical Cavities,’’ Heat Transfer-Sov. Res., **25**, No. 2, pp. 196–203.
[5] Bearman, P. W., and Harvey, J. K., 1993, ‘‘Control of Circular Cylinder Flow by the Use of Dimples,’’ AIAA J., **31**, No. 10, pp. 1753–1756.
[6] Kimura, T., and Tsutahara, M., 1991, ‘‘Fluid Dynamic Effects of Grooves on Circular Cylinder Surface,’’ AIAA J., **29**, No. 12, pp. 2062–2068.
[7] Kesarev, V. S., and Kozlov, A. P., 1994, ‘‘Convective Heat Transfer in Turbulized Flow Past a Hemispherical Cavity,’’ Heat Transfer-Sov. Res., **25**, No. 2, pp. 156–160.
[8] Terekhov, V. I., Kalinina, S. V., and Mshvidobadze, Y. M., 1995, ‘‘Flow Structure and Heat Transfer on a Surface With a Unit Hole Depression,’’ Russ. J. Eng. Thermophys., **5**, pp. 11–33.
[9] Zhak, V. D., 1995, ‘‘The Taylor–Goertler Vortices and Three-Dimensional Flow Evolution in Cavity,’’ Russ. J. Eng. Thermophys., **5**, pp. 165–176.
[10] Schukin, A. V., Koslov, A. P., and Agachev, R. S., 1995, ‘‘Study and Application of Hemispherical Cavities for Surface Heat Transfer Augmentation,’’ ASME Paper No. 95-GT-59.
[11] Chyu, M. K., Yu, Y., Ding, H., Downs, J. P., and Soechting, F. O., 1997, ‘‘Concavity Enhanced Heat Transfer in an Internal Cooling Passage,’’ ASME Paper No. 97-GT-437.
[12] Lin, Y.-L., Shih, T. I.-P., and Chyu, M. K., 1999, ‘‘Computations of Flow and Heat Transfer in a Channel With Rows of Hemispherical Cavities,’’ ASME Paper No. 99-GT-263.
[13] Gortyshov, Y. F., Popov, I. A., Amirkhanov, R. D., and Gulitsky, K. E., 1998, ‘‘Studies of Hydrodynamics and Heat Exchange in Channels With Various Types of Intensifiers,’’ Proc. 11th International Heat Transfer Congress, **6**, pp. 83–88.
[14] Moon, H. K., O’Connell, T., and Glezer, B., 2000, ‘‘Channel Height Effect on Heat Transfer and Friction in a Dimpled Passage,’’ ASME J. Eng. Gas Turbines Power, **122**, pp. 307–313.
[15] Hedlund, C. R., and Ligrani, P. M., 1999, ‘‘Local Swirl Chamber Heat Transfer and Flow Structure at Different Reynolds Numbers,’’ ASME J. Turbomach., **122**, pp. 375–385.
[16] Moffat, R. J., 1988, ‘‘Describing the Uncertainties in Experimental Results,’’ Exp. Therm. Fluid Sci., **1**, No. 1, pp. 3–17.
[17] Kays, W. M., and Crawford, M. E., 1993, *Convective Heat and Mass Transfer*, McGraw-Hill, New York.

Flow and Heat Transfer in a Rotating Square Channel With 45 deg Angled Ribs by Reynolds Stress Turbulence Model

Yong-Jun Jang
Turbine Heat Transfer Laboratory,
Department of Mechanical Engineering,
Ocean Engineering Program,
Texas A&M University,
College Station, TX 77843-3123

Hamn-Ching Chen
Ocean Engineering Program,
Department of Civil Engineering,
Texas A&M University,
College Station, TX 77843-3136

Je-Chin Han
Turbine Heat Transfer Laboratory,
Department of Mechanical Engineering,
Texas A&M University,
College Station, TX 77843-3123

Numerical predictions of three-dimensional flow and heat transfer are presented for a rotating square channel with 45 deg angled ribs as tested by Johnson et al. (1994). The rib height-to-hydraulic diameter ratio (e/D_h) is 0.1 and the rib pitch-to-height ratio (P/e) is 10. The cross section of the ribs has rounded edges and corners. The computation results are compared with the experimental data of Johnson et al. (1994) at a Reynolds number (Re) of 25,000, inlet coolant-to-wall density ratio ($\Delta\rho/\rho$) of 0.13, and three rotation numbers (Ro) of 0.0, 0.12, and 0.24. A multiblock numerical method has been employed with a near-wall second-moment turbulence closure model. In the present method, the convective transport equations for momentum, energy, and turbulence quantities are solved in curvilinear, body-fitted coordinates using the finite-analytic method. Pressure is computed using a hybrid SIMPLER/PISO approach, which satisfies the continuity of mass and momentum simultaneously at every time step. The second-moment solutions show that the secondary flows induced by the angled ribs, rotating buoyancy, and Coriolis forces produced strong nonisotropic turbulent stresses and heat fluxes that significantly affected flow fields and surface heat transfer coefficients. The present near-wall second-moment closure model provided an improved flow and heat transfer prediction. [DOI: 10.1115/1.1333092]

Introduction

Gas turbine blades in modern gas turbine engines are designed to operate with high heat loads as the turbine inlet temperature increases. Sophisticated cooling techniques such as film cooling and convective internal cooling are essential in maintaining acceptable blade life. For the internal cooling of the blades, the walls of the coolant passages are roughened by periodic ribs to enhance heat transfer. These rib turbulators disturb the laminar sublayer and create local wall turbulence due to flow separation and reattachment between the ribs, which greatly enhances the heat transfer. The flow field in real gas turbine engines is further complicated by the presence of secondary flows arising from blade rotation. At present, efforts to understand the flow and local heat transfer characteristics in rotating cooling passages are continuing, especially with angled ribs attached to two opposite walls of a cooling channel.

Han and Park [1] and Ekkad and Han [2] performed experimental studies on heat transfer characteristics in nonrotating rib-roughened channels. Bonhoff et al. [3] and Schabacker et al. [4] studied the flow characteristics in nonrotating rib-roughed channels. Tse and Steuber [5] investigated flow characteristics in a rotating serpentine coolant passage with angled ribs (45 deg) using LDV. Wagner et al. [6], Johnson et al. [7], Parsons et al. [8], and Zhang et al. [9] studied the surface heat transfer coefficient in a rotating, multi-pass square channel with normal and angled ribs. Johnson et al. [7] made the most systematic investigation of the effects of buoyancy and Coriolis forces on heat transfer coefficient distributions of four-pass square channels with trips angled to the flow (45 deg ribs). They concluded that the maximum rotating heat transfer coefficient increased 30-40 percent compared to stationary 45 deg ribbed wall values, while the minimum rotating heat transfer coefficient decreased to 50 percent of the stationary 45 deg ribbed wall model. However, the heat transfer coefficients with angled trip strips are less sensitive to buoyancy effects than the heat transfer in models with either smooth walls or normal trips. They recommended that angled trip strips (45 deg ribs), rather than normal trip strips (90 deg ribs), be used in turbine blade coolant passage design. Since the experiments of Johnson et al. [7] are very close to typical turbine blade cooling conditions, several researchers have used their data as a baseline for comparison.

In recent years, several researchers have made computational studies on internal cooling channels. Prakash and Zerkle [10], Iacovides et al. [11], Bo et al. [12], Stephens et al. [13], Bonhoff et al. [14], and Chen et al. [15] have made predictions on the flow and heat transfer behavior of rotating channels with smooth walls. Stephens et al. [16], using a low-Reynolds-number $k-\epsilon$ turbulence model, investigated three-dimensional flow and heat transfer in a nonrotating rectangular duct (one pass) where one wall was roughened with five equally spaced 90 deg square ribs. Rigby et al. [17] presented the numerical simulations for flow and heat transfer in a nonrotating straight duct with normal (90 deg) ribs. Turbulence was accounted for by a $k-\epsilon$ turbulence model. They made comparisons with the detailed heat transfer distribution data of Ekkad and Han [2]. Stephens et al. [18], using a low-Reynolds-number $k-\epsilon$ turbulence model, investigated flow and heat transfer characteristics in a straight nonrotating duct with inclined, rounded ribs on two opposite walls and provided important characteristics on the inclined rib ducts. Chen et al. [19] and Jang et al. [20] studied flow and heat transfer behavior in a nonrotating two-pass square channel with 90 and 60 deg ribs, respectively. They used two turbulence models: a two-layer $k-\epsilon$ isotropic eddy viscosity model and a near-wall second-moment closure model. By comparing the detailed heat transfer data of Ekkad and Han [2] with their own, they validated the code capability and concluded that the second-moment closure model is necessary for predicting flow and heat transfer characteristics in the ribbed duct.

Contributed by the International Gas Turbine Institute and presented at the 45th International Gas Turbine and Aeroengine Congress and Exhibition, Munich, Germany, May 8–11, 2000. Manuscript received by the International Gas Turbine Institute February 2000. Paper No. 2000-GT-229. Review Chair: D. Ballal.

Prakash and Zerkle [21], employing a high-Reynolds-number $k-\epsilon$ turbulence model with wall function approximation, made a numerical prediction of flow and heat transfer in a ribbed rectangular duct (90 deg rib) with and without rotation. However, their calculations used periodicity and neglected buoyancy effects. They suggested that a low-Reynolds-number model is necessary to simulate real gas turbine engine conditions and a Reynolds stress model is required to capture anisotropic effects. Using the periodicity of the flow, Iacovides [22] computed flow and temperature fields in a rotating straight duct with normal ribs. Two zonal models of turbulence were tested: a $k-\epsilon$ with a one-equation model of k transport across the near-wall region and a low-Re differential stress model (DSM). He concluded that the DSM thermal computations were clearly superior to those of the $k-\epsilon$/one-equation. Rigby [23] presented the numerical prediction of flow and heat transfer in a rotating ribbed (90 deg rib) coolant passage with a 180 deg turn. The computation was performed using a $k-\epsilon$ turbulence model, and the heat transfer coefficient was overpredicted for the stationary case and underpredicted for the rotating case compared to experimental data. Iacovides and Raisee [24] explored turbulence modeling issues related to the computation of flow and heat transfer in internal cooling passages of turbine blades with normal ribs (90 deg). They tested four turbulence models: a zonal $k-\epsilon$, a low-Re $k-\epsilon$, a zonal differential stress model (DSM), and a low-Re DSM. They found that zonal models underpredicted surface heat transfer coefficients because they ignored the effects of transport on the near-wall turbulence scale. The low-Re closures were found to reproduce the correct surface heat transfer coefficients. In their results, the low-Re DSM model reproduced the turbulence field more reasonably than the $k-\epsilon$ model. Bonhoff et al. [14] calculated the heat transfer coefficients and flow fields for rotating **U**-shaped coolant channels with angled ribs (45 deg), which is the same geometry tested by Johnson et al. [7]. They used a Reynolds stress turbulence model with wall functions in the FLUENT CFD code. Their results show that the Nusselt number ratios for the stationary case were close to the data of Johnson et al. [7]. However, the Nusselt number ratios for the rotation case were off from the experimental data. Stephens and Shih [25] and Shih et al. [26] performed an investigation of the effect of angled ribs on the heat transfer coefficients in a rotating two-passage duct using a low-Re number $k-\epsilon$ turbulence model. They studied the effects of Reynolds numbers, rotation numbers, and buoyancy parameters. In comparison with the data of Johnson et al. [7] data, the heat transfer coefficient was underpredicted for the stationary case. However, the results for the rotating case were not clearly verified.

To date, extensive numerical studies of flow and heat transfer in a rotating duct with ribs have not been possible for several reasons. One reason is associated with turbulence models. As indicated in Iacovides and Raisee [24], the wall function approach is inappropriate when there are flow separations. Moreover, the simple isotropic eddy viscosity model cannot capture the physically reasonable flow and heat transfer behavior induced by the anisotropic characteristic of turbulent flow around the ribs. However, recent computational work by Chen et al. [15] for a rotating two-pass duct with smooth walls, and Chen et al. [19] and Jang et al. [20] for the stationary two-pass ribbed ducts in our laboratory, have demonstrated the superiority of the second-moment closure model over simpler $k-\epsilon$ isotropic eddy viscosity models using the finite analytic method. Encouraged by this successful result, the model and method have been applied to predict flow and heat transfer in a rotating duct with 45 deg angled ribs. This paper presents the flow characteristics and heat transfer results in a rotating square duct with 45 deg angled ribs of a rounded cross section. The geometry represents the first passage of the four-pass, serpentine passage that was experimentally investigated by Johnson et al. [7].

The computation was performed by a near-wall second-moment turbulence closure model. The governing equations for this model were described in detail by Chen et al. [15] and will not be repeated here. For completeness, the numerical method will be briefly summarized in the following section.

Chimera and RANS Method

In the present study, the chimera RANS method of Chen [27,28] and Chen et al. [15] was used for calculating the fluid flow and heat transfer in stationary and rotating ribbed channels. The present method solves the mean flow and turbulence quantities in an arbitrary combination of embedded, overlapped, or matched grids using a chimera domain decomposition approach. In this approach, the solution domain is first decomposed into a number of smaller blocks, which facilitate an efficient adaptation of different block geometries, flow solvers, and boundary conditions for calculations involving complex configurations and flow conditions. The finite-analytic numerical method of Chen and Chen [29] and Chen et al. [30] was used within each computational block to solve the unsteady RANS equations on a general curvilinear, body-fitted coordinate system. The coupling between the pressure and velocity is accomplished using a hybrid SIMPLER/PISO algorithm given in Chen and Patel [31] and Chen and Korpus [32]. The method satisfies continuity of mass by requiring the contravariant velocities to have a vanishing divergence at each time step. Pressure is solved using the concept of pseudovelocities and, when combined with the finite-analytic discretization, gives the Poisson equation for pressure. To ensure the proper conservation of mass and momentum between the linking grid blocks, the grid-interface conservation techniques of Hubbard and Chen [33] and Chen and Chen [29] were used to eliminate the unphysical mass source resulting from the interpolation errors between the chimera grid blocks. More detailed descriptions of the chimera RANS method were given in Chen and Chen [29] and Chen and Liu [34].

Results and Discussion

Calculations were performed for the one-pass rotating square channel with 45 deg angled ribbed wall as tested by Johnson et al. [7]. Figure 1 shows the schematic diagram and an enlarged view of the numerical grids around the ribs. Two of the four side walls in the rotation direction are denoted as the leading and trailing surfaces, respectively. The other two side walls are denoted as the inner and outer surfaces. The leading surface is roughened with 13 equally spaced ribs of rounded cross section, and the trailing surface with twelve equally spaced ribs of rounded cross section. The ribs on these two walls were staggered relative to each other, with ribs on the leading surface offset upstream from those on the trailing surface by a half pitch (P). All ribs were inclined at an angle (α) of 45 deg with respect to the flow. The length of the duct was $17.5D_h$ and the radius from the axis of rotation was 42 D_h. The length from the inlet to the first rib (L_1) was $1.62D_h$ and the length from the last rib to the exit (L_2) was $2.6D_h$. The rib height-to-hydraulic diameter ratio (e/D_h) was 0.1 and the rib pitch-to-height ratio (P/e) was 10.

In this study, the Reynolds number (Re) was fixed at 25,000, which is a typical operating condition for medium-sized gas turbines. The rotation number (Ro) was varied from 0 to 0.24 and the coolant-to-wall density ratio($\Delta\rho/\rho$) was fixed at 0.13.

The present calculations used a fully developed turbulent boundary layer profile at the inlet of the duct. Since the fully developed profiles for mean flow and turbulence quantities are not known analytically, a separate calculation was performed for a straight duct to provide the inlet conditions at the duct entrance. The flow was assumed to be parabolic at the exit of the duct with zero-gradient boundary conditions for mean velocity and all turbulence quantities, while linear extrapolation was used for the pressure field. All walls, including the rib surfaces, are heated to a constant temperature. The coolant fluid at the entrance of the duct

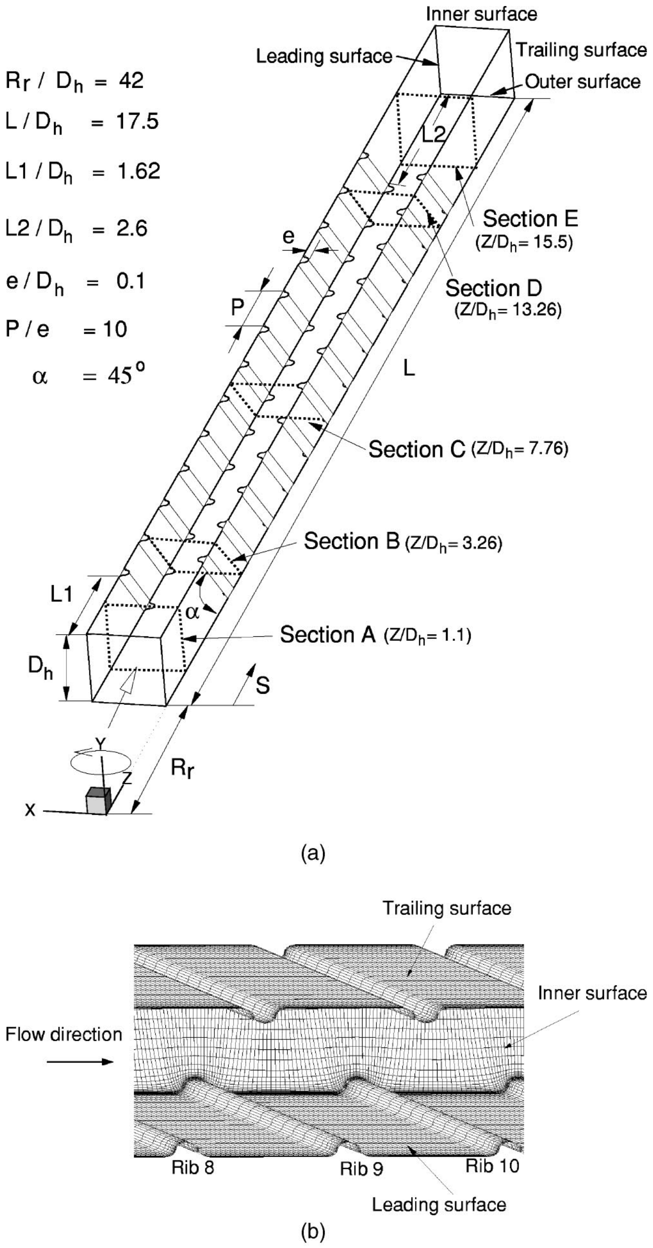

(a)

(b)

Fig. 1 Geometry and numerical grid

was air at a uniform temperature T_0 (i.e., $\theta=(T-T_0)/(T_w-T_0)=0$), and the wall temperature, including the ribs, was kept constant at $T=T_w$ ($\theta=1$).

The Nusselt numbers were normalized with a smooth tube correlation (Kays and Crawford [35]) for fully developed, nonrotating, turbulent flow:

$$\mathrm{Nu}_0=0.0176\ \mathrm{Re}^{0.8}$$

The present numerical grid was generated using the interactive gridding code GRIDGEN developed by Steinbrenner et al. [36]. It was then reblocked into several interlocked computational blocks to facilitate the implementation of near-wall turbulence models and specification of boundary conditions. To provide adequate resolutions of the viscous sublayer and buffer layer adjacent to a solid surface, the minimum grid spacing in the near-wall region was maintained at $D_h\times10^{-4}$, which corresponds to a wall coordinate y^+ of the order of 0.1. In all calculations, the root-mean-square (rms) and maximum absolute errors for both the mean flow and turbulence quantities were monitored for each computational block to ensure complete convergence of the numerical solutions. A convergence criterion of 10^{-5} was used for the maximum rms error in all computational blocks.

A grid-refinement study was performed using four different grid distributions. In the first test, three grid systems $21\times21\times570$, $41\times41\times570$, and $61\times61\times570$ (570 in the streamwise direction and 21, 41, and 61 in each of the two cross-stream directions) were evaluated. The maximum improvement in the spanwise-averaged Nusselt number ratio was about 40 percent when the numerical grid was refined from $21\times21\times570$ to $41\times41\times570$. However, further grid refinement to $61\times61\times570$ produced only a 4 percent improvement in the predicted spanwise averaged Nusselt number ratio. In the second test, two grid systems of $41\times41\times285$ and $41\times41\times570$ were examined to determine the grid resolution in the axial direction. The Nusselt number ratio improved by 5 percent with the $41\times41\times570$ grid when compared to the $41\times41\times285$ grid. As indicated in Stephens et al. [18], the Nusselt number is more sensitive to the grid spacing in the cross-stream direction than in the streamwise direction. This investigation concluded that the $41\times41\times570$ grid system was nearly grid independent. All the results in the following discussion were based on the $41\times41\times570$ grid distribution. The grid was divided into five computational blocks with a total grid point count of approximately 1,000,000.

Velocity and Temperature Fields. This section presents three-dimensional mean flow and temperature fields for the rotating square duct with 45 deg angle ribs. Computations were performed for three rotation numbers of 0.0, 0.12, and 0.24, at a Reynolds number of 25,000 and an inlet coolant-to-wall density ratio of 0.13.

Figure 2 shows the calculated secondary flow vectors and constant temperature contours at five axial stations (the first and fifth planes are normal while the second through the fourth are inclined) as defined in Fig. 1 for the nonrotating case. Each figure is viewed from upstream. Before the flow reached the first rib (Fig. 2(*a*)), four corner vortices were generated as a result of the Reynolds stress anisotropy in the straight duct. The magnitude of those vortices, which is less than $0.02W_b$, cannot be seen clearly in this figure. Figures 2(*b*–*d*) show the secondary flow field induced by staggered angled ribs of the rounded cross section. It can be seen that the staggered angled ribs produced a pair of asymmetric counterrotating secondary flows in the inclined cross-stream plane. These figures also show that the angled ribs induced the fast flow near the leading and trailing surfaces between the ribs, which impinged on the outer surface and then returned along the centerline of the inclined cross-stream plane. This secondary flow structure convected the cooler fluid from the core toward the inner surface and then moved back along the ribbed surface. This led to steep temperature gradients and high heat transfer coefficients on both the inner and ribbed surfaces. It is important to note that the secondary flows became stronger as the fluid moved downstream along the staggered angled ribbed ducts. The magnitude of the secondary flow velocity in the middle of the inclined cross-stream plane at section B (Fig. 2(*b*)) was $0.13W_b$ and at section D (Fig. 2(*d*)) it doubled to $0.25W_b$. Figure 3 shows the cross-stream velocity vectors and temperature contours for rotation number Ro = 0.12 and inlet coolant-to-wall density ratio, $\Delta\rho/\rho=0.13$ at the same planes as the nonrotating case. Figure 3(*a*) (before the ribs) shows a secondary flow pattern that is similar to the one in the smooth wall rotating duct (Chen et al. [15]). That is, the Coriolis forces produced two counterrotating flows that pushed the cooler fluid from the core toward the trailing surface and then returned along the inner and outer surfaces. However, its magnitude was small when compared to the rib-induced flow. The Coriolis force started to distort the secondary flow set up by the angled ribs in section B (Fig. 3(*b*)). In sections C and D (Figs. 3(*c*) and (*d*)), the Coriolis force effect can be clearly seen when compared with Figs. 2(*c*) and 2(*d*). A vortex near the lead-

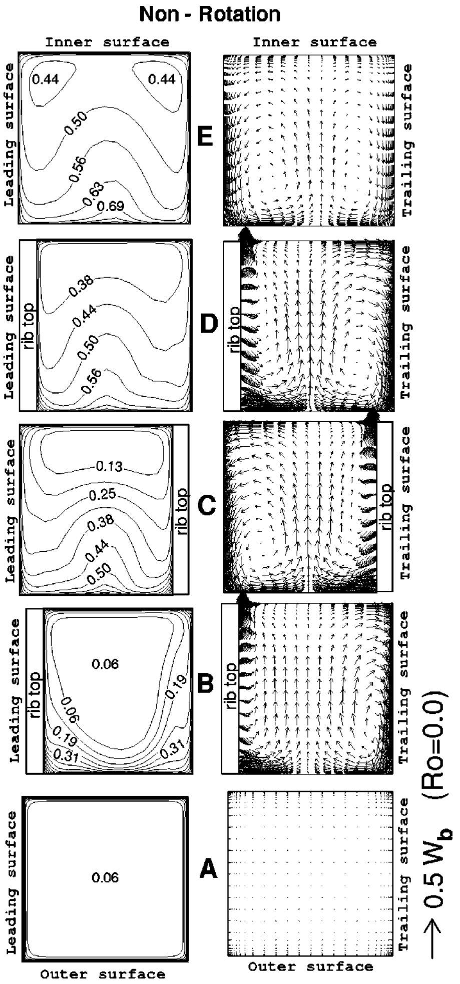

Fig. 2 Dimensionless temperature (*θ*) and secondary flows for ribbed nonrotating duct

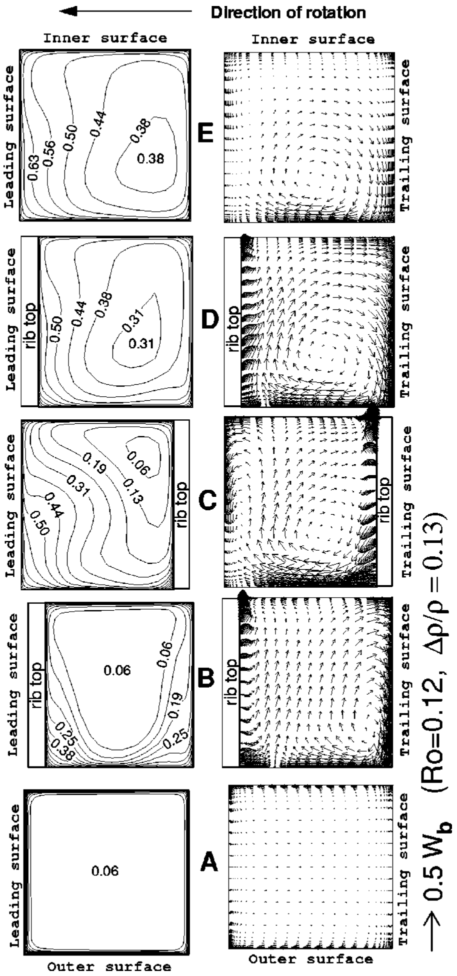

Fig. 3 Dimensionless temperature (*θ*) and secondary flows for ribbed rotating duct (Ro=0.12)

ing surface generated by the angled ribs was weakened by the Coriolis force and became smaller (Fig. 3(*c*)), while the vortex near the trailing surface generated by the angled ribs was strengthened. This vortex combined with the Coriolis-induced vortex and became larger (Fig. 3(*c*)). In this rotating case, the cooler fluid was pushed by the Coriolis force toward the trailing surface where it was expected that the temperature gradients would be high.

For a higher rotation number (Ro=0.24), the effect of the Coriolis force on the flow field was severe, as shown in Fig. 4. Figure 4(*a*) (before the ribs) shows that the two Coriolis-induced, counterrotating cross-stream flows became stronger due to the higher rotation. Figure 4(*b*) shows that the secondary flow and temperature field were not changed much when compared with the rotation number Ro=0.12. However, Fig. 4(*c*) shows the secondary flow patterns were further distorted by the high rotation. The stronger Coriolis forces produced a larger vortex near the trailing surface and destroyed the rib-induced fast flow near the leading surface. Simultaneously, the core fluid was pushed farther toward the trailing surface. Two counterrotating vortices caused by the Coriolis force reappeared farther downstream of this duct, as shown in Fig. 4(*d*). Figure 4(*e*) clearly shows two counterrotating vortices caused by the Coriolis force, and also shows that the flow on the leading surface was disturbed by the reversed flow in the streamwise direction which was caused by the centrifugal buoyancy force.

In order to facilitate a more detailed understanding of the three-dimensional flow field for the nonrotating case, Fig. 5 shows the three-dimensional particle traces around the ninth, tenth, and eleventh ribs near the leading surface. Unlike the prediction of Stephens et al. [18], that there was no separation around the ribs, Fig. 5 shows that the rib-induced separations (vortices) were generated downstream of each rib and next to the inner surface (i.e., rib leading corner), then pushed away diagonally between the angled ribs and then damped out by the spiral-like streamwise flow (not shown). Figure 6(*a*) shows the streamwise velocity vector distribution for nonrotation, which presents only half of the section of the plane between the leading and trailing surfaces, because of the flow symmetry, at three locations: in the middle of the rib, near the inner surface ($0.018D_h$ from the inner surface), and near the outer surface ($0.018D_h$ from the outer surface). This figure helps show the three-dimensional flow characteristics of this configuration. Flow separation was present near the inner surface but not at the middle of the ribs or near the outer surface. Figure 6(*b*) shows the streamwise velocity vector distribution for the entire section of the plane between the leading and trailing surfaces in the middle of the ribs at a rotation number of 0.24 and inlet density ratio of 0.13. Unlike the nonrotating case, flow separation was present on the leading surface due to the centrifugal buoyancy force, which tended to slow down the lighter fluid (lower density fluid) near the leading surface. It is also observed that high-momentum cooler fluid was pushed toward the trailing surface by the Coriolis force.

Surface Heat Transfer. Figures 7(*a*) and 7(*b*) present enlarged views of the detailed Nusselt number ratio distributions on all four walls for the stationary case around the ninth and tenth ribs. The highest heat transfer coefficients took place on the front of the rib due to flow impingement, while the heat transfer was

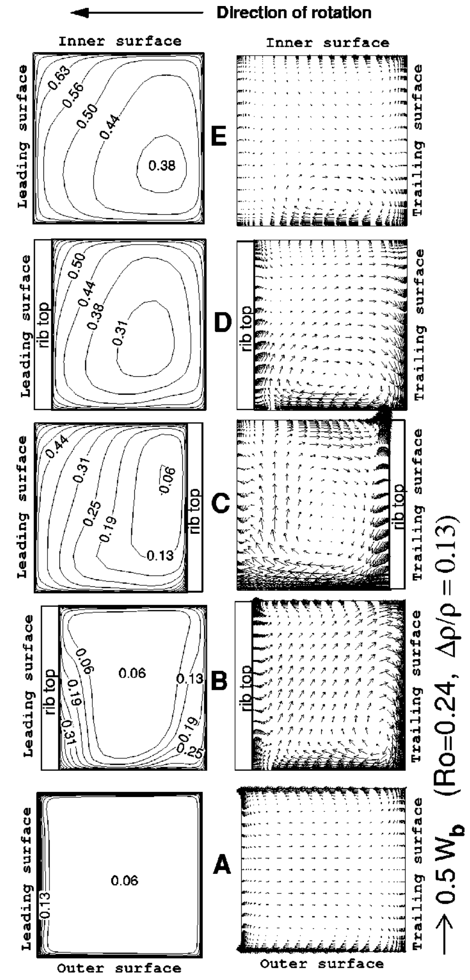

Fig. 4 Dimensionless temperature (θ) and secondary flows for ribbed rotating duct (Ro=0.24)

low on the back of the rib where the flow tried to separate. The leading and trailing surfaces have similar heat transfer patterns. In the regions between the ribs, the heat transfer was high next to the inner surface because flow reattachment took place, creating a thinner thermal boundary layer. Due to the rib-induced secondary flow characteristics of this configuration, the heat transfer decreased diagonally downstream of the rib leading edge to upstream of the next rib trailing edge. Another high heat transfer spot is seen on the outer surface next to both the leading and trailing surfaces and is caused by the impingement of the secondary flow (Fig. 7(*a*)). The present calculations created higher heat transfer on the inner surface than the outer surface due to the secondary flow, which pushed cooler fluids from the core regions toward the inner surface where the temperature gradient was higher compared to the outer surface (see also Fig. 2).

Detailed Nusselt number ratios are shown in the same location as the nonrotating case for a higher rotation number ($Ro=0.24$, $\Delta\rho/\rho=0.13$) (Figs. 7(*c*, *d*)). On the leading surface (Fig. 7(*c*)), the high heat transfer next to the inner surface cannot be seen in this rotating flow because the Coriolis force caused the core fluid to be pushed toward the trailing surface, and the Coriolis-induced vortex prevented flow reattachment on the leading surface, which usually caused a high heat transfer coefficient. The high heat transfer location (Fig. 7(*c*)) on the outer surface and next to the trailing surface was caused by the secondary flow impingement, which was higher than the nonrotating case. The surface heat

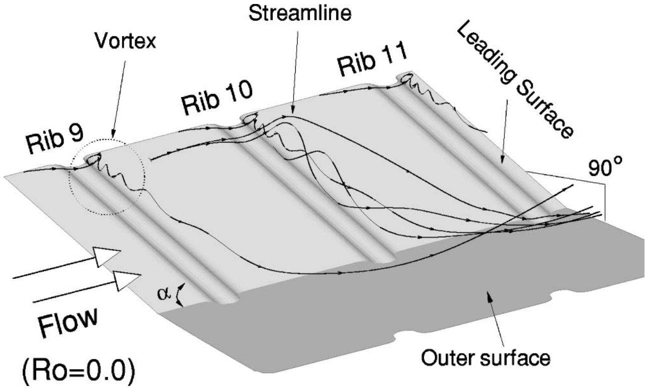

Fig. 5 Three-dimensional particle trace around ribs for nonrotating duct

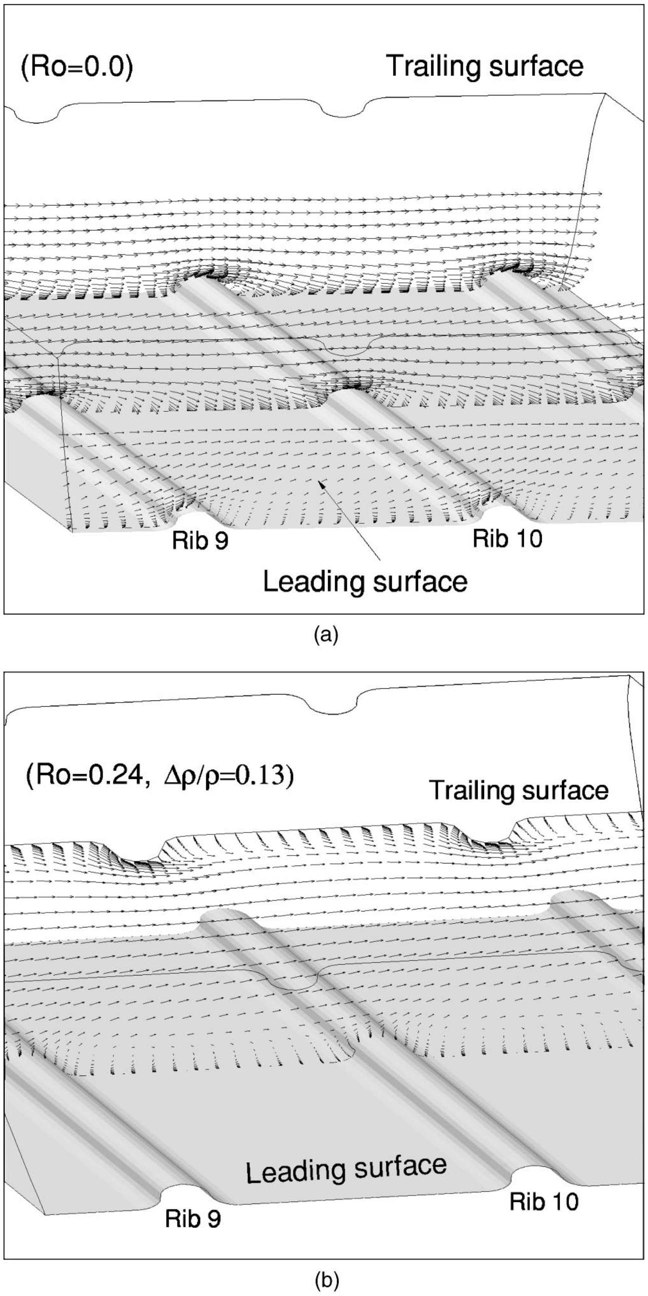

(a)

(b)

Fig. 6 Streamwise velocity vector distribution for ribbed duct

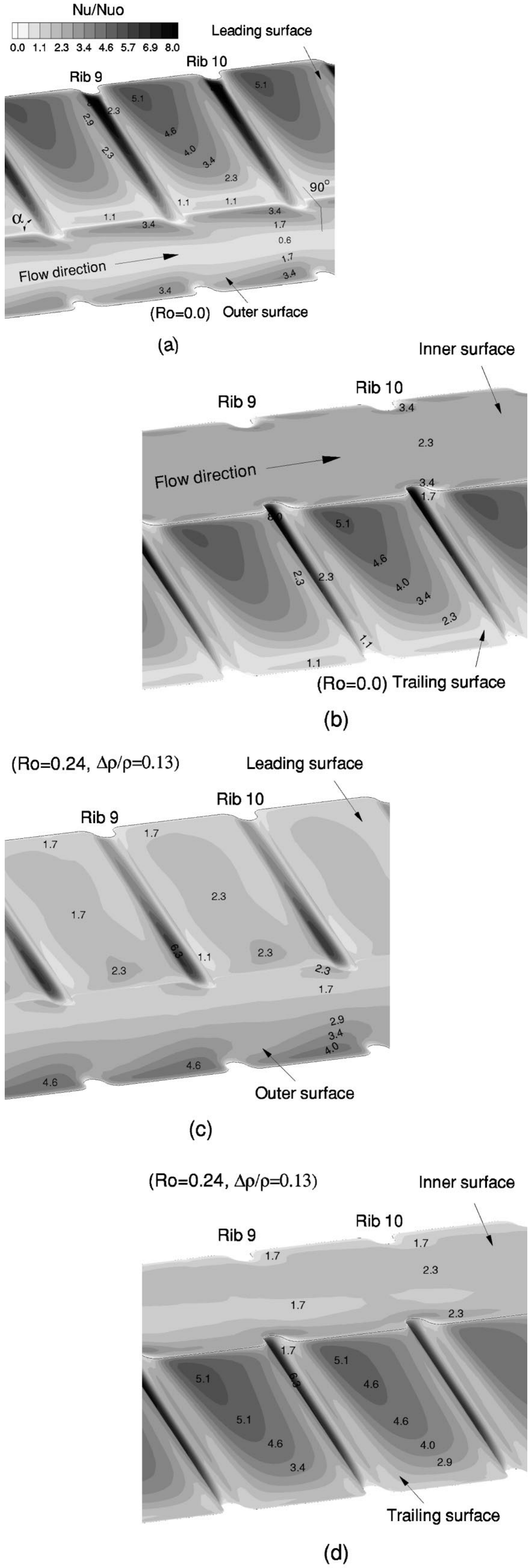

Fig. 7 Enlarged view of detailed Nusselt number ratio for all four surfaces

(a) Leading and Trailing surface (Ro=0.0)

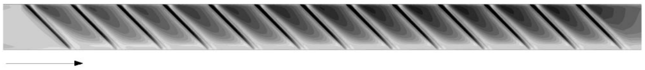

(b) Leading surface (Ro=0.12, Δρ/ρ=0.13)

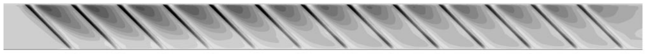

(c) Leading surface (Ro=0.24, Δρ/ρ=0.13)

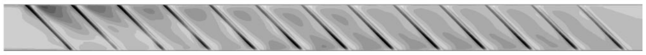

(d) Trailing surface (Ro=0.12, Δρ/ρ=0.13)

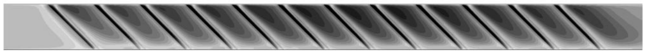

(e) Trailing surface (Ro=0.24, Δρ/ρ=0.13)

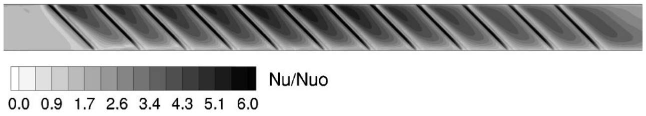

Fig. 8 Detailed Nusselt number ratio distribution

transfer on the trailing surface (Fig. 7(*d*)) looks similar to the nonrotating case; However, the heat transfer level was higher than the nonrotating case due to the stronger vortex caused by the Coriolis force. The heat transfer patterns on both the inner and outer surfaces were reversed, as compared to the nonrotating case. In other words, the heat transfer on the inner surface was less than that of the outer surface.

Figure 8(*a*) shows the Nusselt number ratio contour plots on both the leading and trailing surfaces for the nonrotating case. The entrance and exit regions were cut off so that the rib regions could be seen more clearly. The Nusselt numbers between the ribs increased along the duct until the flow approached the ninth rib and then decreased after the eleventh rib. This was because the heat transfer in this region was strongly affected by the secondary flows, which became stronger as the flow moved downstream. This feature was a unique characteristic for the angled rib arrangement, which was not found in the normal rib case. Another feature was that in every section between the ribs, the Nusselt number ratios were higher next to the inner surface and then decreased to the outer surface, which was consistent with the experimental data (Ekkad and Han [2]). This was because of the flow reattachment next to the inner surface. The flow started to redevelop in this location and caused the thermal boundary layer to become thinner. Figures 8(*b*, *d*) show the Nusselt number ratio contours on both the leading and trailing surfaces at a rotation number of 0.12 and inlet density ratio of 0.13. On the leading surface (Fig. 8(*b*)), the Nusselt number ratios decreased from the first rib to the last rib due to the Coriolis force, which pushed the cooler fluid from the leading surface toward the trailing surface. The Nusselt number ratios on the trailing surface (Fig. 8(d)) increased from the first rib and reached a maximum between the seventh and ninth ribs and decreased after that. Figures 8(*c*,*e*) show the Nu/Nu_0 contours on the leading and trailing surfaces at a rotation number of 0.24 and inlet density ratio of 0.13. In general, the higher rotation number induced stronger Coriolis and centrifugal buoyancy forces. As expected, the Coriolis forces further pushed the cooler fluid toward the trailing surface, where the heat transfer became higher as seen compared with the low rotation number (Ro=0.12). On the leading surface, the heat transfer decreased further due to the presence of hotter fluid.

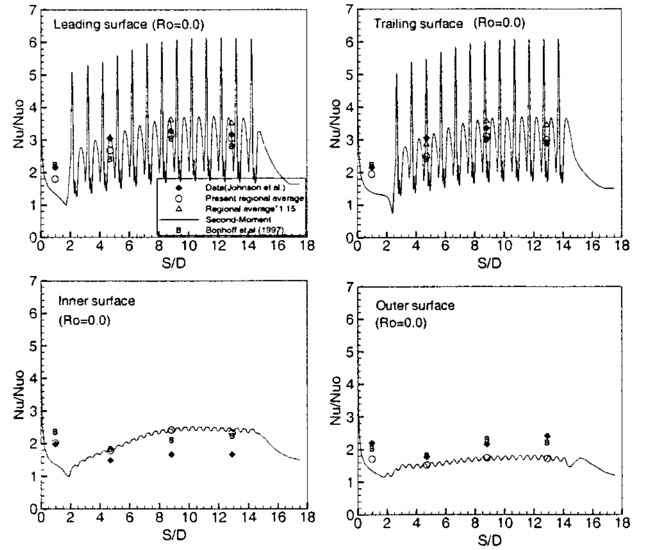

Fig. 9 Calculated and measured Nusselt number ratio: Re =25,000, Ro=0.0, $\Delta\rho/\rho$=0.13

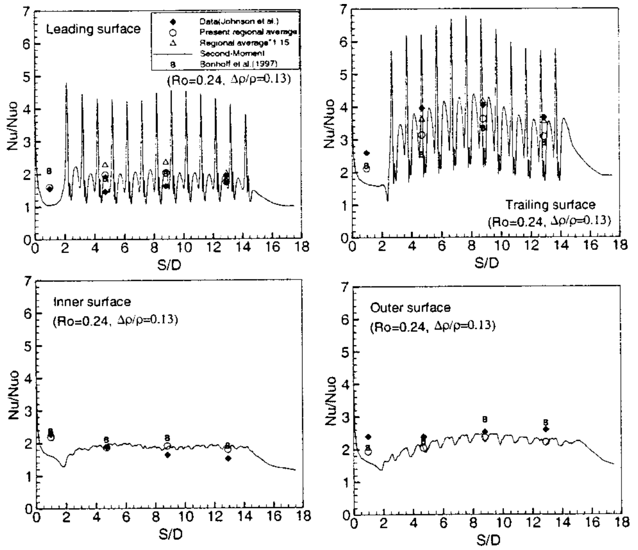

Fig. 11 Calculated and measured Nusselt number ratio: Re =25,000, Ro=0.24, $\Delta\rho/\rho$=0.13

Spanwise-Averaged and Regional-Averaged Heat Transfer Distribution. Comparisons were made with the experimental data of Johnson et al. [7] in order to provide a thorough evaluation of the present second-moment closure model. Figures 9–11 show the spanwise-averaged and regional-averaged Nusselt number ratios (Nu/Nu_0) for each of the three rotation numbers (Ro=0.0, 0.12, and 0.24). The Reynolds number, inlet density ratio, and the radius from the axis of rotation were held constant at the values of 25,000, 0.13, and 42, respectively. Note that the heat transfer coefficients in Johnson et al. [7] were based on the projected area rather than the true heat transfer surface area due to the trip geometry. The true heat transfer area for the test surfaces with trip strips was 1.15 times the projected area. Therefore, the present regionally averaged Nusselt number ratios should be multiplied by 1.15 to compare reasonably with the data of Johnson et al. [7], except for the first point on the leading and trailing surfaces and every point on the inner and outer surfaces where there were no ribs. In Fig. 9 (Ro=0.0), the spanwise-averaged Nusselt number distributions on the leading and trailing surfaces show the periodic spikes. The higher ones were caused by the flow impingement on the ribs and the smaller ones were caused by the flow reattachment between the ribs. The smaller Nusselt number ratios were low just upstream and downstream of the ribs and higher in the regions between the ribs. Unlike the normal rib case, the Nusselt number ratios increased until about the ninth rib. This phenomenon was caused by the rib-induced secondary flow, which became stronger along the duct, as mentioned by Han and Park [1]. There was no spike on the inner and outer surfaces and the inner surface had a higher heat transfer coefficient than the outer surface. Figure 10 (Ro=0.12, $\Delta\rho/\rho$=0.13) shows that the heat transfer coefficients decreased approximately 30 percent on the leading surface, as compared to the stationary case. The decrease in heat transfer coefficients was due to the Coriolis force. The heat transfer on the trailing surface increased approximately 17 percent as compared to the stationary case. The heat transfer coefficients decreased slightly on the inner surface, but increased slightly on the outer surface (data points for both the inner and outer surfaces from Johnson et al. [7] in Fig. 10 were not available). Figure 11 shows that for a higher rotation number (Ro=0.24, $\Delta\rho/\rho$=0.13), the heat transfer coefficients on the leading surface decreased approximately 40 percent, and on the trailing surface increased by 35 percent when compared to the stationary case. The heat transfer on both inner and outer surfaces is found to be fairly insensitive to the rotation number. The overall predicted Nusselt number behavior was relatively close to the data of Johnson et al. [7], except on the leading surface of rotating channel case.

For completeness, the numerical results by Bonhoff et al. [14] were also plotted on the same figure. They presented regional-averaged Nusselt numbers only for the case of Ro=0.0 and 0.24. Thus, we could not compare our data with their data for the case of Ro=0.12. Note that they did not mention whether they included the rib increased area (i.e., 1.15 times the smooth surface) in their data calculations. For the stationary case (Fig. 9), the Bonhoff et al. [14] data on the leading and trailing ribbed surfaces and inner surface were slightly lower than ours but higher on the outer surface. For the rotating case (Fig. 11, Ro=0.24), their data on the leading ribbed surface and inner and outer surfaces were about the same, but their trailing ribbed surface heat transfers were lower.

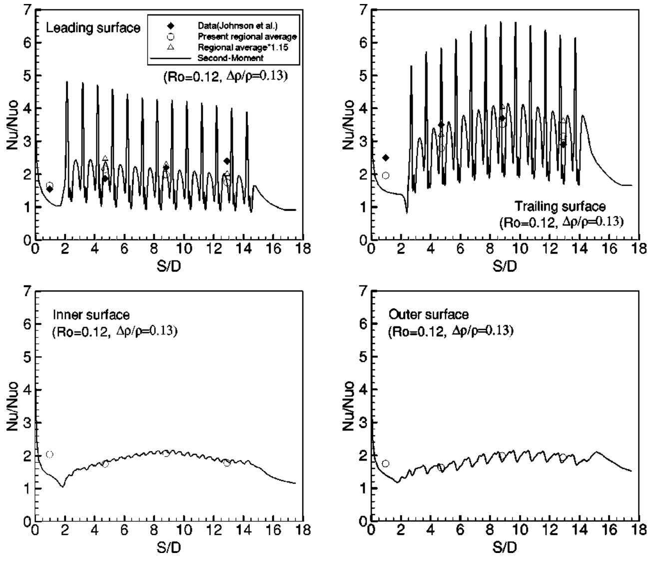

Fig. 10 Calculated and measured Nusselt number ratio: Re =25,000, Ro=0.12, $\Delta\rho/\rho$=0.13

Conclusions

A multi-block RANS method was employed to calculate of dimensional flow and heat transfer in a rotating square channel with two opposite walls roughened and with equally spaced, angled, and three-rounded ribs. The method solved the Reynolds-Averaged Navier–Stokes equations in conjunction with a near-wall second-order Reynolds stress closure model for accurate resolution of the turbulent flow and thermal fields produced by the 45 deg angle ribs as well as rotating and buoyancy effects.

Even for the stationary case, two asymmetric counterrotating secondary flows, induced by the ribs, produced strong nonisotropic turbulence. The flow fields are further complicated by the presence of secondary flows induced by rotation. These nonisotropic characteristics of turbulence significantly influence development of momentum and thermal boundary layers along the ribbed duct. Therefore, it is important to employ second-moment closure models that solve each individual Reynolds stress component directly. The present near-wall second-moment closure model predicted fairly well the complex three-dimensional flow and heat transfer characteristics resulting from the angled ribs, rotation, and centrifugal buoyancy forces.

Acknowledgments

This work was supported by the Texas Higher Education Coordinating Board–Advanced Technology Program under grant number 999903-165. The computations were performed on the Cray J90 at the Texas A&M Supercomputer Center under a supercomputer research grant, and on the Cray C90 at Cray Research, Inc., in Eagen, MN, under the sponsorship of Frank Kampe. Their support is greatly appreciated.

Nomenclature

D_h, D = hydraulic diameter
e = rib height
h = heat transfer coefficient
K = thermal conductivity of coolant
L = length of the duct
L_1 = length from the inlet to the first rib
L_2 = length from the last rib to exit
Nu = local Nusselt number$=hD_h/K$
Nu_0 = Nusselt number in fully developed turbulent nonrotating tube flow without ribs
P = rib pitch
Pr = Prandtl number
Re = Reynolds number$=\rho W_b D_h/\mu$
Ro = rotation number$=\Omega D_h/W_b$
R_r = radius from axis of rotation
S = streamwise distance
T = local coolant temperature
T_0 = coolant temperature at inlet
T_w = wall temperature
W_b = bulk velocity in streamwise direction
α = rib angle
θ = dimensionless temperature$=(T_w-T_o)/(T_w-T_o)$
μ = dynamic viscosity of coolant
ρ = density of coolant
$\Delta\rho/\rho$ = coolant-to-wall density ratio $=(T_w-T_o)/T_w$
Ω = rotational speed

References

[1] Han, J. C., and Park, J. S., 1988, ''Developing Heat Transfer in Rectangular Channel With Rib Turbulators,'' Int. J. Heat Mass Transf., **31**, No. 1, pp. 183–195.

[2] Ekkad, S. V., and Han, J. C., 1997, ''Detailed Heat Transfer Distributions in Two-Pass Square Channels With Rib Turbulators,'' Int. J. Heat Mass Transf., **40**, No. 11, pp. 2525–2537.

[3] Bonhoff, B., Parneix, S., Leusch, J., Johnson, B. V., Schabacker, J., and Bolcs, A., 1999, ''Experimental and Numerical Study of Developed Flow and Heat Transfer in Coolant Channels With 45 Deg Ribs,'' Int. J. Heat Fluid Flow, **20**, pp. 311–319.

[4] Schabacker, J., Boelcs, A., and Johnson, B. V., 1999, ''PIV Investigation of the Flow Characteristics in an Internal Coolant Passage With 45 Deg Rib Arrangement,'' ASME Paper No. 99-GT-120.

[5] Tse, D. G. N., and Steuber, G. D., 1997, ''Flow in a Rotating Square Serpentine Coolant Passage With Skewed Trips,'' ASME Paper No. 97-GT-529.

[6] Wagner, J. H., Johnson, B. V., Graziani, R. A., and Yeh, F. C., 1992, ''Heat Transfer in Rotating Serpentine Passages With Trips Normal to the Flow,'' ASME J. Turbomach., **114**, pp. 847–857.

[7] Johnson, B. V., Wagner, J. H., Steuber, G. D., and Yeh, F. C., 1994, ''Heat Transfer in Rotating Serpentine Passage With Trips Skewed to the Flow,'' ASME J. Turbomach., **116**, pp. 113–123.

[8] Parsons, J. A., Han, J. C., and Zhang, Y. M., 1995, ''Effect of Model Orientation and Wall Heating Condition on Local Heat Transfer in a Rotating Two-Pass Square Channel With Rib Turbulators,'' Int. J. Heat Mass Transf., **38**, No. 7, pp. 1151–1159.

[9] Zhang, Y. M., Han, J. C., Parsons, J. A., and Lee, C. P., 1995, ''Surface Heating Effect on Local Heat Transfer in a Rotating Two-Pass Square Channel With 60 Deg Angled Rib Turbulators,'' ASME J. Turbomach., **177**, pp. 272–280.

[10] Prakash, C., and Zerkle, R., 1992, ''Prediction of Turbulent Flow and Heat Transfer in a Radially Rotating Square Duct,'' ASME J. Turbomach., **114**, pp. 835–846.

[11] Iacovides, H., Launder, B. E., and Li, H. Y., 1996, ''The Computation of Flow Development Through Stationary and Rotating U-Ducts of Strong Curvature,'' Int. J. Heat Fluid Flow, **17**, pp. 22–33.

[12] Bo, T., Iacovides, H., and Launder, B. E., 1995, ''Developing Buoyancy-Modified Turbulent Flow in Ducts Rotating in Orthogonal Mode,'' ASME J. Turbomach., **117**, pp. 474–484.

[13] Stephens, M. A., Shih, T. I.-P., and Civinskas, K. C., 1996, ''Computations of Flow and Heat Transfer in a Rotating ∫-Shaped Square Duct With Smooth Walls,'' AIAA Paper No. 96-3161.

[14] Bonhoff, B., Tomm, U., Johnson, B. V., and Jennions, I., 1997, ''Heat Transfer Predictions for Rotating **U**-Shaped Coolant Channels With Skewed Ribs and With Smooth Walls,'' ASME Paper No. 97-GT-162.

[15] Chen, H. C., Jang, Y. J., and Han, J. C., 1999, ''Computation of Flow and Heat Transfer in Rotating Two-Pass Square Channels by a Reynolds Stress Model,'' ASME Paper No. 99-GT-174.

[16] Stephens, M. A., Shih, T. I.-P., and Civinskas, K. C., 1995, ''Computation of Flow and Heat Transfer in a Rectangular Channel With Ribs,'' AIAA Paper No. 95-0180.

[17] Rigby, D. L, Steinthorsson, E., and Ameri, A. A., 1997, ''Numerical Prediction of Heat Transfer in a Channel With Ribs and Bleed,'' ASME Paper No. 97-GT-431.

[18] Stephens, M. A., Chyu, M. K., and Shih, T. I.-P., 1996, ''Computation of Convective Heat Transfer in a Square Duct With Inclined Ribs of Rounded Cross Section,'' ASME Paper No. 96-WA/HT-12.

[19] Jang, Y. J., Chen, H. C., and Han, J. C., 2000, ''Computation of Flow and Heat Transfer in Two-Pass Channels With 90° Parallel Ribs,'' presented at the 8th Int. Symp. on Transport Phenomena and Dynamics of Rotating Machinery (ISROMAC-8), Honolulu, HI, Mar. 26–30.

[20] Jang, Y. J., Chen, H. C., and Han, J. C., 2000, ''Computation of Flow and Heat Transfer in Two-Pass Channels With 60 deg Ribs,'' AIAA Paper No. 20001036.

[21] Prakash, C., and Zerkle, R., 1995, ''Prediction of Turbulent Flow and Heat Transfer in a Ribbed Rectangular Duct With and Without Rotation,'' ASME J. Turbomach., **177**, pp. 255–264.

[22] Iacovides, H., 1998, ''Computation of Flow and Heat Transfer Through Rotating Ribbed Passage,'' Int. J. Heat Fluid Flow, **19**, pp. 393–400.

[23] Rigby, D. L., 1998, ''Prediction of Heat Mass Transfer in a Rotating Ribbed Coolant Passage With a 180 Degree Turn,'' ASME Paper No. 98-GT-329.

[24] Iacovides, H., and Raisee, M., 1999, ''Recent Progress in the Computation of Flow and Heat Transfer in Internal Cooling Passages of Turbine Blades,'' Int. J. Heat Fluid Flow, **20**, pp. 320–328.

[25] Stephens, M. A., and Shih T. I.-P., 1997, ''Computation of Compressible Flow and Heat Transfer in a Rotating Duct With Inclined Ribs and a 180 Deg Bend,'' ASME Paper No. 97-GT-192.

[26] Shih, T. I.-P., Lin, Y.-L., Stephens, M. A., and Chyu, M. K., 1998, ''Flow and Heat Transfer in a Ribbed U-Duct Under Typical Engine Conditions,'' ASME Paper No. 98-GT-213.

[27] Chen, H. C., 1995, ''Assessment of a Reynolds Stress Closure Model for Appendage-Hull Junction Flows,'' ASME J. Fluids Eng., **117**, No. 4, pp. 557–563.

[28] Chen, H. C., 1995, ''Submarine Flows Studied by Second-Moment Closure,'' J. Eng. Mech., **121**, No. 10, pp. 1136–1146.

[29] Chen, H. C., and Chen, M., 1998, ''Chimera RANS Simulation of a Berthing DDG-51 Ship in Translational and Rotational Motions,'' Int. J. Offshore Polar Engineering, **8**, No. 3, pp. 182–191.

[30] Chen, H. C., Patel, V. C., and Ju, S., 1990, ''Solutions of Reynolds-Averaged Navier–Stokes Equations for Three-Dimensional Incompressible Flows,'' J. Comp. Physiol., **88**, No. 2, pp. 305–336.

[31] Chen, H. C., and Patel, V. C., 1989, ''The Flow Around Wing-Body Junctions,'' *Proc. 4th Symposium on Numerical and Physical Aspects of Aerodynamic Flows*, Long Beach, CA.

[32] Chen, H. C., and Korpus, R., 1993, ''Multi-block Finite-Analytic Reynolds-Averaged Navier–Stokes Method for 3D Incompressible Flows,'' *ASME Fluids Engineering Conference*, ASME FED-Vol. 150, pp. 113–121.

[33] Hubbard, B. J., and Chen, H. C., 1994, ''A Chimera Scheme for Incompressible Viscous Flows With Applications to Submarine Hydrodynamics,'' AIAA Paper No. 94-2210.

[34] Chen, H. C., and Liu, T., 1999, ''Turbulent Flow Induced by a Full-Scale Ship in Harbor,'' J. Eng. Mech., **125**, No. 7, pp. 827–835.

[35] Kays, W. M., and Crawford, M. E., 1993, *Convective Heat and Mass Transfer*, 3rd ed., McGraw-Hill.

[36] Steinbrenner, J. P., Chawner, J. R., and Fouts, C. L., 1990, ''The GRIDGEN 3D Multiple Block Grid Generation System,'' Vols. I & II, WRDC-TR-90-3022, Wright Patterson AFB, OH.

Lateral-Flow Effect on Endwall Heat Transfer and Pressure Drop in a Pin-Fin Trapezoidal Duct of Various Pin Shapes

Jenn-Jiang Hwang
Professor,
Mem. ASME
e-mail: jjhwang@chu.edu.tw

Chau-Ching Lu

Department of Mechanical Engineering,
Chung-Hua University,
Hsinchu, Taiwan 300

The effects of lateral-flow ejection $(0<\epsilon<1.0)$*, pin shapes (square, diamond, and circular), and flow Reynolds number* $(6000<Re<40,000)$ *on the endwall heat transfer and pressure drop for turbulent flow through a pin-fin trapezoidal duct are studied experimentally. A staggered pin array of five rows and five columns is inserted in the trapezoidal duct, with the same spacings between the pins in the streamwise and spanwise directions:* $S_x/d=S_y/d=2.5$*. Three different-shaped pins of length from* $2.5<l/d<4.6$ *span the distance between two endwalls of the trapezoidal duct. Results reveal that the pin-fin trapezoidal duct with lateral-flow rate of* $\epsilon=0.3-0.4$ *has a local minimum endwall-averaged Nusselt number and Euler number for all pin shapes investigated. The trapezoidal duct of lateral outlet flow only* $(\epsilon=1.0)$ *has the highest endwall heat transfer and pressure drop. Moreover, the square pin results in a better heat transfer enhancement than the diamond pin, and subsequently than the circular pin. Finally, taking account of the lateral-flow rate and the flow Reynolds number, the work develops correlations of the endwall-averaged heat transfer with three different pin shapes.*

[DOI: 10.1115/1.1333093]

Introduction

The desire for increased gas turbine reliability and efficiency has spurred research in all areas of turbine blade cooling. As shown in Fig. 1, various blade cooling methods have been developed over the years, for example, convection augmented by rib-turbulators in the leading and midchord regions and by pin fins for the trailing edge. This study focuses on the internal cooling channels at the trailing edge of a turbine blade. Aerodynamic considerations demand a small wedge angle for the blade profile and, thus, the narrow channels in the trailing-edge region should be trapezoidal in cross section. Pin fins spanning the suction and pressure surfaces are used not only to promote turbulence to enhance internal heat transfer, but also serve as a means to bridge the narrow cavity for the structure purpose. In common cooling designs, the coolant from the blade bases either exits through the blade-tip slots or traverses the trapezoidal-shaped pin-fin channel and then is ejected from the slots along the edge of the airfoil [1].

Pin fin heat transfer has received much attention by many investigators for several decades. Relevant studies by several groups are briefly surveyed below.

Van Fossen [2] measured the overall heat transfer coefficients in rectangular ducts with staggered arrays of short pin fins $(0.5<l/d<2.0)$. All arrays had four rows of pins in the streamwise direction. Heat transfer rates were averaged over the four-row array. It was found that the overall heat transfer coefficients for short pins were lower than those for long pin fins $(I/d=8.0)$. Then, Brigham and Van Fossen [3] investigated the effects of row number of pin in streamwise direction and pin length (height) on array-averaged heat transfer. The results showed that the row number of the pin has a slight effect on the array-averaged heat transfer. When the pin length-to-diameter ratio is lower than two $(l/d<2)$, the array-averaged heat transfer was not affected by the pin length. For $I/d>2$, the heat transfer increased significantly with an increase in l/d.

Metzger et al. [4] studied experimentally the local heat transfer variation in rectangular ducts with staggered pin array for $SJd=1.5$ and 2.5, and $1/d=1.0$. Results showed that heat transfer increased in the first few rows, reached a peak value, and then slowly decreased to a fully developed value. Metzger et al. [5] further studied the effects of using flattened pins and of varying the orientation of the pin fin array with respect to the main flow direction on the heat transfer and pressure drops in pin fin channels. They observed that, by varying the orientation of the pin-fin array, it was possible to increase the heat transfer and, at the same time, reduce the pressure drop. They also found that the use of flattened pins increased the heat transfer slightly but doubled the pressure loss.

Lau et al. [6] further measured the overall heat transfer and friction factor in rectangular pin fin channels with lateral ejection. It was shown that the overall heat transfer for a rectangular pin fin channel with lateral ejection holes was lower than that for rectangular channel with no ejection holes.

Chyu [7] used a mass transfer sublimating system to evaluate the effects of fillets at the cylinder-endwall junction and array geometry on the endwall heat transfer in rectangular ducts. Then, Chyu et al. [8] examined the pin-shape effect on the heat/mass transfer characteristics in a narrow rectangular channel. The staggered cube array was recommended since it produced a significant heat transfer enhancement and a moderate pressure penalty. Chyu et al. [9] further conducted experiments to compare the contribution of heat transfer enhancement by the endwall and that by the pins in a pin-fin rectangular duct. Results revealed that the pin has about 10–20 percent higher heat transfer than the endwall. However, such a difference in heat transfer coefficient imposed very insignificant influence on the overall array-averaged heat transfer since the wetted area of the uncovered endwalls was much greater than that of the pins.

All of the aforementioned studies are for flow through rectangular channels with a uniform pin length. Recently, Hwang et al.

Contributed by the International Gas Turbine Institute and presented at the 45th International Gas Turbine and Aeroengine Congress and Exhibition, Munich, Germany, May 8–11, 2000. Manuscript received by the International Gas Turbine Institute February 2000. Paper No. 2000-GT-232. Review Chair: D. Ballal.

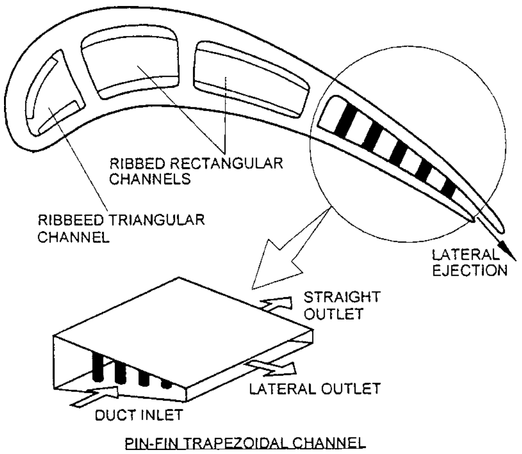

Fig. 1 Typical modern internally cooled turbine blade and the modeled pin-fin trapezoidal duct

[1] extended the rectangular-duct works to a more realistic geometry of the trapezoidal pin-fin-cooling cavity in a typical turbine blade. The log-mean heat transfer and overall pressure drop in a pin-fin trapezoidal duct are measured. Results revealed that the trapezoidal pin-fin duct with lateral outlet flow only has higher log-mean Nusselt numbers and pressure-drop coefficient than the straight counterpart. However, the local heat transfer characteristics, which are highly desired in the turbine-blade cooling design, were not determined. This study is a continuation of the previous work to measure the detailed heat transfer coefficient on the endwall of a trapezoidal duct with lateral ejection. Several issues that have not been studied are discussed in the present paper. First, we examine the pin-shape effect on the local heat transfer characteristics in the trapezoidal duct with lateral ejection. It is known that the square pin can provide a higher heat transfer than the circular pin in a rectangular duct of a straight outlet flow [8]. It is very interesting to know whether such a trend is true in a trapezoidal duct with lateral ejection. Then, we study the combined effects of the pin shape and lateral-flow rate on the overall pressure drops in a pin-fin trapezoidal duct. Finally, we developed the empirical correlations for heat transfer in a pin-fin trapezoidal duct by considering the effects of the lateral-flow rate and the flow Reynolds number for three different pin shapes.

To resolve the highly localized heat transfer distributions mentioned above, a transient liquid-crystal technique [10] is employed to measure the local heat transfer on the endwall surfaces. Thin coatings are sprayed directly on the endwall of the pin-fin duct, and observed during a transient test with an automated computer vision and data acquisition system. The detailed distributions of heat transfer coefficient that are provided by the present work could afford a better understanding of the endwall heat transfer enhancement by variously shaped pin fins in a trapezoidal duct with lateral-flow ejection. They could also provide a reference of computational-fluid-dynamic-based studies relating to the pin-fin-duct heat transfer.

Experimental Apparatus

Flow Loop. Figure 2 shows the schematic layout of the experimental apparatus. A 15-hp centrifugal blower sucks air from the laboratory room into the flow circuit. Before entering the test section, the air is first ducted into an electric heater to be heated to a required temperature, subsequently traverses a noise-reduction chamber, and an entrance plenum. Finally, the air exits from the straight and/or lateral outlets. A flow meter associated with a valve situated at each outlet controls and measures the volume flow rate of the air. Note that the arrangement of the noise-reduction chamber associated with a nozzle-like contraction can provide a fairly uniform flow with turbulence intensity less than 1 percent in the plenum entrance. The uniformity of the flow and turbulence level were checked by hot-wire measurements [11].

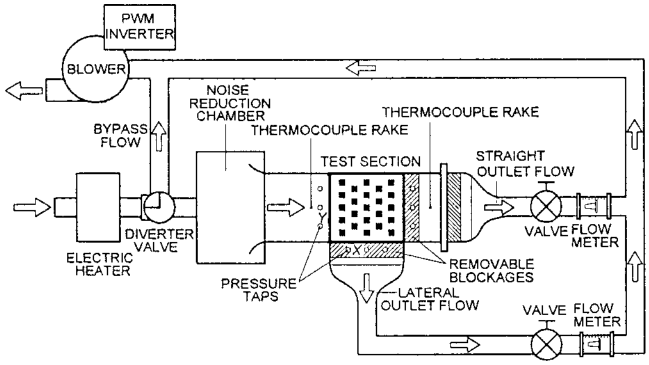

Fig. 2 Sketch of the experimental apparatus

Test Model. As shown in Fig. 3, the trapezoidal-shaped test section and the pins are made of Plexiglas®. The bottom endwall of a square area of 120 mm×120 mm (L by W) is sprayed with liquid crystals, representing the heat transfer active surface. Twenty-three pins span the distance between two principal duct walls. The characteristic dimension of the pin, i.e., diameter of the circular pin and the side length of the square (diamond) pin, is fixed at $d=9$ mm. All pins are screwed in place from the bottom endwall, and thus stand vertically on the endwall. They have different lengths from $l/d=2.5$ to 4.6 depending on the location within the trapezoidal duct. The pin spacings along the longitude and transverse directions are the same, i.e., $S_x=S_y=22.5$ mm. The heights of the duct entrance (H_1) and straight exit (H_2) are 40.0 mm and 18.0 mm, respectively, forming a wedge angle of about 10.4 deg. As shown in Fig. 2, two thermocouple rakes (each with five beads) are located at the test-section entrance and exit (straight or lateral), respectively, to measure the mainstream temperatures. A real-time hybrid recorder (Yokogawa, AR 1100A) records the time-dependent mainstream temperatures. In addition, nine pressure taps are installed at the entrance and two exits of the test section (each with three taps) for the static-pressure measurement. They are connected to a transmitter (Modus) to display the pressure-drop signals.

The image-processing system includes a digital color camcorder (Sony DCR-TRV7), a frame grabber card, and a Pentium II personal computer. The camcorder is focused on the liquid-crystal-coated surfaces to view and record their color change during the transient test. The frame grabber interface is programmed to analyze the color change using image-processing software. The

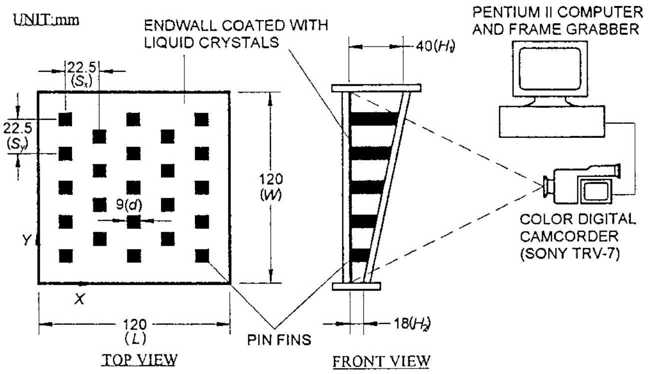

Fig. 3 Dimensions and coordinate system of the test section

software analyzes the picture frame-by-frame and simultaneously records the time lapse as the liquid crystals change from colorless to green during the transient test.

Experimental Procedure. The test section is assembled after spraying the liquid crystals (Hallcrest, BW/R38C5W/C17-10) uniformly on the endwall surface. The coating is a light spray of thickness on the order less than 10 μm. The response time of the liquid crystals should be only a few milliseconds [12], which is much more rapid than the wall temperature transient. The camcorder is set up and focused on the endwall surface. Each test run is thermal transient, initiated by suddenly exposing the hot air to the test section, which results in a color change of the surface coatings. The calibration of color to temperature is carried out on a copper rod coated with liquid crystals [13]. The liquid crystals are colorless at room temperature. They then change to red, green, blue, and finally colorless again during the heating process. The color change temperatures to red, green, and blue are 38.2°C, 39.0°C, and 43.5°C, respectively. Before the test run, the hot air bypasses the test section so that the endwall remains at the laboratory ambient temperature. The valve keeps in the diverted position until a required mainstream temperature (typically about 60–70°C) has been achieved in the diversion of the flow loop. Then, the valve turns to route the hot air into the test section and, simultaneously, the recorder is switched on to record the mainstream temperature history. The image processing system records the transition time for the color change to green, and transfers the data into a matrix of time of the color change over the entire surface. The time and temperature data are entered into a computer program to obtain the local heat transfer coefficient.

Heat Transfer Theory. The local heat transfer coefficient over the test surface can be obtained by assuming one-dimensional transient conduction over a semi-infinite solid. The one-dimensional transient conduction, the initial condition, and boundary conditions on the liquid crystal coated surface are

$$k\frac{\partial^2 T}{\partial Z^2}=\rho c_p\frac{\partial T}{\partial t} \tag{1}$$

When $t=0$, $T=T_i$; when $t>0$, $k(\partial T/\partial Z)=h(T_w-T_m)$ at $z=0$; when $z\rightarrow\infty$, $T=T_i$.

The surface temperature response to Eq. (1) is shown as:

$$\frac{T_w-T_i}{T_m-T_i}=1-\exp\left(\frac{h^2\alpha t}{k^2}\right)\cdot\mathrm{erfc}\left(\frac{h\sqrt{\alpha t}}{k}\right) \tag{2}$$

The heat transfer coefficient h can be calculated from Eq. (2), by knowing the wall temperature (T_w), the initial surface temperature (T_i), the oncoming mainstream temperature (T_m), and the corresponding time (t) required to change the coated-surface color to green at any location. The time required for the color change in a typical run is about 15 to 90 seconds depending on the location, mainstream temperature, and throughflow rate. This testing time is so short that the heat flow does not penetrate the depth of the acrylic. Therefore, the assumption of the semi-infinite solid on the test surface is valid. It is noteworthy that in the region where the heat transfer coefficient varies significantly in spatiality, the heat transfer coefficient measured may be somewhat averaged by the axial conduction in the Plexiglas® plate (i.e., two- or three-dimensional effect). To check this effect, two thermocouples are cemented into small holes drilled into the Plexiglas® plate approximately 1.0 mm in depth to measure the time-dependent axial conduction. The locations of these two thermocouples are behind the pin and ahead of the next pin, respectively, where the heat transfer is expected to be highly localized. The results show that the maximum axial conduction is less than 5 percent of the convection heat transfer from the fluid to the surface in the test duration.

Since the mainstream temperature is time dependent, the solution in Eq. (2) should be modified. First, the mainstream temperature history is simulated as a series of time step changes. Then, the time step changes of the mainstream temperature are included in the solution for the heat transfer coefficient using Duhamel's superposition theorem. The solution for the heat transfer coefficient at every location is therefore represented as

$$T_w-T_i=\sum_{j=1}^{n}\left\{1-\exp\left[\frac{h^2\alpha(t-\tau_j)}{k^2}\right]\times erfc\left[\frac{h\sqrt{\alpha(t-\tau_j)}}{k}\right]\right\}\times[\Delta T_{m(j,j-1)}] \tag{3}$$

where $\Delta T_{m(j,j-1)}$ and t_j are the temperature and time step changes obtained from the recorder output.

Data Analysis and Uncertainty. The nondimensional heat transfer coefficient on the endwall of the trapezoidal duct is represented by the Nusselt number as

$$\mathrm{Nu}=hDe/k_f \tag{4}$$

The Reynolds number used herein is based on the mean throughflow velocity at the duct entrance and the equivalent hydraulic diameter of the trapezoidal duct, i.e.,

$$\mathrm{Re}=G\cdot De/\mu \tag{5}$$

The pumping power required to drive a fixed volumetric flow rate V [overdot] in the trapezoidal duct with both straight and lateral outlets can be written as

$$\Delta P\dot{V}=\Delta P_1\dot{V}_1+\Delta P_2\dot{V}_2$$

where $\dot{V}_1$ and $\dot{V}_2$ are the volumetric flow rates, and ΔP_1 and ΔP_2 are the measured pressure drops for flow through the straight and lateral exits, respectively. If the density of the flowing air does not vary significantly in the test section, the pressure drop across the finite-length duct of trapezoidal cross section with both straight and lateral outlets, can be made dimensionless as follows:

$$\mathrm{Eu}=2\Delta P/(G^2/\rho)$$

The pressure-drop coefficient obtained is based on adiabatic conditions (i.e., test with ambient-temperature mainstream).

By using the estimation method of Kline and McClintock [14], the maximum uncertainties of the investigated nondimensional parameters are as follows: Re, 6.4 percent; Nu, 8.5 percent; and Eu, 7.7 percent.

Results and Discussion

Before the subsequent discussion, it is necessary to make a comparison of the present data with those in previous works to validate present experimental procedure and results. As shown in Fig. 4, the Nusselt number and Darcy friction factor are measured in the region $18.0\leqslant X/De\leqslant 20.2$ of the present smooth trapezoidal duct, and are plotted as a function of Reynolds number. The correlations selected for comparison are the Dittus–Boelter [15] correlation for heat transfer and the Blasius equation and the equation by Petukhov [16] for friction. All of these equations represent well the data for a fully developed flow in a smooth duct. It is seen from this figure that, within the range of Reynolds number investigated, the agreement between these correlations and the present experimental heat transfer and friction data is good. The good agreement of this comparison confirms an adequate experimental procedure employed and reliable results obtained in the current work.

Detailed Heat Transfer Coefficient Distributions. Typical examples showing the effects of lateral-flow rate and pin shape on the detailed Nusselt number distributions on the endwall surfaces of a pin-fin trapezoidal duct are given in Figs. 5 and 6. The trapezoidal duct is inserted with a staggered pin array at a fixed Reynolds number of Re=40,000. The flow is from left to right and/or bottom of each figure. The lateral-flow rate varies from $\epsilon=0$ to 1.0.

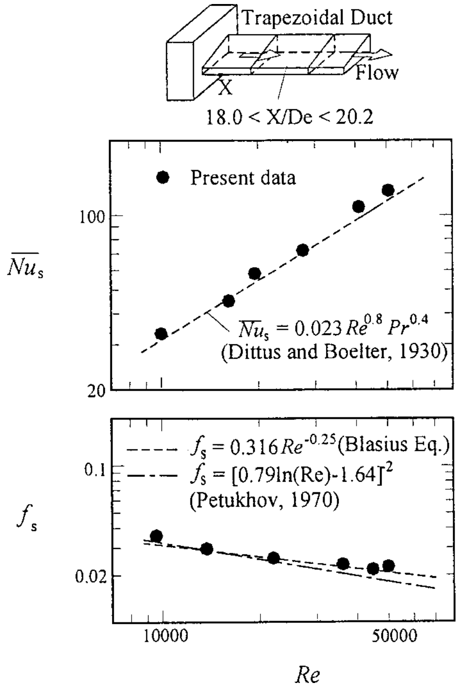

Fig. 4 Comparison of the averaged Nusselt number and friction factor of the present smooth trapezoidal duct with the previous correlations

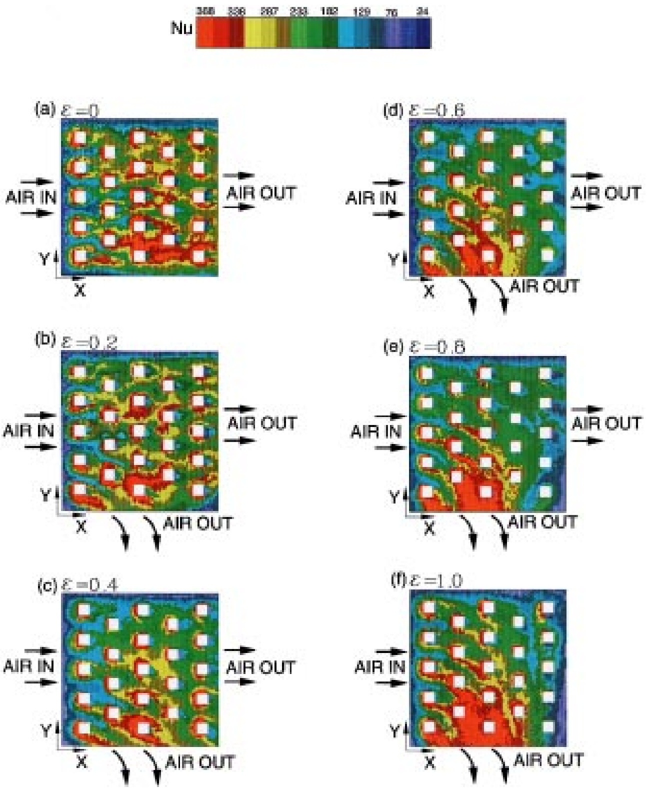

Fig. 5 Detailed heat transfer coefficient distribution on the endwall of the trapezoidal duct: effect of the lateral-flow rate, Re=40,000

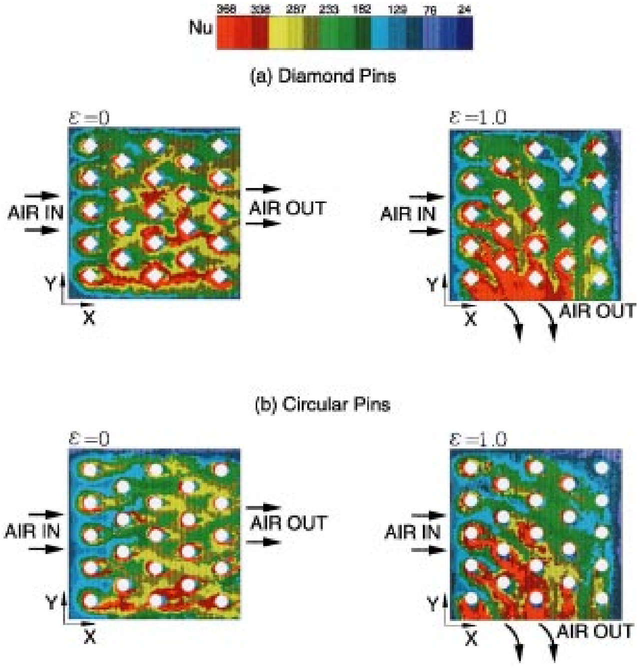

Fig. 6 Detailed heat transfer coefficient distribution on the endwall of the trapezoidal duct: effect of the pin shapes, Re =40,000

Effect of Lateral-Flow Rate. For the duct of a straight outlet flow only (Fig. 5(*a*), $\epsilon=0$), since the duct is trapezoidal, the two sidewalls are of different widths, which leads to asymmetry in local heat transfer coefficient distributions. In addition, the distributions become higher after the third rib array from the duct entrance [4]. When the lateral exit is open with $\epsilon=0.2$ (Fig. 5(*b*)), only a small portion of fluid turns laterally and most of the fluid still traverses the trapezoidal duct and exits from the straight exit. Therefore, the pattern of heat transfer distribution on a large portion of endwall shown in Fig. 5(*b*) is not changed too much as compared to Fig. 5(*a*). The notable differences are a slight reduction in Nu value and the deflection of wake shedding behind the pins adjacent the lateral exit for Fig. 5(*b*). It is seen that the wake shedding behind the pins adjacent to the lateral exit, except for the last row, is slightly deflected toward the lateral exit by the lateral flow. Interestingly, the pin around the corner formed by tow openings of the duct (i.e., the last-row pin adjacent the lateral exit) has a shedding wake directed from the lateral exit toward the straight exit. This means that some fluids enter the duct from the lateral opening and exit from the straight opening. Such complex flow transportation will be illustrated in Fig. 7. As the lateral-flow rate increases further (Figs. 5(*c*), 5(*d*), and 5(*e*)), the deflection of wake shedding behind the pins becomes significant, and the heat transfer in the region near the lateral exit has been enhanced by increasing ϵ. Meanwhile, the heat transfer coefficient adjacent to the longer sidewall is evidently degraded. The former is attributed to the effect of the accelerating flow through the convergent lateral exit and, partly, the flow turning effect. The latter is because of the less forced convection along the straight (X) direction of the trapezoidal duct. In contrast to the results of small lateral-flow ejection shown in Fig. 5(*b*), the direction of the wake shedding by the pin around the corner formed by tow openings is from the straight exit to the lateral exit for the high lateral ejection of $\epsilon=0.8$, indicating that the flow across this pin is from the straight opening to the lateral opening. When the straight exit is blocked (Fig. 5(*f*), $\epsilon=1.0$), the total main flow has to turn laterally, and thus enhances the most heat transfer near the lateral exit. How-

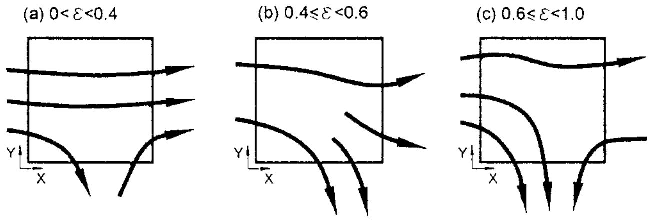

Fig. 7 Relation of the lateral-flow rate and the main flow direction in the trapezoidal duct

ever, due to the flow recirculation, a heat transfer deterioration is observed around the remote corner formed by the longer sidewall and the blocked straight exit.

From the heat transfer traces given above, the flow direction across the trapezoidal duct under various ϵ, which strongly affects the local heat transfer distribution on the endwall surfaces, can be sketched in Fig. 7. For $0<\epsilon<0.4$, due to a strong vacuum at the straight exit, the total straight outlet flow is induced not only from the duct entrance but also from the lateral opening (Fig. 7(*a*)). For the duct with $0.6\leq\epsilon<1.0$ (Fig. 7(*c*)), in contrast, the fluids exiting from the lateral exit are provided by the duct entrance as well as the straight opening. As for $0.4\leq\epsilon<0.6$, the straight and lateral outflows are almost even (Fig. 7(*b*)) due to the vacuum balance in the two exits.

Effect of the Pin Shape. Figures 6(*a*) and 6(*b*) shows the detailed heat transfer distributions on the endwall of the trapezoidal ducts with diamond and circular pin-arrays, respectively, for $\epsilon=0$ and 1.0. Comparing Figs. 5(*a*) and 5(*f*) with Fig. 6 gives an indication of the effect of pin shape on the distributions of local heat transfer coefficient on the endwall of a trapezoidal duct with straight or lateral outlet flows. For the duct of a straight outlet flow ($\epsilon=0$), the wake shedding behind the square pin (Fig. 5(*a*)) spreads much wider than that behind the diamond pin fin (Fig. 6(*a*)) and subsequently wider than that behind the circular pin. In general, a square fin element located in an array interior may be subjected to a complex pattern of wake shedding [8], which consists of wakes shed sideways for the adjacent elements immediately upstream and that from the element directly aligned two rows ahead. However, the effect of the sideways wake-shedding for the circular pin fin is relatively insignificant. Observations of Figs. 5(*f*) and 6(*a*) further indicate that the local heat transfer coefficient distributions are quite similar for the square and diamond pins for the trapezoidal duct of lateral outlet flow only ($\epsilon=1.0$). Further examination of the endwall-averaged Nusselt number will be conducted later for evaluating the heat transfer performance in trapezoidal ducts of various pin shapes.

Endwall-Averaged Heat Transfer. Figure 8 shows the effect of the lateral-flow rate on the endwall-averaged heat transfer for three different pin shapes at Re=40,000. The symbols are actual experiments and the lines passing through these symbols are curve-fitting results. As given in this figure, all pin shapes have a similar trend, i.e., the endwall-averaged Nusselt number starts a decrease from $\epsilon=0$, reaches a local minimum at about $\epsilon=0.3$–0.4, and then increases with increasing ϵ. The first decrease is because the apparent cross-sectional area for the throughflow becomes large when the lateral exit is open. An increase in the apparent cross-sectional area reduces the average throughflow velocity; hence endwall-averaged heat transfer. Further increasing the lateral-flow rate augments the convective heat transfer by accelerating fluid through the convergent lateral exit and by enhancing the flow turning effect. The more the lateral flow, the stronger the fluid acceleration becomes. This is the reason that the endwall-averaged heat transfer increases with the increase in the lateral-flow rate at high lateral-flow conditions. It should be noted that this trend is true for the present duct of a 10.4-deg wedge angle, and may not be valid when the wedge angle is varied, especially for a relatively small wedge angle. For example, the previous results by Lau et al. [6] showed that the overall heat transfer decreased monotonically with increasing lateral-flow rate from $\epsilon=0$ to 1.0 in the pin-fin rectangular duct. The disagreement in the ϵ-dependence of the overall heat transfer between the present and previous results may be due to the difference in the cross section of the test duct investigated [1]. As for the effect of pin shape, in general, the endwall-averaged heat transfer for the square pin-array is higher than that for the diamond pin-array, and subsequently higher than that for the circular pin-array at a fixed lateral-flow rate. Chyu et al. [8] found a similar trend for a pin-fin rectangular channel without lateral-flow ejection. Careful inspection of this figure shows that at high lateral flow conditions ($\epsilon>0.8$), the endwall-averaged heat transfer for the diamond and square pins are almost the same. This is very reasonable because the square pin appears to be a diamond pin with respect to the turning main flow. Therefore, these two pin shapes are not different from each other too much relative to the turning flow. Indeed, this fact has been clearly shown in Figs. 5(*f*) and 6(*a*) for the local Nusselt number distributions.

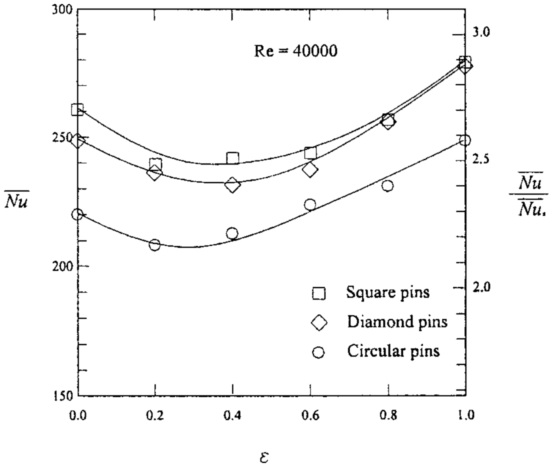

Fig. 8 Effect of the lateral-flow rate on the endwall averaged Nusselt number for Re=40,000

The dependence of the endwall-averaged Nusselt number on the Reynolds number and the lateral-flow rate can be correlated by the equation of the form

$$\overline{\mathrm{Nu}}=a_1\,\mathrm{Re}^{a2}(1+a_3\epsilon+a_4\epsilon^2)$$

The coefficients and exponent of these equations for three different pin shapes are given in Table 1. The maximum deviations between these equations and the experimental data are less than ±5, ±6, and ±8 percent for the square, diamond, and circular pins, respectively. The combined effects of lateral-flow rate and Reynolds number on the endwall-averaged heat transfer of the trapezoidal duct with an array of various-shaped pins are shown in Fig. 9. For simplicity, the effect of lateral-flow rate is expressed explicitly in the ordinate of the figure. In addition, the present smooth trapezoidal duct results (Fig. 4) are also displayed as a solid line in this figure for comparison. As shown in Fig. 9, the

Table 1 Constants for the heat transfer correlation

Pin shapes	$\overline{Nu}=a_1 Re^{a_2}(1+a_3\varepsilon+a_4\varepsilon^2)$				
	a_1	a_2	a_3	a_4	Maximum Deviations
Square	0.234	0.662	-0.30	0.38	± 5 %
Diamond	0.296	0.636	-0.28	0.40	± 6 %
Circular	0.222	0.651	-0.22	0.36	± 8 %

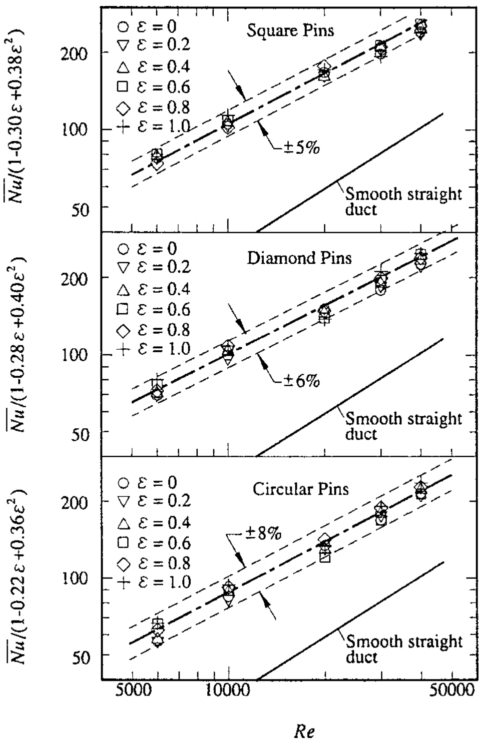

Fig. 9 Endwall-averaged Nusselt number as a function of the Reynolds number

data for various ϵ gather closely at a fixed Reynolds number, meaning that the dependence of Nu on ϵ in Eq. (8) is appropriate. From Fig. 9 or Table 2, in general, it can be seen that the endwall-averaged Nusselt number of the trapezoidal pin-fin duct increases with increasing Reynolds number. In a comparison of the smooth duct results of the straight flow (solid line), the enhancement in the endwall averaged heat transfer is about 170–260, 160–260, and 130–210 percent for the square, diamond, and circular pins, respectively.

Pressure Drops. The results of the pressure-drop experiments are presented in Fig. 10. In this figure, the Euler number, defined in Eq. (7), is plotted as a function of the flow Reynolds number for various lateral-flow rates. For all lateral-flow rates, the Euler number depends mildly on the flow Reynolds number over the range of Reynolds number studied.

As for the effect of lateral-flow rate, similar to the heat transfer results, the Euler number is first decreased and then increased with increasing ϵ. The minimum Eu occurs at about $\epsilon=0.4$. Increasing the lateral-flow rate from $\epsilon=0$ to 0.4 has two counteracting effects that influence the overall pressure drop across the trapezoidal duct. The first is the reduction in the volumetric flow rate of the air in the duct due to an increase in the apparent exit area, which reduces the pressure drop across the trapezoidal duct. The second effect is an enhancement in the flow turning effect, which increases the pressure drop. Obviously, the former effect is more significant than the latter effect for $\epsilon<0.4$. As ϵ increases further, the flow-turning effect gradually becomes crucial. After $\epsilon\geqslant0.8$, the Eu is higher than that of $\epsilon=0$ (solid circles), meaning that the flow-turning effect has overcome the area-increment effect. For all pin shapes, the duct of $\epsilon=1.0$ has the highest Euler numbers, which are about 50–80, 100–120, and 100–150 percent higher than that of straight duct inserted with square, diamond, and circular pin-arrays, respectively. The turning of the flow through a 90-deg angle and the recirculation of trapped air at the corner between the longer sidewall and the blocked straight exit for $\epsilon=1.0$ cause a significant pressure drop in the pin-fin channel.

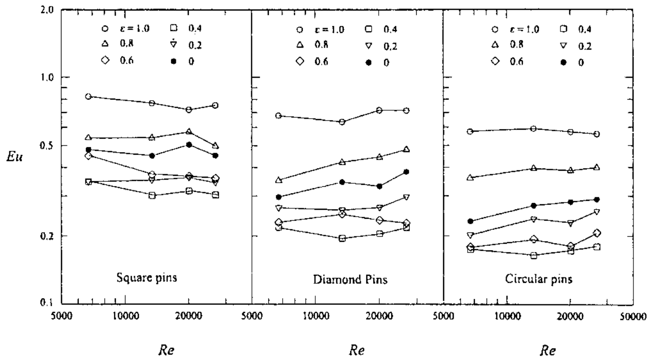

Fig. 10 Reynolds-number dependence of Euler number for the trapezoidal duct of the square pins

Summary and Conclusions

Experiments have been conducted for the measurements of endwall heat transfer and pressure drop in a trapezoidal duct with a short pin-fin array, simulating the trailing edge cooling cavity of a turbine blade. The effects of pin shape, lateral-flow rate and flow Reynolds number have been examined. New information on detailed heat transfer distributions on the endwall surfaces of a pin-fin trapezoidal channel with various lateral-flow rates has been provided in this study. When some fluid turns laterally out of the pin-fin trapezoidal cooling cavity, both the variation in the apparent duct throughflow area and the flow turning effect would affect the local forced-convection phenomena. The main findings based on the present experiments are as follows:

1 Increasing ϵ enhances the local heat transfer in the region near the lateral exit but degrades the local heat transfer in the region adjacent to the longer sidewall. The former is attributed to the effect of the accelerating flow through the convergent lateral exit together with the flow-turning effect. The latter is because of the lower forced convection along the straight (X) direction of the trapezoidal duct.

2 As for the effect of ϵ, the endwall-averaged heat transfer decreases with increasing ϵ from zero to a small lateral-flow rate (say, $\epsilon=0.3$–0.4) due to an increase in the duct throughflow area, which reduces the forced convection in the trapezoidal duct. At high lateral flow conditions ($\epsilon>0.4$), however, the endwall-averaged heat transfer increases with increasing ϵ due to the significance of flow-turning effect. Consequently, a local minimum in $\overline{\mathrm{Nu}}$ occurs at about $\epsilon=0.4$ for the square and diamond pins and at about $\epsilon=0.3$ for the circular pins.

3 As for the effect of pin shape, the square pin performs a better endwall heat transfer than the diamond pin, and subsequently than the circular pin for $\epsilon<0.8$. However, under a high lateral flow condition, $\epsilon>0.8$, the endwall-averaged Nusselt numbers are largely identical between the square and diamond pins. As compared to the fully developed smooth duct results, the heat transfer enhancement for the square, diamond, and circular pins are about 170–260, 160–260, and 130–210 percent, respectively. When the lateral-flow rate increases from $\epsilon=0$ to 1.0, the pressure drop across the trapezoidal duct decreases first, reached a local minimum at about $\epsilon=0.4$ and then increases to a local maximum at $\epsilon=1.0$. In addition, the square pins yield the highest pressure drop, while the circular pin has the lowest pressure drop in the trapezoidal duct under a fixed Reynolds number and lateral-flow rate. Correlations for endwall-averaged heat transfer in the trapezoidal duct with different pin shapes are developed in terms of the lateral-flow rate and the flow Reynolds number for the first time.

Acknowledgments

Support for this work was provided by the National Science Council of Taiwan under Contract No. NSC 89-TPC-7-216-001.

Nomenclature

c_p = specific heat at constant pressure
De = equivalent hydraulic diameter at the test duct inlet
d = diameter or length of the side wall of the pin
Eu = Euler number, Eq. (7)
f_s = Darcy friction factor for smooth trapezoidal duct
G = total mass flux
H_1 = height of longer side wall of trapezoidal duct
H_2 = height of short side wall of trapezoidal duct
h = heat transfer coefficient
k = thermal conductivity of endwall material
k_f = air thermal conductivity
L = trapezoidal duct length along streamwise direction
l = fin length (or height)
$\overline{\mathrm{Nu}}$ = endwall-averaged Nusselt number of pin fin channel
$\overline{\mathrm{Nu}}_s$ = fully developed Nusselt number for smooth duct
P = pressure
Pr = Prandtl number
ΔP = pressure drop across test section entrance and exit
Re = Reynolds number $= UDe/\nu$
S_x = streamwise spacing between the pins
S_y = spanwise spacing between the nearby pins
T_i = initial wall temperature
T_m = mainstream temperature
T_w = wall temperature
t = time
U = bulk mean velocity of air at duct inlet
V = volume flow rate of air
W = spanwise distance of heated plate, Fig. 3
X = axial coordinate, Fig. 3
X_s = axial coordinate from smooth-duct entrance, Fig. 6
Y = transverse coordinate, Fig. 3
Z = coordinate normal to the endwall
α = thermal diffusivity of the endwall material
ϵ = ratio of the lateral-to-total flow rate
μ = viscosity of air
ρ = air density
τ_j = time step

Subscripts

i = initial
m = mainstream
s = smooth wall
t = total
w = wall

References

[1] Hwang, J. J., Lai, D. Y., and Tsia, Y. R., 1999, ''Heat Transfer and Pressure Drop in Pin-Fin Trapezoidal Ducts,'' ASME J. Turbomach., **121**, pp. 264–272.
[2] Van Fossen, G. J., 1982, ''Heat-Transfer Coefficients for Staggered Arrays of Short Pin Fins,'' ASME J. Heat Transfer, **104**, pp. 268–274.
[3] Brigham, B. A., and Van Fossen, G. J., 1984, ''Length to Diameter Ratio and Row Number Effects in Short Pin Fin Heat Transfer,'' ASME J. Eng. Gas Turbines Power, **106**, pp. 241–245.
[4] Metzger, D. E., Berry, R. A., and Bronson, J. E., 1982, ''Developing Heat Transfer in Rectangular Ducts With Staggered Pin Fins,'' ASME J. Heat Transfer, **104**, pp. 700–706.
[5] Metzger, D. E., Fan, C. S., and Haley, S. W., 1984, ''Effects of Pin Shape and Array Orientation on Heat Transfer and Pressure Loss in Pin Fin Arrays,'' ASME J. Heat Transfer, **106**, pp. 252–257.
[6] Lau, S. C., Han, J. C., and Kim, Y. S., 1989, ''Turbulent Heat Transfer and Friction in Pin Fin Channels With Lateral Flow Injection,'' ASME J. Heat Transfer, **111**, pp. 51–58.
[7] Chyu, M. K., 1990, ''Heat Transfer and Pressure Drop for Short Pin-Fin Arrays With Pin-Endwall Fillet,'' ASME J. Heat Transfer, **112**, pp. 926–932.
[8] Chyu, M. K., Hsing, Y. C., and Natarajan, V., 1998, ''Convective Heat Transfer of Cubic Fin Arrays in a Narrow Channel,'' ASME J. Turbomach., **120**, pp. 362–367.
[9] Chyu, M. K., Hsing, Y. C., Shih, T. I. P., and Natarajan, V., 1999, ''Heat Transfer Contributions of Pins and Endwall in Pin-Fin Arrays: Effects of Thermal Boundary Condition Modeling,'' ASME J. Turbomach., **121**, pp. 257–263.
[10] Hwang, J. J., and Chen, C. S., 1999, ''Augmented Heat Transfer in a Triangular Duct by Using Multiple Swirling Jets,'' ASME J. Heat Transfer, **121**, pp. 683–690.
[11] Lu, C. C., 1999, ''An Experimental Study of Heat Transfer and Fluid Flow in a Pin-Fin Wedge Duct,'' Masters Thesis, Chung-Hua University, Taiwan.
[12] Ireland, P. T., and Jones, T. V., 1987, ''The Response Time of a Surface Thermometer Employing Encapsulated Thermochromic Liquid Crystals,'' J. Phys. E, **20**, pp. 1195–1199.
[13] Vedula, R. J., and Metzger, D. E., 1991, ''A Method for the Simultaneous Determination of Local Effectiveness and Heat Transfer Distributions in Three-Temperature Convection Situation,'' ASME Paper No. 91-GT-345.
[14] Kline, S. J., and McClintock, E. A., 1953, ''Describing Uncertainties in Single-Sample Experiments,'' Mech. Eng. (Am. Soc. Mech. Eng.), **75**, pp. 3–8.
[15] Dittus, F. W., and Boelter, L. M. K., 1930, University of California at Berkeley, Publications in Engineering, **2**, p. 443.
[16] Petukhov, B. S., 1970, *Advances in Heat Transfer*, Vol. 6, Academic, New York, pp. 503–504.

Augmentation of Stagnation Region Heat Transfer Due to Turbulence From a DLN Can Combustor

G. James Van Fossen
NASA Glenn Research Center,
Cleveland, OH 44135

Ronald S. Bunker
General Electric,
Schenectady, NY 12309

Heat transfer measurements have been made in the stagnation region of a flat plate with a circular leading edge. Electrically heated aluminum strips placed symmetrically about the leading edge stagnation region were used to measure spanwise-averaged heat transfer coefficients. The maximum Reynolds number obtained, based on leading edge diameter, was about 100,000. The model was immersed in the flow field downstream of an approximately half-scale model of a can-type combustor from a low NO_x*, ground-based power-generating turbine. The tests were conducted with room temperature air; no fuel was added. Room air flowed into the combustor through six vane-type fuel/air swirlers. The combustor can contained no dilution holes. The fuel/air swirlers all swirled the incoming airflow in a counterclockwise direction (facing downstream). A five-hole probe flow field survey in the plane of the model stagnation point showed the flow was one big vortex with flow angles up to 36 deg at the outer edges of the rectangular test section. Hot-wire measurements showed test section flow had very high levels of turbulence, around 28.5 percent, and had a relatively large axial-length scale-to-leading edge diameter ratio of 0.5. X-wire measurements showed the turbulence to be nearly isotropic. Stagnation heat transfer augmentation over laminar levels was around 77 percent and was about 14 percent higher than predicted by a previously developed correlation for isotropic grid-generated turbulence.* [DOI: 10.1115/1.1330270]

Introduction

Firing temperatures of modern turbine engines often exceed the melting temperature of the downstream blade and vane alloy material, thus requiring the hardware to be cooled by compressor discharge air or some other means. The design of these cooling systems requires a knowledge of the heat transfer coefficients between the hot gas and the blade or vane. Turbulence in the combustor exit stream plays a major role in determining the level of heat transfer. The stagnation region is an area of high heat transfer and is very sensitive to the level of free-stream turbulence. The objective of the present work is to determine the level of stagnation region heat transfer augmentation due to turbulence produced by a scaled, can-type combustor from a ground-based, gas-fired turbine operating at room temperature and compare the results with heat transfer augmentation from isotropic grid-generated turbulence.

It has been known for a long time that a small increase in free-stream turbulence from laminar levels can cause a large increase in heat transfer from the stagnation region of a bluff body such as a turbine vane or blade [1,2]. Early attempts at correlation, e.g., [3,4], ignored the effect of turbulent length scale and tried to correlate heat transfer augmentation with only turbulence intensity and Reynolds number. These attempts resulted in large, unexplained scatter when compared to the data of other researchers. The works of Ames [5] and Van Fossen et al. [6] showed that length scale was also an important parameter.

Van Fossen et al. [6] studied the augmentation of stagnation region heat transfer due to isotropic turbulence from square-bar, square-mesh grids. A correlating parameter was developed from experimental data taken with several different grids, which grouped the augmentation data very tightly (±4 percent). The isotropic data of several other studies were compared to the correlation and found to agree within ±10 percent. Data from an array of parallel, fine wires that generated non-isotropic turbulence were correlated by the parameter but showed a much higher level of augmentation than the isotropic turbulence.

Ames [5] fabricated turbulence generators that resembled a combustor liner, having primary air inlets and dilution holes. Using the rapid distortion theory of Hunt and Graham [7], he developed a correlating parameter based on intensity, Reynolds number, and what he called an energy-scale, the average size of the energy containing eddies. The correlation fit his and other data quite well.

Results to be presented from the present work include heat transfer measurements in the stagnation region of a flat plate with a circular leading edge, a five-hole probe flow field survey, turbulence intensity survey using a single hot wire, and X-wire results downstream of the simulated combustor liner.

Test Facility, Instrumentation and Data Acquisition

Wind Tunnel. The experiments were carried out in the wind tunnel shown in Fig. 1. Air drawn from the test cell passed through the six-scaled combustor fuel/air swirlers into the 32.4 cm diameter × 26.4 cm long can, through a 68.5 cm long transition section and into the 15.2 cm × 54.1 cm × 77.5 cm long test section. Air leaving the test section then passed through another transition section to a 10 in. pipe that contained an orifice for flow measurement and a butterfly valve for flow control. Flow through the swirlers could be choked so the control valve was set to supply the maximum test section pressure that gave the maximum flow rate. The ratio of test section static pressure to test cell barometric pressure was typically 0.63. This gave a leading edge Reynolds number of about 100,000. A Kiel probe located in the test section was used to measure the total pressure for each run. Four chromel-alumel thermocouples near the inlet of the swirlers measured the

---

Contributed by the International Gas Turbine Institute and presented at the 45th International Gas Turbine and Aeroengine Congress and Exhibition, Munich, Germany, May 8–11, 2000. Manuscript received by the International Gas Turbine Institute February 2000. Paper No. 2000-GT-215. Review Chair: D. Ballal.

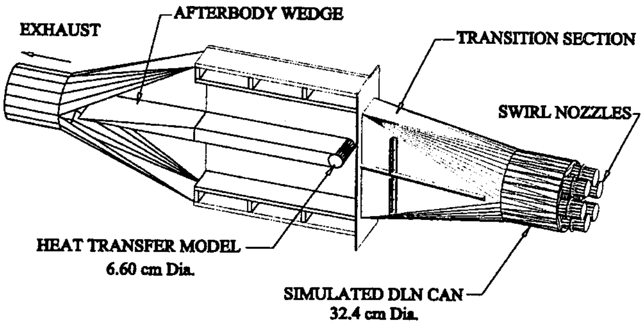

Fig. 1 Rig layout

total inlet temperature. A two-dimensional actuator system allowed hot-wire and five-hole probe surveys in a plane perpendicular to the flow that passed through the stagnation line of the heat transfer model. The model was not present when the flow surveys were conducted.

Simulated Combustor. The combustor liner model is of the natural gas fired, Dry-Low-NO$_x$ (DLN), can-type having no dilution or film cooling air injection. Six identical, scaled DLN-type fuel-air swirlers are set into the upstream end, or head end, of the combustor liner. Each swirler, shown in Fig. 2, was composed of a set of 12 large air swirl vanes (outer) and a 16-vane diffusion gas tip (inner). The air swirler vane sets were cast stainless steel with about 45 deg of turning. The diffusion gas tips were fabricated from aluminum for this mockup. Swirl is in the same direction for each of the inner and outer vanes. Each swirler is also provided with a 7.62 cm diameter × 6.11 cm long inlet duct to model the inlet region existing in typical engine hardware. In this mockup, the head end has no additional flow orifices other than the swirlers. This configuration results in a cold flow combustor mockup, generating both swirl and large-scale turbulence typical of a land-based power turbine. While this cold flow combustor mockup does not achieve the pressure and temperature levels of an actual engine, nor does it have the reaction and combustion chemistry, previous work of Zimmerman [8] and Goebel et al. [9] indicates that the inclusion of the major geometry and flow features in such a cold flow device does result in the generation of free-stream turbulence and swirl representative of a pressurized and fired system.

Five Hole Pressure Probe. Mean flow angle and velocity were measured with a standard, commercially available, five-hole pressure probe. Pressures were measured with strain gage-type transducers and recorded using the Laboratory steady-state data recording system.

Hot-Wire Instrumentation. Turbulence measurements were obtained using a two-channel constant-temperature anemometer system. The turbulence intensity survey in the plane of the model stagnation point was conducted with a single hot wire oriented parallel to model spanwise direction with the model removed. Bridge voltage was converted to mean and rms components with special purpose analog meters whose output was recorded with the Laboratory state data acquisition system. Length scale and isotropy measurements were made with a crossflow X-wire probe. The wires were oriented perpendicular to the model spanwise direction. Bridge voltage was passed through an eight pole, six zero, constant-delay anti-aliasing filter set to begin roll-off at 6 kHz. A total of 2^{20} samples were recorded at an 18 kHz sampling frequency with a high-speed, digital-to-analog conversion (DAC) board and stored in a personal computer. In order to obtain good resolution of the fluctuating component of the signal, it was necessary to subtract a known DC voltage from the raw signal, then amplify the result before passing to the DAC. For all hot-wire measurements the frequency response was estimated to be about 90 kHz using the standard square wave test.

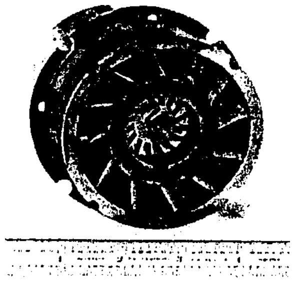

Fig. 2 DLN fuel–air swirler looking upstream

Heat Transfer Model. The heat transfer model was a 65-cm-long flat plate with a circular leading edge with a radius of 3.30 cm. The model spanned the 15.2 cm test section width. A 52-cm-long wedge-shaped afterbody designed to eliminate vortex shedding extended downstream into the outlet transition section, as shown in Fig. 1. The model contained 19 heat flux gages consisting of aluminum strips 6.6 cm long × 0.48 cm wide × 0.32 cm deep with a thin foil electric heater glued to the rear and a chromel-alumel thermocouple embedded in a groove. Each gage averaged the heat transfer over its 6.6 cm span. The farthest downstream gages were used as guard heaters to minimize losses in the streamwise direction. A guard heater behind the gages prevented conduction to the interior of the model. The average gap between the aluminum strips was 0.25 mm and was filled with epoxy. The aluminum strips were maintained at constant temperature (±0.25°C) by a specially designed control circuit [10].

Data Reduction

Flow Field. The five-hole probe was calibrated in an atmospheric jet over a range of pitch and yaw angles using the technique described in Giel et al. [11]. Yaw and pitch angles were least-square curve fit with fourth-order polynomials. Symmetry was not assumed in any of the curve fits.

Turbulence

Intensity. Hot-wire probes were calibrated in an atmospheric jet. A fourth-order polynomial was used to fit bridge voltage versus density-velocity product. Density-velocity product was used because the test section pressures were below atmospheric thus calibration density was different than test section density. The mean and rms voltages recorded for the intensity survey with the steady state recording system were converted to density velocity product and turbulence intensity was calculated as

$$Tu=\frac{\left[\frac{d(\rho u)}{dE}\right]_E e_{\text{rms}}}{\rho U} \tag{1}$$

where E is the mean bridge voltage, e_{rms} is the rms component of the bridge voltage, and the derivative is the slope of the calibration curve at E.

Integral Length Scale. Length scale was calculated from the autocorrelation function by fitting an exponential curve

$$R(\tau)=e^{-C_\tau \tau} \tag{2}$$

between the arbitrary limits of $1>R(t)>0.33$. Integrating $R(t)$ between zero and infinity and multiplying by the mean velocity gives the integral length scale,

$$\Lambda_x=U\int_0^\infty R(t)dt=\frac{U}{C_\tau} \tag{3}$$

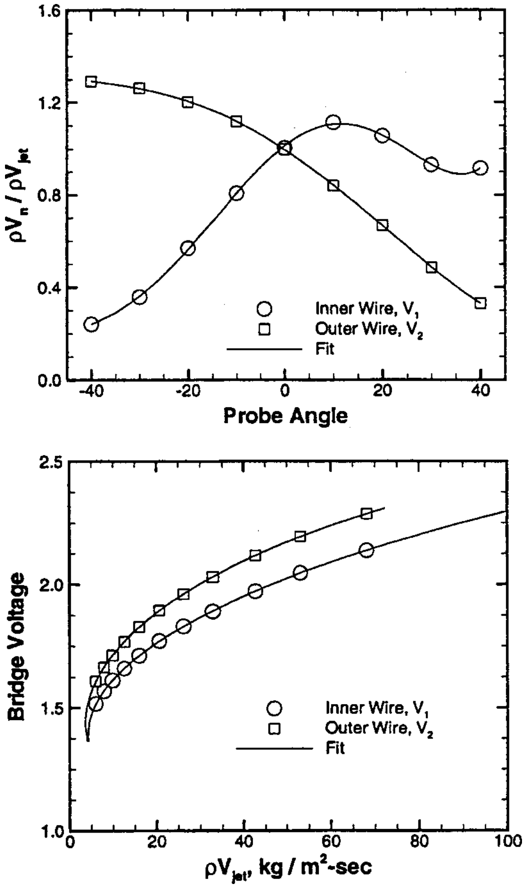

Fig. 3 Crossflow X-wire calibration curves

Although not a problem with this data set, this method of computing the length scale eliminates inconsistent results from some data that contain low-frequency noise; see Van Fossen et al. [6].

Isotropy. The X-wire probe was calibrated in the same air jet used to calibrate the single-wire probe. The procedure was to set the probe angle so both wires were as close as possible to 45 deg to the flow, and perform a velocity calibration as was done for the single wire. This produced a curve fit of bridge voltage versus jet velocity for each wire. A directional calibration was accomplished by setting the jet density-velocity product at the value expected in the test section and recording bridge voltage over a range of probe angles between -40 and $+40$ deg. Using the velocity curve fit for each wire, a density-velocity product was calculated for each probe angle and normalized by the actual jet density-velocity product. These data sets were then curve-fit with polynomials. Figure 3 shows the resulting calibration curves with the data points superimposed.

It can be seen in the directional calibration that wire 2, the outer wire, looks like a cosine curve, which is normal behavior for an angled hot wire. Wire l, however, looks like the cosine for angles between -40 and 0 deg, but at angles greater than 0 deg it does not. This is a problem inherent to the crossflow probe design; at angles greater than 0 deg, wire 1 is in the wake of the prongs that support wire 2. Several features of this type of probe outweigh this inconvenience: (1) The wire angle can be changed by simply rotating the probe stem without a change in the streamwise or cross-stream position; (2) the probe can be inserted through a small (6.4 mm) hole in an actuator or tunnel wall without having other access to the test section such as a window or door to install the probe tip. This shortcoming of the crossflow probe can be overcome by limiting the flow angles relative to the probe to the range -40 to 0 deg. The curve fits from Fig. 3 were used to construct a lookup table of the ratio $\rho V_1/\rho V_2$ versus probe angle. The data reduction procedure was then: (1) Calculate ρV_1 and ρV_2 using the curve fits of velocity versus bridge voltage. (2) Using the ratio of $\rho V_1/\rho V_2$ and the lookup table, find the angle of the velocity vector relative to the probe. (3) Using the curve fit of $\rho V_2/\rho V_{\text{jet}}$ versus angle, compute ρV_{jet} (ρV_{jet} is now the magnitude of the mass-velocity vector).

Heat Transfer. An energy balance was used to determine the Frossling number for each gage:

$$\mathrm{Fr}(s/R)=\frac{(q_{EI}-q_{\text{rad}}-q_{\text{gap}})d}{A[T_W-T_r(s)]k\sqrt{\mathrm{Re}_d}} \tag{4}$$

where q_{EI} is the heat added to the gage by the electric heater, q_{rad} is the heat lost by radiation, q_{gap} is the heat conducted away from the gage to the epoxy gap and the unguarded ends of the heaters, A is the exposed gage surface area, T_W is the gage temperature, $T_r(s)$ is the local recovery temperature, k is the thermal conductivity of air, and Re_d is the Reynolds number based on leading edge diameter, d. Corrections for radiation heat loss, q_{rad}, were made assuming gray body radiation to black surroundings and an emissivity of 0.05 for the aluminum gage.

An estimate of the gap loss, q_{gap}, can be obtained from an exact solution for two-dimensional heat conduction in a rectangle; see Van Fossen et al. [10] for details. The gap loss was about 10 percent of the total heat flow while the radiation heat loss was on the order of 0.2 percent.

The recovery temperature was calculated as

$$T_r(s)=T_{st,\infty}+r(s)(T_t-T_{st,\infty}) \tag{5}$$

where $T_{st,\infty}$ is the static temperature upstream of the model. The local recovery factor, $r(s)$, was calculated as

$$r(s)=1-\left(\frac{\rho U(s)}{(\rho U)_\infty}\right)^2(1-\sqrt{\mathrm{Pr}}) \tag{6}$$

The local mass flow ratio, $\rho U(s)/(\rho U)_\infty$, was found from a numerical solution of flow over the model that included the tunnel walls [12].

Following the results of Rigby et al. [12], the thermal conductivity and viscosity of air were evaluated at the free-stream total temperature from equations given in Hillsenrath et al. [13].

The Reynolds number, Re_d, was based on the diameter of the leading edge, d, and the mass-velocity averaged between the flow area with maximum model blockage and the unblocked flow area, that is,

$$(\rho U)_{avg}=(\rho U)_\infty\frac{(2-B)}{2(1-B)} \tag{7}$$

where the blockage, B, is the ratio of maximum model thickness to tunnel height. Blockage was 0.122 for this test.

Uncertainty Analysis

Frossling Number. Estimates of the bias error of each measuring instrument were made and combined by the method of Kline and McClintock [14]. Estimates of the precision of each measurement were calculated from 20 samples of each steady-state measurement and combined by the same method. The maximum Frossling number uncertainty occurred at the stagnation gage and was 5.7 percent.

Flowfield Measurements. Estimates of error in the hot-wire and five-hole probe measurements were made using a method suggested by Yavuzkurt [15]. Estimated error in turbulence intensity was 12.9 percent and in length scale 18.3 percent.

Results and Discussion

Flow Field. Results of the five-hole probe survey are shown in Fig. 4. The figure shows streamlines and vectors that represent the components of velocity perpendicular to the axial direction. The length of the vector at the top of the figure is representative of the magnitude of the axial velocity. It can be seen that vortices from the six individual swirl nozzles add together to form a single vortex at the inlet to the test section. The center of the vortex is displaced from the tunnel centerline. Flow angles of up to 36 deg were measured at the extreme spanwise positions and angles near 0 deg were recorded at midspan.

Figure 5 shows the mean flow velocity components in the axial and cross-stream directions measured with the X-wire. The axial component varies about 17 percent in the spanwise direction with a minimum near midspan. The cross-stream component varies linearly with span with zero velocity corresponding with the midspan position.

Turbulence. A survey of turbulence intensity measured with the single hot wire is shown in Fig. 6. Intensity was stratified in the spanwise direction with a maximum of around 30 percent at midspan and tapering off to around 21 percent at the full test section span. Intensity averaged over the span of the stagnation heat transfer gage was 28.5 percent.

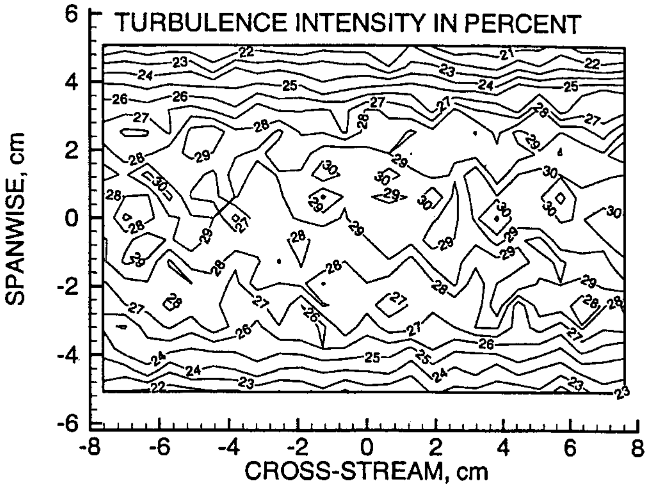

Fig. 6 Turbulence intensity contour plot

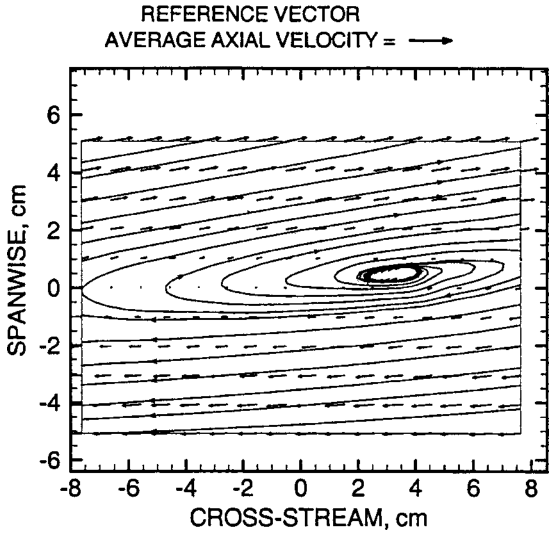

Fig. 4 Five-hole probe survey; cross-stream vector and streamline plot

Figure 7 gives the fluctuating components of axial and cross-stream velocity. The axial component is nearly constant, while the cross-stream component has a dip near midspan. This, at first, appears contrary to the results of the single-wire survey, but closer examination shows that it is consistent. The single wire was oriented in the spanwise direction and thus would respond to axial and cross-stream components as:

$$Tu=\sqrt{\frac{(u'^2+v'^2)}{(U^2+V^2)}} \tag{8}$$

The zero velocity of the cross-stream mean component, V, causes the intensity to peak in the center of the span.

Figure 8 shows the ratio of the two fluctuating velocities, u'/v'. The average ratio over the span is equal to 0.97 and varies only about ±10 percent, indicating that the flow is nearly isotropic.

Typical autocorrelation functions used to determine the length scale are shown in Fig. 9. Also shown on the figure are the exponential curve fits used to determine the length scale. These figures

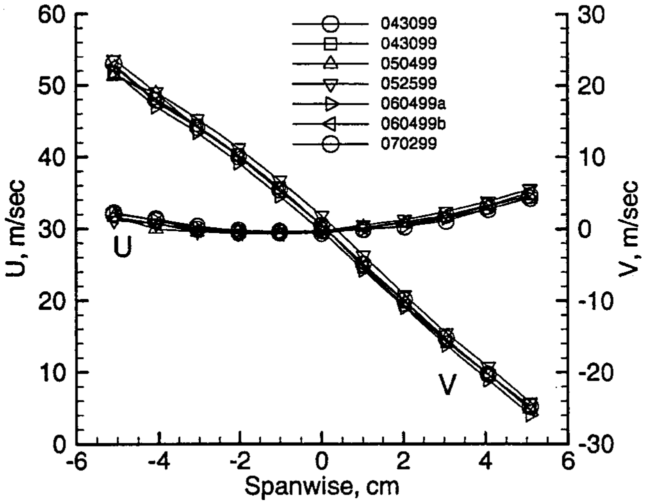

Fig. 5 X-wire traverse: mean axial flow and cross-stream velocity components

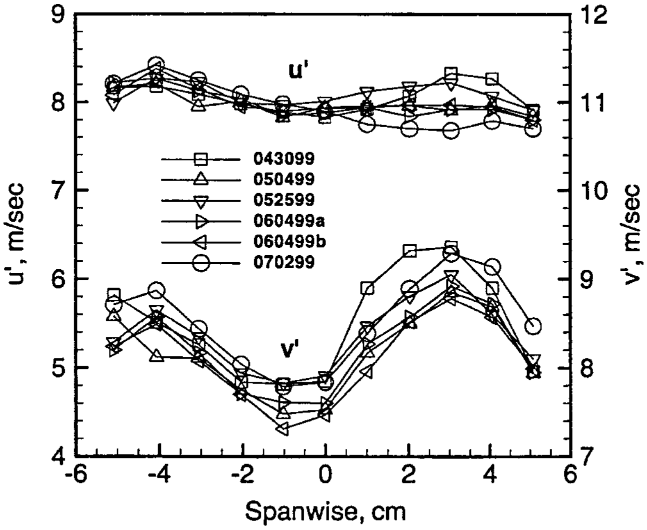

Fig. 7 X-wire traverse: rms fluctuating axial and cross-stream velocity components

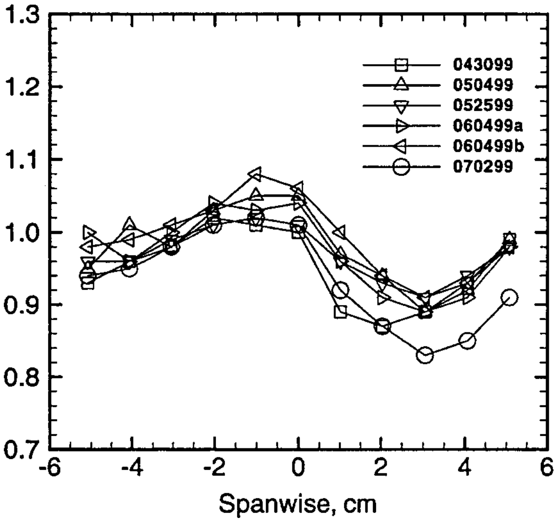

Fig. 8 X-wire traverse: ratio of rms fluctuating axial and cross-stream velocity components

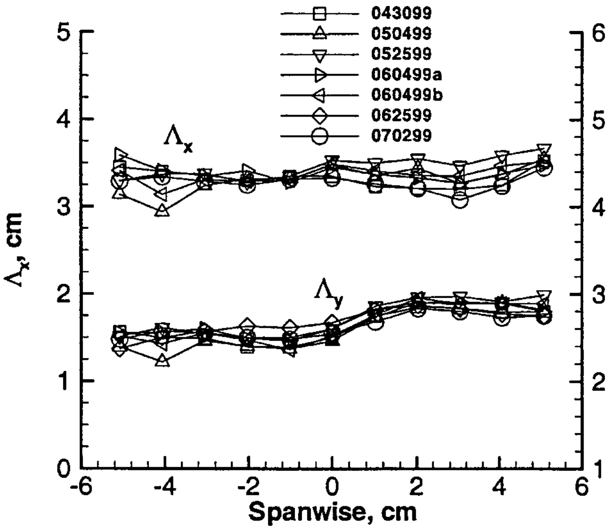

Fig. 10 X-wire traverse: axial and cross-stream length scales

are typical of autocorrelations for all the data taken. The axial direction autocorrelation is closely approximated by the exponential curve fit while the cross-stream component has a large area of negative correlation.

The spanwise distribution of length scale is shown in Fig. 10. The average axial length scale was 3.34 cm, while the cross-stream length scale was 2.64 cm, making the ratio of axial to cross-stream length scale about 1.26. Axial and cross-stream components of the power spectrum in wave number space are shown in Fig. 11. Both components exhibit the $-5/3$ slope indicative of the inertial subrange. The rolloff in the spectrum at wave numbers greater than about 1500 is caused by the anti-aliasing filter. The spectra shown in Fig. 11 are typical of all spanwise locations.

Heat Transfer. The heat transfer distribution in the stagnation region is shown in Fig. 12 where Frossling number (Nusselt number/$(\mathrm{Re}_d)^{1/2}$) is plotted versus the ratio of surface distance to leading edge radius. For comparison, a numerical solution for the cylindrical leading edge for a laminar free stream obtained using the PARC-2D code taken from Rigby and Van Fossen [12] is shown. Also shown are the PARC-2D code results multiplied by the factor 1.77 in order to match the experimental data at the stagnation point. The augmentation of stagnation heat transfer due to the DLN turbulence is about 77 percent above the laminar case. Frossling numbers for heat flux gages off the stagnation line generally follow the laminar distribution multiplied by the augmentation factor until s/R of roughly ± 0.9 ($\sim \pm 52$ deg). Beyond this value of s/R, the augmentation is greater than the 1.77 of the stagnation region.

Figure 13 shows a comparison of the DNL turbulence augmented stagnation heat transfer compared with a correlation for stagnation region heat transfer taken from Van Fossen et al. [16]. The stagnation heat transfer due to the DLN turbulence is about 14 percent higher than the correlation predicts. The correlation was derived using turbulence generated with square-bar, square-mesh grids that produced nearly isotropic turbulence; the data were all contained within the ± 4 percent bands shown in Fig. 13. Van Fossen et al. [16] showed that nonisotropic turbulence could produce augmentation levels higher than that of isotropic turbulence. It was suspected that this was the cause of the increased augmentation by the DLN combustor turbulence, but the turbulence measurements show that this is not the case; the DLN turbulence is nearly isotropic. The cause of this increased augmentation above isotropic grid turbulence levels remains unknown. One possibility could be the swirl in the mean flow, causing an

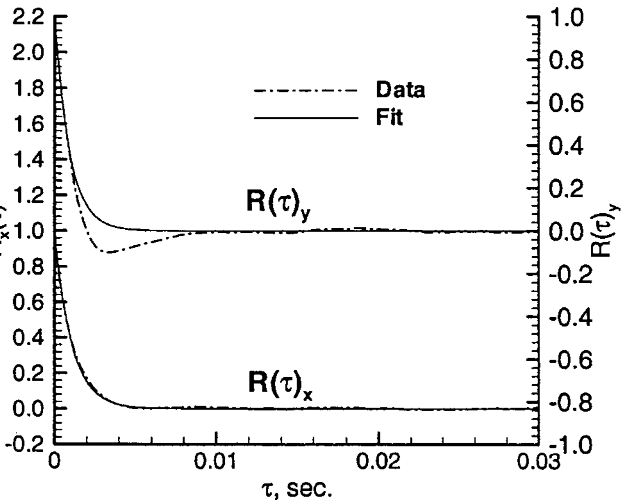

Fig. 9 Typical axial and cross-stream autocorrelation functions with curve fits

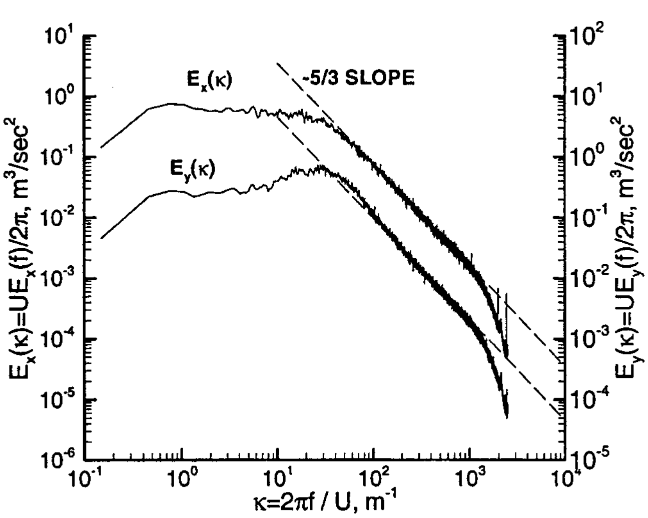

Fig. 11 Typical axial and cross-stream wave number spectrum

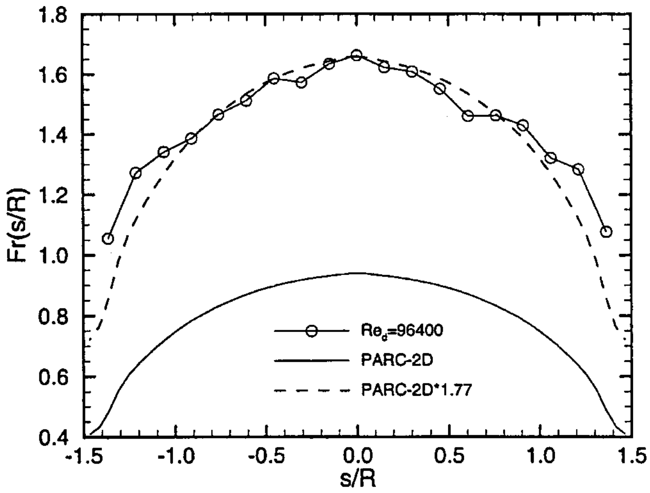

Fig. 12 Heat transfer distribution over the model leading edge

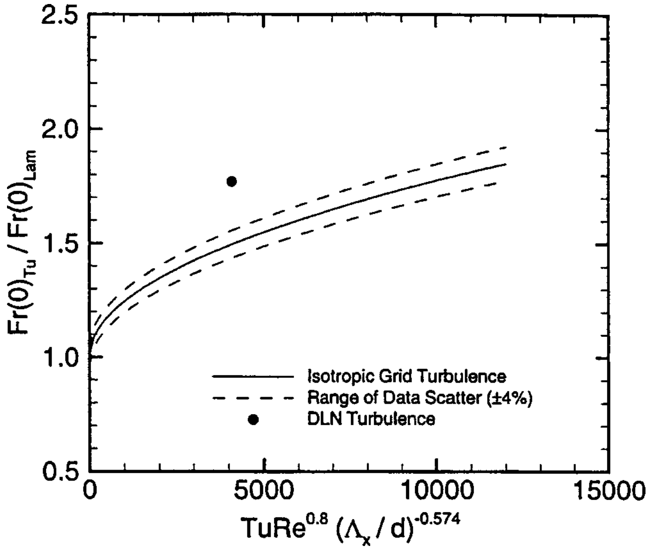

Fig. 13 Comparison of stagnation heat transfer augmentation due to DLN turbulence and correlation derived from square bar grid data

effective angle of attack on the leading edge; positive on one half of the span and negative on the other half. This has not been investigated.

Conclusions

Spanwise-averaged heat transfer measurements were made in the stagnation region of a flat plate with a 3.3 cm radius circular leading edge. The heat transfer model was placed downstream of a scaled, simulated, gasfired, combustor liner from a ground based, power turbine. Conclusions drawn from this study are:

1 The DLN combustor used in the present test with the swirl vanes from each of the six nozzles oriented in the same direction produced a single large swirl entering the test section. Flow angles up to 36 deg from axial were recorded at the outer edge while flow angles of nearly zero were found at the center.

2 Very high levels of free-stream turbulence were generated. Spanwise-averaged turbulence intensity was found to be 28.5 percent.

3 The turbulence generated appeared to be isotropic. Fluctuating components of velocity in the axial and cross-stream directions were nearly identical in magnitude. The wave number spectrum for both components demonstrated the $-5/3$ slope characteristic of an inertial subrange.

4 The average length scale in the axial direction was found to be 3.34 cm, while the cross-stream direction length scale was 2.64 cm.

5 Stagnation heat transfer in the turbulent exhaust of the DLN combustor liner was found to be higher than that for a laminar free stream by a factor of 1.77.

6 Stagnation heat transfer augmentation was found to be 14 percent higher than predicted by a correlation developed from isotropic grid-generated turbulence.

Nomenclature

B = wind tunnel blockage
C_τ = constant in fit of autocorrelation, s^{-1}
d = leading edge diameter, cm
E = hot wire bridge voltage, V
e = fluctuating component of bridge voltage, V
Fr = Frossling number=Nusselt/(Re)$^{1/2}$
f = frequency, Hz
Pr = Prandtl number
R = radius of model leading edge, cm
r = recovery factor
$R(\tau)$ = autocorrelation function
Re = Reynolds number
s = surface distance from stagnation point, cm
T = temperature, K
Tu = turbulence intensity
U, V = axial and cross-stream components of velocity, m/s
u', v' = fluctuation components of U and V, m/s
Λ = length scale, cm
κ = wave number, m^{-1}
ρ = density, kg/m^3
τ = delay time in autocorrelation, s

Subscripts

avg = averaged over time
d = leading edge diameter
rms = root mean square
r = recovery
st = static condition
t = total condition
x = axial direction
y = cross-stream direction
∞ = free-stream condition

References

[1] Zapp, G. M., 1950, ''The Effect of Turbulence on Local Heat Transfer Coefficient Around a Cylinder Normal to an Air Stream,'' M. S. Thesis, Oregon State College, Corvallis, OR.

[2] Giedt, W. H., 1951, ''Effect of Turbulence Level of Incident Air Stream on Local Heat Transfer From Cylinders,'' J. Aeronaut. Sci., **18**, No. 11, pp. 725–730.

[3] Smith, M. C., and Kuethe, A. M., 1966, ''Effects of Turbulence on Laminar Skin Friction and Heat Transfer,'' Phys. Fluids, **9**, No. 12, pp. 2337–2344.

[4] Lowery, G. W., and Vachon, R. I., 1975, ''Effect of Turbulence on Heat Transfer From Heated Cylinders,'' Int. J. Heat Mass Transf., **18**, No. 11, pp. 1229–1242.

[5] Ames, F. E., 1994, ''Experimental Study of Vane Heat Transfer and Aerodynamics at Elevated Levels of Turbulence,'' NASA CR 4633.

[6] Van Fossen, G. J., Simoneau, R. J., and Ching, C. Y., 1994, ''Influence of Turbulence Parameters, Reynolds Number, and Body Shape on Stagnation Region Heat Transfer,'' NASA TP-3487.

[7] Hunt, J. C. R., and Graham, J. M. R., 1978, ''Free-Stream Turbulence Near Plane Boundaries,'' J. Fluid Mech., **84**, pp. 209–235.

[8] Zimmerman, D. R., 1979, ''Laser Anemometer Measurements at the Exit of a T63-C20 Combustor,'' NASA CR-159623.

[9] Goebel, S., Abuaf, N., and Lee, C.-P., 1993, ''Measurements of Combustor Velocity and Turbulence Profiles,'' ASME Paper No. 93-GT-228.

[10] Van Fossen, G. J., Simoneau, R. J., Olsen, W. A., and Shaw, R. J., 1984, ''Heat Transfer Distributions Around Nominal Ice Accretion Shapes Formed on a Cylinder in the NASA Lewis Icing Research Tunnel,'' presented at the

AIAA 22nd Aerospace Sciences Mtg., Jan. 9–12, Reno, NV (also NASA TM-83557).

[11] Giel, P. W., Thurman, D. R., Lopez, I., Boyle, R. J., and Van Fossen, G. J., 1966, ''Three-Dimensional Flow Field Measurements in a Transonic Turbine Cascade,'' ASME Paper No. 96-GT-113.

[12] Rigby, D. L., and Van Fossen, G. J., 1992, ''Increased Heat Transfer to Elliptical Leading Edges Due to Spanwise Variations in the Freestream Momentum: Numerical and Experimental Results,'' AIAA Paper No. 92-3070.

[13] Hillsenrath, J., Beckett, C. W., Benedict, W. S., Fano, L., and Hobe, H. J., 1955, ''Tables of Thermal Properties of Gases,'' NBS Circular 564.

[14] Kline, S. J., and McClintock, F. A., 1953, ''Describing Uncertainties in Single-Sample Experiments,'' Mech. Eng. (Am. Soc. Mech. Eng.), Jan., pp. 3–8.

[15] Yavuzkurt, S., 1984, ''A Guide to Uncertainty Analysis of Hot-Wire Data,'' ASME J. Fluids Eng., **106**, pp. 181–186.

[16] Van Fossen, G. J., Simoneau, R. J., and Ching, C. Y., 1995, ''Influence of Turbulence Parameters, Reynolds Number, and Body Shape on Stagnation-Region Heat Transfer,'' ASME J. Heat Transfer, **117**, pp. 597–603.

An Experimental Evaluation of Advanced Leading Edge Impingement Cooling Concepts

M. E. Taslim

L. Setayeshgar

Mechanical, Industrial, and Manufacturing
Engineering Department,
Northeastern University,
Boston, MA 02115

S. D. Spring

GE Aircraft Engines,
Lynn, MA 03885

The main objective of this experimental investigation was to measure the convective heat transfer coefficient of impingement for different target wall roughness geometries of an airfoil leading edge, for jet to wall spacings and exit flow schemes. Available data in the open literature apply mostly to impingement on flat or curved smooth surfaces. This investigation covered two relatively new features in blade leading-edge cooling concepts: curved and roughened target surfaces. Experimental results are presented for four test sections representing the leading-edge cooling cavity with cross-over jets impinging on: (1) a smooth wall, (2) a wall with high surface roughness, (3) a wall roughened with conical bumps, and (4) a wall roughened with tapered radial ribs. The tests were run for two supply and three exit flow arrangements and a range of jet Reynolds numbers. The major conclusions of this study were: (a) There is a heat transfer enhancement benefit in roughening the target surface; (b) while the surface roughness increases the impingement heat transfer coefficient, the driving factor in heat transfer enhancement is the increase in surface area; (c) among the four tested surface geometries, the conical bumps produced the highest heat transfer enhancement. [DOI: 10.1115/1.1331537]

Introduction

Various methods have been developed over the years to keep the blade or nozzle temperatures below critical levels. One main objective in turbine blade and vane cooling design is to achieve maximum heat transfer coefficients while minimizing the coolant flow rate. One such method is to route coolant air through serpentine passages within the airfoil and convectively remove heat from the blade. The coolant is then ejected either at the tip of the blade, through the cooling slots along the trailing edge, or through the film holes on the airfoil surface. To enhance the heat transfer further, the channels and walls are often roughened with ribs. Extensive research on geometric aspects of the rib-roughened channels such as the passage aspect ratio (*AR*), the rib height to passage hydraulic diameter or blockage ratio (e/D_h), the rib angle of attack (α), the manner in which the ribs are positioned relative to one another (in-line, staggered, criss-cross, etc.), the rib pitch-to-height ratio (*S/e)* and the rib shape (round versus sharp corners, fillets, the rib aspect ratio (AR_{rib}), and the skewness toward the flow direction) all have shown pronounced effects on both local and overall heat transfer coefficients. The reader is referred to Burggraf [1], Chandra and Han [2], El-Husayni et al. [3], Han [4], Han et al. [5–7], Metzger et al. [8–10], Taslim and Spring [11,12], Taslim et al. [13–15], Webb et al. [16], and Zhang et al. [17].

Leading edge cooling cavities in modern gas turbine airfoils play an important role in maintaining the leading edge temperature at levels consistent with airfoil design life. These cavities often have a complex cross-sectional shape to be compatible with the external contour of the airfoil at the leading edge. Furthermore, to enhance the heat transfer coefficient in these cavities, they are often roughened on three walls with ribs of different geometries. The cooling flow for these geometries usually enters the cavity from the airfoil root and flows radially to the tip or, in the most recent designs, enters the leading edge cavity from the adjacent cavity through a series of crossover holes on the partition wall between the two cavities. In the latter case, the crossover jets impinge on a smooth leading-edge wall and flow exits through the ''showerhead'' film holes, ''gill'' film holes on the pressure and suction sides, and, in some cases, forms a crossflow in the leading-edge cavity and moves toward the airfoil tip. This study focuses on the leading-edge jet impingement and effects that roughening of the leading-edge surface have on the impingement heat transfer coefficient. A survey of airfoil geometries shows that, for analytical as well as experimental analyses, such cavities can be simplified by simulating the shape as a four-sided polygon with one curved side that forms the leading edge curvature, a rectangle with one curved side (often a smaller side) or a trapezoid with the smaller base replaced by a curved wall. The available data in open literature are mostly for the jet impingement on flat smooth or rib-roughened surfaces and occasionally for impingement on smooth concave surfaces. These studies include the works of Chupp et al. [18], Metzger et al. [19], Kercher and Tabakoff [20], Florschuetz et al. [21–23], Bunker and Metzger [24], Metzger and Bunker [25], Van Treuren et al. [26], Chang et al. [27], Huang et al. [28], and Akella and Han [29]. However, as dictated by the external shape of an airfoil leading edge, the test section in this investigation was a symmetric channel with a circular nose, two tapered side walls, and a flat fourth wall on which the cross-over jets were positioned. Depending on the flow arrangement, the impingement jet (air) exited from the test section through two rows of holes on the side walls representing the pressure and suction side gill film holes, or through one open end of the channel representing an airfoil tip. Furthermore, data were obtained for jet Reynolds numbers as high as 40,000, which is well beyond any published impingement data for gas turbine applications.

Test Sections

Figures 1 and 2 show schematically the layout, cross section, and the target surface geometries for the four test sections investigated. A conventional technique of heated walls in conjunction with thermocouples was used to measure the heat transfer coefficient. The test wall, where all measurements were taken, consisted of three removable cast brass pieces, which were heated by foil heaters attached on the back of the pieces. By adjustment of the ohmic power to the foil heater, the desired surface temperature was obtained. All test sections were 85.5 cm long. The circular

---

Contributed by the International Gas Turbine Institute and presented at the 45th International Gas Turbine and Aeroengine Congress and Exhibition, Munich, Germany, May 8–11, 2000. Manuscript received by the International Gas Turbine Institute February 2000. Paper No. 2000-GT-222. Review Chair: D. Ballal.

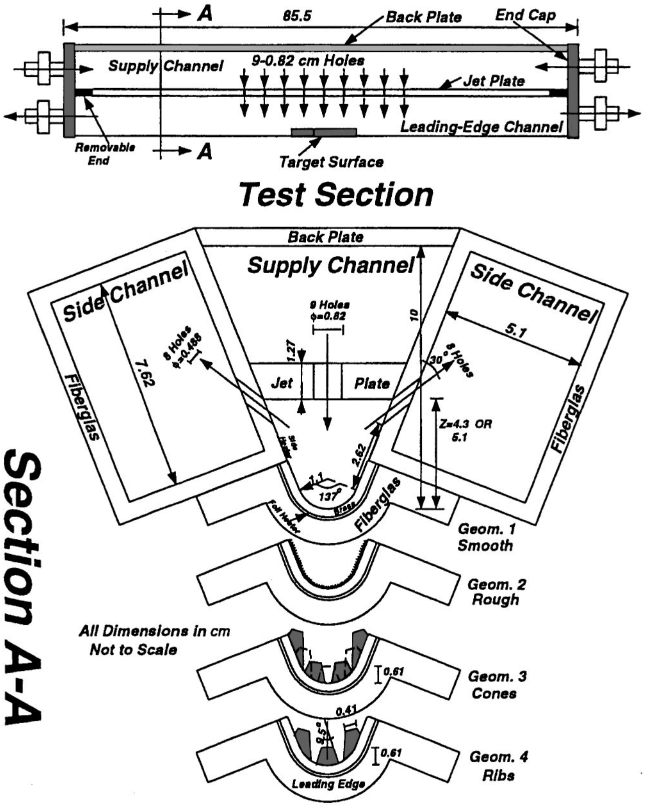

Fig. 1 Schematic of the test apparatus

wall simulating the leading-edge nose had an inner radius of 1.1 cm and an arc angle of 137 deg, and was made up of an outer fiberglass shell with the brass pieces installed on the inner radius. A flange on each side of the leading-edge piece facilitated the connections of the side walls. A circular recess along the inner radius with a depth of 3.2 mm and a length of 9.9 cm allowed the brass pieces to be fitted into the fiberglass shell. The two identical side channels with a cross-sectional area of 38.86 cm^2 (5.1 cm by 7.62 cm) and the same length as the leading-edge piece were also made of fiberglass. The side channels' main function was to maintain the dump pressure to consequently control the amount of flow through the ''gill'' holes on the blade suction and pressure sides. Eight angled cylindrical holes with a diameter of 4.88 mm and a center-to-center distance of 3.25 cm were drilled on each side channel wall at an angle of 30 deg with the sidewall to simulate gill holes on the suction and pressure sides of an airfoil. These holes were staggered along the length of the test section with respect to the crossover jet holes on the jet plate.

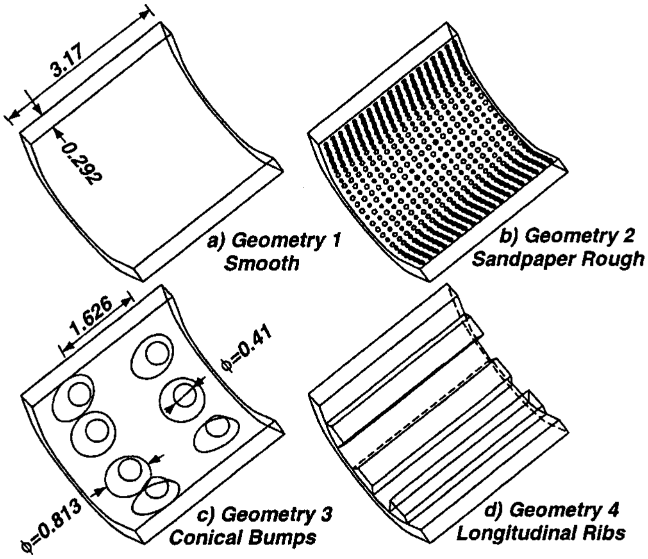

a) Geometry 1 Smooth

b) Geometry 2 Sandpaper Rough

c) Geometry 3 Conical Bumps

d) Geometry 4 Longitudinal Ribs

Fig. 2 Target surface geometries

Two removable 1.27-cm-thick jet plates corresponding to two values of $Z/d_{\mathrm{jet}}=5.2$ and 6.2 were made of acrylic plastic to produce the impinging jets. Nine cylindrical holes with a diameter of 0.82 cm were drilled at a distance of 3.25 cm from each other (center-to-center) on each jet plate. For each Z/d_{jet} test, the corresponding jet plate was attached and sealed to the side channel walls to simulate the partition wall between the leading-edge and its adjacent cavities. The cylindrical holes were centered along both the length and width of the jet plate. For the nominal position of the jet plate, a jet impinged at the center of each brass piece. To move the impinging jets to an off-center position, two removable 0.82-cm-thick pieces were attached to each end of the jet plates to allow three different impingement locations.

The removable brass pieces, installed in the fiberglass outer shell, provided the ability to change the impingement surface geometries in the test rig. Four different geometries were manufactured and tested: (1) a smooth wall that served as a baseline, (2) a sandpaper-rough wall with an average roughness of 0.5 mm corresponding to e/D_h of 0.0133, (3) a roughened wall with conical bumps, (4) a roughened wall with tapered radial ribs.

For each geometry, a Unigraphics® model was created for a LOM (Laminated Object Model) machine. This LOM model was used to mold and create a cast brass test piece for each of the four geometries. A 3 cm by 6.1 cm custom-made thin etched-foil heater with a thickness of about 0.2 mm was glued around the outer curved surface of each brass piece to provide the necessary heat flux. For each geometry, three identical brass pieces, separated by a 1-mm-thick rubber insulator, were mounted next to each other. Heat transfer coefficients were measured on the middle piece, while the other two pieces acted as guard heaters to minimize the heat losses to the adjacent walls. In addition, two custom-made thin etched-foil heaters were also mounted on the test section side channel walls next to the middle brass piece free edges, again acting as guard heaters. The test section wall temperature was adjusted to a desirable level by varying the ohmic power to these heaters. Six thermocouples embedded in the middle brass piece and three thermocouples embedded in each guard brass piece measured the wall temperatures. The average of the six thermocouple readings in the middle brass piece, which, if different only differed by a fraction of a degree, was used as the surface temperature in the data reduction software for the average heat transfer coefficient. The selected nominal surface temperature was 45°C. With a jet temperature of about 20°C, a reasonable 25°C temperature difference between the wall surface and air was attained. Two thermocouples embedded in the wall behind the guard heaters were used to measure the side wall temperature adjacent to the middle brass piece. By proper adjustment of the power to the side heaters, the wall temperature under the side heaters was set to be around 45°C. The conduction heat loss from the test piece to the fiberglass wall was calculated to be negligible (less than 0.02 percent of the total heat flux). AC power was supplied to individual heaters through an existing power panel with individual Variacs for each heater. Typical amperage and voltage levels for each heater varied from 0.23–0.4 Amps and 20–45 V, respectively. Air properties were evaluated at jet temperature.

The trapezoidal supply channel was formed by the exterior walls of the side channels, the jet plate, and a 1.27-cm-thick aluminum back plate. The end caps with throttling valves controlled the flow and pressure in each channel, thus simulating many variations that may occur in a real airfoil. Static pressure taps and thermocouples in each channel measured the pressure and temperature at different locations. The test sections were covered on all sides, by 5-cm-thick glasswool sheets to minimize heat losses to the environment. The radiational heat loss from the heated wall to the unheated walls as well as losses to ambient air through the fiberglass nose piece were taken into consideration when heat transfer coefficients were reduced. A contact micromanometer with an accuracy of 0.025 mm of water as well as a series of oil and mercury manometers measured the pressures and pressure differences between the static pressure taps mounted on both sides of the target wall for each geometry. For all cases, a critical venturimeter was used to measure the total air mass flow rate entering the supply channel.

Results and Discussion

A total of 47 tests were run in this investigation. All tests had several common features described as follows. There were always nine impinging jets issuing from the jet plate. The middle jet (fifth) always impinged on the brass test piece in the middle of the test section and the reported heat transfer results are always for that middle brass test piece. The fourth and sixth jets impinged on the side brass pieces that acted as guard heaters. The remaining six jets impinged on the fiberglass leading-edge wall to simulate the flow field in a typical leading-edge cavity. The jet Reynolds number is based on the total measured mass flow rate and the total area of the nine impingement holes. Two inflow arrangements to the channel, as shown in Fig. 3*(a)*, where air entered either from one end or both ends, were tested. A one-dimensional flow analysis of the test setup, shown in Fig. 4, reveals a slight variation of the air mass flow rate through different impingement holes for the case of flow entering the supply channel from one or both ends. It is also noted that the fifth jet, the one impinging on the brass test piece, has a flow rate that is very close to the average for both inflow arrangements. The remaining impingement holes carry mass flow rates that are only a fraction of a percent different from the average. Static pressure taps in the middle and at each end of the supply channel did not measure a significant difference (about 1 cm of water column for a supply pressure ranging from 110 to 172 kPa, absolute). Three outflow arrangements for the exiting cooling air, shown in Fig. 3(*b*), were tested. For the ''nominal flow'' case the air, after impinging on the leading-edge wall, ejected equally through the side channel holes, which simulate the gill holes on the pressure and suction sides of an airfoil. For the ''one-sided'' case the air, after impinging on the leading-edge wall, ejected through the gill holes on one side only. For the ''crossflow'' case the air, after impinging on the leading-edge wall, ejected from one end of the leading-edge channel, simulating exit flow, through an airfoil tip. In this flow arrangement, all side channel valves were closed and the only way out for the cooling air after impingement was through the end of the leading-edge channel. The four jets upstream of the middle jet (spent air) formed a crossflow that severely affected the impingement heat transfer coefficient. Two jet plate positions corresponding to two Z/d_{jet} values of 5.2 and 6.2 were tested for all geometries. The smaller Z/d_{jet} (5.2) consistently produced higher heat transfer coefficients for the nominal and one-sided cases. For the crossflow case, however, the smaller Z/d_{jet} (5.2) produced a slightly lower heat transfer coefficient for all geometries except the sandpaper-roughened wall. Those cases are discussed next. Experimental uncertainties in heat transfer coefficient and jet Reynolds number, following the method of Kline and McClintock [30] were determined to be 6 and 1.5 percent, respectively.

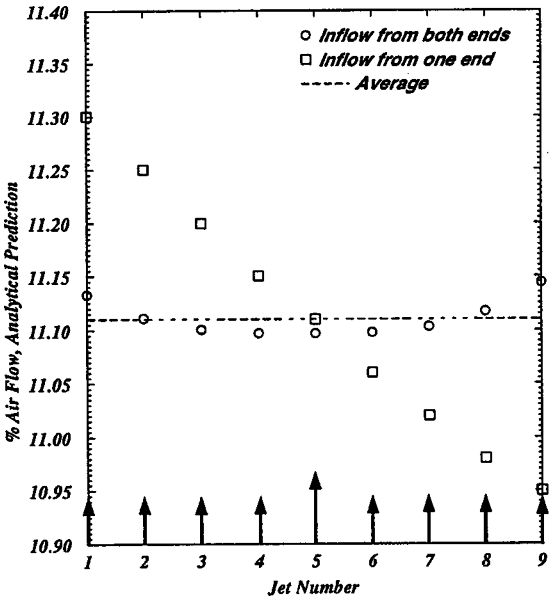

Fig. 4 Percentage of air-flow rate through each impingement hole for the two inflow arrangements

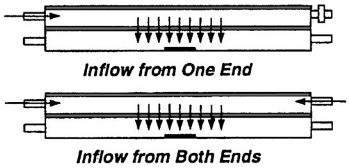

a) Inflow

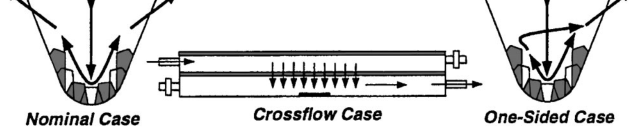

b) Outflow

Fig. 3 ***a)*** **Inflow and** ***b)*** **outflow arrangements**

Geometry 1. Impingement on a smooth leading-edge wall, shown in Fig. 2*(a)*, was tested in this baseline geometry. Figures 5 and 6 show Nusselt number versus jet Reynolds number for air entering the supply channel from one and both ends, respectively. The nominal and one-sided outflow cases produced almost the same level of heat transfer coefficients, indicating that impingement action is the dominant phenomenon and the manner in which the cooling air departs the target surface does not play a significant role. For the inflow from one end (Fig. 5), the results of one-sided case were slightly higher than those of nominal flow, while for inflow from both ends, the trend was reversed. The crossflow cases, in all geometries tested, produced the lowest heat transfer coefficients, indicating that the crossflow generated by the four upstream jets was strong enough to deflect the fifth jet and reduce its impingement effectiveness. Figure 5 also shows an increase of about 4 percent in Nusselt number in the nominal flow case when the jet plate is brought close to the target wall and Z/d_{jet} decreases from 6.2 to 5.2. The same trend is observed for the one-sided exit flow and the crossflow cases. One data point, corresponding to a jet Reynolds number of 10,000, from Akella and Han [29] is also shown in Fig. 5. Their investigation dealt with impingement on a smooth flat surface of a channel in stationary as well as orthogonally rotating modes. The value shown was at their highest jet Reynolds and the present data seem to extrapolate well to that data point. A data point from Chupp et al. [18] who measured impingement heat transfer on a smooth semi-circular surface, again for their highest jet Reynolds number of 10,000, falls right on the data point of Akella and Han. In Fig. 7, where the two inflow arrangements are compared, it is seen that Nusselt numbers increase slightly when the supply channel is fed

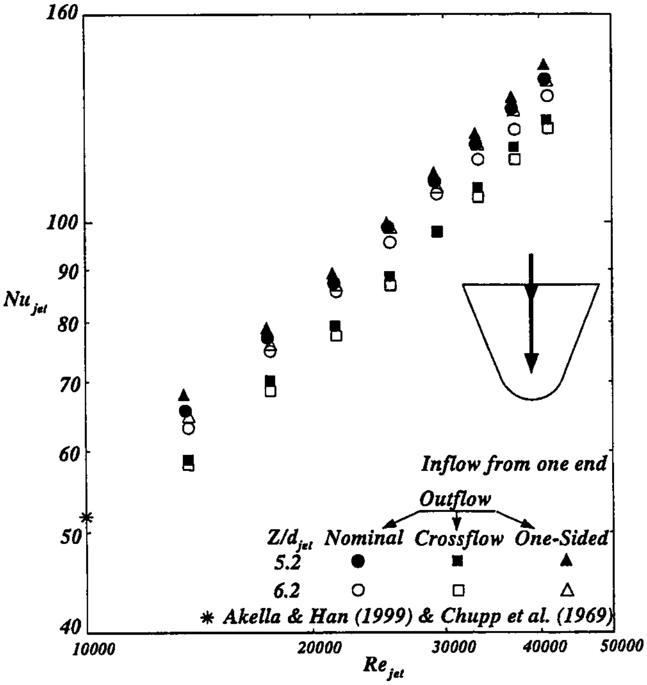

Fig. 5 Nusselt number variation with Reynolds number for geometry 1 (smooth wall), flow from one end

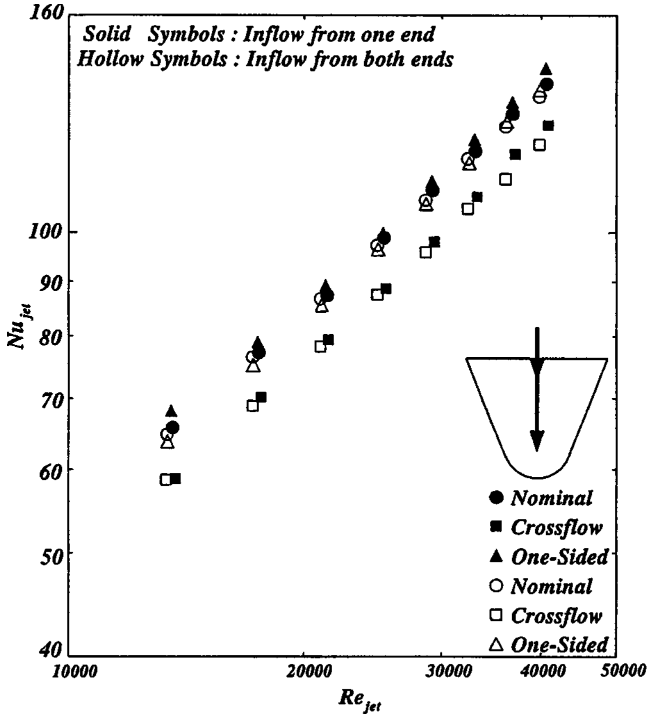

Fig. 7 A comparison between the results of inflow from one end and inflow from both ends for geometry 1 (smooth wall), $Z/d_{jet}=5.2$

from one end for the nominal and one-sided outflow cases. This behavior is due to a slightly higher air mass flow through the fifth impingement hole seen in Fig. 4. Almost no difference was measured for the crossflow case whether the supply channel was fed from one end or both ends.

Geometry 2. The leading-edge wall was roughened and looked like the surface of a very coarse file. The roughness elements were in the shape of very small pointed-bumps (16 per cm^2) with an average height of 0.5 mm. This is a scaled dimension that corresponds to bumps approximately 0.025 mm high in an actual airfoil. The roughening process was done manually and the calculated increase in heat transfer area was about 4 percent compared to the baseline surface. A total of twelve tests were run

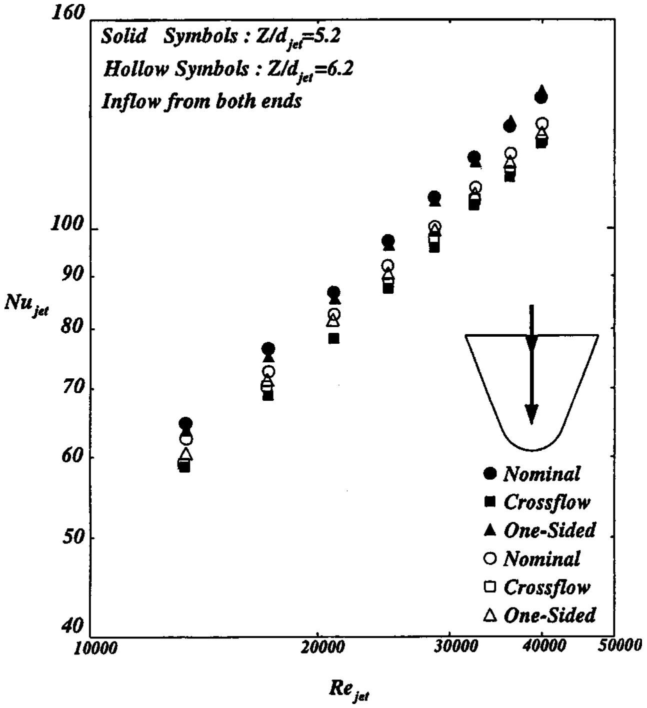

Fig. 6 Nusselt number variation with Reynolds number for geometry 1 (smooth wall), flow from both ends

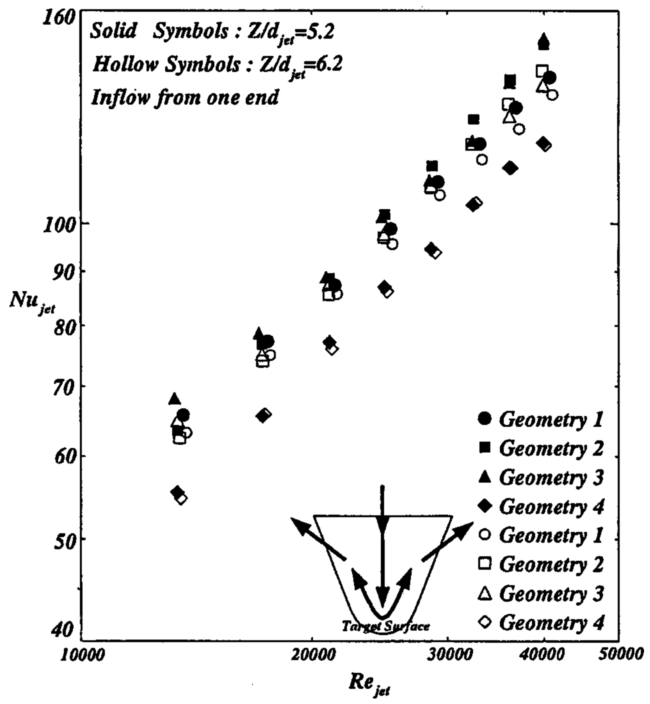

Fig. 8 A comparison between the heat transfer results of all four target wall geometries in nominal flow arrangement

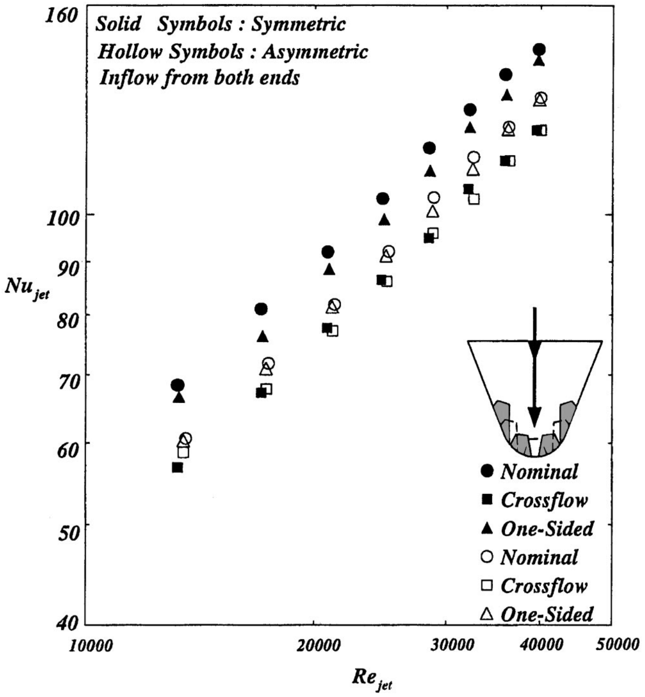

Fig. 9 A comparison between the heat transfer results of symmetric and asymmetric impingement on geometry 3 (cones), $Z/d_{\mathrm{jet}}=5.2$

for this geometry and the results are shown in Figs. 9–11, along with the results of other geometries to be discussed next. A comparison of the nominal cases of geometry 2 shows the maximum increases in the Nusselt number of about 12 and 10.5 percent for $\mathrm{Re}_{\mathrm{jet}}=40{,}000$ and for $Z/d_{\mathrm{jet}}=6.2$ and 5.2, respectively, compared to those of geometry 1. Figures 12–14 include the contribution of

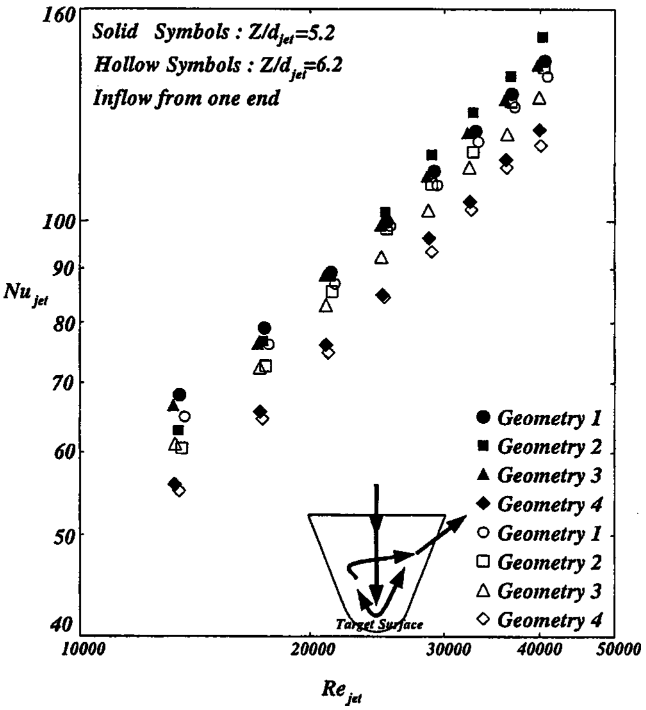

Fig. 10 A comparison between the heat transfer results of all four target wall geometries in one-sided outflow arrangement

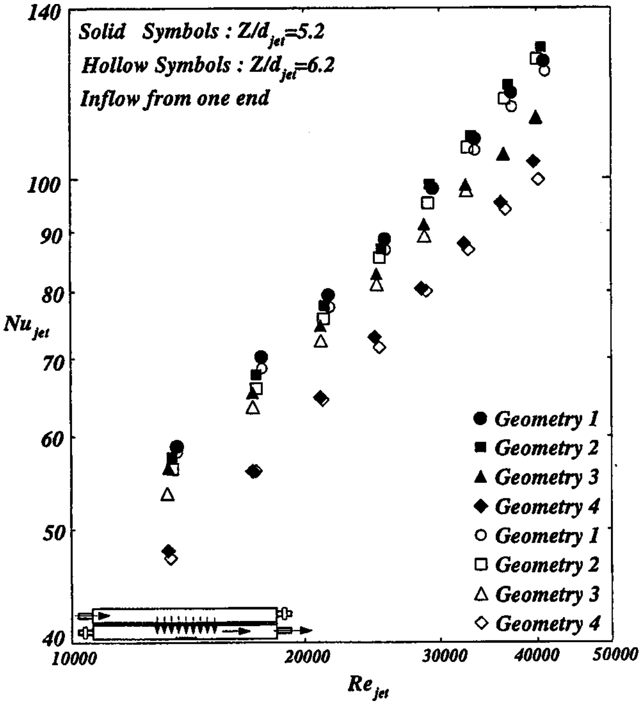

Fig. 11 A comparison between the heat transfer results of all four target wall geometries in crossflow arrangement

the increased area in the overall heat transfer from the target surface ($\mathrm{Nu}_{\mathrm{jet}}[A_{HT}/A_{\mathrm{base}}]$) in the data reported in Figs. 8, 10, and 11. When the area increase for geometry *2* is included in these comparisons (base area used), these percentages increase to 17.2 and 15 percent, respectively.

Geometry 3. The target wall for this geometry was roughened with conical bumps (Fig. 2(*c*)). This configuration consisted

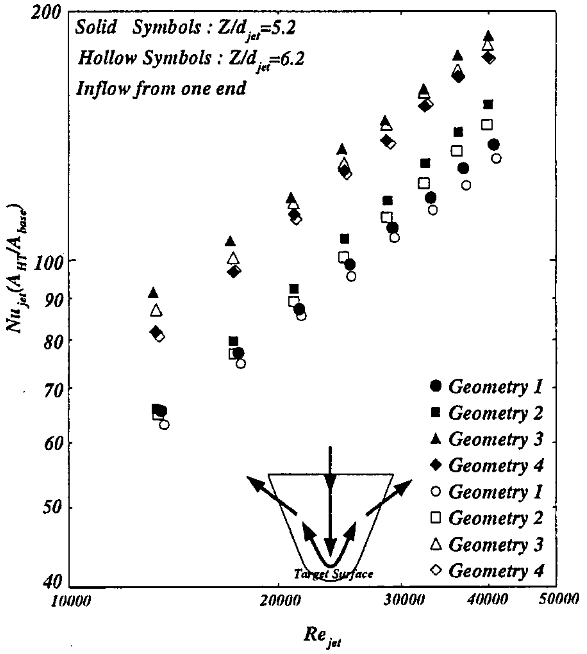

Fig. 12 A comparison between the area-augmented heat transfer results of all four target wall geometries in nominal outflow arrangement

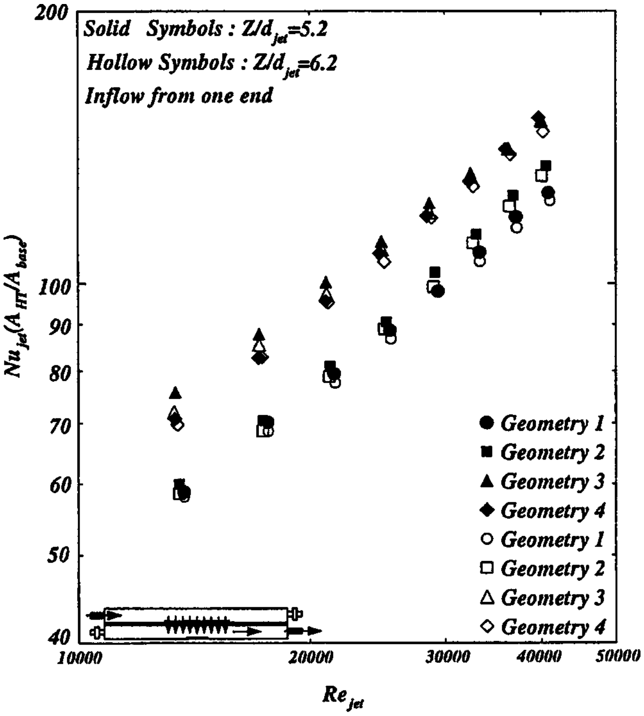

Fig. 13 A comparison between the area-augmented heat transfer results of all four target wall geometries in crossflow arrangement

of a total of seven conical bumps made up in two staggered rows of four and three cones each. Compared to the baseline geometry, the total wetted heat transfer area on the middle brass piece was increased by about 34 percent. A comparison of the nominal cases of geometries 1 and 3, presented in Fig. 8, shows for geometry 3 a maximum increase in the Nusselt number of about 7.5 percent for $\mathrm{Re}_{\mathrm{jet}}$=40,000 and Z/d_{jet}=6.2, and a maximum increase in the Nusselt number of about 7.8 percent for $\mathrm{Re}_{\mathrm{jet}}$=40,000 and Z/d_{jet}=5.2 as compared to geometry 1 (baseline). However, when the increased area for geometry 3 is included in these comparisons, the percentages increase to 44 and 44.7 percent (Fig. 12), respectively. These are the largest percentage increases for all geometries. A total of 17 tests were run for this geometry. The additional tests were the results of investigating symmetric and asymmetric impingement on the middle brass piece. In tests called ''Symmetric,'' the middle jet impinged at the geometric center of the middle brass piece in between the two rows of cones while the ''Asymmetric'' tests represent the impingement on the row of four cones (Fig. 2*(c)*). Testing of latter position was accomplished by offsetting the jet plate to the right. Therefore, test runs were conducted for all outflow cases (nominal, crossflow, and one-sided), both Z/d_{jet} values (5.2 and 6.2), both inflow arrangements, and the symmetric and asymmetric impingement arrangements. For consistency, only the symmetric results for geometry 3 are compared with the other geometries in Figs. 8, 10, and 11. Figure 9 shows that symmetric impingement (between the two rows of cones) is much more effective than asymmetric impingement for the nominal as well as the one-sided case. For the crossflow case, however, the asymmetric impingement shows almost the same level of heat transfer coefficient. This behavior further proves the strong effect of crossflow in deflecting the impinging jets and reducing their effectiveness in heat removal from the target surface, regardless of their impingement position on the target surface.

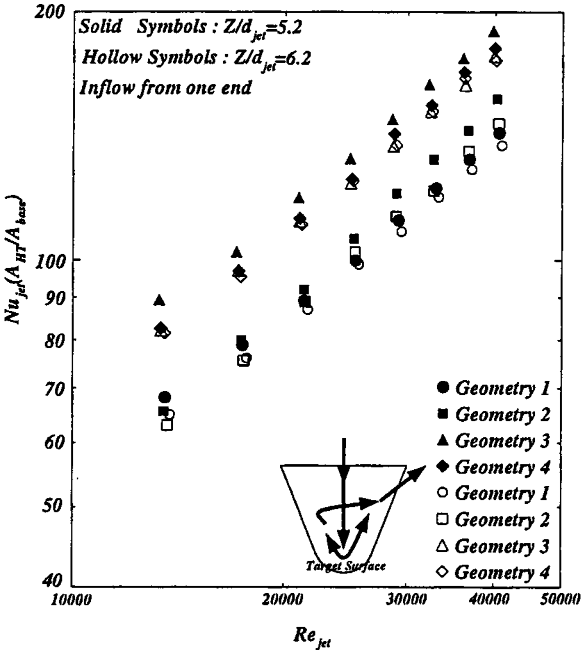

Fig. 14 A comparison between the area-augmented heat transfer results of all four target wall geometries in one-sided outflow arrangement

Geometry 4. The target wall for this geometry was roughened with longitudinal ribs (Fig. 2(*d*)). There were three ribs along each brass piece one on the leading-edge nose and one on each side, parallel to the middle one. The total heat transfer area on the middle brass piece measured to be 47.3 percent higher than that of the baseline geometry. A total of twelve tests were run for this geometry to cover the three outflow cases (nominal, crossflow, and one-sided), the two Z/d_{jet} values of 5.2 and 6.2, and the two inflow arrangements. Test results of geometry 4 are also compared with those of other geometries in Figs. 8, 10, and 11. Geometry 4 did not show much sensitivity to the manner in which the supply channel was fed; thus, the results of inflow from both ends are not shown due to space limitations. Again, the smaller Z/d_{jet} (5.2) produced higher heat transfer coefficients than the larger Z/d_{jet} (6.2) for all cases. However, on a percentage basis it was not nearly as high as in geometry *3*. For example, at $\mathrm{Re}_{\mathrm{jet}}$=25,000 and nominal outflow case, the increase in heat transfer coefficient from Z/d_{jet}=6.2 to 5.2 for this geometry was about 3.5 percent while this increase for geometry 3 was about 6.2 percent. As geometry changes from 1 to 4, Nusselt number decreases by about 5, 15, and 8 percent for the nominal, crossflow, and one-sided cases, respectively, all for $\mathrm{Re}_{\mathrm{jet}}$=40,000 and Z/d_{jet}=6.2, and decreases by about 10, 15, and 11.5 percent for the nominal, crossflow, and one-sided cases, respectively, all for $\mathrm{Re}_{\mathrm{jet}}$=40,000 and Z/d_{jet}=5.2. It appears that cooling air did not come in good contact with all available heat transfer areas around the ribs, particularly the outer most surfaces. When the total wetted area for geometry 4 is used in comparison, the percentages change to increases in the amounts of 40, 24, and 35 percent, and 32, 25, and 30 percent, respectively. In spite of its higher overall heat transfer area, geometry 4 was not as effective as geometry 3.

Conclusion

Without the inclusion of the heat transfer area increase, the conical bumps and the sandpaper roughness cases produced comparable results. However, when the contribution of the increased area in the overall heat transfer is taken into consideration, geometry 3 for all inflow and outflow cases as well as the two Z/d_{jet} values proved to be the most effective geometry. Also an overall increase of about 40 percent in heat transfer can be accomplished by roughening the leading-edge wall with conical bumps The contribution of the heat transfer coefficient to this enhancement is about 8 percent while the balance is attributed to the increase in the heat transfer area.

Acknowledgments

The authors wish to thank the US Army Aviation Applied Technology Directorate and Mr. Stephen P. Kinney for their involvement and support during this investigation.

Nomenclature

A_{base} = leading-edge base area for the smooth case
A_{hole} = total area of all nine crossover holes
A_{HT} = total heat transfer area including the surface roughness
AR = cooling channel aspect ratio
AR_{rib} = rib aspect ratio
d_{jet} = jet diameter
D_h = cooling channel hydraulic diameter
e = roughness height
h = average heat transfer coefficient on the leading-edge wall $= [(vi/A_{HT}) - q_{\text{loss}}]/(T_s - T_{\text{jet}})$
i = current through the foil heater on the middle brass piece
k = air thermal conductivity
m = air total mass flow rate through all nine crossover holes
Nu_{jet} = average Nusselt number based on the jet diameter $= hd_{\text{jet}}/k$
P = channel perimeter without ribs
q_{loss} = heat losses from the middle brass piece to the ambient by conduction and convection as well as the heat losses by radiation to the unheated walls
R_{nose} = channel radius at the leading edge
Re_{jet} = Reynolds number based on the jet diameter $= (\rho U_{\text{jet}} d_{\text{jet}}/\mu)$
S = rib pitch
T_{jet} = air jet temperature
T_s = surface temperature
U_{jet} = jet mean velocity $= m/\rho A_{\text{hole}}$
v = voltage drop across the foil heater on the middle brass piece
Z = jet place distance to the target surface (Fig. 1)
α = rib angle of attack
μ = air dynamic viscosity at jet temperature
ρ = air density at jet temperature and pressure

References

[1] Burggraf, F., 1970, ‘‘Experimental Heat Transfer and Pressure Drop With Two Dimensional Turbulence Promoters Applied to Two Opposite Walls of a Square Tube,’’ *Augmentation of Convective Heat and Mass Transfer*, A. E. Bergles and R. L. Webb, eds., ASME, pp. 70–79.
[2] Chandra, P. R., and Han, J. C., 1989, ‘‘Pressure Drop and Mass Transfer in Two-Pass Ribbed Channels,’’ J. Thermophys. Heat Transfer, **3**, No. 3, pp. 315–319.
[3] El-Husayni, H. A., Taslim, M. E., and Kercher, D. M., 1994, ‘‘An Experimental Investigation of Heat Transfer Coefficients in a Spanwise Rotating Channel With Two Opposite Rib-Roughened Walls,’’ ASME J. Turbomach., **113**, pp. 75–82.
[4] Han, J. C., 1984, ‘‘Heat Transfer and Friction in Channels With Two Opposite Rib-Roughened Walls,’’ ASME J. Heat Transfer, **106**, pp. 774–781.
[5] Han, J. C., Glicksman, L. R., and Rohsenow, W. M., 1978 ‘‘An Investigation of Heat Transfer and Friction for Rib Roughened Surfaces,’’ Int. J. Heat Mass Transf., **21**, pp. 1143–1156.
[6] Han, J. C., Park, J. S., and Lei, C. K., 1985, ‘‘Heat Transfer Enhancement in Channels With Turbulence Promoters,’’ ASME J. Eng. Gas Turbines Power, **107**, pp. 628–635.
[7] Han, J. C., Zhang, Y. M., and Lee, C. P., 1992, ‘‘Influence of Surface Heat Flux Ratio on Heat Transfer Augmentation in Square Channels With Parallel, Crossed, and V-Shaped Angled Ribs,’’ ASME J. Turbomach., **114**, pp. 872–880.
[8] Metzger, D. E., Vedula, R. P., and Breen, D. D., 1987, ’’The Effect of Rib Angle and Length on Convection Heat Transfer in Rib-Roughened Triangular Ducts,’’ *Proc. ASME–JSME Thermal Engineering Joint Conference*, Vol. 3, pp. 327–333.
[9] Metzger, D. E, Chyu, M. K. and Bunker, R. S., 1988, ‘‘7th Contribution of On-Rib Heat Transfer Coefficients to Total Heat Transfer From Rib-Roughened Surfaces,’’ in: *Transport Phenomena in Rotating Machinery*, J. H. Kim, ed., Hemisphere Publishing.
[10] Metzger, D. E., Fan, C. S., and Yu, Y., 1990, ‘‘Effects of Rib Angle and Orientation on Local Heat Transfer in Square Channels With Angled Roughness Ribs,’’ in: *Compact Heat Exchangers: A Festschrift for A. L. London*, Hemisphere Publishing, pp. 151–167.
[11] Taslim, M. E., and Spring, S. D., 1988, ‘‘An Experimental Investigation of Heat Transfer Coefficients and Friction Factors in Passages of Different Aspect Ratios Roughened With 45 deg Turbulators,’’ *Proc. ASME National Heat Conference*, Houston, TX.
[12] Taslim, M. E., and Spring, S. D., 1988, ‘‘Experimental Heat Transfer and Friction Factors in Turbulated Cooling Passages of Different Aspect Ratios, Where Turbulators Are Staggered,’’ Paper No. AIAA-88-3014.
[13] Taslim, M. E., Bondi, L. A., and Kercher, D. M., 1991, ‘‘An Experimental Investigation of Heat Transfer in an Orthogonally Rotating Channel Roughened 45 Degree Criss-Cross Ribs on Two Opposite Walls,’’ ASME J. Turbomach., **113**, pp. 346–353.
[14] Taslim, M. E., Rahman, A., and Spring, S. D., 1991, ‘‘An Experimental Investigation of Heat Transfer Coefficients in a Spanwise Rotating Channel With Two Opposite Rib-Roughened Walls,’’ ASME J. Turbomach., **113**, pp. 75–82.
[15] Taslim, M. E., and Spring, S. D., 1994, ‘‘Effects Turbulator Profile and Spacing Have on Heat Transfer and Friction Factors in a Channel,’’ J. Thermophys. Heat Transfer, **8**, No. 3, pp. 555–562.
[16] Webb, R. L., Eckert, E. R. G., and Goldstein, R. J., 1971, ‘‘Heat Transfer and Friction in Tubes With Repeated-Rib-Roughness,’’ Int. J. Heat Mass Transf., **14**, pp. 601–617.
[17] Zhang, Y. M., Gu, W. Z., and Han, J. C., 1994, ‘‘Heat Transfer and Friction in Rectangular Channels With Ribbed or Ribbed-Grooved Walls,’’ ASME J. Heat Transfer, **116**, pp. 58–65.
[18] Chupp, R. E., Helms, H. E., McFadden, P. W., and Brown, T. R., 1969, ‘‘Evaluation of Internal Heat Transfer Coefficients for Impingement Cooled Turbine Blades,’’ J. Aircr., **6**, No. 1, pp. 203–208.
[19] Metzger, D. E., Yamashita, T., and Jenkins, C. W., 1969, ‘‘Impingement Cooling of Concave Surfaces With Lines of Circular Air Jets,’’ ASME J. Eng. Power, **93**, pp. 149–155.
[20] Kercher, D. M., and Tabakoff, W., 1970, ‘‘Heat Transfer by a Square Array of Round Air Jets Impinging Perpendicular to a Flat Surface Including the Effect of Spent Air,’’ ASME J. Eng. Power, **92**, No. 1, pp. 73–82.
[21] Florschuetz, L. W., Berry, R. A., and Metzger, D. E., 1980, ‘‘Periodic Streamwise Variation of Heat Transfer Coefficients for Inline and Staggered of Circular Jets With Crossflow of Spent Air,’’ ASME J. Heat Transfer, **102**, pp. 132–137.
[22] Florschuetz, L. W., Truman, C. R., and Metzger, D. E., 1981, ‘‘Streamwise Flow and Heat Transfer Distribution for Jet Impingement With Crossflow,’’ ASME J. Heat Transfer, **103**, No. 2, pp. 337–342.
[23] Florschuetz, L. W., Metzger, D. E., Su, C. C., Isoda, Y., and Tseng, H. H., 1984, ‘‘Heat Transfer Characteristics for Jet Arrays Impingement With Initial Crossflow,’’ ASME J. Heat Transfer, **106**, pp. 34–41.
[24] Bunker, R. S., and Metzger, D. E., 1990, ‘‘Local Heat Transfer in Internally Cooled Turbine Airfoil Leading Edge Regions: Part II—Impingement Cooling With Film Coolant Extraction,’’ ASME J. Turbomach., **112**, No. 3, pp. 459–466.
[25] Metzger, D. E., and Bunker, R. S., 1990, ‘‘Local Heat Transfer in Internally Cooled Turbine Airfoil Leading Edge Regions: Part I—Impingement Cooling Without Film Coolant Extraction,’’ ASME J. Turbomach., **112**, pp. 451–458.
[26] Van Treuren, K. W., Wang, Z., Ireland, P. T., and Jones, T. V., 1994, ‘‘Detailed Measurements of Local Heat Transfer Coefficient and Adiabatic Wall Temperature Beneath an Array of Impinging Jets,’’ ASME J. Turbomach., **116**, pp. 269–374.
[27] Chang, H., Zhang, D., and Huang, T., 1997, ‘‘Impingement Heat Transfer From Rib-Roughened Surface Within Arrays of Circular Jet: The Effect of the Relative Position of the Jet Hole to the Ribs,’’ ASME Paper No. 97-GT-331.
[28] Huang, Y., Ekkad, S. V., and Han, J. C., 1998, ‘‘Detailed Heat Transfer Distributions Under an Array of Orthogonal Impinging Jets,’’ J. Thermophys. Heat Transfer, **12**, No. 1, pp. 73–79.
[29] Akella, K. V., and Han, J. C., 1999, ‘‘Impingement Cooling in Rotating Two-Pass Rectangular Channels With Ribbed Walls,’’ J. Thermophys. Heat Transfer, **13**, No. 3, pp. 364–371.
[30] Kline, S. J., and McClintock, F. A., 1953, ‘‘Describing Uncertainty in Single-Sample Experiments,’’ Mech. Eng., **75**, Jan., pp. 3–8.

Heat Transfer and Flow Characteristics of an Engine Representative Impingement Cooling System

Changmin Son
e-mail: changmin.son@eng.ox.ac.uk

David Gillespie
e-mail: david.gillespie@eng.ox.ac.uk

Peter Ireland
e-mail: peter.ireland@eng.ox.ac.uk

Department of Engineering Science,
University of Oxford,
Oxford, OX1 3PJ, United Kingdom

Geoffrey M. Dailey
Rolls-Royce plc,
Derby, DE24 8BJ, United Kingdom
e-mail: geoffrey.dailey@rolls-royce.com

A study of a large-scale model of an engine representative impingement cooling system has been performed. A series of tests were carried out to characterize the behavior of the system fully. These included cold flow diagnostic tests to determine the pressure loss and the static pressure distribution, and flow visualization to assess surface shear. The surface shear stress pattern provided by multiple stripes of colored paint applied to the target surface yielded important information on the near-wall flow features far from the jet axis. The row solved flow and pressure distributions are compared to industry standard predictions. Heat transfer tests using the transient liquid crystal technique were also conducted using coatings comprised of a mixture of three thermochromic liquid crystals. Analysis of the thermochromic liquid crystal data was enhanced by recent developments in image processing. In addition, an energy balance analysis of signals from fast-response thermocouples for air temperature measurement was applied to verify the levels of heat transfer coefficients on surfaces not coated with the temperature-sensitive liquid crystal. [DOI: 10.1115/1.1328087]

Keywords: Impingement Cooling, Transient Heat Transfer, Liquid Crystal, Energy Balance

Introduction

A modern turbine internal cooling system normally employs an optimized combination of several strategies such as film, impingement, and multi-pass passage cooling, as shown in Fig. 1. Several aspects of impingement cooling are attractive to the engine designer. It is a more robust design than film-cooling, in general having larger holes that have no surface in close proximity to the external flow, and thus is more suitable for regions prone to external deposition. It is easier to achieve uniformity of heat transfer when compared to the multi-pass systems: Many impingement holes may be fed from a single plenum, rather than from a duct of decreasing cooling potential.

Because of the wide range of applications of impingement cooling, there have been numerous combinations of different geometric, aerodynamic, and thermodynamic parameters employed. Impingement geometry is generally specified using: (1) the ratio of impingement hole diameter to the thickness of the impingement plate, l/d; (2) the ratio of the channel height to hole diameter, z/d; (3 & 4) the nondimensional orthogonal spacing of the impingement hole array, x_h/d and y_h/d. The flow parameters are the Reynolds number of each jet, Re_j, the ratio of the crossflow mass velocity to the impinging flow mass velocity, G_c/G_j, and the Prandtl number. The Mach number is usually low enough to be of little concern, and this is the case in the current study. Additionally, the nozzle geometry and the shape of jet hole significantly affect the cooling characteristics.

Many efforts have been made to produce a comprehensive correlation that covers the full range of geometric, fluid, and thermal parameters. A two-dimensional array of jets has a three-dimensional flow pattern near the target surface and between the jets where vortical structures form. Kercher and Tabakoff [1] considered the spent air in an array of round impinging jets and proposed a heat transfer correlation based on graphical evaluation of appropriate constants. Florschuetz et al. [2,3] conducted an extensive study of several in-line and staggered impingement arrays. By approximating the discrete impinging jets as a continuous injection process, they produced a simple analytical model of flow field in the channel. The flow field model is widely used throughout industry to calculate Reynolds number of each jet, G_c/G_j, and the pressure drop through the channel. Obot and Trabold [4] studied the effect of crossflow in arrays of circular impinging jets and introduced a correlation employing the concepts of minimum, intermediate and maximum crossflow in defining the exit of the spent flow.

Lucas et al. [5] and Van Treuren et al. [6] studied the contribution of the thermal boundary conditions to the overall heat transfer coefficient at the target plate by controlling the impingement plate temperature. The term ''jet effectiveness'' was used to express the influence of the impingement plate temperature on the target plate adiabatic wall temperature. Lucas et al. [5] reported that, for a

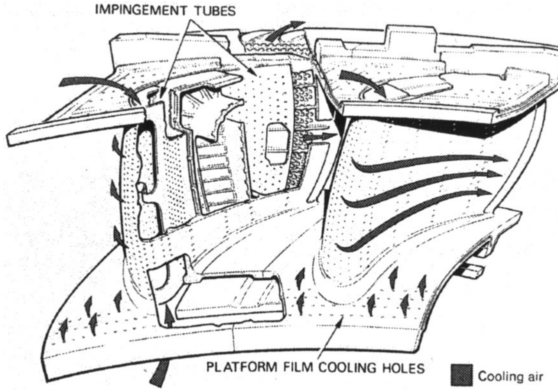

Fig. 1 Nozzle guide vane cooling scheme [15]

Contributed by the International Gas Turbine Institute and presented at the 45th International Gas Turbine and Aeroengine Congress and Exhibition, Munich, Germany, May 8–11, 2000. Manuscript received by the International Gas Turbine Institute February 2000. Paper No. 2000-GT-219. Review Chair: D. Ballal.

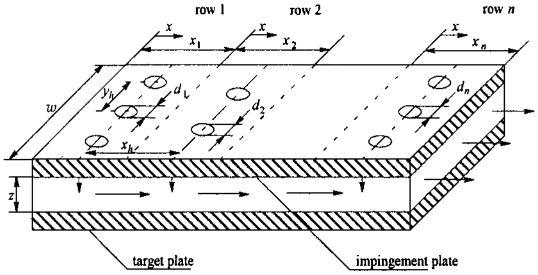

Fig. 2 Impingement cooling system with staggered hole array and nomenclature

single confined jet, the temperature of the impingement plate had a significant effect on the target plate heat transfer for $z/d = 2–3$. Van Treuren et al. [7] conducted a series of experiments for in-line and staggered impingement arrays for $z/d=1$, 2, and 4 with initial crossflow. They accurately controlled the temperature of the impingement plate. In the range of $\mathrm{Re}\,j=10{,}000–40{,}000$, they concluded that the results at $z/d=2$ showed most uniform heat transfer throughout the array. The recirculation in the impingement channel provides a mechanism that thermally couples the impingement plate temperature to the target surface. This coupling influences the adiabatic wall temperature and hence the local heat transfer. Gillespie et al. [8] investigated an integrally cast impingement cooling geometry, in which the impingement air is vented through film cooling holes. There is no existing correlation that covers the entire range of flow and geometric parameters.

The present study investigates the heat transfer and flow characteristics of an existing turbine internal cooling system of one of the family of Rolls Royce engines, and a similar geometry with a uniform array of impingement holes. The particular impingement geometries are in the range $xh/d=3.0–4.8$, $yh/d=3.75–6.0$, and $z/d=1.875–3.0$. A schematic diagram is shown in Fig. 2. The two systems have a staggered array of uniform and nonuniform impingement holes arranged in five columns (spanwise) and six rows (streamwise). The spent air exits from the streamwise downstream edge of the impingement channel.

Experimental Techniques

Theory and Data Reduction. Heat transfer measurements in impingement systems are difficult for a number of reasons. The local heat transfer coefficient changes by a large factor from a peak near the stagnation point beneath the jet to significantly lower values away from the jet in the channel between the impingement and target plates. One difficulty specific to the transient method is the problem of quickly establishing the flow at a temperature different from the starting temperature. In a typical impingement array, the area ratio between the inlet plenum and the total cross-sectional area of the jets means that the flow velocity in the plenum is very low (typically 0.1 m/s). The flow temperature switching in these experiments is achieved using a planar heater mesh fitted across the plenum flow. The experiments start when power is switched to the mesh. Prior to this, room temperature air is drawn through the heater mesh and model to establish the flow field. As the velocity through the heater mesh is low, a step change in the power supplied does not cause the flow temperature to change as a step. The normal surface temperature response of the perspex substrate under a step change in fluid temperature is given by the familiar equation,

$$T_s=T_0+(T_g-T_0)\cdot\left[1-\exp\left(\frac{h^2t}{\rho ck}\right)\times\operatorname{erfc}\left(\frac{h\sqrt{t}}{\rho ck}\right)\right] \tag{1}$$

When the driving fluid temperature changes with a known time constant, τ, i.e., $T=T_0+(T_g-T_0)(1-e^{-t/\tau})$, the equation for the surface temperature rise becomes [9]

$$\begin{aligned}\frac{T_s-T_0}{T_g-T_0}&=1-\frac{\rho ck/h^2\tau}{(1+\rho ck/h^2\tau)}e^{h^2t/\rho ck}\times\operatorname{erfc}(h\sqrt{t}/\sqrt{\rho ck})\\&\quad-e^{-t/\tau}\frac{1}{(1+\rho ck/h^2\tau)}\\&\quad\times\left(1+\frac{\sqrt{\rho ck}}{h\sqrt{\tau}}\left(\frac{1}{\pi}\sqrt{\frac{t}{\tau}}+\frac{2}{\pi}\sum_{n=1}^{\infty}\frac{1}{n}e^{-n^2/4}\sinh n\sqrt{t/\tau}\right)\right)\end{aligned} \tag{2}$$

Equation (2) is then solved numerically for the local heat transfer coefficients from the times, $t=t_1$, t_2, and t_3, at which the surface reaches the calibrated liquid crystal temperatures. At each pixel location, the solution in h, which can minimize the rms residual of three crystals, is chosen.

Progress in the hardware used at Oxford has centered around a change in the frame-grabbing strategy. The card that digitizes the video recording is fitted to a Pentium PC and the data stored directly in computer RAM. The computer has 512 Mbytes of RAM and is capable of acquiring 500 full frames. In practice, partial frames are used to resolve typical heat transfer coefficient results accurately, and this allows more frames to be captured. In addition, not every frame is required for heat transfer data processing. A typical heat transfer test lasts 30 seconds. A time signal is captured in the each frame and used to determine the elapsed time to obtain a referenced signal intensity.

Test Rig. The schematic of the test facility is shown in Fig. 3. The mesh heater and additional plastic meshes equipped with thermocouples are fixed on separate frames and installed in recessed channels in the test plenums to minimize leakage and misalignment. Impingement and target plates are interchangeable. The inlet to the rig is atmospheric; flow is sucked through a mesh heater 210 mm upstream of the impingement plate in the inlet plenum. All of the flow enters the cooling channel through the impingement holes and exits to an exhaust plenum. The mass flow rate is measured using a BS1042 orifice meter installed in the pipe work between the exit plenum and the vacuum pump. A gate valve installed immediately upstream of the pump controls the appropriate mass flow rate for each test.

During transient heat transfer experiments, 5 pressure signals and 12 thermocouple signals are monitored using an 8 channel A/D converter card and a 32 channel multiplexer installed in a PC. The typical sampling rate is 20 Hz and approximately 1500 data points per channel are acquired in each test using National Instruments ''Labview'' software.

Surface temperature measurement was achieved using a coating of three narrow band liquid crystals (supplied by Hallcrest LCT Ltd.). These are able to record single temperature events at 30°C,

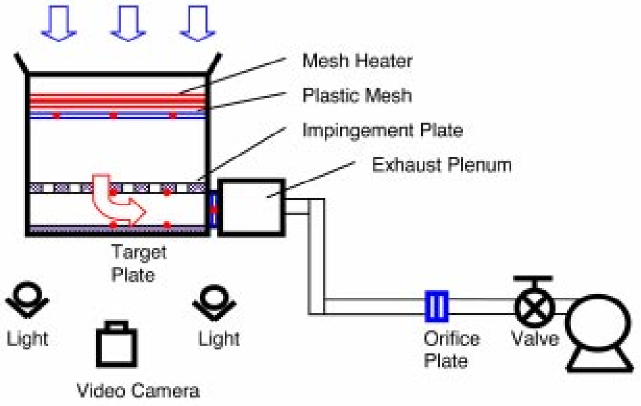

Fig. 3 Schematic of test facility

34.5°C, and 37.5°C with an estimated uncertainty of ±0.2°C. This wide range of temperatures allows heat transfer coefficient data to be obtained over the full surface in a single test. The liquid crystal coating was applied not only to the target surface, but also to the impingement plate downstream surface, where there can be considerable heat transfer. The signal of the three fast response thermocouples located in a noninvasive plastic mesh of low thermal capacity, 10 mm downstream of the mesh heater, shows temperature uniformity of heated air at the inlet plenum within 1°C.

Results and Discussion

Detailed Heat Transfer Data. Full local heat transfer coefficient distributions have been measured on the target and impingement plates using the transient liquid crystal technique. A captured image of the entire target surface is shown in Fig. 4.

The dotted rectangular area represents the selected symmetric area used in subsequent data processing. The locations of the surface thermocouples installed to monitor the temperature rise during the transient experiments are also shown in the figure. The portion of the original image taken for processing has a resolution of 60×300 pixels and the processed data were interpolated onto a 40×140 pixel grid.

The Nusselt number distributions on the smooth target plate with the uniform and nonuniform staggered impingement hole arrays are shown in Figs. 5 and 6, respectively. The difference in distribution caused by the changing hole size and reduced early crossflow is apparent. At the left-hand side of the channel, it is notable that the heat transfer footprint under each jet is approximately circular. At exit of the channel these are larger and highly distorted, the footprint of the nonuniform array at exit being both larger and less distorted than that of the uniform array. The Nusselt number distribution on the smooth target surface can be characterized by the following three zones: first, the stagnation area under each impinging hole, which includes the peak value of heat transfer; second, the wall jet where high Nusselt numbers persist; third, the mixing boundary between adjacent jets.

Figures 7 and 8 show the target plate longitudinal centerline Nusselt number distributions under uniform and nonuniform array arrays of impingement holes. The distributions are normalized by the tried and tested Dittus–Boelter correlation using the channel exit condition. In the figure, each x-direction grid line indicates the center of an impingement hole. So the displacement between the peak values of Nusselt number and the x-grid lines shows the effect of crossflow on the position of the stagnation point. Bouchez and Goldstein [10] reported that crossflow moves the position of peak heat transfer coefficient downstream and reduces its level. The stagnation values increase with increasing local Re_j for uniform array. This is not the case between holes 3 and 4 in the nonuniform array, where the hole diameter increases by 33.3 percent. This is due to the need to nondimensionalize the heat

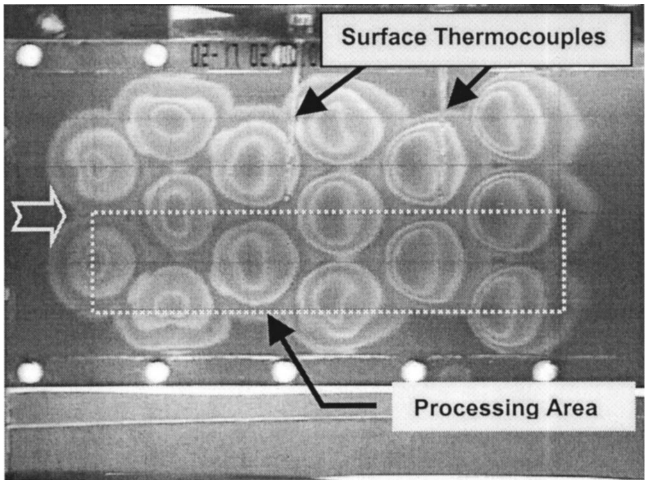

Fig. 4 Captured image and selected area for processing

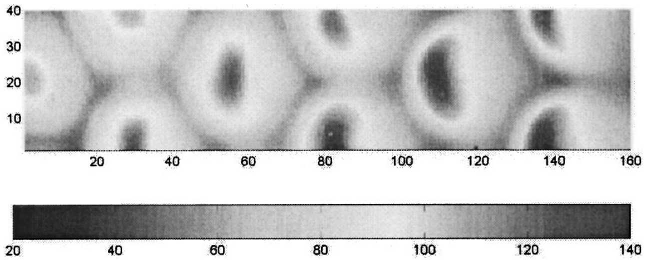

Fig. 5 Nusselt number distribution on target surface under uniform impingement array at $\mathrm{Re}_{j\,\mathrm{avg}}=28{,}870$

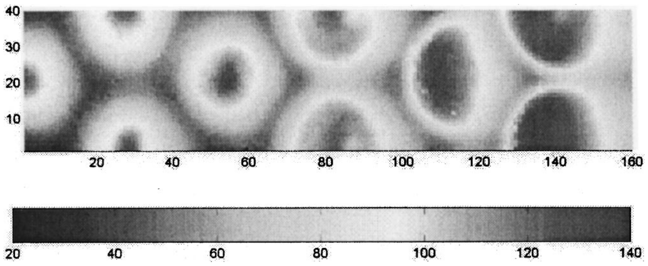

Fig. 6 Nusselt number distribution on target surface under nonuniform impingement array at $\mathrm{Re}_{j\,\mathrm{avg}}=29{,}440$

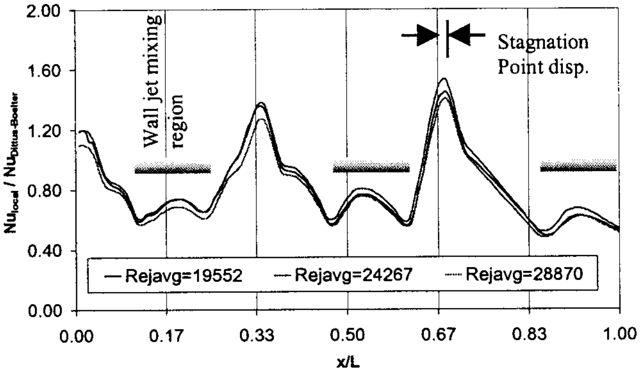

(a) Centreline of row 1, 3, and 5

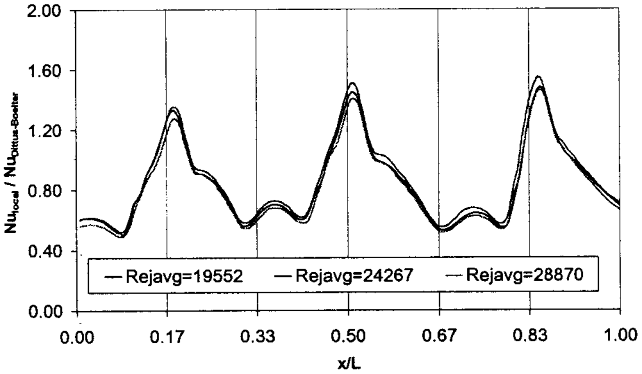

(b) Centreline of row 2, 4, and 6

Fig. 7 Variation of local Nusselt number along the jet centerlines: uniform hole array

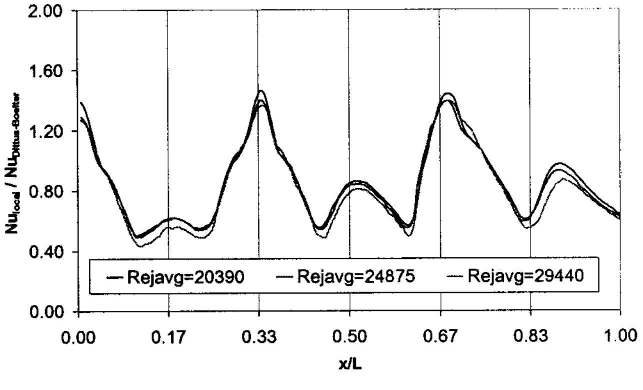

(a) Centreline of row 1, 3, and 5

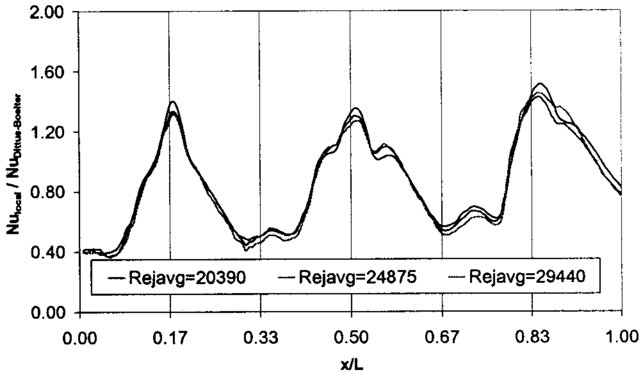

(b) Centreline of row 2, 4, and 6

Fig. 8 Variation of local Nusselt number along the jet centerlines: nonuniform hole array

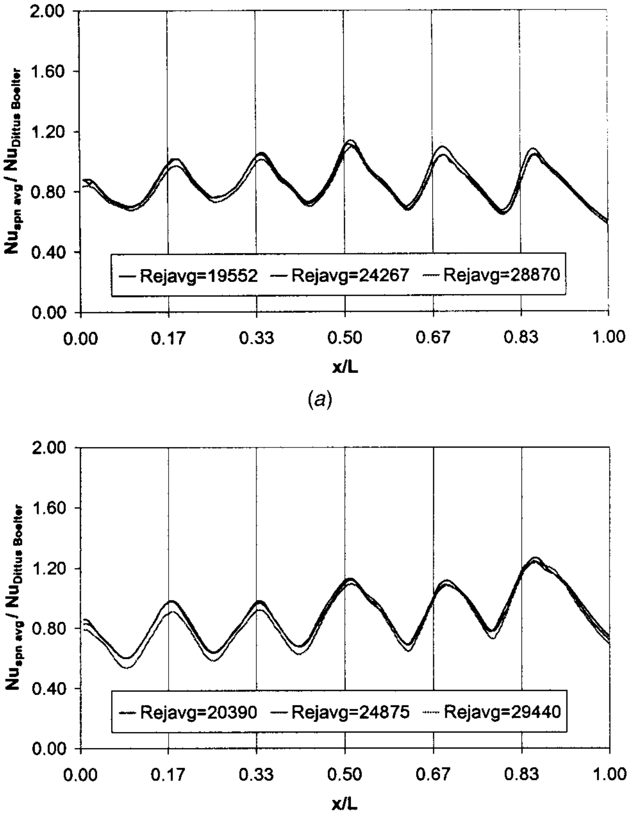

(*a*)

(*b*)

Fig. 9 Spanwise-averaged Nusselt number distribution: (*a*) uniform hole array; (*b*) nonuniform hole array

transfer coefficient by a single value of hole diameter to avoid having a discontinuity through the array. The average diameter was chosen. This has the effect of increasing the stagnation point Nusselt number level by 25 percent in the first three rows of holes, reducing the level by 3.8 percent in rows 4 and 5 and reducing the level by 21.9 percent in row 6.

The effect of crossflow can be seen in the shape of the Nusselt number distribution surrounding the stagnation region. On the upstream side of the stagnation point, the drop in Nusselt number is generally much steeper than on the downstream side, where an attenuation in this drop, at about 1–1.8 jet diameters from the jet axis is more pronounced. This attenuation is usually attributed to transition from a laminar to a turbulent wall jet on the target surface. The sharp drop in Nusselt number on the upstream side of the jet may be attributed to rapidly decelerating flow in these regions.

Compared with the high performance region of the stagnation area, the Nusselt number in the mixing boundary area has levels of order 30–50 percent of the peak heat transfer coefficients. Gardon and Akfirat [11] observed that secondary peaks in heat transfer rate occur midway between impingement jets where the walls jets meet and interact. Koopman and Sparrow [12] explained the higher level of heat transfer of multiple jet is due to the action of adjacent jets in inhibiting spanwise dispersion. In Figs. 7 and 8 it is clear that the secondary peak in this region is deflected much farther downstream than the stagnation point in the presence of crossflow.

Taking the high resolution data from the liquid crystal images, it is possible to produce spanwise-averaged Nusselt number distributions, shown in Fig. 9. For the uniform array, the distribution is reasonably uniform through the entire array, compared to the nonuniform array, where the trend in average heat transfer coefficient is to increase moving toward the exit of the array. This trend is caused by the increasing hole diameter of the nonuniform array. It is not initially obvious why this should be the case, as in each case the Nusselt number distributions at the stagnation point show an upward trend through the array. If we, however, consider the shape of the footprint surrounding each jet, the effect of additional crossflow is to steepen the drop in Nusselt number. Looking at the uniform array (Fig. 8(*a*)), in the first row the Nusselt number drops to 70 percent of the stagnation point level 1.87*d* downstream of the hole. At the third row, while the stagnation point Nusselt number has risen by 15.9 percent, 70 percent of this level occurs at an average of 1.37*d* from the stagnation point. At the fifth row, the stagnation point Nusselt number is 28.0 percent higher than the level in row 1, but 70 percent of this level now lies an average of 1.00*d* from the stagnation point. Remembering that a symmetric jet profile covers a linearly increasing area moving away from the jet axis (as each point lies on a circumference of increasing radius), the coefficient region toward the jet axis can counteract the increasing Nusselt number at the stagnation point. In the case of the uniform array tested, this happens to produce an approximately uniform variation through the array.

In the nonuniform array the hole size increases through the array, and the crossflow that degrades the jet footprint in the way described above is not as strong; see Fig. 15. This is clear from the nearly circular patterns seen under rows 1–3 in Fig. 8. The region of high heat transfer coefficient is reduced in the first three rows as the holes are 25 percent smaller than in the uniform array. The drop in Nusselt number to 70 percent of its value at the stagnation point occurs at approximately 1.6*d*. Even at row 5 this value occurs at an average 1.35*d* from the jet axis; however, here the jet diameter is close to that of the uniform array (cf. 1.00*d*) in the uniform array. The spanwise-averaged values of Nusselt number therefore show an increasing trend moving through the array.

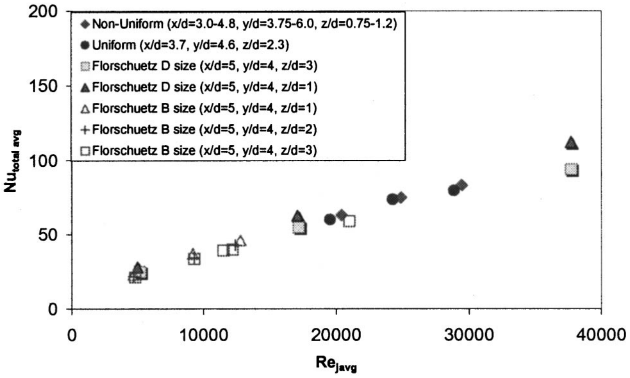

Fig. 10 Comparison of total average Nusselt number

In fact the total average Nusselt number for the two arrays turns out to be nearly the same, and the values are shown in Fig. 10. Data from Florschuetz et al. [3] for a similar hole configuration are also shown in the figure for comparison to the present experimental data. While there are no data in the $Re_{j\ avg}$ range tested, Florschuetz' data lie on either side of these tests. The experimental data appear to be very well matched to the Florschuetz data.

The uncertainty in values of h measured using the transient method employed above was calculated and reported in detail by Son et al. [13]. The total uncertainty is calculated as 7.2 percent.

Heat Flux Measurements. The validity of the assumption of one-dimensional conduction to a semi-infinite substrate, and an unchanging heat transfer coefficient, used to solve the Fourier equation can be investigated by the considering the local heat flux at the model surface. A typical comparison between the measured initial temperature and gas inlet temperature and the adiabatic wall temperature before and after heating the flow is shown in Fig. 11. The thermocouple analyzed was positioned at $x/L=0.42$ and $y/w=0.5$. At this position the heat transfer is influenced by flow from the fourth row of holes and the upstream crossflow. Any upstream wall temperature effect on the local driving gas temperature should be apparent at this position. The local heat flux can be determined numerically from the time-temperature history at a local surface thermocouple using an algorithm given in Schultz and Jones [14]. The constant slope of the locus of heat flux with temperature indicates an unchanging heat transfer coefficient. Notably this is unchanged when heating or cooling the substrate. By extrapolation, the temperatures at which there would be zero heat flux to the wall are found. In the case of heating this adiabatic wall temperature is the theoretical inlet driving gas temperature, and with the subsequent cooling it is the temperature of the cold flow (the initial model temperature). A maximum difference of less than 2°C between the calculated and measured inlet driving gas temperature was found over several test runs. This difference is due to the heat loss through the plenum wall upstream of impingement plate. The results verified the validity of the assumptions used in the transient heat transfer technique for this experimental rig.

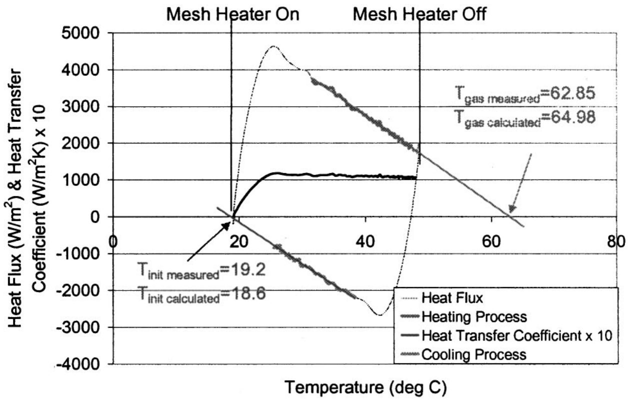

Fig. 11 Heat flux analysis and adiabatic wall temperature

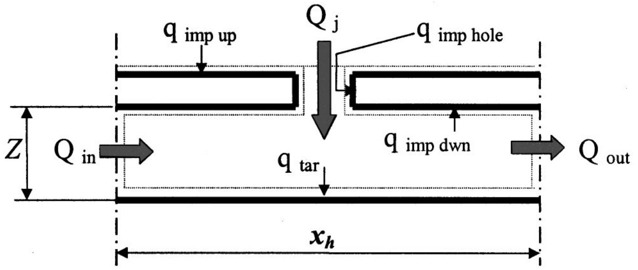

Fig. 12 Simple model of wall cooling

Energy Balance Techniques. The results presented so far account only for heat transferred to the target surface of the impingement channel. Another approach was applied to estimate overall heat flux on all surfaces of the channel using an energy balance between the enthalpy of the flow through the system and the heat transferred to all wetted surfaces. These surfaces included the upstream impingement surface, downstream impingement surface, impingement holes, side and end walls, and target surface as shown in Fig. 12.

For the analysis, each row was considered in turn: G_c and G_j were calculated from the flow analysis model described below, and were used along with Eq. (3) to estimate Q_{in}, Q_j, and Q_{out}:

$$Q_{in}+Q_j=\sum q_{\text{wall}_i}\cdot A_{\text{wall}_i}+Q_{\text{out}} \tag{3}$$

where

$$q_{\text{wall}_i}=\{q_{\text{impup}},q_{\text{imphole}},q_{\text{impdown}},q_{\text{tar}},q_{\text{side \& endwalls}}\}.$$

From the measured detailed heat transfer data, the average heat flux to the target surface, q_{tar}, was calculated. The heat flux $q_{\text{wall }i}$ for the other walls were assigned values correlated by Gillespie [9] in a cast passage impingement geometry. His correlation equations were developed for a slightly different cooling configuration, which included film cooling fed from the impingement cavity. The overall change in enthalpy was calculated for each test case and the calculated exit gas temperature was compared to measured gas temperature at the exit of impingement cooling channel, Fig. 13(*b*). The calculation showed good agreement between the measured ($T_{\text{ext mess}}$) and calculated ($T_{\text{ext cal}}$) exit gas temperature with a maximum difference of 2°C in the case of the uniform array and 2.5°C for the nonuniform array.

Figure 13 shows distribution of heat flow through rows. For the first row, heat flow rate through the end wall was included. In each row Fig. 13(*a*) shows the contribution of each surface to the overall heat transfer. The target plate has the most significant contribution, while heat flow to the impingement plate, which may be in good thermal contact with the blade surface, lies at approximately 50 percent of this level.

Flow Visualization. Mixtures of powder suspended in oil were employed to visualize the surface shear on the target surfaces. Color visualization techniques were used to identify the mixing region of neighboring jets. A zinc oxide and lampblack powder and methylsalicylate oil mixture were used; later yellow, green, and red colored powders mixed with the same base oil were used to produce striped regions. A 1:1 mixture of powder and oil was found to provide the best results. For increased visibility, the target plate was covered by a white plastic sheet prior to the tests. This also protected the perspex from the oil. Black grid lines,

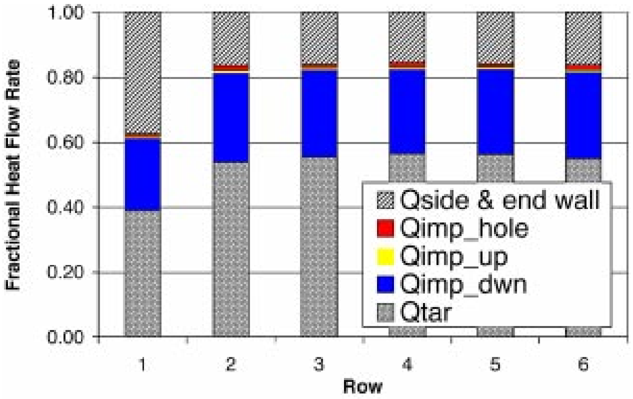

(a) Fractional Heat Flow Rate

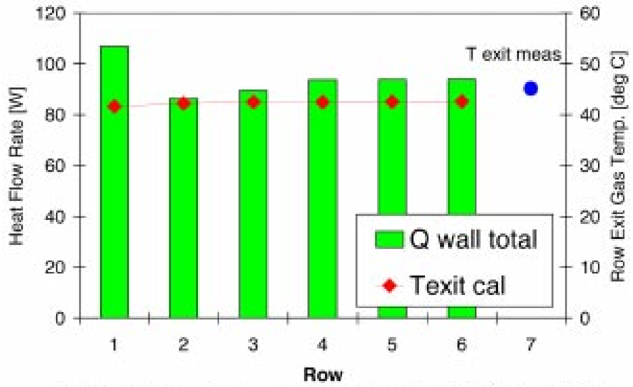

(b) Total Heat Flow Rate and Row Exit Gas Temp

Fig. 13 Heat flow rate distribution: uniform array, $Re_{j\,avg}=28{,}870$

representing the position of the centerline of the impingement holes in the array, were drawn on the sheet. The oil–powder mixture was painted onto the sheet using an artist's paint brush to ensure a smooth finish. For color visualization, different colors were used in strips under adjacent row of holes. Each color covered half a hole pitch upstream and downstream of each row of holes. In Fig. 14 the surface shear pattern is shown on the target surface. The impingement plate used was of uniform hole diameter with a staggered array of holes. The area on the surface directly affected by each of the impinging jet has a repeatable approximately hexagonal shape, surrounded by a mixing area where the flow interacts with the adjacent jets. The area covered by each hexagon is slightly smeared downstream in the presence of increasing crossflow. It was noted that the color of the downstream stripe is predominantly seen in the mixing region between the wall jets from adjacent rows of holes. Where the flows from the neighboring wall jets meet, they coalesce and leave the surface, migrating toward the impingement plate. The figure also shows the location of the stagnation point under each jet. While under row 1 the stagnation point lies on the centerline of the jet, for row 6 it is clear that the jet deformation caused by the increasing crossflow the stagnation point is moved slightly downstream.

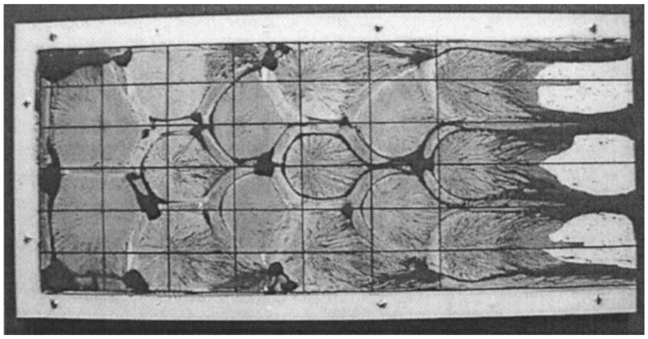

Fig. 14 Shear stress visualization on a smooth target plate

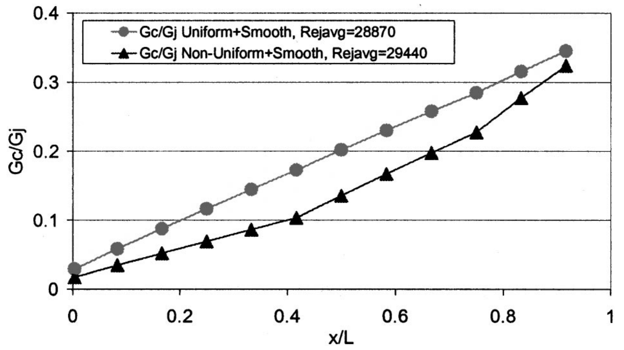

Fig. 15 Comparison of G_c/G_j distribution through the impingement channel

Static Pressure Distribution and Pressure Drop. For impingement into a smooth cooling channel, Florschuetz et al. [3] presented an analytical flow field model, which can predict the flow parameters in an impinging system. This employs a continuous injection model, where discrete injection at rows of impinging jets is distributed over the full impingement plate. The predictions from the model were compared to the static pressure distribution and overall pressure drop measured through the impingement duct.

Static pressure measurements were made along the streamwise centerline of the channel using a hypodermic tube. The measurements were taken at midheight between the plates. A radial hole of diameter 1 mm was drilled in the hypodermic tube (internal diameter 1 mm) 10 mm from the sealed end of the tube. Measurements were made relative to atmospheric pressure using a digital pressure transducer in the data acquisition system. The flow was unheated; otherwise the flow conditions were identical to those in the heat transfer tests.

The measurements were conducted at two different orientations of the static pressure tapping on the probe. This demonstrated the effect of the impinging jet and crossflow on the measured static pressure. The results are compared in Fig. 16. The three excursions in the measured static pressure are caused by the proximity of the impinging jet to the probe at these sites. In all the cases presented, the Florschuetz model predicts the flow field well for

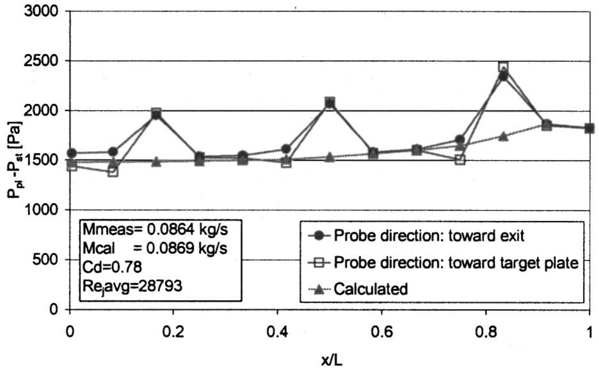

Fig. 16 Static pressure distribution through the impingement channel: nonuniform array

the impinging duct. It is also notable that the hole orientation of the hypodermic probe did not affect the measured static pressure.

Summary

The performance of an impingement cooling system was carefully investigated by conducting flow field and transient heat transfer experiments.

The detailed heat transfer coefficient distributions on the target surface, measured using the transient liquid crystal technique, showed the effect of changing hole diameter and increasing crossflow in the channel.

Using existing data on heat transfer on the other surfaces of the cooling channel, it was possible to estimate the heat flow to all the wetted surfaces accurately, suggesting that they are less strongly affected by changing impingement geometry. The heat flow through the impingement downstream surface is about 50 percent of the target surface value.

Thermocouple data showed that the assumptions of constant heat transfer coefficient and a semi-infinite substrate were valid for this series of tests.

Shear stress patterns on the smooth target plate under the staggered impingement hole array clearly showed detailed information such as the stagnation point of the jets, the development of the wall jet, the mixing area between jets, and crossflow effects.

Acknowledgments

This work has been carried out with the support of Rolls-Royce plc, DERA, DTI CARAD, and MOD ARP26c, the continuance of which is greatly appreciated by the authors, as is their permission to publish this work. The lead author would also like to thank the British Chevening & Korean Government for the support to study at the University of Oxford. The experimental apparatus was manufactured by Mr. Pat Timms.

Nomenclature

A = area, m^2
C_d = discharge coefficient $= m_{\mathrm{actual}}/m_{\mathrm{ideal}}$
c = specific heat capacity, J/kg·K
d = hole diameter, m
G = mass velocity, $\mathrm{kg/m^2 \cdot s}$
h = heat transfer coefficient, $\mathrm{W/m^2 \cdot K}$
k = thermal conductivity, W/m·K
L = length of the channel, m
l = thickness of the impingement and target plate, m
m = mass flow rate, kg/s
Nu = Nusselt number $= h \cdot d/k$ for uniform array or $h \cdot d_{\mathrm{avg}}/k$ for nonuniform array
P = pressure, $\mathrm{N/m^2}$
Q = heat flow rate, W
q = heat flux, $\mathrm{W/m^2}$
Re = Reynolds number $= G_j \cdot d/\mu$
T = temperature, °C
u = velocity, m/s
t = time, s
w = width of the impingement channel, m
x = streamwise distance, m
y = spanwise distance, m
z = channel height, m
μ = dynamic viscosity
ρ = density
τ = time constant for the exponential temperature change

Subscripts

avg = average
c = crossflow
cal = calculated
d = hole diameter
imp = impingement
ext = channel exit
g = gas
h = impingement hole
dwn = downstream
j = impingement jet
meas = measured
pl = plenum
s = surface
spn = spanwise
st = static
stg = stagnation
tar = target
0 = initial condition

References

[1] Kercher, D. M., and Tabakoff, W., 1970, ''Heat Transfer by a Square Array of Round Air Jets Impinging Perpendicular to a Flat Surface Including the Effect of Spent Air,'' ASME J. Eng. Power, **92**, pp. 73–82.
[2] Florschuetz, L. W., Metzger, D. E., Takeuchi, D. I., and Berry, R. A., 1980, ''Multiple Jet Impingement Heat Transfer Character—Experimental Investigation of In-Line and Staggered Arrays With Crossflow,'' NASA Contractor Report No. 3217.
[3] Florschuetz, L. W., Metzger, D. E., and Truman C. R., 1981, ''Jet Array Impingement With Crossflow Correlation of Streamwise Resolved Flow and Heat Transfer Distributions,'' NASA Contractor Report No. 3373.
[4] Obot, N. T., and Trabold, T. A., 1987, ''Impingement Heat Transfer Within Arrays of Circular Jets: Part 1—Effects of Minimum, Intermediate, and Complete Crossflow for Small and Large Spacings,'' ASME J. Heat Transfer, **109**, pp. 872–879.
[5] Lucas, M. G., Ireland, P. T., Wang, Z., and Jones, T. V., 1993, ''Fundamental Studies of Impingement Cooling Thermal Boundary Conditions,'' AGARD CP-527, Paper No. 14.
[6] Van Treuren, K. W., Wang, Z., Ireland, P. T., and Jones, T. V., 1994, ''Detailed Measurements of Local Heat Transfer Coefficient and Adiabatic Wall Temperature Beneath an Array of Impinging Jets,'' ASME J. Turbomach., **116**, pp. 369–374.
[7] Van Treuren, K. W., Wang, Z., Ireland, P. T., Jones, T. V., and Kohler, S. T., 1996, ''Comparison and Prediction of Local and Average Heat Transfer Coefficients Under an Array of In-Line and Staggered Impingement Jets,'' ASME Paper No. 96-GT-163.
[8] Gillespie, D. R. H., Wang, Z., Ireland, P. T., and Kohler, S. T., 1998, ''Full Surface Local Heat Transfer Coefficient Measurements in a Model of an Integrally Cast Impingement Cooling Geometry,'' ASME J. Turbomach., **120**, pp. 92–99.
[9] Gillespie, D. R. H., 1996, ''Intricate Internal Cooling Systems for Gas Turbine Blading,'' D. Phil. Thesis, Department of Engineering Science, University of Oxford, United Kingdom.
[10] Bouchez, J.-P., and Goldstein, R. J., 1975, ''Impingement Cooling From a Circular Jet in a Crossflow,'' J. Heat Mass Flow, **18**, pp. 719–730.
[11] Gardon, R., and Akfirat, J. C., 1966, ''Heat Transfer Characteristics of Impinging Two-Dimensional Air Jets,'' ASME J. Heat Transfer, **88**, pp. 101–108.
[12] Koopman, R. N., and Sparrow, E. M., 1976, ''Local Average Transfer Coefficients Due to an Impingement Row of Jets,'' Int. J. Heat Mass Transf., **19**, pp. 673–683.
[13] Son, C. M., Michaelis, M., Robertson, A., Ireland, P. T., and Bather, S., 1998, ''Detailed Heat Transfer Measurements in an Engine Representative Impingement Cooling System Using Liquid Crystals,'' *Proc. ASME International Mechanical Engineering Congress and Exposition*, HTD-Vol. 361-3, pp. 389–397.
[14] Schultz, D. L., and Jones, T. V., 1973, ''Heat Transfer Measurements in Short-Duration Hypersonic Facilities,'' AGARD-AG165.
[15] Rolls Royce plc., 1996, *The Jet Engine*.

X. Li

J. L. Gaddis

T. Wang[1]

Department of Mechanical Engineering,
Clemson University,
Clemson, SC 29634-0921

Mist/Steam Heat Transfer in Confined Slot Jet Impingement

Internal mist/steam blade cooling technology has been considered for the future generation of Advanced Turbine Systems (ATS). Fine water droplets of about 5 μm were carried by steam through a single slot jet onto a heated target surface in a confined channel. Experiments covered Reynolds numbers from 7500 to 25,000 and heat fluxes from 3 to 21 kW/m^2. The experimental results indicate that the cooling is enhanced significantly near the stagnation point by the mist, decreasing to a negligible level at a distance of six jet widths from the stagnation region. Up to 200 percent heat transfer enhancement at the stagnation point was achieved by injecting only ~1.5 percent of mist. The investigation has focused on the effects of wall temperature, mist concentration, and Reynolds number. [DOI: 10.1115/1.1331536]

Introduction

To improve the overall efficiency of gas turbine engines, the turbine inlet temperature and compressor pressure ratio are continuously increasing for the next generation of gas turbine systems. As a result, even with the potential advancement of future high-temperature materials, highly efficient gas turbine engines are expected to continue to operate at temperatures much higher than the allowable metal temperature of the turbine airfoils, which, in turn, makes effective cooling of the airfoils essential.

With recent adoptions of closed-loop steam cooling by two major gas turbine manufacturers [1,2] for their heavy-frame Advanced Turbine Systems (ATS), a major part of external air-film cooling load will be replaced by internal steam cooling. Generally, the internal heat transfer coefficient is required to be in the range of 8000~10,000 W/m^2 K in order to replace the cooling load currently shared by external air-film cooling. Liquid water can achieve this goal easily, but problems with instability when boiling occurs have discounted its chances. With the availability of steam from the bottom cycle of a heavy-frame ATS, mist/steam cooling has been introduced by this research group [3] as a potential means to enhance the internal cooling effectiveness of turbine airfoils significantly. The advantages and reasons for using mist/steam cooling, a comparison of mist/air and mist/steam cooling, and a review of previous related studies have been presented by Guo et al. [3] and are not repeated here.

Basically, the concept of using mist/steam cooling to enhance cooling effectiveness is based on its following features: (*a*) latent heat of evaporation, (*b*) increased specific heat, (*c*) steeper temperature gradient near the wall, (*d*) lower bulk temperature, (*e*) increased flow mixing induced by steam-particle interactions and particle dynamics, and (*f*) additional momentum and mass transfer induced by evaporation of liquid droplets on/near the wall.

Jet impingement cooling has been applied widely to provide high heat transfer rates in many industrial processes, including the hardening and quenching of metals, tempering of glass, and cooling of electronic components. The early studies show that jet impingement cooling is better than channel cooling for gas turbines, especially for the leading edge of the turbine blades. Single-phase jet impingement has been studied extensively, including heat transfer at the stagnation point, local heat transfer, and effects of turbulence intensity and nozzle geometry. However, few studies have been found on mist jet impingement, including air–water mist and steam–water mist.

Wachters et al. [4] considered the impact of droplets about 60 μm impacting a heated surface in the range of 5 m/s. Impinging droplets could only maintain the spheroidal state with relatively high surface temperatures. The required temperature depended on thermal properties and roughness of the surface as well as the Weber number of the droplets. In the spheroidal state very low rates of heat flow were observed.

Goodyer and Waterston [5] considered mist/air impingement for turbine blade cooling at surface temperatures above 600°C. They suggested that the heat transfer was dominated by partial contact between the droplets and the target surface, during which the droplets vaporized at least partially. A vapor cushion and the elastic deformation of the droplets were responsible for rejecting the droplets. Addition of 6 percent water was found to improve the stagnation point heat transfer by 100 percent, diminishing away from the stagnation point. Droplet size was found to have little effect for 30 $\mu m < d_{32} < 200$ μm.

Takagi and Ogasawara [6] studied mist/air heat and mass transfer in a vertical rectangular tube heated on one side. They identified wet-type heat transfer at relatively low temperatures and post-dryout type at higher temperatures. In the wet region the heat transfer coefficient increased with increased heat flux. In the post-dryout region the heat transfer coefficient increased with droplet concentration and flow velocity and with decreased droplet size.

Ganic and Rosenhow [7] studied the effects of dispersed droplets on heat transfer in a gas flow. They demonstrated that the total heat transfer flux is the sum of a single-phase component and a component due to direct impact of the droplets. In trajectory analysis of droplets in the temperature boundary layer, they included a lift term arising from faster evaporation on the side of the droplet nearer the wall where the gas temperature is higher. The higher evaporative rate gives rise to a momentum imbalance equivalent to lift.

Mastanaiah and Ganic [8] conducted experiments on mist/air in the post-dryout region in a vertical circular tube. Performance depended mainly on wall temperature and was independent of the mass velocity for a range of temperatures in film boiling. They confirmed the heat transfer coefficient decreased with increased wall temperature.

Yoshida et al. [9] focused on the effect on turbulent structure with a suspension of 50-μm glass beads. In the impinging jet region, the gas velocity decreased due to the rebound of beads, accompanied by an increase in the normal direction velocity fluc-

---

[1] Current address: University of New Orleans, New Orleans, LA.

Contributed by the International Gas Turbine Institute and presented at the 45th International Gas Turbine and Aeroengine Congress and Exhibition, Munich, Germany, May 8–11, 2000. Manuscript received by the International Gas Turbine Institute February 2000. Paper No. 2000-GT-221. Review Chair: D. Ballal.

tuations. In the wall-jet region the effect was slight. The Nusselt number was found to increase by a factor of 2.7 for mass flow ratios (solid/gas) of 0.8.

Lee et al. [10] studied the dynamic depositional behavior of droplets in a mist/air flow in a vertical rectangular channel with one side heated. It was found that when the droplet diameter was 30∼80 μm, a ''superbly'' effective cooling scheme with ten times the heat transfer enhancement could be established by the evaporation of an ''ultrathin'' liquid film (50∼100 μm).

Buyevich and Mankevich [11,12] modeled the particles in the mist as liquid discs separated from the wall by a vapor layer whose thickness is that of the wall roughness. A critical impact velocity was identified to determine whether a droplet rebounds or is captured. They applied the model to dilute mist impingement and reported agreement with experiment.

Fujimoto and Hatta [13] studied deformation and rebound of a water droplet on a high-temperature wall. For Weber numbers of 10–60, they computed the distortions of the droplet as it flattened, contracted, and rebounded. They used a simple heat transfer model to confirm that surface tension dominates vapor production in the rebounding process. Hatta et al. [14] gave correlations of contact time and contact area of the droplet with Weber number.

Guo et al. [3,15] studied the mist/steam flow and heat transfer in a straight tube under highly superheated wall temperatures. Droplet size and distribution were measured by a Phase Doppler Particle Analyzer (PDPA) system. It was found that the heat transfer performance of steam could be significantly improved by adding mist into the main flow. An average enhancement of 100 percent with the highest local heat transfer enhancement of 200 percent was achieved with 5 percent mist. Guo et al. [16] performed an experimental study on mist/steam cooling in a highly heated, horizontal 180 deg tube bend with the same experimental facility as above. Due to the effect of centrifugal force, the outer wall of the test section always exhibited a higher heat transfer enhancement than the inner wall. The highest enhancement occurred at about 45 deg downstream of the inlet of the test section. Only a small number of droplets could survive the 180 deg turn and be present in the downstream straight section. The overall cooling enhancement of the mist/steam flow ranged from 40 to 300 percent with maximum local cooling enhancement being over 800 percent. It increased as the main steam flow increased, but decreased as the wall heat flux increased.

Experimental Facility

Experimental System. The overall experimental system is shown in Fig. 1, which consists of four subsystems: steam system, water system, atomizing system, and test section. The steam system supplies the main steam flow used in the experimental study. The high-pressure (about 8 bar) steam extracted from the steam pipeline existing in the building becomes clean and dry saturated steam after passing through a strainer, a regulatory system, a desuperheater, and a filter tube. The saturated steam at about 1.5 bar then enters the mixing chamber and mixes with the mist from the atomizer system. The mist/steam flow enters the test section through a flexible silicone tube and goes to the condenser, where it is cooled down to water. Water supplies the atomizer (Mee Industries, Inc.) through a high-pressure pump to produce droplets with an average diameter (d_{10}) less than 10 μm at 68 bar. Any extra water in the mixer goes to drain through a steam trap. The arrangement of nozzles in the mixer has an important effect on the mist/steam flow. Four nozzles are connected by two valves to allow one, three, or four to operate together.

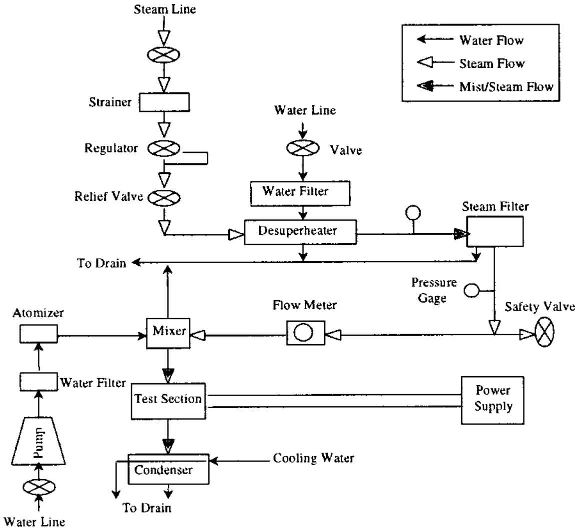

Fig. 1 Schematic of experimental system

The test section is designed to implement heat transfer measurement as well as optical penetration. It consists of a single slot jet, heaters, thermocouples, and optical windows. Figure 2 shows the layout of this test section. A tube 25 mm in diameter and 125 mm long connects the 50 mm flexible tube to the settling chamber, which is 70 × 100 mm in cross section and 60 mm long. The collecting pipes are at both ends. The whole test section slides horizontally and moves vertically by insertion of shims. Flexible silicone rubber tubes are used to connect the test section with the mixer and the condenser to implement movement in both directions. The container is made of aluminum to reduce the total weight and assembled by bolts. Based on other studies and the recommendations from industry and limited by the steam-line capability, the rounded-entrance slot size is 7.5 × 100 mm with a nozzle-to-target spacing of 22.5 mm. The channel length is 250 mm. This size of slot jet gives a Reynolds number of about 25,000 with a jet velocity of about 30 m/s. Droplets with very high velocity may damage the heated surface, especially for a long period of operation. Therefore, the jet used in this study is scaled up from the industrial application to achieve the current Reynolds number. On the plus side, these dimensions are convenient for optical measurement.

To cover more extensive areas and prevent overheating, five discrete heater elements are used. The segmented heated surface is mounted firmly to a backup plate of high temperature and low thermal conductivity. The middle one, which covers the stagnation point, is only the half width of the other four identical elements (38 × 76 mm). Five heater elements are in series electri-

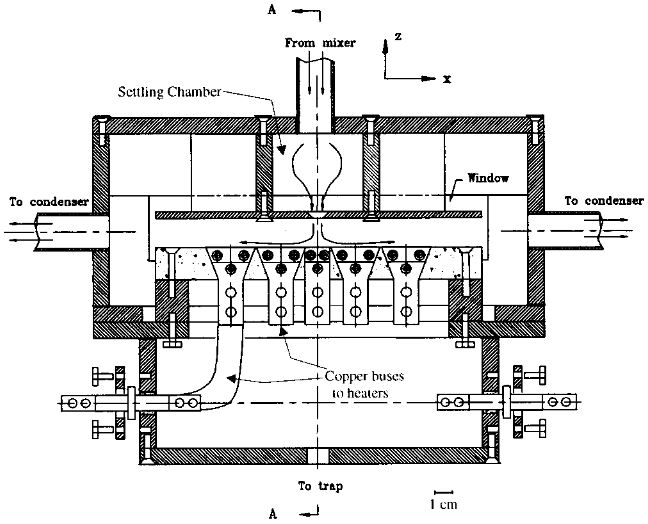

Fig. 2 Design of test section

cally. Stainless steel sheet (Type 316), with a thickness of 0.4 mm, is used for the four larger elements. The center element is copper nickel with one-fourth the electrical resistivity of stainless steel. This yields an approximately constant heat flux within 10 percent.

Two large, flat Pyrex windows are used to cover the whole side-confining wall of the channel. Such big windows make the optical measurement easier and the direct examination on the condition of heated surface possible. The data at different locations can be obtained by moving the test section or the optical system. Compared with moving the jet issuing plate while a small window is used, this scheme can always make a symmetric flow condition and cause little sealing problem. O-rings are used to seal the optical windows.

The test section is directly heated by a DC power supply, which has a maximum voltage of 7 V and a maximum current of 750 A. To maintain a dry and clean window, hot air (200°C) from an auxiliary heater is used to heat the window.

Experimental Instrumentation

Droplet Measurement. The droplet measurement is conducted by a Phase Doppler Particle Analyzer (PDPA). Two laser beams (488 nm, green) with a waist diameter of 0.115 mm are issued from the transmitter and focused on the same region, which generate the fringes for the PDPA system. The PDPA receiver and analysis software (Aerometrics) produce data on velocity parallel to the heater surface, droplet size distribution, and droplet count rate. The PDPA system is fixed; different measurement locations are achieved by moving the test section.

Temperature Measurement. All temperatures are measured by Omega 30-gage (wire diameter about 0.25 mm) Chromega/Alomega (K type) thermocouples with braided fiberglass insulation. A data logger (FLUKE Model 2250) is used to monitor and record the temperature. The thermocouples, along with the data logger, were calibrated against a standard Resistance Temperature Device (RTD) system for nominal temperature uncertainty of 0.3°C. To measure the temperature distribution on the heated surface, thermocouples are strategically placed at the stagnation point and at about 1, 2, 3, 5, 8, and 11 slot widths away from the jet center. Only half of the heated surface is measured, while a single thermocouple at the other side is placed to check for symmetry. The temperature at the inlet of the test section and the temperature of water for the atomizer are also measured.

Flow Rate and Others. Steam flow rate is measured by an orifice flow meter. The catch-and-weigh method is also used to measure the flow rates and calibrate the flow meter in-situ. Water flow from the trap under the mixer is essential to determine the water concentration in the mist. The water flow rates from the traps just before the test section and at the bottom of the test section are also measured. The water flow rate to the atomizer can be adjusted by changing the pump pressure.

The heating power to the test section is obtained from the current and the voltage across the test section. The current is given by the voltage across the precision shunt (with a resistance of $1.333 \times 10^{-4}\ \Omega$) of the power supply. The voltage across the test section is measured directly by a voltmeter. Pressure gages before and after the steam filter indicate the pressure of the steam.

Data Reduction and Uncertainty Analysis

Heat Transfer Coefficient. For jet impingement, the heat transfer coefficient is usually defined as

$$h(x)=\frac{q''(x)}{T_w(x)-T_j} \tag{1}$$

where q'' is the wall heat flux, T_w is the local wall temperature, and T_j is the jet temperature. The steam saturation temperature is taken as the jet temperature for the current study. The wall temperatures are measured by thermocouples electrically insulated by mica at the back of the heater. Since the temperature drop across the heater is less than 0.5°C, which is negligible compared with (T_w-T_j), the temperatures of the thermocouples are used as the wall temperatures.

Table 1 Results of uncertainty analysis

Resultants	Nominal Value	Nth-order Uncertainty (%)	Largest Source
m_l/m_s	$2.43\text{x}10^{-2}$	19.3	Δt
Re	15300	1.65	μ_s
q''	13.4 (kW/m^2)	5.43	V_{shunt}
h	268 (W/m^{2}K)	6.27	V_{shunt}
Nu	161	6.50	V_{shunt}

The heat flux on the heater can be obtained from the heating power divided by the heating area, assuming the heater has a uniform thickness. In fact, the heating power can be obtained directly from the electrical resistance of the heater components and the current passing through the heater as follows:

$$q''=I^2\xi/\delta B^2 \tag{2}$$

where I is the current passing through the heater and ξ is the resistivity of the heater materials. δ and B are the heater thickness and width, respectively. Calculation by this equation avoids measurement error of the heater length and of the voltage across the test section due to contact resistance. In the current design, the supporting block for the heaters is ceramic with low heat conductivity and it is surrounded by saturated steam. A simple one-dimensional heat conduction model is used to provide a correction of back heat loss less than 5 percent in data processing.

Flow Parameters. Steam traps in the mixer, immediately upstream of the test section and from the condenser, allow determination of average liquid flow in the test section. The velocity and size of the droplets are given directly by the PDPA system. The concentration of the liquid phase can be found from the droplet average diameter, d_{30}, and the data rate (n) of the PDPA system:

$$m_l=\frac{\pi}{6}\rho_l d_{30}^3 n \tag{3}$$

In our experiment there appears to be frequent interruption of the signal by droplets on the glass. Thus, the value of n is taken as the largest value of many observations. The liquid concentration obtained by the PDPA system is usually smaller than that obtained by the balance of flow rates.

Uncertainty Analysis. Based on the methodology developed by Moffat [17], the nth-order uncertainty analysis is conducted on both heat transfer and flow rate in this study. The results of uncertainty analysis are summarized in Table 1. It is found that the uncertainty for heat transfer is about 5～7 percent and the largest source is the heating voltage of the power supply. For the flow rate, although the uncertainty for the steam phase is very small, the mist concentration has a large uncertainty, about 40 percent, and the largest source is Δt (sampling time). The main sources for the uncertainty of Reynolds number are the steam viscosity, μ_s, and the slot length. The uncertainty of Reynolds number is not large either. The detailed uncertainty analysis is documented by Li [18].

Experimental Results and Discussions

Preliminary Experiments and System Verification. Preliminary studies on single-phase steam jet impingement were conducted first to verify that the whole experiment system was reliable. The results also serve as a baseline for mist/steam jet impingement. Different heat fluxes as well as different jet veloci-

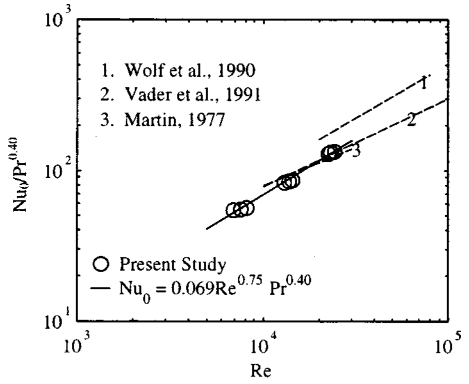

(a) Heat Transfer at Stagnation Point

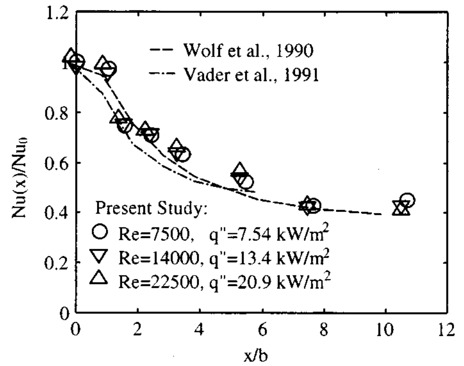

(b) Local Heat Transfer Coefficient Distribution

Fig. 3 Heat transfer results for steam-only flow

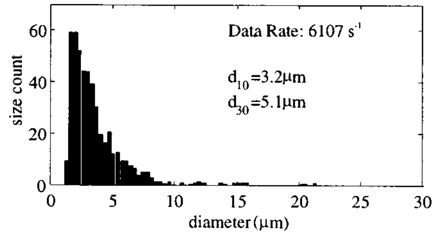

(a) Droplet Size Distribution

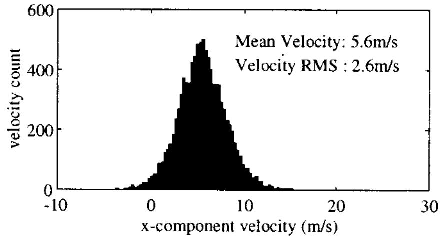

(b) Droplet Velocity Distribution

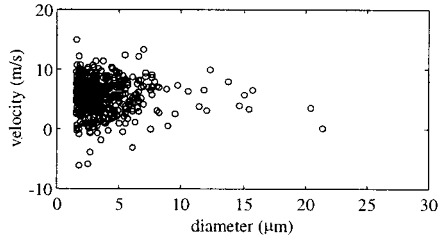

(c) Droplet Size vs. Droplet Velocity

Fig. 4 A typical result of PDPA measurement with one nozzle at Re=15,000, $x/b=2$, and $z/b=0.5$

ties have been tested. Figure 3(*a*) shows the heat transfer results at the stagnation point. The following correlation can be used to represent the data at the stagnation point:

$$Nu_0 = 0.069\,Re^{0.75}\,Pr^{0.40} \tag{4}$$

The characteristic scale used in the Reynolds number and Nusselt number is $2b$, two times the slot width. Figure 3(*b*) shows the distribution of local heat transfer coefficient. The present results are in basic agreement with prior studies. The power of the Reynolds number in Eq. (4) is higher than in other studies due to the narrow range of Reynolds number. In fact, the heat transfer results for jet impingement are subject to variations because of different nozzle designs, different heated surface condition, target distances, and different turbulence intensity. The power for Reynolds number can range from 0.5 to 0.8 [19]. Since the present study does not focus on the effect of different flow parameters and different configurations but only on the effect of water droplets on heat transfer, the steam-only tests support that this experiment system is reliable without large bias error sources.

The symmetric character of the flow was examined by both temperature and velocity measurements. The measurement results, including both steam-only flow and mist/steam flow, indicate, though not shown, that the flow is highly symmetric.

Two-Phase Mist/Steam Jet Impingement

Results of Droplet Measurement for a Typical Case. With the experimental system proven by preliminary studies, the typical behavior of mist/steam jet impingement is examined. The Reynolds number is 15,000 and the heat flux is 13.4 kW/m^2. Figure 4 shows the typical distributions of the droplet size and x-component velocity obtained by the PDPA system at a specific location close to the stagnation region ($x/b=2$ and $z/b=0.5$). The droplet size ranges from 1 to 15 μm with an arithmetic average diameter of 3.2 μm. The velocity of the droplet has a large range from -2 to 12 m/s with an average value of 5.6 m/s, which is due to the high turbulence of the shear layer in a jet impingement flow. It can also be seen that the droplet size does not have a close relationship with the droplet velocity, which suggests the droplets follow the main flow well. The distribution of the average droplet size obtained at different locations throughout the test section indicates that the droplet size remains the same at all locations except for the region close to the heated surface, where the droplets become smaller along the wall because of evaporation.

Liquid Concentration Measurement. By using both the catch-and-weigh method and the PDPA data, liquid flow rate was measured for different steam flow rates and with different numbers of nozzles. The results are listed in Table 2. The data range indicates the measurement uncertainty. The liquid concentration was found to decrease with the main flow rate. It was believed initially that a higher steam flow rate would transport more liquid. However, further study found that the liquid flow rate itself decreases with increasing steam flow rate. The possible reason is that high-velocity agitation of mist and steam in the mixer makes more droplets hit the wall and drain out.

More nozzles produce higher liquid concentration, which is also indicated by heat transfer measurements. Direct observation found that liquid streams along the unheated walls, which means some of the liquid collected by catch-and-weigh does not affect the heated surface and the true liquid concentration in the main

Table 2 Results of liquid concentration measurement

Reynolds Number of Steam-Only Flow	Mist Concentration (%)		
	One Nozzle	Three Nozzles	Four Nozzles
7500	3.0~4.0	6.0~8.0	8.0~10.0
15000	1.0~2.0	2.0~3.5	3.0~4.5
22500	0.5~1.0	1.0~1.5	1.5~2.0

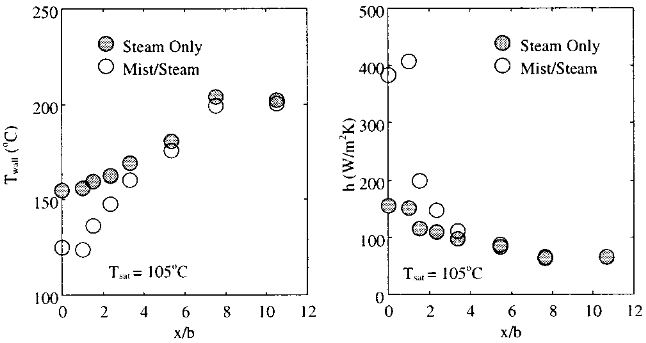

(a) Wall Temperature

(b) Heat Transfer Coefficient

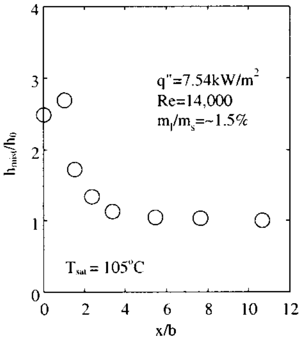

(c) Ratio of Heat Transfer Coefficient

Fig. 5 A typical heat transfer result of mist/steam jet impingement ($q''=7.54$ kW/m^2, Re=14,000 and $m_l/m_s=\sim 1.5$ percent)

flow is lower than the calculated value. This effect, varying with the main flow rate, can be used to explain partially the lower value given by the PDPA method.

Results of Heat Transfer for a Typical Case. With a Reynolds number of 14,000 and a heat flux of 7.54 kW/m^2, the typical heat transfer performance of mist/steam jet impingement cooling is summarized as shown in Fig. 5. In Fig. 5(*a*) the temperature distribution with mist is compared to that without mist, showing clearly the depression in temperatures caused by the mist. The heat transfer coefficient calculated by Eq. (1), as shown in Fig. 5(*b*), is considerably larger near the stagnation point. For $x/b<2$ the mist effect is strong, declining to about $x/b=6$ where it becomes negligible. Figure 5(*c*) shows the enhancement, which is the ratio of mist to dry heat transfer coefficient of Fig. 5(*b*). The enhancement for this typical case is 150 percent for ~1.5 percent mist content at the referenced conditions. The mist effect is depressed at the centerline compared with $x/b=1$, attributed to the divergence of path lines resulting in defocusing of the mist together with the existence of droplet rebound and multiple contacts.

The reduction in enhancement downstream could be due to lack of survival of droplets past the stagnation point or because the droplets become thermally remote from the wall. In this case, as is typical, only a small fraction of the droplets must be evaporated to account for the heat transfer in the stagnation region. Therefore the droplets do survive, a fact corroborated by the PDPA surveys in the downstream region. Therefore the only plausible reason for negligible enhancement for $x/b>6$ is that the droplets have become thermally remote. This contrasts with the observations of Guo [15] in a straight tube, where the mist always maintained a 10 to 20 percent enhancement even far downstream.

An extensive study has been performed by Li [18] to model the dynamics of liquid droplets impinging on a hot surface and transported in the boundary layer. Only a brief summary is given here. A study of the droplet trajectory shows the droplet has little time to evaporate inside the boundary layer. Near the stagnation point, assuming an elastic rebound at expected velocities, the exposure to superheated vapor causes about 0.1 percent of the liquid mass to evaporate. Therefore, it is deduced that most of the heat transfer enhancement is caused by other mechanisms. One possible mechanism would be the direct heat transfer from wall to droplet. Some of the droplets may be captured on the wall for a short time before they rebound, especially at low wall temperature. The in-

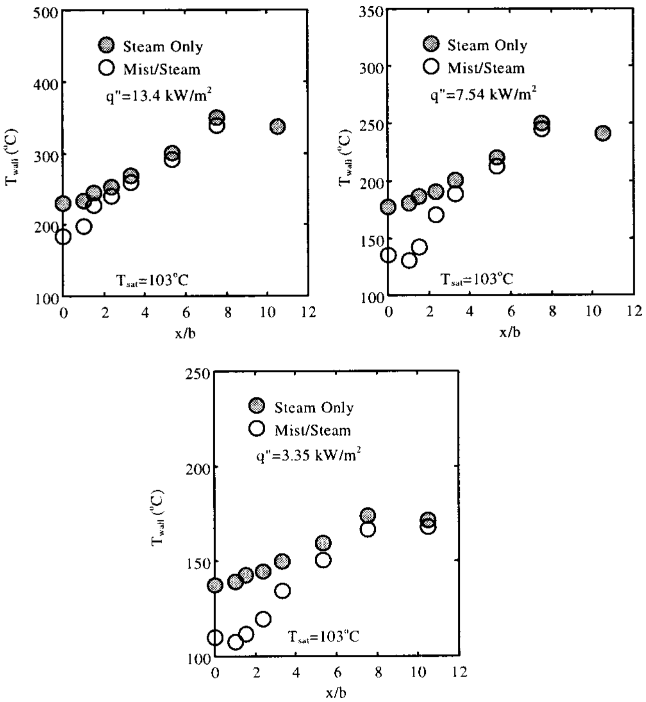

Fig. 6 Wall temperature distribution at different heat fluxes (Re=7500 and $m_l/m_s=\sim 3.5$ percent)

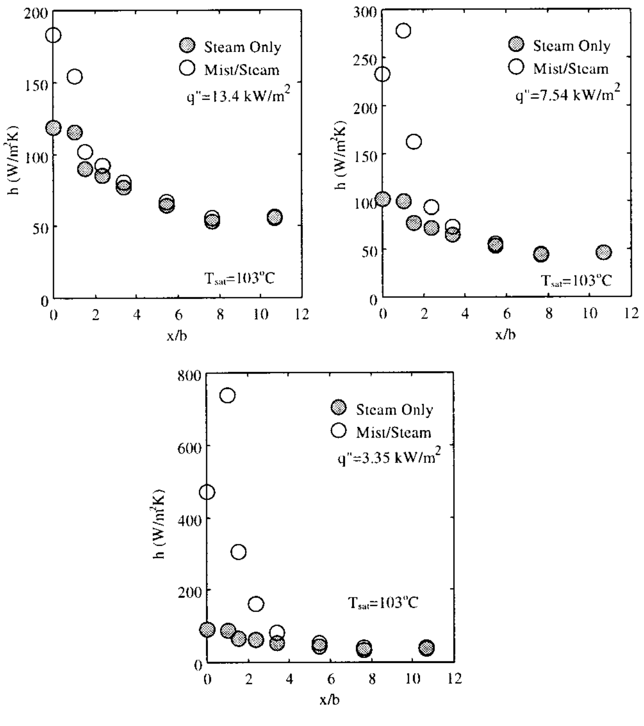

Fig. 7 Heat transfer coefficient at different heat fluxes (Re=7500 and $m_l/m_s=\sim 3.5$ percent)

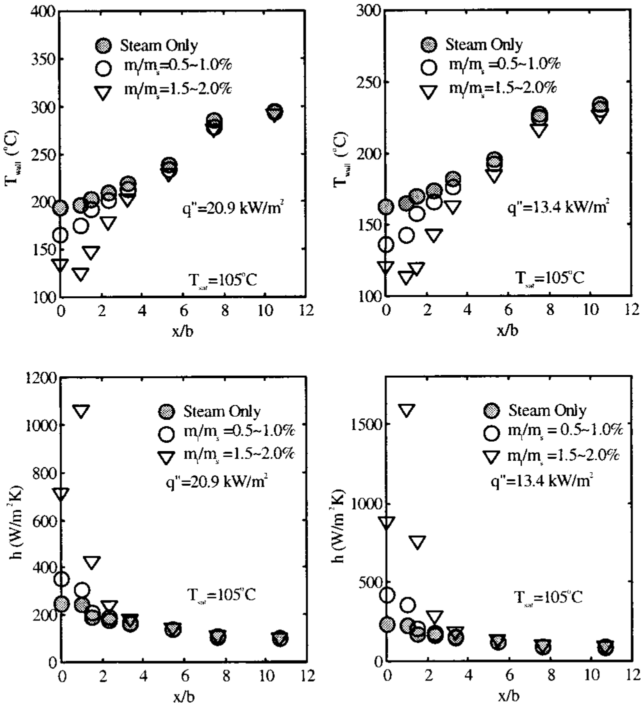

Fig. 8 Effect of liquid concentration on wall temperature and heat transfer coefficient at Re=22,500 and different heat fluxes

creased mixing and turbulence in the boundary layer due to the droplet injection may also contribute to the enhanced heat transfer. This can be supported by the experimental studies on single-phase flow with solid particles inside [9,20].

Effect of Target Wall Temperature on Heat Transfer. The wall temperature plays an important role in the mist heat transfer. The droplets are slowed as they approach the wall and are acted on by the evaporative lift force. As they penetrate the boundary layer and contact the wall, the droplets are expected to deform, as suggested by Hatta et al. [14] for a time dependent on the wall temperature. At low enough temperatures, the droplets could wet the wall and evaporate completely, while for higher temperatures the droplet will overcome any subcooling associated with the pressure of deformation, form vapor, and be repelled from the wall. Direct observation of the surface at all heat fluxes showed no evidence of droplet residence or any accumulated film. The complicated phenomenon noted by Guo et al. [15] resulted from a pre-existing liquid film and is not relevant here. The downstream region of Guo's observation is more comparable. In the present study, data with several heat fluxes are available to examine the temperature effect. Figure 6 shows the temperature distributions under different heat fluxes. Figure 7 shows the corresponding heat transfer coefficient. The variation in single-phase heat transfer coefficient produces a constant Nu using the conductivity evaluated midway between wall and saturation temperature. The stagnation point heat transfer is enhanced by 40 percent at high heat flux, $q''=13.4$ kW/m^2 and the enhancement increases to over 400 percent at low heat flux, $q''=3.35$ kW/m^2. Similar results about the effect of the wall temperature on two-phase heat transfer were reported by Guo et al. [15] and Takagi and Ogasawara [6].

Effect of Liquid Concentration on Heat Transfer. Figure 8 shows results obtained with different liquid concentrations. As expected, increasing the liquid content significantly improves the heat transfer performance. The enhancement can rise to higher than 300 percent from 80 percent when the liquid content increases to 1.5~2.0 percent from 0.5~1.0 percent for Re $=22{,}500$ and $q''=20.9$ kW/m^2. However, increasing liquid content does little to improve the heat transfer far away from the stagnation point.

Effect of Steam Flow Rate on Heat Transfer. A high steam flow rate, which means high jet velocity in the present study, will force more droplets to approach the wall. Therefore, more heat can be removed by mist if the mist concentration is the same. However, since the single-phase heat transfer also increases with the main flow rate, the enhancement ratio of the heat transfer coefficient is more complicated. Because the liquid content depends on the main flow rate, it is very difficult to control the experiment under identical liquid concentration and different Reynolds number, although a different number of nozzles can be used. Based on the limited data, it is found that the enhancement ratio is proportional to Re$^{0.3}$ at $T_w=200°$C, which means that increasing the main flow rate will improve the heat transfer enhancement. Guo et al. [15] gave a similar conclusion based on mist/steam cooling in a straight pipe.

Relevance to Turbine Applications. Actual application is expected at 25~35 bar, and Reynolds number to 400,000. Projections to the higher Reynolds numbers of gas turbine applications will increase the single-phase heat component and improve the mist component, based on the trends herein. At the increased wall superheat values, which may reach 700°C, there may be a decline in the mist effect. But the trends indicate that the mist concentration continues to influence the mist effect and it is expected that the higher fluid density will permit carrying increased mist concentration. More study will be required to establish whether higher pressures and temperatures will support useful mist enhancement.

Conclusions

A heat transfer enhancement has been observed due to mist added to steam in an impingement flow. A 150 percent enhancement with a mist concentration of 1.5 percent is typical in the stagnation region. The highest effect is in the stagnation region $x/b<2$, where b is the slot width. From $x/b=2$ to $x/b=6$ the effect wanes, and for $x/b>6$ there is no significant effect. The stagnation point enhancement is strongly influenced by heat flux, increasing from 40 percent at the highest flux to over 400 percent as the flux is reduced by a factor of four. The increase in enhancement is roughly proportional to the liquid content at the stagnation point, but positions downstream remain unaffected at any liquid rate. The heat transfer enhancement is modestly affected by steam velocity (Reynolds number). Tentatively the enhancement varies with Re$^{0.3}$, based on limited data. For low heat flux and high liquid flow conditions the maximum cooling effect is located away from the stagnation point.

Mechanisms noted include the systematically dry condition of the heated surface, having neither film nor visible droplets for long enough to be seen by eye. Calculations of droplet trajectory and thermal boundary layer indicate the droplets have too little residence time to evaporate significantly. The PDPA data indicate relatively large ranges of velocity parallel to the heater surface. Surveys downstream on the plate do indicate smaller droplets near the heated wall, but no elevation in concentration. Estimates suggest that the direct contact heating of droplets is responsible for most of the enhancement, consistent with these observations. Few or no droplets evaporate completely.

Acknowledgments

The authors would like to thank Graver Separations (Wilmington, DE) for donating the steam filters for the experiment. We also want to thank Mee Industries, Inc. (El Monte, CA) for donating the pressure atomizers and the high-pressure pump. We appreciate the help from Dr. T. Guo in setting up the test facility. This research was sponsored by the U.S. Department of Energy under contract No. DOE/AGTSR 95-01-SR-034, and was managed by Dr. N. Holcombe at the Federal Energy Technology Center and by Dr. Larry Golan at the South Carolina Institute for Energy Studies.

Nomenclature

B = width of heat element
b = jet width$=7.5$ mm
d = diameter of droplet
d_{10} = arithmetic mean diameter
d_{30} = volume mean diameter
d_{32} = Sauter mean diameter
h = heat transfer coefficient
I = current through the heater
k = thermal conductivity of vapor
m = mass flow rate
Nu = Nusselt number$=h2b/k$
n = data rate, s^{-1}
Pr = Prandtl number
q'' = heat flux
Re = Reynolds number$=\rho_s V_j 2b/\mu_s$
T = temperature
t = time
V_j = average jet velocity at jet exit
V_{shunt} = voltage cross the shunt
x = coordinate along the target wall
z = coordinate along the jet centerline
δ = thickness of heater elements
μ = dynamic viscosity
ρ = density
ξ = resistivity, Ωm

Subscripts

0 = stagnation point
j = jet
l = liquid phase
s = steam
sat = saturated
w = wall

References

[1] Bannister, R. L., and Little, D. A., 1993, ‘‘Development of Advanced Gas Turbine System,’’ *Proc. Joint Contractor Meeting: FE/EE Advanced Turbine System Conference; FE Fuel Cells and Coal-Fired Heat Engine Conference*, Aug., Morgantown, WV, pp. 3–15.

[2] Mukavetz, D. W., 1994, ‘‘Advanced Turbine System (ATS) Turbine Modification for Coal and Biomass Fuels,’’ in: *Proc. Advanced Turbine System Annual Program Review Meeting*, Nov. 9–11, ORNL/Arlington, VA, pp. 91–95.

[3] Guo, T., Wang, T., and Gaddis, J. L., 2000, ‘‘Mist/Steam Cooling in a Heated Horizontal Tube: Part 1 — Experimental System,’’ ASME J. Turbomach., **122**, pp. 360–365.

[4] Wachters, L. H. J., Smulders, L., Vermeulen, J. R., and Kleiweg, H. C., 1966, ‘‘The Heat Transfer From a Hot Wall to Impinging Mist Droplets in the Spheroidal State,’’ Chem. Eng. Sci., **21**, pp. 1231–1238.

[5] Goodyer, M. J., and Waterston, R. M., 1973, ‘‘Mist-Cooled Turbines,’’ *Proc. Conf. Heat and Fluid Flow in Steam and Gas Turbine Plant*, IMechE, pp. 166–174.

[6] Takagi, T., and Ogasawara, M., 1974, ‘‘Some Characteristics of Heat and Mass Transfer in Binary Mist Flow,’’ *Proc. 5th Int. Heat Transfer Conf.*, Tokyo, pp. 350–354.

[7] Ganic, E. N., and Rohsenow, W. M., 1973, ‘‘Dispersed Flow Heat Transfer,’’ Int. J. Heat Mass Transf. **20**, pp. 885–866.

[8] Mastanaiah, K., and Ganic, E. N., 1981, ‘‘Heat Transfer in Two-Component Dispersed Flow,’’ ASME J. Heat Transfer, **103**, pp. 300–306.

[9] Yoshida, H., Suenaga, K., and Echigo, R., 1988, ‘‘Turbulence Structure and Heat Transfer of a Two-Dimensional Impinging Jet With Gas–Solid Suspensions,’’ ASME HTD-Vol. 2, pp. 461–467.

[10] Lee, S. L., Yang, Z. H., and Hsyua, Y., 1994, ‘‘Cooling of a Heated Surface by Mist Flow,’’ ASME J. Heat Transfer, **116**, pp. 167–172.

[11] Buyevich, Yu. A., and Mankevich, V. N., 1995, ‘‘Interaction of Dilute Mist Flow With a Hot Body,’’ Int. J. Heat Mass Transf., **38**, pp. 731–744.

[12] Buyevich, Yu. A., and Mankevich, V. N., 1996, ‘‘Cooling of a Superheated Surface With a Jet Mist Flow,’’ Int. J. Heat Mass Transf., **39**, pp. 2353–2362.

[13] Fujimoto, H., and Hatta, N., 1996, ‘‘Deformation and Rebounding Processes of a Water Droplet Impinging on a Flat Surface Above Leidenfrost Temperature,’’ ASME J. Fluids Engineering, **118**, pp. 142–149.

[14] Hatta, N., Fujimoto, H., Kinoshita, K., and Takuda, H., 1997, ‘‘Experimental Study of Deformation Mechanism of a Water Droplet Impinging on Hot Metallic Surfaces Above Leidenfrost Temperature,’’ ASME J. Fluids Eng., **119**, pp. 692–699.

[15] Guo, T., Wang, T., and Gaddis, J. L., 2000, ‘‘Mist/Steam Cooling in a Heated Horizontal Tube: Part 2—Results and Modeling,’’ ASME J. Turbomach., **122**, pp. 366–374.

[16] Guo, T., Wang, T., and Gaddis, J. L., 2000, ‘‘Mist/Steam Cooling in a 180-Degree Tube,’’ ASME J. Heat Transfer, in press.

[17] Moffat, R. J., 1985, ‘‘Using Uncertainty Analysis in the Planning of an Experiment,’’ ASME J. Fluids Eng., **107**, pp. 173–178.

[18] Li, X., 1999, ‘‘Cooling by a Mist/Steam Jet,’’ Ph.D. Dissertation, Dept. of Mechanical Engineering, Clemson University, SC.

[19] Downs, S. J., and James, E. M., 1987, ‘‘Jet Impingement Heat Transfer—A Literature Survey,’’ ASME Paper No. 87-HT-35.

[20] Chen, J. C., and Costigan, X. Y., 1992, ‘‘Review of Post-Dryout Heat Transfer in Dispersed Two Phase Flow,’’ in: *Post-Dryout Heat Transfer*, G. F. Hewitt et al., eds., CRC Press Inc., FL, pp. 1–37.

[21] Martin, H., 1977, ‘‘Heat and Mass Transfer Between Impinging Gas Jets and Solid Surfaces,’’ Adv. Heat Transfer, **13**, pp. 1–60.

[22] Vader, D. T., Incropera, F. P., and Viskanta, R., 1991, ‘‘Local Convective Heat Transfer From a Heated Surface to an Impinging, Planar Jet of Water,’’ Int. J. Heat Mass Transf., **34**, pp. 611–623.

[23] Wolf, D. H., Viskanta, R., and Incropera, F. P., 1990, ‘‘Local Convective Heat Transfer From a Heated Surface to a Planar Jet of Water With a Nonuniform Velocity Profile,’’ ASME J. Heat Transfer, **112**, pp. 889–905.

R. J. Boyle
e-mail: R.J.Boyle@grc.nasa.gov

C. M. Spuckler
e-mail: C.M.Spuckler@grc.nasa.gov

B. L. Lucci
e-mail: B.L.Lucci@grc.nasa.gov

W. P. Camperchioli
e-mail: W.P.Camperchioli@grc.nasa.gov

NASA Glenn Research Center,
Cleveland, OH 44135

Infrared Low-Temperature Turbine Vane Rough Surface Heat Transfer Measurements

Turbine vane heat transfer distributions obtained using an infrared camera technique are described. Infrared thermography was used because noncontact surface temperature measurements were desired. Surface temperatures were 80°C or less. Tests were conducted in a three-vane linear cascade, with inlet pressures between 0.14 and 1.02 atm, and exit Mach numbers of 0.3, 0.7, and 0.9, for turbulence intensities of approximately 1 and 10 percent. Measurements were taken on the vane suction side, and on the pressure side leading edge region. The designs for both the vane and test facility are discussed. The approach used to account for conduction within the vane is described. Midspan heat transfer distributions are given for the range of test conditions.

[DOI: 10.1115/1.1333693]

Introduction

It is important to understand the effects of surface roughness on turbine blade heat transfer. Surface roughness is expected to increase blade surface heat transfer. Whether blade temperature increases, depends on the nature of the surface roughness. If the surface roughness results from low thermal conductivity material deposited onto the blade surface, the heat load, and therefore blade temperature, may decrease due to the thermal resistance of the deposition layer. If surface roughness results from material erosion, understanding blade heat transfer becomes more critical, since blade strength decreases, and average blade temperature increases due to higher gas side heat transfer.

Experimental heat transfer for rough surface turbine blades has been reported by several investigators. Dunn et al. [1] and Blair [2] used different techniques to measure rotor heat transfer in rotating facilities. Tarada [3], Tarada and Suzuki [4], and Abuaf et al. [5] reported measurements of vane heat transfer for rough surfaces. While these tests indicated higher heat transfer for rough surfaces, the heat transfer ratio between rough and smooth surfaces varied considerably. This may have been due to differences in Reynolds number as well as roughness characteristics.

To help clarify the consequences of surface roughness, a program to measure the heat transfer on a rough surface turbine vane was undertaken. It was felt that true surface temperatures, as opposed to temperatures between the roughness and the free stream, should be measured. Also, it was felt important to generate the heat flux at the vane surface, so as not to introduce an insulating layer between the heater and the vane surface. Temperature differences across an insulating layer of unknown thickness would adversely affect the measurements, especially at higher Reynolds numbers. These requirements led to a test configuration in which the rough surface was used to generate the heat flux, and temperatures were measured using an infrared camera. An infrared measurement technique was used because this technique does not rely on contact with the test surface, and does not disturb the surface profile. The infrared camera system generates a temperature map of the portion of the vane surface seen by the camera. Heat transfer measurements using an infrared camera have been reported by several investigators. Sargent et al. [6], Baldauf et al. [7], Johnston et al. [8], and Sweeney and Rhodes [9] used infrared cameras to measure different aspects of film cooling heat transfer.

The test facility allowed accurate flow measurements over a range of Reynolds numbers that varied by more than a factor of 20. A single vane was tested. Consequently, while the physical vane roughness remained constant, the surface went from being nearly hydraulically smooth to fully rough as the Reynolds number was varied. While the lower Reynolds numbers tests are lower than those for a typical high-pressure turbine application, they are approached in low power engine applications.

The purposes of the work reported herein are to show the effects of surface roughness on heat transfer, and to quantify when surface roughness is important. A companion paper, Boyle et al. [10], describes an analysis useful for predicting rough surface turbine heat transfer.

Description of Experiment

The measurements were taken in the three-vane linear cascade illustrated in Fig. 1. The center vane was the test vane. Air entered the test section at pressures between 0.14 and slightly greater than 1 atm. The air was at ambient temperature. Valves between the test section and a low-pressure altitude exhaust section were adjusted to maintain the desired vane exit isentropic Mach number. Periodicity was achieved by adjusting the tailboards. Further details of the test configuration are given by Boyle et al. [11]. This reference documented the inlet turbulence intensity and length scale for the range of Reynolds and Mach numbers used in the present work. Tests were done with and without the turbulence grid in place.

The vane was heated, and when steady state was achieved, vane surface temperatures were measured using an infrared camera system. The Inframetrics 600 camera was operated in the open mode (3 to 12 μm), and used a liquid nitrogen cooled detector. The output from the camera and its associated computer was the temperature at each pixel in an array. The pixel array size was 364 $\times 208$. The digital temperature output of the camera system was verified using a black body of known temperatures.

Both the inside and outside of the test section were painted with a flat black paint to reduce reflected thermal energy. This was done to minimize stray thermal energy onto the detector. The vane was viewed through each of the three window locations shown in Fig. 1. A ZnSe window, mounted flush with the inside surface, was used. The ZnSe window had a diamondlike coating to increase its surface hardness, and thus reduce the effects of abrasion from high speed flows. The coating was applied using the method described by Banks and Rutledge [12].

Data were obtained for a range of Reynolds and Mach numbers, and two inlet turbulence intensities. For each test there were three

---

Contributed by the International Gas Turbine Institute and presented at the 45th International Gas Turbine and Aeroengine Congress and Exhibition, Munich, Germany, May 8–11, 2000. Manuscript received by the International Gas Turbine Institute February 2000. Paper No. 2000-GT-216. Review Chair: D. Ballal.

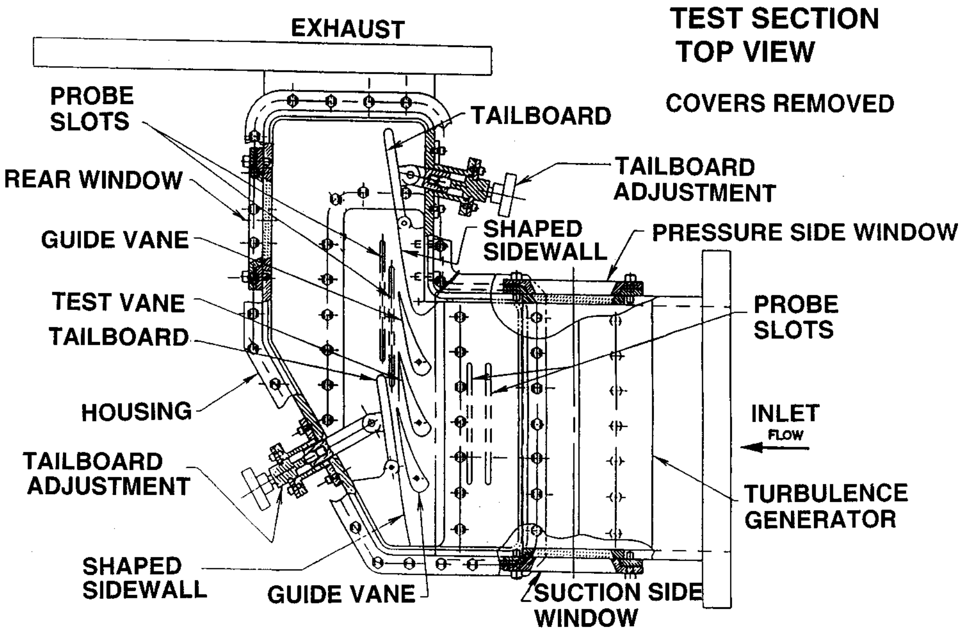

Fig. 1 Overall view of test section

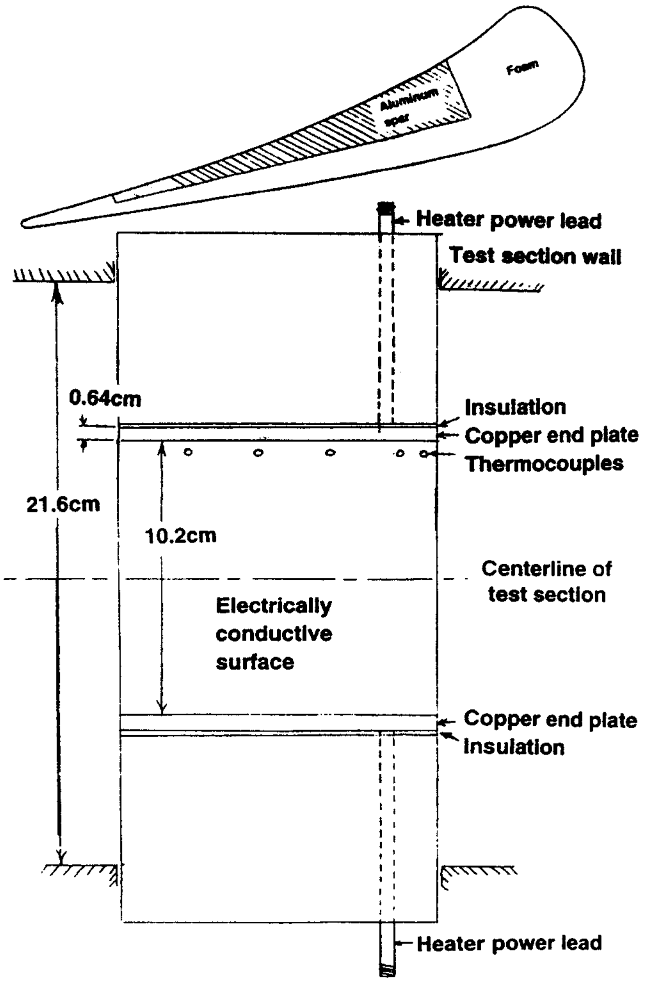

Fig. 2 Construction of heat transfer vane

views of the vane. The forward portion of the pressure surface was viewed through the pressure side window. The forward portion of the suction surface was viewed through the suction side window, and the rear portion of the suction surface was viewed through the rear window. A front-faced, highly reflecting mirror was used when viewing through the rear window. A region of the suction surface forward of the throat was not visible to the infrared camera. However, enough of the vane surface was visible that the effects of surface roughness could be quantified.

Figure 2 illustrates the test vane construction, and Table 1 gives the vane geometric parameters. The intent of the test was to make midspan measurements, away from the endwalls. Consequently, a high aspect ratio of 4.86 was specified, which gives a span-to-true chord ratio of 2.16. An aluminum vane was used, and much of the middle portion was removed. A spar was left in this region to provide rigidity to resist the pressure loads at high Mach and Reynolds numbers. Only the suction surface of the vane and the pressure surface near the leading edge were available for heat transfer measurements. A copper bus bar, shaped to the vane profile, was attached to each end of the opening. The bus bars were insulated from the aluminum vane, and had copper rods extending through the entire test section to provide electrical power. A high-strength, but low-thermal-conductivity foam material, Rohacell 300, was inserted between the copper bus bars. It was also shaped to the vane profile. Roughness was achieved by not smoothing the foam surface. The foam was securely bonded to the copper bus bars. After appropriate masking, an electrically conducting silver paint was sprayed onto the vane surface. This created an electric circuit between the bus bars. As shown in Fig. 2, the forward

Table 1 Test vane characteristics

Axial chord, C_x	4.445cm
True chord, C/C_x	2.25
Pitch-to-axial chord ratio	1.86
Span-to-axial chord ratio	4.86
Heated span-to-axial chord ratio	2.36
Flow turning	80°

Table 2 Average roughness properties

Property	Value	Normalized by C_x
R_{RMS}	$111 \pm 18\mu m$	$25 \pm 4 \times 10^{-4}$
R_a	$92 \pm 15\mu m$	$21 \pm 4 \times 10^{-4}$
Skewness	-0.58 ± 0.34	
Kurtosis	-0.42 ± 0.49	

portion of the pressure surface, all of the suction surface, and a small part of the pressure surface trailing edge region were painted. At room temperature the resistance of the heater was 0.07 Ω.

In addition to instrumentation to measure the heater voltage and current, nine Type E thermocouples were attached to the test section. Three thermocouples were attached to the aluminum spar near midspan. They were located between the foam and aluminum. Six thermocouples were placed on the vane surface at different locations close to the upper bus bar. They were insulated from the heater surface, and were attached with an epoxy covering. Five thermocouple locations are shown in Fig. 2. The sixth thermocouple is on the vane pressure side. The surface thermocouples could not be used for an *in situ* calibration of the infrared camera. Because the surface thermocouples were secured using an epoxy covering, they did not read the surface temperature. The difference between the thermocouple and infrared temperatures varied with the flow condition. The thermocouple locations were known, and because the infrared temperature differed from the thermocouple's surrounding temperature, they were used to locate the pixel coordinates onto the vane surface. The thermocouple locations were especially visible during transient cool down.

Roughness Characteristics. Data from six profilometer traces were used to determine the roughness characteristics of the heated surface. Each trace was approximately 1 cm in length. A summary of the analysis of these traces is presented in Table 2. The rms roughness averaged slightly over 100 μm, while the average absolute roughness height was 92 μm. The 1 σ variation in these parameters among the six traces was approximately 16 percent. The skewness showed considerable variation among the traces, but was always negative. Negative skewness means that the area above the meanline exceeds the area below the meanline. The average kurtosis was negative, with only one trace evidencing a positive value. According to Dagnall [13] a negative kurtosis indicates a bumpy, rather than spiky, surface profile.

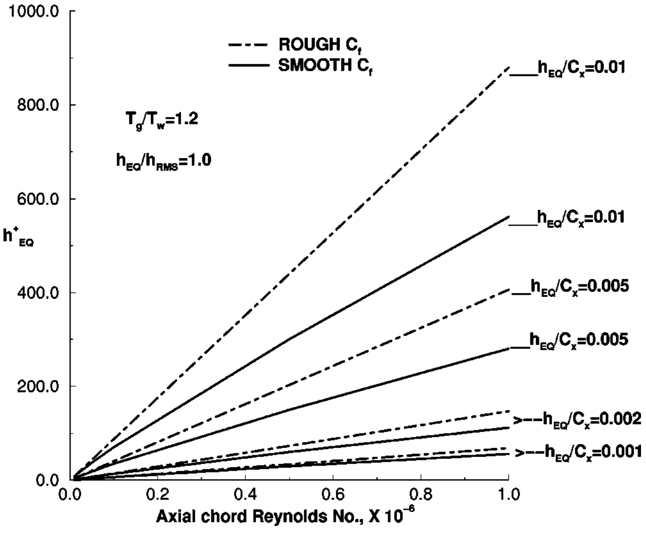

Fig. 3 Estimated maximum equivalent roughness height, h^+_{EQ}

The roughness height of 111 μm corresponds to h_{RMS}/C_x of 0.0025, or h_{RMS}/C of 0.001. Kind et al. [14] reported aerodynamic effects for rotors having bands of roughness in the height-to-chord range of 0.0021 to 0.0063. Aerodynamic tests for uniformly covered sand grain roughness in the range of h_{EQ}/C between 0.001 and 0.01 have been reported by Bammert and Sandstede [15,16] and by Boynton et al. [17].

The degree to which surface roughness affects the flow and heat transfer is determined by its value in wall normalized coordinates. The maximum normalized roughness height, h^+_{EQ}, was estimated using the procedure proposed by Boyle and Giel [18] to estimate the maximum near wall grid spacing prior to a CFD calculation.

$$h^+_{EQ}=0.17\frac{h_{\text{RMS}}}{C_x}\sqrt{\frac{(C_f)_{\text{ROUGH}}}{(C_f)_{\text{SMOOTH}}}}\left(\frac{h_{\text{EQ}}}{h_{\text{RMS}}}\right)\left(\frac{T_{IN}}{T_V}\right)^{1.5}\text{Re}^{0.9}$$

where Re is a Reynolds number based on axial chord, C_x. To maximize h^+_{EQ}, Re is taken as the exit Reynolds number, Re_2. The ratio of h_{EQ} to h_{RMS} was estimated to be about two for the vane tested. Figure 3 shows h^+_{EQ} as a function of Re_2 and h_{EQ}/C_x for two friction factors. The curves labeled SMOOTH are for a C_f ratio of one. The curves labeled ROUGH are for fully rough flow using the relationship for $C_f/2$ given by Kays and Crawford [19]

$$\frac{C_f}{2}=\frac{0.168}{[\ln(864\delta_2/h_{EQ})]^2}$$

This figure shows that h^+_{EQ} increases almost linearly with Reynolds number and with the roughness height. For $h^+_{EQ}>70$, the ROUGH curve is the appropriate curve to use for estimating h^+_{EQ}. For $5<h^+_{EQ}<70$, the appropriate value for h^+_{EQ} lies between the two curves. Fortunately, in this region the differences between the SMOOTH and ROUGH curves are small. Since the equivalent height ratio was estimated to be about two, and $h_{\text{RMS}}/C_x=0.0025$, the maximum equivalent height at each Reynolds number was expected to be on the ROUGH C_f line for $h_{\text{RMS}}/C_x=0.005$. At high Reynolds numbers, the maximum h^+_{EQ} was expected to be given by the dashed curve for $h_{EQ}/C_x=0.005$. As the Reynolds number decreases, the maximum h^+_{EQ} was expected eventually to be given by the solid line at the same value for h_{EQ}/C_x.

Analysis of Data

The measured temperatures were corrected to give the true surface temperature. This correction accounts for the emissivity of the vane surface, the emissivity and temperature of the surroundings, and the ambient temperature. The IR camera system measured the true temperature of a black body when the emissivity was one. The measured temperature, T_M, is determined from a heat balance on the infrared camera receiver. The energy incident on the detector is less than the emitted energy. The camera system cuts off energy at wavelengths above 12 μm. Camera temperatures were determined by energy in the 3 to 12 μm band. Because of the small measured temperature differences, and the wide wavelength band, the variation in the fraction of energy incident on the detector was neglected. The energy on the detector is $q_{\text{IR}}=f(3{,}12)_M\sigma T_M^4$, where $f(3{,}12)$ is the fraction of available radiant energy in the 3–12 μm band, and is a function of temperature. In actuality the heat flux is given by:

$$q_{\text{IR}}=\sigma(\tau_W(\epsilon_V f(3{,}12)_V T_V^4+\rho_V\epsilon_{SR}f(3{,}12)_{SR}T_{SR}^4)+(1-\tau_W)\epsilon_A f(3{,}12)_A T_A^4)$$

The fraction of available energy, $f(3{,}12)$, was assumed constant. Calculations showed that, because of the small temperature differences, no significant error was introduced by assuming $f(3{,}12)$ constant. Equating the two expressions for the heat flux gives the vane temperature as:

$$T_V^4=\frac{T_M^4-(1-\tau_W)\epsilon_A T_A^4-\tau_W\rho_V\epsilon_{SR}T_{SR}^4}{\tau_W\epsilon_V}$$

At each point on the vane the Nusselt number is calculated from:

$$\mathrm{Nu}=\frac{q_{\mathrm{NET}}C_x}{(T_V-T_r)K}$$

The local adiabatic recovery temperature, T_r, was determined from the inlet total temperature, T'_{IN}, and the surface pressure distribution. The surface pressures were determined from a two-dimensional Navier–Stokes analysis [20].

The vane local net heat flux was calculated from:

$$q_{\mathrm{NET}}=q_{\mathrm{ELEC}}-q_{\mathrm{COND}}-q_{\mathrm{RAD}}$$

Null Tests. If the resistivity of the heater were uniform, q_{ELEC} would be given by: $q_{\mathrm{ELEC}}=VI/A=\overline{q}$. However, measurements indicated that the heat flux was not uniform, so that the ratio of local-to-average heat flux, F, had to be determined. Tests were done where the heat transfer was known to be nearly uniform over the vane surface. For these tests heat transfer was by free, not forced convection. For turbulent free convection the heat transfer is independent of the streamwise location. For turbulent flow over a vertical flat plat Burmeister [21] gives a correlation for the local Nusselt number as:

$$\mathrm{Nu}_x=0.1(\mathrm{Gr}_x\mathrm{Pr})^{1/3}$$

Here, x is the spanwise distance. Since $\mathrm{Gr}_x=gx^3(T_V-T'_{IN})/(\nu^2T'_{IN})$, Nu is independent of x, but depends on $T_V-T'_{IN}$ to the one-third power. For this test condition:

$$\frac{q_{\mathrm{ELEC}}}{\overline{q}}=F=\frac{\left(\dfrac{T_V-T'_{IN}}{\overline{T_V-T'_{IN}}}\right)^{4/3}+q_{\mathrm{COND}}/\overline{q_{\mathrm{NET}}}+q_{\mathrm{RAD}}/\overline{q_{\mathrm{NET}}}}{1+\overline{q_{\mathrm{COND}}}/\overline{q_{\mathrm{NET}}}+\overline{q_{\mathrm{RAD}}}/\overline{q_{\mathrm{NET}}}}$$

At each point on the vane surface q_{COND} is evaluated from the temperature distribution around the vane. $\overline{q_{\mathrm{COND}}}$ is evaluated using the average surface temperature and measured metal temperatures. $q_{\mathrm{RAD}}/\overline{q_{\mathrm{NET}}}$ is approximated by:

$$\frac{q_{\mathrm{RAD}}}{\overline{q_{\mathrm{NET}}}}=\frac{\overline{q_{\mathrm{RAD}}}}{\overline{q_{\mathrm{NET}}}}\left(\frac{T_V-T_{SR}}{\overline{T_V-T_{SR}}}\right)$$

$\overline{q_{\mathrm{COND}}}$ was evaluated using a two-dimensional conduction analysis. The analysis used the average surface temperature and measured metal spar temperature.

Flow Tests. For test with flow over the vane, the local Nusselt is given by:

$$\mathrm{Nu}=\frac{(FVI/A-q_{\mathrm{COND}}-q_{\mathrm{RAD}})C_x}{(T_V-T_r)K}$$

The term q_{COND} was evaluated for each test using the same two-dimensional conduction analysis as for the null test. In the flow test the heat transfer distribution was not uniform, but varied with circumferential location. The local value of F was found from the null test.

Since the flow in the cascade is two dimensional, the spanwise-averaged Nusselt number is of interest. This value was obtained by integrating in the spanwise direction. At each distance around the vane, the heat transfer coefficient was averaged over a fraction of the spanwise distance. When the fraction was very small, the result was the midspan values. However, these values, in addition to being noisy, were very sensitive to the spanwise alignment of the infrared camera images. Averaging over a 40 percent of the heated span gave less alignment sensitivity and less point-to-point variations in the heat transfer.

The uncertainty in the Nusselt number was estimated to be about 15 percent over most of the vane surface. The uncertainty in the infrared camera measurements was better than 2°C, and the camera resolved differences of less than 0.2°C. The infrared camera uncertainty was minimized by verifying the camera system output for a calibrated black body, and by comparing the pretest surface temperatures with the inlet thermocouple readings. The maximum uncertainty occurred at the minimum surface-to-gas temperature difference. The maximum surface temperature of 80°C was set based on the temperature capability of the foam material. This temperature occurs at the minimum Nusselt numbers. The large variation in Nusselt numbers meant that at high Nusselt numbers, the surface-to-gas temperature difference was much less than 60°C. The estimate was made by assigning uncertainties to all of the variables used in the data reduction, and doing the analysis repetitively. The local heat flux was determined by properties in addition to the heater voltage and current. The uncertainty analysis treated the determination of F as a part of the analysis, and not as an independent quantity. This has the beneficial effect of reducing heat transfer uncertainty due to some independent variables, such as thermal conductivity. The one region where there is a higher uncertainty in heat transfer is the very rear portion of the suction surface. At the design of the test vane, the assumption was made that the heat transfer rate at the very rear of the suction and pressure surfaces would be the same. This was done on the basis of CFD analyses. However, the experiment was unable to verify this assumption under flow conditions. A temperature difference across the vane near the trailing edge would affect low Nusselt number measurements more than those at higher Nusselt numbers.

There was also a positional uncertainty due to the alignment of the camera. This uncertainty was estimated to be less than $0.05C_x$.

Experimental Results

Table 3 shows the range of test conditions for which data were obtained. Data were obtained at three isentropic exit Mach numbers for a range of inlet total pressures. The Reynolds numbers in this table are based on axial chord, and varied by nearly a factor of 15 over the range of test conditions. At each test point, data were obtained for two inlet turbulence intensities. Boyle et al. [11] reported that the turbulence intensity, measured 1.14 axial chords upstream of the leading edge, was between 13 and 15 percent over the range of test conditions. Air was blown through the grid to achieve a pitchwise uniformity in turbulence intensity.

The results obtained for the entire heated span at a single test condition will be discussed first. This is followed by a discussion of the midspan results for all of the test cases.

Full-Span Results. Figures 4–7 illustrate full span results for a typical test case. The case is for $\mathrm{Re}_2=0.394\times10^6$, $\mathrm{M}_2=0.7$, with the turbulence grid. The temperatures recorded by the infra-

Table 3 Summary of test conditions

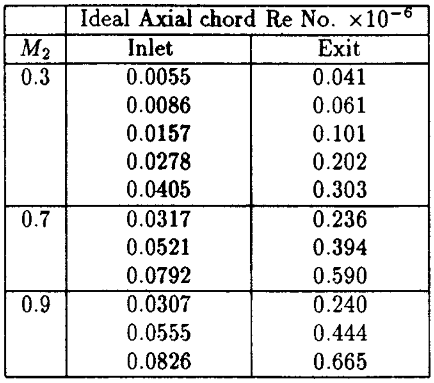

	Ideal Axial chord Re No. $\times10^{-6}$	
M_2	Inlet	Exit
0.3	0.0055	0.041
	0.0086	0.061
	0.0157	0.101
	0.0278	0.202
	0.0405	0.303
0.7	0.0317	0.236
	0.0521	0.394
	0.0792	0.590
0.9	0.0307	0.240
	0.0555	0.444
	0.0826	0.665

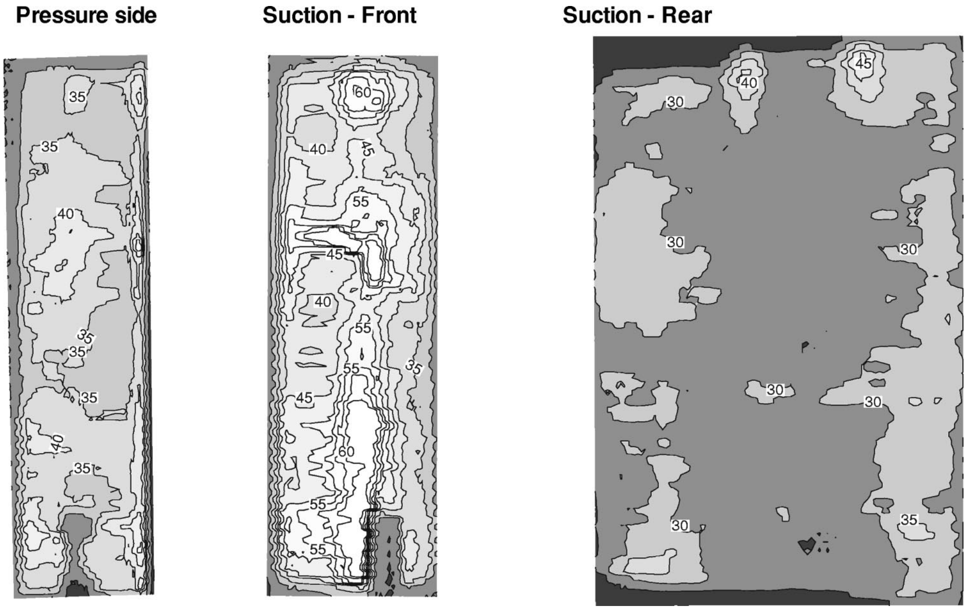

Fig. 4 Temperatures recorded by infrared camera, °C

red camera are given, followed by the calculated vane surface temperatures. Next, the surface Nusselt numbers are shown. The Nusselt number distribution is shown when the heat generation is assumed uniform, and this is followed by the Nusselt number distribution calculated using the local heat generation determined from the null test. Figure 4 shows the infrared camera temperature distribution for the vane for a typical test case. The views as seen through each of the three windows are shown. The heated portion of the pressure surface is followed by the forward portion of the suction surface, and ends with the rear part of the suction surface. Moving from left to right in the pressure side view shows the forward part of the pressure surface, the leading edge region, and a small portion of the suction surface.

Similarly, the forward view of the suction side shows a small portion of the pressure side, the leading edge, and the front portion of the suction side. The rear suction side view begins near the throat region, and continues to the trailing edge. The first two parts overlap in the leading edge region. In the lower region of the two front views there are apparent discontinuities in the surface temperatures. These are the result of sensor probes in the line of sight between the vane and the camera, and were left in the camera's view to help align the images. The spanwise temperature variation is due to heat generation nonuniformity and variations in surface roughness. In each view, near the blade top, there are small islands of large temperature gradients. These islands, labeled 35, 60, 40, and 45°C, correspond to thermocouple locations. A high degree of spatial resolution is visible in these figures. The suction surface rear view shows cold temperatures in the middle of the surface distance. Since this is where the insulating foam is thinnest, it is reasonable to suspect that this is a region of high conductive heat loss. While the conductive heat loss to the cold aluminum spar can be significant in this region, this is also a

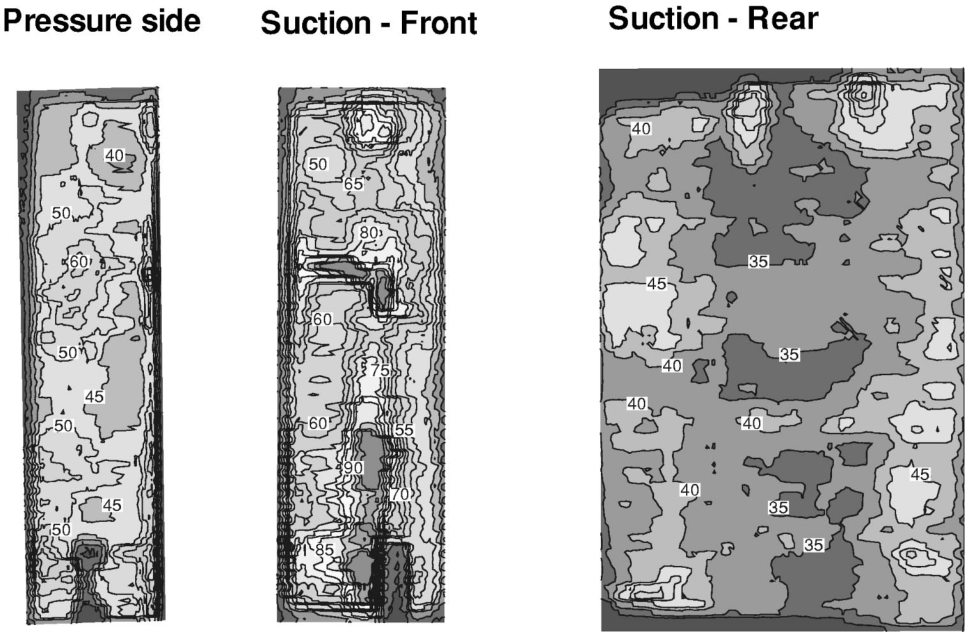

Fig. 5 Calculated surface temperatures, °C

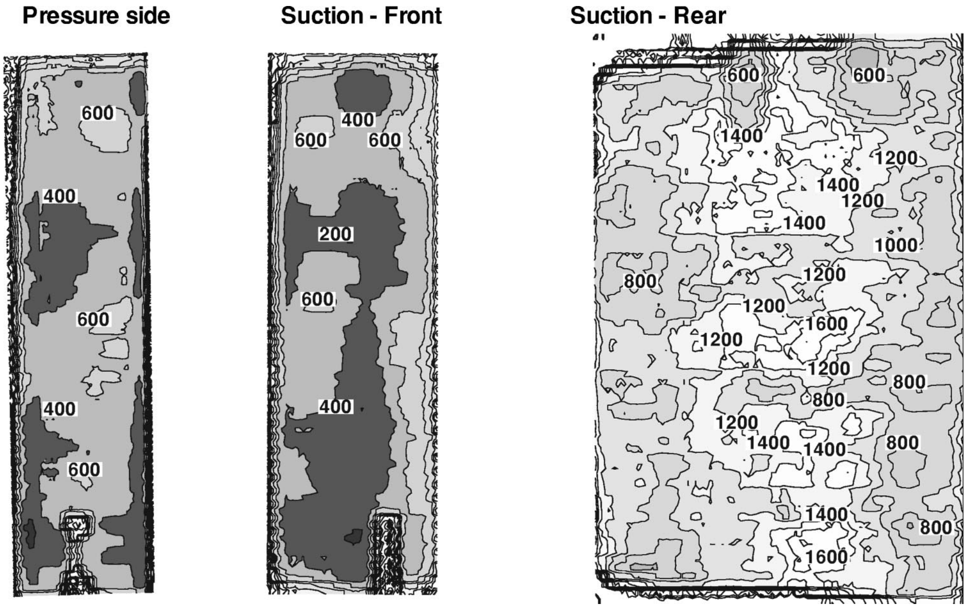

Fig. 6 Nusselt number, uniform heat flux

region of lower than average heat generation. If conduction were the cause of the cold temperatures, its relative importance decreases as the Reynolds number and external heat transfer increase. The temperatures would become more uniform at high convective heat transfer rates. However, this was not the case, and using measured values for the foam thermal conductivity showed that the generated heat flux in this region was lower than average.

Figure 5 shows the calculated temperatures using the measured infrared camera temperatures, the surrounding temperature, the ambient temperature, the vane emissivity, and the window transmissivity. At the two higher Mach numbers, the surrounding temperature varied from view to view. It was calculated as the adiabatic temperature seen on the adjacent vane. Even though the silver paint has a low emissivity on a smooth surface, measurements of the rough vane surface gave an emissivity of approximately 0.75. The measured emissivity was influenced by several factors. Considerable variations in emissivity were observed, and the effect of a variation in emissivity is discussed. The transmission of the ZnSe window was found to be approximately 0.7, when viewing at a near normal angle. This transmissivity was consistent with the calculated value using the index of refraction for the material. When the vane was viewed through the rear window, the transmissivity was reduced to 0.65 to account for both the mirror reflectivity and the highly oblique angle to the window. There is a temperature discontinuity when the camera views a surface other than the heated one. This could be either an adjacent vane or the unheated portion of the test vane. However, this temperature difference is spread out over several pixels when the camera views the vane through the ZnSe infrared window at a nonnormal angle. The thickness of the window displaces the image in the streamwise direction for images passing through at oblique angles.

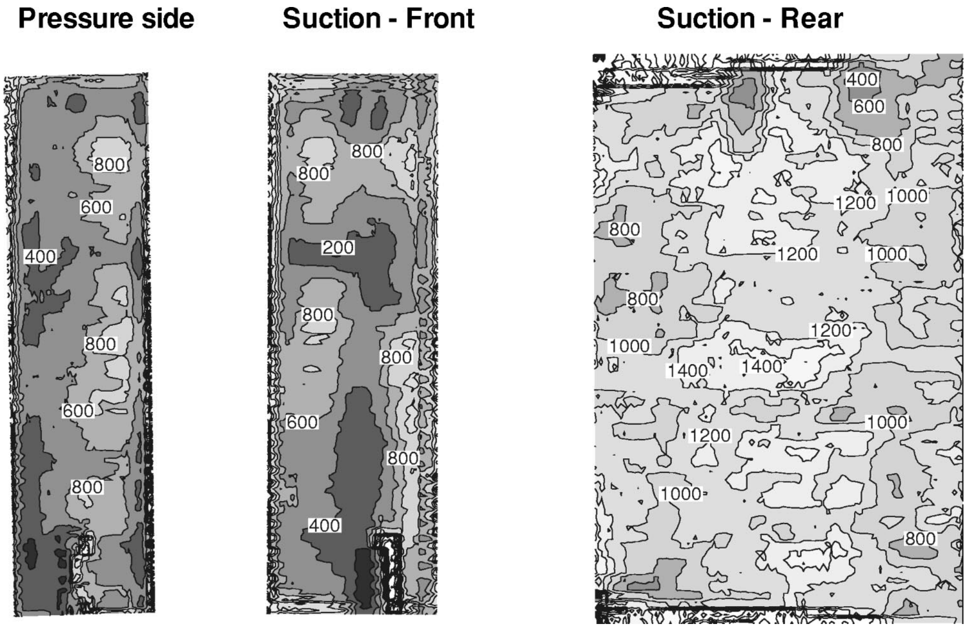

Fig. 7 Nusselt number, nonuniform heat flux

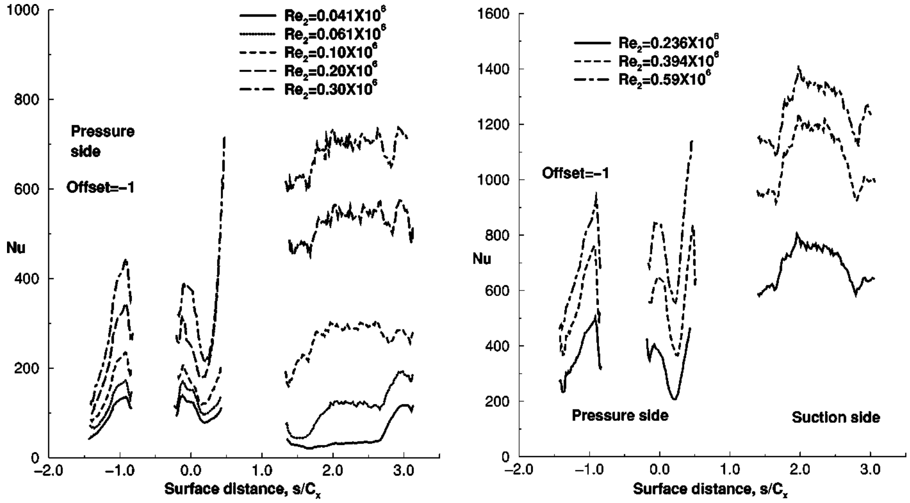

a) Nusselt number for M_2=0.3, No grid

d) Nusselt number for M_2=0.7, Turbulence grid.

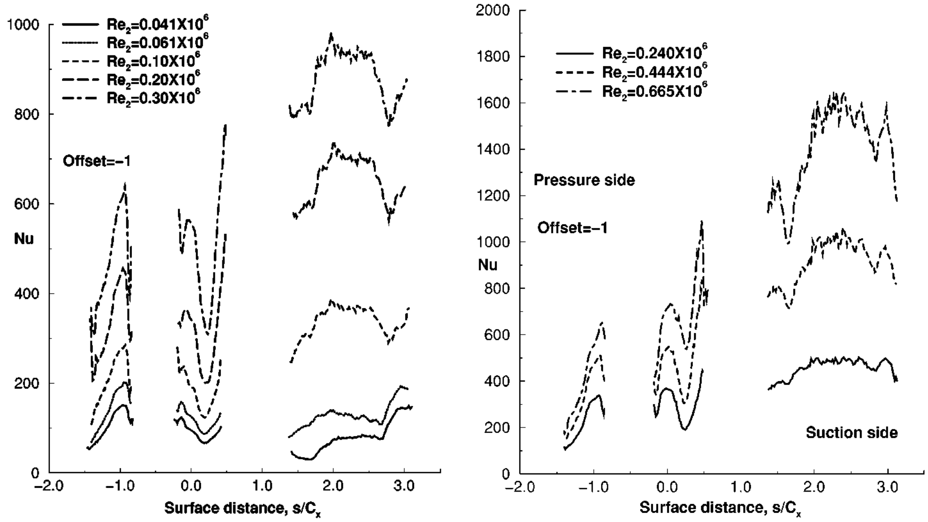

b) Nusselt number for M_2=0.3, Turbulence grid.

e) M_2 =0.9 No grid.

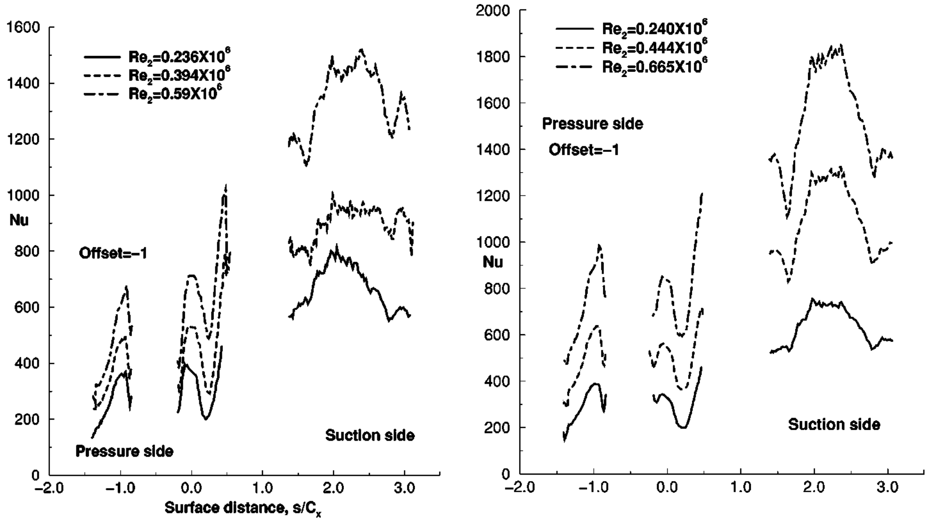

c) Nusselt number for M_2=0.7, No grid.

f) M_2 =0.9 Turbulence grid.

Fig. 8 Midspan Nusselt numbers

Figure 6 shows the Nusselt number distribution based on a uniform heat flux. This Nusselt number distribution includes the corrections for radiation from the heated vane and conduction to the aluminum spar. The correction for radiation was small. At this Reynolds number the correction for conduction to the spar was also small. High temperature regions in Fig. 5 correspond to low Nusselt number regions in Fig. 6.

Figure 7 shows the Nusselt distribution after correcting for the nonuniformity in the electrical heat flux. Since there were variations in surface roughness on the vane surface, there would not be spanwise uniformity in the Nusselt number distribution for a uniform heat flux. Some of the spanwise nonuniformity seen in this figure could be the result of nonuniformity in the surface roughness. The pressure side view shows a low-Nusselt-number region on the pressure side of the leading edge. The heat transfer rises to the leading edge and beyond. The front suction view shows high heat transfer on the pressure side, a decrease in heat transfer, followed by an increase on the suction side of the vane. The suction rear view shows a fairly uniform level over much of the region away from the end bus bars. Midway along the surface of this view, and near midspan there is a high heat transfer region. Either high surface roughness or overestimating heat generation in this region could account for this apparent high heat transfer. An error in calculating the local value of *F* causes a bias in the heat generation throughout the entire range of test conditions.

Midspan Results. The data for each case were averaged over different fractions of the heated span. No significant variation in the spanwise-averaged Nusselt number distribution was observed for averaging regions of 20 and 40 percent of the heated span.

M_2=0.3 Results. Figure 8 shows the midspan heat transfer distribution for the different Reynolds numbers at the three vane exit Mach numbers, and for the two inlet turbulence intensities. Each part of the figure shows data for a single Mach number. Successive parts show data at low and high turbulence levels. High turbulence being the result of the upstream grid. For clarity, the pressure side window data have been offset on the plot by $s/C_x = -1$. In reality there is an overlap in the leading edge region. The two suction surface views have a gap between them, because the camera could not view a region upstream of the throat. The no-grid data at $M_2 = 0.3$ shown in Fig. 8(*a*) clearly show suction surface transition moving forward as the Reynolds number increases. Data for the forward portion of the suction side show a heat transfer peak on the pressure side of the leading edge. Nu increases approaching the leading edge, $s/C_x = 0$, from the pressure side, then decreases. This is followed by a rapid increase, and is most evident at higher Reynolds numbers.

The pressure side data do not show the peak leading edge heat transfer at $s/C_x = -1$ in the plot. The peak is over onto the suction surface. The surface on the far side of the leading edge is nearly tangential to the camera view. The discrepancy between the two views could be due to unaccounted variation in surface emissivity with viewing angle to the surface. In the overlap region the pressure side view heat transfer is somewhat higher.

Figure 8(*b*) gives the Nusselt numbers for the same exit Mach number as in part 8(*a*), but with the grid installed. The presence of the grid increases the Nusselt number, even for the rear portion of the suction surface. For these tests, and those at higher Mach numbers, air was blown through the grid. Tests were done, viewing the rear portion of the suction surface, with no grid air. The turbulence intensity varied significantly in the pitchwise direction for the unblown grid [11]. However, no significant Nusselt number differences were seen for the unblown grid test.

High M_2 Results. At an exit Mach number of one, the flow chokes, so that the flow rate at constant Reynolds number does not increase significantly as the Mach number increases from 0.7 to 0.9. As expected, the data obtained by viewing through the two forward windows at $M_2 = 0.7$ and $M_2 = 0.9$ are similar to those for $M_2 = 0.3$. Even at the higher exit Mach numbers, the upstream Mach numbers are less than 0.3. For the two higher exit Mach numbers there is not as consistent an increase in suction side rear heat transfer with increased turbulence. What was observed, but is not evident in the figures, is an indication of a lower than expected recovery factor for a rough surface. It was observed that measurements with lower wall-to-gas temperature differences gave higher heat transfer rates. The recovery temperatures were calculated using a recovery factor of 0.89. A lower recovery factor, approximately 0.8, resulted in Nusselt numbers for the rear portion of the suction surface independent of the wall-to-gas temperature difference. This is consistent with the observation of Hodge et al. [22] that a rough surface has a lower recovery factor than a smooth one.

Fixed Point Comparisons. Next, specific vane regions are examined to identify the effects of roughness on the vane heat transfer. Figure 9 shows the Frossling number, Fr, at the vane stagnation point. If roughness had no effect, the low turbulence intensity Frossling number is expected to be in the range 0.85–1.0 [23]. The data in Fig. 9(*a*), for low turbulence intensity, show increased Frossling number with increased Reynolds number. The low Frossling numbers, seen for the front suction side data at low Reynolds numbers, may be due to uncertainty in the position of the stagnation point in the camera view. If the leading edge line in the data reduction was not the true leading edge line, then the Frossling number would be less than the stagnation point value.

Figure 9(*b*) shows stagnation point heat transfer for the turbulence grid data. The grid resulted in a high turbulence level, mea-

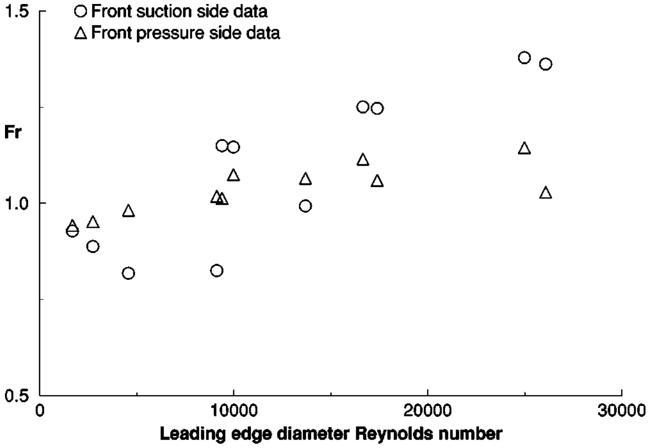

a) No grid - Tu=1%

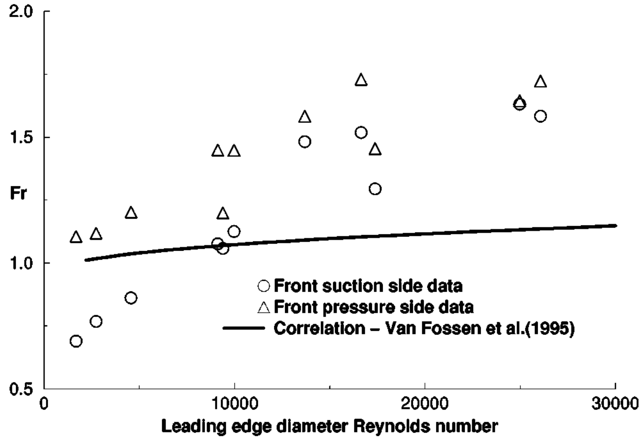

b) Turbulence grid

Fig. 9 Frossling number at vane stagnation point

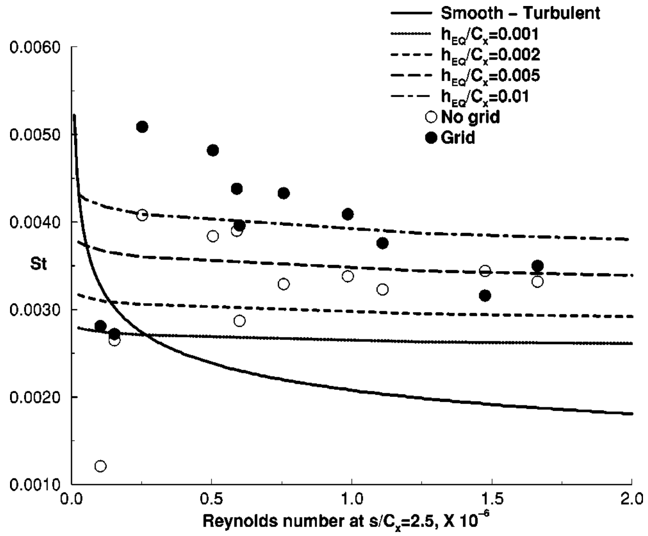

Fig. 10 Stanton number at $s/C_x=2.5$

sured as more than 13 percent approximately one axial chord upstream of the leading edge. The trend of an increased Frossling number with increase Reynolds number is similar to the no-grid results. However, the slope, especially in the lower Reynolds number region, is greater. This figure also shows predictions using a correlation developed by Van Fossen et al. [23] for a smooth leading edge. The correlation accounts for turbulence intensity and length scale effects on leading edge heat transfer. Primarily, because of the large turbulent length scale to leading edge diameter ratio, the correlation gives a relatively small increase in Frossling number. Over much of the Reynolds number range, the effect of roughness on Frossling number is significantly greater.

Figure 10 shows the Stanton number at $s/C_x=2.5$. This location was chosen because the heat transfer coefficient is representative of the rear part of the suction surface. Results are presented in terms of Stanton number, St=Nu/Re/Pr, since this quantity varies slowly with Reynolds number. In addition to the experimental data, correlation curves are shown. The turbulent Stanton number correlation for a smooth surface is shown along with results from a correlation given by Kays and Crawford [19] for rough surfaces. This correlation is:

$$\mathrm{St}=\frac{C_f/2}{\mathrm{Pr}_t+\sqrt{C_f/2}/\mathrm{St}_h}$$

and

$$\mathrm{St}_h=C\left(\mathrm{Re}\,\frac{h_{EQ}}{C_x}\sqrt{\frac{C_f}{2}}\right)^{-0.2}\mathrm{Pr}^{-0.44}$$

The constant, C, which is a function of the roughness geometry is taken as 1. While the appropriate value for this vane geometry is not known, the data of Pimenta et al. [24] for closely packed spheres corresponded to a value of $C=1.0$. The Reynolds number is taken as $\mathrm{Re}=\mathrm{Re}_2 s/C_x$. $C_f/2$ is determined from the rough surface correlation for a range of h_{EQ}/C_x values. The turbulent Prandtl number, Pr_t, was assumed to be 0.9.

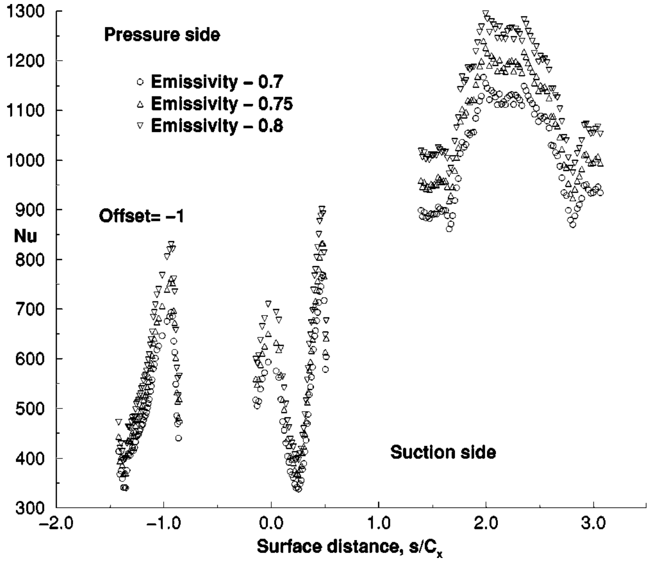

Fig. 11 Effect of emissivity variation, $\mathrm{Re}_2=0.394\times10^6$, $M_2=0.7$, grid

The lowest Reynolds number no-grid case has a Stanton number below the turbulent correlation. This value is consistent with a Stanton number for laminar flow. The data for the next highest Reynolds number are close to the smooth correlation for turbulent flow. At this Reynolds number, and lower, the flow appears to be hydraulically smooth, as it also does for the grid cases. The no-grid cases show a rapid increase in Stanton number, followed by a decrease in Stanton number, eventually approaching the $h_{EQ}/C_x=0.005$ curve at high Reynolds numbers. Stanton numbers just after transition are typically higher than the turbulent value. As was mentioned earlier, the expected value for h_{EQ}/C_x was 0.005. With the turbulence grid in place, the trend shows higher Stanton numbers at lower Reynolds numbers, and a more negative slope of Stanton number versus Reynolds number. The grid Stanton numbers approach the no-grid values at high Reynolds numbers.

Emissivity Variations. As mentioned earlier, measurements of the surface emissivity gave a considerable amount of uncertainty. Among the factors that contributed to the emissivity uncertainty were the angle to the camera; the position on the vane; and uncertainty in the reference black paint emissivity. Figure 11 shows the midspan Nusselt number distribution for three values of the surface emissivity. The three values are the estimated value of 0.75±0.05. Increasing the vane emissivity causes the vane temperature to decrease. This in turn causes the vane-to-gas temperature difference to decrease. While the Nusselt number does increase, as expected, the increase is not large. The number of symbols in each line are the number of pixels in the streamwise direction. The number of pixels per unit length were approximately the same in the spanwise and streamwise directions.

Conclusions

The experimental results showed that an infrared camera technique is a useful tool for measuring turbine heat transfer over the entire blade surface. Knowledge of surface emissivity and window transmission is important to achieving accurate results. Verifying the camera system output with a calibrated black body source, and verifying the agreement between the gas temperature measurement and surface temperatures measured with the infrared camera, results in accurate heat transfer even when the temperature differences are small. The portion of the blade surface for which the heat transfer is measured is controlled by optical access. The portion of the surface viewed through each window is determined by the adjacent blades. The fraction of the surface viewed is determined by the solidity as well as blade shape. Even though in this application the measurements were averaged to obtain the midspan heat transfer, spanwise as well as streamwise variations in surface temperatures were readily measured. This technique is applicable to measuring surface heat transfer resulting from three-dimensional flows.

Leading edge Frossling numbers increased with increasing Reynolds number. The increase was significantly greater than was expected from free-stream turbulence effects. The trend in the low-turbulence intensity data showed Frossling numbers approaching 1.3 at high Reynolds numbers. This is 30–40 percent greater than is expected for leading edge heat transfer of a smooth vane. When the inlet turbulence intensity was increased, the trend in leading edge Frossling number showed a higher initial slope. At high Reynolds numbers, the Frossling number approached 1.7. The increased Frossling number at high turbulence was again greater than expected for a smooth surface, and approached 50 percent at high Reynolds numbers. The heat transfer augmentation due to roughness increased with Reynolds number throughout the range of test conditions.

The heat transfer on the rear portion of the suction surface was greater than would be expected for a smooth vane by nearly a factor of two at high Reynolds numbers. For the low-turbulence test cases, the ratio was less as the Reynolds number decreased. However, with a high turbulence intensity, the ratio remained close to two for Reynolds numbers of 101,000 and greater. Only for Reynolds numbers of 61,000 or less was the heat transfer consistent with that for a smooth surface. The estimated equivalent roughness height, h_{EQ}^{+} was approximately 23 at a Reynolds number of 61,000. This value of 23 corresponds to a transitionally rough equivalent height.

Acknowledgments

The authors wish to thank Dr. James Van Fossen for the two-dimensional computer code used for the analysis of the conduction losses.

Nomenclature

A = area of heat surface
$C_f/2$ = friction factor
C_x = axial chord
D = leading edge diameter
F = local-to-average heat flux
f = fraction of radiant energy
Fr = Frossling number $= \mathrm{Nu}_D/\sqrt{\mathrm{Re}_D}$
Gr = Grashof number
h = roughness height
I = current
K = thermal conductivity
Nu = Nusselt number
Pr = Prandtl number
q = heat flux per unit area
Re = Reynolds number
St = Stanton number
s = surface distance
T = temperature
Tu = turbulence intensity
V = voltage
x = spatial coordinate
δ_2 = momentum thickness
ϵ = emissivity
ν = kinematic viscosity
ρ = reflectivity
σ = Stefan–Boltzmann constant
τ = transmissivity

Subscripts

A = ambient
a = absolute difference from mean
COND = conduction
ELEC = electrical
EQ = sand grain equivalent
IN = gas inlet
IR = infrared
M = measured
NET = net to gas
RAD = radiation
RMS = rms value
r = recovery
SR = test section surroundings
v = vane surface
w = window
1 = inlet
2 = exit

Superscripts

$+$ = normalized
$'$ = total
$-$ = average

References

[1] Dunn, M. G., Kim, J., Civinskas, K. C., and Boyle, R. J., 1994, ''Time-Averaged Heat Transfer and Pressure Measurements and Comparison With Prediction for a Two-Stage Turbine,'' ASME J. Turbomach., **116**, pp. 14–22.
[2] Blair, M. F., 1994, ''An Experimental Study of Heat Transfer in a Large-Scale Turbine Rotor Passage,'' ASME J. Turbomach., **116**, pp. 1–13.
[3] Tarada, F., 1987, ''Heat Transfer to Rough Turbine Blading,'' PhD thesis, University of Sussex, England.
[4] Tarada, F., and Suzuki, M., 1993, ''External Heat Transfer Enhancement to Turbine Blading Due to Surface Roughness,'' ASME Paper No. 93-GT-74.
[5] Abuaf, N., Bunker, R. S., and Lee, C. P., 1998, ''Effects of Surface Roughness on Heat Transfer and Aerodynamic Performance of Turbine Airfoils,'' ASME J. Turbomach., **120**, pp. 522–529.
[6] Sargent, S. R., Hedlund, C. R., and Ligrani, P. M., 1998, ''An Infrared Thermography Imaging System for Convective Heat Transfer Measurements in Complex Flows,'' Meas. Sci. Technol., **9**, pp. 1974–1981.
[7] Baldauf, S., Schulz, A., and Witting, S., 1999, ''High Resolution Measurements of Local Heat Transfer Coefficients by Discrete Hole Film Cooling,'' ASME Paper No. 99-GT-43.
[8] Johnston, C. A., Bogard, D. G., and McWaters, M. A., 1999, ''Highly Turbulent Mainstream Effects on Film Cooling of a Simulated Airfoil Leading Edge,'' ASME Paper No. 99-GT-261.
[9] Sweeney, P. C., and Rhodes, J. F., 2000, ''An Infrared Technique for Evaluating Turbine Airfoil Cooling Designs,'' ASME J. Turbomach., **122**, pp. 171–178.
[10] Boyle, R. J., Spuckler, C. M., and Lucci, B. L., 2000, ''Comparison of Predicted and Measured Vane Rough Surface Heat Transfer,'' ASME Paper No. 2000-GT-0217.
[11] Boyle, R. J., Lucci, B. L., Verhoff, V. G., Camperchioli, W. P., and La, H., 1998, ''Aerodynamics of a Transitioning Turbine Stator Over a Range of Reynolds Numbers,'' ASME Paper No. 98-GT-285.
[12] Banks, B. A., and Rutledge, S. K., 1982, ''Ion Beam Sputter Deposited Diamondlike Films,'' NASA TM 82873.
[13] Dagnall, H., 1986, *Exploring Surface Texture*, 2nd ed., Rank Taylor Hobson Ltd., Leicester, England, p. 158.
[14] Kind, R. J., Serjak, P. J., and Abbott, M. W. P., 1998, ''Measurements and Prediction of the Effects of Surface Roughness on Profile Losses and Deviation in a Turbine Cascade,'' ASME J. Turbomach., **120**, pp. 20–27.
[15] Bammert, K., and Stanstede, H., 1972, ''Measurements Concerning the Influence of Surface Roughness and Profile Changes on the Performance of Gas Turbines,'' ASME J. Eng. Power, **94**, pp. 207–213.
[16] Bammert, K., and Stanstede, H., 1976, ''Influences of Manufacturing Tolerances and Surface Roughness of Blades on the Performance of Turbines,'' ASME J. Eng. Power, **98**, pp. 29–36.
[17] Boynton, J. L., Tabibzadeh, R., and Hudson, S. T., 1992, ''Investigation of Rotor Blade Roughness Effects on Turbine Performance,'' ASME J. Turbomach., **115**, pp. 614–620.
[18] Boyle, R. J., and Giel, P. W., 1995, ''Three-Dimensional Navier–Stokes Heat Transfer Predictions for Turbine Blade Rows,'' J. Propul. Power, **11**, No. 6, pp. 1179–1186.
[19] Kays, W. M., and Crawford, M. E., 1980, *Convective Heat and Mass Transfer*, 2nd ed., McGraw-Hill, New York, p. 327.
[20] Chima, R. V., 1996, ''Application of the $k-\omega$ Turbulence Model to Quasi-Three-Dimensional Turbomachinery Flows,'' J. Propul. Power, **12**, No. 6, pp. 1176–1179.
[21] Burmeister, L. C., 1983, *Convective Heat Transfer*, Wiley, New York, p. 544.
[22] Hodge, B. K., Taylor, R. P., and Coleman, H. W., 1986, ''An Investigation of Surface Roughness Effects on Adiabatic Wall Temperature,'' AIAA J., **24**, No. 9, pp. 1560–1561.
[23] Van Fossen, G. J., Simoneau, R. J., and Ching, C. Y., 1995, ''Influence of Turbulence Parameters, Reynolds Number, and Body Shape on Stagnation Region Heat Transfer,'' ASME J. Heat Transfer, **117**, pp. 597–603.
[24] Pimenta, M. M., Moffatt, R. J., and Kays, W. M., 1995, ''The Turbulent Boundary Layer: An Experimental Study of the Transport of Momentum and Heat With the Effect of Roughness,'' Rep. HMT-21, Dept. of Mechanical Engineering, Stanford Univ., CA.